AD-768 315

TECHNIQUES FOR ASSESSING CASE LINER-BOND INTEGRITY IN SOLID PROPELLANT ROCKET MOTORS

J. McKay Anderson, et al

Hercules, Incorporated

Prepared for:

Air Force Rocket Propulsion Laboratory

September 1973

FOREWORD

This report documents an 18-month Case-Liner-Bond Study, authorized by Contract F04611-72-C-0009. The major portion of the work was accomplished at Hercules Incorporated, Bacchus Works, Magna, Utah.

Preparation of this report is authorized under data item B004 of the data requirements list in the contract. Contract F04611-72-C-0009 was issued to Hercules by the Air Force Rocket Propulsion Laboratory, Director of Laboratories, Edwards, California, Air Force Systems Command, United States Air Force. The Air Force Project officers for this work were Mr. Norman D. Walker and Dr. Randy Peeters.

Propellant/case bond material for testing was cast at Thiokol, Wasatch Division. Subscale motors for the program were also manufactured at Thiokol. Thiokol support was additionally provided in the three-dimensional stress analysis of analog flap termination samples.

Major contributors to the Case-Liner-Bond Study were Terry Pavelka (Task IV), Perry Bruno (Task II, Tensile Sample Analysis), and J. McKay Anderson (Principal Investigator), all of Hercules. Thiokol support was provided principally by Elwin Dickson (3-D stress analysis) and Ned Caldwell (subscale motors).

This Technical Report has been reviewed and is approved.

R. Peeters
AFRPL Project Engineer

NOTICES

AD 768 315

REPORT DOCUMENTATION PAGE

READ INSTRUCTIONS
BEFORE COMPLETING FORM

1. REPORT NUMBER	2. GOVT ACCESSION NO.	3. RECIPIENT'S CATALOG NUMBER
AFRPL-TR-73-75		

4. TITLE (and Subtitle)	5. TYPE OF REPORT & PERIOD COVERED
Techniques for Assessing Case Liner Bond Integrity in Solid Propellant Rocket Motors	Final Report for Period 15 Dec 71 through 15 Jun 73
	6. PERFORMING ORG. REPORT NUMBER

7. AUTHOR(s)	8. CONTRACT OR GRANT NUMBER(s)
J. M. Anderson T. D. Pavelka P. S. Bruno	Contract No. F04611-72-C-0009

9. PERFORMING ORGANIZATION NAME AND ADDRESS	10. PROGRAM ELEMENT, PROJECT, TASK AREA & WORK UNIT NUMBERS
Hercules Incorporated Bacchus Works Magna, Utah 84044	Final Report

11. CONTROLLING OFFICE NAME AND ADDRESS	12. REPORT DATE
Air Force Rocket Propulsion Laboratory Director of Science and Technology Air Force Systems Command Edwards, California	September 1973
	13. NUMBER OF PAGES

14. MONITORING AGENCY NAME & ADDRESS(if different from Controlling Office)	15. SECURITY CLASS. (of this report)
N/A	Unclassified
	15a. DECLASSIFICATION/DOWNGRADING SCHEDULE

16. DISTRIBUTION STATEMENT (of this Report)

Approved for Public Release
Distribution Unlimited

17. DISTRIBUTION STATEMENT (of the abstract entered in Block 20, if different from Report)

N/A

18. SUPPLEMENTARY NOTES

19. KEY WORDS (Continue on reverse side if necessary and identify by block number)

Case Bond Strength, Propellant Grain Structural Analysis, Cylinder
Structural Parameter Study, Right-Angle Corner Integrity

20. ABSTRACT (Continue on reverse side if necessary and identify by block number)

This report documents results of an 18-month study program to develop improved methods for case bond structural analysis. The study was limited to unflawed bond systems in solid propellant rocket motors.

DD FORM 1473 EDITION OF 1 NOV 65 IS OBSOLETE

20.   ABSTRACT (Continued)

In Task I of the program, parametric stress solutions were obtained for cylindrical motor configurations with flapped and right-angle bond terminations. The parametric results indicate that the largest bond stresses occur at the terminations. However, the termination stresses for flapped configurations can be adjusted significantly through variations in flap thickness. The right-angle termination constitutes a discontinuity, and the parametric results were cast in terms of singularity theory.

In Task II of the program, improved test sample configurations were developed for the measurement of case bond tensile and shear strength. The recommended tensile sample is a round-flapped configuration and the recommended shear sample is a very short lap-shear configuration. Strength data were obtained for TP-H1123 and ANB-3066 bond systems.

Analog flap and discontinuity samples for integrity assessment at bond terminations were developed in Task III. Stress analyses of these samples indicate a good match for the case bond normal and shear stresses that occur typically in motors. Strength data were obtained for the TP-H1123 bond system.

Verification of procedures for structural integrity assessment at bond terminations were accomplished in Task IV through pressure testing of four structural test vehicles and comparing measured failure loads with predicted load levels. Correlation between test results and predictions for the flapped vehicles was within 10 percent. The vehicles with right-angle discontinuities failed within 30 percent of the predicted pressure load.

Based on results obtained from this program, techniques for the assessment of case bond integrity have been placed on a level equivalent to existing techniques for the assessment of grain integrity at the centerport. The Task I parametric study provides handbook-type procedures for estimating maximum case bond stresses in cylindrical rocket motor grains. Task II provides proven sample configurations for measuring the tensile and shear strength of case bond systems. Task III provides analog samples and associated techniques for making integrity predictions at flapped and right-angle discontinuity bond terminations.

SUMMARY

The case liner-bond study was organized into four tasks. Task I involved the calculation of case bond stress distributions in motors with cylindrical grain configurations. Emphasis was placed on the critical bond termination areas for motors with flapped ends and/or right-angle bond termination discontinuities. Task II involved the development of improved test sample configurations for measuring the tensile and shear strength of case liner-bond systems. Experimental sample evaluations were made with ANB-3066 and TP-H1123 case bond material. Task III involved the development of analog samples and associated procedures for assessing case bond integrity at flapped and right-angle discontinuity bond terminations. As such, the Task III effort interfaced directly with Tasks I, II, and IV. In Task IV, pressurization tests were conducted to failure on structural test vehicles containing flapped and right-angle bond terminations. Detailed summaries for each of the four program tasks follow.

TASK I - BONDLINE PARAMETRIC STUDIES

Case bond stress distributions were obtained numerically using the finite-element (FE) method for cylindrical motor analogs. The study involved simple cylinorical grains with free ends. The grain bonded surfaces were either flapped or terminated with a right-angle corner on the outer cylindrical diameter. The FE models were developed with highly refined grids in the vicinity of the end terminations so that variations in case bond constituents could be evaluated. The right-angle corner solutions were cast in terms of singularity theory, because this type of bond termination constitutes a discontinuity.

Stress solutions for the flapped-end configuration were completed first, and an interim report (see Appendix) was published. This interim report depicted typical bond stress distributions for thermal, pressure, and axial acceleration loading conditions. The important results obtained from the flap study are as follows:

(1) Case bond stresses for thermal shrinkage and internal pressure loading become larger as web fraction (W/b) and length-to-diameter ratio (L/D) increase. However, as L/D and W/b increase, the end termination stresses decrease relative to the centerport hoop stress and the radial bond stress at the mid-cylinder location.

(2) Case bond stress distributions are a function of the local geometry only and are relatively insensitive to changes in W/b and L/D for the loadings studied.

(3) Modest changes in flap and case bond-liner stiffness have little effect on local case-bond stress levels.

(4) Flap length is a less significant factor than flap thickness in determining stresses at the flap terminations.

(5) Case bond and propellant stresses can be predicted accurately for internal pressure loading from thermal shrinkage solutions.

(6) The case bond radial stress at flap terminations is much larger than the shear stress under axial acceleration, thermal shrinkage, and internal pressure loading.

(7) Flap termination stresses relative to the average case bond shear stress are insensitive to L/D and W/b for axial acceleration loading.

The interim report containing the flap solutions was published before detailed data became available for typical case bond liner moduli. Stress solutions in the interim report considered a minimum liner tensile modulus of one-half the propellant tensile modulus. More typical bond liners have tensile moduli as low as one-fifth the propellant tensile modulus. Additional stress solutions were therefore obtained and included in this final report. These additional solutions confirm that very soft liners have a minor impact on the radial and maximum principal stresses adjacent to the flap termination; however, the shear stress for soft liners is significantly less than for stiff liners. Also, the maximum principal strain in the propellant adjacent to the flap termination is significantly reduced for soft liners; this implies that the local propellant stresses are more hydrostatic.

Stress solutions for the right-angle corner termination considered the discontinuity to occur at the liner-propellant interface, because this appears a priori to be the weakest of all possible configurations. Use of the FE method for analysis of this configuration was validated through comparison with a singularity solution of Zak for a rigid liner situation. The singularity order (i.e., $\sigma(x) \sim x^m$, where m is the singularity order) predicted by Zak and the FE method compare within 1 percent. The shear stress adjacent to the corner for a rigid liner condition is only 53 percent of the radial stress. Right-angle corner solutions were obtained for thermal shrinkage loading only.

Discontinuity stress solutions for typical liner properties indicate a significant perturbation in the local bond stresses, relative to the rigid liner situation. The order of the local singularity for the radial stress is increased from 0.41 for a rigid liner to 0.47 for a liner one-tenth the stiffness of the propellant. The singularity order of the shear stress is increased from 0.41 to 0.62 for the same tensile modulus variation. Thus, a different singularity order is computed for the two stress components for a soft liner condition. This is a significant departure from published singularity solutions for bi-material strips wherein the singularity order is predicted to be the same for all stress components.

Stress solutions were obtained for liner thicknesses of 0.03, 0.06, and 0.12 in. These variations in liner thickness have only a small effect on the stress magnitude and singularity order adjacent to the corner. The total length of the stress perturbation caused by the flexible liner, relative to a rigid liner, is proportional to the liner thickness.

Parametric relationships were developed for the corner stress gradients considering variations in liner modulus and length-to-diameter ratio and web fraction of the cylinder. A scaling law was derived on the basis of the singularity order of 0.41 for a rigid-liner condition.

TASK II - TENSILE AND SHEAR SAMPLE DEVELOPMENT

Test samples were developed for measuring case bond strength in tensile and shear stress fields. The recommended tensile sample is round with a 0.1-inch unbonded ring between the insulator layer and end tab. The recommended shear sample is a short lap-shear sample with the insulator layer unbonded from the end tab over a 0.2-inch length

1. Sample Design/Analysis

Detailed FE stress analyses were performed on five candidate tensile sample configurations, in addition to the current ICRPG "pipe" sample. Stress analyses were also performed on three candidate shear sample configurations. These candidate samples and results of the analyses are as follows:

(a) Pipe Tensile Sample

The pipe tensile sample consists of a cylindrical propellant slug cast in a pipe section and case bonded to an end tab. The stress solution indicates three significant undesirable features of the pipe sample. A strong edge concentration is present at the pipe-propellant bond termination, approximately 0.2 inch from the bond liner-propellant interface. A significant stress concentration is also present at the outer edge of the liner-propellant bondline. Finally, the state of stress in the propellant adjacent to the liner is quite triaxial, with the radial and hoop stresses approximately 70 percent of the axial (bond normal) stress. The axial stress along the bondline is reasonably uniform.

(b) Long, Round-Flapped Tensile Sample

The long, round-flapped tensile sample is a propellant cylinder approximately 3 inch in length and 1 inch in diameter. It is case-bonded to an end tab with a circular ring of unbondedness (flap) around the periphery.

Parametric stress solutions were obtained for variations in the flap length, insulator thickness, and liner modulus. A flap length of 0.1 inch and an insulator thickness of 0.1 inch were the best choice -- liner bond systems typical of composite propellant motors. The stresses in the bond liner are quite triaxial, but the stresses in the propellant adjacent to the bondline are nearly uniaxial. The liner thus acts like a poker chip sandwiched between harder insulator and propellant materials.

(c) Round-Flapped Tensile Sample

The round-flapped tensile sample is similar to the long-round-flapped tensile sample, but has a propellant cylinder length of approximately 1 inch. The 1-inch propellant length in the round-flapped tensile sample, compared with the approximately 3-inch length in the long, round-flapped sample, has little effect on the stresses near the bondline. The bond normal stress is actually more uniform in the shorter sample. Over-all, the longer and shorter round-flapped tensile samples provide very similar bondline stress distributions.

(d) Back-to-Back Tensile Sample

The back-to-back tensile sample is comprised of two round-flapped tensile samples with their insulator layers fully bonded together (i.e., no flap). The bondline stress distribution for this sample is very uniform if the adhesive between the insulator layers has the same modulus as the insulator. However, a high modulus adhesive, like most epoxy resins, produces a mild edge concentration at the crucial liner-propellant bondline.

(e) Round-Filleted Tensile Sample

The round-filleted tensile sample is similar to the round-flapped tensile sample, except that the propellant is flared out (using a fillet) near the bondline to eliminate the edge concentration. Two fillet radii were studied, 0.25 and 0.375 inch. The maximum bondline stresses for both fillet radii are significantly less than the maximum propellant stresses. Thus, if the case bond is strong, the sample will fail in the propellant away from the bondline. This type of sample is considered unsatisfactory.

(f)   Analog Flap Termination Sample Pulled in Tension

This sample is rectangular, a length of 1.5 inches and
a height of 1.3 inches; with 0.3-inch long unbonded
regions occurring between the insulator and end tabs.
A three-dimensional stress analysis was performed on
0.5 and 0.25-inch wide samples. The 0.5-inch sample
provides the best stress distribution for typical liner
stiffnesses. The liner acts like a poker chip and
largely suppresses the stress concentration along the
unflapped edges of the sample; however, a mild edge
concentration exists.

(g)   Torsional Shear (Cylindrical Samples)

The basic torsion sample is cylindrical, with a 2-inch
diameter. The stress solutions indicate it is crucial
that the insulator and liner layers be cut flush with
the propellant cylinder. When the liner/insulator
extend beyond the propellant, a singularity occurs at
the outer edge of the propellant-liner bondline. This
singularity (and implied stress concentration) occurs
only when the liner layer is flexible. When the liner
and insulator are flush with the propellant cylinder,
the bondline stress distribution is consistent with
basic torsional stress solutions for cylinders, inde-
pendent of the moduli of the various layers. Partial
unbonding between the insulator and end tab has little
effect on the liner-propellant bondline stresses.
Thus, "flaps" are ineffective in reducing edge concen-
trations in torsion specimens. Torsional shear samples
with thick walls (in the limit, a solid cylinder) are
undesirable for strength testing of highly yielding
materials, such as propellant.

(h)   Picture-Frame Shear

The linear stress distribution for a material sheet
bonded to rigid links, pinned together at the corners
(i.e., picture-frame shear) is one of pure shear.
However, when a case bond system (with its attendant
multiple layers) is included in the sheet, the stress
distribution deviates significantly from pure shear.
Large stress concentrations occur at the bondline and
terminations. This type of sample is not considered
satisfactory for case bond shear testing.

v

(i) Lap Shear

A strength-of-materials solution was derived for a rectangular sheet bonded on the top and bottom faces to rigid end tabs and subjected to (lap) shear. This solution indicates that bondline normal stresses near the bond terminations are proportional to the length-to-height (aspect) ratio of the sheet. Normal stresses are small when the aspect ratio is large. FE stress solutions were obtained for lap-shear bond sample configurations of different aspect ratios, flap lengths, and liner moduli. These stress solutions confirm the strength of materials solution relative to aspect ratio. Short flaps (i.e., unbonded regions between the end tab and insulator) are effective in suppressing the end concentrations, such that the maximum bondline stress occurs in the shear direction in the sample gage length. Three candidate lap shear configurations evolved from the FE analyses. The propellant layer is only 0.1-inch high in all three configurations, and differ only in flap length and the technique used to bond the propellant to the end tab opposite the case bond side.

2. Manufacturing and Testing Techniques

Procedures were developed to machine the recommended case bond tensile and shear samples from castings with the case bond system on one face. The lap shear samples were cut with a knife from sheets with the propellant milled to a 0.1-inch thickness. The round-flapped tensile samples were machined on a lathe from rectangular blocks cut from the large 9 x 9 x 9 inch castings with a band saw. A special lathe tool was used to cut through the insulator and liner layers and provide a smooth transition into the propellant cylinder. Special dies were used to stamp Teflon rings for use in constructing the 0.1-inch unbonded ring between the insulator and end tab. A ten-shear fixture was used to test the lap-shear samples as single samples without introducing moments into the testing machine linkages. The case bond tensile samples were tested similarly to regular propellant tensile samples.

3. Test Results

Testing was performed on two propellant/case bond systems; ANB-3066 (a CTPB composite) and TP-H1123 (a PBAN composite). The ANB-3066 material was used only for preliminary testing, and the bulk of the testing was performed on TP-H1123 material.

Round-flapped and back-to-back tensile samples and short lap shear samples were tested with the ANB-3066 material (propellant-only samples were also tested). The round-flapped tensile sample and the short lap shear sample worked well with the ANB-3066 bond system. The back-to-back tensile sample was not successful because of premature failure in the low modulus adhesive used to bond the insulator layers together. The test

results indicate that the ANB-3066 bond tensile strength is approximately 80 percent of the propellant tensile strength over a constant displacement rate range of 0.02 to 200 in./min. However, the ANB-3066 bond shear strength is approximately 15 percent greater than the propellant tensile strength under zero superimposed pressure.

Testing on TP-H1123 material involved round-flapped tensile, analog flap samples pulled in tension, short lap-shear samples, and torsional shear samples (propellant only samples were also tested). All material came from five 9-inch cube castings case bonded to NBR rubber sheets on one face. The round-flapped tensile sample and the two shear samples performed well with the TP-H1123 bond system. The analog flap when pulled in tension performed well, except for testing at high rates under superimposed pressure. Stress concentrations at the sample edges apparently caused early failure under this condition. A similar effect also occurred with round-flapped tensile samples fully bonded between the insulator and end tab. Thus, the suppression of edge failures is critical to successful strength testing of the TP-H1123 bond system. The test data indicate that the case bond tensile strength for TP-H1123 material is superior to the propellant tensile strength, particularly at high loading rates. However, the case bond shear strength is only 70 percent of the propellant tensile strength under zero superimposed pressure. At high rate, the case bond shear strength is not enhanced by superimposed pressure to the same extent as is the case bond tensile strength. (The propellant shear strength enhancement is also small.)

4. Sample Selection

The round-flapped tensile sample was selected as the primary configuration for measuring tensile strength of case liner-bond systems, and the short lap-shear sample was selected as the primary configuration for measuring bond shear strength. The selection was made on the basis of superior bond stress distributions, good test performance, and ease of manufacture. Some options were left open to help tailor the samples to the users specific bond systems. These options primarily involve end-tab bonding procedures.

TASK III - BOND TERMINATION INTEGRITY

Analog samples were developed for use in assessment of case bond integrity at flapped and right-angle corner bond terminations. These analog samples are approximately 1.5-inches long, 1.0 inch high, and 0.5-inch wide. The samples are fully machineable and are tested with standard high-rate testing machines (Instron). Special ten-shear pull fixtures are required for sample loading.

The sample for assessing bond integrity at flap terminations is termed the "analog flap termination sample". It has 0.3-inch long regions (flaps) where the insulator is not bonded to the end tabs. Both 2-D (plane stress) and 3-D FE stress analyses were performed on this sample. The 3-D analysis

was accomplished with the Thiokol 3-D program. The 2-D analysis was accomplished with the Hercules quadrilateral-element program. Testing of analog flap termination samples was performed on TP-H1123 case bond material.

The sample for assessing bond integrity at right-angle (discontinuity) bond terminations is termed the "analog discontinuity sample". It has right-angle corners at the liner-propellant interface. Stress analysis of this sample was performed using 2-D (plane stress) methods only. Testing of analog discontinuity samples was performed on TP-H1123 case bond material.

Three-dimensional stress analysis of the analog flap termination sample indicates that a sample width of 0.50 is better than a width of 0.25 inch. Stronger (undesirable) edge concentrations are predicted for the 0.25-width sample. The stress gradient through the sample thickness indicates a significant influence of the bond liner. The maximum bondline stresses are predicted to occur along the width (thickness) midplane of the sample; the normal stresses along this line are computed to be 15 percent larger than the average stress through the sample thickness. The stress concentrations near the sample edges were not well established by the 3-D analysis; however, their presence is definitely indicated.

Two-dimensional stress analyses of the analog flap termination samples were performed to investigate alternate sample configurations, liner moduli, and testing conditions. Excellent correlation was obtained between the 2-D and 3-D stress analyses when the 15 percent thickness factor was applied to the 2-D normal stress values. The 2-D stress solutions indicate that the bond liner modulus has a relatively small effect on the bond stresses for a unit force. Stress distributions for sample pull angles of 0 and 90 degrees are substantially different. A pull angle of 15-30 degrees provides a normal/shear bond stress distribution most like the cylindrical motor model of Task I.

Approximately 60 analog flap termination samples were tested. The samples performed much like the analysis predicted. However, the case bond is stronger under combined normal and shear stress distributions than predicted by a maximum principal stress failure criterion. At high loading rates and under superimposed pressure, the analog samples appear to fail prematurely due to edge effects, similar to some of the case bond tensile samples of Task II. A structural analysis procedure was outlined for the use of the analog flap termination samples in bond integrity assessments. The recommended procedure compensates for sample deficiencies which cause premature edge failures.

Two-dimensional stress analyses of the analog discontinuity samples show that they possess stress gradients of a singular nature near the bond terminations like the cylinders of Task I. Pull angle has only a small effect on the stress distribution near the discontinuity. A complete match for the cylindrical motor model could not be obtained for any pull angle. Singularity exponents for the analog sample were slightly different than for the motor. However, the relative intensity of the normal and shear bondline stresses is very similar for the sample and cylindrical motor

model. Procedures were developed for computing allowable stress intensity factors from tests performed on analog discontinuity samples.

Approximately 20 analog discontinuity samples were tested; testing was performed only at the shear pull angle. Considerable data scatter occurred in the testing, precise alignment of the test fixtures was necessary to obtain acceptable results. Sample failure does not occur at the time of maximum load during testing. Visual observation of low-rate tests indicates that failure (unbonding at the corner) initiates at approximately 75 percent of the maximum load. Rate-dependence of the failure load is similar to that for the propellant tensile strength. However, superimposed pressure has only a small effect on the load at failure.

A detailed procedure was outlined for structural analysis of motors with right-angle bond-termination discontinuities. The procedure is similar to that for a routine, nonsingular analysis but uses stress intensity factors instead of stresses.

TASK IV - SUBSCALE MOTOR STUDIES

FE stress analyses were conducted for several geometrical variations of end-pressurized cylinder (EPC) analog motors to obtain a design having a stress distribution in the forward flap termination region similar to that which exists in the Task I cylinder. Comparisons were based upon the ratios of normal stresses to shear stresses along the bondline.

Initial analyses showed that the value of shear stress relative to normal stress calculated for the cylinder cannot be obtained in the basic EPC configuration. This is a result of the inherently large shear stress associated with axial loading in the EPC. Further comparison of the cylinder stress distribution with forward bond termination stresses in the first stage (FS) Poseidon and second stage (SS) Polaris motors indicated that the low relative shear stress present in the cylinder is not typical, at least not for motors containing bond terminations in curved dome regions. Therefore, the range of stress distributions capable of being produced in the EPC are characteristic of those present in typical solid propellant rocket motors.

A discontinuity EPC configuration was selected which could be manufactured using the same hardware and procedures as the flap-termination EPC. The distribution of stress (stress singularity exponents adjacent to the right-angle discontinuity) did not fully duplicate that for the Task I cylinder; the EPC has less shear than the cylinder.

Results from high-rate pressurization testing of the EPC's were compared to structural integirty predictions based upon analog sample test data. Maximum deviatoric stress was selected as the failure criterion for failure predictions in the flap termination geometry. The stress state at the flap termination is largely biaxial (neglecting superimposed pressure effects), and deviatoric stress includes the effect of the intermediate principal (hoop) stress. The effect of pressure upon the case bond strength, as

determined from propellant uniaxial tensile samples tested under super-
imposed pressure, was accounted for by increasing the allowable maximum
deviatoric stress proportionally as the uniaxial maximum principal stress
capability increased with pressure. The allowable deviatoric stress as a
function of the time to failure was obtained from flap termination analog
samples tested at a zero angle of pull. The analog sample and EPC were
both analyzed by a linear elastic procedure. However, the actual non-
linear effects should be similar for both specimens and were neglected in
the comparison of predicted and allowable deviatoric stress. The viscoe-
lastic effects were considered in a quasi-elastic manner. The deviatoric
stress failure criterion, in conjunction with analog sample failure data,
predicted failures in the flap termination EPC's with a maximum error of
less than 10 percent.

A similar procedure was used in the failure analysis of the right-angle
discontinuity configuration. Analog samples served to provide predicted
failure allowables for the EPC's. A singularity theory approach based upon
maximum effective principal stress ($\sigma_1 + P$) gradients was used in the
discontinuity failure predictions. This approach was selected because the
two modes of failure for the analog sample and EPC are failure due to axial
shear normal to the discontinuity and failure due to tensile loads normal
to the bondline. Maximum principal stress acts in the same plane as the
two failure loadings. Therefore, maximum principal stress better represents
failure, as a vector combination of the two loadings, than does each loading
independently when the ratios of normal stress to shear stress loadings
are not identical in the analog sample and EPC.

The critical stress intensity factor (based upon maximum principal
stress) as a function of time to failure was determined from discontinuity
analog samples tested at various rates at the appropriate pull angle
(zero degrees). Corresponding stress intensity factors were obtained from
the FE stress solution for the EPC and plotted as a function of time based
upon the pressure transients which occurred during high-rate pressurization.
Comparison with the pressure-adjusted critical stress intensity factor curve
indicated that the discontinuity EPC's displayed a structural integrity
capability approximately 30 percent in excess of that predicted.

This error has probably contributed largely to the difference in
"distinctness" of the right angle corner discontinuities in the analog
samples and EPC's. The junctions in the EPC's contained small fillets
which occurred as a result of propellant casting, while the analog samples
contained a more critical geometry obtained by "knife-cutting". Therefore,
the singularity approach may be valid if predictions were based on precise
models of the singularity geometry. Also, since singularity exponents were
shown to vary at a different rate in axisymmetric geometries than in plane
geometries as the liner to propellant modulus ratio is varied, it is im-
portant to consider the correct ratio of their effective elastic moduli,
which corresponds to the actual time to failure.

Overall, both types of analog samples appeared to work well. The less satisfactory performance of the analog discontinuity sample was expected. This type of bond termination is of much less importance than the flapped configuration (at least for zero-burn grain configurations). The conclusion is that engineering procedures now exist, as a result of this work, for case bond integrity evaluation at end terminations involving flaps and/or right-angle discontinuities.

TABLE OF CONTENTS

LIST OF FIGURES

LIST OF FIGURES (Cont)

LIST OF FIGURES (Cont)

LIST OF FIGURES (Cont)

LIST OF FIGURES (Cont)

LIST OF FIGURES (Cont)

LIST OF FIGURES (Cont)

LIST OF FIGURES (Cont)

LIST OF FIGURES (Cont)

LIST OF FIGURES (Cont)

LIST OF FIGURES (Cont)

LIST OF FIGURES (Cont)

LIST OF FIGURES (Cont)

LIST OF TABLES

INTRODUCTION

Propellant grain survivability depends upon the structural integrity of the grain and all bonded interfaces. Although past emphasis has been placed on developing analysis methods applicable to the propellant grain, probably more structural failures of motors occur at case bonds. Only a relatively small effort has been applied to the development of case bond structural analysis methods, and the general ability in the solid propellant industry for case bond structural analysis is quite poor when compared with capabilities related to the propellant. The industry reasons that acceptable structural analysis techniques must first be developed for the propellant before meaningful bonded interface studies can be accomplished. This position has logic, but case bond problems are too important in motor design to continue waiting the development of fully acceptable propellant structural analysis techniques. Many methods are now under consideration for grain structural analysis which can be readily adapted to the case bond analysis problem.

Case bonds impose challenges to the structural analyst which are somewhat greater than those imposed by the propellant grain proper. First, geometrical irregularities, such as right angle corners at bond terminations, are not tractable using classical structural analysis techniques. Second, detailed bond stress analyses often require difficult modeling of multi-layered structures composed of case, insulator, flap, barrier coat, liner, and propellant. Third, development of sample configurations for strength tests which provide pure states of stress, such as uniaxial tension or shear is virtually impossible. Fourth, grain processing and aging often produce propellant property gradients in the vicinity of the bond which are either unknown or are difficult to structurally model. Flaw propagation theories are common to both propellant and case bonds, but the case bond is more difficult to analyze because of the multi-layer materials situation.

The solid propellant industry is in a much improved position to develop workable case bond structural analysis methods than was possible when major analysis development activities were in progress in the early and mid 1960's. FE computer programs for grain stress analysis developed and refined over the past 8 years allow the detailed geometric and multi-layer material modeling at critical bond termination regions. Fracture mechanics theories recently adapted to propellant structural analysis offer great promise for application to the bond termination corner problem and for flaw/separation propagation studies. Bond test sample configurations which provide approximations of pure stress states and stress/strain distributions near critical bond termination regions of motors can be readily explored with the FE method.

The need for a better case bond integrity assessment posture in the solid propellant industry has become increasingly evident in recent motor development and aging programs. In 1971, the AFRPL took positive steps to satisfy this need through the award of separate case bond integrity studies to Hercules Incorporated and United Technology Center (UTC). The Hercules study was directed towards bond integrity assessment for unflawed bond

configurations, with a strong experimental emphasis; whereas, the UTC study placed major emphasis on the development of techniques for analysis of adhesive flaw propagation. However, both studies considered the right-angle corner singularity at bond terminations.

Mechanical properties for the individual components of the case bond system are difficult to obtain. Properties which are routinely measured for materials, such as the liner, often do not cover a broad rate/time/temperature range. Further, the applicability of data obtained using samples of bond layers cast and cured by themselves is uncertain. For example, epoxy resins into which base grains are embedded in double-base bond systems undergo a reduction in modulus by one order of magnitude during subsequent grain processing. Changes in case bond liners for composite propellant systems during grain processing are not expected to be this large. However, the liner is usually under-cured at the time of grain casting, and migration of liner ingredients into the propellant is probable. During the course of the Hercules case liner-bond study, considerable uncertainty prevailed as to typical properties of the case bond liner. Stress solutions performed in the various tasks used slightly different propellant/case bond moduli, depending upon the current knowledge and the need for consistency between solutions.

The Hercules case bond integrity program was organized into four tasks: Task I - Bondline Parametric Studies, Task II - Tensile and Shear Sample Development, Task III - Bond Termination Integrity, and Task IV - Subscale Motor Studies. Work elements in the four tasks were designed to tie the total effort together and provide a proven approach to integrity assessment of unflawed case liner-bond systems in solid propellant rocket motors.

In Task I, parametric stress analyses were performed on cylindrical motor analogs to establish typical case bond/propellant stress distributions in rocket motors. These stress distributions were used as the basis for the development of analog bond termination samples in Task III and subscale motor analogs in Task IV. Case bond strength data obtained in Task II is fundamental to the establishment of failure criteria for use in Tasks III and IV. The parametric stress solutions for cylindrical motor analogs in Task I helps establish the relative requirements on bond strength in tension and shear stress fields.

An interim report on studies completed under Task I of the Hercules program was published in May 1972. This report[1] contains parametric stress solutions for cylinders with flapped bond terminations. Since this interim report was published, parametric stress solutions were obtained for cylinders with right-angle bond termination discontinuities. Also, a minor extension was made to the flap termination study to consider a broader range of liner

---

[1] Anderson, J. M., "Case Bond Stress Calculations for Flapped Cylindrical Analogs of Solid Propellant Rocket Motors", AFRPL-TR-72-55, (May 1972).

stiffnesses. The additional parametric studies accomplished since May 1972 are included in this final report. Little repetition of the results in the interim report is contained herein.

A rigorous structural analysis of a solid propellant rocket motor requires the consideration of many complex features of propellant/case bond mechanical behavior. Among these complex features are: 1) viscoelastic behavior, 2) cumulative damage effects, 3) nonlinear behavior, 4) age dependence, and 5) state-of-stress dependence. Of central focus in the Hercules study is the state-of-stress dependence (i.e., failure criteria). This feature seems to best distinguish the case bond from the propellant proper in most motor integrity assessments.

Viscoelasticity must be considered in case bond integrity analysis, but viscoelasticity enters the case bond analysis in a manner very similar to the propellant analysis. The reader should be well grounded in viscoelastic propellant analysis because little emphasis is placed on viscoelastic aspects in this report. Sample loading procedures in the experimental portions of Tasks II and III and the subscale motors in Task IV were purposely made similar to minimize the use of complicated viscoelastic relationships. Further, the subscale motors were subjected to pressure loading, as opposed to thermal loading, because of the lesser demands for viscoelastic theory in this type of loading program.

Cumulative damage effects are almost totally ignored herein. However, the case bond integrity prediction techniques developed are such that cumulative damage criteria commonly used for propellants should apply. One such criteria is the stress cumulative damage theory of Bills[2].

Nonlinear aspects of propellant and case bond structural response are very important. However, the nonlinear problem was only partially addressed herein. Case bond stresses are almost totally determined by the propellant response, either linear or nonlinear. Case bond stresses occur only because the grain deforms differently from the insulator or case. The most critical case bond stresses in rocket motors usually occur during thermal loading and grain ignition. Ignition pressurization appears to provide the most linear propellant structural response because of the suppression of dewetting by superimposed pressure, the constant grain temperature (except in the combustion zone), and the relatively simple time-dependence of the applied loads. Therefore, pressure loading was selected for the subscale motor test program in Task IV.

Attempts were made to minimize propellant/case bond aging in the testing program. The ANB-3066 propellant/bond system (Minuteman III Stage III) was initially chosen for the experimental program. However, this material indicated significant post curing, plasticizer loss (in small samples), and oxidation problems. Therefore, a change was made to TP-H1123

---

[2] Bills, K. R., Jr., et al, "Solid Propellant Cumulative Damage Program," Final Report, AFRPL-TR-68-131, (October 1968).

propellant/case bond material (C3 Poseidon Stage I) approximately 9 months into the program. Aging and handling effects are minimal with this material. Some minor benefits were derived from the fact that two case bond systems were tested in the subject program. The relatively large difference in the liner formulations provided a good test for the candidate tensile and shear sample configurations developed in Task II. However, only a minimum of testing was accomplished with the ANB-3066 material, and handling/aging changes in the test specimens made it unreasonable to quote absolute values for measured propellant/case bond strengths.

The remaining portions of this final report are organized according to task. The write-ups for each of the four tasks are largely self-contained. Objectives, introductions, backgrounds, analyses, and experimental sections are provided under each task, as appropriate. A relatively close relationship is present among Tasks I, III, and IV. The reader should cover the material in these sections in that order to obtain the proper background material. The report concludes with a section providing conclusions and recommendations.

SECTION I

TASK I - BONDLINE PARAMETRIC STUDIES

A. OBJECTIVE

The objective of this task is to obtain case bond stress and strain distributions typical of unflawed solid propellant rocket motors. Parametric relationships are to be developed for use in the design of grains with flap and/or right-angle end terminations.

B. INTRODUCTION

This task is intended to provide case bond stress distributions which are typical of unflawed solid propellant rocket motors. As such, this task is basic to the total case bond study program. It provides the standard of comparison for use in the design of analog bond termination samples in Task III and subscale motors in Task IV. The parametric data generated in this task will permit bond termination design and analysis (considering flaps and right-angle corners) to be elevated to a level comparable to that of the grain centerport.

Stress analyses performed on the flap and right-angle end terminations comprise two distinct units of work. Models for both end configurations are cylinders. However, the case bond stress distributions adjacent to the two end terminations are fundamentally different, and results must be cast in different forms. Because the analysis results for the flapped configuration have already been published in detail as an interim report under this program[1] (see Appendix), only a modest treatment of this configuration is provided in this section. Additional results are presented only for more extreme variations in bond liner stiffness. Stress analysis results for the right-angle corner configuration are presented in detail.

The remainder of the Task I section of this final report is organized to first discuss the additional results for the flapped end configuration. A short background is given and then a discussion of results for variations in liner-flap-insulator stiffness. Next is an extensive presentation of the stress solutions for the right-angle end termination. The writeup for the right-angle configuration first provides background material. Then, a perspective of the right-angle corner problem is given and its relationship to fracture mechanics. This is followed by a paragraph discussing the application of the FE method to corner singularities. A presentation of results is then provided for cylindrical motor analogs containing flexible bond liners.

C. FLAPPED END TERMINATION

    1. Background

        Except for the interim report[1] previously published under this
program, only limited information has been published which depicts typical
case bond stress distributions in rocket motors. Experimental studies us ng
photoelasticity have been made to evaluate stress distributions at bond
terminations[3]. However, these studies did not consider case-bond detail
and were restricted to configurations involving fillets and grooves in the
propellant grain adjacent to the bond termination. Published numerical
stress analyses have considered the case bond in varying degrees. Reference
4 contains case bond stress distributions in cylinders with flat ends; no
attempt was made to deal with the actual termination geometry or bond
constituents. However, in later studies[5] some consideration was given to
the case bond liner and bond termination configurations.

        The reader should be familiar with the previously published
interim report because little discussion will be provided with respect to
method of analysis and modeling details. The basic cylinder configuration
analyzed is shown in Figure 1-1. The flap termination studies were based
on an FE model containing insulator, flap, liner, and propellant layers.
Thicknesses and moduli representative of rocket motors were selected for
study. The basic cylinder diameter was chosen to be 32.0 inches which is
intermediate to larger strategic and smaller tactical motors.

        The interim report showed that the stress distribution adjacent
to the flap termination is insensitive to the length-to-diameter ratio
or web fraction of the cylinder. The conclusion was that the largest bond
stresses are in the radial direction, even for axial acceleration loading.
The bond stresses adjacent to the flap termination are strongly influenced
by the total flap-liner thickness but are not significantly affected by
the stiffness of the flap or liner moduli (at least, for liner moduli with
minimum values of one-half the propellant stiffness). The need to consider
softer bond liners more representative of motor situations prompted the
additional work contained in this section for the flapped end configuration.
Results are presented only for thermal shrinkage loading. However, the

[3]Robinson, C. N. et al, "Effect of Grain End Shape on Stress Concentrations
    at the Case-Propellant Interface", Technical Report AFRPL-TR-69-124-Vol I,
    Contract F04611-68-C-0015, Atlantic Research Corp., (May 1969).

[4]Messner, A. M., and D. Schiessmann, "Parameter Calculation of Simple Pro-
    pellant Grains for Temperature Cycling, Pressurization, and Acceleration",
    Appendix D, Study of Mechanical Properties of Solid Propellants, Aerojet-
    General Report No. 0411-10F, (March 1962), and Lockheed Propulsion Com-
    pany Structures Manual, (December 1969).

[5]Shearly, R. N., and A. M. Messner, "Stresses in Propellant Grain Bond
    Systems", Bulletin of the 3rd Meeting ICRPG Working Group on Mechanical
    Behavior, Vol I, (October 1964).

thermal-pressure loading equivalence described in Reference 1 indicates that the thermal loading behavior is directly applicable to the pressure loading situation. Based on the similarity of the flap area stress distributions for axial acceleration loading and thermal loading, the thermal loading effects for soft bond liners should relate to axial acceleration loading as well.

2. Liner-Flap-Insulator Modulus Effects

Reference 1 (page 7) contains a discussion of liner-flap-insulator modulus variations on the stresses adjacent to the flap termination. This paragraph is basically a revision of parts of the referenced discussion. Figures 1-2 through 1-4 provide the maximum principal stress, τ_{rz} shear stress, and maximum principal strain in the propellant 0.01 inch inboard of the bond liner, adjacent to the flap termination.

The "basic" material property set considered tensile moduli of the insulator, flap, liner, and propellant of 1000, 1000, 200, and 200 psi, respectively. The bulk modulus of all materials was kept at 333,000 psi for all variations in the tensile modulus. The stiff flap solution depicted in Figures 1-2 through 1-4 considered the basic material property set. The first variation from the basic set involved softening of the flap material from E_f = 1000 to 200 psi, thus making it the same as propellant. Overall effects of this change are very small. Radial and maximum principal stresses show almost no change from the stiffer flap solution. The shear stress has the largest change, with an increase in the positive peak of approximately 6.3 percent, but no appreciable change in the larger and more meaningful negative peak. The largest effects were in the axial stress (not shown) and maximum principal strain. The changes are summarized in Figure 1-5 (the shear values are for the negative peak).

The next variation in material properties involved a decrease in the tensile modulus of the liner, reducing it from 200 to 100 psi. For this solution, the tensile modulus of the flap was kept at 200 psi, as opposed to the basic value of 1000 psi. Propellant stresses and strains next to the liner were influenced little by this decrease in liner modulus. Another solution was then obtained for a decrease in the liner modulus to 200 psi, i.e., one-tenth of the propellant modulus. However, the flap modulus for this solution was changed back to the basic value of 1000 psi. These changes still had little effect on the maximum principal stress or radial stress (not shown), but significantly influenced the shear stress and the maximum principal strain. The extra-soft liner flattens out the shear stress gradient and makes the stress state more hydrostatic (i.e., a large decrease in maximum principal strain with little change in the maximum principal stress). The significance of this change in stress-strain state is somewhat problematical. If the propellant/case bond failure criterion is based on deviatoric or maximum shear/equivalent stress parameters, then softening of the liner ought to be advantageous (as long as it does not fail cohesively). However, if the failure criterion is based on the magnitude of the principal stress, then softening of the liner will have little effect. The effects of the above liner modulus variations are summarized

3

in Figure 1-6. The solution for the 100 psi liner modulus was adjusted, on the basis of Figure 1-5, to a flap modulus of 1000 psi. Because this adjusted solution fits so well with the overall trend expressed in Figure 1-6, apparently little interaction of the flap and liner modulus variables is occurring. The two variables can thus be considered separately.

The final variation in material properties considered the insulator to have the same tensile modulus as the propellant, liner, and flap (E = 200 psi). As indicated in Figures 1-2 through 1-4, the soft insulator provided one of the largest overall decreases in stresses and strains. The decrease was a uniform 11.0 percent in all stress components, as compared with the soft-flap solution. Because the same decrease was evident in all of the stress components, the state of stress was not affected by softening the insulator. Apparently, a soft insulator simply offers less restraint to the grain, allowing the grain cylinder to pull in more on the ends and thus reducing the stress level. The effect of the insulator modulus on the key stress-strain parameters is summarized in Figure 1-7 for $E_L = E_f = 200$ psi. Little interaction is expected between the insulator, flap, and liner modulus variations, and thus softening of the insulator should cause the same percentage change in the bond stresses, independent of the liner or flap stiffness.

D. RIGHT-ANGLE CORNER STUDY

1. Background

Right-angle bond terminations occur frequently in solid propellant grains, and this is a structurally undesirable condiction. Flaps, grooves, and fillets are used to eliminate the occurrence of any right-angle configuration. However, at advanced burn times the right-angle corner configuration may occur, at least as a limit condition, even when flaps, grooves, and fillets are used in the motor design. Thus, development of rigorous procedures for structural evaluation of right-angle corners is important.

Original work relating to stress distributions at corners was accomplished by Williams[6]. He showed that angular corners of clamped-free plates in extension produced singular conditions when the included angle was greater than 63°. Zak[7] extended the work of Williams to include corner conditions at the end terminations of rigidly-bonded cylinders and showed that the cylinder solution reduced to a singularity criterion similar to that for clamped-free plates under conditions of plane strain. The

[6]Williams, M.L., "Stress Singularities Resulting From Various Boundary Conditions in Angular Corners of Plates in Extension," J. Appl. Mech., Vol 19, Transactions of the ASME, Vol 74, p. 26 (1952).

[7]Zak, A. R., "Stresses in the Vicinity of Boundary Discontinuities in Bodies of Revolution", J. Appl. Mech., Vol 31, No. 1, p. 150, (March 1964).

order of the singularity was shown to vary with Poisson's ratio (with higher Poisson's ratios providing the higher singularity orders) and the wedge angle. In a recent paper[8], Zak computed the stress distributions in the region further removed from a right-angle corner by using more terms in the solution series expansion.

The stress distribution in the vicinity of a crack along a bi-material interface was studied by Williams[9]. The stress was shown to vary as a damped trigonometric function of the form $\sigma(r) \sim r^{-m} \cos(\lambda \log r)$. The strength of the singularity, m, was shown to be a function of shear modulus ratio for the two component materials. A crack emanating from a harder material to the interface with a softer material was shown to produce the strongest singularity, with a maximum value of 1.0 for m. A further conclusion was that the crack would most likely propagate along the material interface and not into the softer material.

More recent work relative to singularities at the bi-material interfaces has been accomplished by Hein and Erdogan[10]. Some of their results are reproduced in Figure 1-8a which shows that a right-angle corner produces oscillatory behavior (nonzero value for imaginary portion of of eigenvalue, p) only when the tensile modulus of the foundation material, E_2, is less than 0.1 times the modulus of the adjoining material. The singularity exponent, $m = P_{real} + 2$, varies only slightly from 0.5 over the typical propellant/liner tensile modulus range of $1 < E_1/E_2 > 10$. For the case of a crack parallel to the material interface, Hein and Erdogan calculated a singularity exponent of 0.5, independent of the modulus ratio, as shown in Figure 1-8b. Nonoscillatory behavior occurs only for equal values of the tensile moduli of the two adjacent materials.

2. The Right-Angle Corner Problem

Right-angle corners can be potentially viewed as limit cases of separated bonds with a zero length of separation. However, this viewpoint is not reasonable for cracks in a homogeneous stress field because the limit case no longer constitutes a singularity, and a minimum crack length (greater than the "inherent flaw size") must be present before fracture mechanics theory is applicable. Because the limit case for a bond separation emanating from a right-angle corner is itself a singularity, fracture mechanics theory bears further consideration in this regard.

---

[8] Zak, A. R., "Elastic Analysis of Cylindrical Configurations with Stress Singularities", J. Appl. Mech., Vol 39, No. 2, p. 501, (June 1972).

[9] Williams, M. L., "The Stresses Around a Fault or Crack in Dissimilar Media," Bulletin of the Seismological Society of America, Vol 49, p. 199, (April 1959).

[10] Hein, V. L., and F. Erdogan, "Stress Singularities in a Two-Material Wedge", International Journal of Fracture Mechanics, Vol 7, No. 3, (September 1971).

The basic assumption of (elastic) fracture mechanics theory is that a flaw will propagate under load whenever the rate of strain energy released through an increase in the flaw length is greater than the rate of surface energy expended; i.e., $\frac{\partial U}{\partial A} > \gamma_c$. The strain energy is a cubic function and the surface area is a squared function of the characteristic body size. Therefore, fracture mechanics theory implies that the applied (area distributed) load for which a flaw will propagate in a scaled (including the flaw length) larger body, $B' = \alpha B$, is inversely proportional to the square root of the scale factor, α; i.e., $(P_c)_{\text{Large Body}} = \frac{1}{\sqrt{\alpha}} (P_c)_{\text{Small Body}}$. Flaw propagation can be approached in terms of balance or stress intensity factor relationships; the two approaches are mathematically equivalent, as shown by Irwin[11], and further discussed in Reference 12. The stress intensity factor approach to flaw analysis provides a close parallel with the analysis of singularities not of the flaw type, such as right-angle corners.

The effect of scaling on the stress distribution adjacent to a singularity, such as a right-angle corner at a propellant-liner junction is outlined in Figure 1-9. It is shown that the stress intensity factor for a given load distribution acting on two scaled bodies is proportional to the scale factor "α" raised to the mth power, where m is the order of the singularity. Based on fracture mechanics theory, bodies are expected to undergo flaw propagation whenever the stress intensity factor reaches a certain critical value. A scaled larger body is expected to fail (propagate the "flaw") at an applied (distributed) load level equal to α^{-m} times that at which the smaller body failed.

The work of Hein and Erdogan showed a distinct difference in the singularity order for a right-angle bond termination and a separated bond (See Figures 1-8a and 1-8b). Further, the singularity order for the right-angle corner is greatly influenced by the bi-material modulus ratio; whereas, it is independent of this modulus ratio for the separated bond configuration. In view of these results, approaching the right-angle bond problem as a limit case to the separated bond problem would be a mistake. Therefore, in the subject study, right-angle corners are considered as singularity problems separate from the energy balance considerations of fracture mechanics.

[11] Irwin, G. R., "A Critical Energy Rate Analysis of Fracture Strength," Welding Journal (Research Supplement), (1965).

[12] "Fracture Toughness Testing and Its Applications", ASTM STP 381, (1965).

3. Application of the Finite-Element Method to Corner Singularities

The corner configuration shown in Figure 1-10 was chosen for study in the subject work, primarily because it is difficult to "design out" for advanced burn geometries of solid propellant grains, and because it appears a priori to be the weakest of the various possible termination configurations. Thus, it should provide the most conservative prediction for integrity of grain and terminations.

The FE method is the current best choice of the various analysis tools for study of right-angle bond terminations of the type shown in Figure 1-10, when it is considered that such geometrical features as bond liner thickness may be important to the solution. Numerous studies have shown the FE method to provide accurate propagation solutions for bodies containing flaws. The most accurate use of the FE method has proved to be in terms of global energy changes considering finite (but small) changes in flaw length[13]. Procedures involving local energy changes, stress gradients, and crack displacements provide less accurate results.

Of primary concern in the current study is an assessment of the local magnitudes of the various discontinuity stresses; in particular, the normal and shear stresses adjacent to the corner. To make this assessment, the most logical approach would be to develop a FE model with numerous small elements adjacent to the corner and simply plot the stresses in the local vicinity to derive the appropriate gradient parameters. However, this is among the less accurate approaches to crack studies, and care must be taken to ensure solution adequacy.

The basic cylinder configuration used for analysis of flap terminations (see Figure 1-1) was selected for study of right-angle bond termination discontinuities. Discontinuity stress solutions were obtained only for L/D = 1.0 and W/b = 0.8. Based on the insensitivity of the local flap termination stress distribution to changes in L/D and W/b, it seems reasonable that stress gradients adjacent to right-angle bond terminations will be equally insensitive to changes in L/D and W/b. Parametric variations in key discontinuity stress parameters can logically be derived by application of the flap termination stress variation with L/D and W/b to the discontinuity solution for L/D = 1.0 and W/b = 0.8.

The FE grid network, containing 1863 nodes, for the right-angle discontinuity cylinder is shown in Figure 1-11. The grid is graduated such that the element sizes near the discontinuity form an arithmetic progression in both the radial and axial directions. (See Figure 1-12.) The smallest element adjacent to the discontinuity is 0.0032 inch Δr by 0.0020 inch Δz. The first five element columns aft of the discontinuity were kept at a uniform value of $\Delta z = 0.0020$ inch to minimize stress oscillation inherent in the constant strain triangle/quadrilateral FE formulation. The minimum

---

[13] Deverall, L. I., and Lindsey, G. H., "A Comparison of Numerical Methods for Determining Stress Intensity Factors," 8th Meeting JANAF Working Group on Mechanical Behavior, CPIA Publication No. 193, Vol I, (March 1970).

element dimension of 0.002 inch is 1/8 the diameter of the "large 400μ (0.016 inch) filler particles used in typical solid propellants.

A standard value of 0.06 inch was used for the case bond liner thickness in the cylinder model. However, stress solutions were obtained for liner thicknesses of 0.03 and 0.12 inch through minor modification of the FE grid shown in Figures 1-11 and 1-12. The number of element rows in the liner and propellant was adjusted such that the radial grid sizes adjacent to discontinuity were the same as for the 0.06 liner model.

Material property values were chosen to be consistent with TP-H1123 propellant and case bond tensile samples loaded at a constant displacement rate of approximately 2.0 inch/minute. The propellant tensile modulus was selected as $E_p = 850$ psi, the case bond liner as $E_L = 200$ psi, and the insulator as $E_I = 1100$ psi. The bulk modulus selected for all three materials was 333,000 psi. All materials were assumed to have the same coefficient of thermal expansion. The outside surface of the insulator was rigidly restrained in all solutions. The axial displacement coordinates were set to zero along the left edge of the insulator-liner piece that extends 1 inch beyond the propellant grain, to ensure that the extended insulator piece acts as if it were very long. Symmetry boundary conditions were also specified along the right side of the cylinder model to double the effective length.

To evaluate the proposed approach to singularity analysis of right-angle corners, the FE cylinder model was specialized to the condition wherein the grain is rigidly constrained along the outer circumference; i.e., the displacement coordinates were set to zero along the liner-propellant interface. The local corner stresses were then compared with the singularity solution of Zak[7]. Zak's solution is for a clamped-free cylinder subjected to pressure loading. However, because of the close relationship between pressure and thermal loading solutions (see Reference 1), solutions for the two types of loading should exhibit similar behavior, at least adjacent to the discontinuity.

The computed shrinkage stresses along the first row of elements (i.e., 0.0016 inch inboard of the interface) in the propellant adjacent to the rigid liner interface are shown in Figure 1-13 as a function of the axial distance, z, from the corner. The solution is plotted on a log-log grid so the singularity order can be readily identified; i.e., $\sigma \sim z^{-m}$, where m is the order of singularity and z is the axial distance from the corner. The shear stress defines a definite exponential form versus z up to 0.3 inch, if the first element value is ignored. Apparently, the FE solution cannot be relied upon in the first element.

The values shown in Figure 1-13 for the radial stress have been averaged in axially adjacent elements to reduce oscillation. These averaged values are thus plotted at the averaged element center distance from the corner. The oscillation in the radial stress should not be

confused with the oscillatory behavior predicted by Zak and Williams for bi-material interfaces[14]. The FE normal stress oscillation occurs for Poisson's ratio near 0.5 and always results in stress values greater and less in adjacent elements than an expected smooth curve, independent of the element dimensions.

Both the radial and shear stresses have a singularity order of approximately 0.41 (0.41 $\pm \sim$ 0.02, depending upon how the straight lines are drawn). This compares very favorably with the predicted order of 0.405 from the singularity solution of Zak. Thus, the technique based on the plotting of local stresses on a log-log grid and determining slopes seems to work well.

The radial stress begins to deviate significantly from simple exponential behavior for distances grater than 0.1 inch from the corner, but this is to be expected (for both stress components). Singularity theory attempts only to model the stress behavior only in the very local vicinity of the discontinuity.

The remaining two normal stresses, σ_θ and σ_z, are shown in Figure 1-14. They do not follow any reasonable singularity trend in the decade 0.001 to 0.01 inch from the corner. Thereafter, they are consistent with the radial stress. The radial and shear stresses are of most interest, however, and the flexible-liner stress solutions will consider these stresses only.

The stress distribution shown in Figure 1-13 is for the first row of elements adjacent to the bond interface (i.e., 0.0016 inch inboard of the interface); stresses along the actual bond interface can be estimated through extrapolation. The shear stress is plotted in Figure 1-15 as a function of the radial distance from the bond line for element columns 2 through 14 adjacent to the corner. The extrapolated interface values are compared in Figure 1-16 with the values for the first element row. The extrapolated values indicate a distinct slope change in the region 0.001 to 0.01 inch axially from the corner, and the singularity order is increased to approximately 0.57. A similar extrapolation for the radial stress (though more difficult and less certain due to smoothing procedures) produces a lesser change from the values for the first element row. Since the results for the first element row are consistent with the singularity solution of Zak whereas the extrapolated values are not, extrapolation is not reasonable in this instance. Apparently, the constant strain FE method compensates for the fact that the element centers for the first row are not at the interface and computes stresses more nearly like bond-line stresses than stresses at the location of the physical element centers.

---

[14] Zak, A. R., and M. L. Williams, "Crack Point Stress Singularities at a Bi-Material Interface", J. Appl. Mech., Vol 30, No. 1, p. 142 (March 1963).

4.   Flexible Liner Solutions

Propellant radial and shear stresses along the element row adjacent to the liner are shown in Figures 1-17 and 1-18, respectively, for the basic discontinuity material property set (i.e., $E_P = 850$, $E_L = 200$, and $E_I = 1100$ psi), and $\delta_P = \delta_L = \delta_I = 0.01$ in./in., where δ is the shrinkage coefficient. The rigid liner solution discussed previously is also shown for comparative purposes.

The flexible liner significantly decreases both the radial and shear stresses in the vicinity of the corner, relative to the rigid liner condition. The largest effect occurs for the shear stress, but the trends are similar in both stresses. The liner influence is felt only within the first 0.2 inch (i.e., approximately three times the liner thickness) from the corner, and thereafter the flexible liner solution parallels the rigid liner results.

The order of singularity depicted by the radial stress components is not significantly different for the flexible and rigid liner solutions. However, the singularity order increases significantly for the shear stress in the flexible liner solution, relative to the rigid liner solution. The higher slope of the stress gradient occurs within the diameter of a 400μ filler particle, and thus its significance is of some concern relative to the microstructure of typical solid propellants. In fact, the strong aberration in the stress gradients between approximately 0.01 and 0.2 inch for the flexible liner is perhaps the most significant feature of the solution.

Scaling laws are dependent upon the order of the singularity. True exponential behavior for the flexible liner solution really only occurs at distances from the corner less than the diameter of a large filler particle; between approximately 0.01 and 0.2 inch from the corner, the singularity order is relatively low. This could possibly be the critical region in the vicinity of the corner, rather than the first 0.01 inch, and hence, scaling factors would be much different than based on the behavior up to 0.01 inch. Packing of filler particles is relatively poor adjacent to interfaces, however, and binder-rich layers normally occur immediately adjacent to the bond liner in motor situations. Thus, the first 0.01 inch may still be the critical region. Test results will be required to help ascertain the significance of the stress gradient features.

Zak and Williams[14] concluded that a flaw normal to the interface of a bi-material strip is most likely to propagate along the interface, and not into the softer underlayer because the order of singularity (in terms of the "equivalent" stress) is higher. A comparison of the gradients for the maximum principal stress (a "normal" stress failure criteria) and the maximum shear stress (s "shear" stress failure criteria, like the equivalent stress) is shown in Figure 1-19 for $E_L = 200$ and in Figure 1-20 for $E_L = 850$ psi. Surprisingly, little difference is present between the stress gradients radially and axially away from the corner for the two values of liner modulus. The gradients into the liner are not well defined;

the stress values closest to the corner suggest a decrease in singularity order. However, the behavior of the low modulus liner solution is no different than the high modulus solution. This contradicts the bi-material strip solution.

Two preliminary stress solutions for the right-angle corner were obtained using an FE model with elements 0.01 Δr by 0.02 inch Δz in the propellant adjacent to the corner. This "coarse grid" model thus has a minimum element size 10 times larger than the "fine grid" model. A comparison of the radial and shear stresses in the propellant along the first element row is shown in Figure 1-21 for E_L = 200 psi, and in Figure 1-22 for E_L = 850 psi. The coarse grid solution is close to the fine grid solution in both instances for both stress components. However, the coarse grid model completely missed the exponential behavior which occurs within the first 0.01 inch for the soft liner. This underscores the importance of grid resolution adjacent to the discontinuity.

a.   Liner Modulus Effects

Stress solutions were obtained for values of the liner tensile modulus equal to 850, 425, and 85 psi in addition to the solutions previously presented for 200 psi and a rigid liner. Propellant radial and shear stresses in the first row of elements adjacent to the case bond liner are shown in Figures 1-23 and 1-24, respectively, for the various liner moduli. The results are plotted only within the first 0.1 inch from the corner because the basic trend beyond 0.1 inch is well defined by Figures 1-17 and 1-18.

Softening the case bond liner significantly reduces the propellant stresses in the very local vicinity of the corner. The largest reduction occurs in the shear stress, but the radial stress is strongly affected as well. The aberration in the stress gradient between approximately 0.01 and 0.1 inch is more extreme as the liner modulus is decreased. However, beyond approximately 0.5 inch, the liner modulus (within the range studied) has no effect on the stresses.

The order of the stress singularity is influenced by the liner modulus and the largest effect is felt in the shear stress. In this regard, the behavior of the FE stress solution deviates significantly from the singularity solutions of Zak and Williams[14] and Hein and Erdogan[10] for discontinuities at bi-material interfaces. Both of the referenced solutions predict that all of the stress components have the same order of singularity. However, Sih[15] has calculated that some of the stress components adjacent to a three-dimensional crack in a plate remain finite,

---

[15] Sih, G. C., "A Review of the Three-Dimensional Stress Problem for a Cracked Plate", International J. Fracture Mech., Vol 7, No. 1, (March 1971).

whereas, others are singular. This corresponds in some sense to this situation wherein the stress components have different orders of singularity. To better define this singularity order for the cylinder, the FE stress solutions were expanded in the region 0.001 to 0.01 inch from the corner, as shown in Figures 1-25 and 1-26. Consistent procedures for fitting straight-line segments to the various element stress values provide an increase in (negative) slope from 0.41 to 0.47 for the radial stress and from 0.41 to 0.62 for the shear stress as the liner modulus is decreased from rigid to 0.1 of the propellant modulus. This change in slope is summarized in Figure 1-27a, where m_I refers to the radial stress and m_{II} refers to the shear stress.

The stress gradient adjacent to the corner (i.e., within the first 0.01 inch) can be expressed in the form:

$$\sigma_r(z) = \frac{K_I}{(2 \pi z)^{m_I}} \tag{1-1}$$

and

$$\tau_{rz}(z) = \frac{K_{II}}{(2 \pi z)^{m_{II}}} \tag{1-2}$$

The parameters K_I and K_{II} are the normal and shear stress intensity factors, respectively. The dependence of K_I and K_{II} on the liner modulus is summarized in Figure 1-27b; the values are normalized by the solution for a rigid liner. A significant decrease in both normal and shear stress intensity factors occurs as the liner modulus is decreased.

The singularity exponents for the flexible liner solutions differ relative to radial and shear components of stress. Failure would be expected to be greater with the stress component which has the higher exponent; i.e., the shear stress. However, the radial stress magnitude is approximately twice the shear stress over distances from the corner equivalent to the characteristic microstructural size of the propellant. The stress intensity (within a filler particle size of the corner) rather than the gradient may therefore be most meaningful relative to failure initiation.

    b.   Liner Thickness Effects

Stress solutions were obtained for liner thicknesses of 0.03 and 0.12 inch, in addition to solutions previously presented for 0.06 inch liner thickness. Propellant radial and shear stresses in the first row of elements adjacent to the case bond liner are shown in Figures 1-28 and 1-29, respectively. Solutions were obtained for a liner modulus of 200 psi only. Liner thickness variations in the range 0.03 to 0.12 inch have surprisingly little effect on the stresses within the first 0.01 inch of the corner.

The stress solution for the thinnest liner approaches the rigid liner solution quickest, as expected, with the radial stress being less influenced than the shear stress. A somewhat arbitrary inflection point is noted in Figure 1-29 for the shear stress. This inflection appears to occur consistently at an axial distance from the corner equal to two-thirds of the liner thickness. It would be expected, a priori, that the length of the flexible liner perturbation would be directly related to the liner thickness. The analysis results seem to bear this out.

c. Parametric Representation of Corner Stresses

Parametric representation of rigid-liner stress solutions for cylindrical motor configurations is relatively straightforward. The key stress parameters are the radial and shear stress intensity factors, as defined in Equations (1-1) and (1-2). Scaling considerations are as outlined in Figure 1-9. Nondimensionalization of the stress intensity factors thus provides parameters of the form

$$ \frac{\overline{K}_I}{b^{.41} E_\delta} \quad \text{and} \quad \frac{\overline{K}_{II}}{b^{.41} E_\delta} $$

where b is the radius to the outside of the grain and 0.41 is the singularity exponent for a rigid liner condition.

All of the stress solutions for right-angle corners involved a cylinder with $L/D = 1.0$, $W/b = 0.8$, and $b = 16.0$ inches. From values given in Figure 1-13, $\overline{K}_I = 116.0$. Thus, $\overline{K}_I/b^{.41} E_\delta = 4.36$; $\overline{K}_{II}/\overline{K}_I = 0.53$, from the stress values shown in Figure 1-13. Stress intensity values for other W/b and L/D ratios can be obtained by simply applying the relative maximum radial stress values from the flap-termination study[1] to the stress intensity values for $L/D = 1.0$ and $W/b = 0.8$. This is justified since both the corner and flap stress distributions are very local. The stress distribution for the flapped configuration was shown to vary little with changes in L/D and W/b, and a similar situation is only logical for the right-angle corner. Parametric results thus obtained are given in Figure 1-30. Results are strictly applicable only for a Poisson's ratio of 0.49958. However, as indicated in Reference 16, the solution should be insensitive to Poisson's ratio between 0.499 and 0.5 over the range of web fractions analyzed.

Parametric representation of flexible-liner stress solutions is much more difficult than the rigid-liner solution. The flexible liner seems to perturbate the rigid-liner stresses within an axial distance of,

---

[16] Anderson, J. M., "Final Report Cumulative Damage Studies of Conventional-Cast, Composite-Modified, Double-Base Propellant", Report No. AFRPL-TR-69-258, (February 1970).

at most, three liner thicknesses from the corner. The re-established "local" singularity order for the flexible-liner solutions, relative to the rigid-liner solution, occurs axially within approximately one-fifth liner thickness of the corner. This distance is roughly equivalent to the diameter of larger filler particles for typical propellants and liner bond systems, and thus, the applicability of this very local singularity order is uncertain.

The most rational approach to nondimensionalization of flexible-liner solutions is to base the scaling law on the singularity order for the rigid-liner solution. This assumes that the basic (unperturbated) exponential form of the stress distribution adjacent to the corner spans an axial distance much greater than a liner thickness (liner thickness is generally independent of motor size). For a cylinder diameter of 32.0 inches this assumption is quite reasonable, as Figure 1-13 indicates, and the exponential form of the stresses extends at least 0.5 inch (i.e., 10 times the liner thickness). However, for a small cylinder such as a strain evaluation cylinder (SEC), which is roughly one-tenth the diameter of the above, exponential form will not begin at a distance greater than one liner thickness from the corner. (An actual SEC will probably not contain a corner of the configuration studied.) The point is, the proposed nondimensionalization scheme for flexible liners is designed for application to "large" cylinders of diameters larger than approximately 16.0 inches. For smaller cylinders, the proposed scheme will most likely provide an unconservative integrity prediction. However, the error should be small since the scheme does consider the correct "local" singularity order, even for small cylinders.

Typical liner thicknesses for state-of-the-art rocket motors vary between approximately 0.03 and 0.12 inch. The effect of thickness variation on the radial and shear stresses over this thickness range for a liner-propellant modulus ratio of 0.24 is small, as shown in Figures 1-28 and 1-29. Liner thickness effects are most likely less for stiffer liners and greater for more flexible liners because the thickness effect for a rigid liner is zero. The liner modulus is by far the most significant factor in perturbating the exponential stress gradient adjacent to the corner for typical liner thicknesses and moduli. The liner thickness effect will therefore be ignored.

The rigid-liner radial stress gradient adjacent to the corner can be expressed as:

$$\sigma_{rigid}(z) = \frac{\overline{K}_I}{(2\pi z)^{0.41}} . \qquad (1-3)$$

14

That for the flexible liner is similarly:

$$\sigma(z) = \frac{K_I}{(2 \pi z)^{m_I}} \tag{1-4}$$

For the three liner thicknesses and all the liner moduli studied, the local exponential form is established within 0.01 inch from the corner. The ratio of the flexible-liner stress value to the rigid-liner stress value at 0.01 inch will be defined as H_I for the radial stress and H_{II} for the shear stress. This, $\sigma(z = 0.01) = H_I \sigma_{rigid} (z = 0.01) \longrightarrow$

$$\frac{K_I}{(0.0628)^{m_I}} = \frac{\overline{K}_I H_I}{(0.0628)^{0.41}} .$$

$$\text{So: } K_I = (0.0628)^{m_I - 0.41} H_I \overline{K}_I \tag{1-5}$$

and similarly,

$$K_{II} = (0.0628)^{m_{II} - 0.41} H_{II} \overline{K}_{II} . \tag{1-6}$$

Values for H_I and H_{II} are given in Figure 1-31 as a function of the liner/ propellant modulus ratio; the functional form of the stresses within 0.01 inch of the corner is given on the figure.

SECTION II

TASK II - TENSILE AND SHEAR SAMPLE DEVELOPMENT

A. OBJECTIVE

The objective of this task is the development of improved test sample configurations and procedures for the measurement of case bond tensile and shear strength.

B. INTRODUCTION

This task is motivated primarily by the industry need for a quantitative measure of bond strength. Task I provides tensile and shear stress requirements for the case bond system under a variety of motor conditions. Tasks III and IV provide the means for evaluating potential case bond failure criteria based on tensile and shear strength. Thus, Task II interfaces with all other tasks in the program.

No standardized bond tests currently exist in the solid propellant industry. The JANNAF Working Group on Mechanical Behavior recognizes several bond tests, but recommends them only as quality control or research tools. Individual companies have defined "in-house" standards, but these are not generally considered as satisfactory for purposes of a quantitative motor integrity analysis. Thus, there is a real need to develop bond test sample configurations which will provide quantitative engineering data relative to actual motor requirements. To this end, an attempt was made in the subject program to concentrate on the two most basic states of stress; i.e., uniaxial tension and shear.

The remainder of the Task II section of this final report is organized into separate discussions for tensile and shear states of stress. The discussion for the tensile condition is given first and begins with background material relating to bond tensile tests. Stress analyses are then given for five candidate tensile sample configurations. A detailed description is provided for the most promising candidate, the "round-flapped tensile sample". Procedures follow for manufacture, testing, and data reduction of this sample. Test results are then provided for a representative propellant/case bond system, TP-H1123 (a Thiokol PBAN propellant).

The discussion for the shear state-of-stress is patterned after that for the tensile condition. It begins with background information, and then stress analysis results are given for four candidate shear sample configurations. A detailed description is provided for the most promising candidate, the "short lap-shear sample". Procedures follow for manufacture, testing, and data reduction of this sample. Test results are then provided for the TP-H1123 propellant/case bond system. Limited data are provided for the ANB-3066 propellant/case bond system.

C. CASE BOND TENSILE STRENGTH.

    1. Background

        Testing in a "tensile" mode for propellant by itself usually
refers to uniaxial tension. The connotation of "tensile" relative to case
bond testing is much broader. This most probably stems from the fact that
it is virtually impossible to develop a uniaxial case bond tensile sample.
The presence of the multiple, thin, component layers in the case bond
system generally precludes the establishment of a simple uniaxial state-
of-stress at the bond. Thus the broader definition of "tension" for
bond samples, such extreme configurations as poker chips are often included.
However, poker chip (and related thin samples) are herein considered to
be poor case bond tensile samples, in the same sense that they are poor
propellant tensile samples; i.e., because of the triaxial stress state.

        The manufacture of case bond tensile samples, like the design,
is basically more difficult than the manufacture of propellant tensile
samples. The tendency has been to cast the various case bond tensile
samples individually. Casting of individual samples eliminates the need
to machine the bond constituents and generally results in higher-quality
sample finishes; it also allows for relatively complex sample geometries.
However, casting of individual bond samples brings with it undesirable
side effects, not representative of motor conditions. It also precludes
testing of case bond material cut from full scale motors. Considering
the increasing role of motor aging in structural integrity programs,
this is a serious drawback to cast samples.

        The major undesirable side effect relative to the casting of
individual bond test samples concerns propellant curing/aging reactions.
Thiokol has considerable evidence[17] that cure reactions in small quan-
tities of PBAN propellant progress at a different rate than in large
propellant quantities, such as in motors. This "carton-to-motor" dif-
ference for PBAN propellant is tolerable, though undesirable.

        In cast case bond samples, the "sample-to-motor" difference can
be much worse than the carton-to-motor difference. This derives from the
fact that the case bond liner is usually the propellant binder which is
more lightly filled and loaded with significantly more curing and cross-
linking agents. The case bond liner is not fully cured when the propel-
lant is cast. Liner crosslinking curing agents migrate into the adjacent
propellant. For example, note the increased hardness of the propellant
adjacent to the case bond liner for TP-H1123 propellant, as shown in
Figure 2-1. This is advantageous relative to increased strength of the

_____

[17] Bennett, S. J., "Carton/Motor Sample Correlation," Tech Report
     AFRPL-TR-72-117, (30 October 1972).

adjacent propellant. However, the magnitude of this strength increase relates strongly to the volume of adjacent propellant. An important condition is that the volume of adjacent propellant be sufficiently large that materials migration and subsequent curing occurs in the test samples similar to the motor. For example, consider the study described in Reference 18, which was performed using individually-cast poker chip samples. At equivalent loading rates, the bond liner-only failed at 325 psi, the propellant-only failed at 190 psi, and the case bond failed (containing propellant) at 275 psi. The propellant in the case bond sample was obviously stronger than the propellant in the propellant-only test. This may be representative of the actual motor condition, but additional data (involving samples with a higher propellant volume) are necessary before the relevance of the cast sample data can be established. A basic ground-rule that case bond sample configurations must be machineable was thus established for this program.

The most accepted joint-in-tension test for use with composite propellants is described in the ICRPG Solid Propellant Mechanical Behavior Manual.[19] The sample configuration (Figure 2-2) is such that propellant is cast in the test fixture composed of a pipe section butted into an anvil base plate. A Teflon washer is used to provide a short unbonded surface along the cylinder adjacent to the case bond. The sample is loaded by pulling on the pipe and restraining the anvil.

A smaller "button" sample (See Figure 2-3) is often used for liner cohesive/adhesive strength evaluation during screening and quality control programs. This button sample has an aspect ratio much like a poker chip, and thus it does not relate directly to the uniaxial tensile condition.

Special bond tensile sample configurations have been developed for double-base propellants. The individual samples (See Figure 2-4) are machined rather than cast. The double-base bond tensile sample has edge discontinuities at the outer circumference of the bond. Plots of $\sigma_z/(\sigma_z)_{avg}$ and $\tau_{rz}/(\sigma_z)_{avg}$ are shown in Figure 2-5 from an FE stress analysis of the double-base sample. At the outer edge, the shear and normal stresses are unbounded. Data reduction techniques for this sample are questionable; it is reasonable to assume that the bond strength is greater than that derived from the average normal stress at failure. A similar situation occurs for the composite propellants. However, the order of the singularity is strongly influenced by the thickness and modulus of the bond liner.

---

[18] Corley, B. M., et. al., "Evaluation of Propellant-to-Substrate Bonds in a Multiaxial Stress Field," Bulletin 6th Meeting ICRPG Working Group on Mechanical Behavior, Vol, II, (March 1968).

[19] "ICRPG Solid Propellant Mechanical Behavior Manual," CPIA Publication No. 21, (September 1963).

In the subject study, five candidate bond tensile samples were evaluated, in addition to the "joint-in-tension" sample. The five samples evaluated are:

(1) Long, round-flapped tensile sample

(2) Round-flapped tensile sample

(3) Back-to-back tensile sample

(4) Round-filleted tensile sample

(5) Analog flap termination sample pulled in tension

FE stress analyses were performed on these five candidate samples, plus the joint-in-tension sample; the analog flap termination sample pulled in tension is discussed in detail in Section III. Testing was performed only on the most promising configuration as determined from the stress analysis (plus the analog flap termination sample).

2. Stress Analysis

a. Joint-in-Tension (Pipe) Sample

An FE stress analysis was performed on the "pipe" tensile sample of the configuration given in Figure 2-2. The FE model used for the analysis is shown in Figure 2-6 and contains 529 nodes, with four element columns through the insulator and three through the case bond liner. The right-angle corner at the junction of the outer propellant cylinder and the liner constitutes a singularity. A singularity also occurs at the end terminations of the pipe; the end termination closest to the liner is of most interest because the stress intensity will be the highest. The Teflon washer was not included in the model because the propellant will not contact it during loading. The grid density adjacent to the important pipe singularity and the propellant-liner discontinuity is of equivalent refinement. The adjacent element dimensions of 0.01 Δr by 0.02 Δz are not sufficiently small to quantify the stress gradients in the immediate vicinity of the singularities. However, this is not considered necessary and appropriate because the pipe sample is not supposed to be a fracture mechanics or singularity specimen.

The computed axial stress distribution in the pipe sample for a typical set of propellant and bond properties is shown in Figure 2-7. The insulator was restrained radially and axially along its left face and the pipe was displaced axially 0.03 inch. The axial stress decreases linearly with axial distance into the pipe. A significant stress concentration occurs at the end termination of the pipe.

Lines of constant maximum principal stress in the vicinity of the pipe and liner-propellant discontinuities are shown in Figure 2-8. The stress intensity adjacent to the pipe discontinuity is much greater than adjacent to the liner-propellant discontinuity. This mismatch in intensities is probably a result of the flexible liner and may not occur for a stiffer liner. Based on a maximum principal stress failure criteria (and a good case bond strength), the sample is expected to fail at the pipe discontinuity. Limited information available to the writer indicates that this is indeed a common mode of failure.

The stress distribution as a function of radial position in the first column of propellant elements adjacent to the liner is given in Figure 2-9. At the axis of the sample, the τ_{rz} shear stress is zero as required by symmetry considerations; the hoop and radial stresses are 77 percent of the axial stress. Thus, the sample provides a state of stress considerably removed from "uniaxial" tension. The discontinuity adjacent to the outside radius of the propellant cylinder is well defined in the τ_{rz} shear stress. However, the reduction in triaxiality of the normal stresses near the outside radius tends to overshadow the singularity in the normal stresses. The discontinuity trend is only evident in the last (element averaged) point for the hoop, axial, and principal stresses.

In summary, the pipe tensile sample has been shown on the basis of stress analysis to have several serious shortcomings:

(1) If the case bond is strong, failure is likely to occur in the propellant at the pipe termination.

(2) If the case bond has only fair tensile strength and is not edge sensitive and thus fails near the axis at the liner-propellant interface, the state of stress is strongly triaxial, not uniaxial at the point of failure.

(3) The sample has a built-in edge discontinuity which will become more serious as the liner stiffness increases. The bond "tensile" strength cannot be quantified when failure precipitates at the edge.

b. Long, Round-Flapped Tensile Sample

The "long, round-flapped" tensile sample (Figure 2-10) was designed to overcome many of the deficiencies of the pipe tensile sample. The gage length was made long to minimize end effects. A ring of unbondedness was provided at the outside edge of the insulator to reduce the edge concentration at the insulator-to-liner and liner-to-propellant bondlines. The basic sample configuration is machineable or castable.

The analysis of the round-flapped tensile sample (Figure 2-10) considered variations in the following parameters:

(1) Tensile modulus of the liner

(2) Insulator thickness, t_I

(3) Flap length, L

The finite element model for the round-flapped tensile sample is shown in Figure 2-11. The rigid end plate and flap length on the case bond end of the sample were modeled by displacement boundary conditions. The tensile load was applied to the sample by means of a uniform displacement at the necked-down end of the sample.

Stress solutions were obtained for case bond liner, E_L, moduli of 230 psi and 700 psi; the propellant was assumed to have a tensile modulus of 700 psi and the insulator 1000 psi. Insulator thicknesses, t_I, of 0.1 inch and 0.2 inch were analyzed. With two variations of three parameters, eight different finite-element solutions for the round-flapped tensile sample were obtained, as indicated below:

	Solution Number	E_L (psi)	t_I (inch)	L (inch)
Flexible Liner	1	230	0.1	0.1
	2	230	0.2	0.1
	3	230	0.1	0.2
	4	230	0.2	0.2
Stiff Liner	5	700	0.1	0.1
	6	700	0.2	0.1
	7	700	0.1	0.2
	8	700	0.2	0.2

The analysis properties are approximately those of TP-H1123 propellant/case bond and V-45 insulation pulled at 2.0 in./min.

Lines of constant maximum principal stress adjacent to the bondline and into the gage section of the sample are shown in Figure 2-12 for solution No. 1 considering a sample elongation of 0.1 inch. The primary stress concentration occurs in the insulator next to the flap termination as expected. No significant stress concentration occurs in the liner or propellant. The stress is uniform approximately 1.0 inch from the liner.

One of the most desirable characteristics of a case bond tensile sample is a uniform bond stress from the centerline to the flap termination or outside radius of the sample. The ratios of bondline tensile (axial - "Z") stress to the tensile stress in the gage section ($\sigma_{bond}/\sigma_{gage}$) as a function of radial location are shown in Figures 2-13 and 2-14. Stress values for the "bond" are for the first column of elements in the propellant adjacent to the bond liner (see Figure 2-11).

Figure 2-13 shows $\sigma_{bond}/\sigma_{gage}$ for a soft liner bond system. The bond stresses from the sample centerline (radius = 0) to the flap termination are more uniform for the shorter flap length, L = 0.1 inch, than for the longer flap length, L = 0.2 inch. The insulator thickness, t_I, alters the magnitude and the location at which the peak bond stress occurs. The bond stresses are maximum at the sample centerline for the "thick" insulators, t_I = 0.2 inch. For "thin" insulators, t = 0.1 inch, the maximum bond stress occurs between the centerline and the flap termination.

Figure 2-14 shows $\sigma_{bond}/\sigma_{gage}$ for case bond systems with a stiff liner (i.e., as stiff as propellant). The shorter flap length, L = 0.1 inch, gives a better bond stress distribution than L = 0.2 inch. The insulator thickness alters the location of the peak bond stress. The peak bond stress is nearer the flap termination (farther from the sample centerline) with the thin insulator (t_I = 0.1 inch); however, the peak stress is approximately 4 psi higher for the thin insulator than for the thick insulator. Considering the overall stress distribution, both insulator thicknesses appear to provide comparable configurations.

The objective of Task II is to develop a "uniaxial" bond tensile sample. The distribution of the stresses other than the bond normal (axial) stress is given in Figures 2-15 and 2-16 for solution Number 1. Figure 2-15 provides the stresses in the propellant immediately adjacent (0.01 inch outboard) to the critical liner-to-propellant bondline. Figure 2-16 provides the stresses in the liner immediately adjacent (0.01 inch inboard) to the liner-to-propellant bondline. The radial and hoop stresses at the propellant side of the bondline are at most 25 percent of the axial stress; the τ_{rz} shear stress is at most 20 percent of the axial stress. The peak shear stress occurs outboard of the flap termination where the axial stress is low and, hence, where the sample integrity is high. The radial and hoop stresses inside the bond liner are a significant percentage of the axial stress. (See Figure 2-16.) Near the axis of the sample they are approximately 80 percent of the axial stress. The shear and axial stresses must be continuous across the bondline; whereas, the radial and hoop stresses can be discontinuous when the liner modulus is different from the propellant modulus as it is in solution Number 1. The relatively flexible liner acts like a poker chip sandwiched in between the stiffer insulator and propellant layers. However, these triaxial liner stresses are not transmitted to the propellant. The stress uniaxiality for the long, round-flapped tensile sample is thus greatly improved over the pipe sample.

The triaxilality of the principal stresses inside the bond liner and the propellant immediately adjacent to the liner-to-propellant bondline is summarized in Table 2-1 for the eight solutions. The parameter, α, is a measure of the deviation from uniaxiality of the principal stresses. In terms of principal stresses and strains,

$$\epsilon_1 = \frac{\sigma_1}{E} \; 1 - \nu \; \frac{\sigma_2 + \sigma_3}{\sigma_1}$$

For $\nu \approx 0.5$, $\alpha = \frac{\sigma_2 + \sigma_3}{2\sigma_1}$ is a conventient measure of the deviation from uniaxial relationship between the maximum principal stress and strain, σ_1 and ϵ_1, respectively; thus, $\epsilon_1 = (1 - \alpha) \sigma_1/E$. For a uniaxial condition, $\alpha = 0$. For a condition of triaxial hydrostatic tension, $\alpha \approx 1.0$.

TABLE 2-1

TRIAXIALITY OF CASE BOND STRESSES FOR LONG.,
ROUND-FLAPPED TENSILE SPECIMEN

Solution Number	$\alpha^*_r = 0.1$		$\alpha_r = 0.24$	
	Liner Side of Bond	Propellant Side of Bond	Liner Side of Bond	Propellant Side of Bond
1	0.77	0.26	0.73	0.15
2	0.72	0.11	0.69	0.04
3	0.78	0.26	0.71	0.13
4	0.70	0.10	0.64	0.01
5	0.40	0.33	0.29	0.22
6	0.20	0.17	0.14	0.10
7	0.35	0.29	0.22	0.15
8	0.14	0.10	0.07	0.03

$* \; \alpha \approx \frac{\sigma_2 + \sigma_3}{2\sigma_1}$ and $\epsilon_1 = \frac{\sigma_1}{E}(1 - \alpha)$

The value of α is given in Table 2-1 for four different locations in the sample: (1) on the liner side of the liner-to-propellant bondline (0.01 inch into the liner) at a radial distance 0.1 inch from the axis, (2) on the propellant side of the liner-to-propellant bondline (0.01 inch into the propellant) at the 0.1 radial distance, (3) on the liner side of the liner-to-propellant bondline at a radial distance 0.24 inch from the axis, and (4) on the propellant side of the liner-to-propellant bondline at a radial distance of 0.24 inch from the axis. As indicated in Figure 2-13 and 2-14, these radial locations are close to the location of the maximum bond normal stress. Because the τ_{rz} shear stress is small at these two radial locations, the principal stresses are essentially in the r, θ, Z coordinate directions.

When the bond liner is flexible relative to the propellant, the state of stress will be basically triaxial in the liner for reasonable variations in the flap length or insulator thickness. When the bond liner is as stiff as the propellant, the insulator thickness and flap length has a significant effect on the triaxiality of the liner stresses. The thickest insulator and longest flap configuration (Solution No. 8) provides the most uniaxial stress condition; whereas, the thinnest insulator and shortest flap provides the most triaxial stress condition. On the propellant side of the bondline (which is of more interest than the liner side because failures tend to initiate here), the state of stress is more uniaxial for flexible liners than for stiff liners. The triaxial stress state in the liner is not transmitted to the propellant.

The best combination of insulator thicknesses and flap lengths, which are selectable parameters in the sample configuration, is a compromise of the various features of the bondline stress distribution. The flap length should be as short as possible to minimize the deviation of the bond stress from the average "gage" stress, yet still suppress the edge concentration at the liner-to-propellant bondline. A flap length of 0.1 inch appears to be the most appropriate choice, even though it leads to a more triaxial stress state than a flap length of 0.2 inch. An insulator thickness of 0.2 inch significantly reduces the triaxiality of the bond stresses and flattens out the bond stress distribution as compared with an insulator thickness of 0.1 inch. However, the insulator thickness cannot in general be chosen as freely as the flap length.

The relationship between the maximum bond normal stress and the average stress (load/area) in the gage length of the sample is shown in Figure 2-17 for the eight different solutions. Results are plotted against the relative liner-to-propellant modulus since this may vary greatly for different bond systems over a broad rate/temperature range. However, variation over the range $0.2 < E_L/E_P < 1.0$ has only a small effect on the stress concentration factor, particularly for the thinner insulator. As expected, the longest flap length provides the highest concentration factor; the thickest insulator provides the lowest concentration factor.

In plotting the data for Figure 2-17, the relative stiffness of the insulator to the propellant was held constant at 1.43. This parameter is expected to have only a small effect in the stress distribution for typical insulator/flap materials and hence was not varied in the solution.

An estimate for the "true" bond stress can be made using approximations similar to those for uniaxial propellant tensile samples. Thus, $\sigma_{true} \approx (1 + \epsilon_z) \sigma_{eng}$, where the "engineering" bond stress is derived from the load at failure, the initial gage area, and Figure 2-17. The calculated value of ϵ_z in the propellant adjacent to the location of highest bond stress is given in Figure 2-18 for the various sample parameters, considering a unit sample elongation, u.

c. Round-Flapped Tensile Sample

The "round-flapped" tensile sample (Figure 2-19) is a modification of the long, round-flapped tensile sample. The modification involves shortening of the gage section to use a smaller quantity of propellant yet still retain the desirable features of the longer sample. A stress analysis was performed on the shortened sample using the finite-element model shown in Figure 2-20. The end plates were modeled as rigid boundaries and the tensile load was applied by displacement boundary conditions.

In the analysis of the long, round-flapped tensile sample, a flap length (L = 0.1 inch) and an insulator thickness (t_I = 0.1) were shown to be good compromises for the flexible liner case bond systems. For bond systems with stiffer liners, L = 0.1 inch and t_I = 0.2 inch were best. FE solutions for the shorter sample were obtained from these two conditions:

Solution Number	Liner Modulus, E_L (psi)	Insulator Thickness, t_I (inch)	Flap Length, L (inch)
1	230	0.1	0.1
2	700	0.2	0.1

The elastic properties of the insulator, liner, and the propellant used in the analysis were:

Material	Tensile Modulus (psi)	Poisson's Ratio	Bulk Modulus (psi)
Insulator	1000	0.499500	350,000
Flexible Liner	230	0.499891	350,000
Stiff Liner	700	0.499667	350,000
Propellant	700	0.499667	350,000

The ratios of bond line tensile stress to the tensile stress in the gage section ($\sigma_{bond}/\sigma_{gage}$) as a function of radial location are shown in Figure 2-21 for the two conditions studied. The bond stresses from the sample centerline (radius = 0) to the flap termination are nearly uniform for both the flexible liner (E_L = 230) and the stiff liner (E_L = 700) conditions. In fact, the distribution is slightly better in these short samples than in the longer samples (see Figures 2-22 and 2-23). In the longer sample the bond stress peaked between the centerline and the flap termination and then decreased nearer the centerline; this effect is much less in the shorter sample.

The triaxiality of the shorter (standard) round-flapped tensile sample is compared in Table 2-2 to that for the long, round-flapped tensile sample. In terms of the triaxiality index, α, the state of stress in the critical areas is virtually identical in both samples.

TABLE 2-2

COMPARISON OF TRIAXIAL STATE OF STRESS IN LONG,
ROUND-FLAPPED AND ROUND-FLAPPED TENSILE SPECIMENS

E_L (psi)	t_I (in.)	L (in.)	$\alpha*$ (r = 0.1) (Propellant Side of Bond)		α (r = 0.24) (Propellant Side of Bond)	
			Long Sample	Standard Sample	Long Sample	Standard Sample
230	0.1	0.1	0.26	0.24	0.15	0.15
700	0.2	0.1	0.17	0.17	0.10	0.11

$$* \; \alpha \approx \frac{\sigma_2 + \sigma_3}{2\,\sigma_1} \quad \text{and} \quad \dot{\epsilon}_1 = \frac{\sigma_1}{E}\,(1 - \alpha)$$

In summary, the round-flapped tensile sample is superior (and is thus recommended) to the long, round-flapped tensile sample. This superiority results from two factors: (1) the round-flapped sample uses much less propellant and (2) the bond normal stress distribution is more uniform.

The factor for determining bond stress from the gage stress (load/area) for the round-flapped sample is given in Figure 2-24. Because of the similarity between the factors for the long and short samples (See Figure 2-17), only one liner modulus was directly evaluated for the 0.2 insulator thickness. However, three liner modulus solutions were obtained for the 0.1 insulator thickness to better define the curve shapes for all four conditions.

26

The factor to estimate the true stress from the engineering stress for the round-flapped sample is given in Figure 2-25. The shorter propellant length approximately doubles the axial strain per unit sample displacement in the propellant (at the location of the maximum bond stress) when compared with the longer sample results in Figure 2-18. Of interest is that two opposing factors influence the local axial propellant strain as the liner modulus is decreased: (1) the state of stress becomes more uniaxial in the propellant and (2) the liner strains more (overall) due to its increased flexibility, and hence the propellant less (overall). The first factor is dominant because the axial strain in the propellant adjacent to the liner increases with decreasing liner modulus for a unit change, u, in sample length.

d. Back-to-Back Tensile Sample

The "back-to-back" tensile sample is simply two round-flapped tensile samples containing 0.1 inch insulator thickness bonded together (see Figure 2-26). However, no ring of unbondedness is used at the outside edge of the insulator layer. Two assumptions were made relative to the insulator-to-insulator bonding layer: (1) the adhesive bonding the two insulator pieces together was assumed to have the same modulus as the insulator and negligible thickness and (2) the bonding layer was rigid. These conditions will provide reasonable bounds on lateral restraint at the insulator surface.

The FE model of this sample is shown in Figure 2-27. The rigid end plate and applied tensile load were modeled by displacement boundary conditions. FE solutions were obtained for the four conditions listed below:

Solution Number	Adhesive Layer	Liner Modulus (psi)
1	Soft	230
2	Soft	700
3	Rigid	230
4	Rigid	700

The liner thickness was 0.06 inch and the insulator thickness was 0.10 inch on each side of the insulator-to-insulator adhesive layer.

The moduli of the various materials comprising the sample were:

Material	Tensile Modulus (psi)	Poisson's Ratio	Bulk Modulus (psi)
Insulator	1000	0.499500	350,000
Flexible Liner	230	0.499891	350,000
Stiff Liner	700	0.499667	350,000
Propellant	700	0.499667	350,000

Calculated stresses in the first row of elements inside the propellant adjacent to the case bond liner are shown in Figures 2-28 through 2-31. The two solutions for the flexible adhesive layer (Figures 2-28 and 2-29) are particularly attractive relative to a uniaxial stress condition. The flexible liner causes a small stress perturbation near the outside edge; the maximum "bondline" tensile stress is only 6 percent greater than the gage stress. The stiff liner condition ($E_L = E_p = 700$ psi) provides the most uniaxial stress condition, as would be expected. The stiffer insulator layer tends to perturbate the hoop and radial stresses.

The bondline stress distributions for the rigid adhesive condition (Figures 2-30 and 2-31) are much less favorable than that for the flexible adhesive condition. A strong stress concentration (not shown) occurs at the outer edge of the insulator adjacent to the rigid adhesive boundary. This stress concentration causes a reduction in the normal (axial) stress at the outer edge of the liner-to-propellant bondline. The perturbation in the shear, radial, and hoop stresses near the outer edge is similar for both of the flexible liner solutions. However, the rigid adhesive solution for a stiff liner is much less favorable than that considering a flexible adhesive.

Solutions presented in Figures 2-30 and 2-31 represent the "round-flapped" tensile sample without the 0.1 inch ring of unbondedness between the end tab and the insulator. These solutions indicate a suppressed normal stress at the edge, which is desirable, and a more uniform stress distribution across the bondline than for the flapped sample. Thus, the round-flapped sample without the flap is a good candidate tensile sample. The back-to-back sample with a flexible adhesive layer is an even better tensile sample.

e. Round-Filleted Tensile Sample

The "round-filleted" tensile sample, Figure 2-32, was designed to suppress the edge concentration at the liner-propellant interface. Two fillet radii were studied; 0.25 and 0.375 inch. The finite element model of the sample with a 0.25 inch fillet radius is shown in Figure 2-33. The rigid end plates and the tensile load were modeled with boundary displacements.

The elastic properties of the insulator, liner, and the propellant used in the analysis were:

Material	Tensile Modulus (psi)	Poisson's Ratio	Bulk Modulus (psi)
Insulator	1000	0.499500	350,000
Liner	230	0.499891	350,000
Propellant	700	0.499667	350,000

The computed "bond" normal stress distribution (stresses in the first row of elements inside the propellant) is shown in Figure 2-34 for the two sample configurations; the stresses are normalized by the average gage stress. The stress distribution is highly non-uniform. As desired, the stress diminishes to almost zero at the sample edge. However, the maximum bond stress is only 88 percent and 82 percent of the gage stress, respectively, for the 0.25 and 0.375 inch fillet radii. This is highly undesirable because the sample will fail at the bondline only when the bond is weak relative to the propellant. The highest propellant stress does not occur in the gage but instead occurs in the fillet radius. Figure 2-35 indicates the maximum principal stress around the fillet arc. The peak stress occurs approximately 10° around the arc from the gage-fillet intersection. For the 0.25 radius sample, the peak propellant stress is 35 percent higher than the gage stress and 53 percent higher than the peak bond stress. For the 0.375 inch radius sample, the peak propellant stress is 29 percent higher than the gage stress and 57 percent higher than the peak bond stress. Thus, both fillet radii provide highly unacceptable stress distributions.

3. Experimental

The round-flapped sample was chosen as the primary case bond tensile sample. Therefore, detailed procedures were developed for manufacture, testing, and data reduction. These procedures were evaluated through testing with two different propellant/case bond systems, ANB-3066 and TP-H1123. Preliminary studies were performed using the ANB-3066 formulation, and TP-H1123 was used for final evaluation. The analog flap termination sample pulled in tension (90° pull angle) was selected as the secondary case bond tensile sample. Details concerning this sample are given in Section III.

a. Configuration for Round-Flapped Tensile Sample

The recommended configuration for the round-flapped tensile sample is shown in Figure 2-36. This configuration deviates from that studied by FE analysis (Figure 2-19) through the addition of a short 1/8 inch lip of propellant on the end opposite the case bond. This lip was

29

added to ensure better uniformity among the test samples. Accurate truncation of the samples is difficult in the fille section. Also, the length of the gage section from the insulator-liner interface should be specified; the waviness of typical liners leads to more uncertainty if the liner-propellant interface is chosen as the reference plane.

b.   Manufacturing Procedure for Round-Flapped Tensile Samples

During the course of the program, three different procedures were used to machine round-flapped tensile samples. All procedures involved the lathe. The most elementary (hand trimming) procedure is outlined in Figure 2-37. Step No. 1 involves cutting a rectangular block, approximately 1.7 inches on a side and 2.5 inches long. Cutting is accomplished using a band or rotary saw. In Step No. 2, the rectangular block is placed in a lathe. The propellant end is held by a metal box which has been placed in the chuck. The case bond end is butted against a live center. A small compression is used to keep the insulator against the live center; double-back tape can be used to improve the grip. A lathe tool with a 0.375 inch radius is used to machine the propellant cylinder of 1.0 inch diameter and the radius section. A small layer of propellant is left on the liner. The lathe tool is also used to cut the 1.5 inch diameter flange. A shallow groove is then cut 1/16 inch from the intersection with the 0.375 inch radius. The sample is trimmed using a knife after removal from the lathe. The propellant is first trimmed to form the lip at the 1.5 inch diameter section opposite the case bond. The insulator, liner, and small layer of propellant at the case bond are then trimmed progressively around the circumference of the sample.

The hand-trimming procedure was used on the ANB-3066 bond system. It produced relatively crude samples and is not recommended as a production procedure. However, because the outer 0.1 inch of the insulator is flapped (unbonded from the end tab), a smooth edge cut is not of prime importance.

The intermediate procedure for machining the round-flapped tensile sample used a special die for cutting through the insulator and liner layers. The die was made according to Figure 2-38, and a photograph of the finished part is shown in Figure 2-39. Step No. 1 of the die-cut procedure involves the cutting of a 1.7 x 1.7 x 2.5 inch rectangular block as outlined in Figure 2-40. The block end is placed in a metal box and tightened into the lathe chuck. The die is placed in the dead center of the lathe, opposite the chuck. The lathe is turned at low speed and the die driven into the insulator and liner layers to approximately 0.2 inch into the propellant. The die is then backed out and a 1.0 inch metal disc centered over the circular cut into the insulator. This disc is then placed against a live center and held securely using double-back tape and a small sample compression. Step No. 3 involves machining of the propellant cylinder using a 0.375 inch radius tool. The tool-machined cylinder can usually be blended into the section cut by the die to within 0.005 inch. The flange is made using the procedure described earlier. The loose

insulator piece is slipped over the end of the sample during removal from
the lathe. This intermediate procedure produced high quality samples.
Figure 2-41 is a photograph of a TP-H1123 sample made with this procedure.
(However, the flange on this sample is greater than 1/8 inch.) The inter-
face between the die-cut section and the machined cylinder is readily
apparent. However, the mismatch in diameters is within 0.005 inch tolerance.

Friction as the die moves into the propellant is somewhat
hazardous when live propellant is cut dry and unfrozen. Therefore, alter-
native procedures were investigated. An attempt was made to press the die
through the insulator without rotary motion. However, this did not work
satisfactorily with TP-H1123 propellant and was not tried on ANB-3066.
Rotary motion is definitely needed with TP-H1123 propellant for proper
cutting. Friction can be minimized by wiping a thin film of oil onto the
die before cutting. Also, the more shallow the propellant cut, the less
chance for propellant heating.

Based upon the success of the die machining technique, a
special apparatus was designed for making round-flapped tensile samples
quicker and more precise on the lathe. A drawing for this special
apparatus is shown in Figure 3-42 and a photograph is shown in Figure
3-43. This apparatus incorporates the die cutter head and the subsequent
live center of the intermediate procedure into one part. When the cutter
is retracted, the apparatus provides a live center. The cutting sleeve
is placed around the live center and is pressed into the sample by a
level-actuated cam. Cutting of the case bond layers is accomplished before
the sample gage is machined. Using this apparatus, Hercules has been able
to machine round-flapped tensile samples almost as rapidly as any other
lathe-machined test sample. Sample finish is comparable to that shown
in Figure 2-41. No damage to the critical edges between the liner-insulator
and liner-propellant layers of the bondline has been noted to date. How-
ever, cutting of rubber tends to dull the tool at a moderately rapid pace,
and resharpening is necessary after approximately 50 samples.

Bonding of the propellant end of the sample to an end tab
for testing is straightforward. Construction of the 0.1 inch ring of
unbondedness to the end tab in the case bond end is critical. The recom-
mended procedure is to cut Teflon rings of 0.8 inch ID and 1.0 inch OD
out of tape material with contact adhesive on one side. Since Teflon
tape is easy to tear, Hercules constructed a special die (see Figures
2-44 and 2-45) and stamped the rings. However, materials other than
Teflon can just as well be used for the rings. All that is necessary is
to assure that the end tab adhesive (Hercules uses Dexter-Hysol Epon 913.1)
does not contact the insulator. A paper ring may work just as well, but
a weak contact adhesive would have to be used on the insulator side of the
ring.

The procedure for bonding the insulator to the sample end tab is summarized in Figure 2-46. Step No. 1 involves cutting the Teflon rings. In Step No. 2 the Teflon ring is centered on the insulator (a well-defined insulator edge is important at this time). The adhesive side is placed against the insulator to ensure that extra end tab adhesive does not run onto the insulator in the flapped area. The contact adhesive on the Teflon tape is assumed to be so weak that it will fail at a low stress level (experience to date bears this out). However, the use of Teflon further assures a weak bond to the end tab adhesive on the other side of the ring.

c.   Test Results

Constant displacement rate tensile tests were performed on ANB-3066 and TP-H1123 propellant/case bond systems. However, data for the ANB-3066 propellant/case bond system are not presented herein because the samples had been exposed to air for approximately 3 weeks prior to testing and behaved much differently than "typical" ANB-3066. Testing was accomplished on three different bond tensile sample configurations for TP-H1123, as well as the propellant by itself. Propellant and case bond testing was performed with the (primary) round-flapped tensile sample and the (secondary) analog flap termination sample at three loading rates and two levels of superimposed pressure. In addition, two tests at 1000 psi superimposed pressure and 100 in./min were performed on round-flapped tensile samples without the flap.

Test data obtained from the tensile testing of TP-H1123 propellant/case bond are summarized in Table 2-3. The key strength parameter, the maximum true stress, is plotted in Figure 2-47 and Figure 2-48. Figure 2-47 indicates that, at the two lowest loading rates, the propellant and case bond are essentially of equal strength. However, at the highest loading rate, the case bond is significantly stronger than the propellant. Further, the primary and secondary bond sample configurations deviate in their strength values.

It is not surprising that the rate-dependence of the bond strength is different than that for the propellant by itself. This can be at least partially explained by the hardness gradient in the propellant adjacent to the liner interface (Figure 2-1). However, it is surprising that the rate dependence of the bond strength as measured by the primary and secondary bond samples is different. This difference at the highest loading rate (100 in./min) is exaggerated by superimposed pressure (Figure 2-48). The bond strength measured by the round-flapped sample increases with superimposed pressure similar to the propellant by itself. However, the bond strength measured by the analog sample does not increase in the same proportional manner with increasing superimposed pressure. Apparently, edge effects become more significant in the analog sample as loading rate and superimposed pressure levels are increased.

32

TABLE 2-3

TENSILE TEST DATA FOR TP-H1123 PROPELLANT/CASE BOND AT 77° F AND 50 PERCENT RELATIVE HUMIDITY

Sample Configuration	Loading Rate (in./min)	Superimposed Pressure (psi)	Time to Failure(2) (min)	Crosshead Displacement at Failure (in.)	Maximum Engineering Stress (psi)	Maximum True Stress (psi)
Round-Flapped Case Bond	0.01	0	21.2[1]	0.212	84[3]	98.4[4]
	1	0	0.333	0.333	132	167
	100	0	0.00501	0.508	253	356
	100	200	0.00432	0.443	384[8]	520
	100	1000	0.00509	0.523	507	719
(No Flap)	100	1000	0.00273	0.270	350	426[4]
Analog Flap Case Bond	0.01	0	15.2[1]	0.152	85.3[5]	98.5[6]
	1	0	0.212	0.212	136	165
	100	0	0.00324	0.340	253	339
	100	200	0.00262	0.260	304[8]	384
	100	1000	0.00258	0.255	364	457
Propellant	0.02	0	34.4[1]	0.692	69	89[7]
	2	0	0.455	0.910	108.5	151
	200	0	0.00565	1.160	186	278
	200	200	0.00536	1.120	300[8]	445
	200	1000	0.00598	1.250	428	656

NOTES:
(1) Four samples tested per condition - average value given in table
(2) Failure defined as maximum load
(3) Engineering stress =(maximum load) x 1.38
(4) True stress = (Engineering stress) x $(1 + 0.8\,u)$; u = crosshead displacement at failure
(5) Engineering stress = (maximum load) x 2.36
(6) True stress = (Engineering stress) x $(1 + u)$
(7) True stress = (Engineering stress) x $(1 + u/2.33)$
(8) Load % area (i.e., not maximum principal stress under superimposed pressure)

33

The two fully-bonded "round-flapped" case bond tensile samples were tested at conditions of 100 in./min and 1000 psi superimposed pressure, because these conditions provide the most demanding test for a candidate sample configuration with the TP-H1123 bond system. The tensile strength and time-to-failure measured with this sample configuration were significantly less than for the standard round-flapped tensile sample. Thus, the edge effect is apparently significant in the fully bonded sample, and flapping is definitely required for the TP-H1123 bond system.

D. CASE BOND SHEAR STRENGTH

1. Background

Shear strength for case bond systems has been primarily measured with lap shear or torsional shear test specimens. Testing in a torsional mode requires special equipment, and most rocket facilities have preferred not to test this type of sample. Thus, the major emphasis has been placed on the testing of lap shear samples of various types.

The single lap shear sample shown in Figure 2-49a is not desirable or often used because of bending moments imparted by the offset of the grips. Perhaps the most used configuration is the double lap shear sample shown in Figure 2-49b, which eliminates the bending moment effect through symmetric load transmission. However, the double lap-shear sample has the potential for nonuniform restraint perpendicular to the direction of pull. The quadruple lap-shear sample shown in Figure 2-49c was developed to provide uniform lateral restraint.

Lap-shear samples have undesirable stress concentrations at the edges similar to tensile samples. Chevrons are sometimes used to minimize these edge effects. However, the stress concentrations cannot be fully suppressed by chevrons, and test samples tend to fail at the edges where quantitative strength values cannot be determined.

The torsion specimen shown in Figure 2-50 has been used to measure case bond shear strength for double-base propellants. Swanson[20] performed an FE stress analysis of the torsion sample. He showed the lack of edge discontinuity when the propellant is butted directly into a rigid base plate. However, if an elastic substrate (insulator and/or liner) is present, an edge discontinuity occurs.

[20] Swanson, S. R., and A. K. Phifer, "Case Bond Failure Criteria Study," Specific Data Report No. S44/6/40-153, Hercules Incorporated, (31 October 1966).

2. Stress Analysis

a. Torsional Shear

Four modifications of the sample configuration shown in Figure 2-51 were investigated for torsional shear loading. The basic sample is 2.0 inches in diameter and length. The variations in the sample configuration studied are: (1) a solid sample with the liner and insulator cut off flush with the propellant at 1.0 inch outside radius and the insulator uniformly bonded to an end plate, (2) a solid sample with the liner and insulator cut off flush with the propellant at 1.0 inch outside radius and the insulator bonded to an end plate over the area between r = 0.6 and 0.8 inch, (3) a hollow sample with the liner and insulator cut off flush with the propellant at 1.0 inch outside radius and the insulator bonded to an end plate, and (4) a hollow sample with the liner and insulator extended to 1.2 inches outside radius and the insulator bonded to an end plate.

Three FE models were constructed to stress analyze the four sample configurations. The first model (Figure 2-52) considered the solid torsion sample involved in configurations (1) and (2). Models for configurations (3) and (4) are shown in Figures 2-53 and 2-54, respectively. In all three models the insulator was considered to be 0.1 inch thick and the liner 0.06 inch thick.

FE stress solutions were obtained using Hercules Asymmetric Loads (Torsion) Finite Element Program. Material properties used in the analysis are as follows:

Material	E (psi)	v
Insulator	1000	0.4995
Liner	50	0.499975
Propellant	200	0.4999

The samples were loaded by twisting the case bond end through an angle of 1.0 radian and holding the opposite end to zero circumferential displacement.

Computed shear ($\tau_{\theta z}$) stresses in the propellant along the column of elements immediately adajacent to the liner are shown in Figure 2-55 for configurations (1) and (2). The fully-bonded solution exhibits a linear dependence of the shear stress versus radial position. Thus, the solution for the insulator-liner-propellant sandwich is similar to that for a sample of uniform composition.

35

The computed shear stress distribution for the partially-bonded sample configuration is very similar to that for the fully-bonded configuration. Apparently, the insulator is sufficiently more stiff than the liner and propellant that it does not experience significant shear strain; it basically acts as though it were fully bonded to the end plate. The use of flaps to relieve edge stresses or partially-bonded regions to level out stress distributions does not appear to be feasible, although they would be more effective if the liner and propellant were more nearly equal to the insulator in stiffness.

Computed shear stresses in the propellant along the column of elements immediately adjacent to the liner for configurations (3) and (4) are shown in Figure 2-56. The solution for the liner and insulator cut flush with the propellant (configuration 3) is linear and is similar to the solid torsion sample solutions. However, the solution for configuration (4) indicates a strong discontinuity at the outside propellant diameter. This is somewhat surprising (though consistent with the work of Swanson) because no discontinuity would occur if the insulator/liner were rigid. This was verified for the FE torsion model by increasing the insulator and liner moduli to 1×10^6 psi and obtaining a new stress solution; no discontinuity occurred, as shown in Figure 2-56. Thus, for a discontinuity to occur at the outer edge of the bond, the bond substrate (insulator and liner) must extend outward beyond the propellant diameter and be of modulus approximately equal to or less than the propellant. If the substrate is machined flush with the propellant, no discontinuity will occur regardless of modulus differences.

The stresses adjacent to the case bond, other than the $\tau_{\theta z}$ shear stress, are negligible (within computer round-off error) for the conditions wherein a discontinuity does not occur. However, for configuration (4) and a flexible liner, significant stresses other than $\tau_{\theta z}$ occur. This configuration is not of interest as a case bond shear sample and thus the $\tau_{\theta z}$ stress distributions shown in Figures 2-55 and 2-56 fully characterize the total nontrivial stress picture.

The computed shear stress distribution for all nonsingular conditions is consistent with the well-known torsion solution for a hollow/solid cylinder:

$$\tau_{\theta z}(r) = (\frac{r}{b}) \ \tau_{max}$$

Where:
$$\tau_{max} = \frac{2 \ Tb}{\pi(b^4 - a^4)}$$

and: a = inner radius of hollow sample

         b = outer radius of hollow sample

 T = torque applied to sample

For example, when the solid torsion sample (configuration 1) is twisted 1 radian, the computed torque from the finite element solution is 49.7 in./lb. The maximum shear stress based on the above relationship is 31.6 psi. This compares identically with the results shown in Figure 2-55. Thus, the only additional information that the FE solution has accomplished over and above the simple torsion solution is to identify the singular condition for configuration 4. The FE method can be used to relate torque and the angle of twist. However, because both are routinely measured during testing, the computed relationship is of little value. No measure of strain is necessary for relating true and engineering stresses since the change in cross-sectional area is minimal (zero in the FE solution) during twisting. The local propellant strain adjacent to the bondline is easily determined from the stress if the modulus is known. The case bond torsion test is not an accurate means for determining this effective propellant shear modulus; a propellant torsion test is much better.

The wall thickness of the torsion sample should be selected to be as thin as possible to minimize the stress gradient across the thickness. When a solid torsion specimen of a ductile material (gradual or sharp yielding) is twisted, the outer material fibers begin to yield first and transfer some of the load to the inner fibers. The maximum stress at failure can only be determined from highly local measurements or a plastic stress analysis of the test sample, and neither is practical. The wall thickness selected for analysis is 0.2 inch, which provides a ± 11 percent variation around the mean. The minimum allowable wall thickness is determined by a buckling criterion, best established by testing for a sandwich structure like the case bond torsion sample. Metal tubes with a wall thickness 1/20 of the average radius are routinely tested to failure without buckling. However, no buckling studies were performed in this program.

b. Picture Frame Shear

A FE stress analysis was performed on the "picture frame" shear sample (Figure 2-57) for plane stress conditions. The propellant and case bond materials were assumed to be bonded to four rigid links around the periphery. The rigid links were pinned at each of the four corners. Opposite corners were loaded along a diagonal to generate a scissor-type shearing condition. Considering a uniform material between the plates, conditions of pure shear exist in the linear solution.

A FE model was constructed for the stress analysis using only the right, upper quadrant of the sample. The sample has symmetry about vertical and horizontal lines as indicated in Figure 2-57. The applied load is not symmetric about either axis. However, the load can be broken up into two load distributions, one which is symmetric and one which is antisymmetric about both axes as follows:

SYMMETRIC   ANTISYMMETRIC
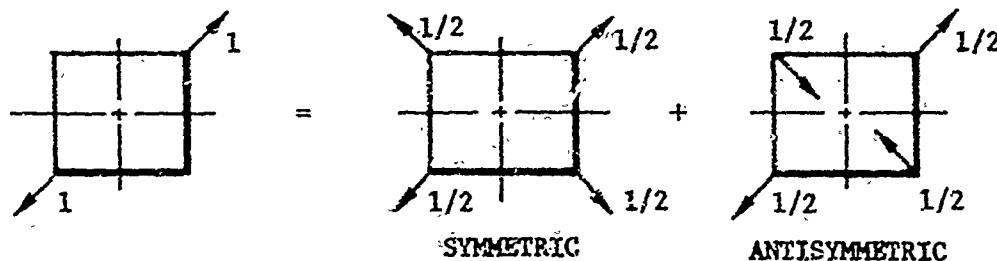
Considering the rigid link restraint, the symmetric loading condition will produce zero stresses in the propellant/case bond because the links must elongate to deform the material inside. Thus, the antisymmetric solution provides the total result.

A FE stress solution was first obtained with the liner and insulator assumed to be propellant; i.e., uniform properties throughout. The computed stresses indicated pure shear conditions as desired and verified the FE model. A solution was then obtained assuming:

Material	E (psi)	ν
Propellant	200	0.4999
Insulator	1000	0.4995
Liner	50	0.499975

The computed stresses indicate a surprisingly large gradient in both shear (τ_{xy}) and normal (σ_y) stresses as shown in Figures 2-58 and 2-59 (the σ_y and σ_x normal stresses should be zero). Apparently, the flexible liner has an effect like a void, causing discontinuity-type stress concentrations where the insulator and propellant intersect the rigid links at the liner bondlines. Thus, the picture-frame shear sample appears to be unsuitable as a case bond shear sample. Even if the linear stress solution had looked good, there are still important considerations relating to buckling, large deformation effects, and stress conditions at the corners.

c.   Lap Shear

Lap shear tests are routinely performed in the solid propellant industry to measure the shear strength of propellant and case bond systems. Achieving a pure shear condition in any test configuration is difficult, except perhaps torsion. Normal stresses are known to occur in lap shear samples in addition to shear stresses. These normal stresses are suspected to be the cause of propellant failure in some instances, instead of the shear stresses. The chevron sample configuration has been

used as a means to suppress the normal stresses at the end of the sample where the stress is tensile. However, as outlined in Reference 21, the chevron sample does not have a desirable shear stress distribution.

A basic understanding of the lap shear test can be obtained from a strength of materials estimate of the stress distribution. Consider the rectangular sample configuration outlined in Figure 2-60. The upper and lower surfaces are assumed to be bonded to rigid bars of infinitesimal thickness which are designed so that the force, F, passes through the vertical midplane of the sample. The bars should not tend to rotate under these conditions, at least in a linear isotropic situation. Along each of the upper and lower faces, F translates to cause a moment, $M = F \, h/2$. If the bars do not rotate, this moment must be reacted by a normal stress at the bondline.

By ignoring the stress singularities at the four corners, a strength-of-materials solution can be obtained. A reasonable assumption is that the bond shear stress is uniform along the length and the bond normal stress is linear; i.e.,

$$\sigma(x) = 2\bar{\sigma} \, \frac{x}{L} \quad (\bar{\sigma} \text{ is the maximum stress})$$

$$\tau(x) = \bar{\tau}$$

Then:
$$M = 2t \int_0^{L/2} \sigma x \, dx = \frac{1}{6} \bar{\sigma} L^2 t \quad (t \text{ is sample thickness})$$

But:
$$M = F \frac{h}{2} = \frac{1}{6} \bar{\sigma} L^2 t$$

So:
$$\bar{\sigma} = 3 \left(\frac{h}{L^2}\right) \left(\frac{F}{t}\right)$$

However:
$$\bar{\tau} = \frac{F}{Lt}$$

So:
$$\bar{\sigma} = 3 \left(\frac{h}{L}\right) \bar{\tau}$$

Thus the aspect ratio, L/h, of the sample should be large to minimize the normal stress relative to the shear stress.

----

[21] Cost, T. L., and C. H. Parr, "Analysis of the Biaxial Strip and Shear Lap Tests for Solid Propellant Characterization," Rohm and Haas Company, Report No. S-73 (May 1967).

The normal-shear stress relationship predicted by the strength-of-materials solution can be evaluated from the work in Reference 21, wherein FE stress analyses were performed on lap shear samples of differing aspect ratios. Figures 2-61 and 2-62 are reproduced from Reference 21 to illustrate the bondline shear and normal stress distribution for different aspect ratios, $\alpha = L/h$. The stresses are only plotted for half the length of the bondline because of symmetry considerations. The discontinuity which occurs at the right end of the sample is recognized by the FE solution. The normal stress distribution becomes more linear as the aspect ratio decreases. For the high aspect ratios, the normal stress distribution deviates significantly from a linear distribution. However, the normal stress predicted by the strength of materials solution for $\xi = 0.9$, which is not strongly affected by the discontinuity, is still quite accurate, as indicated below:

α	τ_{avg}	$\bar{\sigma}$ at $\xi = 0.9$	$3\alpha \bar{\tau}_{avg}$
1	0.230	0.70	0.69
2	0.284	0.48	0.43
3	0.300	0.36	0.30
4	0.309	0.27	0.23
5	0.311	0.20	0.19

When case bond tests are performed, case bond liner and insulator layers must be included in the test sample. The insulator layer can be used to advantage as a flap to suppress the effects of the end discontinuity.

The basic case bond (lap) shear sample configuration selected for initial FE stress analysis is shown in Figure 2-63. The sample is symmetric about two axes, one at the vertical midplane and one at the longitudinal midplane. The propellant layer is only 0.1 inch thick; the liner and insulator layers are assumed to be standard 0.06 and 0.1 inch thick, respectively.

Stress solutions were obtained for the basic sample configuration and three variations. The first two variations involved changes in the flap length to zero and 0.2 inch. The third variation involved an increase in the propellant thickness (height) to 0.5 inch.

The FE grid network for the 0.5-inch model is shown in Figure 2-64. The grid for the 0.1 inch model is similar, but has fewer rows of propellant elements. The elements in the liner have a minimum thickness of 0.01 inch and a minimum length of 0.02 inch.

Solutions for the zero and 0.1 flap lengths were obtained with the basic (0.1 inch) model by varying the flap length. The liner was assumed to have the same mechanical properties as the propellant; i.e., $E_{liner} = E_{prop} = 200$ psi and $K_{liner} = K_{prop} = K_{insulator} = 325,000$ psi. The insulator modulus was considered to be $E_{insulator} = 1000$ psi.

The normal and shear stresses computed in the element row in the liner adjacent to the insulator for a unit shear displacement are shown in Figure 2-65 as a function of the length coordinate for zero and 0.1 flap lengths. The insulator tends to soften the discontinuity in the zero flap-length solution much more in shear than in normal stresses. In fact, the shear stress does not indicate a discontinuity. The flap tends to soften both the shear and the normal stress near the discontinuity. The value of the flap in shifting the maximum stress away from the discontinuity to the gage length is evident. The normal stress distribution based on the relationship $\sigma = 3\alpha \tau$ is also shown in Figure 2-65. This simplified solution better predicts the distribution for the flapped configuration than it does for the non-flapped configuration. Apparently, the moment for both configurations tends to be balanced out by the normal stress nearer to the sample ends than the middle. Thus, the normal stress discontinuity in the non-flapped solution balances out more of the moment near the ends than does the normal stress near the ends for the flapped solution.

The maximum principal stress in the element row in the liner adjacent to the insulator is shown in Figure 2-66. If the case bond liner were to fail as a result of the maximum principal stress, then the un-flapped sample would fail at the edge; whereas, the flapped sample would fail in the gage length where a condition of almost pure shear exists.

Normal and shear stresses in the element row in the propel-lant adjacent to the liner are shown in Figure 2-67. The normal stress next to the left edge of the sample indicates less of a gradient that in the liner, adjacent to the insulator. This is to be expected because the normal stress must be zero along the vertical mid-plane of the sample. The normal stress peak at the left edge of the sample is less than the shear stress in the gage section. Thus, if the bond liner is significantly stronger than the propellant and/or liner-propellant bond, the non-flapped sample is likely to fail due to shear in the sample gage length.

41

Three stress solutions were obtained for variations in the
liner modulus considering a 0.1 inch flap length for the sample. Values
for the maximum principal stress in the element row in the propellant
adjacent to the liner are plotted in Figure 2-68. As the liner becomes
lower in modulus, the average shear stress decreases considering a unit
shear displacement. However, the more flexible liner condition tends to
cause a slight stress concentration near the flap termination, which is
undesirable. This can be alleviated by increasing the flap length to 0.2
inch as shown in Figure 2-69.

The effect of propellant height is shown in Figure 2-70.
The ratio of the radial stress in the row of propellant elements nearest
the liner to the case bond shear stress in the gage clearly demonstrates
the value of a short sample. Trends are predicted quite well by the
strength-of-materials solution $\bar{\sigma} = 3 (h/L) \bar{\tau}$. However, the maximum value
near the flap termination is missed by a substantial amount for the 0.5
inch propellant height. The shorter sample has small normal stresses
relative to the shear stress as desired. The large normal stress near the
flap termination in the thicker sample would cause the propellant/case
bond to fail near the flap termination instead of near the axial midplane
in shear.

Lap shear samples based on the configuration outlined in
Figure 2-63 with two liner layers cannot be machined from blocks contain-
ing large propellant quantities. Thus, this configuration is not practical.
However, stress solutions based on this configuration have been helpful
in establishing the effects of sample height/length, flap length, and
liner modulus. Three candidate sample configurations which are machinable
were thus chosen for further study (see Figure 2-71). All three samples
use the same basic insulator/liner/propellant sandwich, but differ in
the end tab bonding procedure. Configuration No. 1 uses an additional
0.1 inch rubber layer bonded to the bottom face of the propellant with
with an epoxy resin. This additional rubber layer is used to flap the
epoxy bondline and thus relieve end-termination stresses. In configuration
No. 2, the propellant is bonded directly to the end tab. Configuration
No. 3 is similar to configuration No. 2, but the insulator layer is fully
bonded to the end tab.

The height of the propellant layer is 0.1 inch, and the
length is 1.5 inches in the proposed lap shear samples. The width need
not be specified for the analysis because two-dimensional stress solutions
will be obtained; i.e., plane stress (infinitesimally thin) or plane
strain (infinitely thick).

Stress solutions were obtained for all three candidate
configurations using the FE model shown in Figure 2-72. The assumption
made was that the end tabs were longer than the samples, and the flapped
ends would thus be made by placing Teflon strips between the end tabs and
the insulator layers. This will cause an asymmetric boundary condition
with respect to the axial mid-plane of the sample; therefore, the full

42

sample was modeled. The sample loading was simulated by specifying the horizontal (x) and vertical (y) displacements at the insulator-end tab interface. For sample configuration No. 1, the x displacement was set to zero along the bottom interface and set to -1.0 along the top interface between the flap terminations (i.e., x = 0.2 - 1.3 inches); the y displacement was set to zero along the left flapped side of the bottom interface to simulate flap-end tab contact which will occur when the top insulator-end tab interface is displaced to the left in the x direction; a similar y-displacement boundary condition was also used for the right flapped side of the top interface. For sample configuration No. 2, the x and y displacements were set to zero along the propellant-resin interface for the full sample length; the y displacement was set to zero along the top (insulator-end tab) interface to the right of the left flap termination (i.e., x > 0.2 inches); the x displacement between the flap terminations of the top interface was specified to be -1.0. For configuration No. 3, the x and y displacements were set to zero along the propellant resin interface for the full sample length; the y displacement was set to zero and the x displacement specified to be -1.0 along the full length of the top interface. The following material properties were used in the stress analyses:

Material	E (psi)	ν
Insulator	1000	0.4995
Liner	50	0.499975
Propellant	200	0.4999
Epoxy Resin	10,000	0.4

The calculated τ_{xy} shear stress and the maximum principal stress in the propellant adjacent to the liner are shown in Figure 2-73 for sample configuration No. 1, assuming conditions of plane stress. The shear stress is quite uniform between the flap terminations but drops off significantly 0.1 inch from the sample ends. The maximum principal stress is less than the shear stress everywhere along the bondline. If the sample fails at the liner-propellant interface, then the failure should result from pure τ_{rz} shear near the mid-plane of the interface.

Lines of constant maximum principal stress throughout the sample are shown in Figure 2-74. Stress concentrations occur as expected in the insulator layers adjacent to the bond terminations. However, no stress concentrations are evident in either the liner or the propellant. Lines of constant τ_{xy} shear stress for the liner and propellant layers of the sample are shown in Figure 2-75. Except for a small concentration near the bottom-right flap termination, the stress distribution is well behaved. The ratio of the maximum liner-propellant interface shear stress to the average shear stress (assuming a bond length of 1.5 inches) is 1.13.

The calculated shear and principal stresses in the propellant adjacent to the liner are shown in Figure 2-76 for sample configuration No. 2 assuming conditions of plane stress. The shear stress is larger than the maximum principal stress except near the right flap termination; however, even here the two stress components are almost identical, indicating a small normal stress component. Thus if the sample fails at the liner-propellant interface, it should fail basically as a result of τ_{xy} shear stress near the mid-plane of the interface. Lines of constant maximum principal stress for the full sample are shown in Figure 2-77. Stress concentrations occur in the insulator adjacent to the flap terminations. However, an additional concentration occurs at the propellant-end tab bond termination on the right side (the left side is in compression). The additional stress concentration in the propellant is expected and is a shortcoming in the sample design. However, the sample may or may not fail here depending upon relative propellant/case bond strength and plasticity effects. Lines of constant τ_{xy} shear stress in the liner and propellant layers of the sample are shown in Figure 2-78. This stress distribution is well behaved, and indicates a fairly uniform stress level between the flap terminations. The ratio of the peak τ_{xy} shear stress along the propellant-liner interface to the average shear stress (considering a 1.5 inch bond length) is 1.08.

The calculated shear and principal stresses in the propellant adjacent to the liner are shown in Figure 2-79 for sample configuration No. 3, assuming conditions of plane stress. A peak is present in the principal stress adjacent to the left side of the sample. This peak stress is approximately 15 percent higher than the τ_{xy} shear stress and is thus undesirable; otherwise, the stress distribution is good. Lines of constant maximum principal stress in the full sample are shown in Figure 2-80. The expected stress concentrations occur at the upper left insulator-end tab bond termination. However, additional stress concentrations occur at the left liner-insulator bond termination and near the left liner propellant bond termination. Further, the stress intensity at the lower right propellant end tab bond termination is significantly higher for configuration No. 3 than for configuration No. 2. Configuration No. 3 is likely to fail at a location other than the liner-propellant bondline. Lines of constant τ_{xy} shear stress for the liner and propellant layers of sample configuration No. 3 are shown in Figure 2-81. Small concentrations occur inside the propellant layer near the sample ends; otherwise, the stress distribution is very uniform. The ratio of the peak τ_{xy} shear stress to the average shear stress (considering the 1.5 inch bond length) is 1.05.

Stress solutions for the three candidate short lap shear samples assuming plane strain were not obtained. No significant difference will result from the two basic assumptions, plane stress or plane strain, if only trivial normal (σ_x, σ_y) stresses relative to the shear stress (τ_{xy}) are present. Further, 3-D effects in samples of finite width will result only from the normal stresses. The plane stress solutions obtained for the three candidate sample configurations should be representative

since the normal stresses in the areas of interest are small, particularly in Configurations No. 1 and 2. Stress solutions for variations in the insulator, liner, and propellant moduli also were not obtained. The properties studied are representative of a fairly stiff insulator in combination with a flexible propellant (low rate loading) and a very flexible liner. The effect of increasing the insulator stiffness would be to make configuration No. 1 more like configuration No. 3. A decrease in the insulator stiffness would tend to make the bond stress distribution less flat, similar to the liner stiffening effect shown in Figure 2-68 for a fully symmetric sample.

3. Experimental

The short lap shear sample, configuration No. 1, was chosen as the primary case bond shear sample. Procedures were developed for manufacture, testing, and data reduction. These procedures were evaluated through testing with the TP-H1123 propellant/case bond system. Preliminary testing of configuration No. 1 and 2 samples was performed on ANB-3066 material. Minimum testing of lap shear samples, configuration No. 1 and 2 was also accomplished for the TP-H1123 system. The round-flapped tensile sample (Figure 2-36), with the insulator fully bonded to the end tab, was selected as the secondary case bond shear sample. A minimum of torsion testing on this "tensile sample" was accomplished only for the TP-H1123 propellant/case bond system.

a. Configuration for Short Lap Shear Sample

The recommended configuration for the short lap shear sample is shown in Figure 2-82. The propellant layer is nominally 0.1 inch thick (high). For milling purposes, the total thickness of the liner and propellant layers should be specified because the liner usually has some waviness. A sample width of 0.5 inch was chosen on the basis of machining and handling convenience.

b. Manufacturing Procedure for Short Lap Shear Sample

The short lap shear samples were made by first cutting rectangular blocks of insulator/liner/propellant 1.5 inches long and several inches wide (9 inches for the 9 x 9 x 9 castings used in the program); the propellant thickness was greater than 0.1 inch. The rectangular blocks were individually placed on the milling machine and cut to a uniform liner-plus-propellant thickness of 0.16 inch. The milled blocks were then cut with a sharp knife into samples of 0.5 inch width.

The extra rubber layer for the primary (configuration No. 1) samples was cut from sheet stock with a knife. It was bonded to the propellant layer with Dexter-Hysol Epon 913.1 adhesive. Pieces of Teflon tape 0.2 inch long were then placed on the insulator ends and the unprotected rubber bonded to metal end tabs using Epon 913.1 adhesive.

(However, several good adhesives for bonding rubber to metal are available; the adhesive to bond propellant to the extra insulator layer will vary somewhat with the propellant formulation.)

The end tabs should be of the same 0.5 inch width as the sample. This helps in sample alignment and in the removal of extra end-tab adhesive.

c. Testing Procedure for Short Lap Shear Sample

All testing of lap shear samples under this program was accomplished using single sample grips. Hercules has a set of general purpose "ten-shear" fixtures (see Figure 2-83) which are used primarily for testing analog bond termination samples (Section III). These fixtures can be adjusted such that a single lap shear specimen can be tested without introducing moments into the Instron linkages. These fixtures performed well in the testing of the lap shear samples under this program. The two end tabs of the sample remained parallel all the way to sample failure. Testing of the samples using the ten-shear fixtures was accomplished in a manner similar to a uniaxial tensile sample using an Instron or high rate testing machine. Alternatively, special purpose grips can be designed to accommodate a fixed sample height.

d. Test Results

Preliminary testing was performed on lap shear samples of ANB-3066 propellant/case bond. Because of sample aging problems, data will not be given herein. However, the behavior of the bond samples is of interest because of the difference between the TP-H1123 and ANB-3066 propellant/liner bond systems.

Initial testing was accomplished at 2.0 in./min crosshead rate on four lap shear samples of configuration No. 3 (no extra rubber layer and no flaps). The samples failed in the sample gage section approximately midway along the sample length. Based on the FE stress analysis, this was somewhat unexpected. However, the liner layer for this bond system is very flexible and underwent a large shear deformation before failure occurred in the liner-to-propellant bondline. Thus, the linear FE stress solution is inaccurate near sample failure. Using the linear factor of 1.05 to derive the maximum bond shear stress from the average bond shear stress provides a standard (normalized by itself) shear strength of 1.0.

Testing was also accomplished on four ANB-3066 lap shear samples of configuration No. 2. Based on the linear factor of 1.08 to derive the maximum shear stress from the "average" shear stress, a normalized shear strength of 0.90 resulted. In these tests the large shear deformation of the liner caused the flapped insulator layer to curl around the one propellant end, putting a 90 degree bend in the insulator. In this

46

condition the flap should not transmit the shear load from the end tab to the liner than it does when the flap is parallel to the end tab. A more appropriate factor to derive the maximum bond shear stress from the "average" bond shear stress will probably lie closer to the value of 1.5/1.3, which is the sample length ÷ effective bond length. This factor of 1.15 provides a normalized bond shear strength of 0.96.

No lap shear (configuration No. 1) or torsional shear testing was accomplished on the ANB-3066 bond system. However, additional lap shear tests at crosshead rates of 0.2 and 200 in./min were accomplished using configuration No. 3 samples.

Shear testing on TP-H1123 propellant/case bond material was performed for a variety of sample configurations and test conditions. Test data are summarized in Table 2-4. No correction for cross-sectional area changes was made in any of the data reductions. Torsion tests were run on hollow propellant samples of 0.5 inch ID and 0.875 inch OD in the sample gage section; the ends were flared to suppress end failures (Refer to Reference 19 for details regarding this test). The propellant testing was performed at loading rates of 2, 12, and 128 rpm; testing at 128 rpm was performed at 0, 200, and 1000 psi superimposed pressure. Tests were performed on case bond torsion samples at 2 rpm; the sample configuration was the "round flapper" case bond tensile sample with the insulator fully bonded to the end tab. Lap shear tests were performed on the case bond using all three candidate sample configurations. However, the bulk of the lap shear testing was accomplished with configuration No. 1 samples.

Propellant and case bond shear strength for unpressurized conditions are shown in Figure 2-84 as a function of the time to failure. The propellant is significantly stronger than the case bond. The configuration No. 2 lap shear sample provided the highest case bond strength; the failure in these samples initiated at the liner/propellant interface midway along the sample length as desired. Failures in the configuration No. 3 samples initiated at the liner/propellant interface adjacent to an end; results were more scattered, suggesting an edge effect. Failures in the configuration No. 1 samples initiated at the liner/propellant interface away from the sample ends. However, flap curling similar to that in the ANB-3066 tests occurred in the configuration No. 1 tests to a noticeable degree; the factor to relate load to stress as obtained from the linear stress solution is therefore suspect. Two bond shear strength curves are shown in Figure 2-84. The higher curve is considered to be the best estimate for the strength accounting for the flap curling. The torsion value is slightly above the estimated bond strength curve. Plasticity effects will cause the torsion sample to give an optimistic value for the bond shear strength (this is why a solid torsion sample is a poor choice for a highly yielding material). The relative position of the torsion value suggests that the edge singularity which is predicted to occur when the liner/insulator layers extend beyond the OD of the propellant cylinder was not present (in agreement with the finite element stress analysis). Based on the tests run, the configuration No. 2 lap shear sample appears to work best for the TP-H1123 bond system.

TABLE 2-4

SHEAR TEST DATA FOR TP-H1123 PROPELLANT/CASE BOND
AT 77° F AND 50% RH

Sample Configuration	Loading Rate	Superimposed Pressure (psi)	Time to Failure[3] (min)	Maximum Shear Stress (psi)
Propellant Torsion[1]	2 rpm	0	0.31[3]	161[5]
Propellant Torsion	12 rpm	0	0.056	212
Propellant Torsion	128 rpm	0	0.0054	312
Propellant Torsion	128 rpm	200	0.0055	360
Propellant Torsion	128 rpm	1000	0.0071	452
Case Bond Torsion[2]	2 rpm	0	0.135	132
Case Bond Lap Shear - Conf 3	0.5 in./min	0	0.35	98
Case Bond Lap Shear - Conf 2	0.5 in./min	0	0.41	102
Case Bond Lap Shear - Conf 1	0.01 in./min	0	14.3	52
Case Bond Lap Shear - Conf 1	1.0 in./min	0	0.22	90
Case Bond Lap Shear - Conf 1	50 in./min	0	0.007 est[4]	150 est
Case Bond Lap Shear - Conf 1	50 in./min	200	0.0079	172
Case Bond Lap Shear - Conf 1	50 in./min	1000	0.0093	212

NOTES:
1. Hollow cylinder with 0.50 ID and 0.875 inch OD
2. "Round-flapped" case bond tensile sample, fully bonded to end tab
3. Failure defined as maximum load
4. Tests not performed, strength estimated from data for pressurized conditions
5. Values shown for all tests are averages from tests on 4 samples

It is interesting to compare the tensile (true cross-sectional area) and shear strength (no area correction considered to be necessary) for TP-H1123 propellant and case bond material. As shown in Figure 2-85, the propellant tension and shear and case bond tensile strengths are fairly close, particularly at lower loading rates. The case bond shear strength is significantly less, even considering the estimated strength curve. The tests on the four different types of shear samples all indicate a low value for the case bond shear strength; thus, the evidence is quite strong.

A propellant-case bond strength comparison for the ANB-3066 material (with approximately 3 weeks of sample exposure to the lab environment before testing) is shown in Figure 2-86. The data were normalized through division by the propellant tensile strength at 14 minutes time to failure. At this same failure time, the TP-H1123 propellant tensile strength is 100 psi. Thus, a relative comparison of loading rate effects for the two systems is easily made using Figures 2-85 and 2-86. No torsion tests were performed on ANB-3066 propellant. For the ANB-3066 system, the case bond tensile strength is significantly less than the propellant tensile strength. The case bond shear strength is higher than the propellant tensile strength, particularly at high loading rates. This is in contrast to the behavior of the TP-H1123 material. Rate effects on the case bond tensile and shear strengths are somewhat different for the two materials. For both materials, the evidence is overwhelming that the case bond does not behave like propellant by itself.

The effect of superimposed pressure on the shear strength for TP-H1123 propellant and case bond material is summarized in Figure 2-87 for the highest loading rates in each case. The times to failure at 120 rpm and 50 in./in. for the torsion and lap shear samples are reasonably close. (Refer to Table 2-4.) Superimposed pressure has a relatively small effect on the shear strength of both the propellant and case bond materials. A comparison of the effect of superimposed pressure under tensile and shear conditions is given in Figure 2-88. Superimposed pressure enhances the tensile strength much more than the shear strength. Under zero superimposed pressure, the propellant shear strength is equivalent to the tensile strength. However, at 1000 psi superimposed pressure, the propellant tensile strength is 50 percent greater than the propellant shear strength. Superimposed pressure enhances the case bond shear strength by approximately the same percentage as the propellant shear strength. The pressurized strength increase (relative to the zero pressure value) for case bond lap shear is similar to analog flap samples pulled in tension. The small pressure effect for the analog flap samples is attributed to the dominance of the edge stress concentration as the pressure suppresses dewetting. However, this edge stress concentration results from stresses normal to the bondline. The normal stresses are minimal compared with the shear stresses in the short lap shear sample. Thus, the edge concentration should not be a factor in the shear sample behavior under superimposed pressure. This position is fully supported by the fact that superimposed pressure has only a small effect on propellant shear strength as measured by torsion samples (with no edge concentration).

SECTION III

TASK III - BOND TERMINATION INTEGRITY

A. OBJECTIVE

The objective of this task is to develop simple analog test samples and procedures for the assessment of bond integrity at flap and right-angle bond terminations.

B. INTRODUCTION

This task interfaces directly with Tasks I, II, and IV. The parametric studies performed in Task I will be used to help design analog sample configurations which are representative of flap and right-angle corner bond terminations. Data from tests on the flap termination samples can be used to evaluate candidate failure criteria based on tensile and shear strength data obtained in Task II. Empirical bond strength data obtained from this task will be used to predict the performance of subscale motors tested in Task IV.

The bondline parametric studies of Task I, as well as motor experience, have shown that the bond terminations are the most critical regions for case bond structural integrity. Flaps and right-angle corners are among the bond termination configurations that occur most commonly in rocket motors. Flaps are used extensively to reduce both case bond and interport stresses/strains. Although the right-angle corner condition does not commonly occur in zero-burn grain configurations, it occurs often at advanced burn times.

The assessment of bond integrity at burning corners poses a highly complex problem. A right-angle corner constitutes a mathematical singularity (discontinuity), as indicated in Task I. For an operating motor, this discontinuity is continually being turned away. Both modulus (stress) and strength parameters are time- and temperature-dependent quantities for a solid propellant. Thus, bond integrity is determined by an interaction of several time varying processes. A first step in the assessment of integrity at regressing corners is the assessment of integrity at nonregressing corners. Further, integrity at nonregressing corners provides an upper bound on the integrity assessment for the regressing corner problem. Therefore, the nonregressing corner problem was addressed in this study.

Stress and strain gradients are very sharp in the local vicinity of flap terminations. (See Figures 1-2 and 1-3.) Because of the complex combination of normal, shear, and maximum principal stresses and strains that occur in the vicinity of flap terminations, which stress condition (shear, normal, maximum principal, or a complex combination) actually precipitates the case-bond failure is not certain. Further, large deformations occur next to the flap terminations. These large deformations occur

primarily in the flap and insulator rubber, but they affect the case bond as well. Thus, the most appropriate approach is to develop analog samples to simulate these complex conditions at flap terminations. Integrity predictions can then be made in terms of most any of the stress parameters, providing the motor condition is closely matched by the analog sample.

The basic analog flap termination sample configuration proposed for study is outlined in Figure 3-1. The top and bottom faces of the sample are bonded to end tabs and pulled at different angles to vary the relative level of bond normal and shear stress adjacent to the flap termination. A similar configuration is proposed for the right-angle bond termination discontinuity. (See Figure 3-2.)

The analog flap termination sample is similar to the lap shear and round-flapped tensile samples developed in Task II, in the sense that all contain flaps. However, a basic difference in philosophy was used in the sample development. Flaps in the tensile and shear samples are used to suppress edge concentrations, such that bond failure will occur away from the edges. Flaps in the analog sample are there solely to simulate the flap termination location in motors, and analog sample failure at the flap termination is crucial. Increased sample height, relative to the lap shear configuration, and combined tension/shear pull angles are used to cause failure as desired.

The flap termination sample configuration underwent considerable development for double-base bond systems prior to the initiation of this program. During this time, the sample length and height were fixed at approximately 1.5 and 1.0 inches, respectively. The sample development evolved primarily from test experience and is outlined in Figure 3-3. The first configuration studied had a single "flap termination" at the upper left corner of the sample. Three layers of rubber were used in the sample. The upper and lower layers represented the insulator and flaps, respectively; the middle layer was included to minimize the end termination stresses in the rubber layers by providing a fillet under load. Samples of this configuration consistently failed at the lower-right corner in the end-tab bond when the upper end tab was pulled to the left. Configuration No. 2 was envisioned to prevent failure at the lower end-tab bond. However, failure then consistently occurred in the case bond at the upper-right corner of the sample. Additional flapping (configuration No. 3) caused failure to again occur at the lower-right corner. The fully symmetric configuration No. 4 finally generated case bond failures consistently at the upper left flap termination as desired; numerous test data were obtained for double-base bond systems using this sample configuration. Configuration No. 4 represented the analog flap termination sample development status at the initiation of the case liner-bond program. Configurations No. 5 and 6 evolved during this program; FE stress solutions were obtained for both of these configurations.

The analog "discontinuity" sample for studying bond integrity at right-angle bond terminations is a parallel to the analog flap sample. Very little had been done with this sample prior to the case liner-bond program. Singularity theory must be used in the analysis of this sample, similar to the cylinder in Task I.

Because the analog flap and discontinuity samples are directly related to the cylinders studied in Task I, much of the background for these samples is presented in Section II. The reader should be familiar with this material. In subsequent discussions of the analog samples, this material will be used freely with minimum repetition.

Subsequent discussions of the Task III material is separated into sections relating to the analog flap termination sample and the analog discontinuity sample. The flap sample discussion begins with the stress analysis; both 2-D plane stress and 3-D finite-element analyses were performed. The experimental portion of the flap sample studies is then given. The discussion concludes with the analog discontinuity sample, as presented in terms of both stress analysis and experimental studies.

C. ANALOG FLAP TERMINATION SAMPLE STUDIES

1. Stress Analysis

The stresses in a given direction at any point "P" in a 2-D symmetric body pulled at an arbitrary angle can be separated into those resulting from tension (90° pull angle) and shear (0° pull angle), as shown in Figure 3-4. The top and bottom sides of the body are assumed to be bonded to rigid members; the force, F, is assumed to pass through the mid-point of the body so that that body is in equilibrium under this force system. At the point "Q" on the top side of the body, forces exist in vertical (y) and horizontal (x) directions; this situation is indicated in the circular key above the point Q. Because of force equilibrium, the bottom side of the body can be assumed to be rigidly fixed without introducing any new system forces. Superposition of the stress solutions for tension and shear loading provides the desired solution for the force inclined at the arbitrary pull angle, α.

A stress component, σ, at point P can be represented mathematically as the result of stresses from forces F_x, F_y, and M applied to point Q on the sample.

$$\text{Thus,} \quad \sigma = k_x F_x + k_y F_y + k_\alpha M \tag{3-1}$$

The coefficients k_x, k_y, and k_α are basically geometrical factors relating the stress component at point P to the forces at point Q. For a force F acting at the angle α,

$$\sigma_\alpha = k_x (F \cos \alpha) + k_y (F \sin \alpha) + k_\alpha (\ell F \sin \alpha) \tag{3-2}$$

For tension loading ($\alpha = 90^{\circ}$), the stress at point P can be defined as σ_{90}. Thus, from Eq. (3-1), $k_y = \dfrac{\sigma_{90}}{F_{90}}$. For shear loading ($\alpha = 0^{\circ}$), the stress at point P can similarly be defined as σ_0. Thus,

$$\sigma_0 = k_x F_0 + k_\alpha (F_0 \ h), \text{ and } k_x = \frac{\sigma_0}{F_0} - k_\alpha h$$

Substituting for k_x and k_y in Eq. 3-2 provides:

$$\sigma_\alpha = \left(\frac{\sigma_0}{F_0} - k_\alpha h\right)(F \cos \alpha) + \left(\frac{\sigma_{90}}{F_{90}}\right)(F \sin \alpha) + K_\alpha (\ell F \sin \alpha).$$

Recognizing that $\ell/h = \cot \alpha$ and regrouping terms results in cancellation of the moment; division by F provides:

$$\frac{\sigma_\alpha}{F} = \left(\frac{\sigma_0}{F_0}\right)\cos \alpha + \left(\frac{\sigma_{90}}{F_{90}}\right)\sin \alpha. \tag{3-3}$$

Eq. 3-3 indicates that the stress at point P for a unit force acting through the mid-point of the body is equal to the vector component of the stress at P per unit force in the shear direction plus the stress per unit force in the tension direction. FE stress solutions for the analog flap termination sample were thus obtained for tension and shear loadings only. Stress values for arbitrary pull angles were obtained from these two solutions through the application of Eq. 3-3.

a. Three-Dimensional Stress Analysis

A 3-D stress analysis was performed on the analog flap termination sample. Stress solutions were obtained primarily to study the effect of sample width (thickness). The stress distribution through the sample thickness is of great importance to the sample design, and this distribution cannot be obtained except with a 3-D model. The 3-D analysis was performed early in the case liner-bond program. The sample configuration analyzed has two layers of rubber adjacent to the case bond (configuration No. 5 in Figure 3-3). Thus, the stress analysis is not fully representative of the final sample, configuration No. 6.

The stress analysis was performed using the Thiokol 3-D FE stress analysis program. This program uses reformulated (for high Poisson's ratio applications) dodecahedron elements, comprised of tetrahedron elements. The runs were made on the CDC 6600 computer (with extended core) at Kirtland AFB, New Mexico. The program has a capacity for approximately 3500 nodes. However, because of the detail required in modeling the case bond system, sample symmetry was used to the maximum extent to remain within the program capacity.

53

The model for the analog flap termination sample is outlined in Figures 3-5 and 3-6. Only 1/8 of the total sample was modeled. The same case bond system was assumed to have been used at both the top and bottom faces of the sample. The sample was loaded by displacing the top face of the insulator layer either vertically (z direction tension loading) or horizontally (y direction shear loading). The boundary conditions for the six faces of the sample are given in Figure 3-5 for both tension and shear loading; the boundary conditions can be specified for the FE model totally in terms of displacements. Material properties used in the analysis are also given in Figure 3-5. The adhesive used to bond the two insulator layers together was assumed to have the same modulus as the insulator. However, 3-D analyses (performed under internal company funding) on analog samples with double-base bond systems have shown that adhesive moduli of 1000 and 100,000 psi cause little difference in the 3-D stress distribution.

The grid for the FE model of the 1/8 section is shown in Figure 3-6. The nodes are contained in 25 repeating planes, with each plane containing 128 nodes (105 elements). All the elements (2520 total) in the model are thus rectangular prisms. The grid structure is graduated near the outside face of the model to pick-up edge concentrations, and graduated near the flap termination to pick-up the high stress gradients expected in this area. The plane of elements comprising the adhesive (element plane 19) was given an infinitesimal modulus and small Poisson's ratio outboard of the flap termination to simulate the gap between the insulator layers.

The computed normal (σ_z) stress distribution for tension loading is shown in Figure 3-7 for Element Plane 8 (i.e., the first row of elements in propellant next to liner). Stress values computed at the element centers are plotted through the sample thickness for the first 12 rows of elements from the y midplane of the sample. Both triaxial and edge effects are present in the solution. The triaxial effect appears to dominate the edge effect; however, due to the relative coarseness of the grid, the edge effect is not fully characterized in the solution. The highest normal stress occurs at the x (thickness) mid-plane of the sample ($x = 0$), independent of position along the sample length. Stresses are highest in Row 6, which is approximately 0.11 inch inboard of the flap termination (i.e., the insulator-to-insulator bond termination). However, the solution has significant stress oscillation. This is normal for 2-D FE solutions with values of Poisson's ratio near 0.5. The pattern of oscillation for the 3-D solution is interesting because the oscillation is noticeable only in the y direction. Stresses plotted as a function of x (or z) do not indicate any oscillation. Smoothing is necessary before the stress distribution can be properly evaluated in the y direction.

The main features of the stress distribution of Figure 3-7 are indicated in Figure 3-8; values are plotted only for Rows 1, 6, and 12 to better identify the stress distribution. The largest difference between the maximum and the minimum stress along any row occurs in Row 6. However, the stress distribution in Rows 1 and 6 are very similar. The triaxial and edge effects both seem to run the length of the sample, in a proportional manner.

The σ_z stress distribution in Rows 1, 6, and 12 of Element Plane 11 is shown in Figure 3-9. Element Plane 11 (see Figure 3-6) is located near the middle of the liner. In Element Plane 11, the triaxial effect suppresses any edge effect. Thus, the modulus of the liner relative to the propellant and insulator has a significant effect on the stress distribution for this sample. As the liner becomes flexible, the triaxial effect should become more dominant; as the liner becomes stiffer, the edge effect may dominate. Actually, the edge effect may be dominant for the liner-to-propellant modulus ratio studied, but the grid resolution is not sufficient to fully characterize it.

Smoothed distributions for the σ_z stress along Element Column 1 (near the thickness midplane of the sample) are shown in Figure 3-10 for Element Planes 8 and 11. The peak stress in Plane 11 occurs at approximately 0.08 inch inboard of the flap termination; for Plane 8, the peak shifts to approximately 0.11 inch. The peak values of 1560 psi for Plane 11 and 1475 for Plane 8 represents the maximum σ_z stress values calculated in these planes.

Smoothed distributions for all of the key stress components along Element Column 1, Plane 8, are shown in Figure 3-11. The maximum principal stress and the σ_z stress are almost identical. The σ_x stress is less than 10 percent of the peak σ_z stress, and the σ_y stress is less than 20 percent of the peak σ_z stress. The only nonzero shear stress at this location is τ_{yz}; it reaches a (negative) peak value of approximately 20 percent of the maximum σ_z stress. Overall, the analog flap termination sample pulled in tension is a fairly good "uniaxial" case bond tensile sample.

The important features of the stress distribution for the analog flap termination sample pulled in shear are summarized in Figures 3-12 through 3-15. The σ_z stress in Element Plane 8 for Rows 1, 6, and 12 is shown in Figure 3-12, through the sample thickness. The triaxial effect is definitely present, but the edge effect is more subdued than for tension loading. In the liner itself, the σ_z stress distribution through the sample thickness for shear loading is similar to that for tension loading. (See Figure 3-13.) Smoothed distributions for the σ_z stress along Element Column 1 are shown in Figure 3-14 for Element Planes 8 and 11. The stress peaks out approximately 0.05 inch inboard of the flap termination, then drops to zero at the midplane of the sample as required by the boundary conditions for antisymmetry. All of the key stress components along Element Column 1, Plane 8, are shown in Figure 3-15 for shear loading. The dominant stresses are σ_z, τ_{yz}, and σ_{max}.

55

A desirable condition is to have the stress distribution through the sample thickness as uniform as possible. The proposed analog flap termination sample has a thickness of 0.50 inch. This moderate thickness provides a state of stress intermediate to plane stress (infinitesimally thin) and the plane strain (infinitely thick). In an attempt to reduce the stress variation through the sample thickness, the thickness was reduced to 0.25 inch. A 3-D stress analysis was performed for the thinner sample using a slight modification of the FE model shown in Figure 3-6. The elements for the 0.25 inch thick model were simply reduced in thickness by half relative to those for the 0.5 inch thick model. Computations were made for tension loading only.

The distribution of the σ_z stress in Element Plane 8 for 0.25 and 0.50 inch thick analog flap samples is compared in Figure 3-16. The 0.25 inch sample exhibits less triaxial effect but has a stronger edge effect than the 0.50 inch sample. The normalized distributions along Row 1 (nearest the y midplane) and Row 6 (nearest the position of peak normal stress) are almost identical.

Overall, the distribution for the 0.25 inch sample is flatter than that for the 0.50 inch sample. However, the sample thickness would probably have to be less than the liner thickness to fully suppress the triaxial effect. Samples of 0.06 inch thickness would be impractical from the standpoint of manufacturing and testing procedures. A very thick (approaching plane strain conditions) sample appears to be a desirable choice from a stress distribution viewpoint. Considering the amount of bond material required, however, very thick samples also have significant limitations. For the TP-H1123 bond system, the 0.50 thick sample seems to be a reasonable compromise.

Data reduction for analog sample tests require the maximum principal stress per unit applied force. The applied force in the 3-D stress analysis was computed by integrating the calculated stress distribution in Element Plane 1. The results are as follows for the 0.5 inch-thick sample, where F is for the full sample:

Loading Direction	σ_z/F $(1/in.^2)$	σ_{max}/F $(1/in.^2)$	Reduction in Cross-Sectional Area, $(\Delta A/A_0)/u$ $(1/in.)$
Tension	2.36	2.36	0.95
Shear	5.23	5.65	0.27

In addition, it is useful to evaluate the approximate change (decrease) in cross-sectional area for a unit displacement. Computed results for the element with the largest maximum principal stress are given above. The 3-D thickness effect is summarized in Figure 3-16. The maximum value of the σ_z stress relative to the average σ_z stress through the sample thickness is approximately 1.15 for the 0.50-inch-thick sample and 1.13 for the 0.25-inch thick sample. These factors should be applied to results from 2-D stress analyses to account for stress variation in the thickness direction.

b. Two-Dimensional Stress Analysis

A 2-D stress analysis was performed on the analog flap termination sample, in addition to the 3-D stress analysis, for at least four reasons:

(1) The 3-D solution involved a fully symmetric sample with two liner layers, which cannot be manufactured practically.

(2) The 3-D stress analysis was performed on an intermediate configuration of the analog sample (configuration No. 5 of Figure 3-3) which contained extra insulator layers; the final sample configuration does not contain these insulator layers.

(3) A study is desirable to investigate the effects of variations in liner moduli at a lower cost than the 3-D analysis allows.

(4) The testing program involved samples with end tabs which extended beyond the flange terminations, similar to the lap shear samples; this extension causes an asymmetric (about the z mid-plane) sample behavior.

The sample configuration analyzed two-dimensionally is shown in Figure 3-1. The full sample FE model used for the 2-D analysis is shown in Figure 3-17. The model includes the 0.005 inch adhesive layer used to bond the propellant to the 0.2 inch-thick insulator layer on the bottom of the sample. The case bond liner was modeled with three element rows; the center of the element row in the propellant next to the liner is 0.015 inch from the bondline. The coordinate system which will be used for discussion of the 2-D stress solution is the same as that for the 3-D analysis; i.e., the vertical axis is the "z" direction, the horizontal axis is the "y" direction, and the "x" axis being normal to the plane of the 2-D solution.

To load the sample model in tension and/or shear on the top and bottom edges, the following displacement constraints were used on the left flap, insulator-to-end tab bond, and right flap:

Loading Condition	Edge	Left Flap		End Tab Bond		Right Flap	
		y Direct.	z Direct.	y Direct.	z Direct.	y Direct.	z Direct.
Tension	Top	--	--	0	1.0	--	--
	Bottom	--	--	0	0	--	--
Shear (symmetric)	Top	--	--	-1.0	0	--	--
	Bottom	--	--	0	0	--	--
Shear (sliding contact)	Top	--	--	-1.0	0	--	0
	Bottom	--	0	0	0	--	--

Thus for tension loading, the left and right flaps were allowed to separate from the end tab. However, two shear loading solutions were obtained. The symmetric solution assumed that the flap could move freely in either direction; the "sliding contact" solution considered that the flap would touch the end tab on the lower left and upper right flap surfaces. By setting the z displacement to zero and letting the y displacement go unrestrained, a sliding contact condition was achieved.

The material properties considered in the stress analysis are as follows:

Material	E (psi)	ν
Insulator	1100	0.49945
Liner	200, 850	0.4995, 0.49958
Propellant	850	0.49958
Adhesive	10,000	0.4

Stress solutions were obtained for a stiff liner (same modulus as propellant) and a flexible liner typical of the TP-H1123 case bond system.

Lines of constant maximum principal stress in the analog flap sample pulled in tension ($E_{liner} = 200$) are shown in Figure 3-18; only 1/2 of the sample need be considered due to symmetry. Plane stress assumptions were used with regard to constraint in the thickness direction. The stress concentrations in the vicinity of the flap terminations are very evident. The distribution is quite symmetric about the vertical midplane of the propellant. However, the stress is higher in the propellant

along the top (propellant-to-liner) bondline, as compared with the bottom (propellant-to-adhesive) bondline, due primarily to the increased insulation thickness on the bottom of the sample. Lines of constant maximum principal stress for the analog flap sample pulled in shear (sliding contact and $E_{liner} = 200$) are shown in Figure 3-19. In the liner and propellant, only two bond terminations have stress concentrations; i.e., the top left and the bottom right. This condition is as expected, and failure is most likely at the most highly stressed locations (assuming a maximum principal stress failure criteria is applicable). The maximum principal stress is a good measure of the combined influence of the bond normal and shear stress, and thus it is a good indicator of the probable bond failure location. Stresses at the top bondline are not greater than at the bottom bondline; thus, failure is equally likely at each bondline, depending upon the relative bond strengths.

The "case bond" normal (σ_z) stress in the first row of elements adjacent to the liner is shown in Figure 3-20 for tension loading. Stress distributions for the two liner moduli are similar. The stiffest liner provides the highest gradient, but the gradient is small between the flap terminations. The stress is normalized by the average σ_z stress for the full 1.5-inch sample length. Thus, if the stress were uniform between the flap terminations and zero outside the terminations, the "peak" normalized σ_z stress would be 1.67. Because the peak σ_z stress is only 1.45 for the sample, the flaps are carrying approximately 18 percent of the load.

The case bond shear stress (τ_{yz} in the first row of propellant elements adjacent to the liner) is shown in Figure 3-21 for tension loading. The values are normalized by the average σ_z stress for the 1.5 inch sample length. Peak values of approximately 0.3 for the shear stress occur outside the flap termination. The shear stress magnitude is small compared with the normal stress.

The maximum principal stress in the first row of propellant elements adjacent to the liner is shown in Figure 3-22 for tension loading. The distribution is very similar to that for the normal stress because of the small shear stress. Difference in the stress distribution for the two liner stiffness values is minor, further substantiating the conclusion that the liner modulus has little influence (within a normal range for case bond systems) on the liner-to-propellant bondline stresses in the analog sample pulled in tension. This is similar to the cylinder of Task I under shrinkage loading.

Results for shear loading of the analog flap termination sample are complicated by the different assumptions relative to contact between the flaps and end tabs. The calculated values for the σ_z, τ_{yz}, and maximum principal stresses in the first row of propellant elements adjacent to the liner are shown in Figures 3-23 through 3-28. Plane stress conditions were used for modeling the thickness direction. All the stress values were normalized by the average τ_{yz} shear stress over the 1.5-inch

sample length. Because of the multiple curves for each stress component, solutions for the 200 and 850 psi liner moduli were plotted separately.

The influence of the flap-to-end tab contact on the stress components for the analog flap sample pulled in shear is large. As shown in Figure 3-23, the case bond normal stress peak is 2.4 with no contact between the flaps and end tabs. However, when the lower left and upper right corners are allowed to contact the end tabs (and the z displacement of the end tab is constrained to zero), a positive stress peak of only 1.1 occurs at the flap termination of interest. The z displacement constraint is unreasonable in a testing situation. A more appropriate constraint is that the net force in the z direction be zero. Forces applied to the sample using the ten-shear fixture should tend to keep the end tabs from rotating. Thus, the "zero z force" solution can be obtained by determining the net z force in the zero-displacement solution; then, applying this force to the analog sample loaded in tension and adding the stresses to those for the zero-displacement shear solution. The result of this exercise is shown in Figure 3-23 for the σ_z stress component; a peak value of 1.7 occurs for this condition.

A moderate difference is present in the σ_z stress components per unit applied shear stress (as well as the other stress components) for the two liner moduli studied. The peak stress value of 2.8 for $E_{liner} = 850$ (See Figure 3-24) is approximately 15 percent larger than the 2.4 peak value of $E_{liner} = 200$ and no flap-end tab contact. The effect of flap-end tab contact on the τ_{yz} shear stress is shown in Figure 3-25 for $E_{liner} = 200$, and in Figure 3-26 for $E_{liner} = 850$. Little difference exists between the solutions for zero net force and zero displacement contact conditions. However, the peak shear stress for the no contact condition is significantly higher than for the sliding contact conditions. The stiffer liner tends to sharpen the shear stress gradient, causing higher positive and negative peaks than the softer liner.

The maximum principal stress (in the y-z plane) in the first row of propellant elements adjacent to the liner is shown in Figure 3-27 for $E_{liner} = 200$ and in Figure 3-28 for $E_{liner} = 850$. Trends for the principal stress near the left flap termination are similar to those for the normal stress. The principal stress shown is in the y-z plane, because a negative value occurs near the right flap termination for $E_{liner} = 200$; the maximum principal stress considering all coordinate directions would be zero here for plane stress conditions. Based on a maximum principal stress failure criteria, the analog flap sample definitely should not fail at the right flap termination. The zero-force, sliding contact solution provides a peak principal stress value of approximately 83 percent of the no-contact solution.

60

A comparison between the 2-D and 3-D stress solutions is given in Figures 3-29 and 3-30. The 2-D solution for the maximum principal stress in the first row of propellant elements adjacent to the liner is shown for tensile and shear loading. No contact was assumed to occur between the insulator layer and end tabs to be consistent with the 3-D model assumptions. The 3-D model (Figure 3-5) has two insulator layers of 0.08 inch thickness each; whereas, the 2-D model has only one insulator layer of 0.10 inch thickness on the liner-bond side, and one insulator layer of 0.20 inch thickness on the adhesive-bond side. Stress values obtained from the 3-D solution were plotted in Element Plane 7 (Row 1) to provide a consistent vertical distance fror the end tab. The 3-D values are significantly higher than the 2-D values. However, this is to be expected. The thickness factor of 1.15 was used to increase the 2-D values to an approximate 3-D solution for the thickness mid-plane location. The adjusted 2-D solution agrees quite well with the 3-D solution for both tension and shear loading. Considering the difference in the sample geometry studied and the slight differences in material properties, the agreement between the adjusted 2-D and 3-D solutions is excellent. Further, it is shown that 2-D solutions are applicable to the analog flap sample when the 1.15 factor is used to derive the maximum bondline stresses from tne "average" (thickness direction) stresses.

The effect of pull angle on the normal and shear stress distribution in the analog flap termination sample is shown in Figure 3-31. The stresses in the first row of propellant elements adjacent to the liner are plotted in the immediate vicinity of the flap termination; the solution shown is for a liner modulus of 200 psi. The stress values are normalized such that the peak normal stress is 1.0 for each pull angle. The stress distributions for pull angles intermediate to 0 and 90 degrees were obtained through the techniques described in Paragraph C.1 of this section; basically, it involves the superposition of vector components of the tensile and shear loading solutions. As the pull angle is increased from 0 to 90 degrees the normal stress gradient flattens and the shear decreases in magnitude.

A comparison of the case bond normal and shear stress distributions for analog samples pulled in shear with and without flap-to-end tab contact is shown in Figure 3-32. Little difference is present in the two stress distributions. The flap-end tab contact tends to flatten the normal stress distribution and increases the shear slightly relative to the no contact condition. The biggest effect of contact apparently occurs in the relative magnitude of the stresses for a unit sample force.

The effect of pull angle on the maximum principal "bond" stress (i.e., propellant stress 0.015 inch inboard of the bond liner) per unit applied sample force is shown in Figure 3-33. Flap-to-end tab contact is calculated to occur at pull angles less than 34 degrees. In the region of 0 to 34 degrees pull angle, two values are shown for the stress, contact, and no-contact. The values are normalized to the stress per unit force at the 90-degree pull angle. Thus, the curves shown can be viewed as effective stress concentration factors for pull angles other than 90 degrees, relative to the 90-degree condition.

A comparison of the case bond stress distribution in the vicinity of the flap termination for the analog sample and the Task-I cylinder is shown in Figure 3-34. A pull angle betwe ˜ 15 and 30 degrees provides a good match for the normal and shear stresses i. the cylinder. Slightly different values were used for the propellant-liner-insulator moduli in the stress solutions for the analog sample and the cylinder as follows:

Configuration	$E_{propellant}$	E_{liner}	$E_{insulator}$
Analog Sample	850	200	1100
Cylinder	200	100	1000

However, these differences should have little effect on the stress distributions. The applicability of the analog sample to rocket motor conditions at flap terminations is thus excellent with respect to the bond normal and shear stresses. The biggest deficiency in the analog sample is its inability to simulate the hoop stress. However, the hoop stress is probably not a large factor in case bond integrity at bond terminations.

2. Experimental

    a. Configuration for Analog Flap Termination Sample

    The recommended configuration for the analog flap termination sample is shown in Figure 3-1. The total height of the liner plus propellant is 1.0 inch. The top insulator layer is 0.1 and the bottom layer 0.2 inch thick. An epoxy resin (such as Epon 913.1) is used to bond the bottom insulator layer to the propellant. The sample is 1.5 inch in length and 0.5 inch wide (thick). The top and bottom insulator faces are bonded to end tabs, with 0.3-inch long unbonded portions left on each end of the insulator layers. The end tabs should be made only 0.9 inch long to allow the unbonded insulator portions to extend out over the end tabs. Alternatively, Teflon tape can be used to ensure no bond between the end tabs and flaps if the end tabs are more than 0.9 inch in length.

    b. Manufacturing Procedure for Analog Flap Termination Sample

    The analog flap termination samples were manufactured at Hercules primarily on the band saw. Rectangular blocks of insulator/liner/propellant were cut 1.5 inch long, 0.5 inch wide, and 1.0 (liner plus propellant) inch high. To provide a uniform sample height, the flat insulator/liner/propellant sheets should first be milled and then cut into the rectangular blocks on the band saw. This procedure was not used in the case liner-bond program, and height variability was greater than desired.

Blocks of TP-H1123 propellant were cut dry at room temperature. The material for the blocks came from the 9 x 9 x 9 castings with the case bond on one face.

The recommended thickness of insulator layer on the bottom of the sample is 0.2 inch. This is not a standard commercial thickness, and a special order was placed with a rubber vendor to obtain the proper thickness. Alternatively, vulcanization can be used to bond two standard 0.1-inch thick insulator sheets together to obtain the 0.2 inch sheet. Rectangular pieces 0.5 x 1.5 inch are then cut with a band saw or knife. The thick insulator block is bonded to the propellant using an epoxy resin. (Epon 913.1 was used in the case liner-bond program.)

The top and bottom faces of the respective insulator layers are bonded to metal end tabs, using an appropriate epoxy resin (Epon 913.1). As stated earlier, the end tabs should be only 0.9 inch long (and 0.5 inch wise to ensure better centering and minimize adhesive runs on the sides of the sample). However, in the case liner-bond program, end tabs longer than 1.5 inches were used; pieces of Teflon tape 0.3 inch long and 0.5 inch wide were used to ensure a debond between the insulator and end tab in the flapped regions of the sample.

c.   Testing Procedure

For testing purposes, the metal end tabs of the samples are attached to "ten-shear" fixtures (see Figure 2-83) set for the appropriate pull angle. Fixture alignment is set to exert the line of force through the midpoint of the sample. Testing is then accomplished as if the sample were an ordinary tensile sample. Zeroing of the load cell is accomplished with the top fixture and sample hooked up. The crosshead (attached to the bottom fixture) is moved to generate negligible stresses as the sample is attached to the bottom fixture.

Failure (initiation of a separation) of the case bond during testing has always been observed to coincide with the peak load on the load versus displacement trace; this is true of the TP-H1123 bond system and double-base systems as well. Photographs showing a double-base analog sample, pulled at 45 degrees, are provided in Figure 3-35. The first photo shows a sample under zero load, then under load and before failure, and finally after failure has initiated.

d.   Test Results

Approximately 60 constant displacement-rate tests were conducted on analog flap termination samples under this program. Testing was performed on TP-H1123 case bond material using Instron and MTS high-rate testers. All testing was performed at $77 \pm 2^{\circ}$ F and 45 ± 10 percent RH. Tests were performed at a variety of pull angles, crosshead rates, and superimposed pressures. The test conditions and associated data are summarized in Table 3-1.

TABLE 3-1

TEST DATA FOR TP-H1123 ANALOG FLAP TERMINATION SAMPLES

Pull Angle (degrees)	Crosshead Rate (in./min)	Superimposed Pressure (psi)	Maximum Load (lb)	Displacement at Maximum Load (in.)	Time to Maximum Load (min)
90	0.01	0	35.8*	0.152*	15.2*
90	1	0	57.1	0.212	0.212
90	100	0	106.2	0.340	0.00324
90	100	200	127.6	0.260	0.00262
90	100	1000	153.0	0.255	0.00253
0	0.01	0	21.0	0.345	34.5
0	1	0	44.6	0.577	0.575
0	100	0	73.5	0.681	0.00581
0	100	200	91.5	0.837	0.00334
0	100	1000	103.7	0.890	0.00885
0	0.2	0	32.2	0.345	1.72
30	0.2	0	27.7	0.267	1.33
45	0.2	0	29.2	0.214	1.07
60	0.2	0	32.2	0.171	0.85
90	0.2	0	53.2	0.161	0.80

*Note: Data are averages for four samples per condition.

64

Failure in all the analog flap termination sample tests occurred at the liner-propellant interface. (A few preliminary tests were run with a 0.1-inch thickness for the insulator layer bonded to the propellant: failure in these tests occurred frequently at the propellant-adhesive bondline; therefore, the thickness of this insulator layer was increased to 0.2 inch, and no further failures occurred at this location.)

Case bond strength data obtained from analog flap samples pulled in tension were presented in Section II (Table 2-4 and Figures 2-47 and 2-48). Figure 2-47 showed that the case bond tensile strength, as measured by the analog flap sample, is comparable to that measured by the round-flapped tensile sample. However, deviation between the analog and tensile samples begins to occur at the higher loading rates. The relatively small effect of superimposed pressure at the highest loading rate (Figure 2-48) suggests that the analog samples are experiencing edge failures for the high-rate, pressurized condition. The case bond (true) tensile strength for the 90-degree pull angle was obtained from the load and displacement at failure using factors derived primarily from the 3-D stress analysis. The load-force factor of 2.36 was used to derive the engineering stress from the measured load. The reduction in cross-sectional area of the sample, (propellant adjacent to the liner at the location of maximum normal stress) was derived from the 3-D solution. However, because the 3-D model contained two extra rubber layers, the area change versus end-tab displacement factor was modified. A modified factor, $(\Delta A/A_0)u = 0.8$, was used. The 2-D analyses were used to help determine this factor.

The effect of pull angle on the failure load for the analog samples tested at 0.2 inch/min is displayed in Figure 3-36. The failure load for the 90-degree pull angle is divided by the failure loads for the other pull angles (i.e., the maximum principal stress concept does not enter directly into the experimental curves). Two curves are presented for the experimental results: one curve presents that load ratio without any consideration for the increase in the time to failure with decreasing pull angle, and the other curve is based upon the load decrease for the 90-degree pull angle as a function of the time to failure.

The experimental data for the various pull angles are compared with the analytical curves for normalized maximum principal stress in Figure 3-36. Because the experimental curves lie below the analytical curves, the case bond appears to be stronger at pull angles less than 90 degrees than predicted by a maximum principal stress failure criterion. The lower pull angles have bond tensile and shear stresses more nearly equal in magnitude than the 90-degree pull angle; thus, behavior of the type observed may be anticipated. Many materials tend to carry tensile and shear stresses in combination better than predicted by a maximum principal stress failure criterion.

The effect of loading rate on the load at failure for samples pulled in shear and tension is compared in Figure 3-37. The different loading rates influence the loads at failure in a similar manner. However, the shear data have more scatter. This is thought to be a result of poor control on sample height, which will affect the shear behavior much more than the tensile behavior.

The effect of superimposed pressure on the load at failure for samples pulled in shear and tension at 100 in./min is illustrated in Figure 3-38. Superimposed pressure increases the failure load by the same amount for tensile and shear pull angles. However, the load increase caused by superimposed pressure is much less than the case bond tensile strength increase, as measured by round-flapped samples. Thus, the theory proposed is that the analog samples are failing at the edges in both tension and shear attitudes.

5. **Motor Application**

In view of the uniqueness of the analog sample approach to assessing bond integrity at flap terminations and the problem with apparent edge failures for the TP-H1123 bond system, it is appropriate to outline a recommended approach for bond integrity predictions at flap terminations in motors. The recommended approach can be broken down into six steps as follows:

a. Calculated Bondline Normal and Shear Stress Distribution

The normal and shear stresses in the propellant next to the liner should be calculated in the vicinity of the flap termination. Moduli for the propellant, liner, and insulator appropriate to the loading time and temperature of interest should be used in the stress calculation. The solution need be only elastic.

b. Determine the Appropriate Pull Angle for the Analog Sample

The bondline normal and shear stress distribution calculated for the motor should be compared with that for the analog sample. For internal pressure loading, it is appropr te that $\sigma + P$ (where P is the internal pressure) be used in the matcl of normal stress distributions. Figure 3-34 is most applicable in this gard for propellant-liner modulus ratios similar to TP-H1123 samples lr ed at moderate rates and near 77° F.

c. Compute Time-Dependent Value for σ_{max} in Motor

The peak value of the maximum principal stress in the propellant, adjacent to the liner at the flap termination, should be calculated for the motor as a function of time. Appropriate viscoelastic theory should be used.

66

d. **Measure Case Bond Strength in Tension**

The case bond strength should be measured in tension over
a range of rates, temperatures, and superimposed pressures bracketing the
calculated response in the motor. The round-flapped tensile sample of
Task II is most appropriate in this regard. However, the analog flap
sample pulled at 90 degrees may provide acceptable data. For the TP-H1123
bond system, the analog sample falls short at high rates under superimposed
pressure, apparently due to edge failures.

e. **Measure Case Bond Strength at Different Pull Angles**

Analog flap samples should be pulled at different angles
at the temperature/rate/pressure combination most appropriate to the motor
loading condition. The pull angles should bracket the pull angle deter-
mined in Step b. As a minimum, samples should be tested at 90 degrees
and the Step b angle.

f. **Compare Predicted and Allowable Bond Strengths**

The predicted value of σ_{max} at the bond termination should
be compared with the allowable value determined from steps d and e. For
pressure loading, it is appropriate to deal with $\sigma_{max} + P$ instead of σ_{max}
for both computed and allowable values. (Task IV shows that the deviatoric
stress is a better stress parameter than $\sigma_{max} + P$ for pressure loading
conditions; the deviatoric stress parameter apparently compensates for
differences in hoop stress effects in the analog samples and motors as
well as for imprecise matching of normal and shear stress distributions.)
The allowable value of σ_{max} can be taken from the tensile test data,
adjusted by the ratio $(\sigma_{max}/F)_{analytical} \div (\sigma_{max}/F)_{experimental}$ at the
Step b pull angle. The analytical/experimental ratio (See Figure 3-36)
adjusts for the increased bond strength due to combined tension and shear
stresses and for finite deformation effects at the flap termination as
well.

D. ANALOG DISCONTINUITY SAMPLE STUDIES

1. **Stress Analysis**

Stress analysis of the analog discontinuity sample (Figure 3-2)
was performed with 2-D plane stress assumptions; no 3-D analyses were
performed. The FE model used for the analysis, as shown in Figure 3-39
is symmetric about horizontal and vertical axes through the midpoint of
the sample. This allows the modeling of only a quarter section of the
sample. Stress solutions were obtained only for tension (90 degree pull
angle) and shear (0 degree pull angle) and the results superposed
using Eq. 3-3. The implied liner configuration on the bottom side of
the sample, due to symmetry assumptions, should have little effect on the
stress distribution at the actual case bond (top) side of the sample.

The grid refinement in the model is consistent with that used in the Task-I cylinder studies. Minimum element dimensions adjacent to the discontinuity are $\Delta y = 0.003$ and $\Delta x = 0.002$ inch. (Coordinate axes relative to the analog flap termination sample studies have been re-defined.)

The FE analysis was performed with the following material properties:

Material	E (psi)	ν (psi)
Insulator	1100	0.049945
Liner	200, 850	0.4999, 0.49958
Propellant	850	0.049958

For tension loading, the vertical (y) displacement was set to zero along the bottom edge of the FE model and to 1.0 along the top edge of the model; the horizontal (x) displacement was set to zero along the top edge and the right side (symmetry boundary conditions). For shear loading, the horizontal displacement was set to zero along the bottom edge of the model and to 1.0 along the top edge; the vertical displacement was set to zero along the top and right edges (anti-symmetric boundary conditions).

The normal (σ_y) and shear (τ_{xy}) stresses in the first element row in the propellant, adjacent to the liner, are shown in Figure 3-40 and 3-41 for unit tension and shear displacements, respectively. The liner modulus for this solution is 200 psi. The singularity adjacent to the corner is readily apparent for both angles of pull. For tension loading, the normal stress dominates the shear stress everywhere along the bond. However, for shear loading, the normal stress is larger only within the first 0.25 inch of the corner. The need for singularity theory in the stress analysis of this sample is readily apparent.

Log plots of the normal and shear stress distribution within 0.1 inch of the corner are shown in Figures 3-42 and 3-43 for unit tension and shear displacements, respectively. For the tensile pull condition, the singularity exponent for the τ_{xy} shear stress (i.e., slope of the stress gradient on log-log paper) is quite sensitive to the liner modulus; whereas, for the shear pull condition the τ_{xy} stress gradient is not sensitive to the liner modulus (over the range studied). The singularity exponent for the normal stress is insensitive to the liner modulus for both tension and shear pull angles. However, the relative singularity orders for the normal and shear stresses vary considerably with the pull angle.

For conditions of plane stress, the FE solution does not exhibit oscillation in the normal stresses, as it does for plane strain and axisymmetric conditions. Thus, the normal stresses are plotted at the element centers and are not averaged.

The analog sample is relatively small compared with the liner thickness. Therefore the distinct perturbation in the stress gradient that occurred near the discontinuity in the cylinder is not expected to be as evident in the analog sample solution. However, use of a more flexible liner still tends to perturb the stress gradient, particularly for the shear loading condition. (See Figures 3-42 and 3-43.)

The Task I cylinder analysis showed that neither the maximum principal nor the maximum shear stress gradient was significantly larger parallel to the bond than normal to the bond into the liner (See Section I, Paragraph D.4). This was true for liner moduli of 200 psi and 850 psi, in conjunction with a propellant modulus of 850 psi. Figure 3-44 shows the maximum principal stress gradient for the analog sample (pulled in shear) both parallel and perpendicular to the bondline. Again, the stress gradient parallel to the bond is not significantly different from that perpendicular to the bond, even for the flexible liner. However, the distribution for the maximum shear stress (Figure 3-45) is substantially different. The singularity exponent for the stress distribution parallel to the bond is significantly higher than that for the stress distribution perpendicular to the bond. This effect occurs for both the stiff and flexible liners, and is thus in contradiction to the work of Zak and Williams.[14] As the analog sample fails, it is not readily apparent from the stress solution which direction the failure will propagate (i.e., into the liner or along the bondline). However, this report deals only with the initiation of propagation herein, and an answer to this question is of secondary importance.

The "case bond" normal and shear stresses (i.e., propellant stress adjacent to the liner) for pull angles intermediate to 0° and 90° can be readily calculated. The stress at any point for a unit end-tab displacement in the "α" direction is simply:

$$\sigma_\alpha = \sigma_0 \cos \alpha + \sigma_{90} \sin \alpha \qquad (3\text{-}4)$$

The terms σ_0 and σ_{90} are the stresses at that point for unit displacements in the shear and tension directions, respectively.

The stress distribution within 0.1 inch of the corner is shown in Figure 3-46 for pull angles of 0, 15, 30, 45, and 90 for a liner modulus of 200 psi. The stress values have been normalized by the magnitude of the τ_{xy} shear stress at 0.003 inch from the corner. The singularity exponent for the shear stress increases with increased pull angle; whereas, that for the normal stress decreases slightly with increasing pull angle.

69

The normalized radial and τ_{yz} shear stress distribution adjacent to the discontinuity in the Task I cylinder is compared in Figure 3-46 with that for the analog sample. The propellant, liner, and insulator layers have identical corresponding moduli for the respective solutions (i.e., E_L = 200, E_I = 1100, and E_p = 850 psi). A pull angle of 15° provides an excellent match for the shear stress distribution in the sample and cylinder. The singularity orders and relative stress magnitudes for the cylinder cannot be identically matched by the analog sample for any pull angle. However, the discrepancy between the two configurations is surprisingly small, and a pull angle of approximately 15° should provide a reasonable match for the cylinder.

The normalized bond stress distribution for different pull angles with a liner modulus equal to 850 psi (i.e., same as the propellant) is shown in Figure 3-47. The analog sample does not completely match the cylinder (with E_L = 850) for any pull angle. The discrepancy between the cylinder and the analog sample is larger for the stiff liner condition than for the more flexible liner condition. A pull angle of 0° provides the best match.

The effect of pull angle on the relative normal and shear stresses adjacent to the corner discontinuity of the analog sample is surprisingly small. Apparently, the relationship between the normal and shear stresses is determined primarily by the local corner "constraint". The stress distribution at distances greater than 0.1 inch from the corner is a more significant function of the pull angle. (See Figures 3-42 and 3-43.) However, the analog discontinuity sample analysis must be cast in terms of singularity theory. As such, the stress gradient adjacent to the corner is of fundamental importance.

To allow reduction of data from tests on analog discontinuity samples, the curves in Figures 3-48, 3-49, and 3-50 were prepared. Figure 3-48a shows the normal and shear stresses at a distance 0.01 inch in the "x" direction (and 0.0014 inch in the "y" direction) from the corner for a unit applied load in tension. A sample width of 0.5 inch was used in making these plots. The normal stress dominates the shear stress at 0.01 inch from the corner. However, the singularity exponent for the shear stress is the larger, and hence there is a dilemma about the significance of the singularity exponent for a filled material, as discussed in Section II.

The stress intensity factors, K_I (normal stress) and K_{II} (shear stress) per unit applied load in tension, are given in Figure 3-48b. The stress intensity factors are defined as:

$$\sigma_y(x) = \frac{K_I}{(2\pi x)^{M_I}} \text{ and } \tau_{xy}(x) = \frac{K_{II}}{(2\pi x)^{M_{II}}}$$

70

The higher singularity exponent for the shear stress causes K_I to dominate K_{II} even more than the normal stress at 0.01 inch does the shear stress. Changes in liner modulus have a relatively small effect on both the stress intensity factors and the stresses at 0.01 inch from the corner. This is advantageous with respect to data reduction, because liner moduli are not well known over a range of strain rates and temperatures. Corresponding stresses and stress intensity factors per unit applied load in shear are given in Figure 3-49. Relative values of the normal and shear stresses are similar to those for tension loading. The effects of variation in the liner modulus are also similar. The effective concentration factor is significantly higher for a unit shear force than for a unit tensile force; this is evidenced by both the stress intensity factors and the stresses at 0.01 inch from the corner.

The effect of intermediate pull angles on the K_I stress intensity factor and the normal stress 0.01 inch from the corner is given in Figure 3-50 for a liner modulus of 200 psi; values are normalized to a pull angle of 90°. The two stress magnitude parameters vary little as a function of pull angle. The slight increase in singularity order for the shear pull angle relative to the tensile pull angle causes the stress intensity factor to be less than the stress 0.01 inch from the corner.

An interesting comparison is the effect of liner modulus variation on the stress parameter for the analog sample and the Task-I cylinder. Figure 3-51 compares the relative effects on the singularity exponent and the stresses 0.01 inch from the corner for an analog sample pulled in tension. Figure 3-52 compares the relative effects for an analog sample pulled in shear. An analog sample pulled in tension is qualitatively more like the cylinder relative to variations in the liner modulus; however, the singularity exponents are less correct than those for the shear pull angle. Neither pull angle provides a good match for the cylinder with varying liner modulus. When the analog sample is pulled in shear, the τ_{xy} shear stress is less influenced by the liner modulus than is the normal stress. The opposite effect occurs when the analog sample is pulled in tension. Thus, this behavior points out that an intermediate pull angle is appropriate to best match the cylinder behavior over the widest possible range of liner modulus variations.

2. Experimental

a. Configuration for Analog Discontinuity Sample

The recommended configuration for the analog discontinuity sample is shown in Figure 3-2. The total thickness of the liner plus the propellant is 1.0 inch. The insulator layers are assumed to be 0.1 inch thick. The top insulator is bonded to the propellant through the liner. An epoxy resin bonds the bottom layer to the propellant. The propellant length is 1.5 inch, with 0.25 inch of insulator/liner extending out on each end. Both top and bottom insulator faces are completely bonded to end tabs. The sample width is 0.5 inch, however, this dimension is quite arbitrary.

b. Manufacturing Procedure for Analog Discontinuity Sample

The analog discontinuity samples were manufactured at Hercules primarily on the band saw. Rectangular blocks of insulator/ liner/propellant were cut 2.0 inch long, 0.5 inch wide, and 1.0 (liner plus propellant) inch high. Blocks of TP-H1123 propellant were cut dry at room temperature. The material for the blocks was 9 x 9 x 9 inch castings with the case bond on one face. The two ends of the blocks were then trimmed back 0.25 inch by hand using a sharp knife. Cutting a precise right angle corner without nicking the liner is very difficult due to the waviness in the liner. In actual practice, some nicking of the liner or sepration between the liner and the propellant at the corner did occur. (See Figure 3-53.) This is highly undesirable, but nc better way has been found to machine this type of sample.

The extra layer of rubber on the bottom face of the sample can be bonded to the propellant using one of several epoxy resins. Because Hercules has had good success with Epon 913.1, this resin was used for bonding in the case liner bond program. Actually, the insulator piece on the bottom of the sample is of questionable value. It does tend to soften the stress gradient adjacent to the corner and provides a more symmetric sample configuration; however, it may not be needed.

The top and bottom faces of the respective insulator layers are bonded to metal end tabs using an appropriate epoxy resin; Hercules uses Epon 913.1. For the case liner-bond samples, the rubber layers were fully bonded to the end tabs. However, failure of the insulator-resin-propellant bond at the bottom corner of the sample can be best suppressed through the use of short (~0.2 inch long) unbonded regions (flaps). This was not necessary with TP-H1123 propellant.

c. Testing Procedure

For testing purposes, the metal end tabs of the samples are attached to the ten-shear fixtures, set for the appropriate pull angle. Fixture alignment is set to exert the line of force through the midpoint of the sample. Testing is then accomplished as if the sample were an ordinary tensile sample. Zeroing of the load cell is accomplished with the top fixture and sample hooked up. The crosshead (attached to the bottom fixture) is moved to cause negligible stresses when the sample is connected to the bottom fixture. If the weight of the bottom end tab is not negligible, it should be added to the load cell reading to determine the actual load on the sample at the time of failure.

Failure (initiation of a separation) of the liner-propellant
bond during testing may not coincide with the peak load on the load versus
displacement trace. This is particularly true of pull angles approaching
shear (zero degrees). Initial testing should be performed at a low rate
to allow correlation of visual failure observations with the load trace.
In shear, the normal stresses adjacent to the unbond tend to be reduced
as the unbond length increases, up to approximately 0.4 inch separation
length. Failure under high-rate loading may have to be determined from
high-speed movies. Alternatively, an empirical relationship between the
load at the onset of failure and the maximum load achieved may be estab-
lished at low rates for a given angle of pull. This empirical factor can
then be applied to high rate or superimpose: pressure data wherein visual
observation is not practical.

3. Test Results

Approximately 20 constant displacement-rate tests were
conducted on analog discontinuity samples under this program. Testing
was performed on TP-H1123 case bond material using Instron and MTS high-
rate testers. All testing was performed at the zero degree pull angle
(shear), $77 \pm 2^\circ$ F and 45 ± 10 percent RH.

Initial testing was performed at 1.0 in./min so that
sample failure could be observed. Eight tests were performed in the
first series. Quantitative data from these tests will not be reported
herein because the ten-shear fixture had a moderate misalingment. This
misalignment caused corner stresses which were not negligible when the
bottom endplate was attached to the ten-shear fixture, and sample-to-sample
scatter was unexpectedly large. After the ten-shear fixture was realigned,
a second series of tests was accomplished at rates of 0.01, 1, and 100
in./min; tests at 100 in./min were performed at zero and 200 psi super-
imposed pressure. Data from the second series of tests are given in
Table 3-2.

Initial inspection of all of the analog discontinuity
samples indicated no liner nicks or case bond separations. However, the
inspection was done without flexing the samples. When the samples were
subjected to a moderate load during testing, liner nicks (~ 0.01 inch)
and/or short (~ 0.01 inch) bond separations became evident in at least
half of the samples. The liner nicks did not seem to have a strong effect
on failure of the corner; however, the deeper the nick, the more it seemed
to retard failure (strengthen) at the corner. Thus, liner nicks will lead
to unconservative results for the TP-H1123 bond system. The effect of a
short case bond separation on the sample failure was very noticeable.
Samples with small initial separations reached maximum load levels
approximately 25 percent less than good samples. Also, the unbond tended
to propagate at a low load level; i.e., less than 30 percent of the
maximum load.

73

TABLE 3-2

RESULTS FROM CONSTANT DISPLACEMENT RATE TESTING OF TP-H1123 ANALOG DISCONTINUITY SAMPLES

Test No.	Crosshead Rate (in./min)	Superimposed Pressure (psi)	Maximum Load (lb)	Load at Failure (lb)	Time to Maximum Load (min)	Time to Failure (min)
1	1	0	40.9*	37*	0.346	0.27
2	1	0	41.7	34	0.324	0.4
3	1	0	40.9	30	0.315	0.1c
4	1	0	42.5	30	0.340	0.17
Avg 1-4			41.5	32.5	0.331	0.20
5	0.01	0	23.0	17	24.6	15
6	0.01	0	20.9	17	24.0	15
7	0.01	0	18.5	13	23.0	12
8	0.01	0	20.5	14	21.0	11
Avg 5-8			20.7	15.3	23.1	13.2
9	100	0	83.7	--	0.00463	--
10	100	0	83.0	--	0.00374	--
11	100	0	95.5	--	0.00450	--
12	100	0	82.4	--	0.00403	--
Avg 9-12			86.2	64 (est)	0.00423	0.0025 (est)
13	100	200	87.2	--	0.00387	--
14	100	200	105.5	--	0.00377	--
15	100	200	92.5	--	0.00425	--
16	100	200	94.5	--	0.00475	--
Avg 13-16			94.9	70 (est)	0.00416	0.0025 (est)

* Adjusted on the basis of actual sample dimensions to that for nominal sample

Failure of a good sample tended to initiate at a load level of approximately 75 percent of the maximum level achieved in that test as shown in Figure 3-54. Thus, visual means must be used to detect failure in this test. Once a small (~0.01 inch) unbond occurred, it tended to propagate at the crosshead rate. Where the separation was approximately 0.5 inch long, the load peaked out. Separation of the epoxy bond on the opposite end of the sample then occurred. (However, this separation could probably be alleviated through flapping). The length of the unbond was surprisingly uniform across the width (thickness) of the sample. Measurements made during testing at 0.01 in./min did not detect any variation through the sample width. The strip chart for a sample with an initial bond separation is also shown in Figure 3-54. The maximum load is noticeably lower than for a good sample. No inflexion is apparent on either trace to indicate the onset of flaw propagation.

Detection and definition of the load at which the corner failure occurs is somewhat subjective. The higher than usual data scatter in the analog discontinuity test derives from this subjectivity, as well as actual sample differences due to manufacturing. However, this type of behavior is typical of crack propagation testing in general. The strip chart traces for test samples 2 - 4 (see Table 3-2) are shown in Figure 3-55. Failure tends to occur fairly repeatedly at 75 percent of the maximum load.

Visual observation of failure for tests performed at 0.01 in./min crosshead rate indicated that the load at failure is approximately 75 percent of the maximum load (see Table 3-2). Thus, visual observation was used to perform the higher rate tests without high speed photography. The failure load was then derived from the maximum load using the 0.75 factor. This was done for the 100 in./min tests under zero and 200 psi superimposed pressure.

The load to failure (i.e., appearance of bond separation) is plotted in Figure 3-56 as a function of the time to failure. The "viscoelasticity" of the failure load is compared in Figure 3-57 with propellant and case bond tensile strength parameters. The propellant strength is the maximum true stress at failure divided by the true failure stress at the 2.0 in./min loading rate; a similar quotient is presented for the case bond tensile strength. Because the time to failure for the analog sample is less than that for the other samples, the curve goes through unity to the left of the other two. In general, the time-dependence of the three strength parameters is similar. However, the two case bond samples tend to give higher strength values at short times to failure than the propellant by itself. Also, the strength of the analog sample appears to drop off noticeably in the low rate regime.

The effect of superimposed pressure on the failure load for the analog discontinuity sample at the highest loading rate is compared with the propellant and case bond tensile strengths in Figure 3-58. Superimposed pressure increases the load at failure in the analog discontinuity sample very little (i.e., only 10 percent at 200 psi superimposed pressure) relative to the propellant or the round-flapped case bond tensile sample. However, the strength increase is consistent with that for the analog flap termination sample pulled in tension (90° pull angle). Thus, the earlier contention (Section I, Paragraph c.3.c) that analog flap termination samples tested at high rates and under superimposed pressure probably fail due to edge effects, seems to be justified.

3. Motor Application

The proposed procedure for structural analysis of motors with right-angle corners is somewhat new and complex, and an example is shown here. The procedure can be broken down into four steps, similar to any routine grain stress analysis:

(a) Calculate stress gradient near bond-termination corner using linear, elastic FE solution; quantify using fracture mechanics/singularity theory parameters.

(b) Calculate time/temperature dependent stress intensity factors for critical loading conditions using quasi-elastic techniques and superposition.

(c) Determine allowable stress intersity factors from tests on analog discontinuity samples.

(d) Compare calculated and allowable stress intensity factors.

Details relating to each of the four steps follow:

a. Determine Elastic Stress Intensity

The integrity analysis is based on stress intensity factors, which correspond to stresses in a regular stress analysis. Because the quasi-elastic approximation for computing transient viscoelastic values for the stress intensity factor will be used in Step b, the stress intensity factor as a function of the propellant tensile modulus must be obtained. The parameter study of cylinders in Task I has shown that the liner has a significant effect in the stress intensity and singularity exponent at the corner discontinuity. Thus, a numerical solution is the only method wherein the liner can be accurately modeled. When possible, the results for the cylinder of Task I are used, for which a detailed liner model was used.

As a motor example, consider the cylinder shown in Figure 3-59. The grain has a web fraction of 0.64 and an L/D ratio of 1.67. The liner thickness is assumed to be 0.06 inch and the insulator 0.4 inch. The exact insulator thickness is probably not important in the range considered, and the liner thickness is also relatively unimportant as long as it is between 0.03 and 0.12 inch. The motor will be loaded by straining the case; i.e., the outside of the insulator, at a rate of 0.1 in./in./min in the hoop and axial directions. The grain is assumed to be under 200 psi superimposed pressure from time zero on. This is a fictional loading, but it resembles a medium-rate pressure loading of a glass-cased motor. A case strain of 0.01 in./in. would take 0.1 minute to achieve this level.

To calculate the local corner stress gradient, the liner-to-propellant modulus ratio must be known. Assumed tensile relaxation moduli for the propellant and liner are given in Figure 3-60; the propellant curve was measured for TP-H1123, but the liner curve is just an estimate. The ratio of the liner-to-the propellant modulus, shown on the insert in Figure 3-60, indicates that the liner becomes more nearly equal in stiffness to the propellant with increasing time. The range of modulus ratio between 0.22 and 0.56 is probably representative of case bond systems in actual motors. However, estimates must be made because very little data exists for viscoelastic properties of liners, particularly cured in the presence of propellant.

Details of the calculation for the stress intensity factor, K_I, are given in Table 3-3. Six values of time, as indicated in Figure 3-60, were chosen for calculation. The stress intensity factor, K_I, considering a rigid liner was determined from Figure 1-30. For L/D = 1.67 and W/b = 0.64, $\frac{K_I}{E\delta}$ 4.1 $(36)^{0.41}$ = 17.8. The flexibility of the liner was considered using information in Figures 1-27 and 1-31. Figure 1-27 indicates that the singularity exponent is approximately 0.45 over the range of liner-to-propellant modulus ratios considered. The value for H_I, as determined from Figure 1-31, varies between 0.51 and 0.67. Thus, the flexible liner is certainly not negligible. Since K_{II} is directly related to K_I, at least for a rigid liner, K_{II} need not be considered in the calculation.

b.   Compute Viscoelastic Stress Intensity

Calculation of the viscoelastic step solution, K_{I-S}, for the normal stress intensity factor is straightforward. The values under column K_{I-S} in Table -3 are for a unit δ applied as a step loading. Considering a flexible liner, $K_{I-S} = K_I (0.0628)^{.04} H_I$, as specified in Eq. 1-5.

TABLE 3-3

CALCULATION DETAILS FOR EXAMPLE MOTOR WITH RIGHT-ANGLE CORNER BOND TERMINATION

Point No.	Time (min)	E_P (psi)	E_L/E_P (1)	$\bar{K}_I/\delta$ (1)	M_I	H_I	K_{I-S} (1),(3)	δ (2) (in./in.)	K_I (1),(4)	K_I/F (1)	K_{IC} (1)
1	0.003	1300	0.22	23,200	0.45	0.510	10,600	0.0003	3.8	1.41	96
2	0.01	900	0.28	16,000	0.45	0.555	7,950	0.001	9.5	1.45	85
3	0.03	700	0.31	12,500	0.45	0.575	6,430	0.003	23	1.47	73
4	0.1	525	0.39	9,350	0.45	0.615	5,150	0.01	62	1.51	62
5	0.3	420	0.46	7,500	0.45	0.640	4,300	0.03	160	1.55	52
6	1	340	0.56	6,050	0.45	0.670	3,630	0.1	435	1.59	42

Notes: (1) Stress intensity factor has units psi · (in.)^{M_I}

(2) $\delta(t) = 0.1 t$ for t in minutes

(3) K_{I-S} = viscoelastic step solution; i.e., unit δ

(4) Effective tensile modulus for ramp loading assumed to be $E_e(t) = 1.2 E_p(t)$

The stress intensity factor, K_I, for the ramp loading was computed in Table 3-3 using the approximation $K_I(t) \approx K_{I-S}(t)(1 + n)\delta(t)$. The term "n" is the negative slope of the relaxation modulus on log-log paper; for TP-H1123, $n \approx 0.2$. This calculation could have been carried out more exactly using the supposition integral, but it would add little to the example. Step b is thus complete. The computer value for K_I is shown in Figure 3-61.

c. Determine the Allowable Stress Intensity

The test data for TP-H1123 analog discontinuity samples will be used for the strength prediction. The pertinent data are given in Figure 3-56. The pull angle has only a modest influence on the relative values of K_{II} and K_I, and data for zero degrees will be assumed to be close enough to match the motor condition. The calculated relationships between K_I and F as a function of liner modulus (Figure 3-49b) were used to relate the force to K_{IC}. The computed values are given in Table 3-3 and plotted in Figure 3-61. A factor of 1.1 was applied to the unpressurized curve in Figure 3-56 to account for the 200 psi superimposed pressure. Failure is predicted to occur at approximately 0.1 minute, at a value for δ of 0.01 in./in.

In the example, the failure data were obtained for a ramp displacement loading. The stress intensity factor was also computed for a ramp displacement loading. Thus, failure is predicted at the crossing of the K_I and K_{IC} curves, plotted versus time, after the initiation of loading. In general, the problem will not be this simple; however, more complex loadings were not studied herein. For more complex loadings, the cumulative damage criteria of Bills[2] will be used and applied directly to the stress intensity factors. Thus, allowable (creep loading) values for the stress intensity factor would be derived from the constant displacement rate data. Stress intensity factors for variable rate loading would then be applied to the allowable curve using the technique of Bills, as applied to stresses.

SECTION IV

TASK IV - SUBSCALE MOTOR STUDIES

A. OBJECTIVE

The objective of this task is to provide verification oi bond termination failure criteria through tests on structural test vehicles representative of full scale motors.

B. INTRODUCTION

Work performed under Tasks I and III of this program has indicated the structural criticality of bond termination regions in solid propellant rocket motors. The analog bond termination samples of Task III were developed specifically for use in the assessment of bond integrity at flapped and right-angle bond terminations. An evaluation of structural analysis criteria proposed in Task III under motor-like conditions is important. Therefore, a subscale motor testing program was included in the case liner-bond study.

Full scale motors are not generally appropriate for use in the evaluation of new structural analysis procedures. This derives from their complex grain configurations, high relative cost, and poorly controlled failure locations. Subscale motors can be designed to provide stress fields in key structural regions which are similar to full scale motors. One such subscale motor configuration is obviously the Task I cylinder. This cylinder is a good candidate for evaluation of bond integrity criteria developed under this program. However, it was eliminated in the design selection process because Hercules had prior experience with even simpler configurations which appear to provide bond termination stresses representative of full scale motors. Further, the bond stresses in these simpler configurations can be calculated with more certainty than in the Task I cylinders because the propellant modulus does not enter the solution as strongly.

At the beginning of the AFRPL-sponsored case bond study, Hercules had tested two simple structural analogs termed End-Pressurized Cylinders (EPC's). The case bond system in these EPC's was a powder-embedment type used with double base propellants. The basic EPC design concept appeared to offer enough promise that further development was pursued to provide structural test vehicles under this program.

Design studies, manufacturing techniques, and test results for EPC's containing TP-H1123 propellant are reported in this section. A discussion of failure criteria for applying the Task III analog bond data to motor pressure loading conditions culminates the Task IV section of this report.

C. MOTOR DESIGN

The final configurations for the flap termination and right-angle discontinuity EPC's are illustrated in Figure 4-1. Identical geometries were used, with the exception of the unbonded area between the NBR rubber and the asbestos phenolic beaker at the forward end of the flap termination EPC. The similarity of geometries permitted the use of the same casting fixtures for both configurations.

Basic criteria used in the selection of the present design were:

(1) Location of initial failure at the desired points in the EPC's; i.e., at the discontinuity and near the forward flap termination in the respective EPC configurations.

(2) Duplication of the stress fields present near the flap terminations in the thermal shrinkage cylinders of Task I.

(3) Ability to detect failure initiation with standard instrumentation.

(4) Ease of manufacture.

The first consideration pertains primarily to the flap termination EPC design because, if failure initiates at the flap termination, the more critical discontinuity geometry would also experience failure prior to the other regions of stress concentration in the EPC. To reduce the stresses at the aft propellant/case bond junction, a region of unbond between the flap and case was used to produce a flap termination.

The utility of the EPC in assessing case bond integrity depends upon its ability to match the stress fields (hopefully, into the nonlinear range) which exist near the bond terminations. The parameter selected for comparison is the ratio of normal stress to shear stress (in the plane of the bondline) at the point of largest maximum principal stress. This ratio can be altered by adjusting the lengths of the forward and aft flap unbonds on the flap termination EPC. Likewise, the aft flap length for the discontinuity EPC can be adjusted to better match stress gradients near the singularity in a motor.

The stress analysis of the Task I cylinder with right-angle corners was not completed in time for use in the design of the discontinuity EPC's. Therefore, the discontinuity EPC configuration was selected as identical to the flapped EPC, with the forward flap termination fully bonded.

The third factor considered was the ability to detect the exact time of failure initiation in the EPC's. Case strain gages and linear potentiometers were used successfully on the previous EPC's as failure indicators. At failure, inflections occurred in the case hoop strain near the forward bond termination and in the axial displacement of the aft grain surface.

The inflections correspond to the loss of constraint from the forward case bond. The only design restriction for the use of this instrumentation is that the EPC case be flexible enough to provide adequate case hoop strains during pressurization to permit identification of failure inception.

The final design criterion, ease of manufacturing, required special consideration for the discontinuity EPC configuration. A distinct right-angle junction of the propellant and liner is required, with no sharp cuts or tears. This geometry was produced by casting the propellant against an aluminum plug which had been carefully machined and inserted to the correct depth into the forward end of the EPC case.

The prior double-base EPC designs contained a tapered cone at their forward end. In the present design this cone was removed to simplify casting fixture design. The aft flap termination served to control the length of bond and allowed an increased tolerance in the depth of casting, thus eliminating the need for propellant machining after grain casting.

D. MOTOR ANALYSIS

1. Flap Termination EPC

Linear elastic, FE stress analyses were performed for various configurations of the flap termination EPC. The material elastic properties used are as follows:

Material	Modulus (psi)	Poisson's Ratio
Case	2.0×10^6	0.18
Flap	1100.	0.49948
Liner	170.	0.49992
TP-H1123	900., 150.*	0.49957

*Thermal Loading

Initial consideration was given to the residual bond stresses resulting from propellant cure shrinkage and cooldown. The geometry selected for this evaluation consisted of a rigid case, a 0.1-inch forward flap, and no aft flap. This configuration presents the greatest residual bond stresses at the forward flap termination of those EPC's considered. The maximum principal bond stress resulting from cooldown from a stress-free temperature of 145° F to ambient (77° F) is only 3.5 psi. This is well below the allowable bond strength for TP-H1123 propellant under long-term loading conditions. Further, these residual stresses can be neglected when compared to the pressure loading stresses (which will subsequently be shown to be in excess of 200 psi at EPC failure).

The stress distribution in the propellant adjacent to the flap termination for the thermal cylinder geometry analyzed in Task I is presented in Figure 4-2. The data are for the same material properties as those used in the EPC analyses. Also shown in Figure 4-2 are the stress distributions for the flap termination EPC geometrical variations indicated in Table 4-1.

TABLE 4-1

FLAP TERMINATION EPC CONFIGURATIONS

Forward Unbond Length (Inch)	Aft Unbond Length (Inch)	Stress Ratio at Point of Largest Maximum Principal Stress, $\sigma_r + P/\tau_{rz}$
0.5	0.0	2.12
0.5	0.72	2.03
0.5	1.0	1.83
0.5	1.21	1.70
0.5*	0.0	2.09

*This configuration contained a 0.25-inch cone at the forward propellant surface while the others contained flat surfaces.

The stress ratio in the thermal cylinder is 3.01 at the point of largest maximum principal stress. Figure 4-2 and Table 4-1 show that the correct proportion of shear stress to radial stress to satisfactorily model the thermal cylinder cannot be obtained by the basic EPC configuration. The utility of the EPC, however, is not substantially reduced due to this factor because most rocket motors have significantly more shear stress, relative to radial stress, than does the cylindrical thermal shrinkage motor. This apparently results from the typically curved, elongated domes, as opposed to the flat ends on the cylindrical motor; also, thickening of the flap causes larger shear stresses. Comparison of stresses in the FS Poseidon, which has a 0.3-inch thick flap, and SS Polaris, which has a 0.08-inch thick flap, with those of the Task I cylinder (see Figure 4-3) clearly indicates that lower relative shear stress exists in the cylinder.

The EPC configuration containing a 1.0-inch aft flap termination and a 0.5-inch forward flap termination was selected for testing. Its stress distribution is closely matched by the analog flap termination sample at a zero-degree pull angle. The stress ratio for the analog sample is 1.77 and (from Table 4-1) the stress ratio for the selected EPC configuration is 1.83. The case bond normal and shear stress distributions in the propellant adjacent to the liner as a function of axial distance from the flap termination are shown in Figure 4-4 for the analog sample (with flap-end tab contact) and the EPC.

2.   Right-Angle Discontinuity EPC

A linear elastic, FE stress analysis of the selected discontinuity EPC configuration was conducted for a 1 psi pressure loading at the forward end. The material elastic properties used are as follows:

Material	Elastic Modulus (psi)	Poisson's Ratio
Case	2.0×10^6	0.18
Flap	1100.	0.49948
Liner	200.	0.4999
TP-H1123	850.	0.49958

The log of the radial and shear stresses present in the EPC analog samples at various pull angles are shown in Figure 4-5 as a function of the log of the axial distance from the discontinuity. Stresses shown for the EPC are those in the propellant 0.001 inch inward from the liner and those for the analog samples are at 0.0015 inch from the liner. The distributions indicate that the shear stress singularity exponent for the discontinuity EPC is most closely matched by the discontinuity analog sample pulled in shear. Normal stress singularity exponents for the analog samples are shown to increase slightly with decreasing pull angles. The best match with the normal stress singularity exponent for the EPC occurs at the 90-degree pull angle. However, because the shear stress singularity exponent is more affected by variations of the pull angle than is the normal stress singularity exponent, the zero-degree pull angle provides the closest approximation to the combination of stress gradients existing in the discontinuity EPC.

An additional FE stress solution was obtained for the analog discontinuity sample, pulled in shear using grid refinement equal to that used in the discontinuity EPC, to determine the effect of grid resolution on the stress matching. These results indicated no change in the normal stress gradient. However, the shear stress singularity exponent increased to a value corresponding to that previously indicated for the 15-degree pull angle, obtained using the coarser grid.

Recent testing of double-base EPC's containing bond termination singularities(22) has shown that, when an exact duplication of the stress gradients for the motor being analyzed (EPC) is not obtained by the analog sample, closer failure predictions can be obtained by using a critical stress intensity factor based upon effective maximum principal stress $(\sigma_{max} + P)$ rather than normal or shear stresses. Therefore, the log distance from the singularity was plotted in Figure 4-6, for the EPC and zero-degree pull angle analog sample. The stresses shown are per unit internal pressure and unit force applied to the EPC and analog sample, respectively.

E. MANUFACTURING PROCEDURE

The EPC cases were standard Hercules 40-pound charge beakers composed of an asbestos phenolic (RPD-150). The cylinders selected had inside diameters of 8.4 +0.003, -0.005 inches. Case preparation procedures were performed as follows (See Figure 4-7):

(1) Beakers were cut into 10-inch lengths.

(2) Teflon tape was positioned on the inside surface of the beakers to create the regions of flap unbond.

(3) Silica-filled NBR rubber sheet stock (110 mils nominal thickness) was cut to the required dimensions and bonded into the beakers with Epon 943 adhesive applied to a thickness of 0.004 ± 0.001 inch. A tapered lap joint was used at all seams.

(4) Excess adhesive was wiped from the inside of the beakers in the areas indicated in Figure 4-7.

Application of the standard production C3 Poseidon First Stage liner and casting of the propellant were performed by Thiokol Chemical Corporation, Brigham City, Utah, according to the following procedures:

(1) Liner material was applied to the beakers using the sling-lining process to a depth of approximately 60 mils.

(2) A solid aluminum plug was inserted into the forward end of the beakers. The base of the plug was the correct diameter to provide proper axial alignment with the beaker. The leading end contained a 1.5-inch length which had been

(22)"Final Report on Poseidon Propellant Long Term Loads and Grain Structural Analysis Methods," FY 1973 TES Program, Data Item No. SA015-B3A00HTJ-25, (27 June 1973).

machined to the necessary diameter to provide a radial
space of 0.060 ± 0.005 inch between it and the silica-
filled NBR rubber flap. The plug was inserted to a depth
of approximately 1.5 inch past the leading edge of the
flap material.

(3) The liner material at the leading edge of the plug was
smoothed to remove any abrupt change in liner thickness
at this position.

(4) After an appropriate elapsed time for partial cure of the
liner, the aluminum plug was moved to a depth of 0.50 ± 0.05
inch past the forward end of the flap material. The plug
was broken loose from the liner by cooling it with dry ice.
The plug was then positioned, while it was cold, in the
new position and used as the bottom closure during casting.
This is the most critical step in the manufacturing process
for the discontinuity EPC's; the repositioning of the plug
after liner cure provides a reasonably sharp corner for
the liner-propellant grain junction.

(5) The EPC's were then cast from a production lot of TP-H1123
propellant to obtain a solid cylindrical slug 3.00 + 0.25,
- 0.000 inch long.

(6) Following propellant curing, the closure plug was removed
with the aid of an orifice through the plug. This served
to release the vacuum and also provided a means of applying
pressure to aid in plug removal if excessive adhesion
occurred between the aluminum and the propellant surfaces.

This procedure produced a smooth liner surface at the forward end
of the EPC, with a right-angle type discontinuity between the liner and
forward propellant surfaces. Figures 4-8 and 4-9 are photographs of the
two discontinuity EPC's which were tested.

Final machining involved removing the excess 3.2 inches of beaker
at the forward end. This extra length had served to align the aluminum
closure plug during the lining and casting processes. The flap and liner
material were removed flush with the aft propellant surface on both the
flap termination and discontinuity EPC's. These materials were also
removed on the forward end of the flap termination EPC's to permit hydro-
static pressure to be applied in the region of unbond during high-rate
pressurization.

F. TESTING PROCEDURE

The EPC's were instrumented as indicated in Figures 4-10 and 4-11 and Table 4-2. Eight strain gages were placed on the case exterior of each of the EPC's. They were located just aft of the forward bond termination to indicate the increase in hoop strain associated with case bond failure. Six linear potentiometers were located at the aft surface of the propellant grain to permit identification of failure by the abrupt increase in axial grain displacement. Engineering unit line plots and digital printout of the instrumentation output were recorded at 4 ms sampling rate for the duration of each test.

High rate pressurization in the forward cavity of the EPC's was accomplished through gas pressurization of the mineral oil medium with a rapid opening pneumatic valve. Nitrogen gas was used to supply the driving pressure. Figure 4-12 contains a schematic of the pressurization system. The needle valve (Item 7, Figure 4-12) was adjusted to obtain a maximum pressurization rate of 12,000 psi/sec when pressurizing a 6-inch length of 1-inch diameter pipe. Previous EPC testing has shown that this adjustment produces an average pressurization rate of slightly less than 200 psi/sec in the subscales.

The EPC's were preconditioned and tested in a temperature environment of 77 ± 5° F.

G. TEST RESULTS

1. Flap Termination EPC

Flap termination EPC's, designated TCC-2 and TCC-4, were pressurized to failure at the rates indicated by the pressure transient curves of Figure 4-13. Because failure initiates at an internal point along the propellant/liner interface, the initial flaw constitutes a localized stress singularity and produces a very rapid failure. The precise time of failure was determined by plotting normalized axial grain deflection and case hoop strain versus time. (See Figures 4-14 and 4-15 for TCC-2.) The individual data points are shown every 4 milliseconds. Both curves indicate that failure occurred in EPC TCC-2 after 1.096 seconds of pressure application. This corresponds to an applied pressure of 188 psi. Figure 4-16 shows the normalized axial grain deflection (per unit applied pressure) as a function of time for the TCC-4 pressurization. Failure, as indicated by the inflection, occurred at 1.432 seconds. This corresponds to a pressure of 206 psi.

2. Right-Angle Discontinuity EPC

Discontinuity EPC's, designated TCC-6 and TCC-8, were pressurized to failure at the rates indicated by the pressure transient curves of Figure 4-17. Failure of discontinuity EPC's is similar to the discontinuity analog samples because initial bond separation occurs prior to attainment

TABLE 4-2

INSTRUMENTATION FOR EPC TESTING

| Measurement Number | Type | | Purpose of Measurement | Expected Range |
	Measurement	Transducer		
P-1 P-2	Pressure	Taber 1000 psig or equiv.	Chamber Pressure Driving Pressure	700 psig
LP-1 LP-2	Deflection	ElectroTek 3 inch or equiv.	Grain Deflection	2.6 inch
LP-3 LP-4 LP-5 LP-6	Deflection	ElectroTek 1.5 inch or equiv.	Grain Deflection	0.9 inch
SG 1-0 SG 2-45 SG 3-90 SG 4-135° SG 5-180° SG 6-225° SG 7-270° SG 8-315	Strain	BLH-PA-3 or equiv.	Hoop Strain	$\pm$ 1.0%
E-1	Valve Opening	Breakwire	Time "0"	

of maximum applied load. The precise times to failure for the EPC's were determined by noting the inflections in curves of normalized axial grain deflection, as a function of time. (See Figures 4-18 and 4-19.) Failure time and corresponding applied pressure for each EPC are as follows:

EPC No.	Time to Failure (sec)	Applied Pressure at Failure (psi)
TCC-6	0.436	105.
TCC-8	0.720	115.

H. FAILURE CRITERIA EVALUATION

1. Flap Termination EPC

The analog flap termination sample provides the means for matching normal and shear stress gradients and relative intensity to motor conditions. However, cylindrical motors possess significant hoop stresses adjacent to the flap termination (see Task I) which are not present in the analog samples; the match between the normal stress parallel to the bond (σ_z is a cylinder and σ_y in the analog sample) is also not as good as desired.

Failure predictions for a flapped cylinder under thermal loading appears to be relatively straightforward using analog samples. The case bond normal stress level predicted for the cylinder can be compared directly with the allowable normal stress obtained from analog tests at the proper pull angle. However, as stated above, this comparison neglects significant differences in the hoop (sample thickness) stresses. The presence of the tensile hoop stress in the cylinder tends to stiffen the local propellant/ bond constituents relative to the analog sample. The tensile hoop stress will probably allow the bond to carry higher normal and shear stresses than if it were not present. This behavior is consistent with several different failure criteria, including maximum principal strain and equivalent stress. A simple comparison between bond normal stress magnitudes for a cylindrical motor geometry and analog samples should thus lead to a conservative failure prediction for the cylinder.

Failure predictions for a flapped cylinder under internal pressure loading is not as direct as under thermal loading. Direct comparison of the bond normal stress in the cylinder to that in the analog sample (not under superimposed pressure) is not reasonable. For example, the Task II tensile samples pulled at 100 in./min and 1000 psi superimposed pressure failed at a maximum principal stress level of -280 psi. The effect of superimposed pressure must be recognized and compensated for in both the cylinder and the analog sample.

The thermal/pressure loading equivalence discussed in Task I shows that stress distributions at bond terminations (and elsewhere in the cylinder) are virtually identical when compared in terms of $(\sigma + P)/T/\epsilon$ for pressure loading and $\sigma/T/\epsilon$ for thermal (shrinkage) loading. Thus, it seems as appropriate to consider $\sigma_r + P$ as the normal bond stress matching parameter for the cylinder and analog sample under pressure loading as it does σ_r for thermal loading. However, the assumption is that strength data for the analog samples will be derived under superimposed pressure conditions.

Other candidate stress parameters are appropriate for use in applying analog sample strength data to motor conditions. The maximum principal strain in the propellant adjacent to the flap termination is of interest because it is unaffected by the superposition of hydrostatic pressure in the stress analysis. However, the modulus gradient present in the propellant adjacent to the liner interface (at least for TP-H1123 material) tends to discourage the use of strain parameters. The stress distribution is affected very little by local modulus variations, but the strain distribution is not. Further, strain measurements on small bond test samples are difficult to obtain because of the multiple layers in the test samples. Other candidate stress parameters are the maximum principal shear stress and the deviatoric stress. The bondline shear stress (τ_{rz}) is not a particularly good parameter because it is not as large as the bondline normal stress (thus enters less into the failure event) and provides no compensation for the effects of stresses not matched in motors and analog samples. The maximum principal shear stress and the deviatoric stress are quite similar. The deviatoric stress (i.e., $\sigma_1 - \sigma_{avg}$) seems most worthwhile in pursuing because it behaves much like the maximum principal strain relative to changes in the state of stress. In fact for incompressible materials,

$$\sigma_d = \frac{2}{3} E \epsilon_1$$

Maximum principal strain is one of the better criteria for assessing propellant integrity at the center port, where the state of stress (in terms of principal stresses) is surprisingly similar to that at flap terminations. Thus, deviatoric stress is equally appropriate for the flap termination.

Failure of EPC TCC-2 and TCC-4 occurred in the range of 188 to 206 psi applied pressure. Therefore, in order to use the case bond strength data for failure predictions, the effect of a superimposed pressure of 200 psi upon the case bond strength capability was considered. Figure 3-38 indicates that the propellant strength at 100 in./min loading rate is increased by approximately 45 percent for round-flapped tensile samples pulled in tension with 200 psi superimposed hydrostatic pressure. However, the EPC loading rate was significantly slower than the 100 in./min tensile tests; i.e., $t_f = 0.005$ min (case bond tensile) versus $t_f = 0.02$ min (EPC's).

Because of the moderately large discrepancy between the EPC time to failure and the rate at which the effect of superimposed pressure on case bond strength was known, additional data from other programs was reviewed. Under the Poseidon program, Thiokol tested TP-H1123 propellant tensile samples at several rates and pressures, as summarized in Figure 4-20. There is apparently a very strong effect of pressure between 0 and 500 psi in the time to failure range of 0.006 - 0.06 minutes. The EPC time to failure unfortunately falls in the middle of this range.

Smoothed strength curves from the Poseidon data for a time to failure of 0.0208 minutes (i.e., the EPC average failure time of approximately 1.25 seconds) are cross plotted as a function of pressure in Figure 4-21. At 200 psi superimposed pressure, the increase in effective propellant tensile strength is only 19 percent. This is significantly less than the 45 percent strength increase due to pressure at 0.005 minute time to failure. However, the 19 percent factor is more applicable to the EPC failure prediction.

The allowable deviatoric stress for the EPC tests was obtained by applying factors to the case bond tensile strength to account for analog sample/pull angle, superimposed pressure, and state of stress; i.e.,

$$\sigma_d = \sigma_T \times P_f \times S_f \times A_f$$

where:

σ_d = deviatoric stress

σ_T = case bond tensile strength, Figure 2-47

P_f = superimposed pressure factor = 1.19

S_f = factor to obtain deviatoric stress from case bond tensile stress - 0.55

A_f = analog sample pull angle factor = 1.14

The predicted maximum allowable deviatoric stress for 200 psi superimposed pressure, along with the deviatoric stresses existing in the two flap termination EPC's, is shown as a function of time in Figure 4-22. The data are also summarized below:

EPC No.	Time to Failure (sec)	Deviatoric Stress at Failure (psi)	Predicted Allowable Deviatoric Stress (psi)	Error In Predicted Failure Load (percent)
TCC-2	1.096	192.	202	5.2
TCC-4	1.43?	210.	192	8.6

The failure loads for the two tests were predicted within 5.2 and 8.6 percent error. This excellent agreement suggests that deviatoric stress is an appropriate failure parameter for the TP-H1123 case bond system under pressure loading conditions. However, uncertainties in the measured bond strength properties and other aspects of the theory do not allow a firm conclusion as to the applicability of the deviatoric stress failure criteria.

A failure prediction was also made for the EPC tests using the maximum effective principal stress, $\sigma_1 + P$, as the bond strength matching parameter for the EPC's and analog samples. The error using this matching parameter is reasonably small. The EPC's are 27 percent stronger on the average than predicted using the maximum effective principal stress. This error is consistent with the deviation from uniaxiality of the maximum principal stress-strain relationship at the flap termination; i.e.,

$$\epsilon_1 = \frac{\sigma_1}{E} (1-\alpha),$$ where α is the measure of constraint offered by the other principal stresses.

2. Right-Angle Discontinuity EPC

As a basis for determination of the critical stress intensity factor, data from discontinuity analog samples pulled at a zero degree pull angle at various constant crosshead rates were used. (Refer to Table 3-2.) The analytical stress intensity factor per unit force was multiplied by the load at failure from the analog sample tests to obtain the curve of critical stress intensity factor as a function of time to failure shown in Figure 4-23. Due to the variation in stress distribution and stress gradients between the analog sample and the EPC, the stress intensity factor used was based upon effective maximum principal stress (maximum principal stress minus stress from hydrostatic pressure) as shown by the following equation:

$$K = \frac{\sigma_1 (2\pi r)^m}{(\text{Trigonometric Expression})}$$

where r is the distance from the discontinuity, m is the singularity exponent, and the trigonometric expression is a function of the direction from the singularity. For both the analog sample and EPC analysis, the stresses along the bond line were considered. Therefore, the trigonometric function will be identical for both configurations and can be neglected when comparing stress intensity factors. The singularity exponents for the analog sample and EPC were determined from the log-log plots of maximum principal stress versus axial distance from the discontinuity (Figure 4-6) to be 0.462 and 0.436, respectively.

92

The average pressure at failure for the two discontinuity EPC's was 110 psi. Figure 3-58 shows an increase in strength of approximately 5 percent for the discontinuity analog sample when pulled in a 110 psi superimposed pressure environment. The pressure-adjusted critical stress intensity factor curve is presented in Figure 4-24, along with curves displaying loading transient stress intensity factors for each of the two EPC's. Observation of these curves indicates predicted failure loads to be 17.8 and 35.5 percent conservative for EPC's TCC-6 and TCC-8, respectively.

Although these errors are quite large, the predictions were conservative. The most apparent source of error is the variation in "sharpness" of the right angle discontinuities contained in the analog samples and EPC's. The discontinuities in the EPC's were formed by casting the propellant against an aluminum closure, and they contained small stress-relieving fillets. Conversely, the discontinuity analog samples were formed by knife-cutting to obtain the desired geometry and contained distinct right-angle discontinuities. Therefore, although the effect of a small fillet upon the critical stress intensity factor has not been quantitatively evaluated, the analytical curve of Figure 4-24 appears to represent the limiting case of a precise right-angle junction.

In Task III, the quasi-elastic step solution approximation to the viscoelastic case was detailed, along with a cumulative damage approach to failure prediction from incremental critical stress intensity factors. This technique was not used in the present analysis. Instead, the loading rate was considered to be linear, and effective moduli were used for the liner and propellant. Because force boundary loading was used in the analyses of the analog sample and EPC, the stress intensity factors per unit load are not functions of absolute elastic moduli but are the ratios of the component material moduli. The liner-to-propellant modulus ratio used in these analyses was approximately 0.24:1. Figure 3-60 indicates that this is the expected modulus ratio for a time of from 0.003 to 0.01 minute, while the corresponding actual loading time for the EPC's can be seen from Figure 4-24 to be about 0.007 minute (0.43 second). Therefore, any errors resulting from the effective moduli approximation should be minimal.

If the loading of the analog sample and EPC were accomplished in the same elapsed time, the effective liner-to-propellant modulus ratios would appear to be identical for the two tests; and, as long as a similar modulus ratio were employed in both stress analyses, the relative stress intensity factors would vary proportionally and their ratio remain constant, not altering the failure prediction. However, Task III showed that the stress intensity factors are more a function of liner-to-propellant ratios for an axisymmetric geometry, such as the EPC, than for the plane stress (analog sample) geometry. Therefore, the critical stress intensity factor curve in Figure 4-24 is only appropriate for loading times giving an effective liner-to-propellant modulus ratio of 0.24:1 (corresponding to failure times of approximately 0.007 minute).

SECTION V

CONCLUSIONS AND RECOMMENDATIONS

The case liner-bond study comprised a comprehensive effort relative to the "state-of-stress" factor involved in the structural integrity assessment of case bond systems. Several conclusions and recommendations of a general nature evolved from the program, in addition to numerous specific comments relative to the individual tasks. Specific comments relative to the individual tasks will be given first. The general conclusions and recommendations follow.

A. TASK I

The FE stress solutions obtained for cylindrical motor configurations are considered to be accurate. To the author's knowledge, the right-angle corner solutions comprise the first attempt at a rigorous analysis of the end-termination discontinuity problem. Because of the peculiar nature of the solutions, further verification of the FE stress distributions calculated for the corner singularity would be desirable.

The parametric stress solutions considered only modest variations in the insulator and flap stiffnesses. The computed stress values should be used for insulator/flap materials with mechanical properties like these studied. If the insulator is significantly stiffer than that studied, the effect on the stresses is probably small. However, a significantly more flexible insulator may reduce the case bond stresses appreciably. The effects of variation in flap stiffness cannot be readily judged; more stress solutions are needed in this regard.

The technique devised to estimate axial case strain effects for internal pressure loading has significant limitations. As long as the axial strain ranges between 0.5-to-1.0 times the hoop strain, the technique is acceptable. However, if the axial strain is large (i.e., greater than 1.5 times the hoop strain), then the technique over-predicts the case bond and center-port stresses and strains.

FE stress solutions performed at Hercules for domed motor configurations have indicated larger shear stresses relative to the case bond normal stresses than predicted by the flat-ended cylinder solutions. The parametric study ought to be extended to include domed motor configurations.

More specific conclusions from the parametric stress solutions for the flat-ended cylinder are as follows:

> (1) The end termination stresses are generally larger than the mid-cylinder bond stresses.

(2) Flap thickness has a very significant effect on the case bond stresses adjacent to the flap termination; (locally) thicker flaps significantly reduce the bond stresses relative to thinner flaps.

(3) The liner modulus is not a significant factor in determining the case bond stress levels in flapped motors; use of a flexible liner reduces the shear stresses more than the normal stresses at flap terminations. However, the liner modulus has a very strong influence on the case bond stresses locally adjacent to the right-angle bond termination discontinuities. Flexible liners lead to lower termination stress intensities and higher singularity exponents.

(4) Liner thickness (over the range 0.03-0.12 inch) is not a large factor in determining the case bond stress levels. However, changes in liner thickness produce effects on case bond stresses at flap terminations very similar to changes in flap thickness. Thus, increased liner thickness may significantly reduce the bondline stresses if the flap is thin; if the flap is thick, liner thickness changes will have only a small effect on the bondline stresses.

(5) Case bond stresses for thermal shrinkage and internal pressure loadings become larger as the W/b and L/D increase. However, as W/b and L/D increase, the end termination stresses decrease relative to the centerport hoop stress and the radial bond stress at the mid-cylinder location. Thus, cylindrical grains with small web fractions or small length-to-diameter ratios are more likely to experience case bond failure than centerport failure.

(6) Case bond and propellant stresses can be predicted quite accurately (with the axial case strain restricted to 0.5-1.5 times the hoop strain) for internal pressure loading using thermal shrinkage solutions.

(7) The case bond normal stress at bond terminations is larger than the shear stress under axial acceleration loading, shrinkage, or internal pressure loading.

B. TASK II

The round-flapped tensile and short lap shear sample configurations developed in this program are recommended for the determination of case bond strength. A key feature in the design of the lap shear sample is its small (0.1 inch) propellant height. This small height reduces normal stresses at the sample end terminations and thus leads to shear failure in the sample gage length. A key feature in the design of the tensile sample is the flush cutting of the insulator and liner layers to the

95

propellant cylinder diameter. The special tooling for machining of test samples is a worthwhile investment.

The stress analysis performed on the tensile and shear samples considered only a modest range of propellant-liner-insulator moduli. Before the samples are used at extreme temperatures, the user should perform more extensive stress analyses. This implies an approximate measurement of moduli for the insulator and liner materials. Data for liner modulus over a wide range of temperatures and rates are currently very scarce.

The sample configurations recommended herein are somewhat flexible. Not all bond systems are as edge-sensitive as the TP-H1123 propellant system. Thus, edge failures may not always occur in either unflapped tensile or shear sample configurations. Flapping is only desirable when edge failure occurs; otherwise, flaps should not be used because they lead to more uncertain values for the peak bondline stresses relative to the average bondline stresses. The flared end on the tensile sample could probably be eliminated. However, testing experience with the user's own bond system will be necessary to answer this question.

Strength data for the TP-H1123 and ANB-3066 case bond systems were correlated in terms of time-to-failure rather than loading rate. Actual strains in the case bond layer or propellant adjacent to the bond interface cannot be readily measured. The use of the time-to-failure technique for correlating test data eliminates the need for knowledge of local strain/strain rate parameters.

C. TASK III

The analog bond termination samples (and associated strength analyses techniques) developed herein are considered the best means for assessing case bond integrity at flap and right-angle bond terminations. The sample aspect ratio and size appears to be about right for typical flap thicknesses. However, for best results, the flap thickness in the analog sample should be the same as in the motor (to match stress gradients and finite deformation effects). Thus, for motors with thick flaps, the sample size ought to be increased.

The 3-D stress analysis of the analog flap termination sample indicated a 15 percent higher bond stress than calculated using 2-D plane stress assumptions. This was because of stress variation through the sample thickness. The area correction factor for use in the estimation of true stress from engineering stress came primarily from the 3-D analysis. A 3-D stress analysis of the analog discontinuity sample is recommended. If the analog sample analyses are used to derive bond strength factors for propellant/liner/insulator moduli substantially different from those studied, then additional stress solutions should be obtained.

The stress solutions suggest that analog sample configurations symmetrical about the three principal sample axes are desirable. The additional analysis and testing complications introduced by flap-end tab contact are definitely undesirable. Unfortunately, the full ramifications of this contact were not appreciated until the testing program had been completed.

Too much scatter is present in the analog sample data for both discontinuity and flapped configurations. The variation in the discontinuity test results may just be typical of this type of stress concentration; certainly, the stress analysis would support this theory. However, more precise sample controls need to be developed. An obvious improvement is the use of the milling machine to more precisely cut the liner/propellant height to 1.0 inch. Better control of the liner thickness in the bulk castings is also desirable. However, better control cannot be obtained using standard production procedures (as was done in the case liner-bond program). End tabs of the same width as the sample (0.9 inch in length for the flapped sample) will help reduce adhesive runs during propellant-end tab bonding.

Testing of analog flap termination samples indicated that the TP-H1123 bond system is stronger at shallow pull angles than it is in pure tension. This increased strength probably derives from at least two factors. First, the bond is stronger under combined tensile and shear stresses than predicted using a maximum principal stress criterion. Second, the stress gradients are higher for shallow pull angles, and nonlinear effects should tend to smooth-out the stress distribution.

D. TASK IV

The structural test vehicles developed and tested in this program are of relatively simple design and fail in the desired locations. However, a closer simulation to typical motors would be better. The discontinuity EPC does not have enough shear at the bond termination, relative to the Task I cylinder, and the flapped EPC has too much shear. More refinement in the selection of flap/bond length is still needed.

The EPC design studies indicate that case stiffness does not greatly affect the bond stresses. However, since external case strain gages are used as failure event indicators, a moderately flexible case is required

The manufacturing techniques used to make the discontinuity EPC's were fairly elaborate and provided a good right-angle end termination. However, a small propellant fillet still occurred, and this configuration (on the scale of the singularity analysis) was not like that of the analog samples. The EPC corner is probably as square as can be cast. To better match the EPC corner, the analog samples should be cast as well. However, the intent of the analog sample was to provide the weakest (unflawed) corner configuration. As such, the analog sample corner is more appropriate.

97

The overall correlation between failure predictions and test observations for the EPC's was good. As expected, better correlation was obtained for the flapped EPC's.

The use of deviatoric stress as a strength parameter for the flap termination geometry is considered significant. The deviatoric stress tends to compensate for differences in thickness/hoop stresses in the analog samples and cylindrical motor configurations. However, too much emphasis should not be made of the deviatoric stress failure criterion. It should be viewed as a hoop stress adjustment factor for the analog sample-motor stress differences and probably possesses little generality beyond this. It appears to be needed for pressure loading conditions, and further verification is needed for thermal loading conditions.

E.   GENERAL OBSERVATIONS

The experimental program strongly demonstrated the unique structural behavior of case bond systems, as compared with the propellant proper. This program provides ample proof that structural assessment of the case bond should be made using case bond strength properties and not propellant strength properties.

Case bond strength testing should be performed on samples taken from propellant/case bond material with a large propellant quantity in the castings. Case bond strength data obtained from individually-cast, thin samples (such as poker chips) should be considered as inapplicable to motor conditions unless proven otherwise. The hardness gradient measured in TP-H1123 propellant adjacent to the case bond liner indicates that significant migration occurs between the liner and propellant ingredients during and perhaps after curing.

A procedure for assessing case bond integrity at burning right-angles is needed. The corner studies performed in this program are a good beginning for solution of the burning-corner problem. However, considerable effort remains before a solution to the burning corner problem is obtained; the integrity estimate provided by this study is probably too conservative to be of practical use.

Bond integrity assessment procedures for the internal pressure loading conditions appear to be well in hand. Verification of the proposed techniques for thermal loading conditions ought to be accomplished.

Finally, this case bond study program provided some deeper insights into the unique differences between propellant structural response near the bondline and near the centerport for cylindrical motor configurations. Propellant near the centerport is subjected to large stresses and strains in the hoop direction for the most critical (thermal and pressure) loading conditions. The propellant ring at the centerport is pulled outward (Task I "Case Expansion" loading) by the propellant between it and the case bond.

This ring is thus subjected essentially to a displacement loading condition, wherein the hoop stress in the ring is determined by the local (nonlinear) modulus of the propellant in the ring. Thus, long-term constant strain tests to simulate the effects of residual cure shrinkage, etc. are a practical approach.

The Task I study indicates that the modulus of the case bond liner (and hence adjacent propellant) material near flap terminations has only a small influence on the local stresses. (This is obvious for the liner/propellant material in the mid-cylinder location.) This derives from the fact that the bond stresses are primarily radial, whereas the centerport stresses are in the hoop direction. As yielding occurs in the propellant along the bondline, the stress does not decrease. A long-term constant strain sample provides a poor model for the bondline behavior. An assessment of bondline integrity for residual thermal loads in terms of long-term constant stress tests seems more appropriate.

The case bond study adds insight into the dilemma of which mechanical properties of a propellant have the most significance. The centerport requirements suggest that a propellant with a high elongation is desirable, independent of the shape of its stress-strain curve (as long as ballistic-mechanical interaction is minimal). However, the case-bond stresses are generated essentially by the propellant web as a whole. A highly yielding propellant is likely to experience case bond failure much more preferentially than a more linear propellant which provides the same margin of safety at the centerport. Propellant structural performance evaluation criteria are needed to ensure integrity at the case bond as well as the centerport. These criteria would be invaluable in propellant screening programs and seem mandatory for filler-particle coating studies.

FIGURES
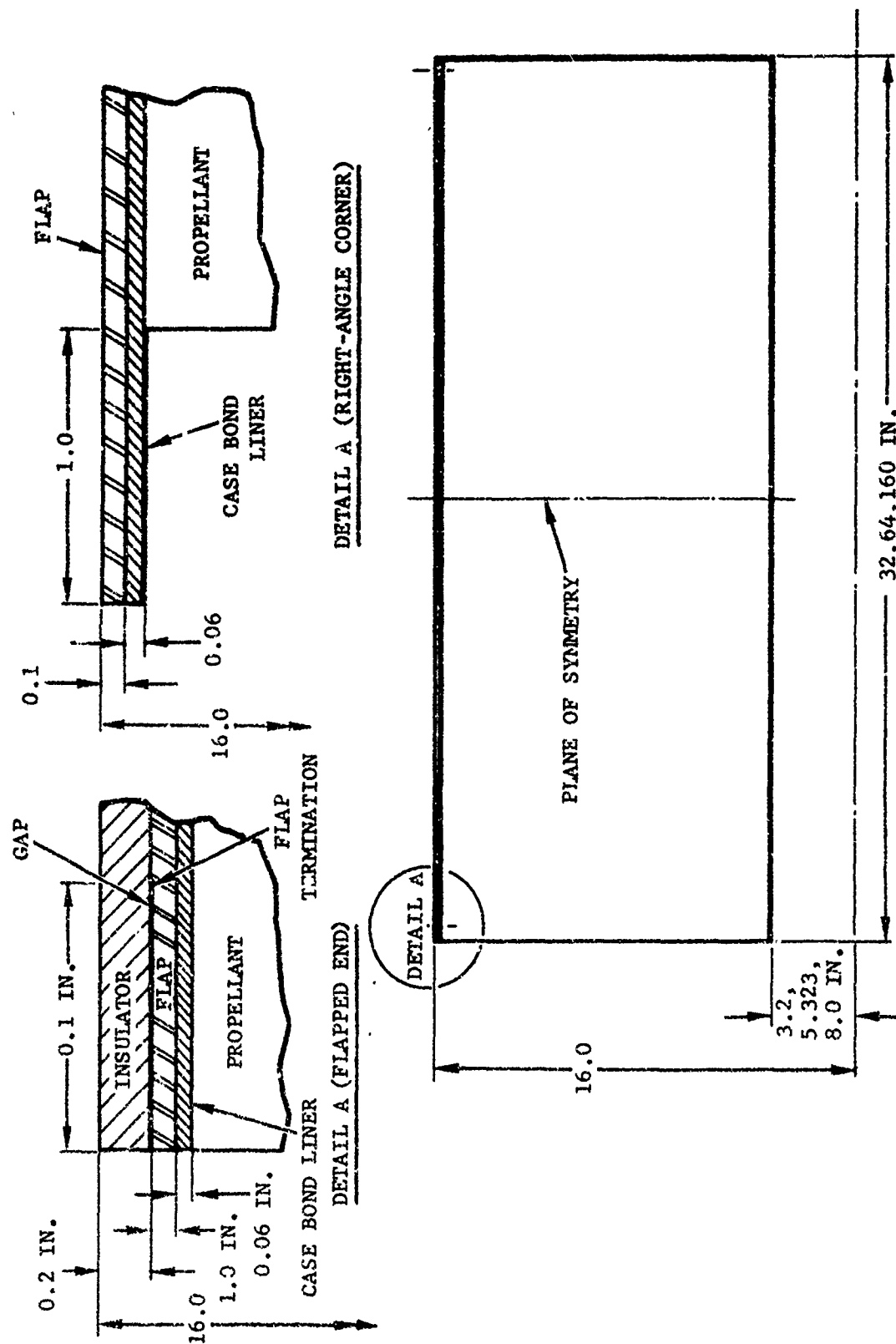
Figure 1-1. Cylinder model for bond termination studies (rigid case).

101
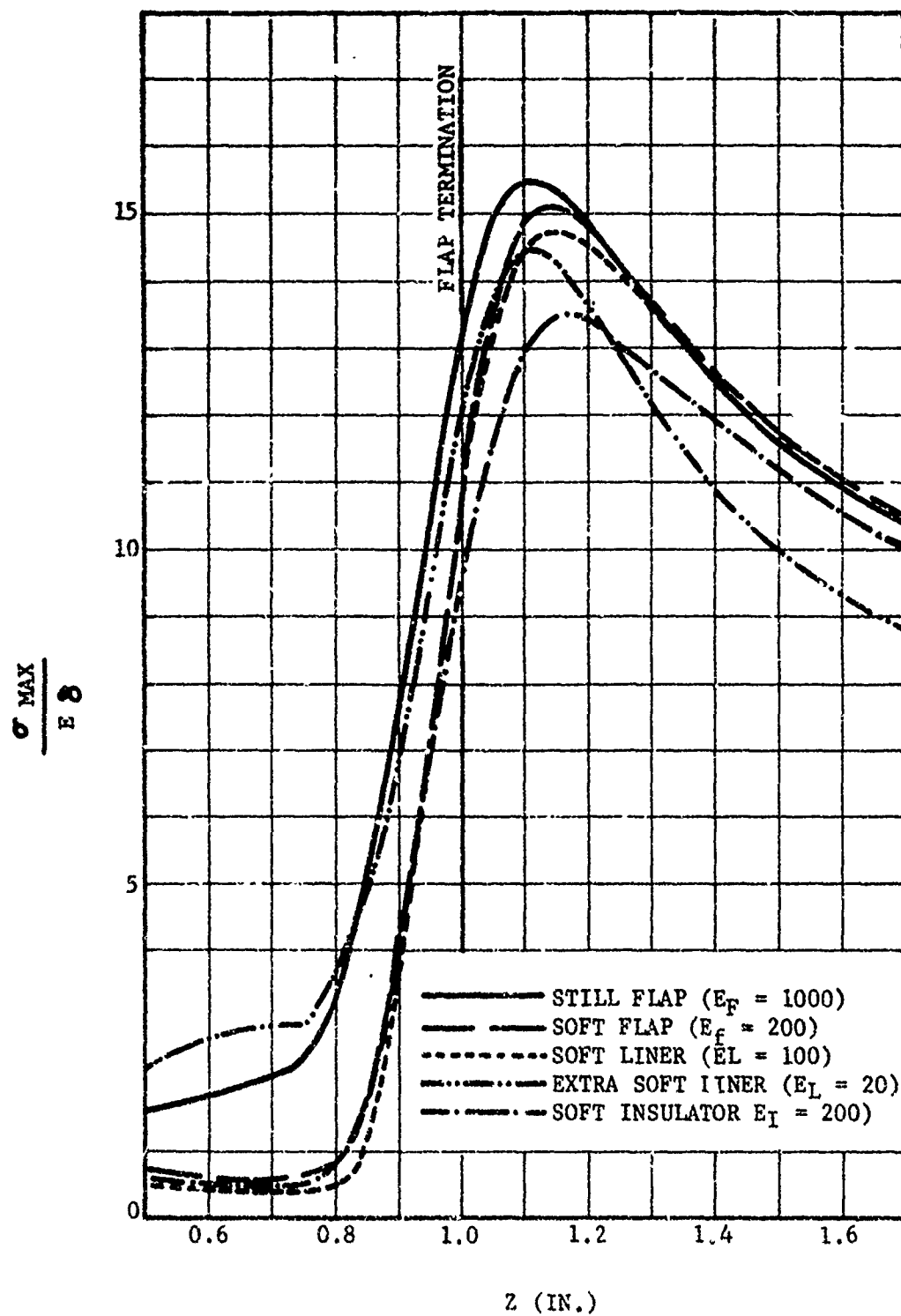
Figure 1-2. Propellant maximum principal stresses at the propellart-to-liner bond adjacent to the flap termination for a cylinder with L/D = 1.0 and W/b = 0.8 under thermal shrinkage loading.

102
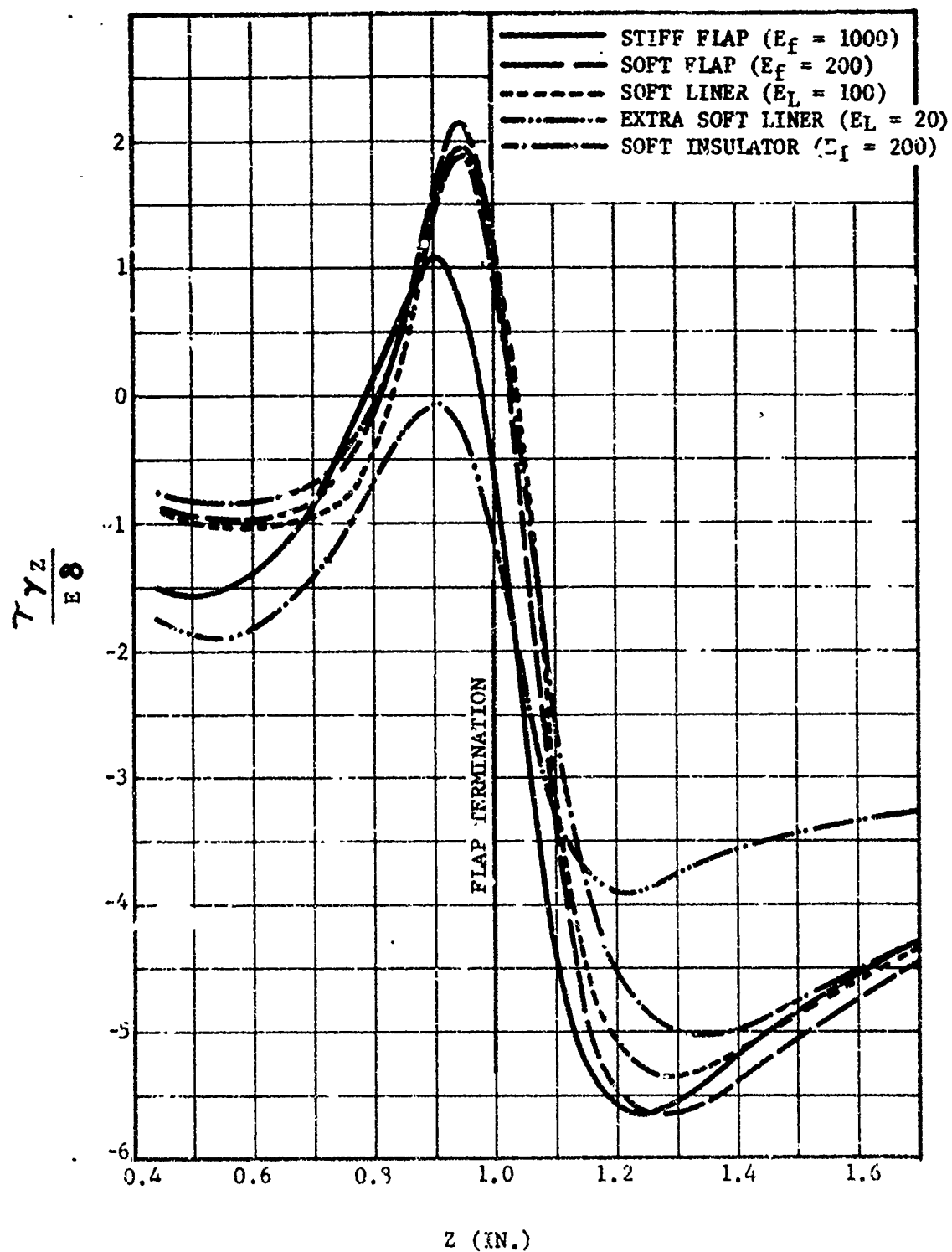
Figure 1-3. Propellant shear strain at the propellant-to-liner bond adjacent to the flap termination for a cylinder with L/D = 1.0 and W/b = 0.8 under thermal shrinkage loading.

103
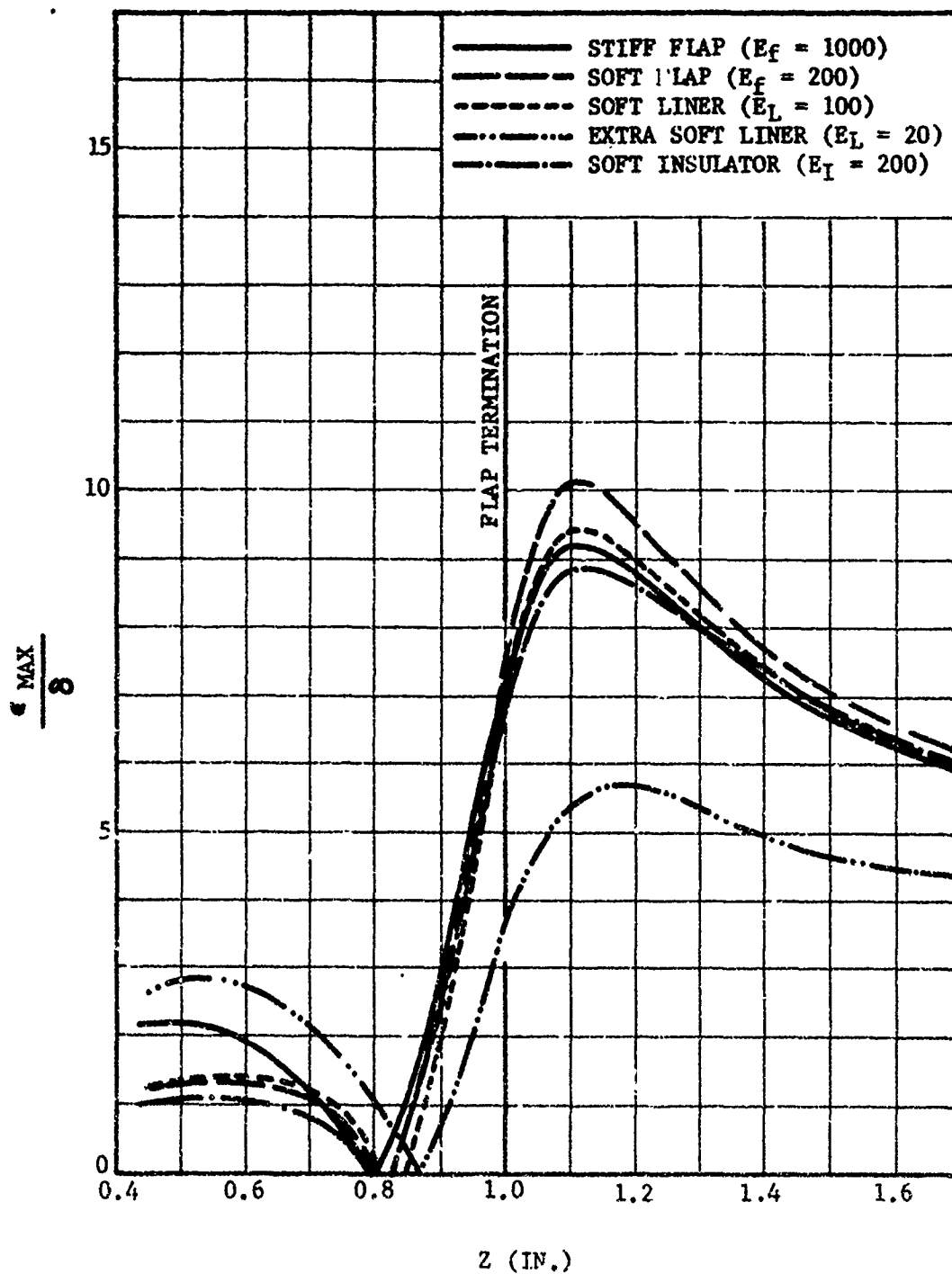
Figure 1-4. Propellant maximum principal strains at the propellant-to-liner bond adjacent to the flap termination for cylinder with L/D = 1.0 and W/b = 0.8 under thermal shrinkage loading.
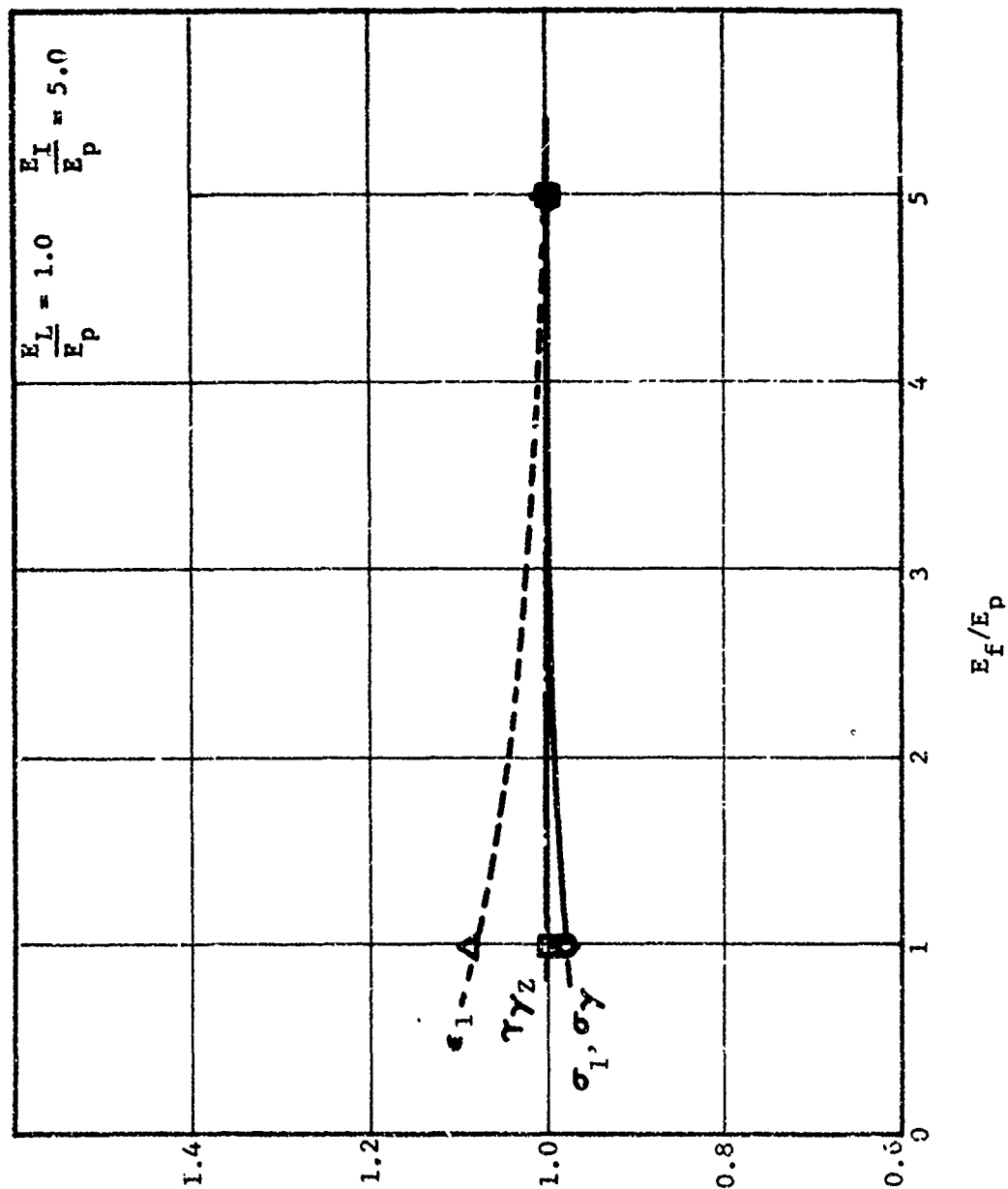
Figure 1-5. Effect of flap modulus on the key bond stress parameters for the flapped cylinder.
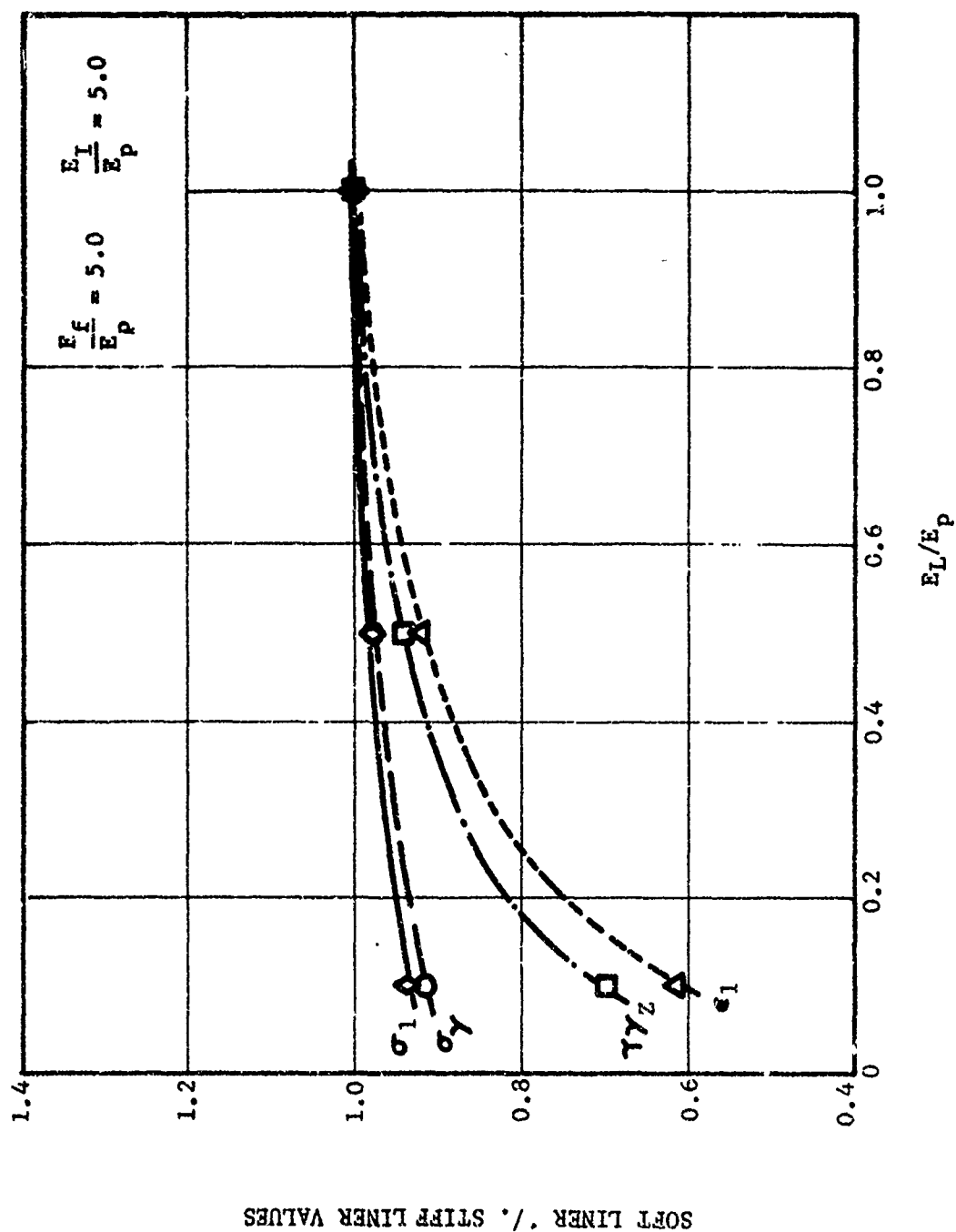
Figure 1-6. Effect of liner modulus on the key bond stress parameters for the flapped cylinder.
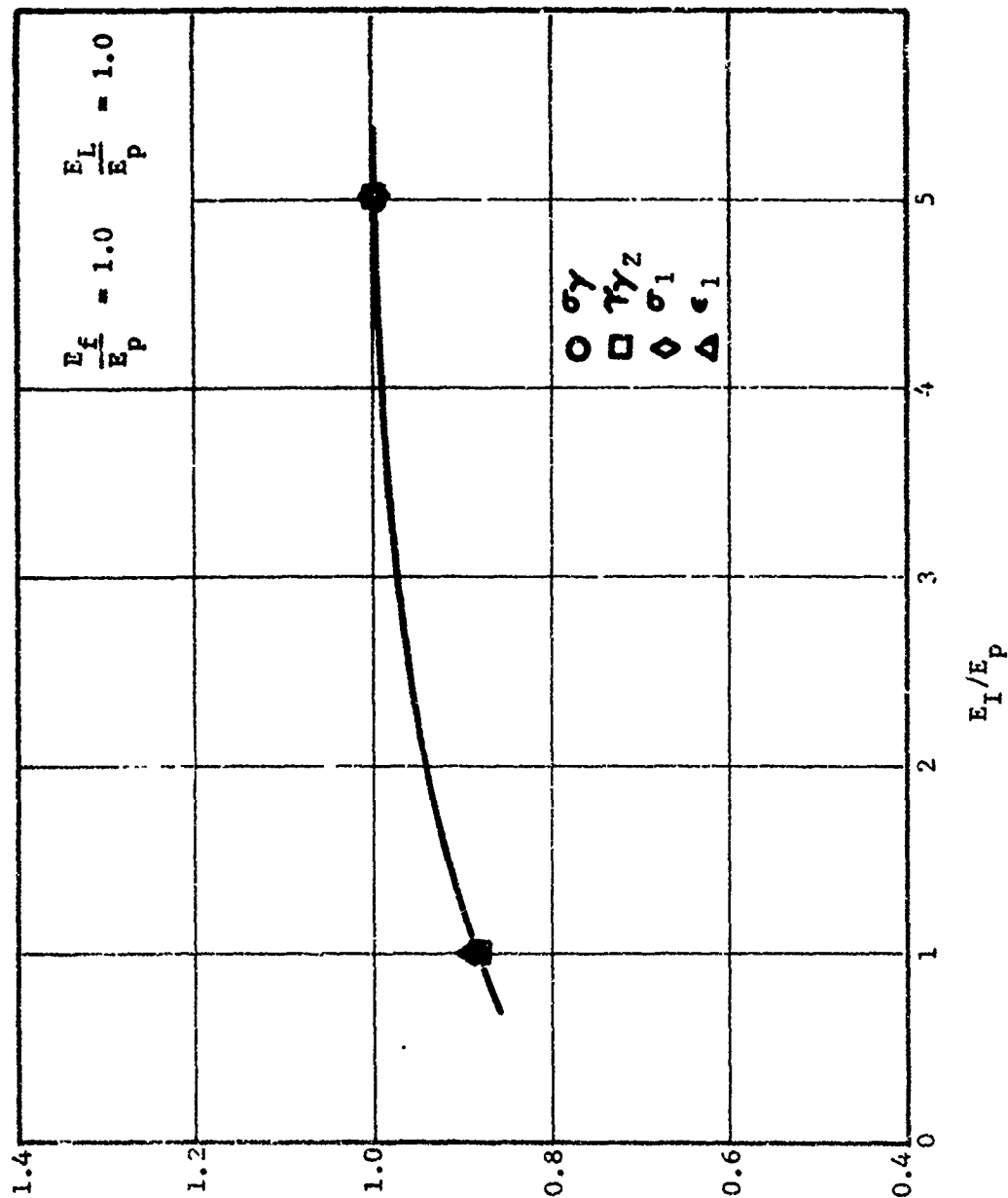
Figure 1-7. Effect of insulator modulus on the key bond stress parameters for the flapped cylinder.

107
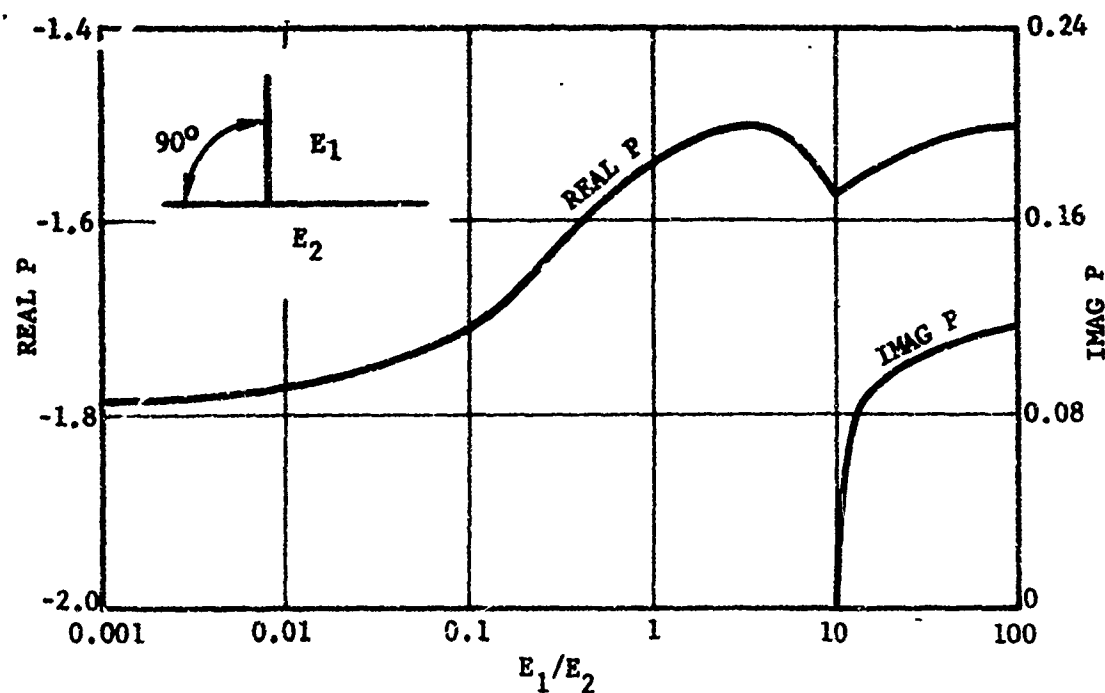
Figure 1-8a. Hein-Erdogan singular eigenvalves for right-angle corner at bi-material interface (poisson's ratio = 0.2).
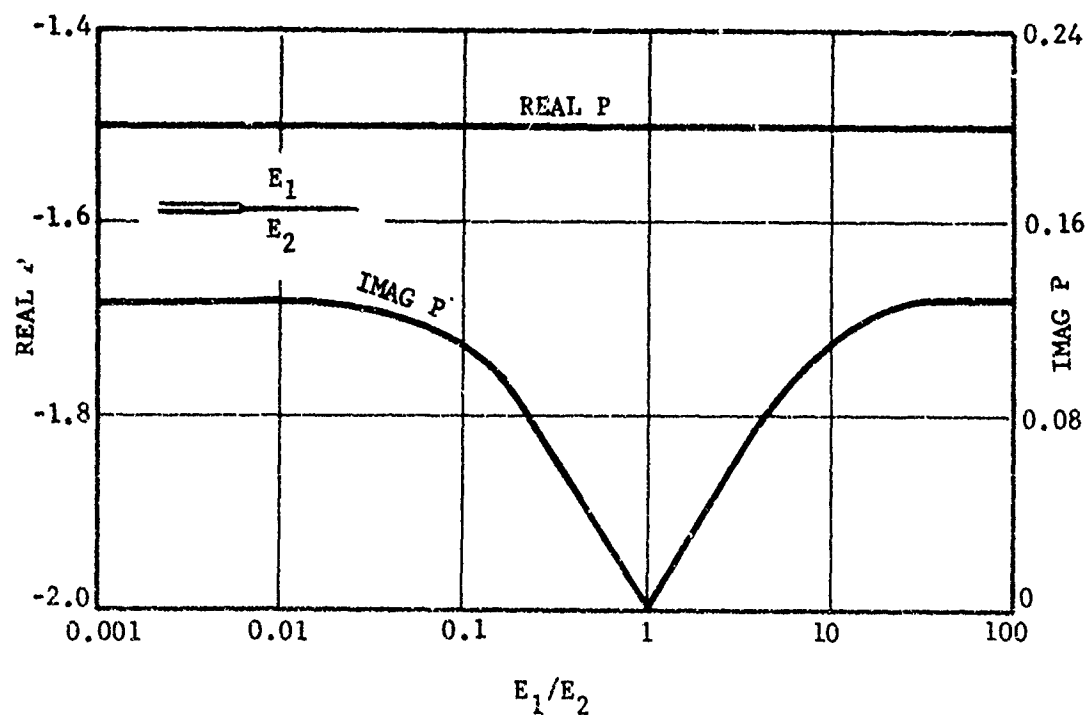
Figure 1-8b. Hein-Erdogan singular eigenvalves for bond crack at bi-material interface (poisson's ratio = 0.2).

108

SMALL BODY, B LARGER SCALED BODY, B' = αB

$\sigma = \dfrac{K_I}{(\pi r)^m}$ FOR BODY, B

$\sigma = \dfrac{K_I}{(\pi r')^m}$ FOR BODY, B'

γ OR γ'
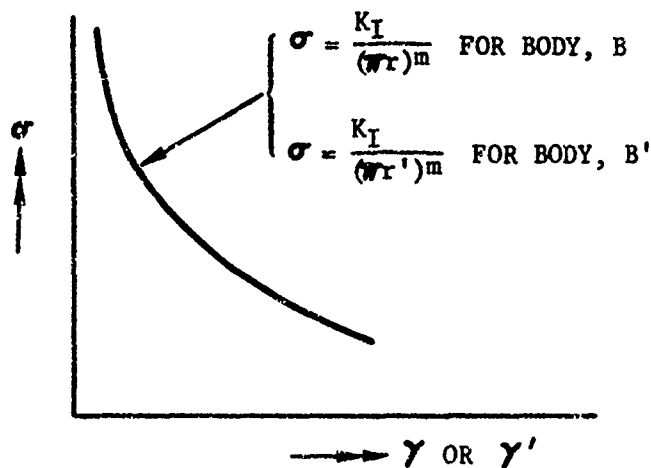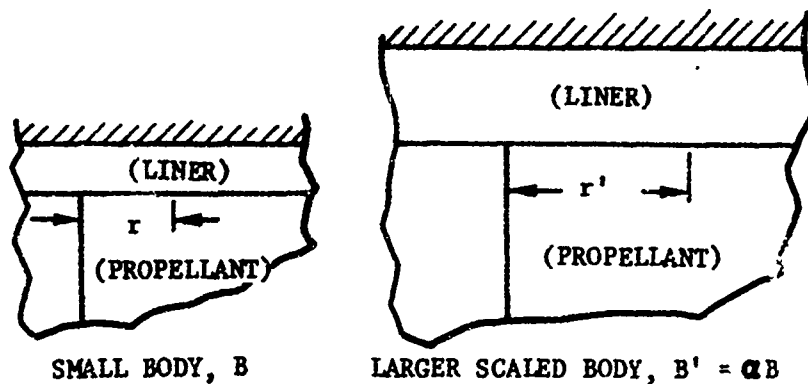
STRESS DISTRIBUTION ADJACENT TO SINGULARITY

DETERMINE K_I FOR
SMALL BODY

DETERMINE K_I FOR
LARGE BODY

$K_I = (\sigma 1_{r=a})\,(\pi a)^m$

$K_I = (\sigma 1_{r=a'})\,(\pi a')^m$

HOWEVER, SINCE $\sigma 1_{r=a} = \sigma 1_{r=a'} = \sigma_a$ AND $a' = \alpha a$:

$$\frac{K_I \ (\text{LARGE BODY})}{K_I \ (\text{SMALL BODY})} = \alpha^m$$

Figure 1-9. Scaling principles for right-angle corners.

105
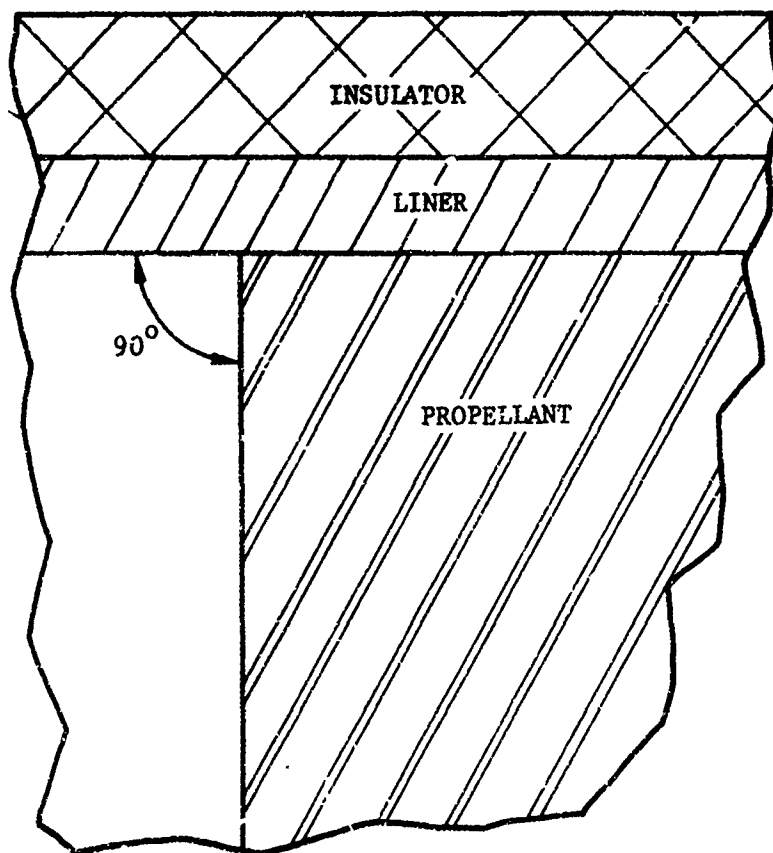
Figure 1-10. Right-angle corner configuration studied.

110
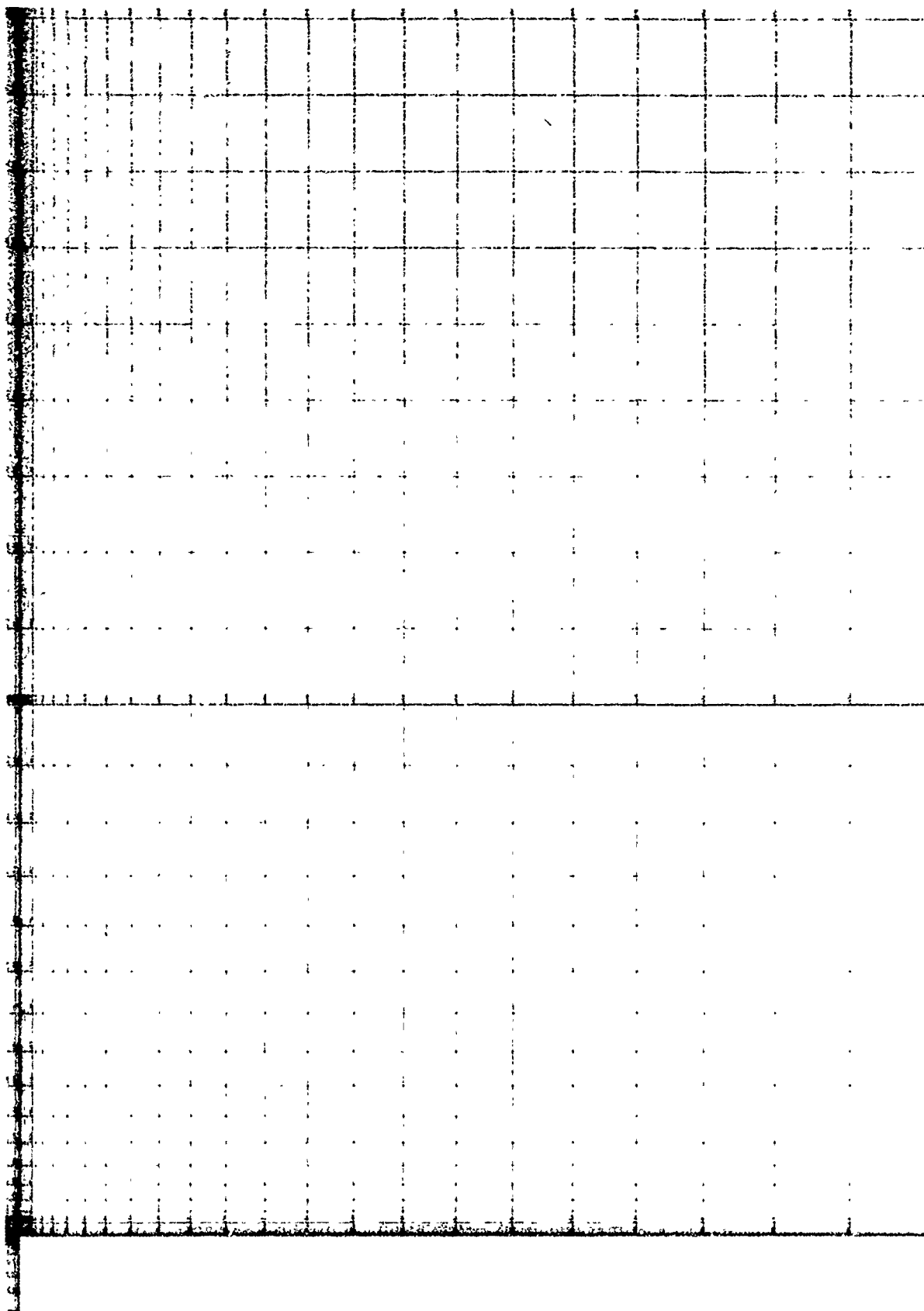
Figure 1-11. Finite-element model used for stress analysis of cylinders containing right-angle bond terminations.

111

FLAP (INSULATOR)

LINER

PROPELLANT

STRESSES PLOTTED ALONG THIS ROW OF ELEMENTS

0.002

0.10

0.06

0.0033

16.0 INCHES (FROM AXIS)
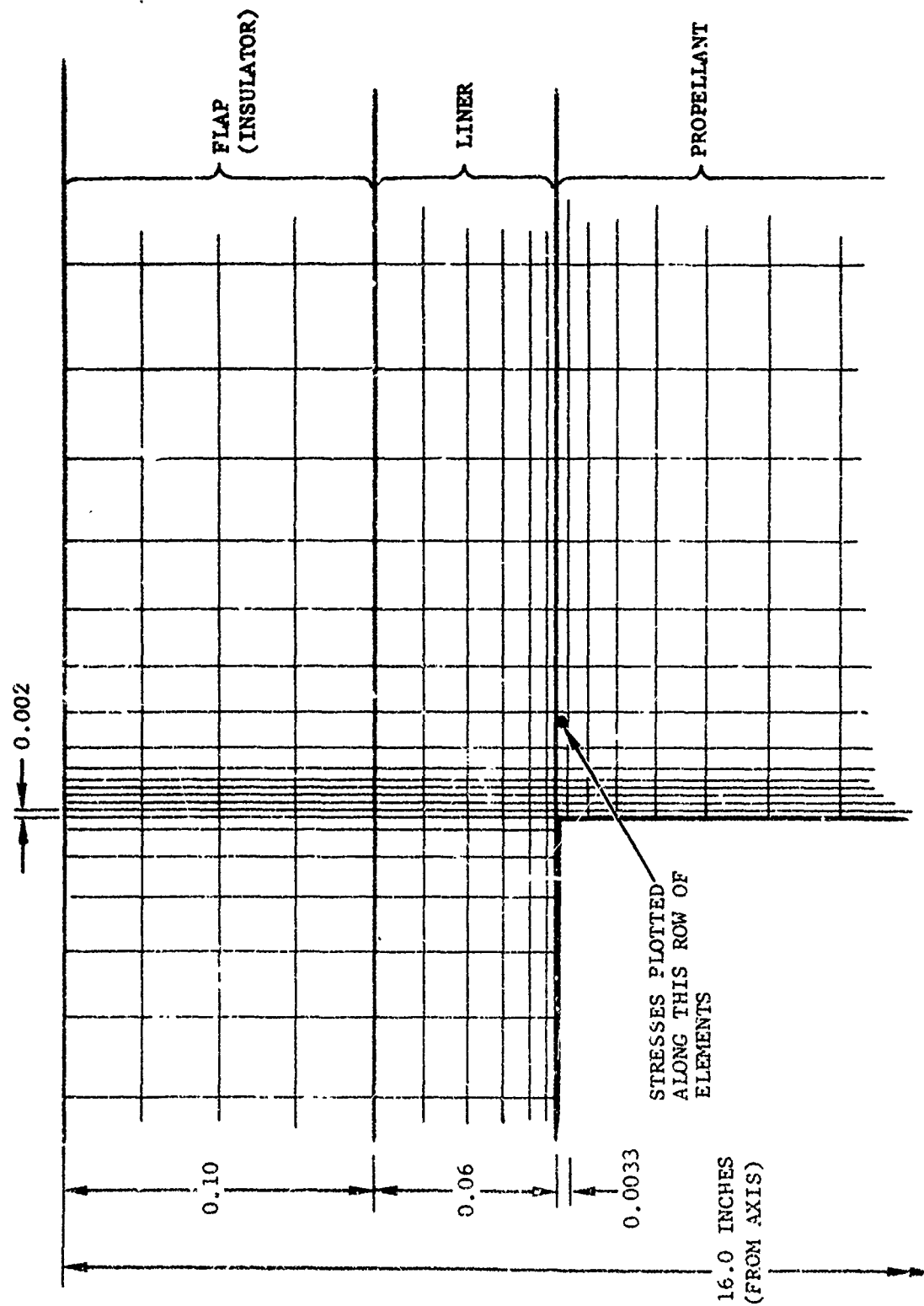
Figure 1-12. Finite element grid detail adajcent to discontinuity bond termination (20:1 scale).

112

NOTE: ZAK PREDICTS SINGULARITY OF ORDER 0.405 FOR THIS CONDITION, VS 0.41 FOR FE SOLUTION

AXIAL DISTANCE FROM CORNER (IN.)
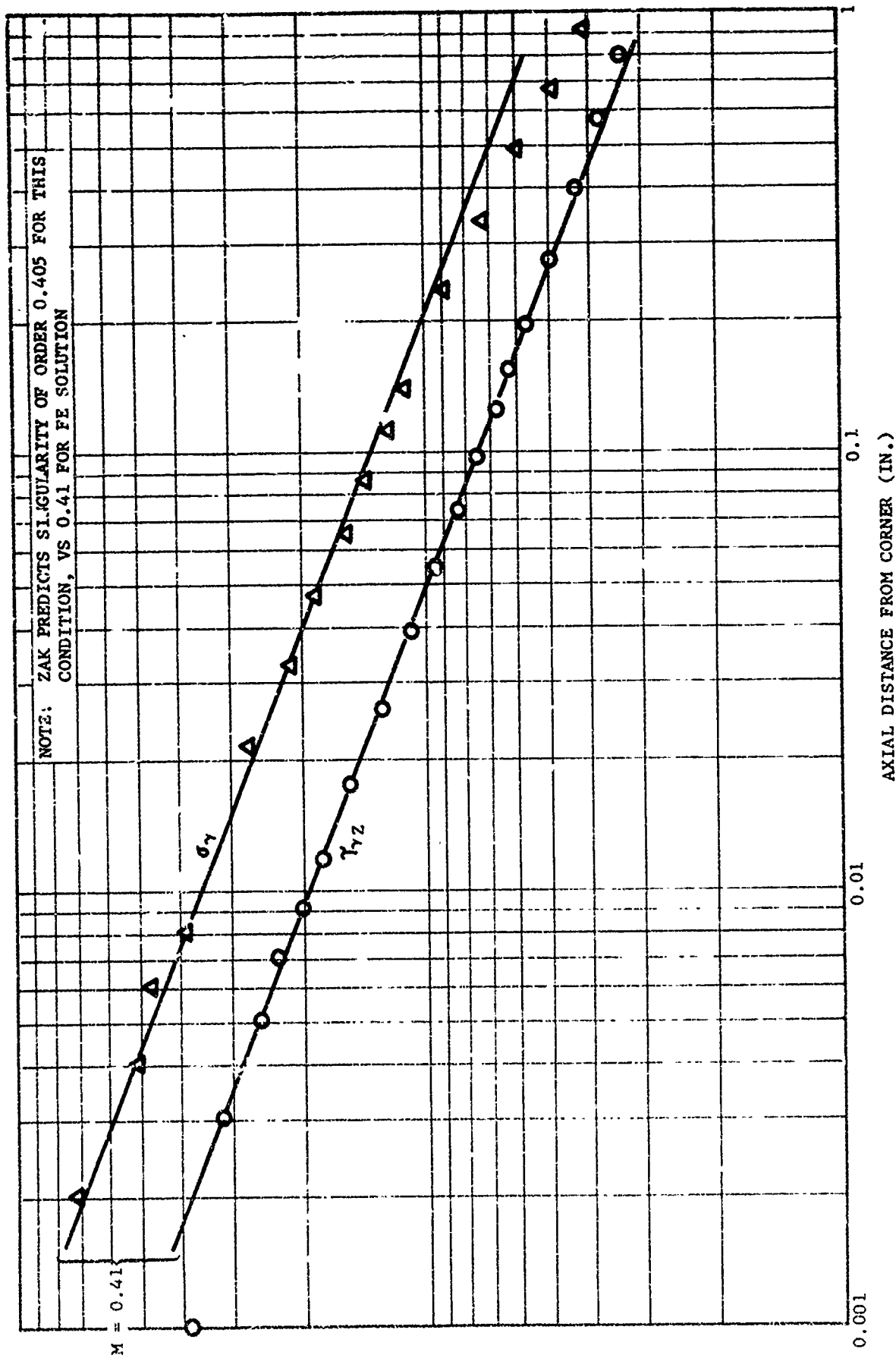
Figure 1-13. Stresses along first element row for rigid-cased cylinder subjected to thermal shrinkage loading ($E = 850$ psi, $\nu = 0.49958$, $\delta = .01$).

113

AXIAL DISTANCE FROM CORNER (IN.)
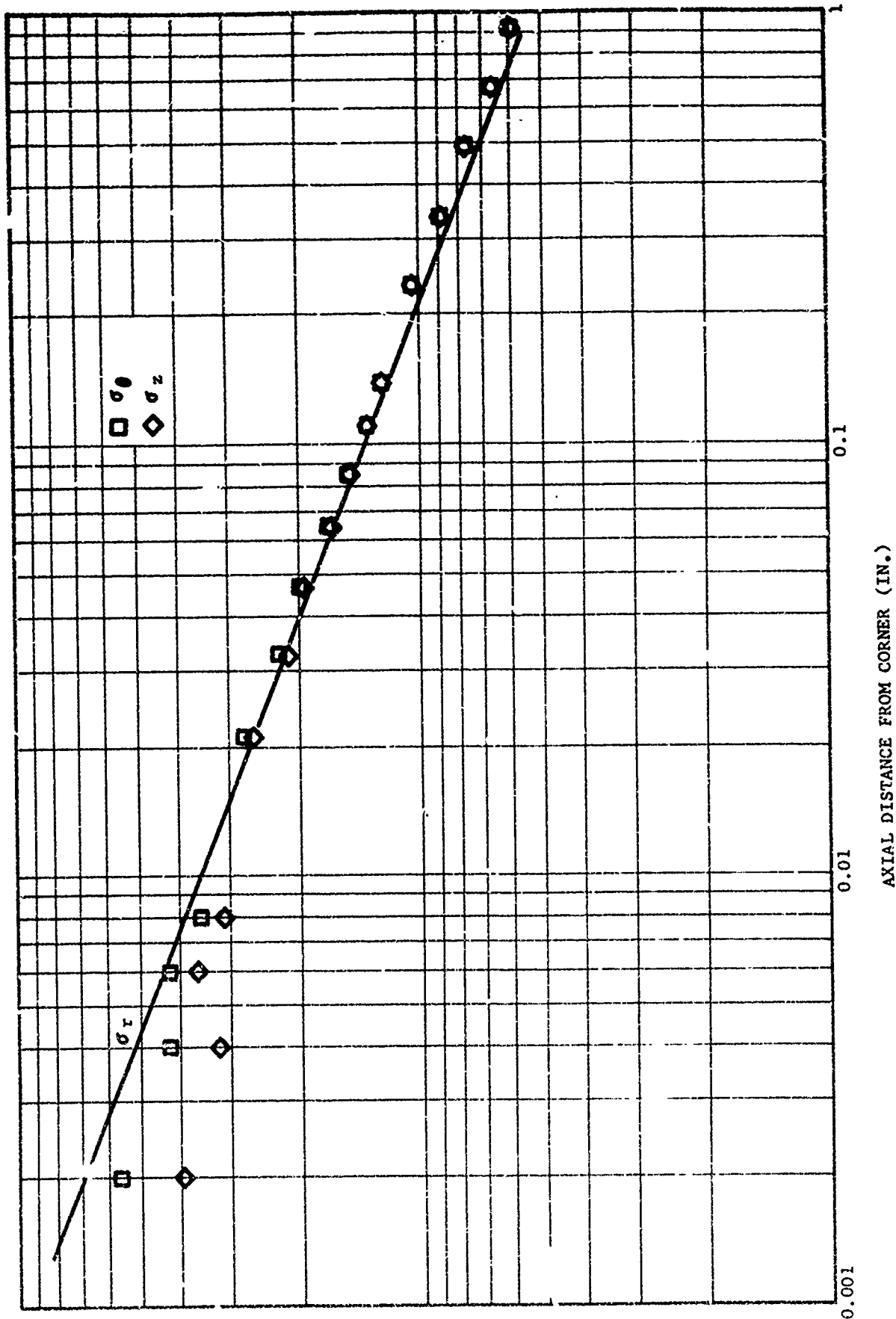
Figure 1-14. Hoop and axial stresses along first element row for rigid-cased cylinder subjected to thermal shrinkage loading.

114
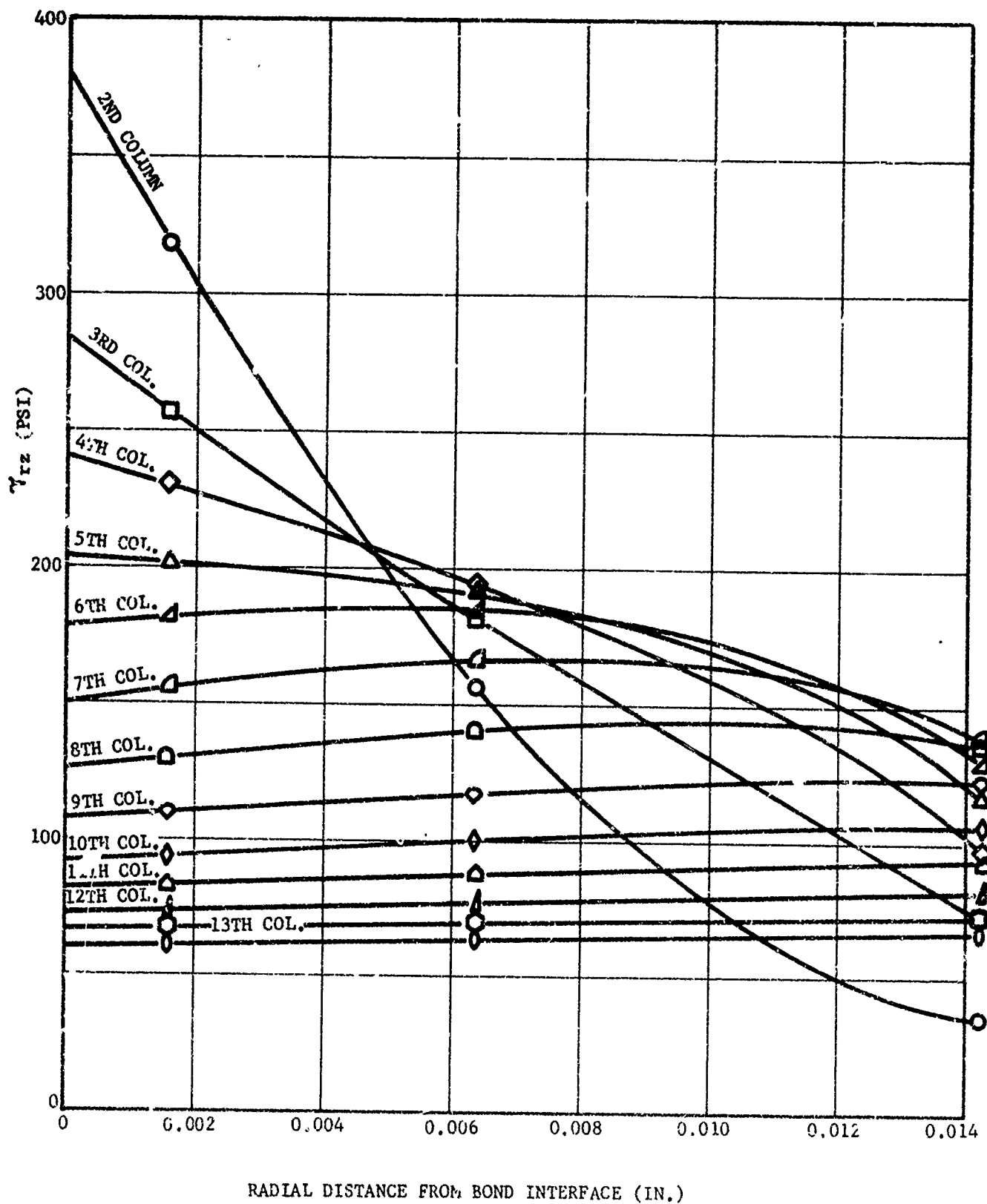
Figure 1-15. Radial distribution of shear stress adjacent to corner for rigid cased cylinder subjected to thermal shrinkage loading.
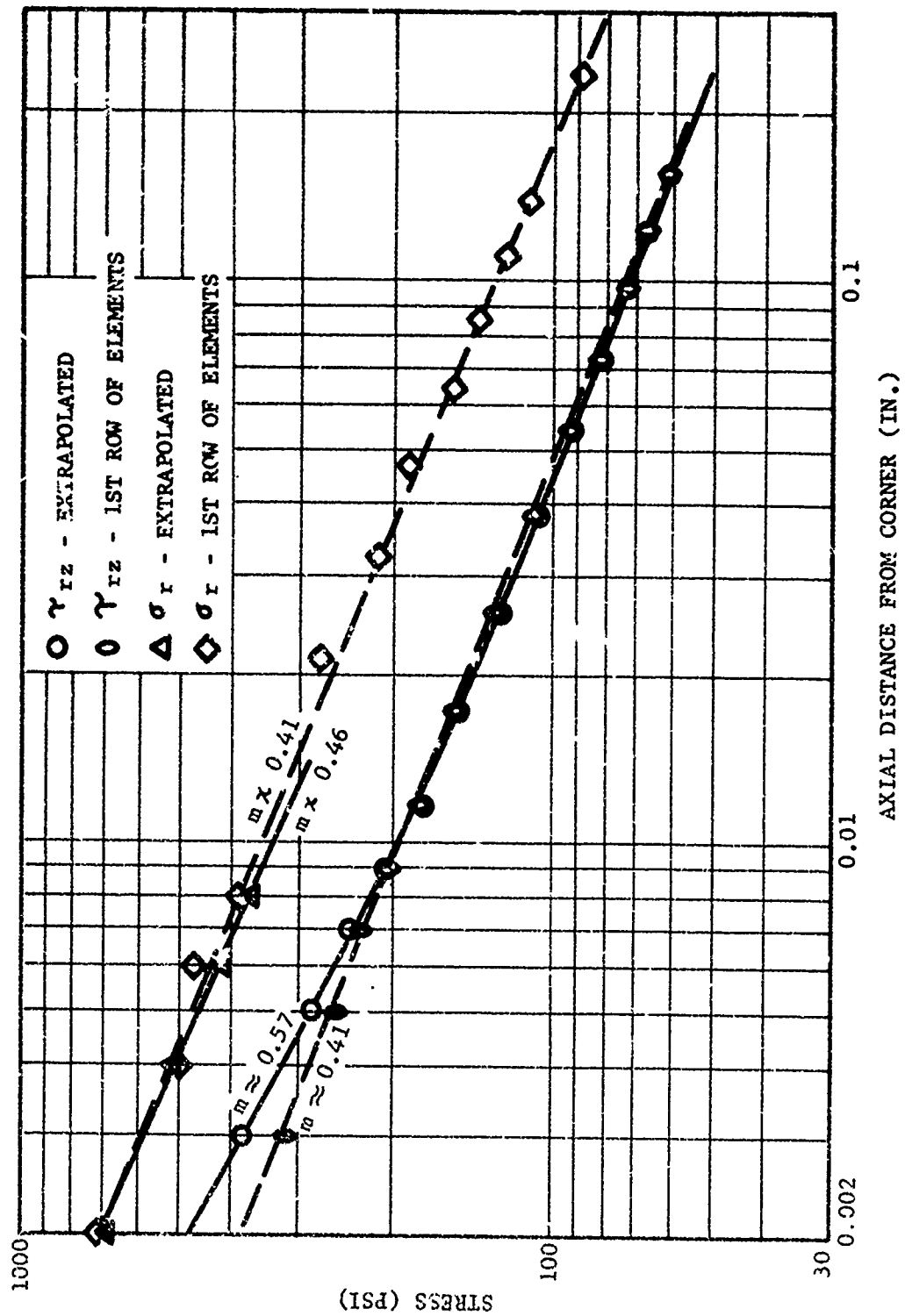
Figure 1-16. Comparison of radial and shear stresses extrapolated to bond interface to stresses along first element row for rigid cased cylinder subjected to thermal shrinkage loading.

116
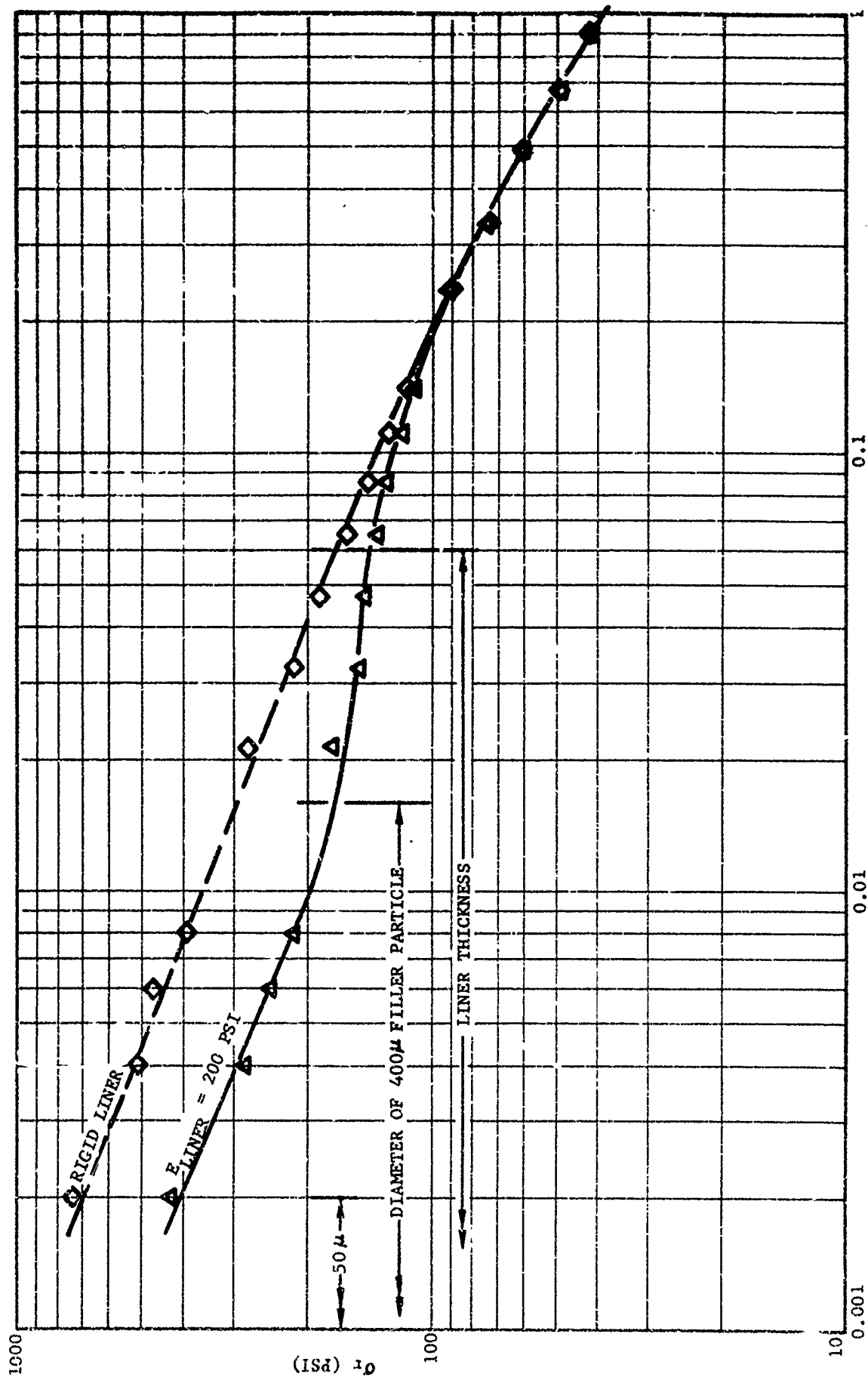
Figure 1-17. Comparison of radial stresses for soft and rigid liner solutions along first row of elements in the propellant for rigid-cased cylinder subjected to thermal shrinkage loading.
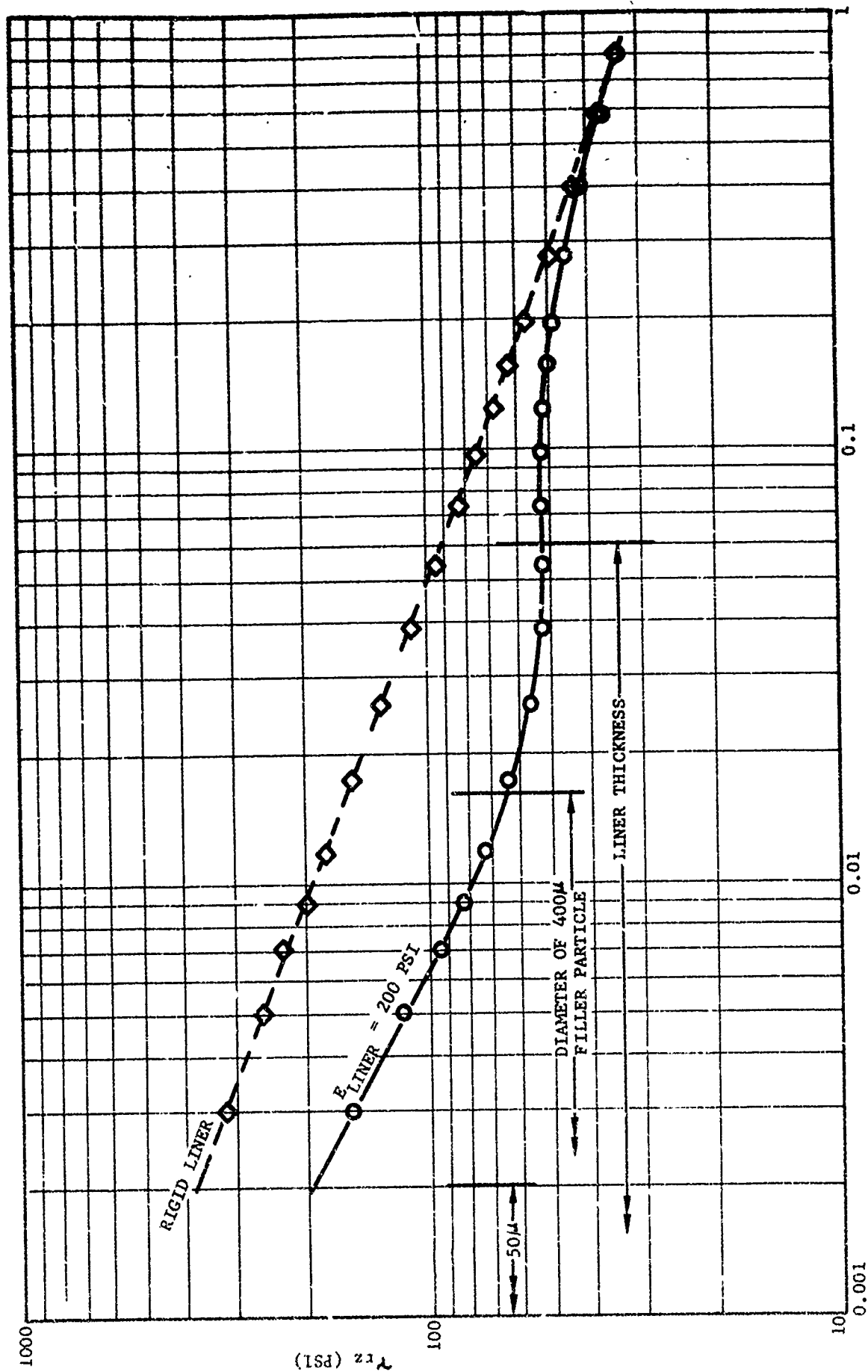
Figure 1-18. Comparison of shear stresses for soft and rigid liner solutions along first row of elements in the propellant for rigid-cased cylinder subjected to thermal shrinkage loading.

118
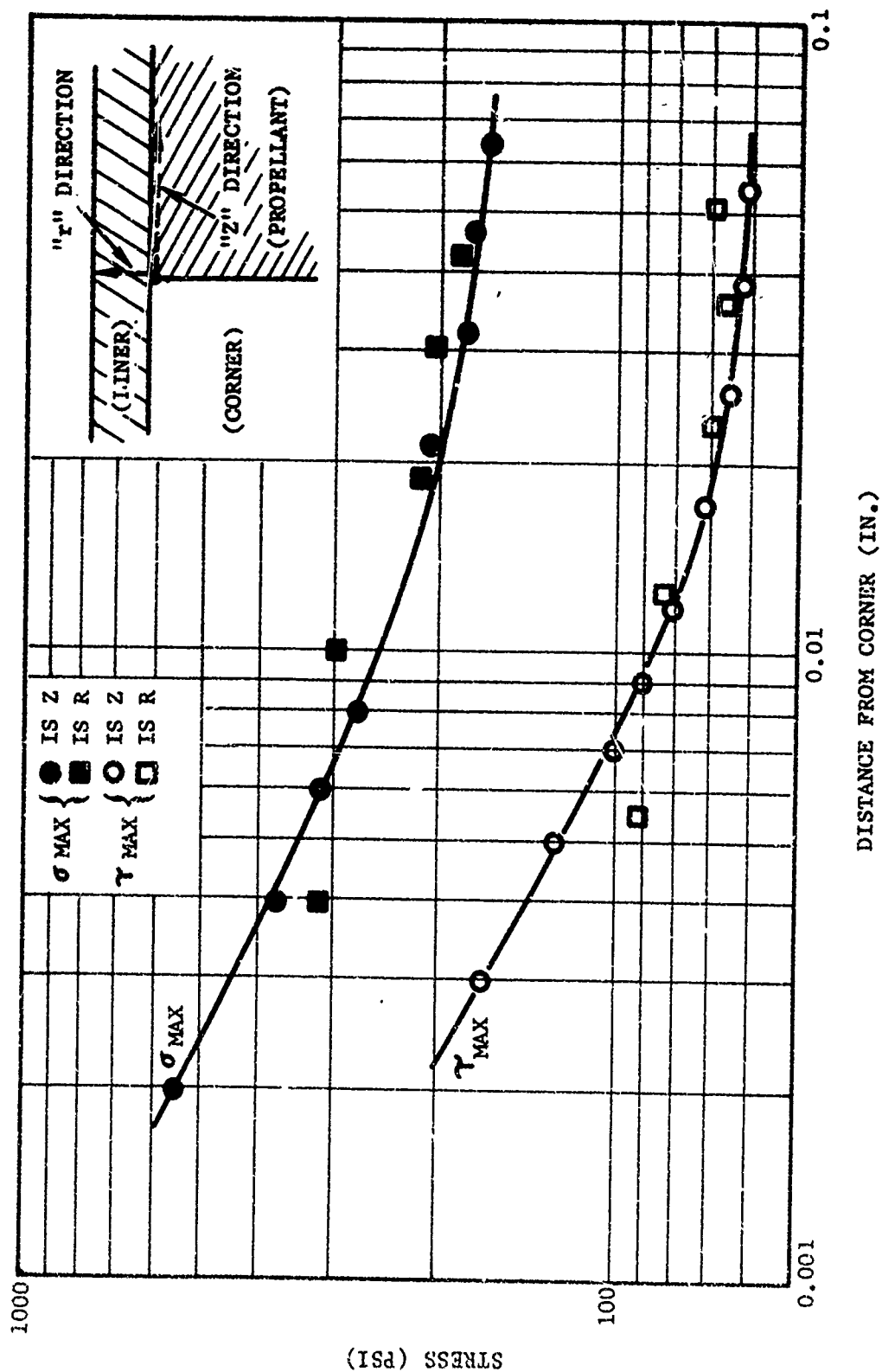
Figure 1-19. Stress gradient in propellant along bond interface (vs z) and in liner normal to bond interface (vs r) for liner modulus - 200 psi.
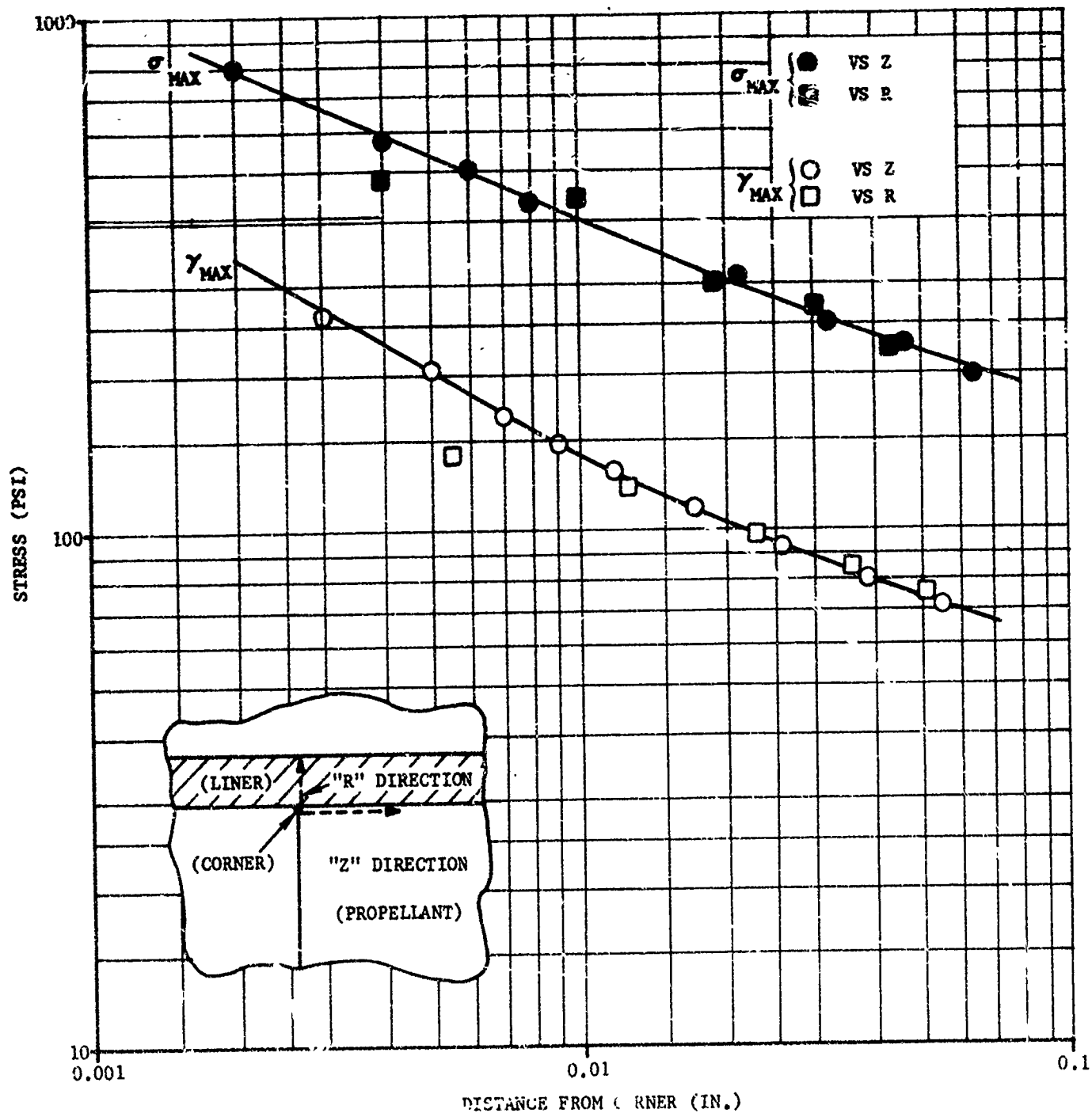
Figure 1-20. Stress gradient in propellant along bond interface (vs z) and in liner normal to bond interface (vs r) for liner modulus = 850 psi (same as propellant).

120
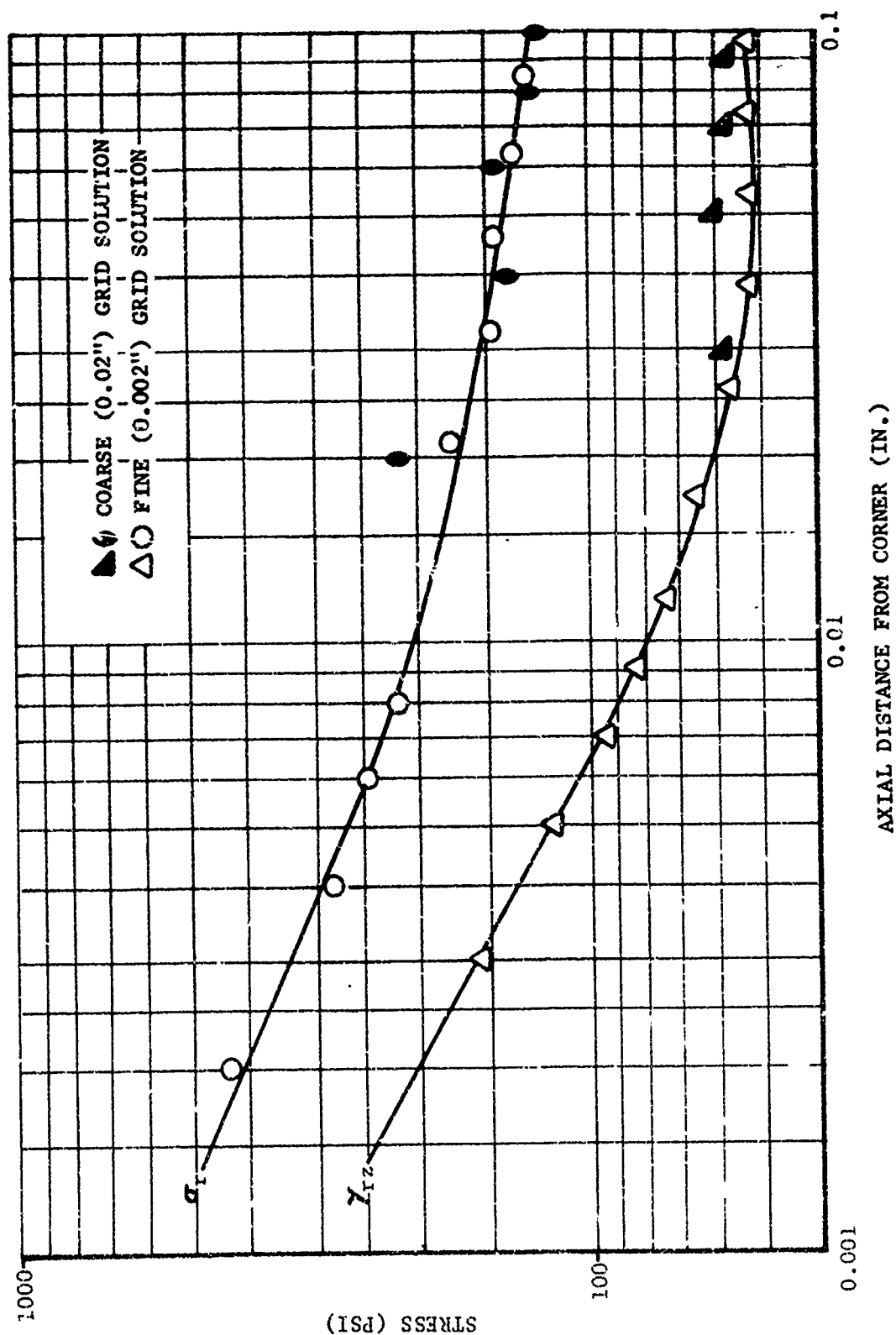
Figure 1-21. Comparison of stresses along first propellant element row of two finite-element models for rigid-cased cylinder subjected to thermal shrinkage loading and Eliner = 200 psi.

121
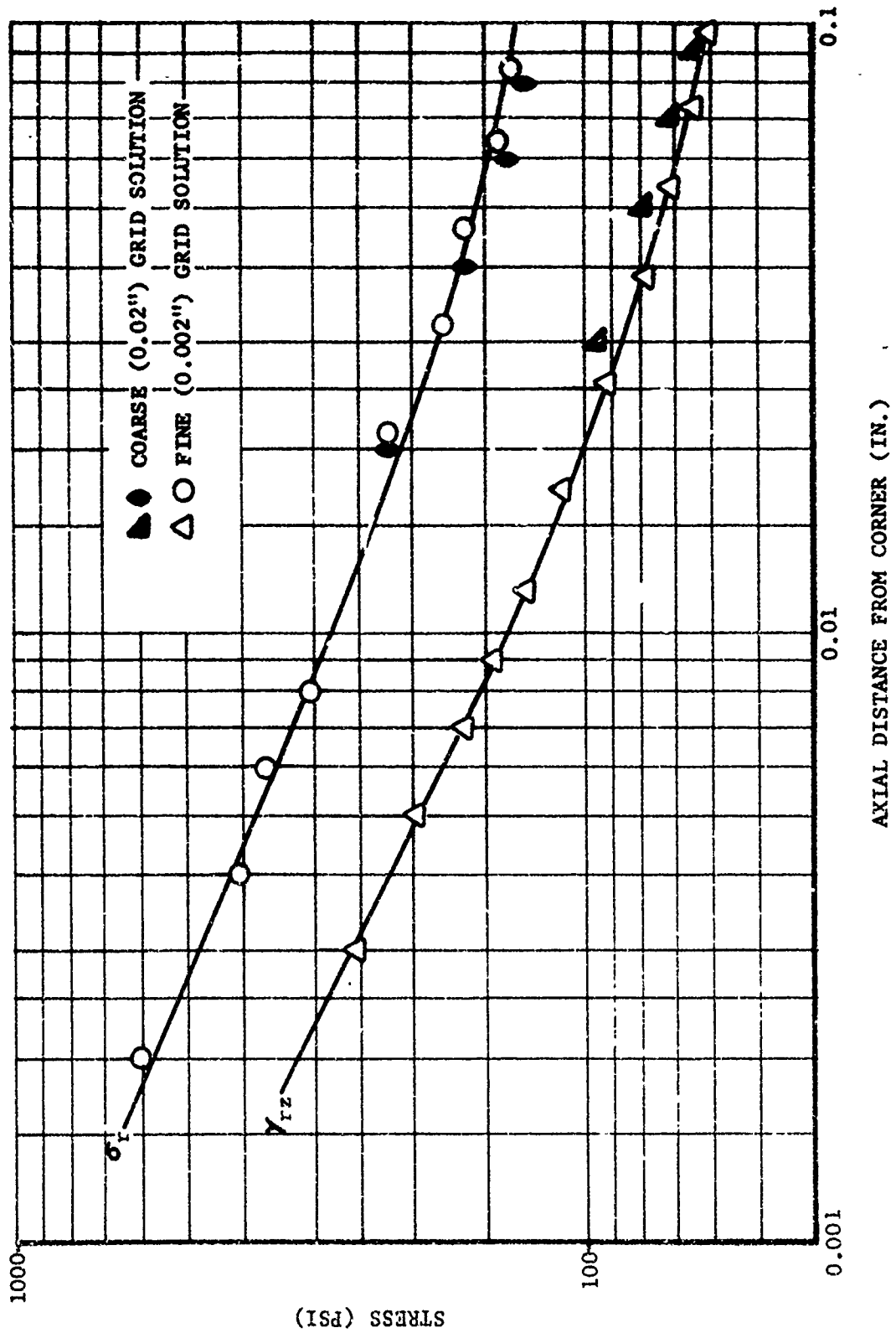
Figure 1-22.   Comparison of stresses along first propellant element row of two finite-element models for rigid-cased cylinder subjected to thermal shrinkage loading and $E_{liner} = E_{propellant} = 850$ psi.

122

RIGID LINER

$E_L/E_p = 1.0$

0.50

0.24

0.10

1000

100

10

σ_r (PSI)

0.001

0.01

0.1

DISTANCE FROM DISCONTINUITY, S (IN.)
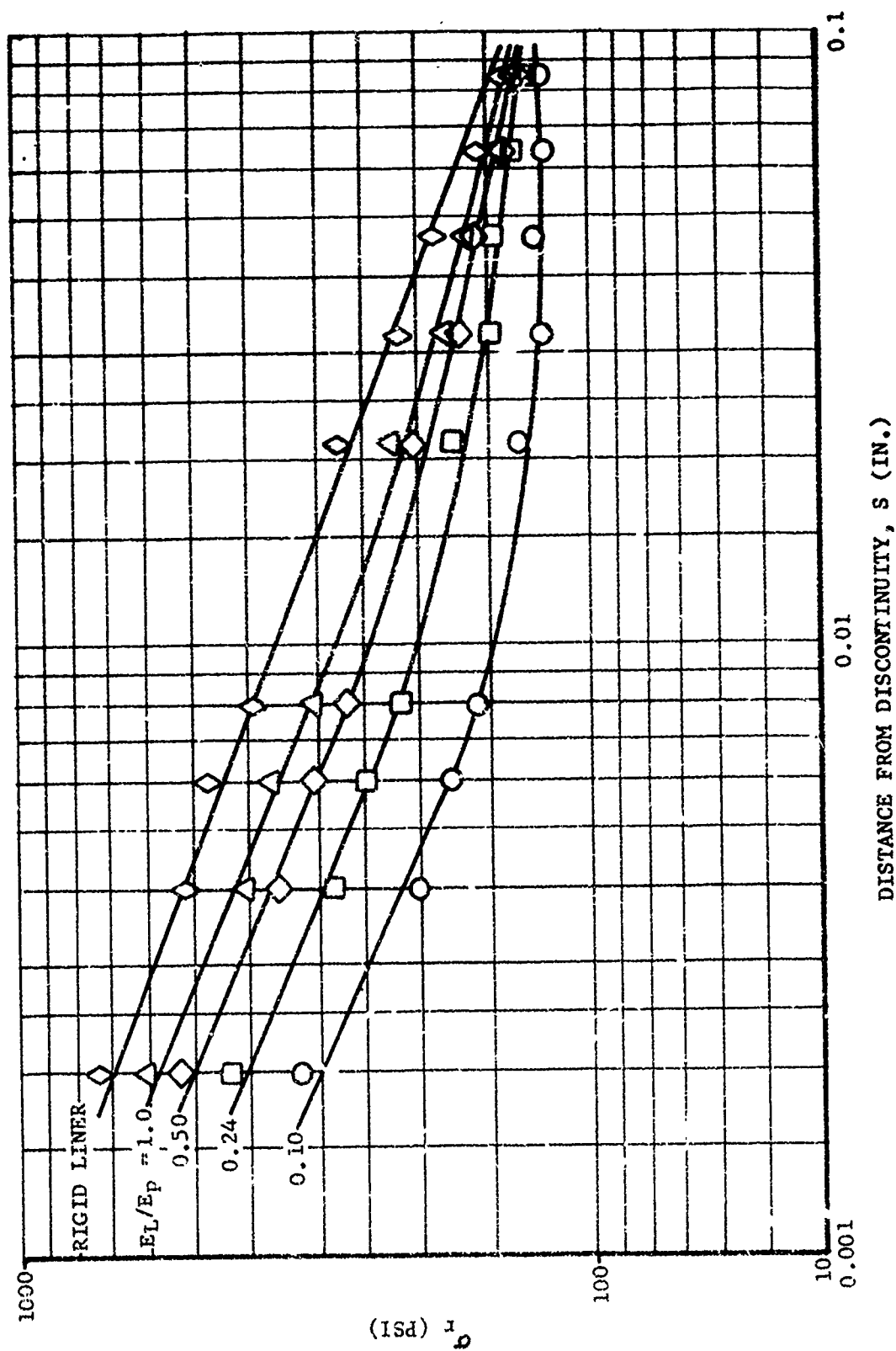
Figure 1-23. F dial stresses along first row of elements in the propellant as a function of liner modulus for rigid-cased cylinder subjected to thermal shrinkage loading.
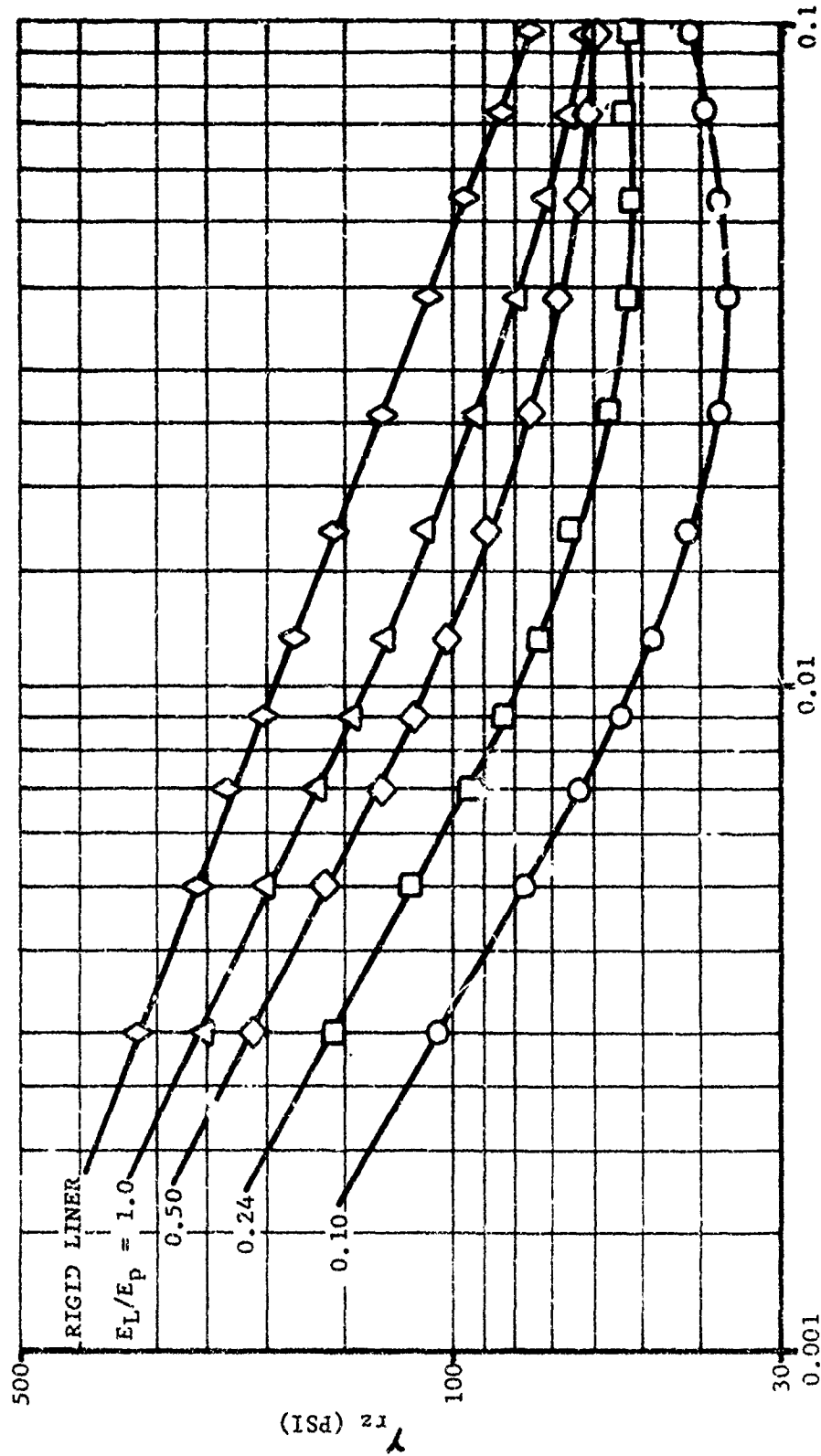
DISTANCE FROM DISCONTINUITY, S (IN.)

Figure 1-24. Shear stresses along first row of elements in the propellant as a function of liner modulus for rigid-cased cylinder subjected to thermal shrinkage loading.

124
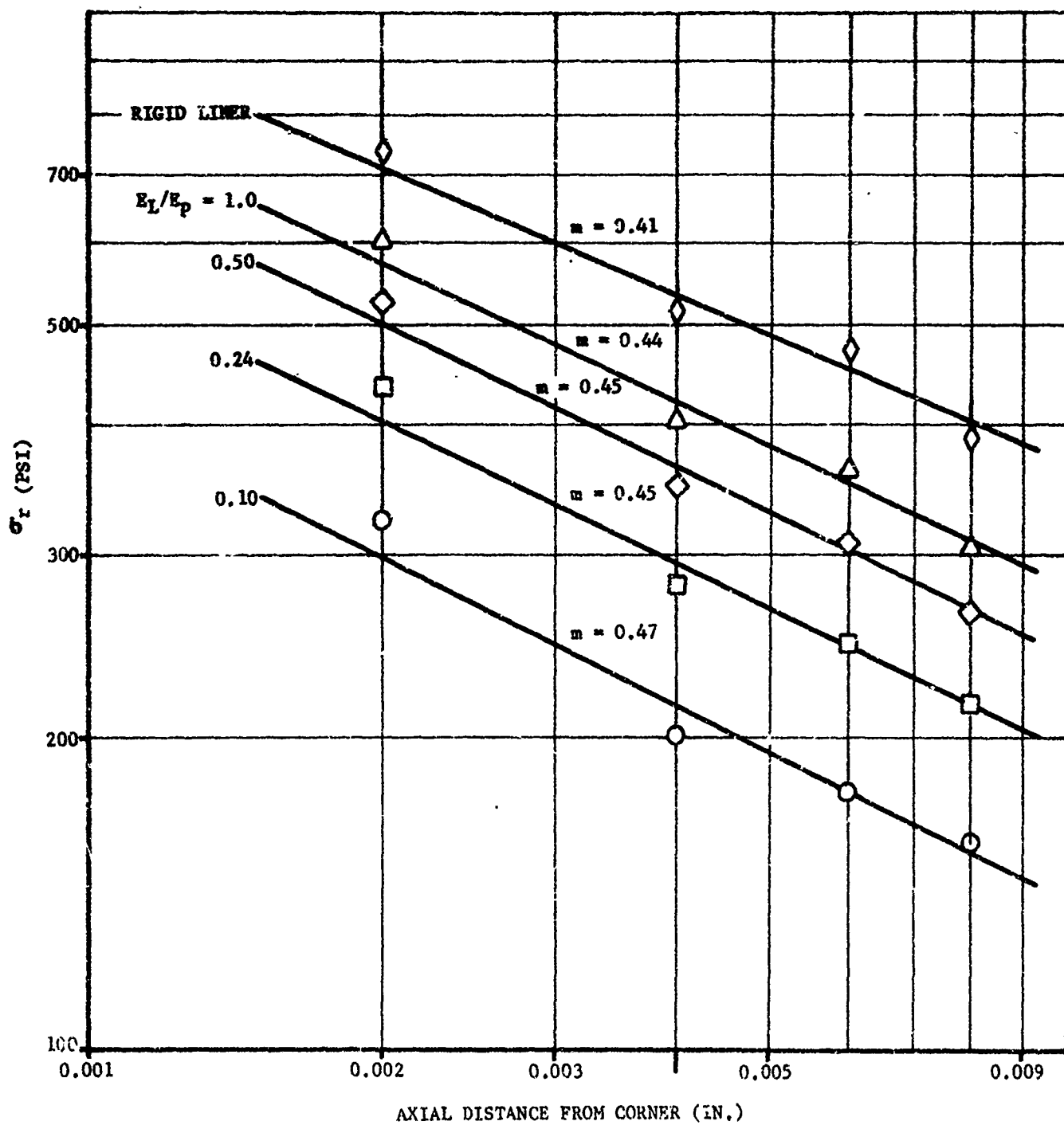
Figure 1-25. Radial stress distribution for different liner-to-propellant tensile modulus ratios.

125
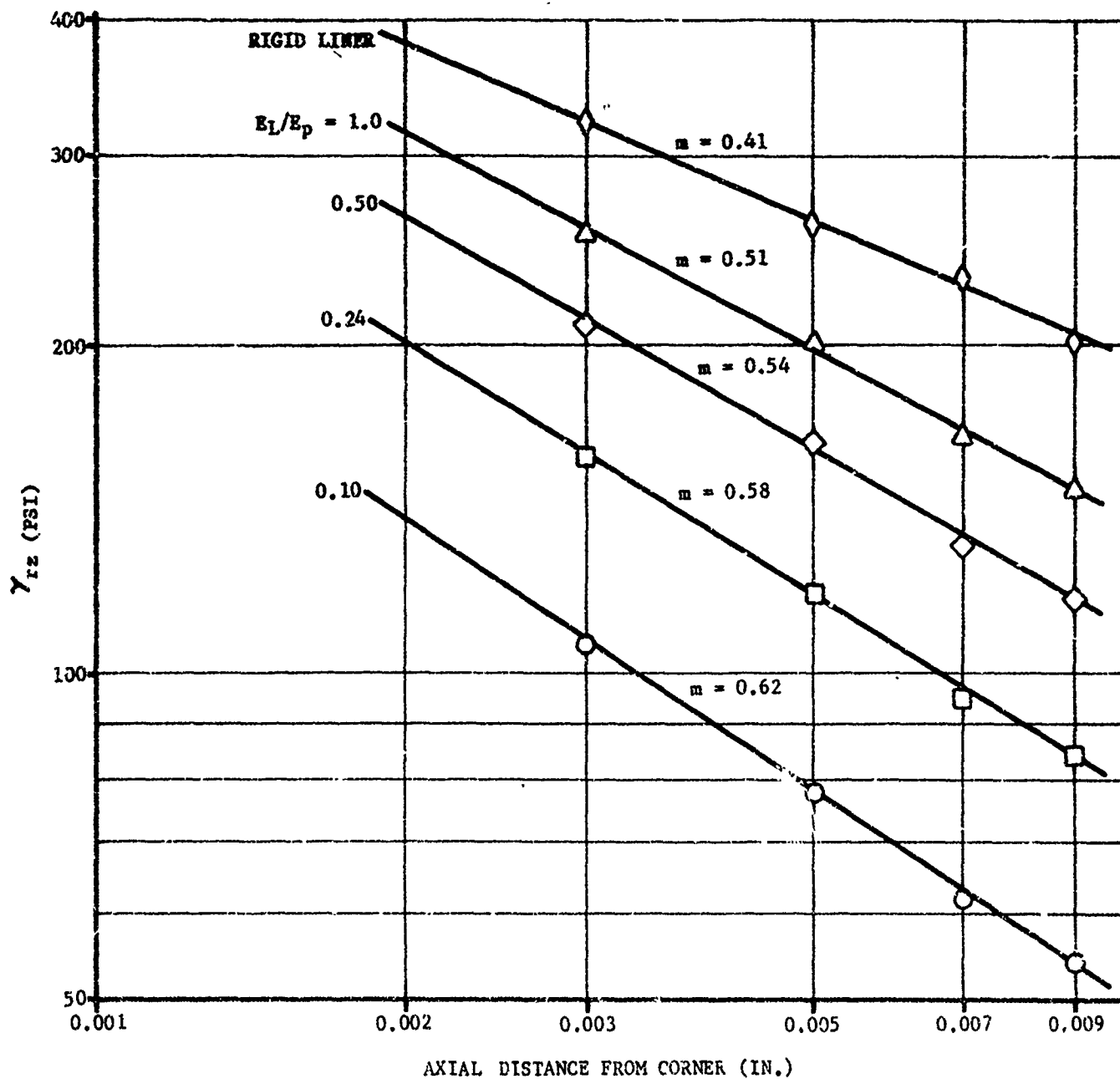
Figure 1-26. Shear stress distribution for different liner-to-propellant tensile modulus ratios.

126
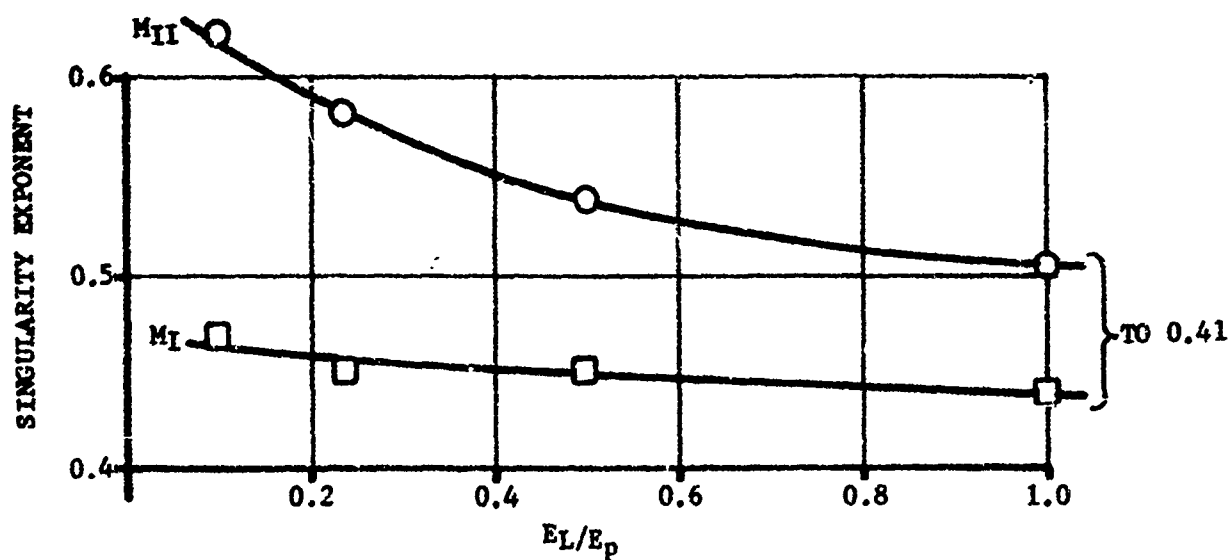
Figure 1-27a. Effect of liner modulus on the singularity exponent.
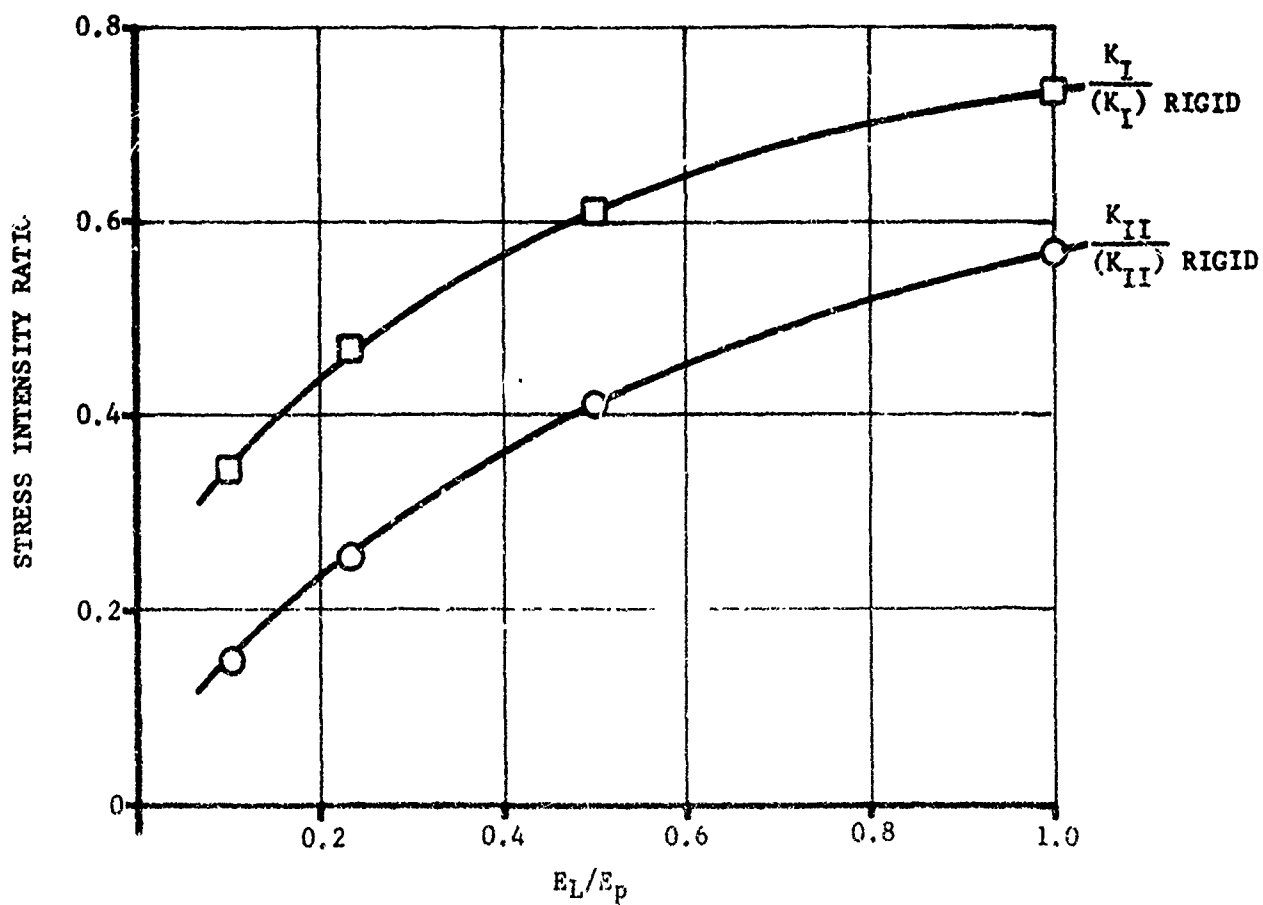
Figure 1-27b. Effect of liner modulus on the stress intensity factor.

127
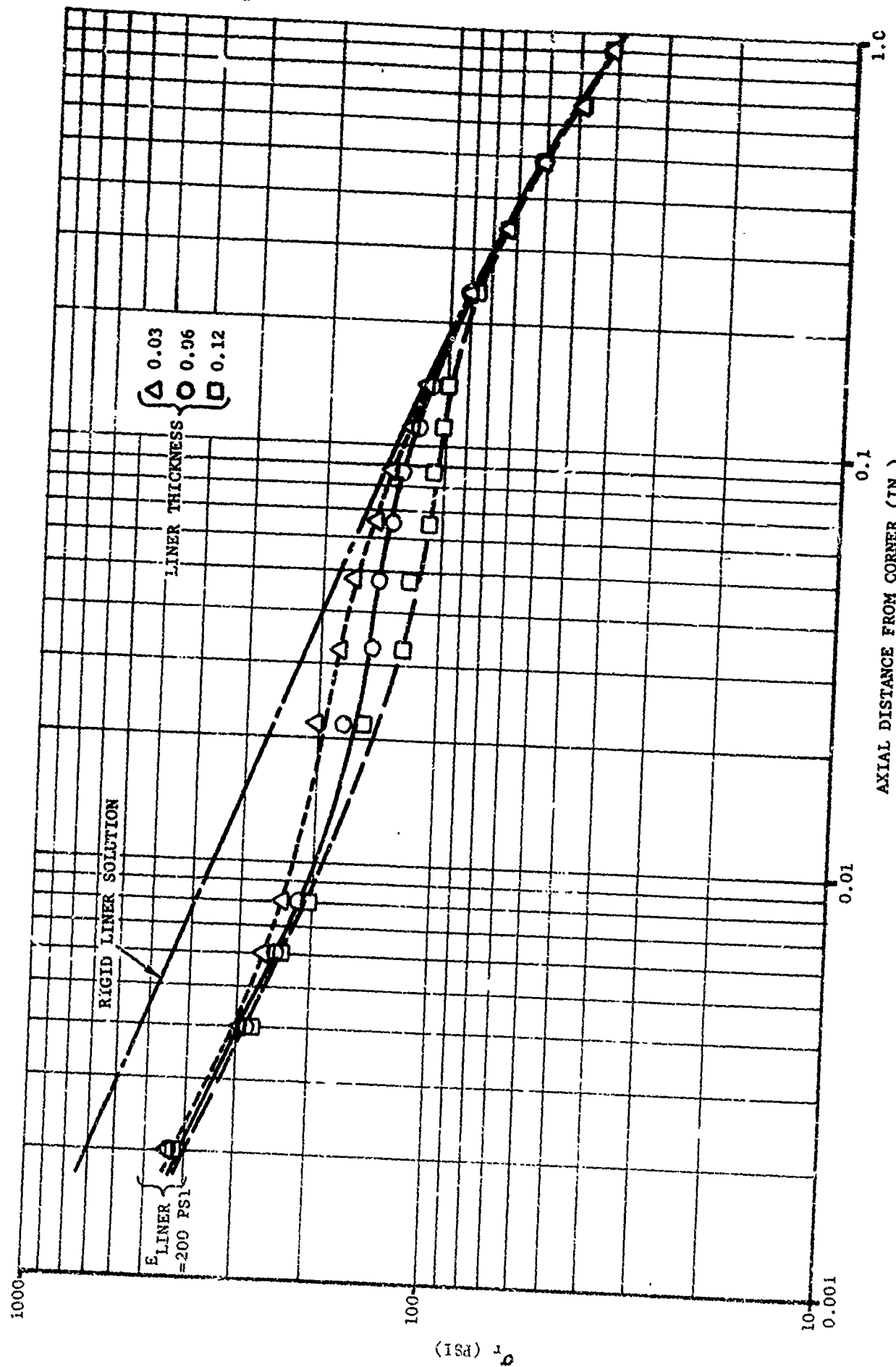
Figure 1-28. Effect of liner thickness on radial stress distribution along first row of elements in the propellant for rigid-cased cylinder subjected to thermal shrinkage loading.

128
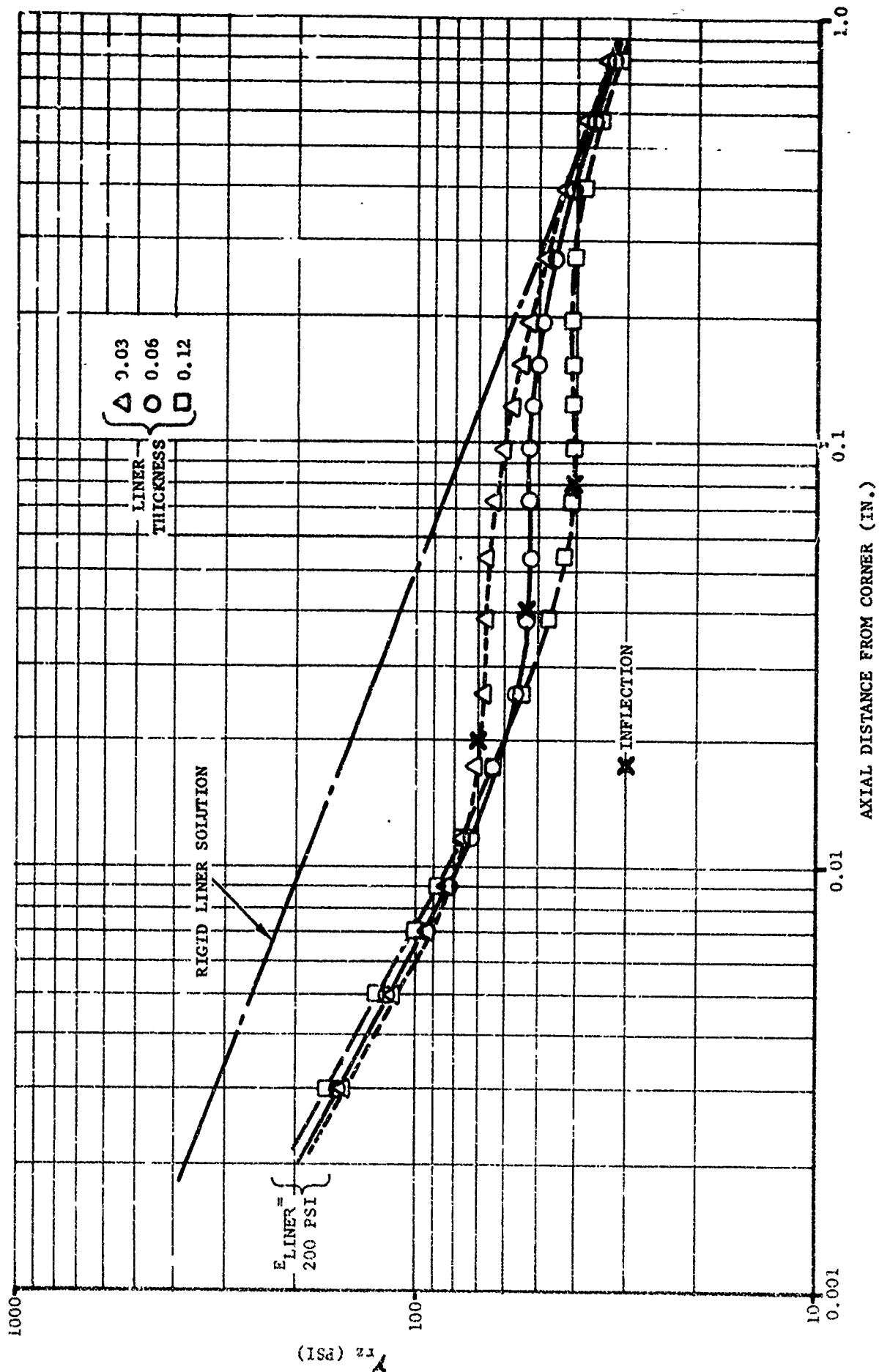
Figure 1-29. Effect of liner thickness on shear stress distribution along first row of elements in the propellant for rigid-cased cylinder subjected to thermal shrinkage loading.

129
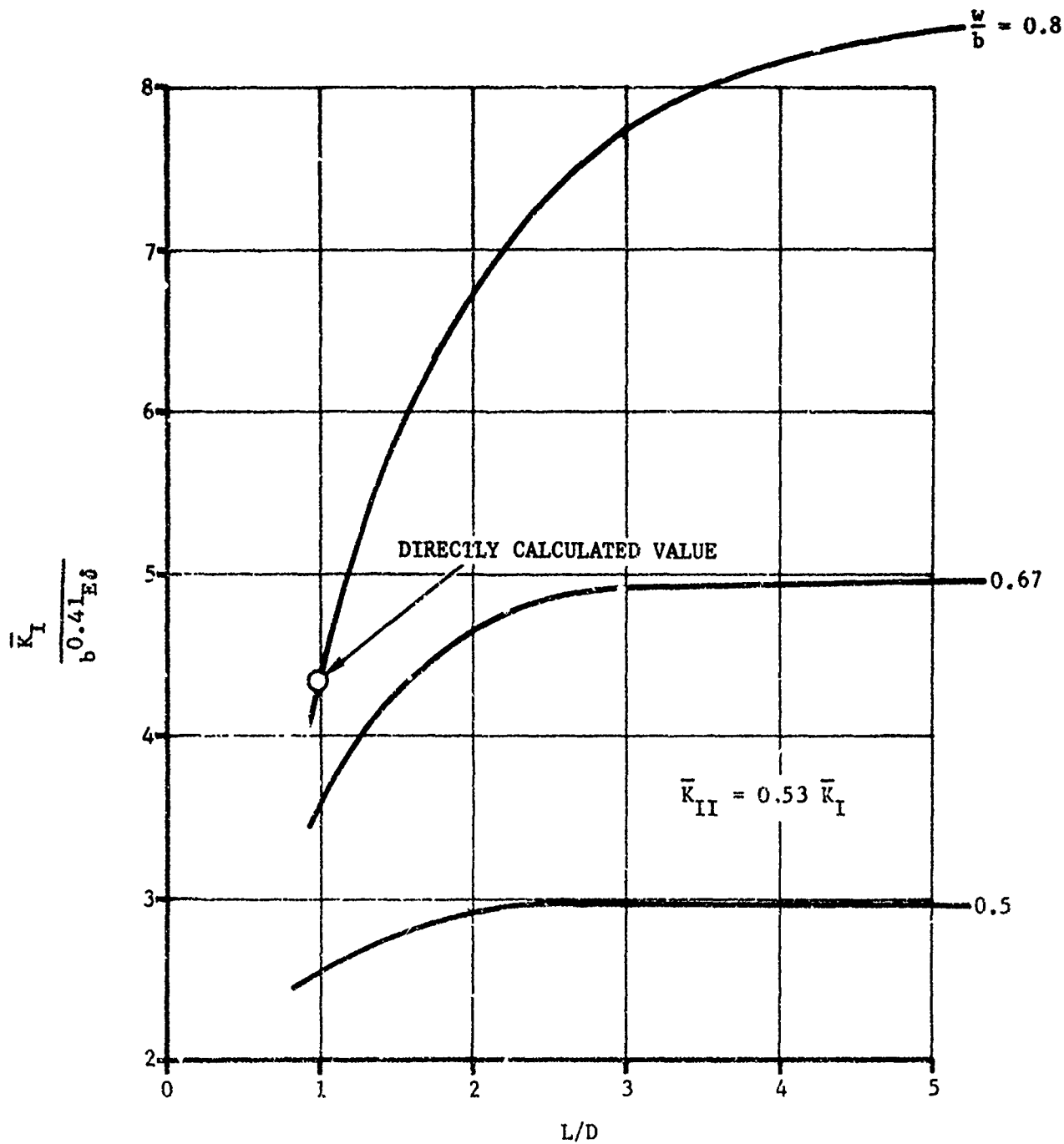
Figure 1-30. Stress intensity factors for thermal shrinkage of a cylinder with a rigid liner, as a function of L/D and W/b.
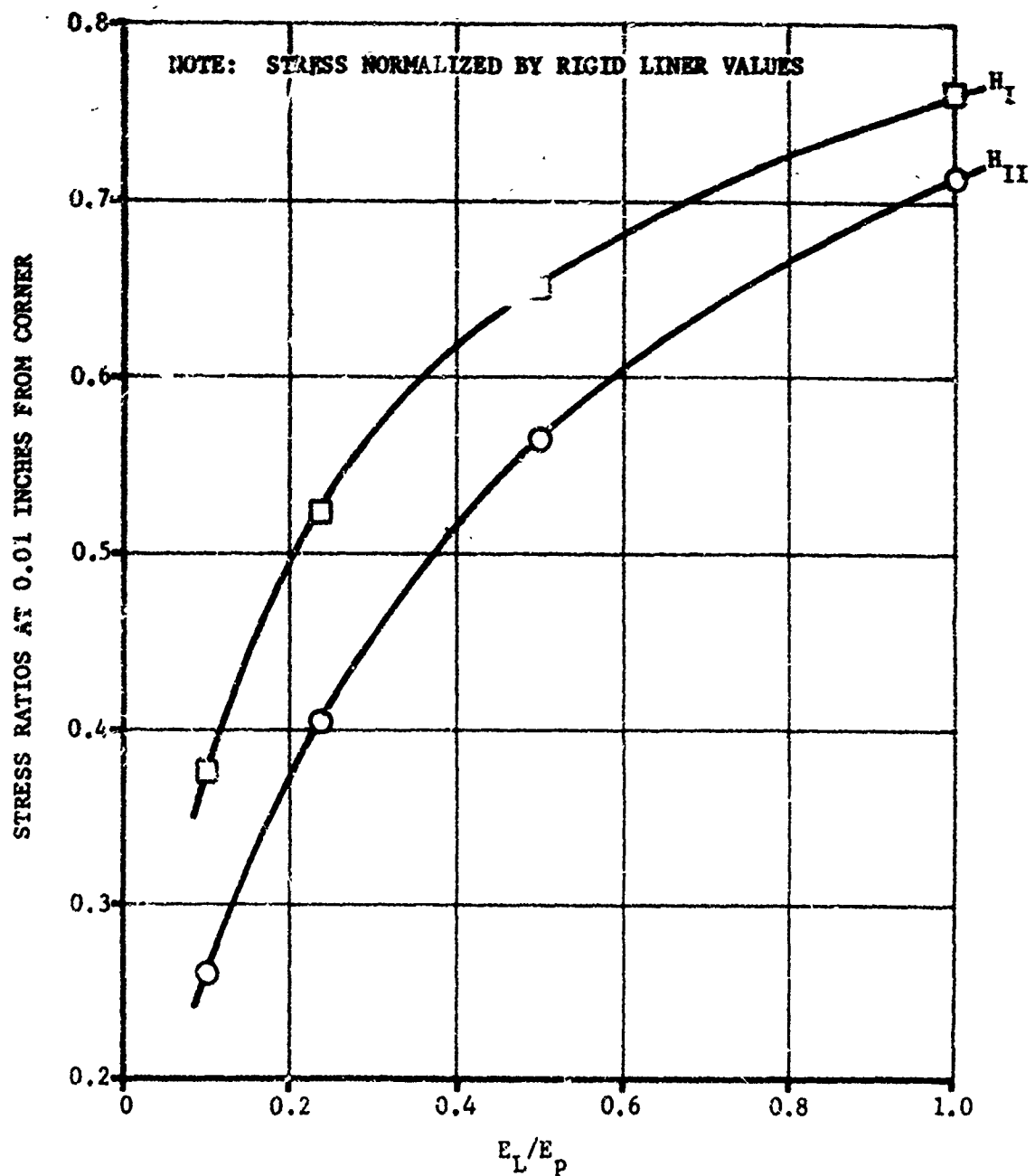
130

Figure 1-31. Effect of liner stiffness on the radial and shear stresses at a distance 0.01 inches axially from the corner.

131
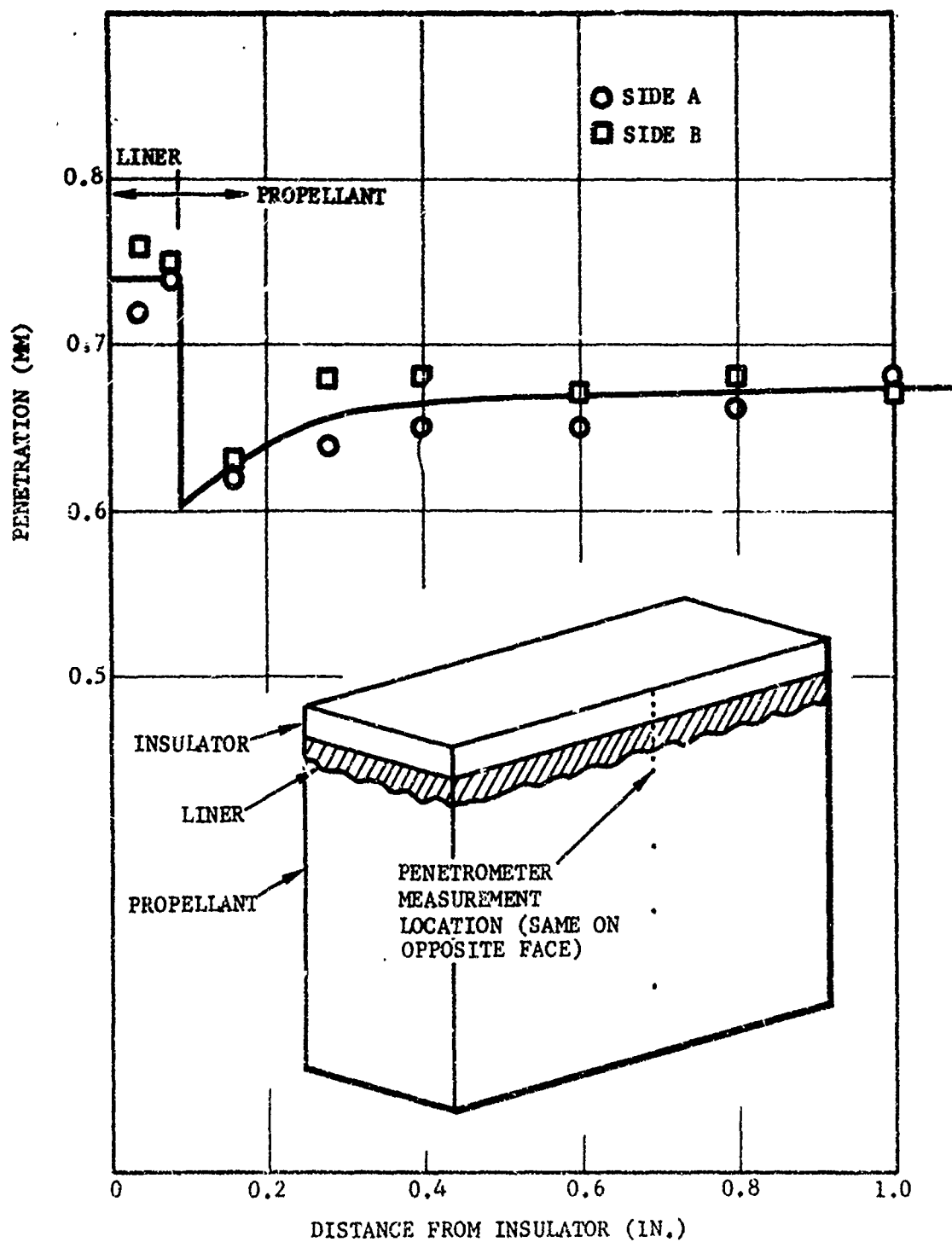
Figure 2-1. Penetrometer results for TP-H1123 propellant/case bond system (9-inch cube casting).
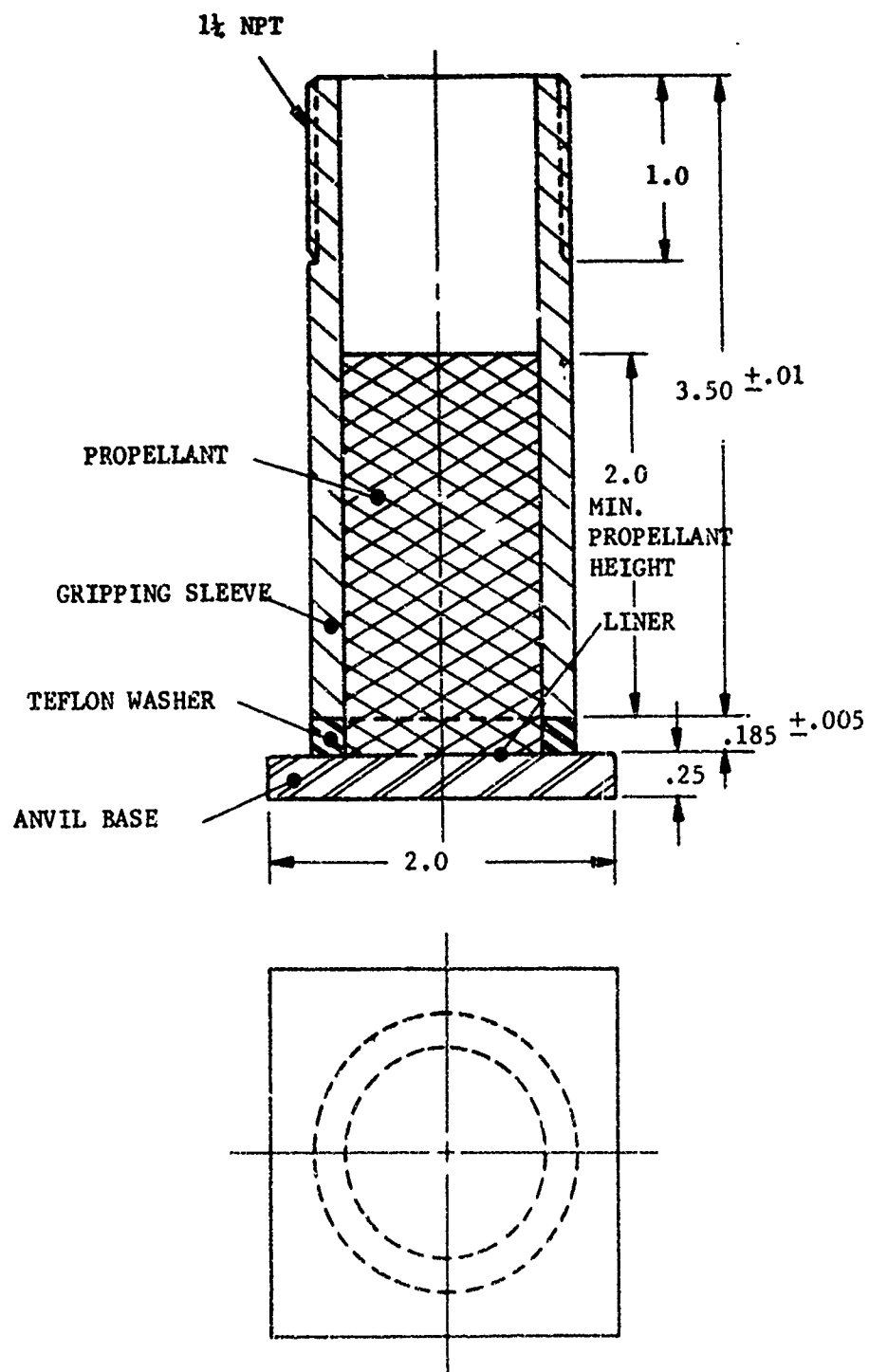
Figure 2-2. Joint in tension (pipe) specimen.

133

DISC, 1020 STEEL

FORMULATION

0.060 + 0.002 IN.
- 0.000 IN.

TEFLON
SPACER

1.128 $\pm$ 0.002 IN.
DIAMETER

DISC, 1020 STEEL
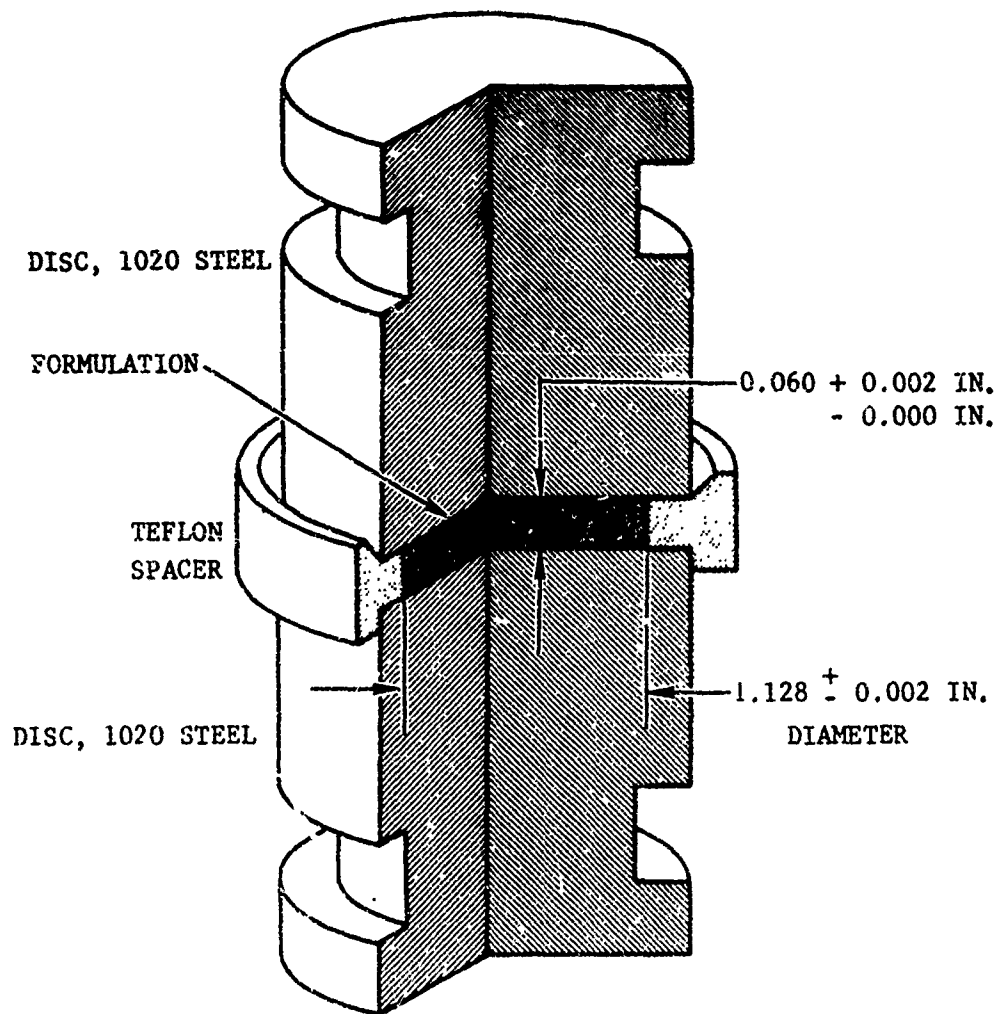
Figure 2-3. Liner strength evaluation sample.
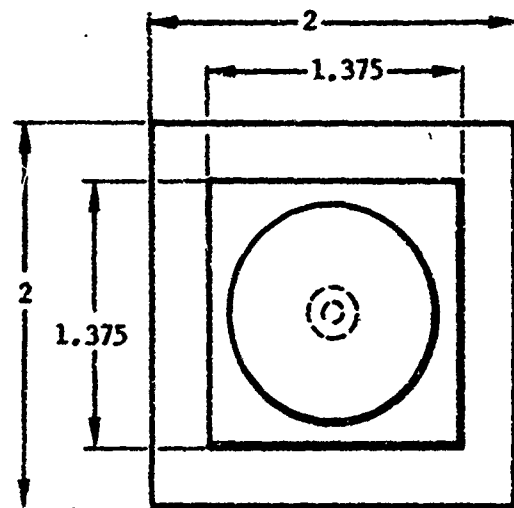
SECTION A-A
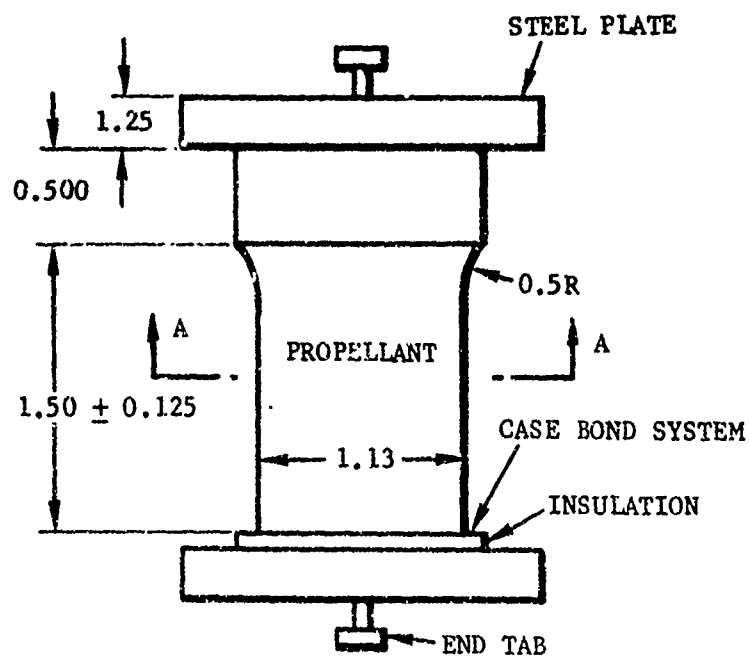
Figure 2-4. Case-bond tensile sample for cast double-base propellants.
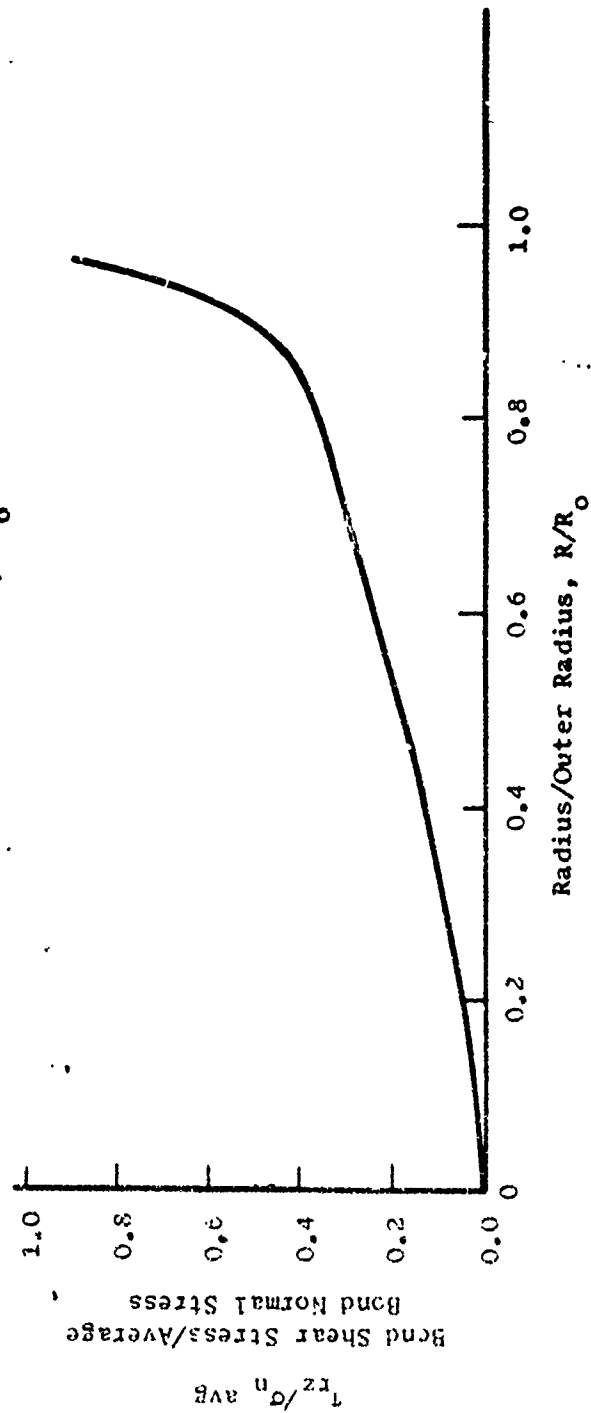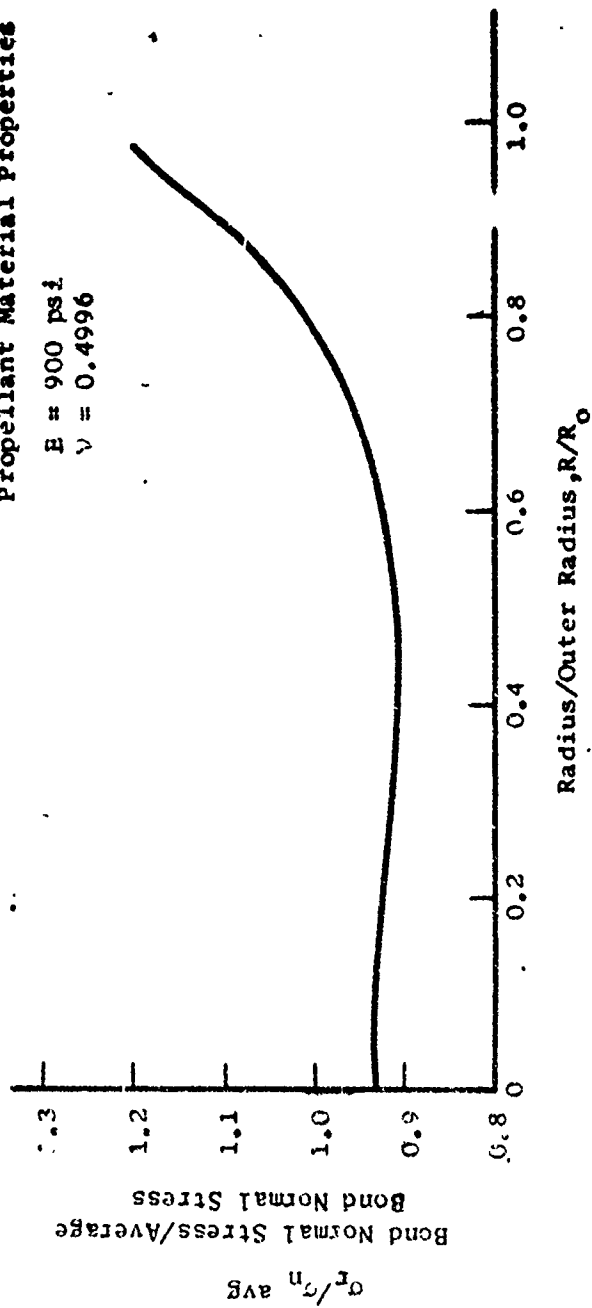
Figure 2-5. Stress distribution at case bond in double-base tension specimen.

136

INSULATOR (0.1 INCH THICK)

LINER (0.06 INCH THICK)

UNIFORM DISPLACEMENT IN "Z" DIRECTION OVER THIS SURFACE OF SAMPLE

Z

Figure 2-6. Finite-element model and boundary conditions for joint in tension (pipe) sample.

STRESSES IN "Z" DIRECTION
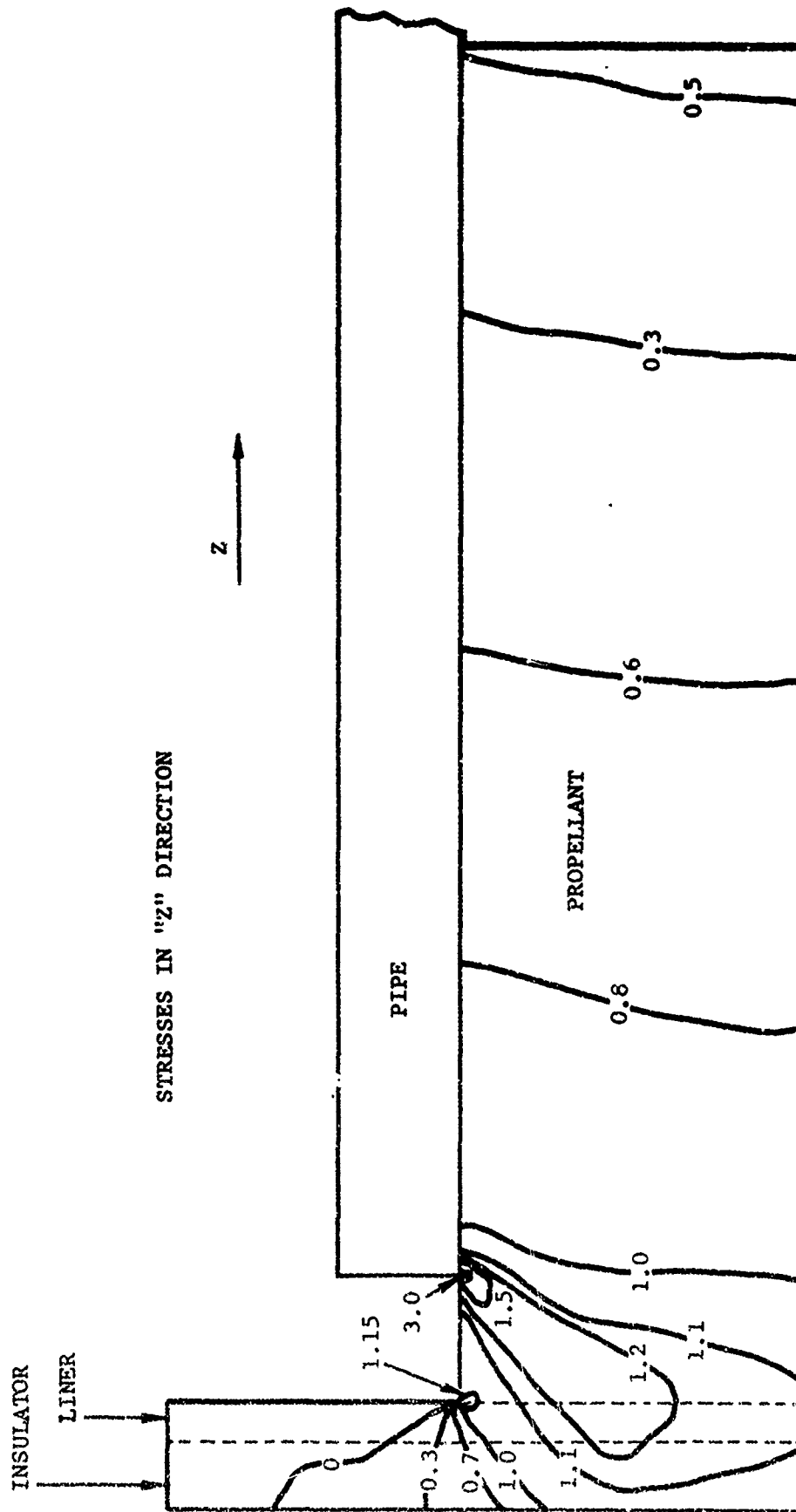
Figure 2-7. Liner of constant axial stress in pipe tensile sample (E_P = 700, E_L = 230, E_I = 1000, U_{pipe} = .03 inches).

138
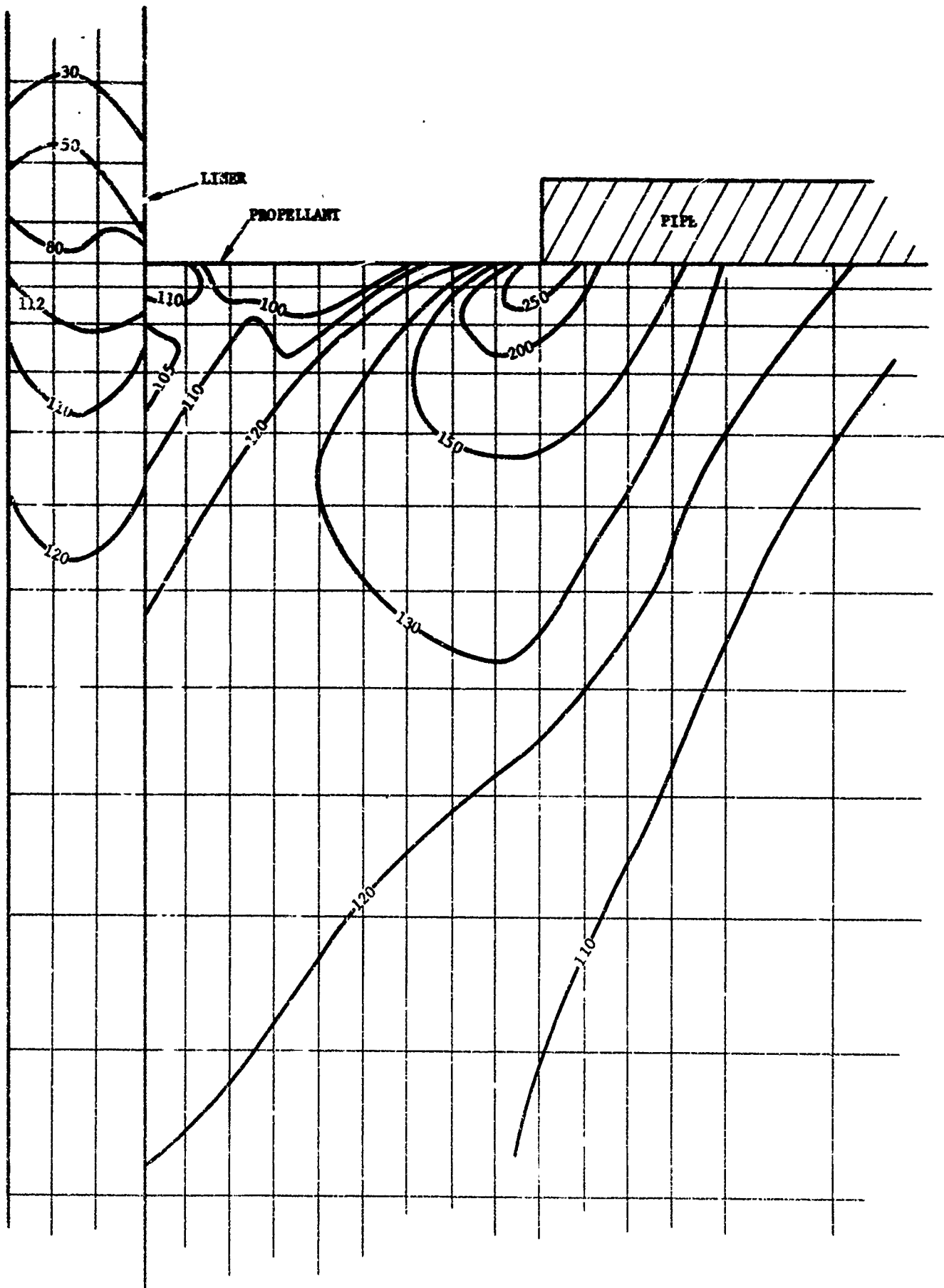
Figure 2-8. Lines of constant maximum principal stress adjacent to bond interface in pipe tensile sample.
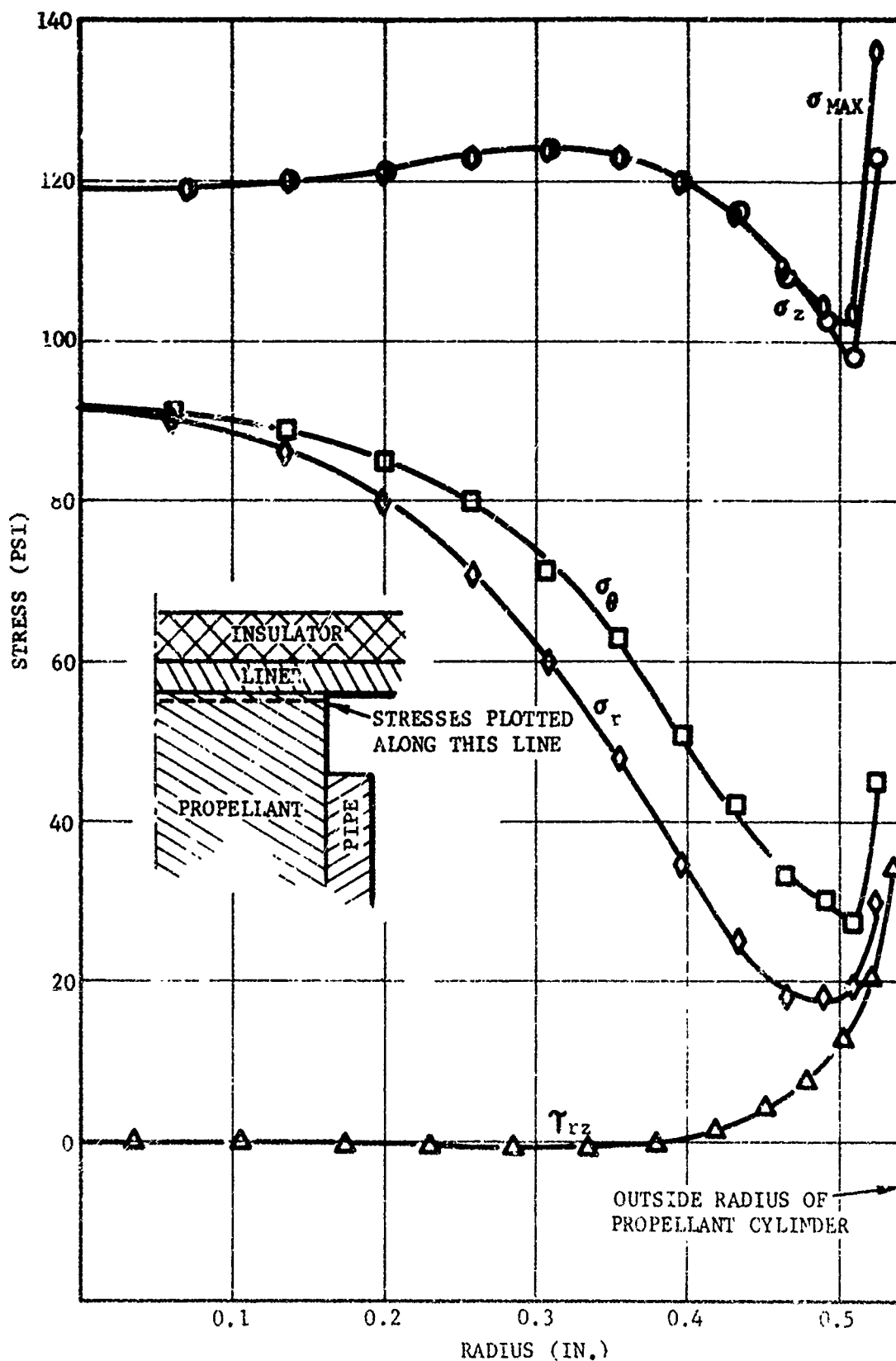
Figure 2-9. Stresses in propellant element column adjacent to case bond liner for pipe tensile sample.

RIGID END TAB

INSULATOR

FLAP (UNBOND, TEFLON WASHERS)

LINER

CASE BOND LINE

PROPELLANT

1.00 DIA.

0.375 R

1.50 DIA

RIGID END TAB

SCALE 2/1
DIMENSIONS IN INCHES
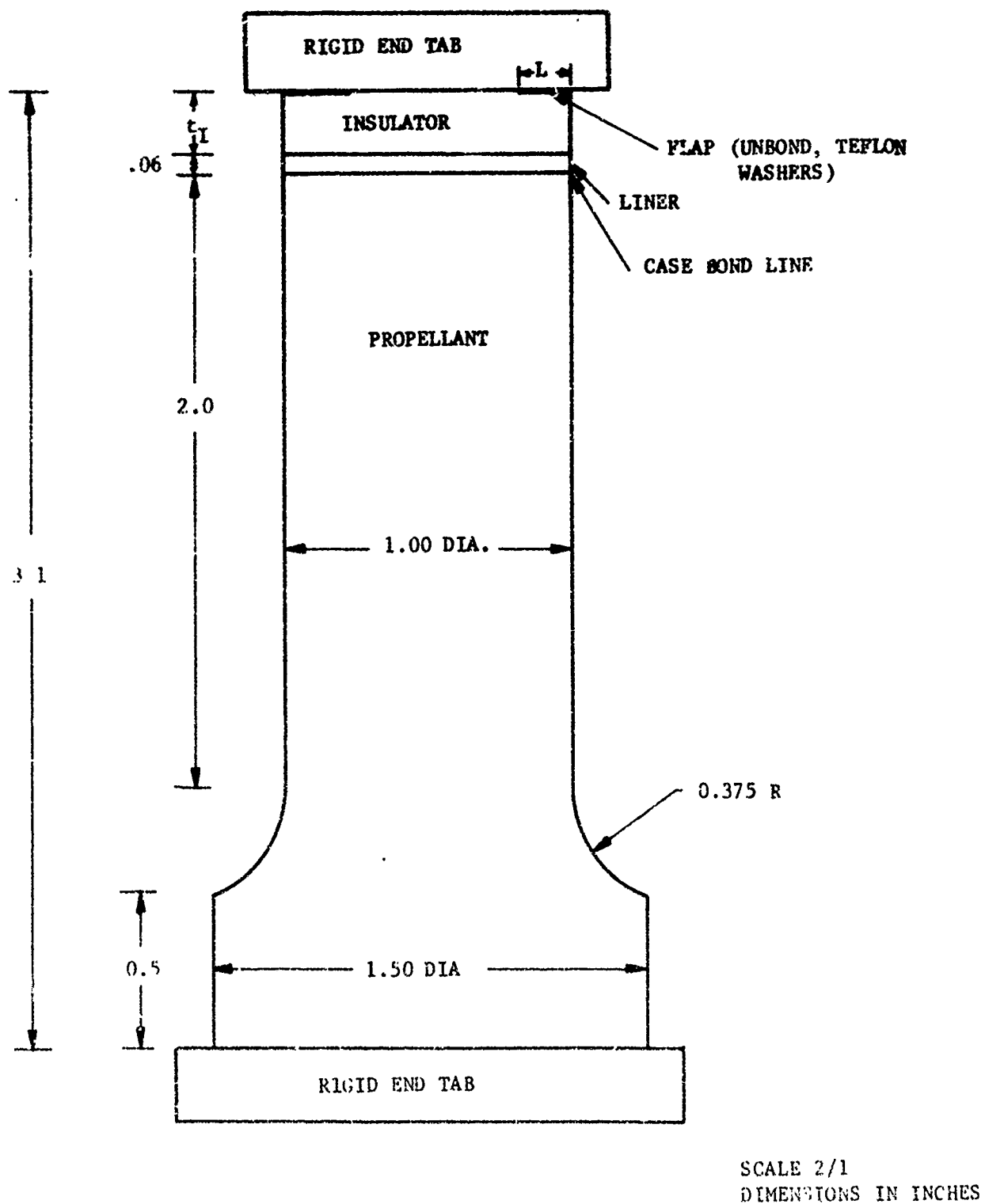
Figure 2-10. Long round-flapped case bond tensile sample.
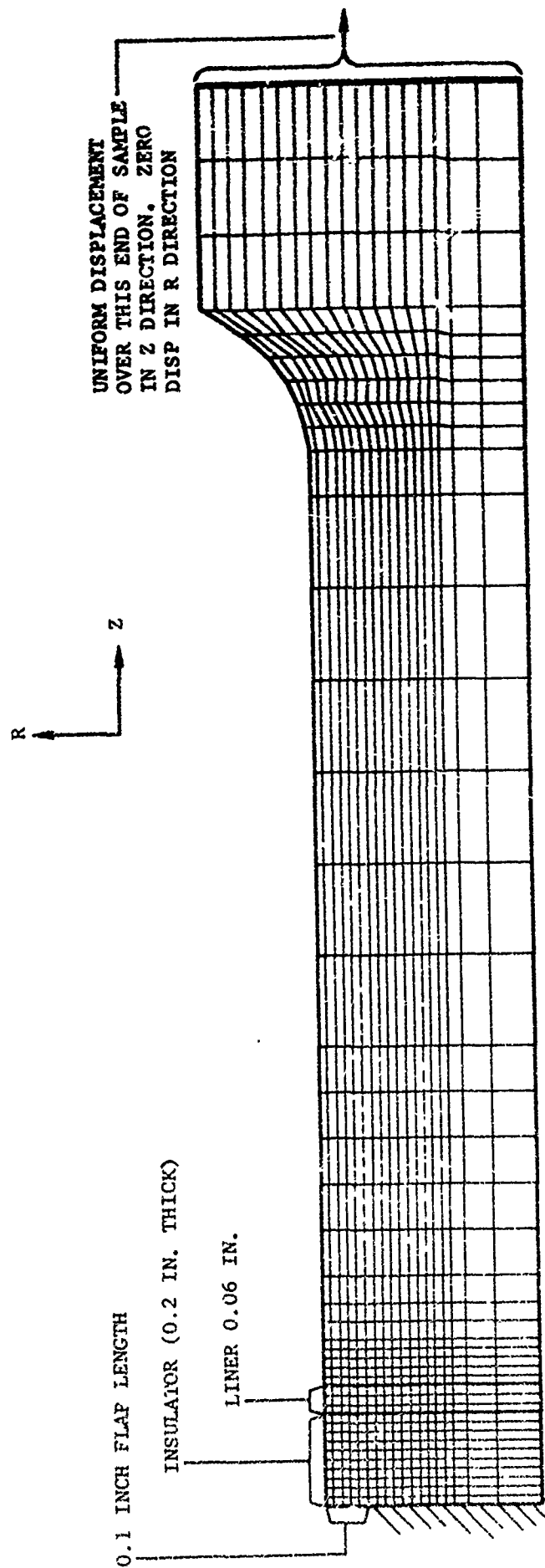
Figure 2-11. Finite element model and boundary conditions for long round-flapped tensile sample.

142
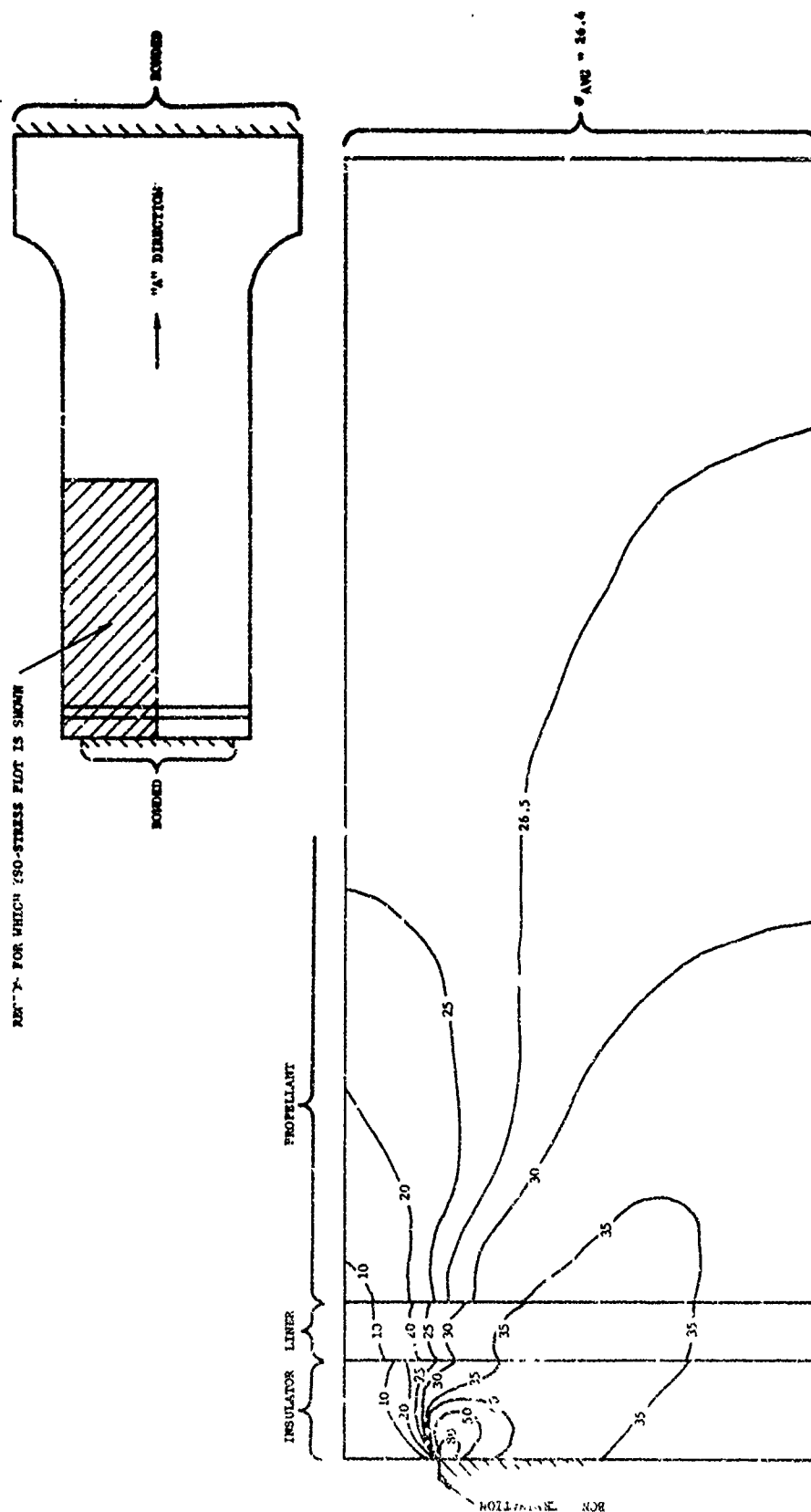
Figure 2-12. Lines of constant maximum principal stress in long, round-flapped tensile sample for soft liner condition ($E_L = 230$, $E_I = 1000$, $E_p = 700$).
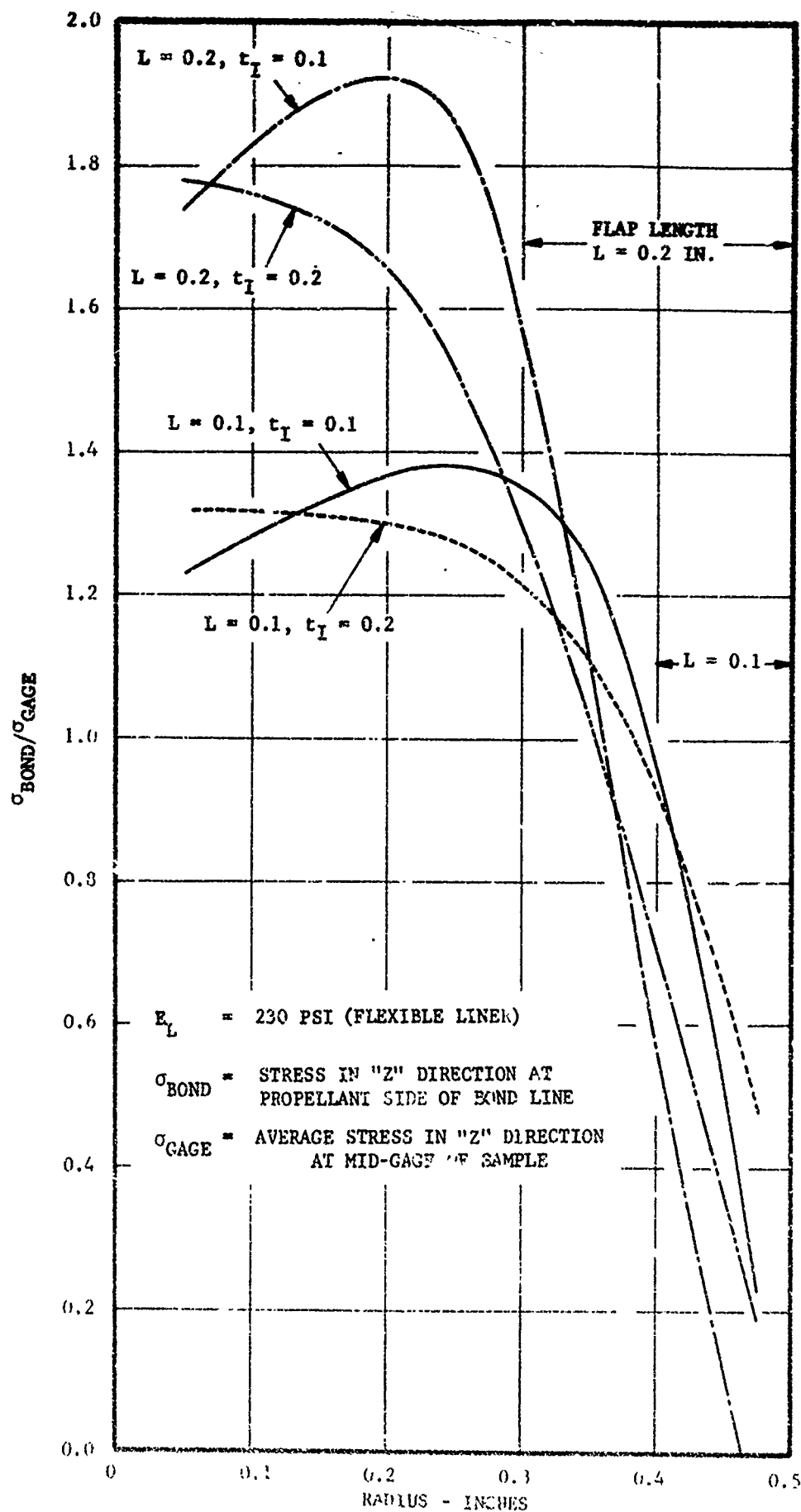
Figure 2-13. $\sigma_{bond}/\sigma_{gage}$ versus radius in long round-flapped tensile
sample ($E_L = 230$)

L=0.2, t$_I$=0.1

L = 0.2, t$_I$ = 0.2

FLAP LENGTH
L=0.2 IN.

L = 0.1, t$_I$ = 0.1

L = 0.1, t$_I$ = 0.2

L = 0.1

$\sigma_{BOND}/\sigma_{GAGE}$

2.0

1.8

1.6

1.4

1.2

1.0

0.8

0.6

0.4

0.2

0.0

E$_L$ = 700 PSI (STIFF LINER)

σ_{BOND} = STRESS IN "Z" DIRECTION AT PROPELLANT SIDE OF BOND LINE

σ_{GAGE} = AVERAGE STRESS IN "Z" DIRECTION AT MID-GAGE OF SAMPLE

0   0.1   0.2   0.3   0.4   0.5

RADIUS - INCHES
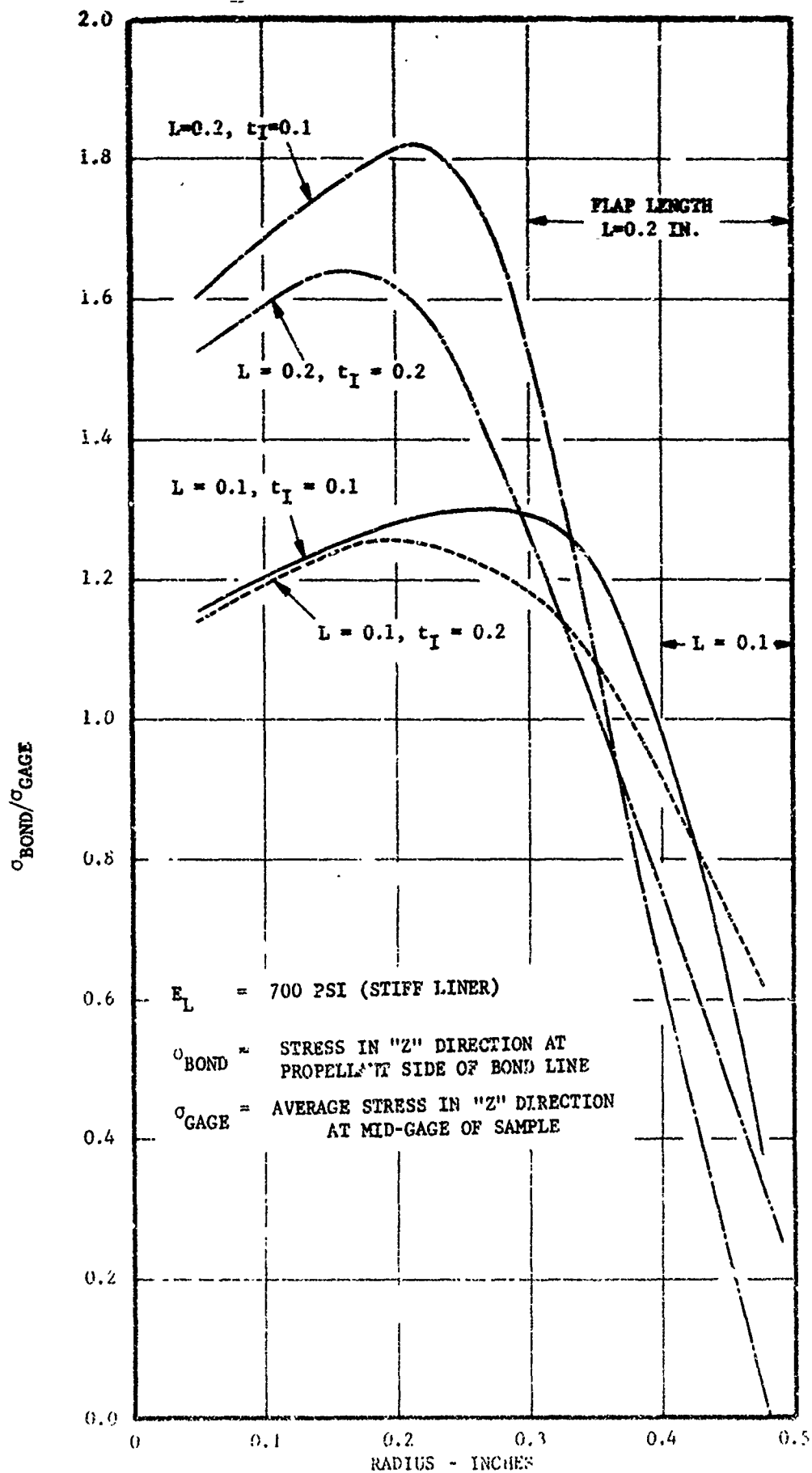
Figure 2-14. $\sigma_{bond}/\sigma_{gage}$ versus radius in long round-flapped tensile sample (E$_L$ = 700).
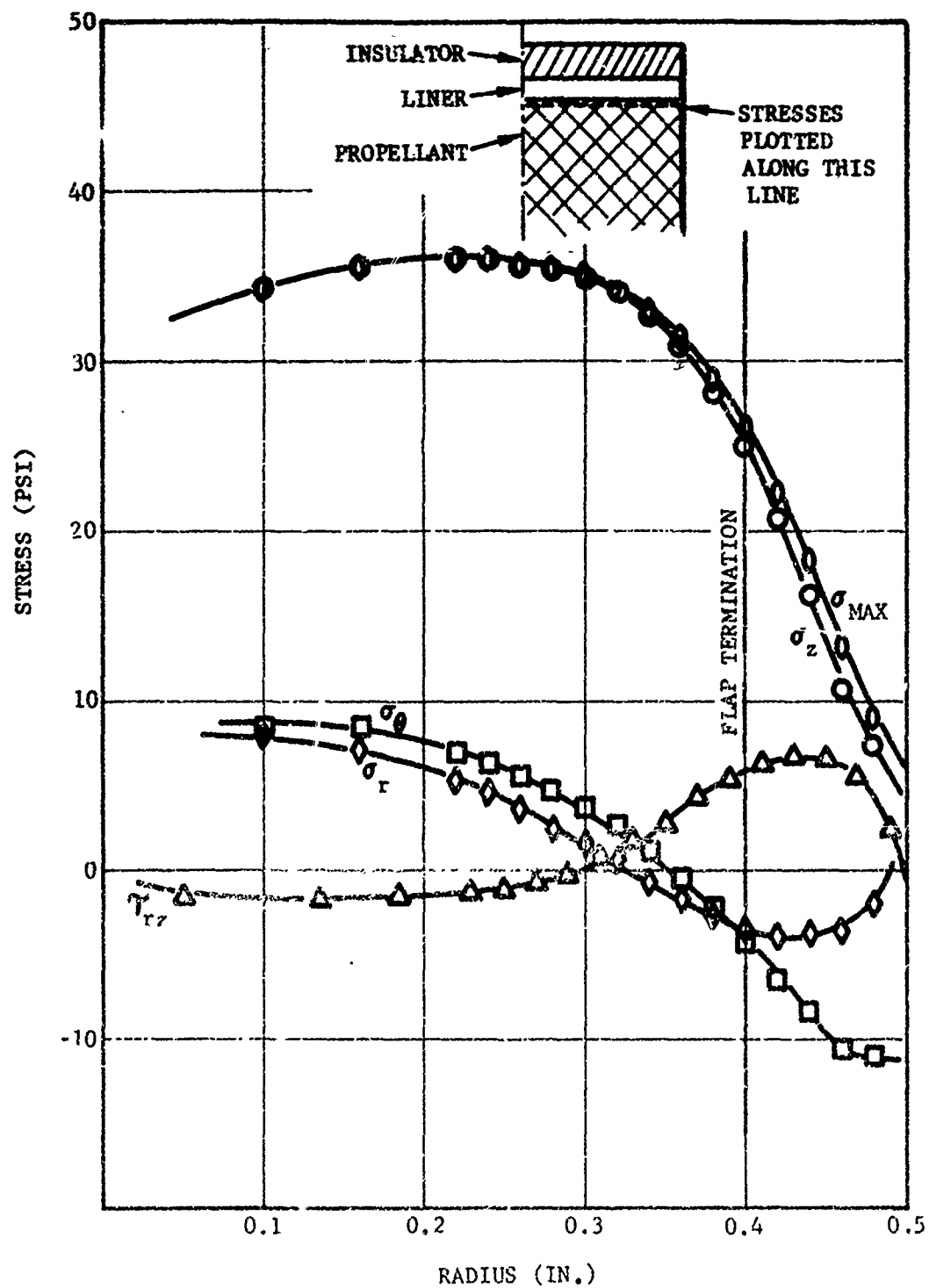
Figure 2-15. Stress distribution in propellant for long, round-flapped
tensile sample ($E_L = 230$, $t_I = 0.1$, $L = 0.1$).

146
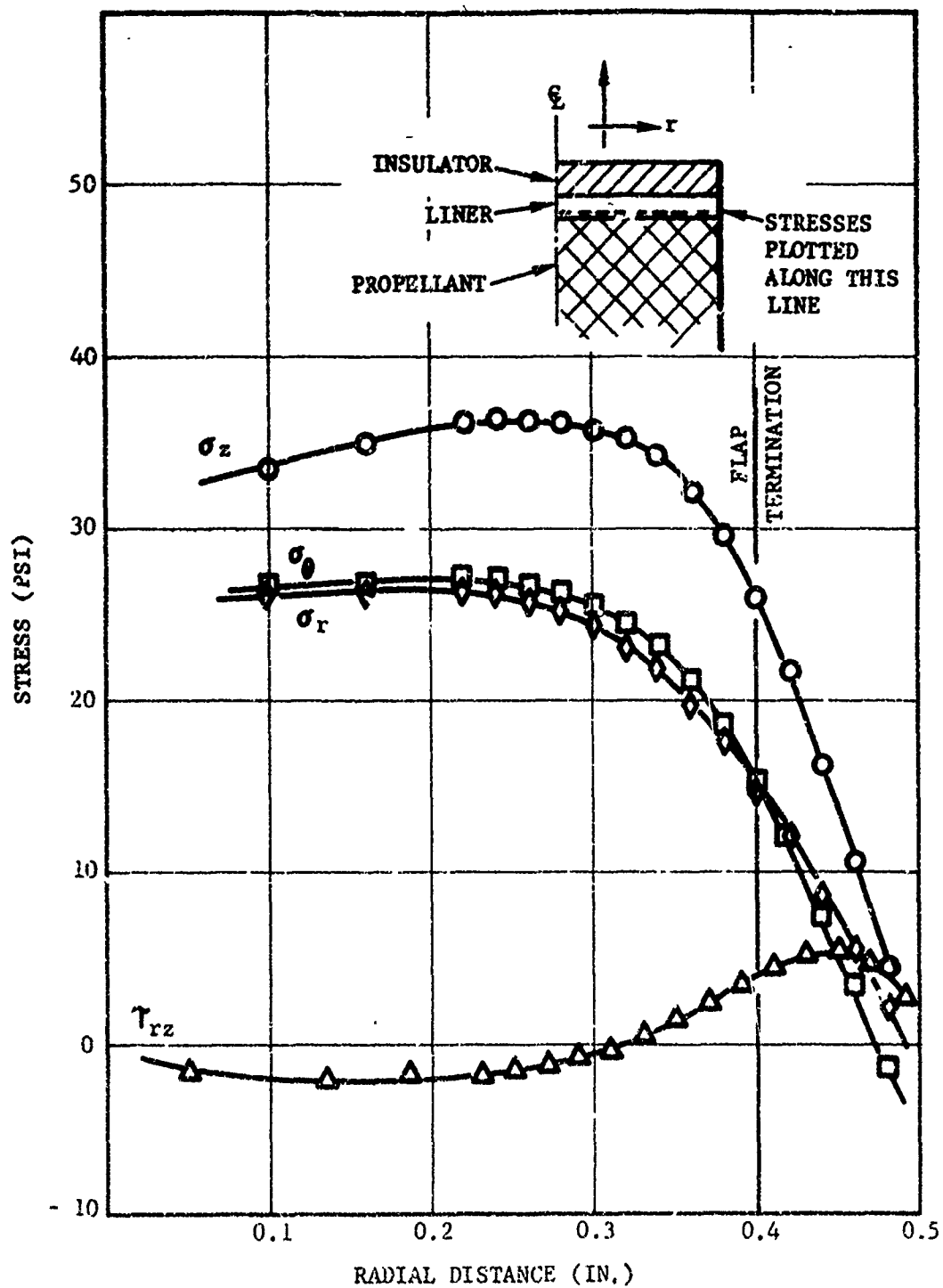
Figure 2-16.   Stress distribution in case bond liner for long, round-flapped tensile sample (E_L = 230, t_I = 0.1, L - 0.1).

147
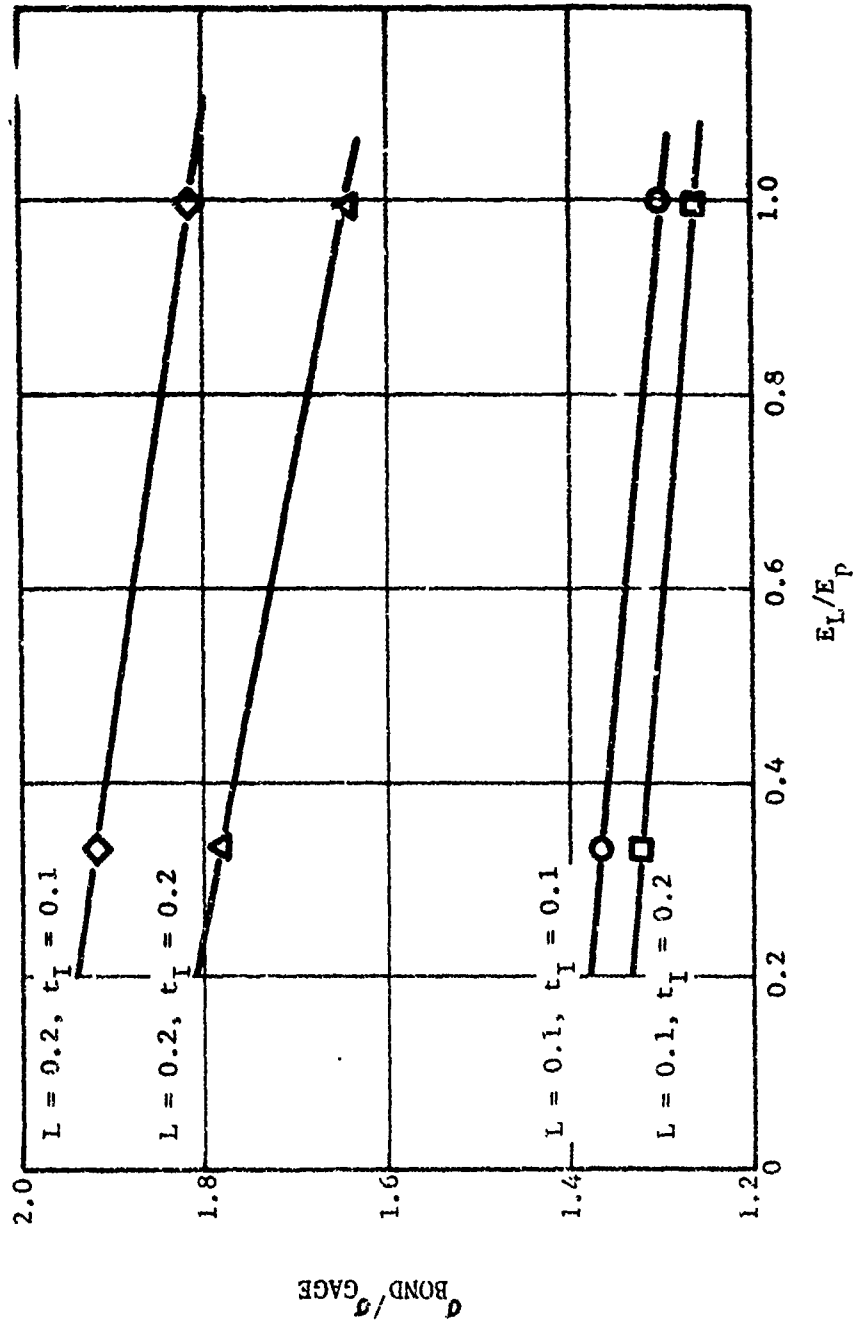
Figure 2-17. Effect of liner stiffness and insulator thickness/bonding on the maximum bond stress for long, round-flapped tensile sample.

148
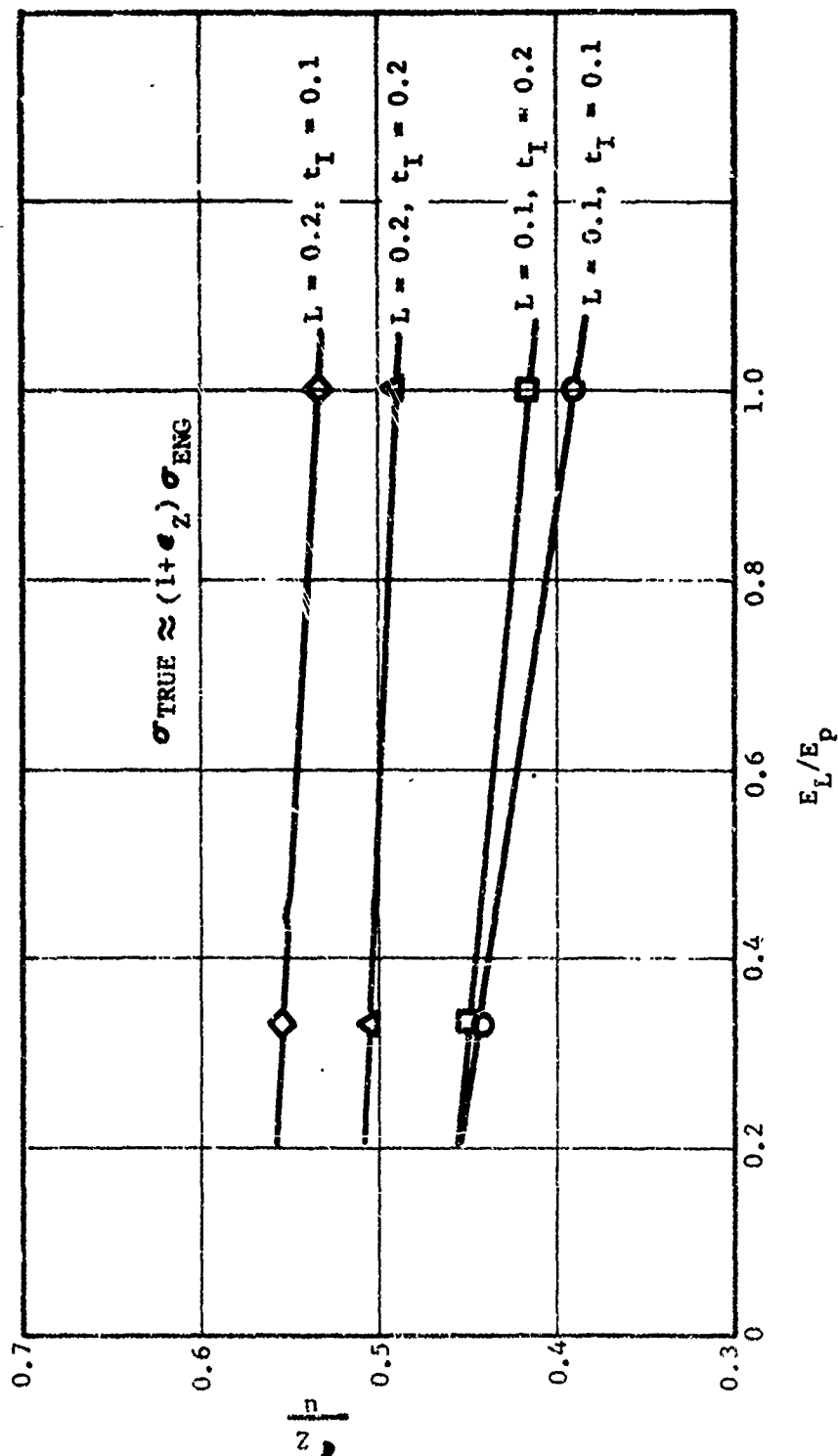
Figure 2-18. Correction factor to convert engineering stress to true stress for long, round-flapped case bond tensile sample.

$\sigma_{TRUE} \approx (1 + \epsilon_Z) \sigma_{ENG}$

L = 0.2, t_I = 0.1

L = 0.2, t_I = 0.2

L = 0.1, t_I = 0.2

L = 0.1, t_I = 0.1

E_L/E_P

ϵ_Z n

149

Figure 2-19. Round-flapped case bond tensile sample.

UNIFORM DISPLACEMENT
IN Z DIRECTION OVER
THIS END OF SAMPLE.
ZERO DISP. IN R DIRECTION

LINER (0.06 INCH THICK)

INSULATOR (0.2 INCH THICK)

0.1 INCH FLAP LENGTH
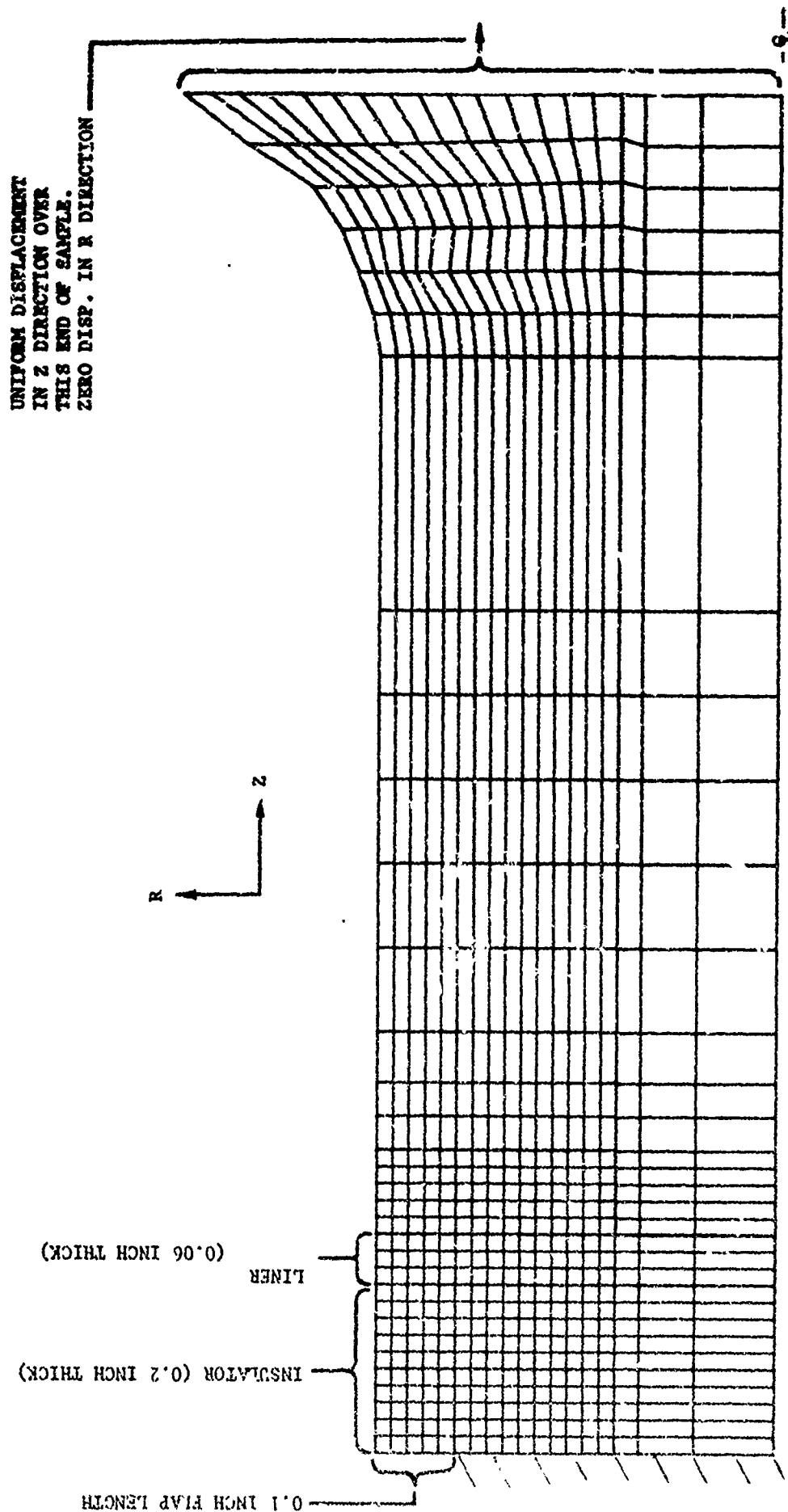
Figure 2-20. Finite-element model and boundary conditions for round-flapped tensile sample.
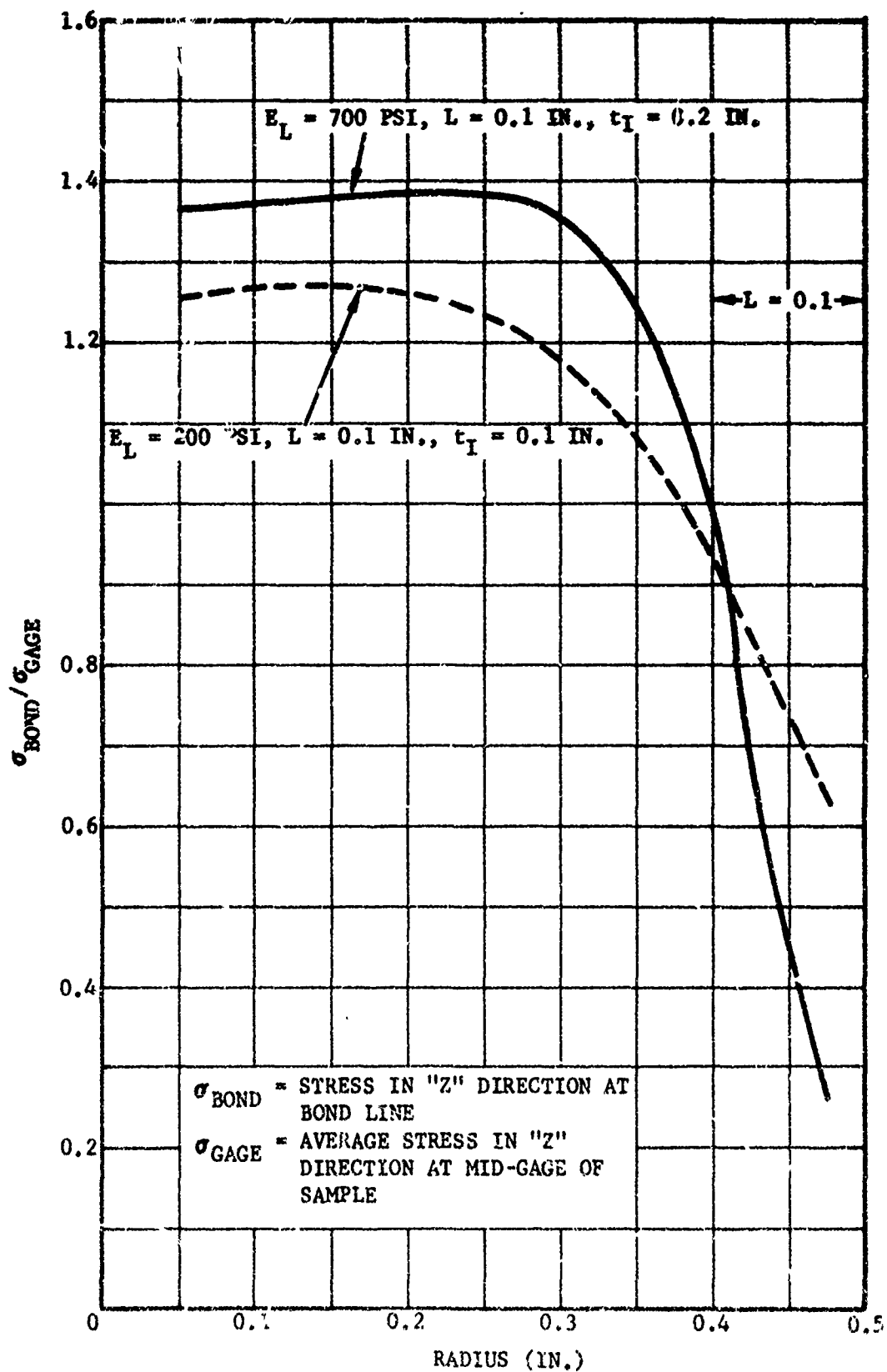
Figure 2-21. σ Bond/σ gage versus radius in round-flapped tensile sample.
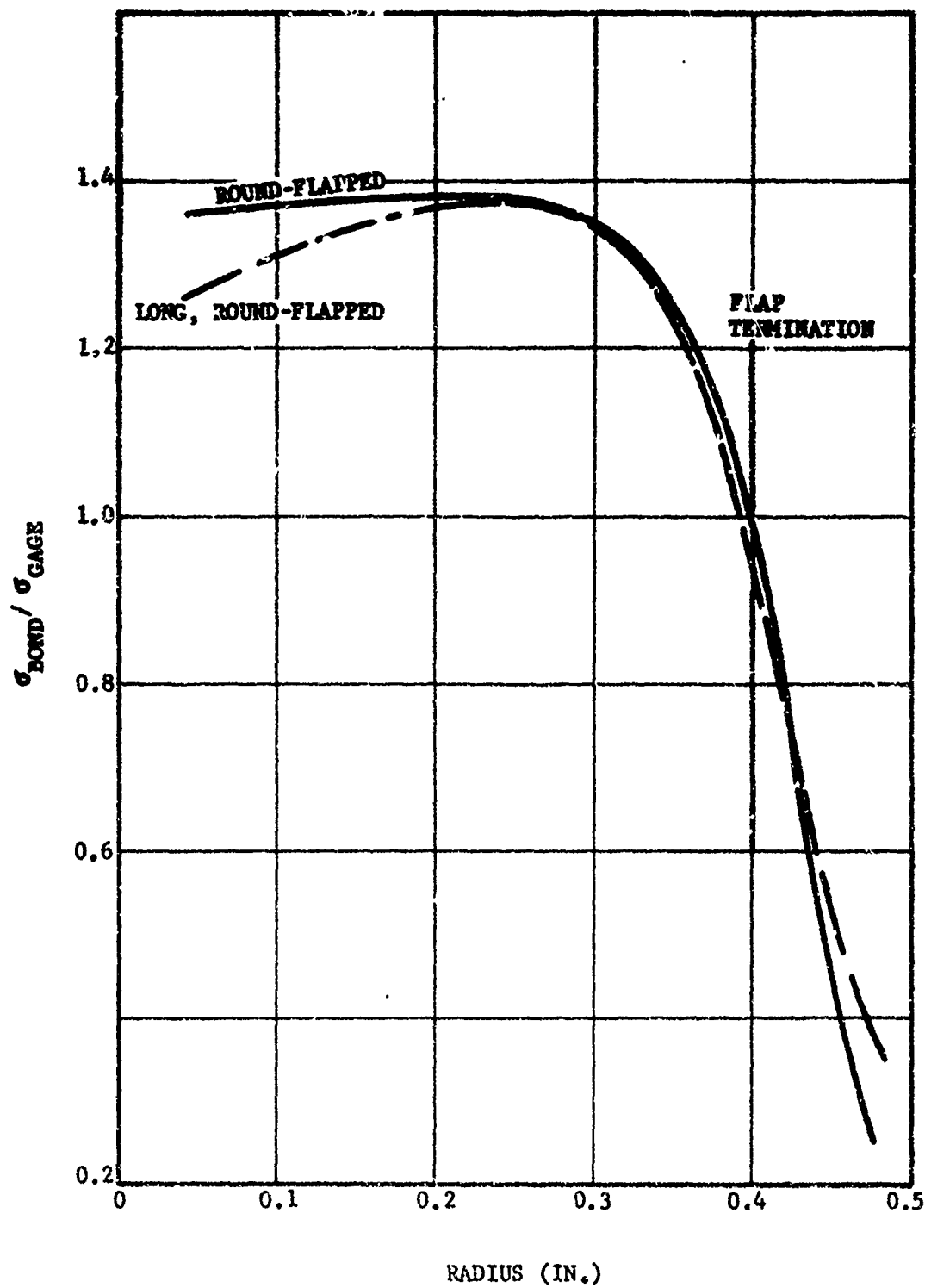
Figure 2-22. Comparision of bond normal (axial) stress distribution for long, round-flapped and round-flapped tensile samples ($E_L = 230$, $t_I = 0.1$).
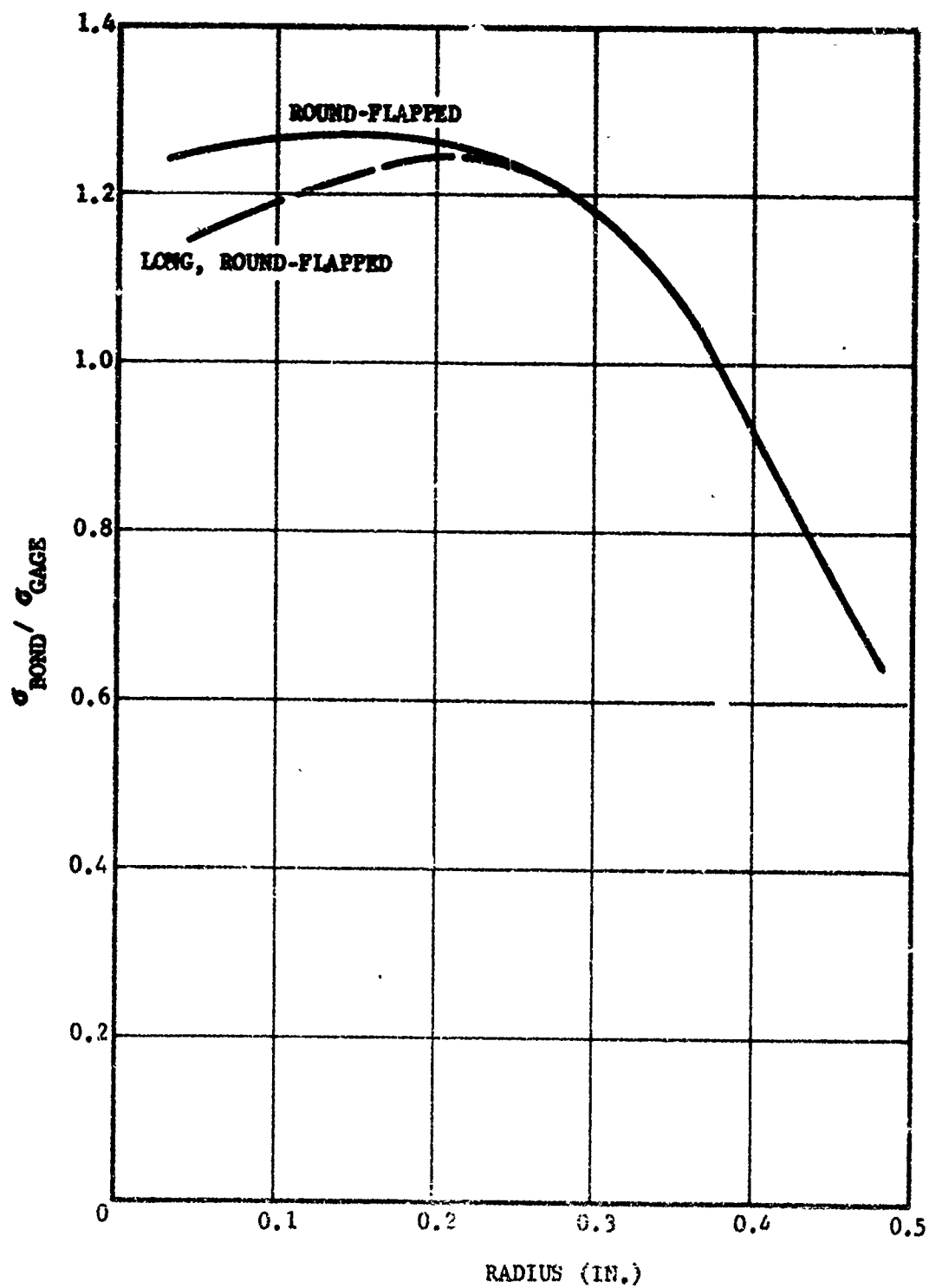
Figure 2-23. Comparison of bond normal (axial) stress distribution for long, round-flapped and round-flapped tensile samples ($E_L = 700$, $t_I = 0.2$).

154
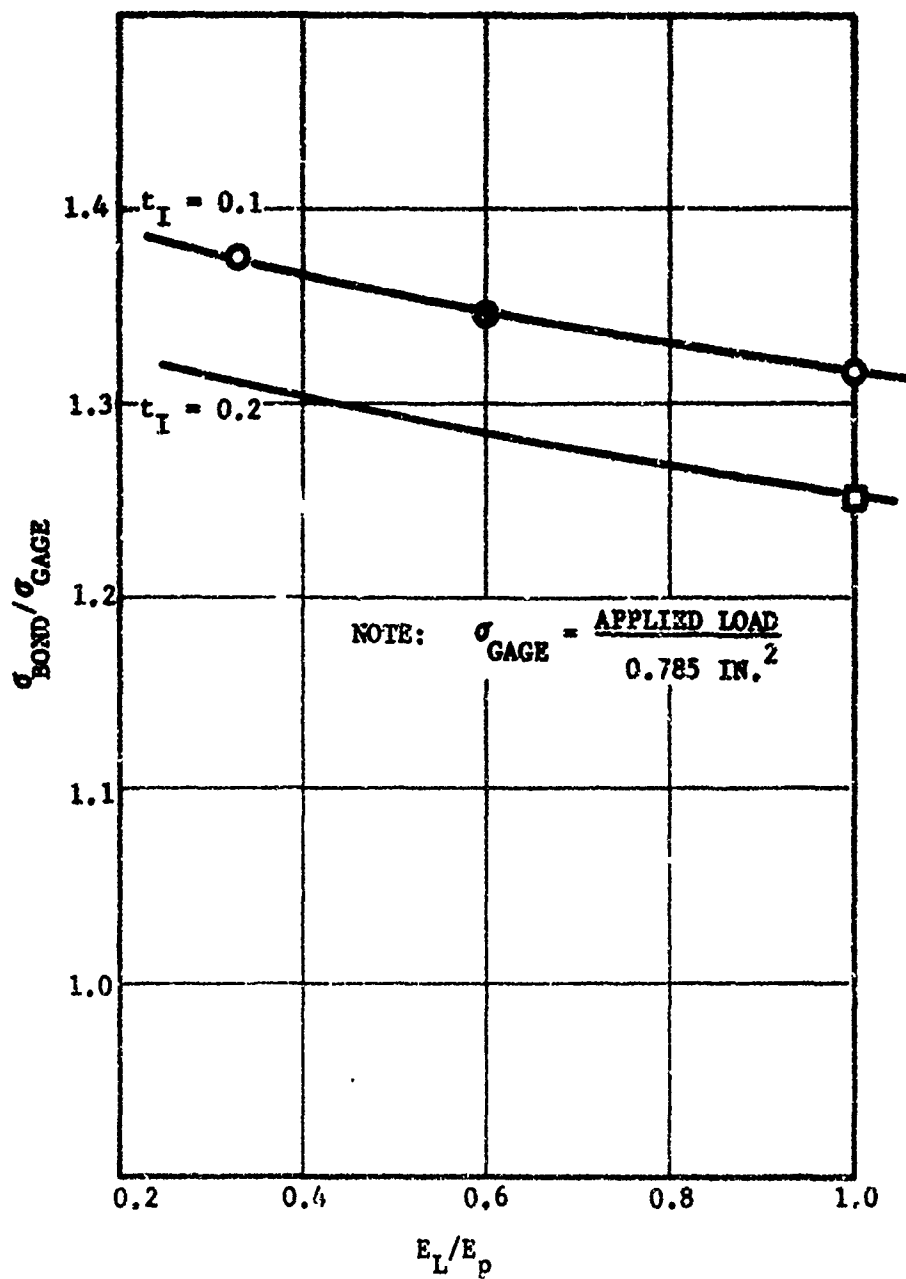
Figure 2-24. Effect of liner stiffners and insulator thickness on the maximum bond stress for round-flapped tensile sample (L = 0.1 inch).
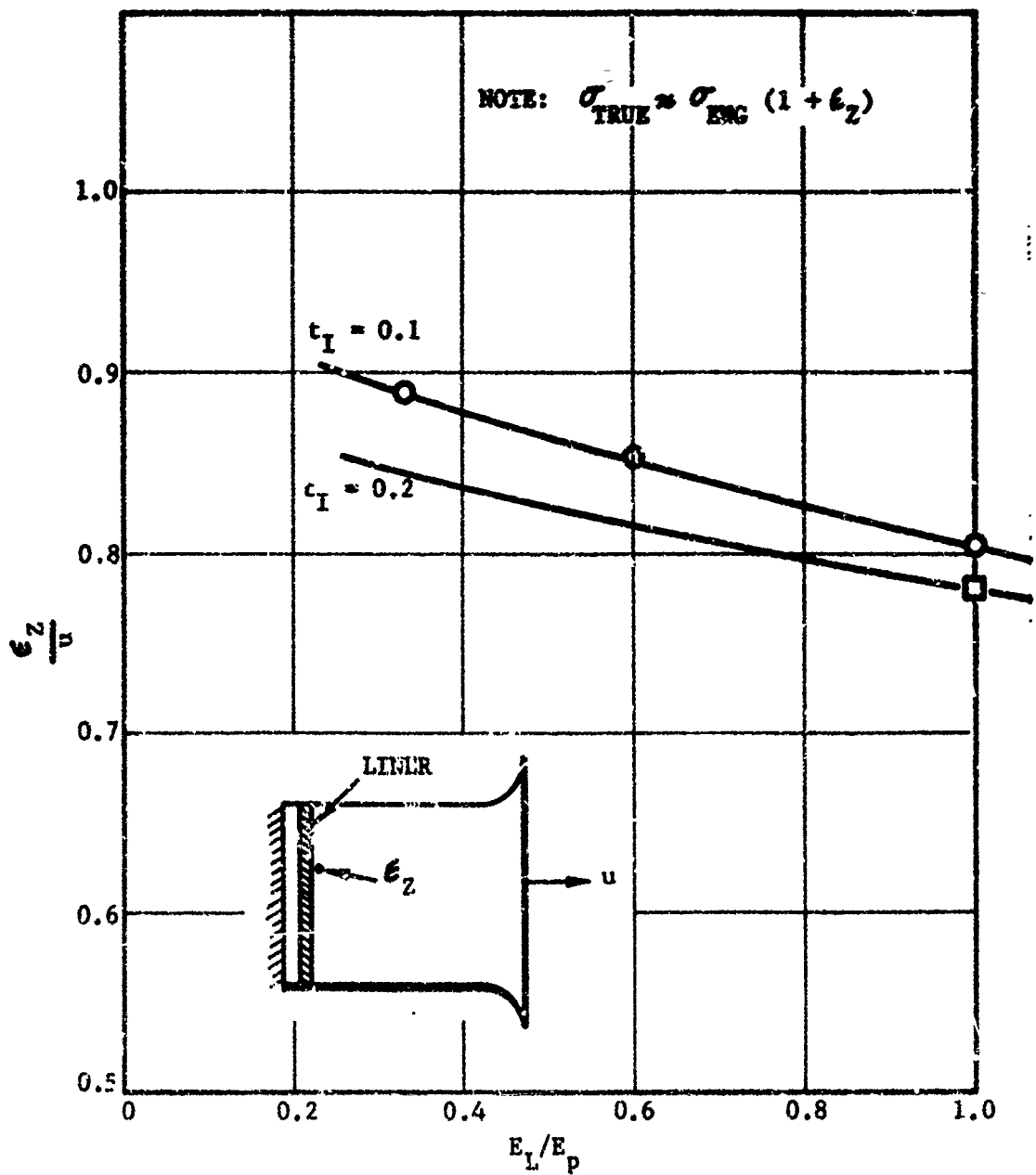
Figure 2-25. Correction factor to convert engineering stress to true stress for round-flapped case bond tensile sample.

156
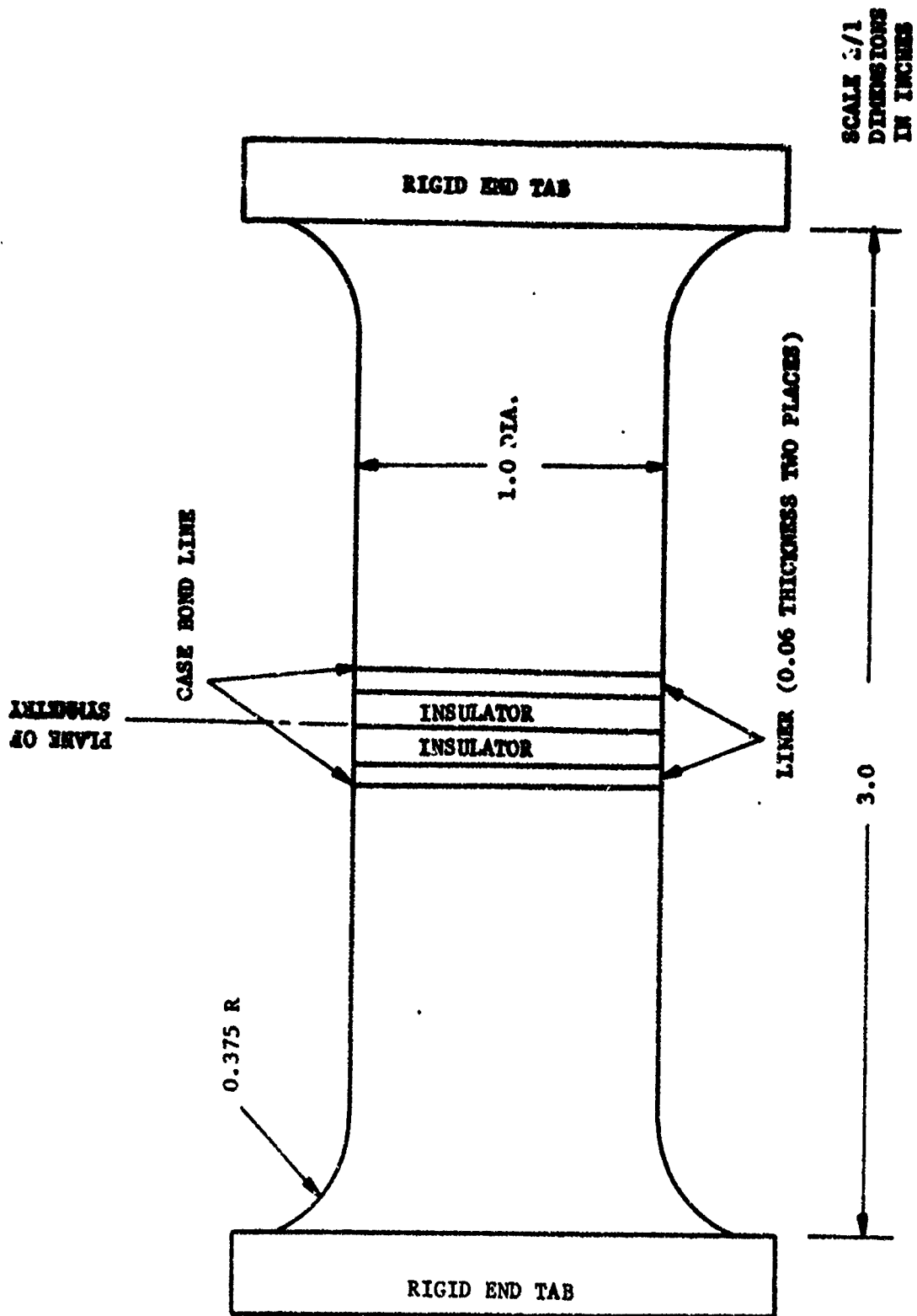
Figure 2-26. Back-to-back case bond tensile sample.

SCALE 2/1
DIMENSIONS
IN INCHES

RIGID END TAB

1.0 DIA.

CASE BOND LINE

PLANE OF
SYMMETRY

INSULATOR

INSULATOR

LINER (0.06 THICKNESS TWO PLACES)

3.0

0.375 R

RIGID END TAB

157

UNIFORM DISPLACEMENT IN "Z" DIRECTION AND ZERO DISPLACEMENT IN "L" DIRECTION OVER THIS END OF SAMPLE

INSULATOR (0.1 INCH THICK)

LINER (0.06 INCH THICK)

PLANE OF SYMMETRY
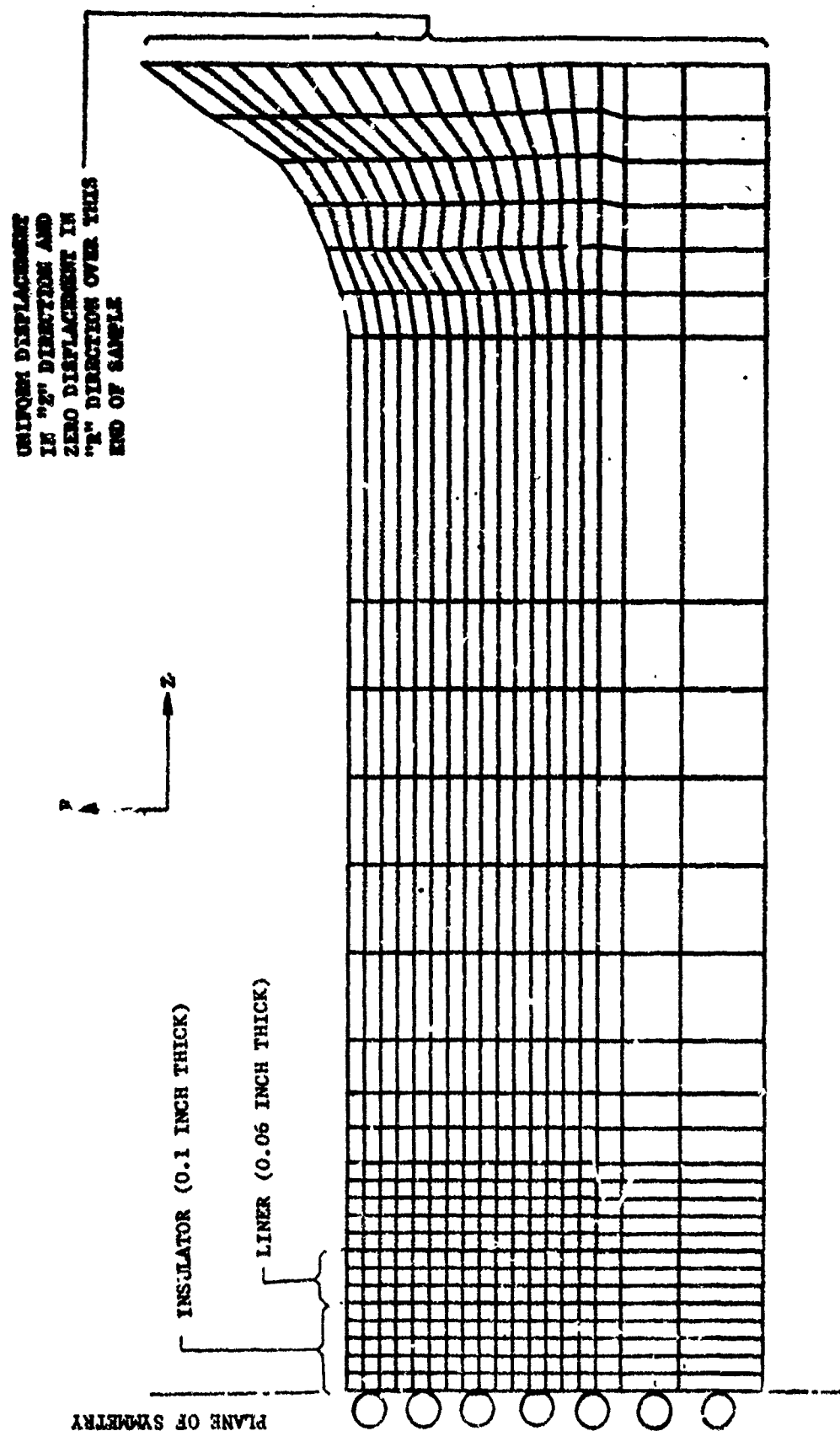
Figure 2-27. Finite element model and boundary conditions for 'back-to-back tensile sample.
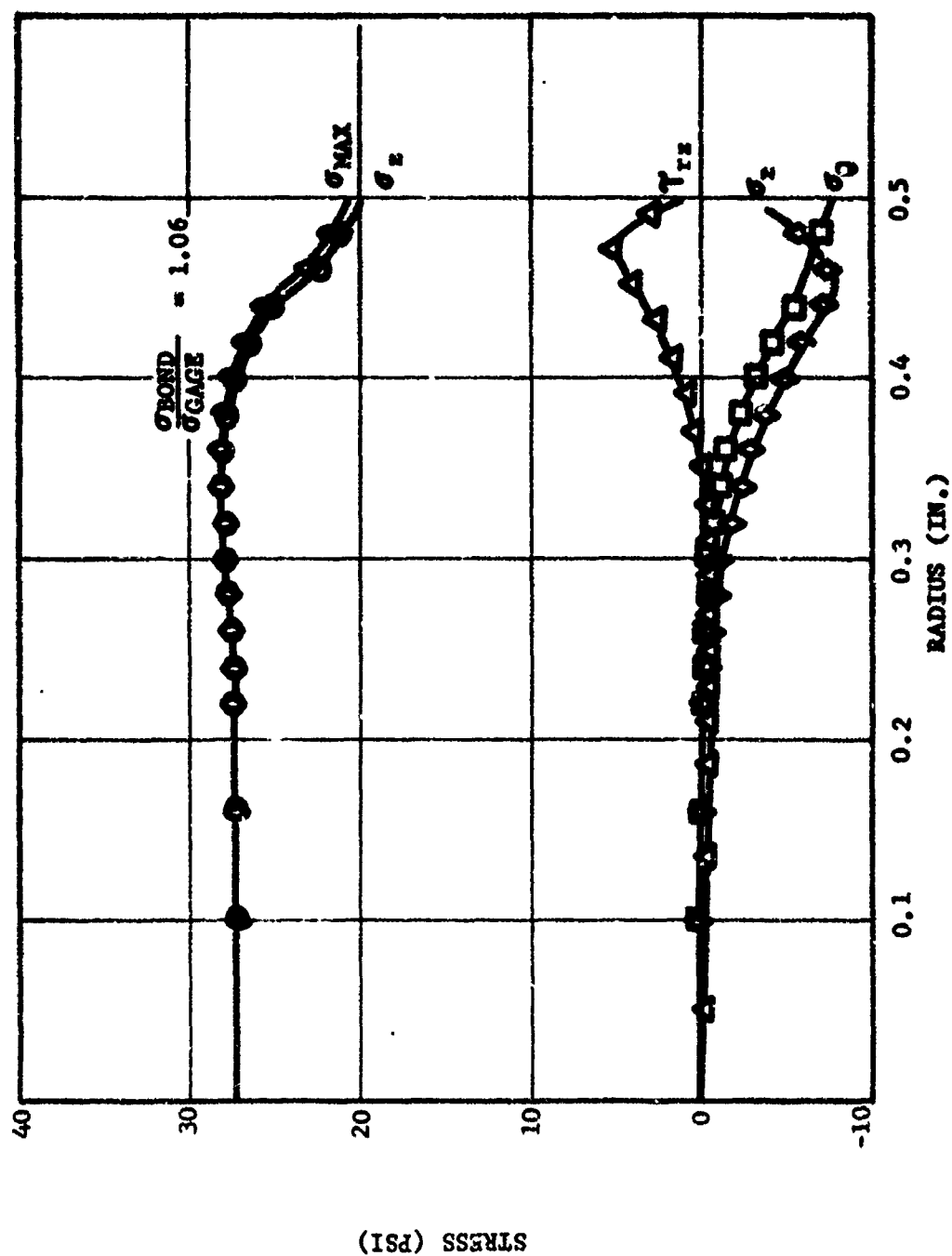
Figure 2-28. Case bond stress distribution in back-to-back tensile sample for flexible adhesive ($E_L = 230$).
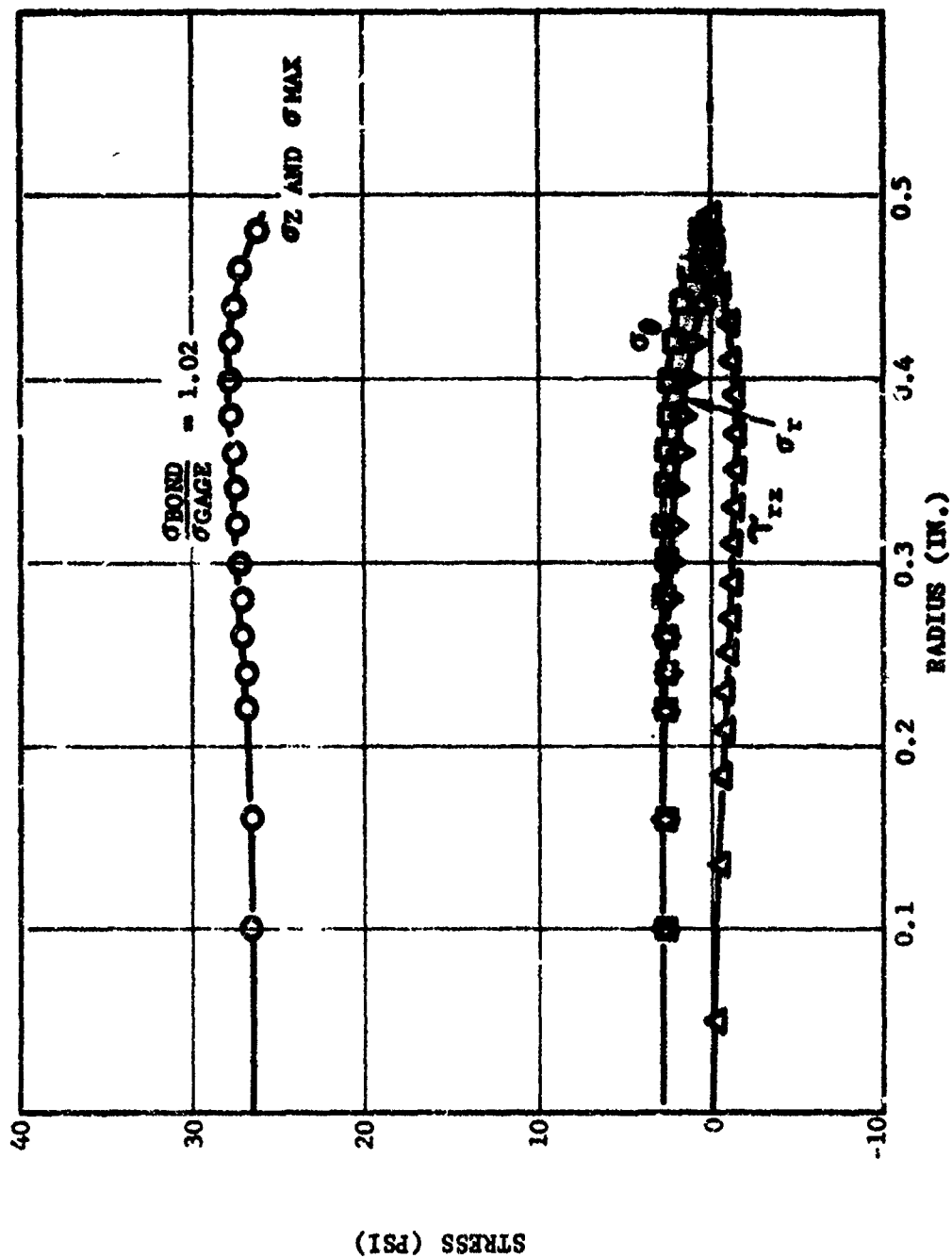
Figure 2-29. Case bond stress distribution in back-to-back tensile sample for flexible adhesive (E_L = 700).

150
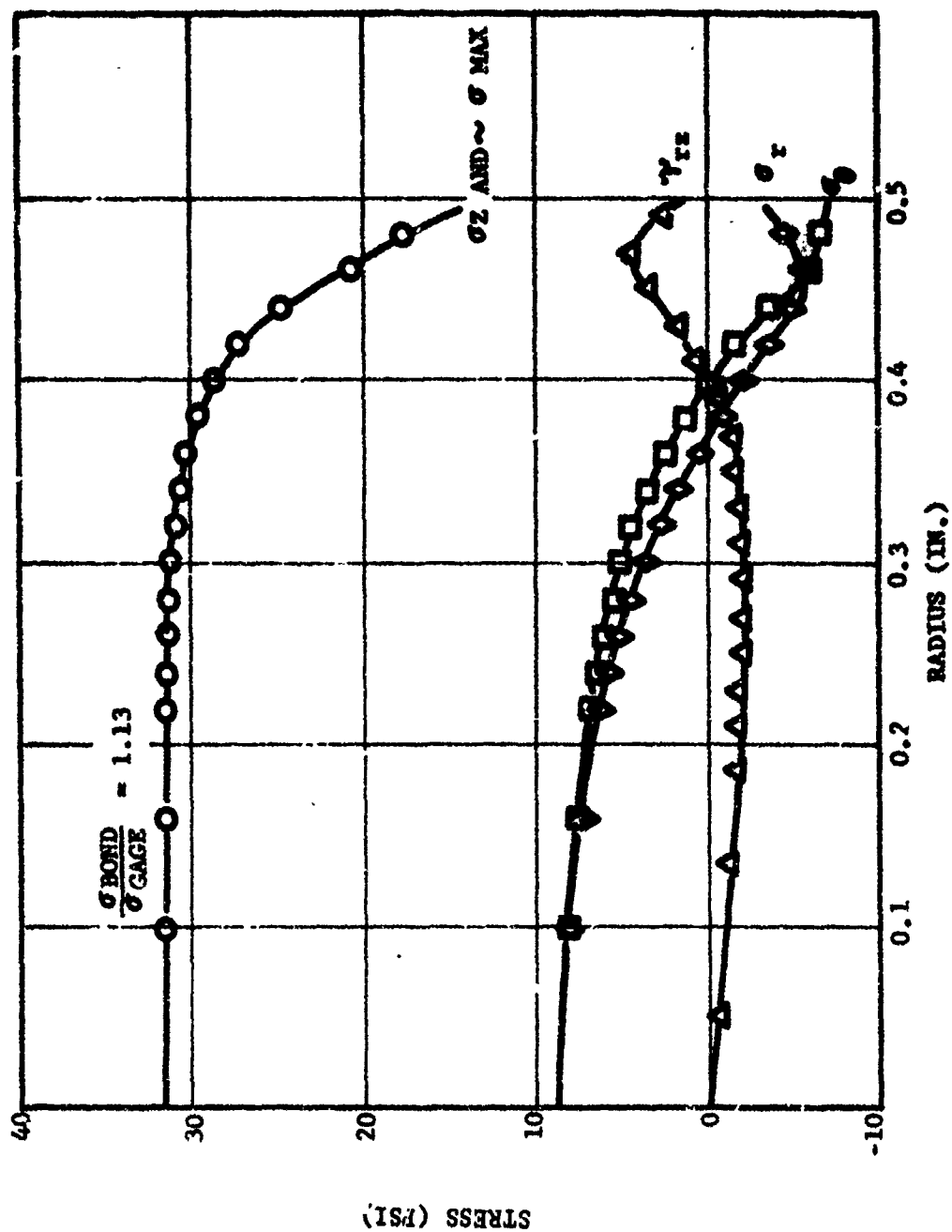
Figure 2-30. Case bond stress distribution in back-to-back tensile sample for rigid adhesive (E_L = 230).
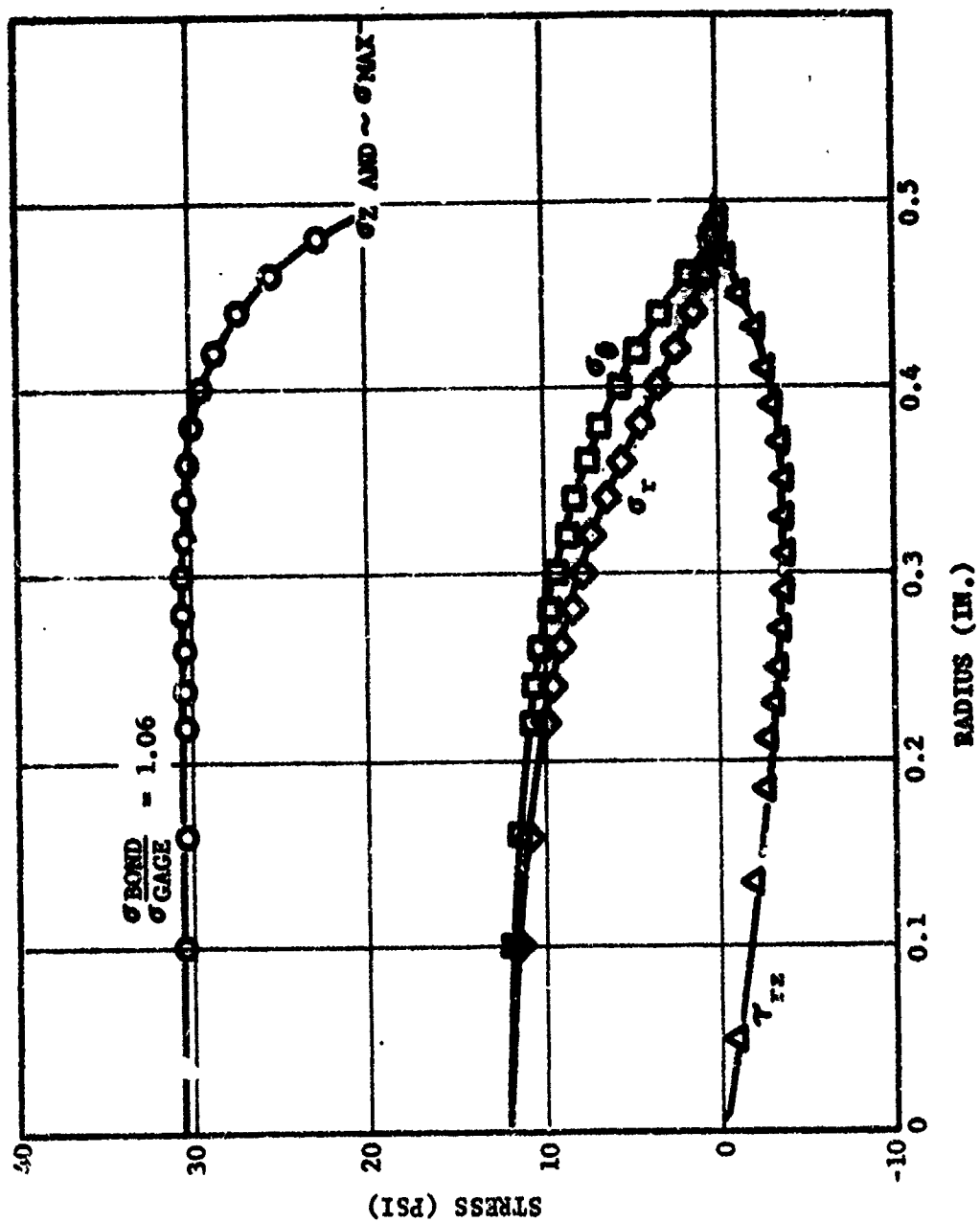
Figure 2-31. Case bond stress distribution in back-to-back tensile sample for rigid adhesive ($E_L = 700$).

162

Figure 2-32. Round-filleted case bond tensile sample.

163

UNIFORM DISPLACEMENT
OVER THIS END OF SAMPLE
IN Z DIRECTION. ZERO
DISP. IN R DIRECTION

R

Z

INSULATOR (0.2 INCH THICK)

LINER OR POWDER EMBEDMENT
LAYER (0.06 INCH THICK)
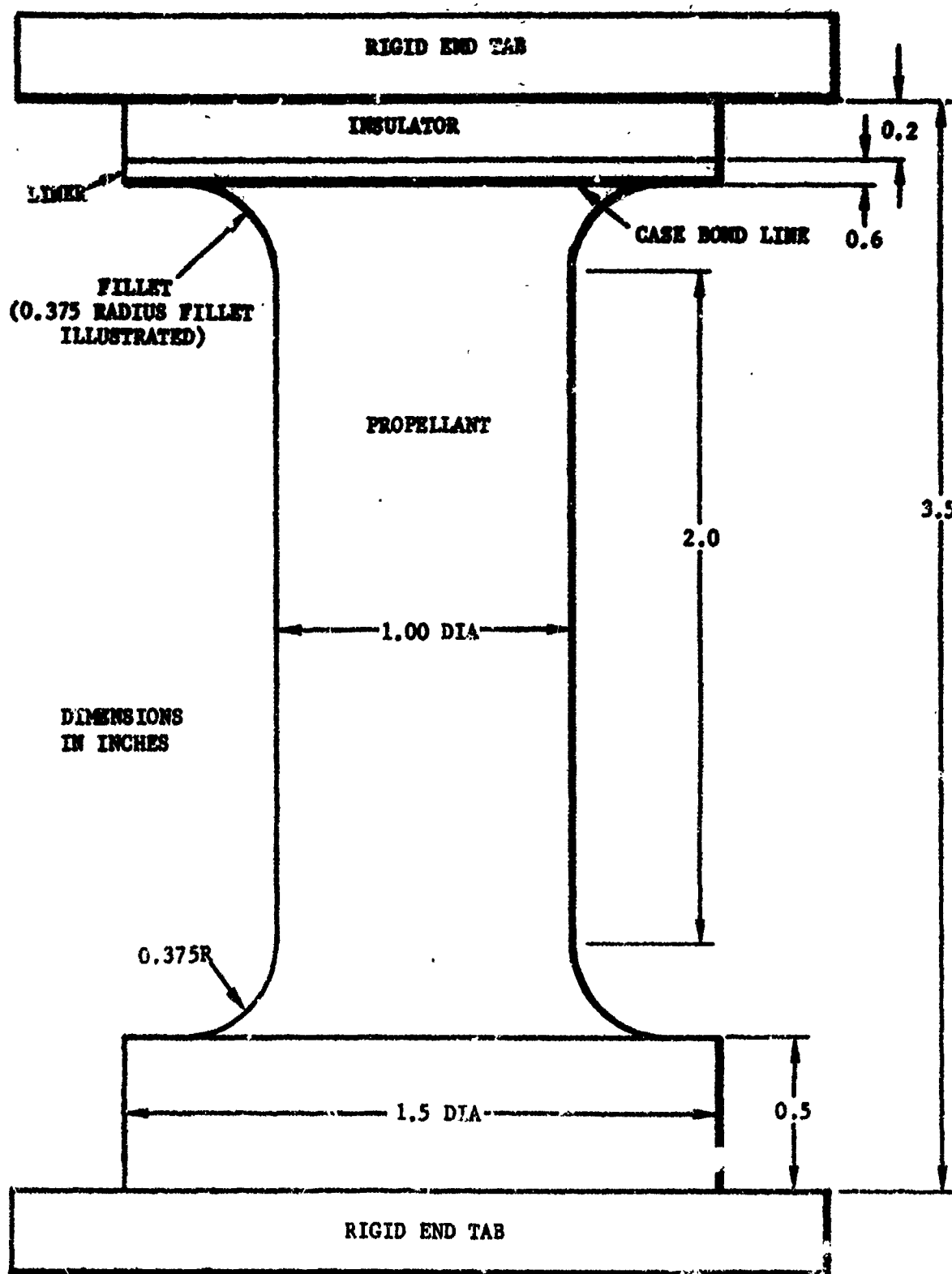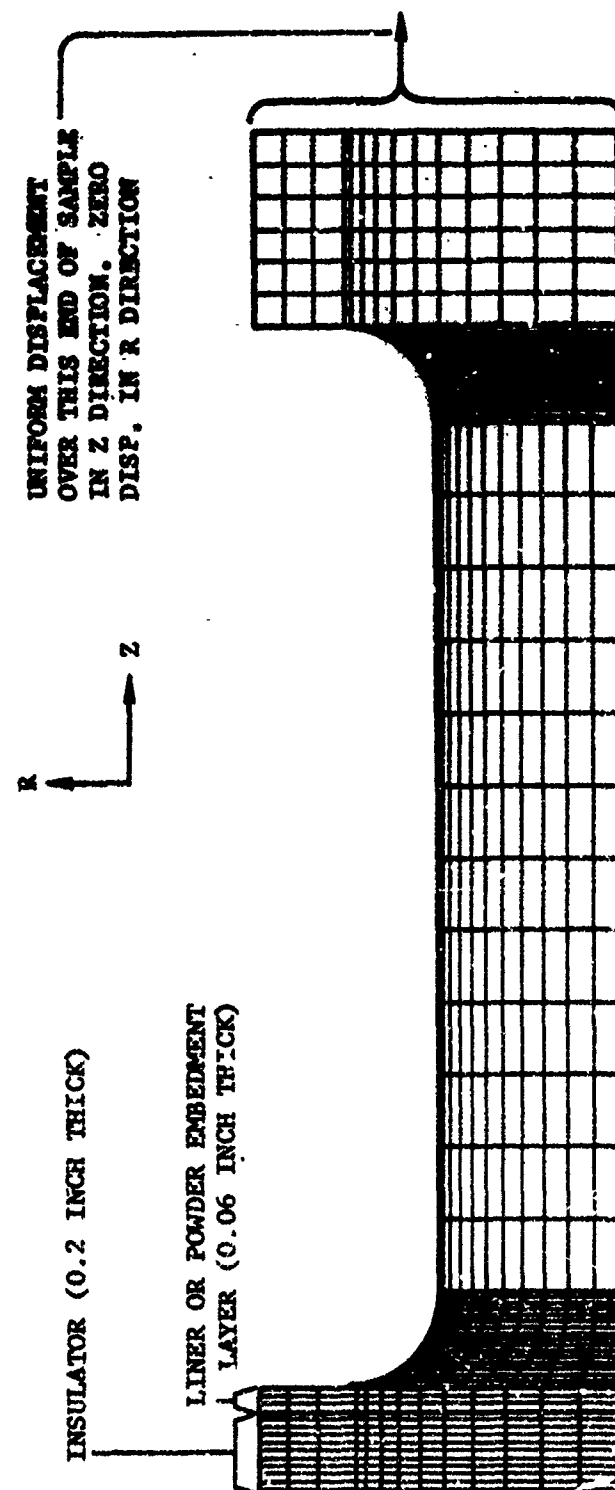
Figure 2-33. Finite-element model and boundary conditions for filleted case bond
tensile sample.

164
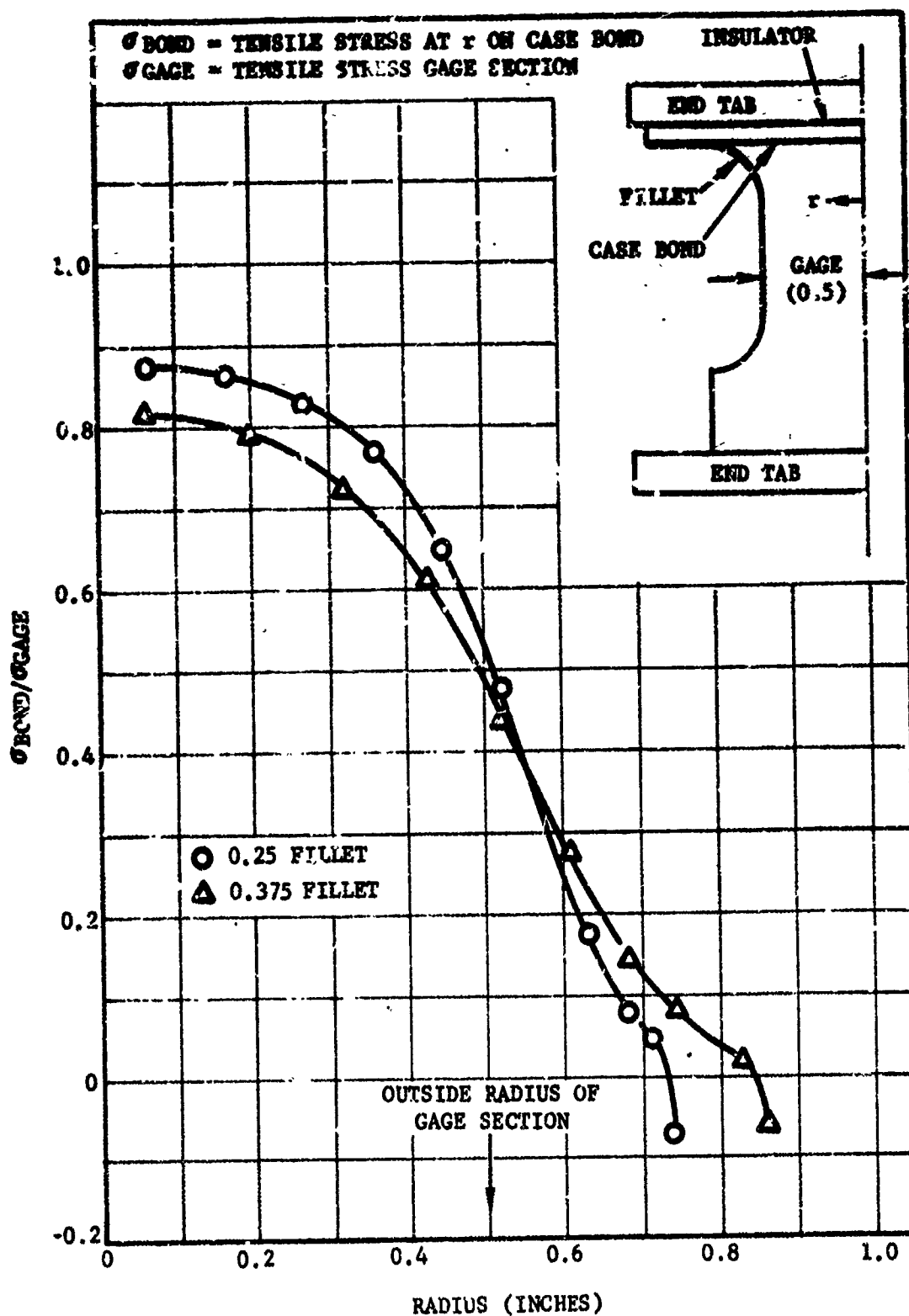
Figure 2-34. Ratio of σ bond to σ gage as a function of radius (filleted case bond tensile sample).
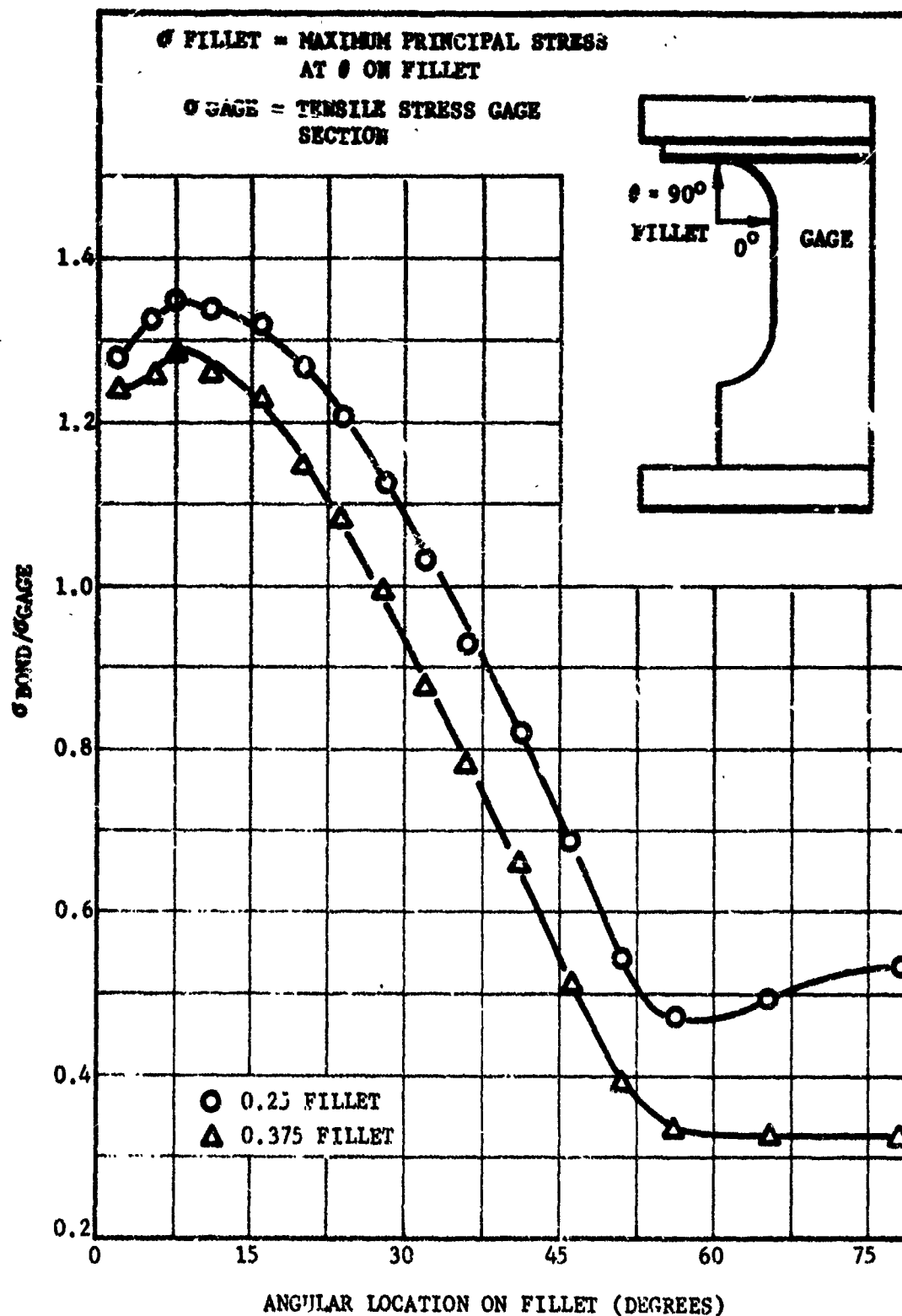
Figure 2-35. Ratio of σ fillet to σ gage as a function of fillet location
(filleted case bond sample).
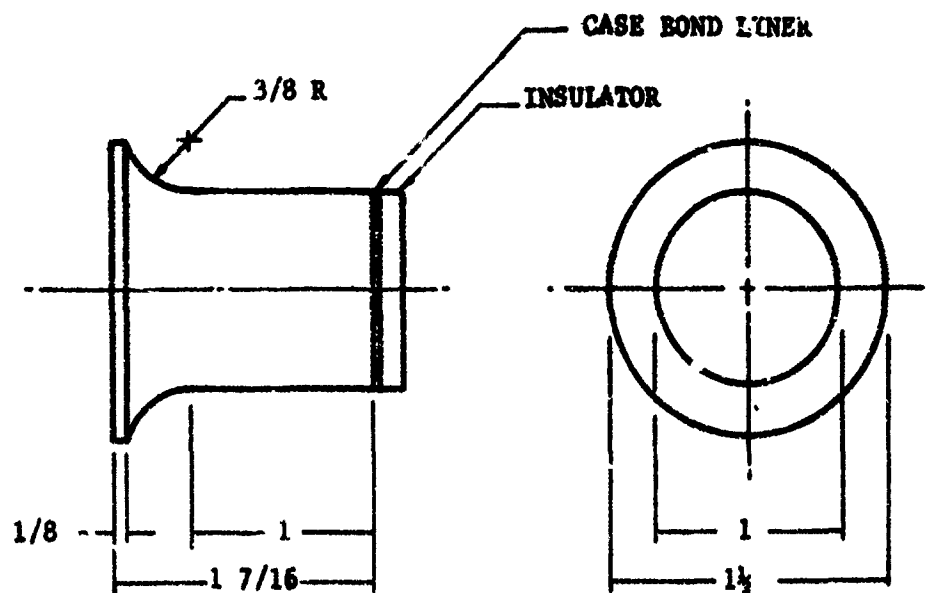
Figure 2-36. Round-flapped case bond tensile sample configuration.

167

METAL
END BOX
(IN CHUCK)

PROPELLANT

CUTTING TOOL
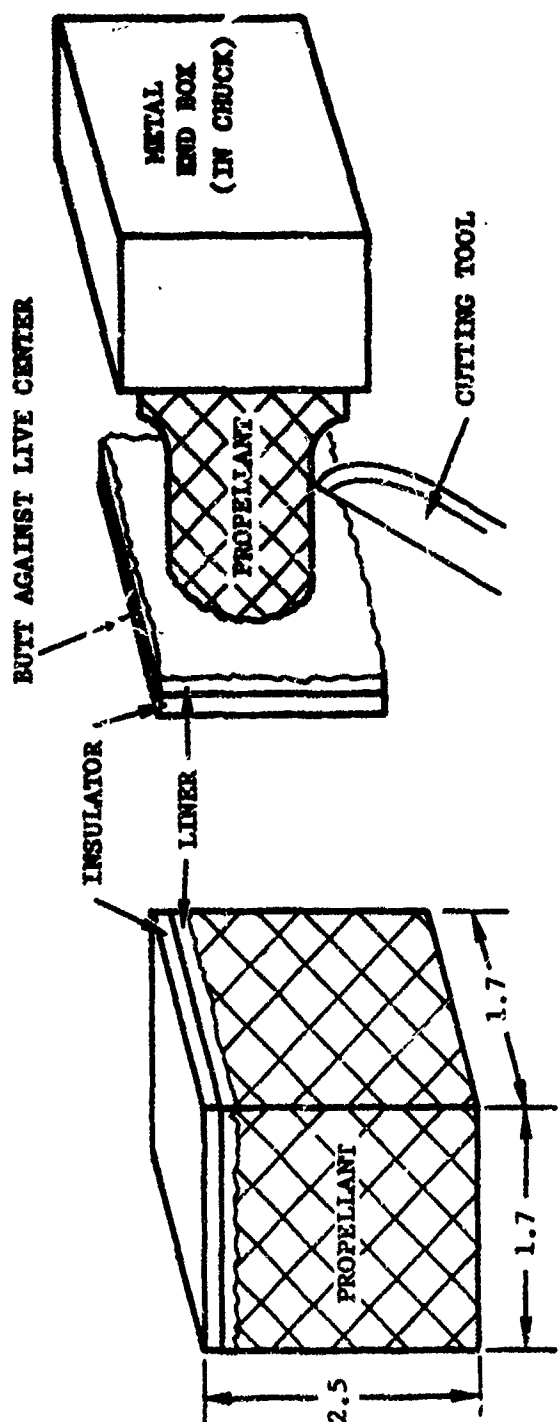
STEP NO. 2
(MACHINE PROPELLANT CYLINDER ON LATHE)

BUTT AGAINST LIVE CENTER

INSULATOR

LINER

PROPELLANT

2.5

1.7

1.7

1.7

STEP NO. 1
(CUT RECTANGULAR BLOCK ON BANDSAW)

THIS SURFACE
CUT ON OUTER EDGE BY LATHE TOOL
AND FINAL TRIMMED USING A KNIFE
STEP NO. 3

PROPELLANT

INSULATOR LINER

KNIFE
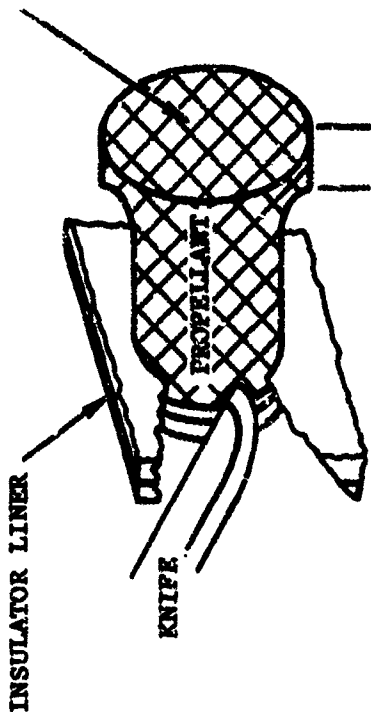
STEP NO. 3
(HAND TRIM INSULATOR AND LINER LAYERS AND PROPELLANT LIP ON OPPOSITE END)

Figure 2-37. Hand-trimming procedure for making round-flapped tensile samples.

168
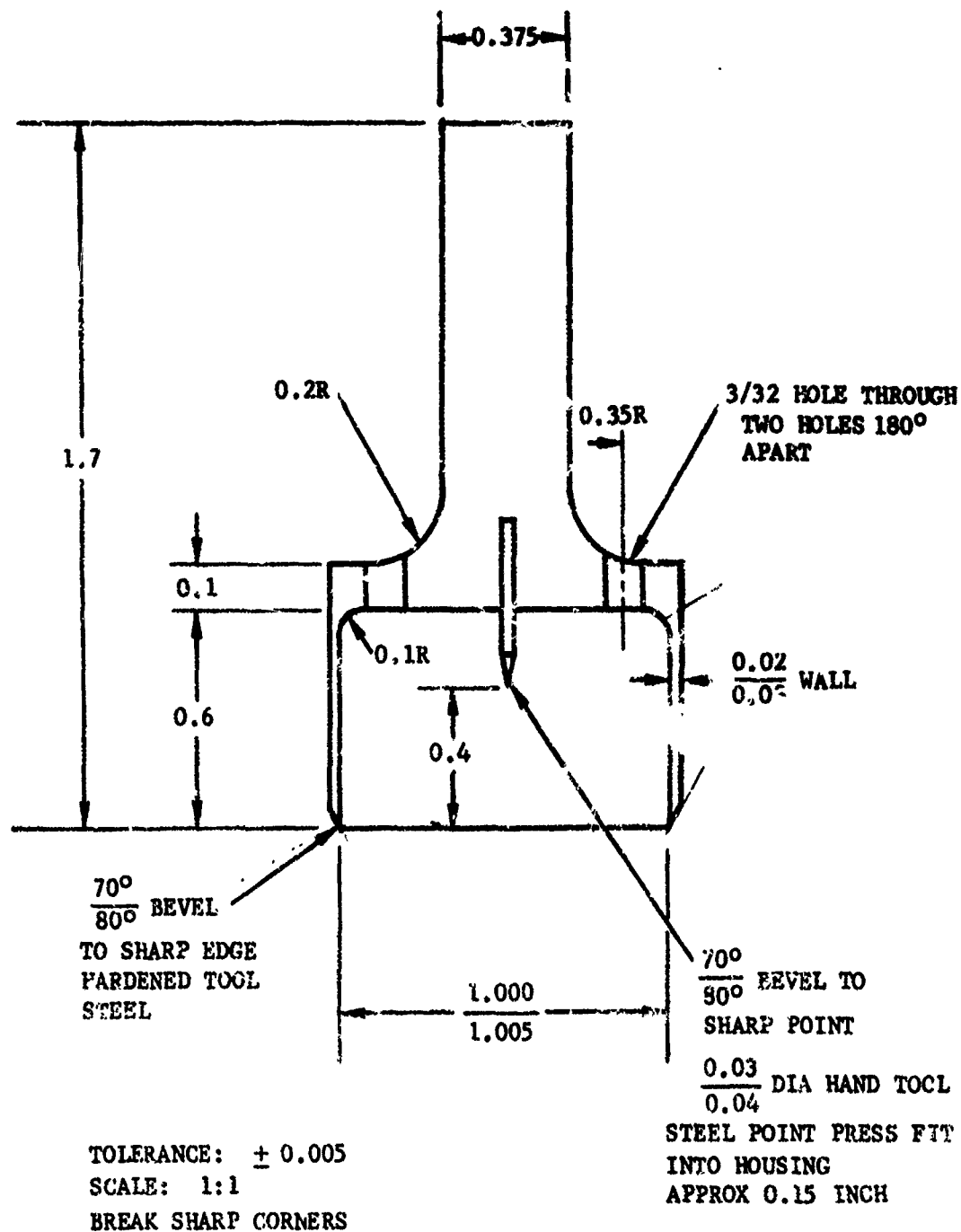
Figure 2-38. Sketch of die for cutting through case bond layer
of round-flapped tensile sample.
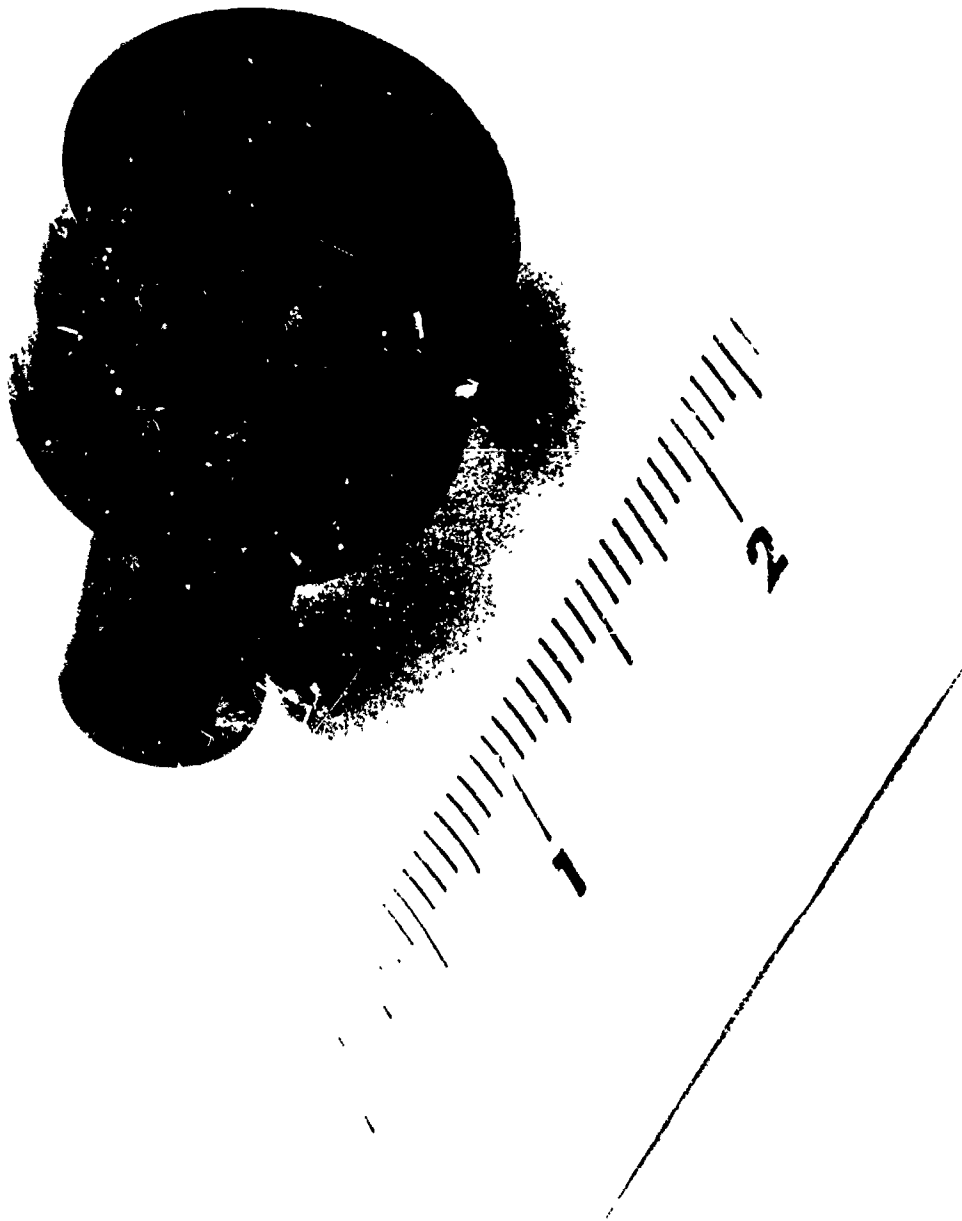
Figure 2-39. Photo of die for cutting through case bond layer of round-flapped tensile samples.

INSULATOR
LINER

PROPELLANT

STEP NO. 1
(CUT RECTANGULAR BLOCK ON BANDSAW)

METAL END BOX (IN CHUCK)

LINER
INSULATOR

DIE (PLACE IN DEAD CENTER,
THEN CUT INTO PROPELLANT)
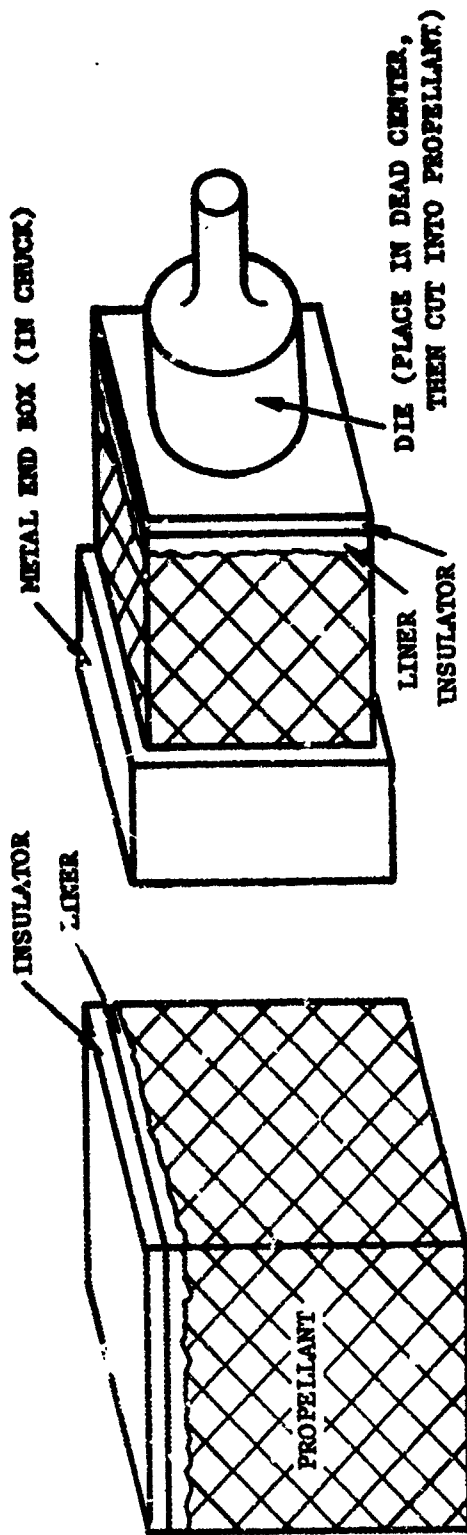
STEP NO. 2
(CUT THROUGH INSULATOR/LINER AND INTO PROPELLANT
USING CYLINDRICAL DIE ON LATHE)

METAL DISC, 1.0 DIA
(CENTER OVER DIE CUT,
PLACE AGAINST LIVE CENTER)

CUTTING TOOL
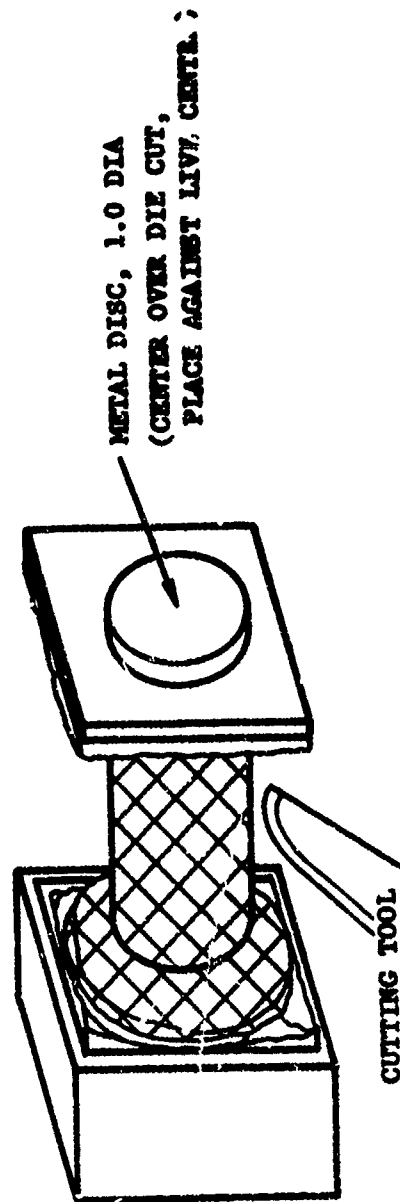
STEP NO. 3
(MACHINE PROPELLANT CYLINDER ON LATHE)

Figure 2-40. Die-cut procedure for machining round-flapped tensile samples.

171
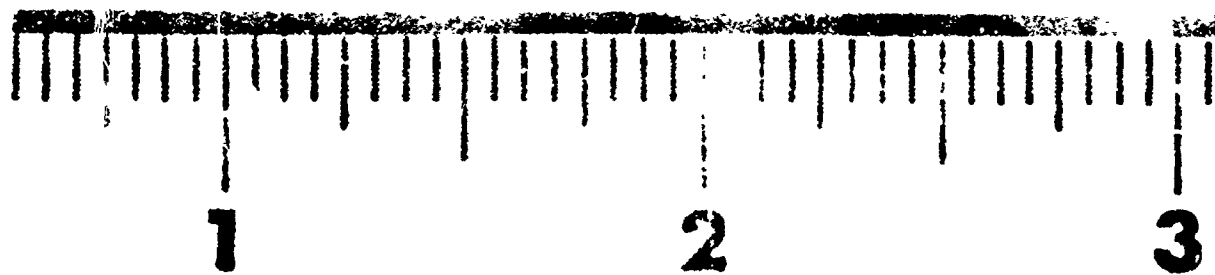
Figure 2-41. Round-flapped tensile sample machined with the rectangular (die cut) procedure — JP-BJ124 propellant
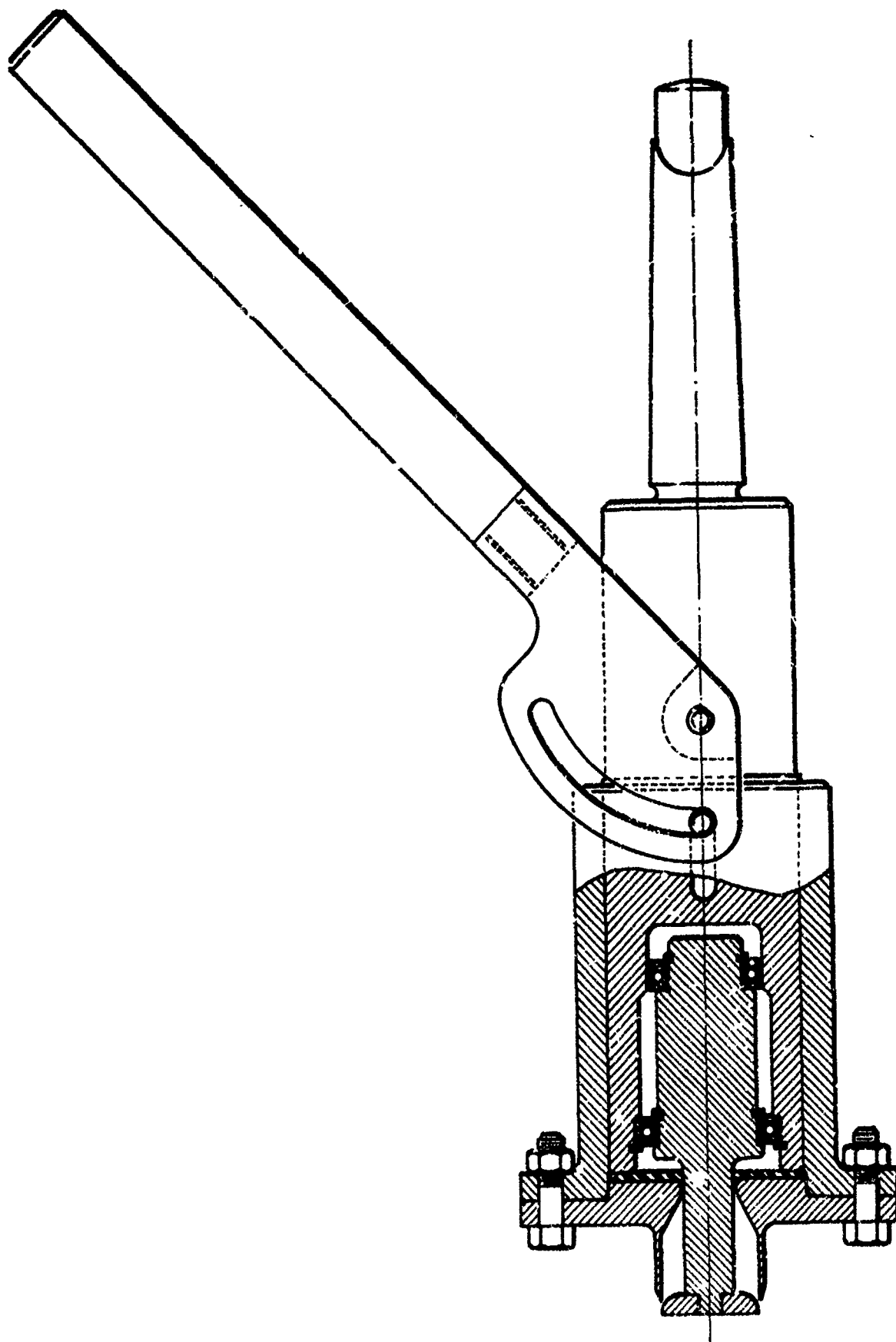
Figure 2-43. Apparatus for cutting through case bond to make round-flapped tensile sample.
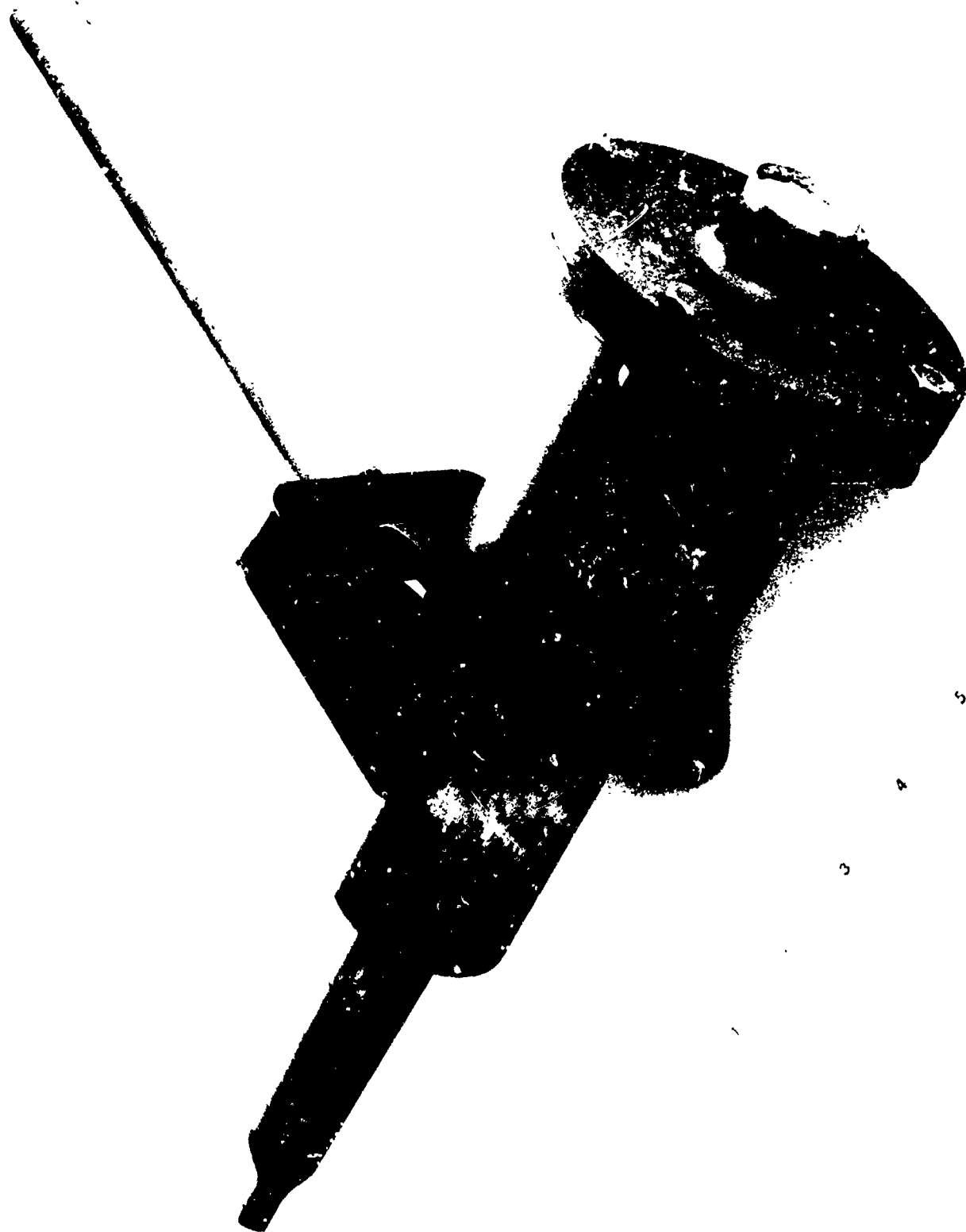
Figure 2-43. Photo of apparatus for machining round-flapped tensile samples.

0.5

3/16 HOLE THROUGH

3.95

3/16R

0.45R

1/16 HOLE THROUGH
TWO HOLES 180° APART

0.2

$\dfrac{0.03}{0.04}$ WALL TWO PLACES

0.25

$\dfrac{0.04R}{0.05R}$

$\dfrac{0.04R}{0.05R}$

$\dfrac{65°}{75°}$ BEVEL TO SHARP EDGE
HARDENED TOOL STEEL
TWO PLACES

$\dfrac{0.400}{0.402}$ R

$\dfrac{0.500}{0.502}$ R

FLAP WASHER DIE

Figure 2-44. Flap washer die.

175

Figure 2-45. Photo of die to cut Teflon rings for round-flapped tensile samples.

WASHER (STICKY SIDE INSULATOR)

INSULATOR

LINER
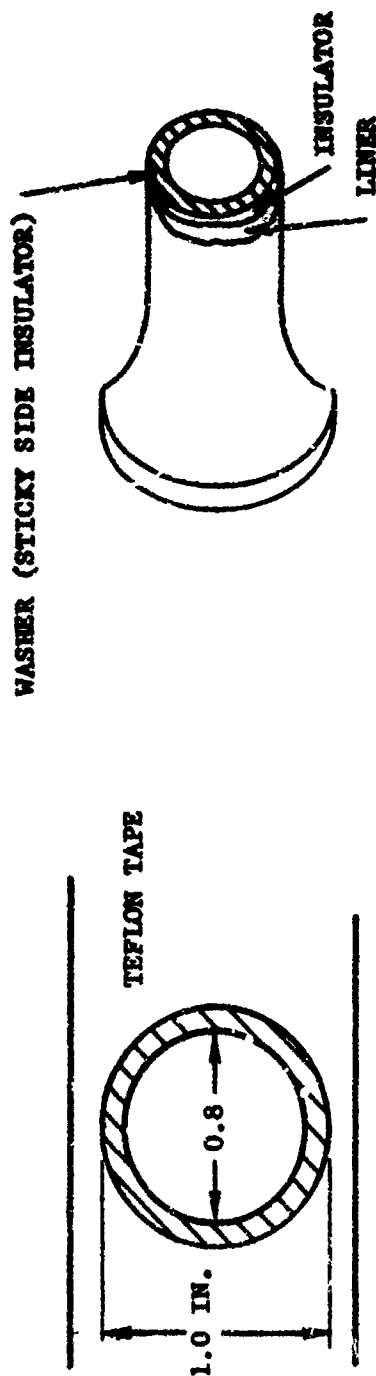
STEP NO. 2
(PLACE RING ON INSULATOR)

TEFLON TAPE

0.8

1.0 IN.

STEP NO. 1
(CUT TEFLON RING)

WRAP 1/4-INCH WIDE TEFLON TAPE AROUND INSULATOR
NEXT TO END TAB BEFORE BONDING; I.E.,
TO AVOID BONDING OF ADHESIVE
HEAD TO OUTSIDE EDGE OF
INSULATOR
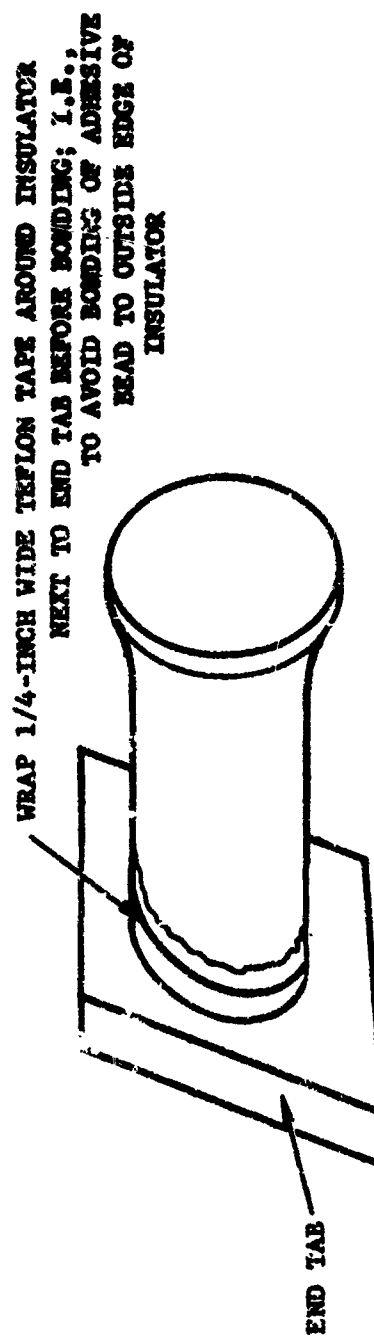
END TAB

STEP NO. 3
(BOND TO END TAB)

Figure 2-46. Bonding insulator end of round-flapped tensile sample to
end tab.

177
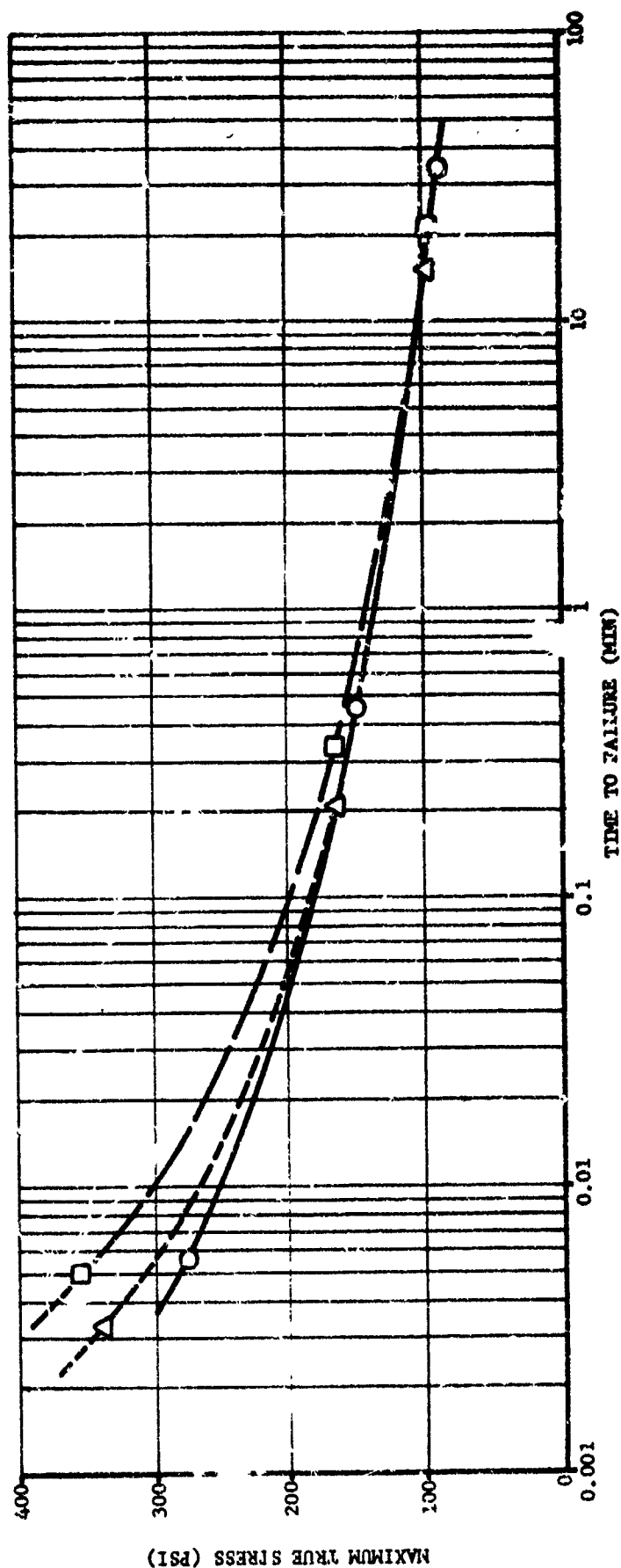
Figure 2-47. Tensile strength for TP-H1123 propellant/case bond, 77° F, 50% R.H.

178
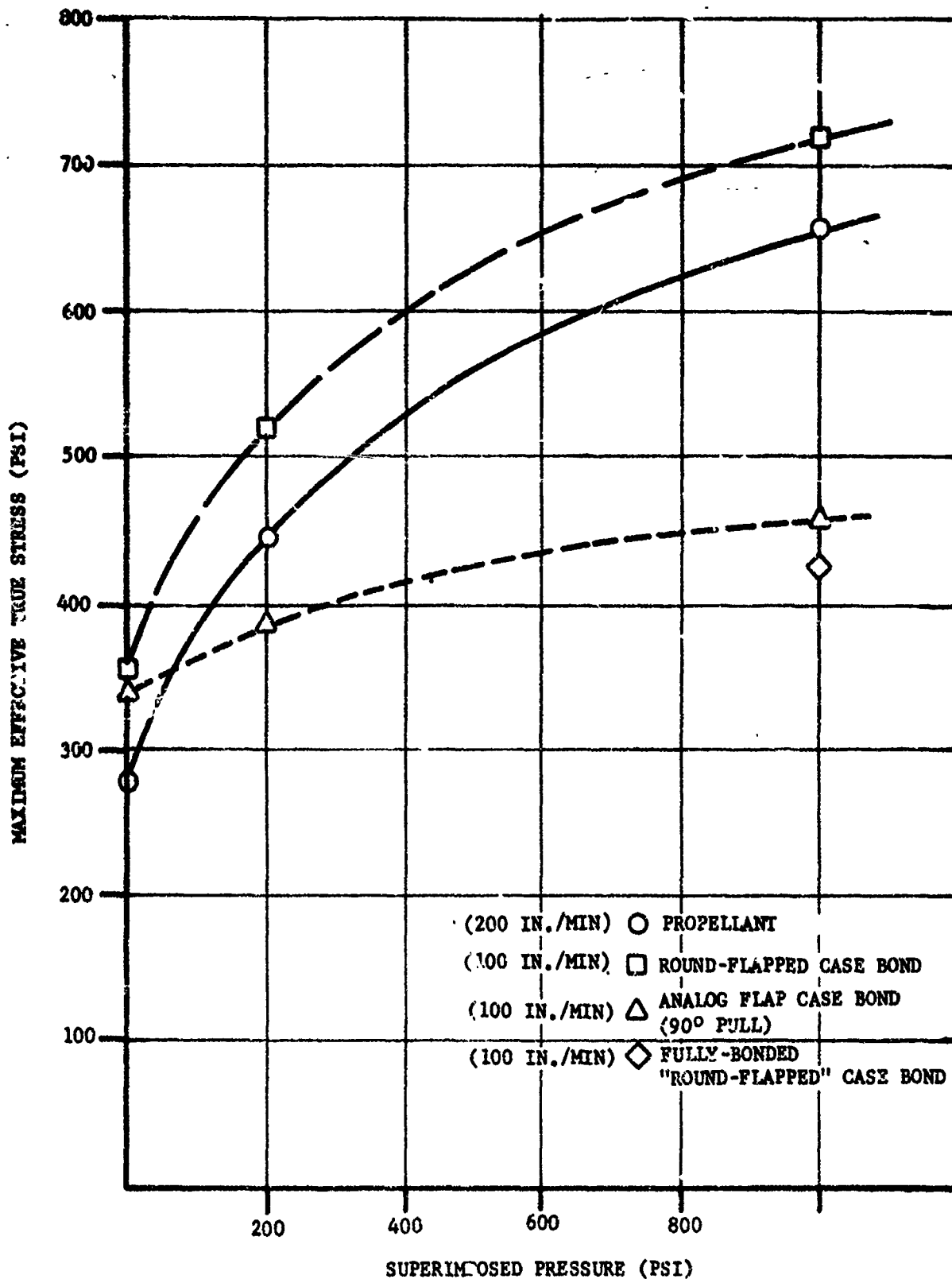
Figure 2-48.   Effect of superimposed pressure on tensile strength of
TP-H1123 propellant/case bond, at high loading rate,
77° F, 50% R.H.

179
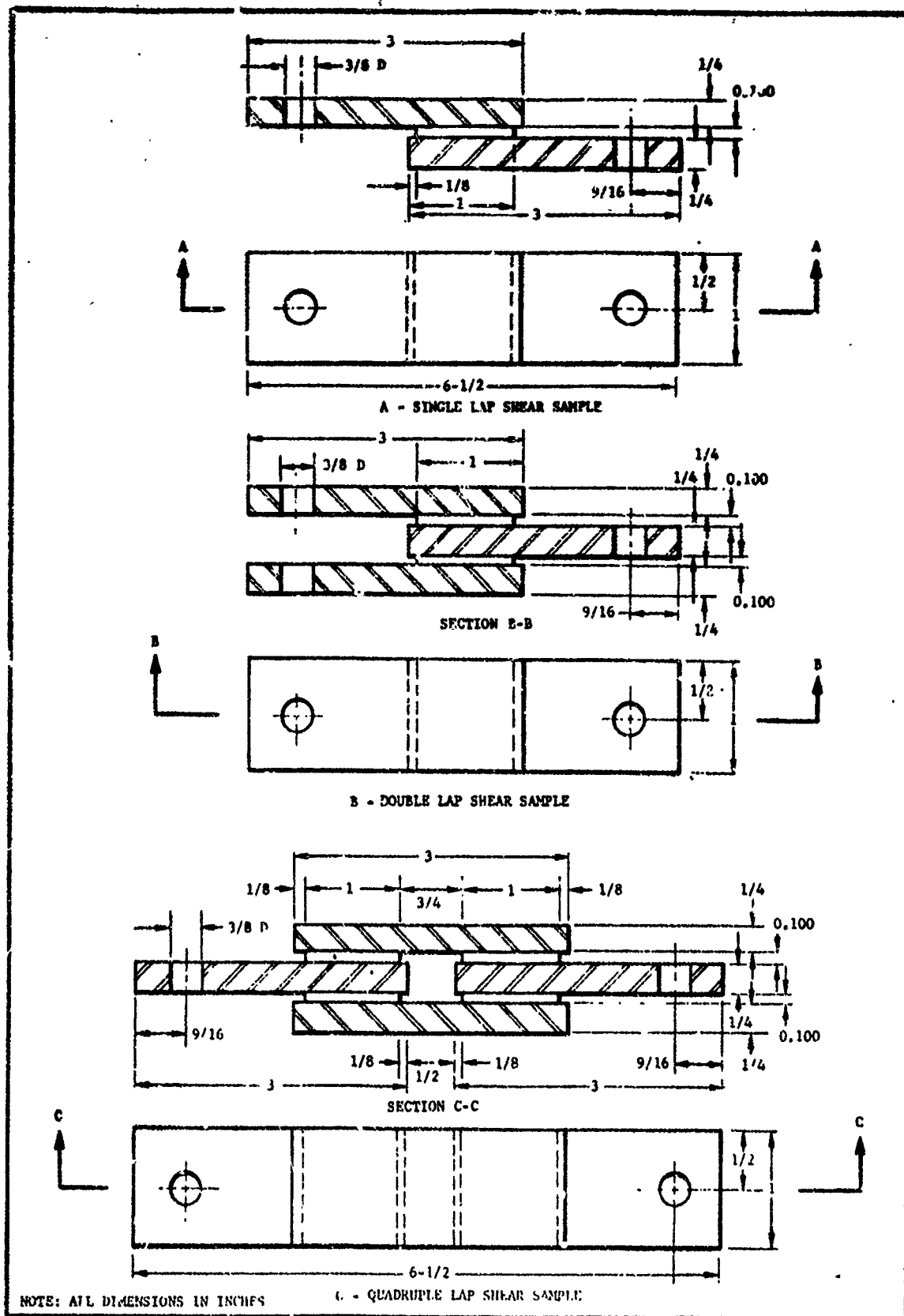
Figure 2-49. Lap shear sample configurations.

180
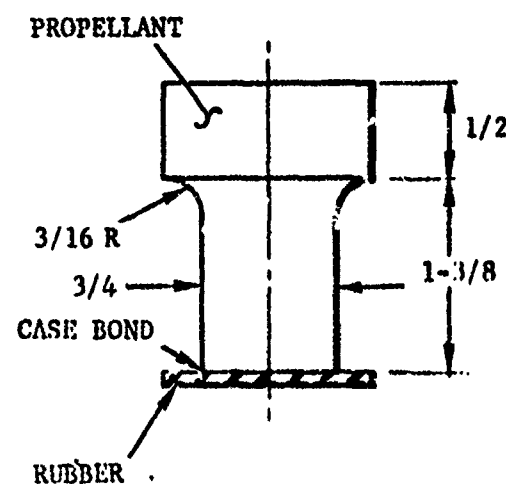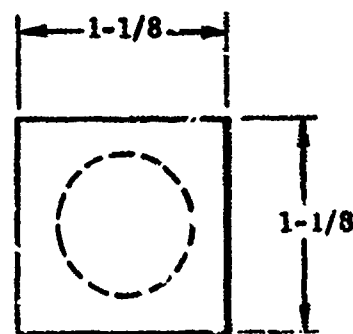
Figure 2-50. Case bond torsion sample used with double-base propellants.
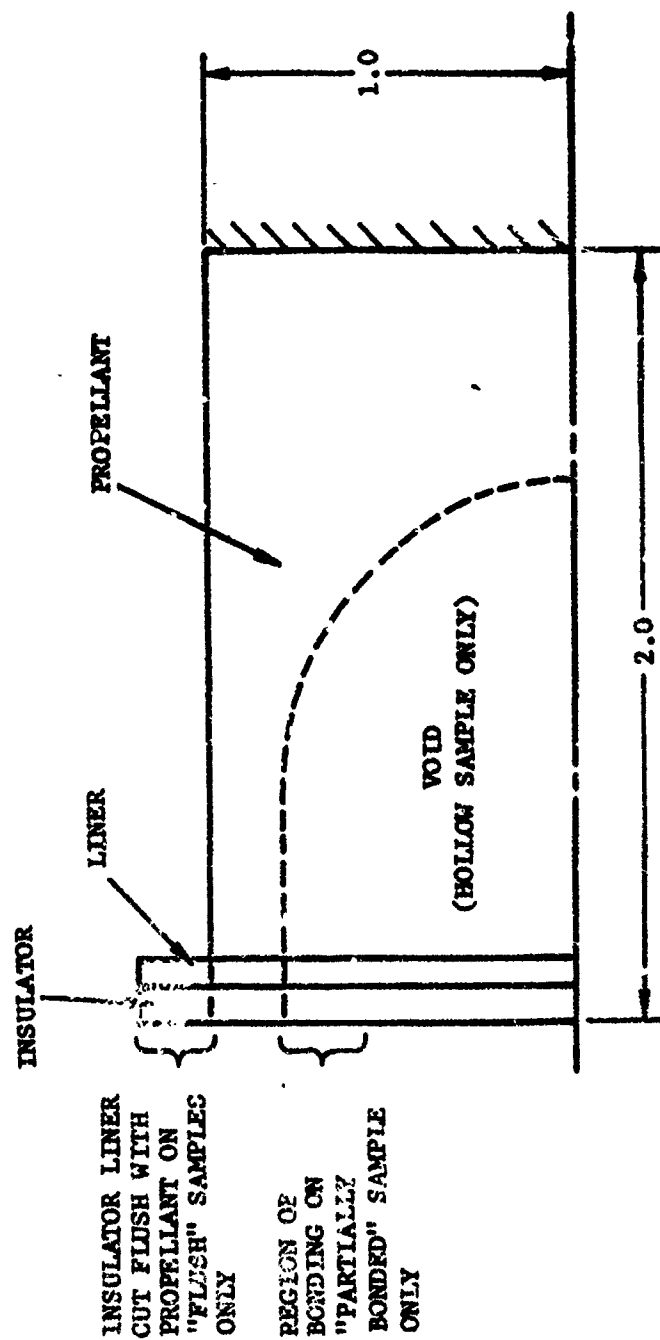
Figure 2-51. Case bond torsion sample configuration analyzed in case liner-bond program.
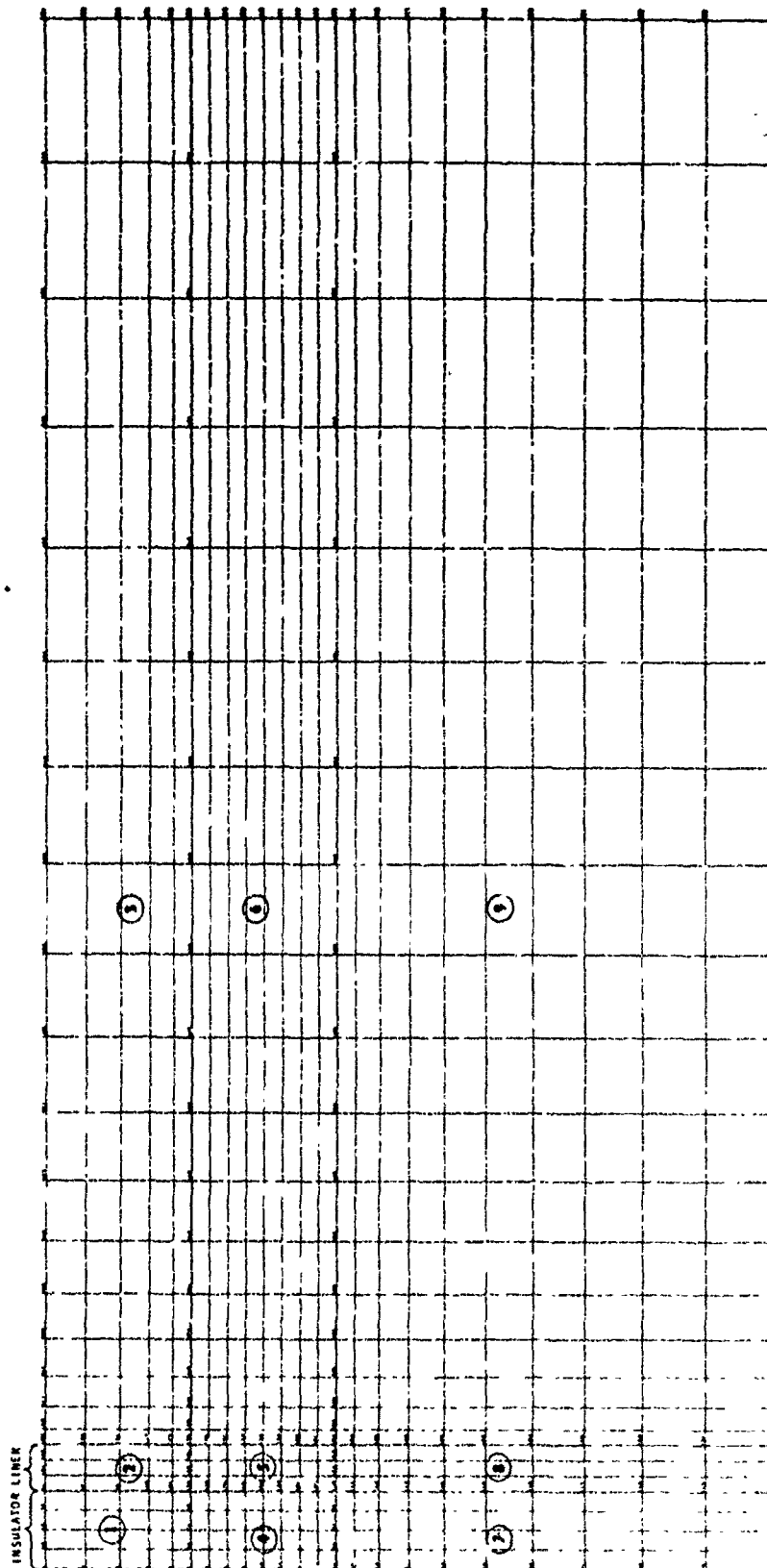
Figure 2-52. Finite-element model for case bond torsion samples of configurations 1 and 2.

183
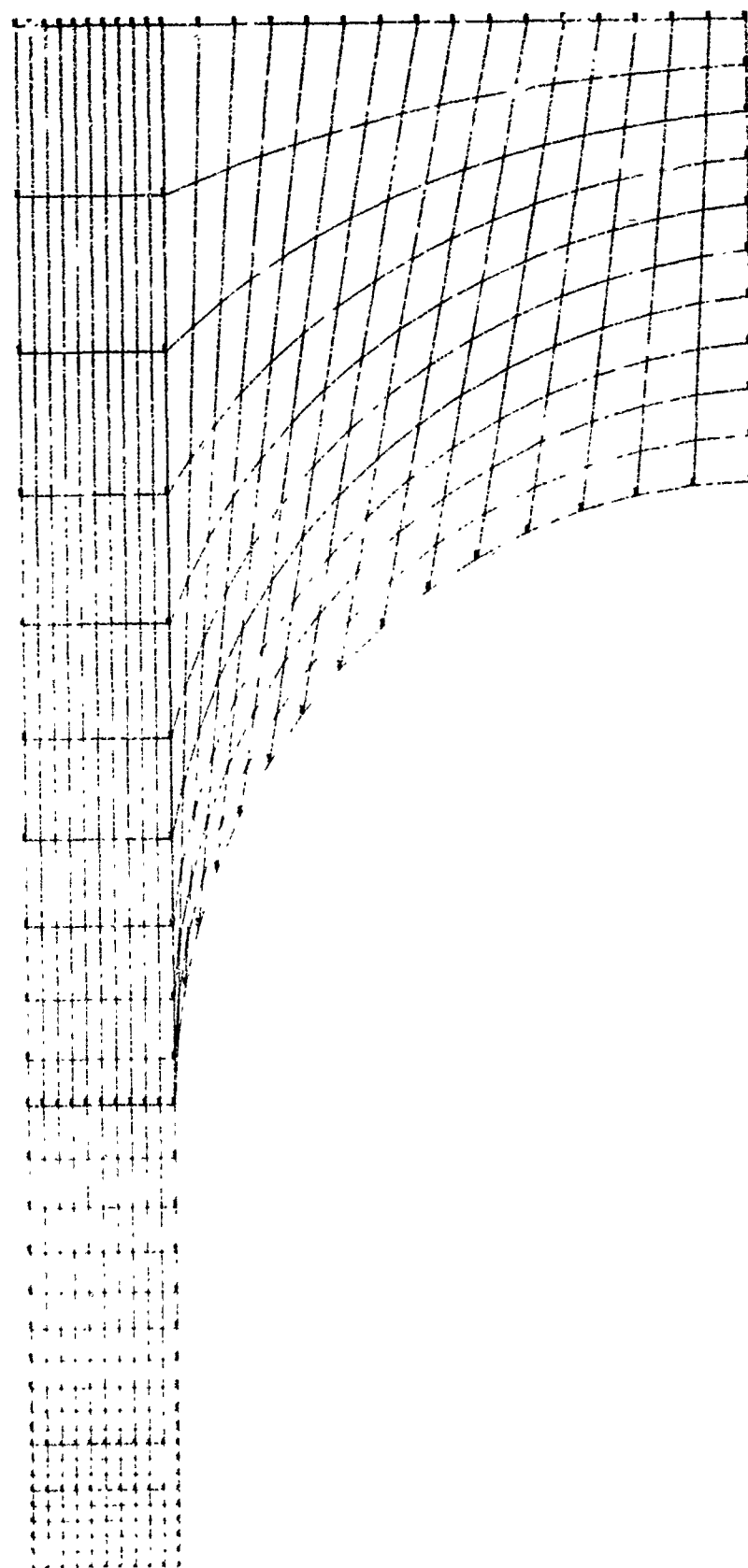
Figure 2-53. Finite-element model for case bond torsion sample of configuration 3.

184
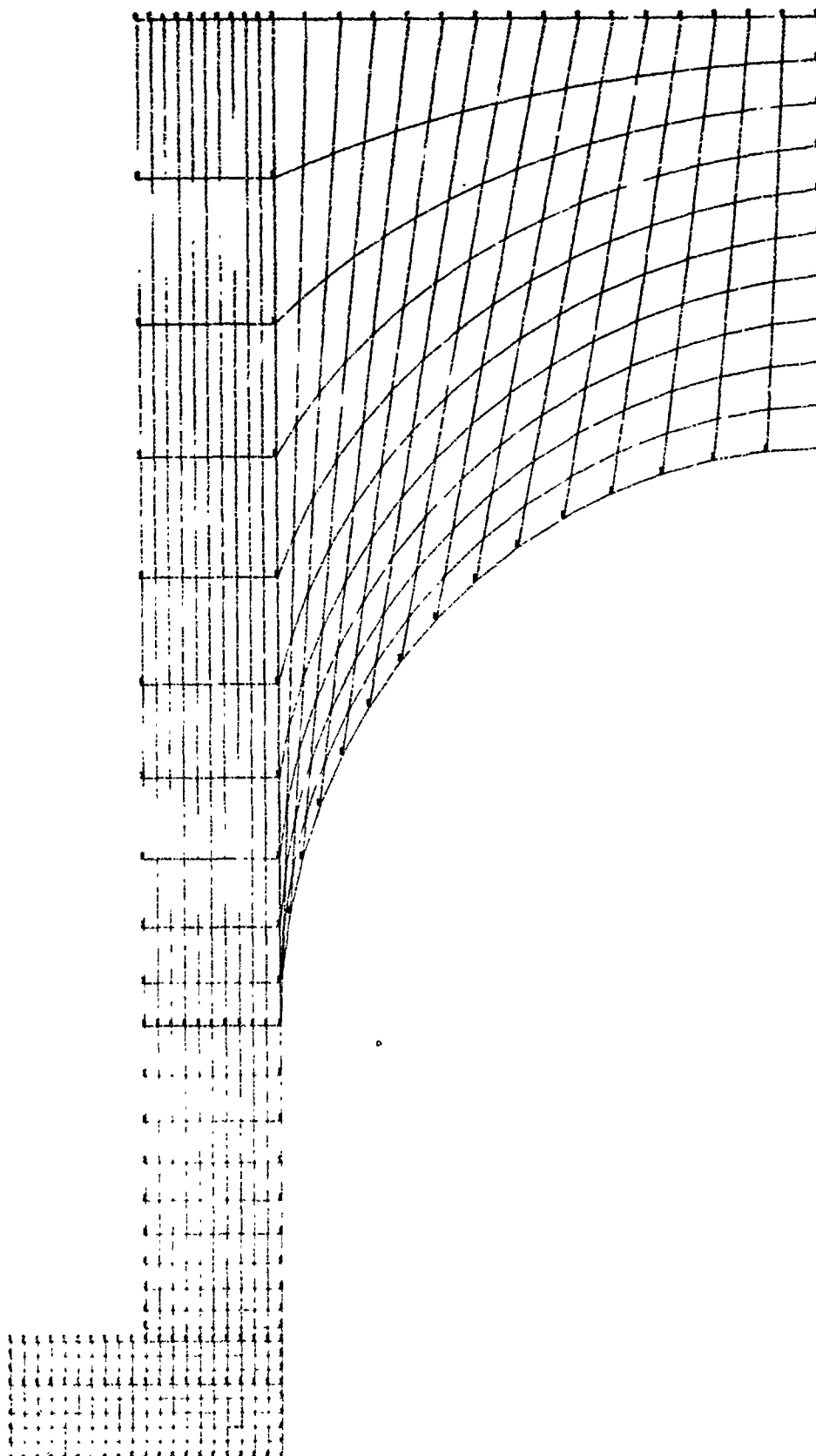
Figure 2-54. Finite-element model for case bond torsion sample of configuration 4.

185
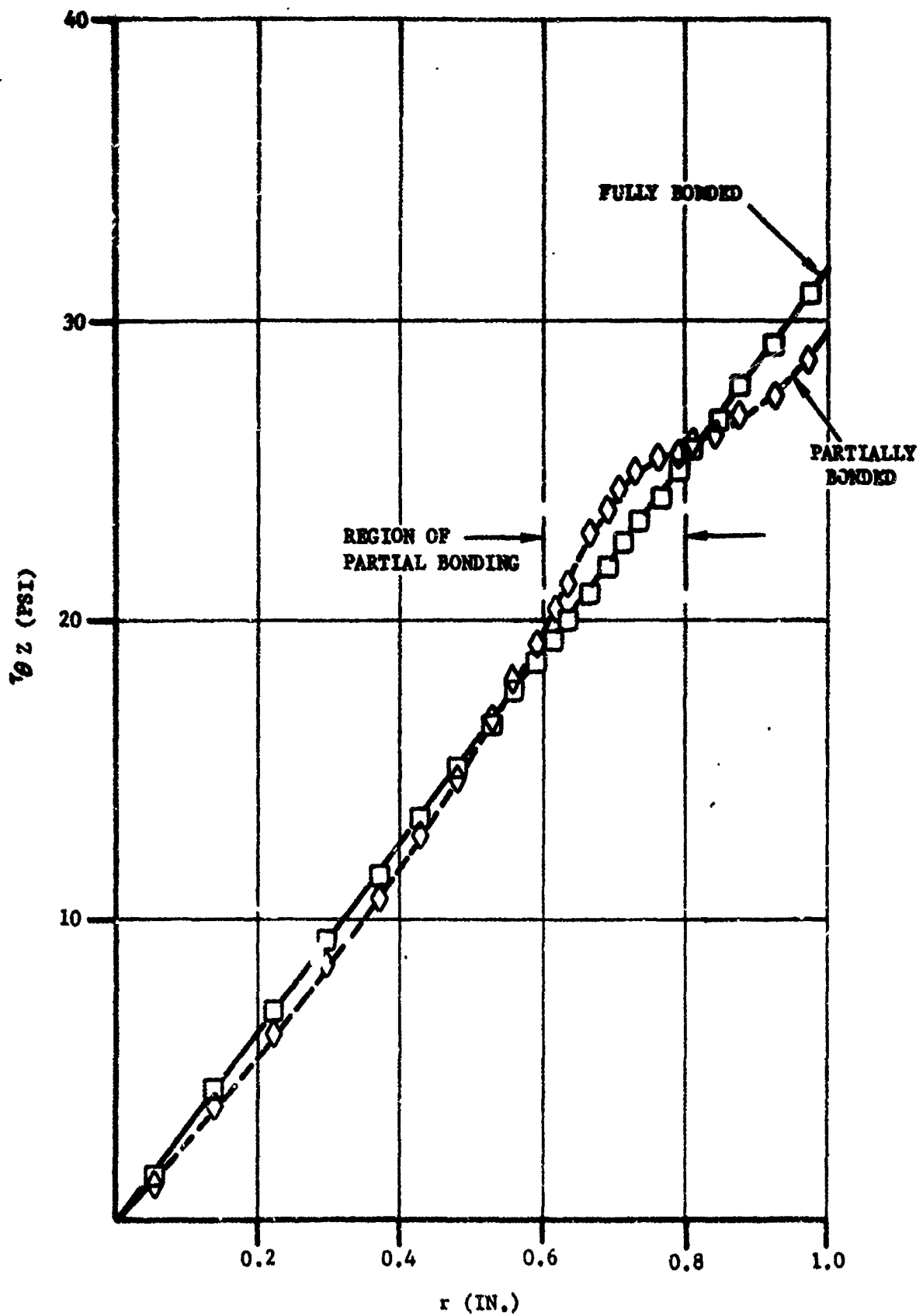
Figure 2-55. Shear stress in propellant adjacent to liner in solid torsion samples.
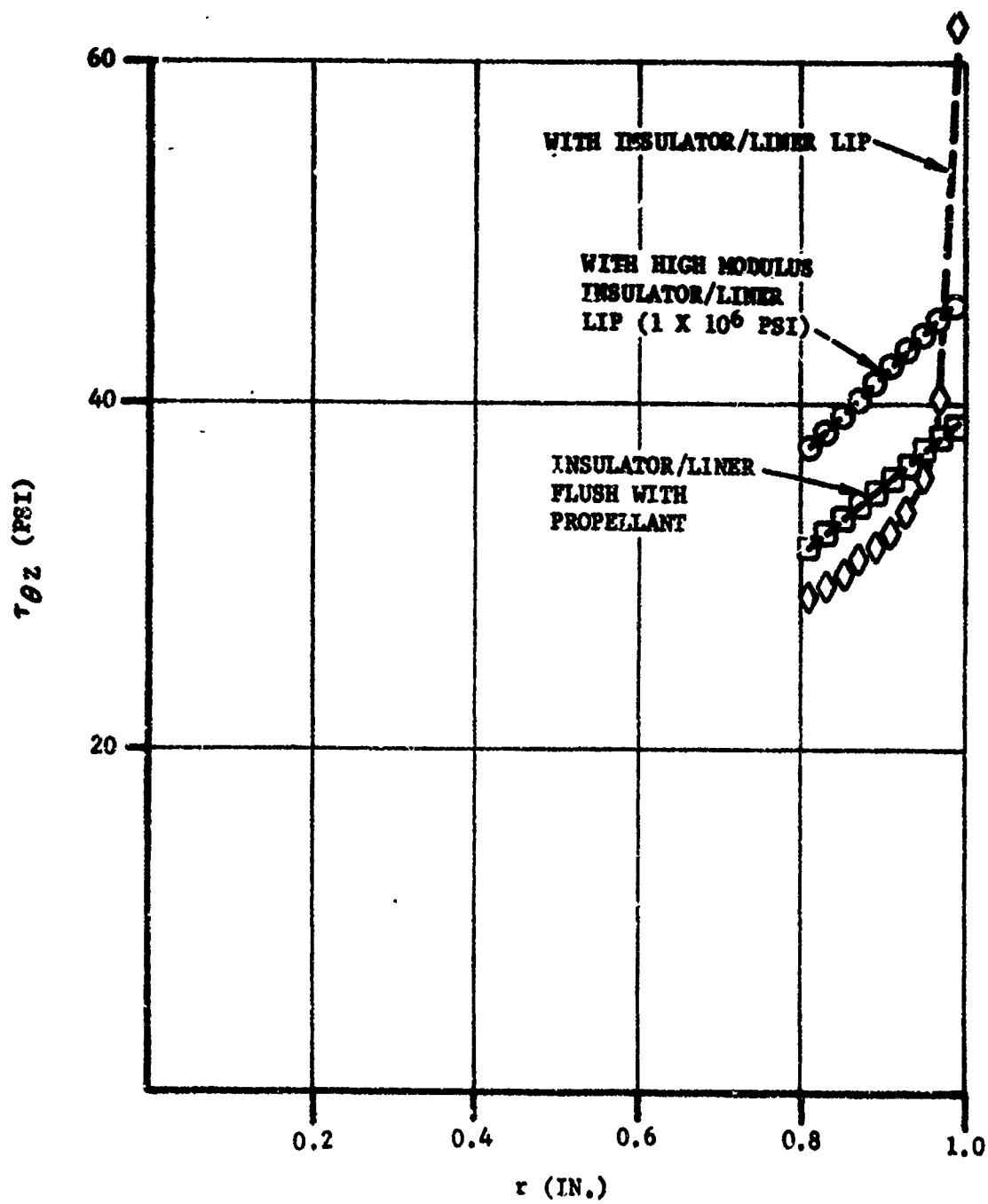
Figure 2-56. Shear stress in propellant adjacent to liner in hollow torsion samples.

187
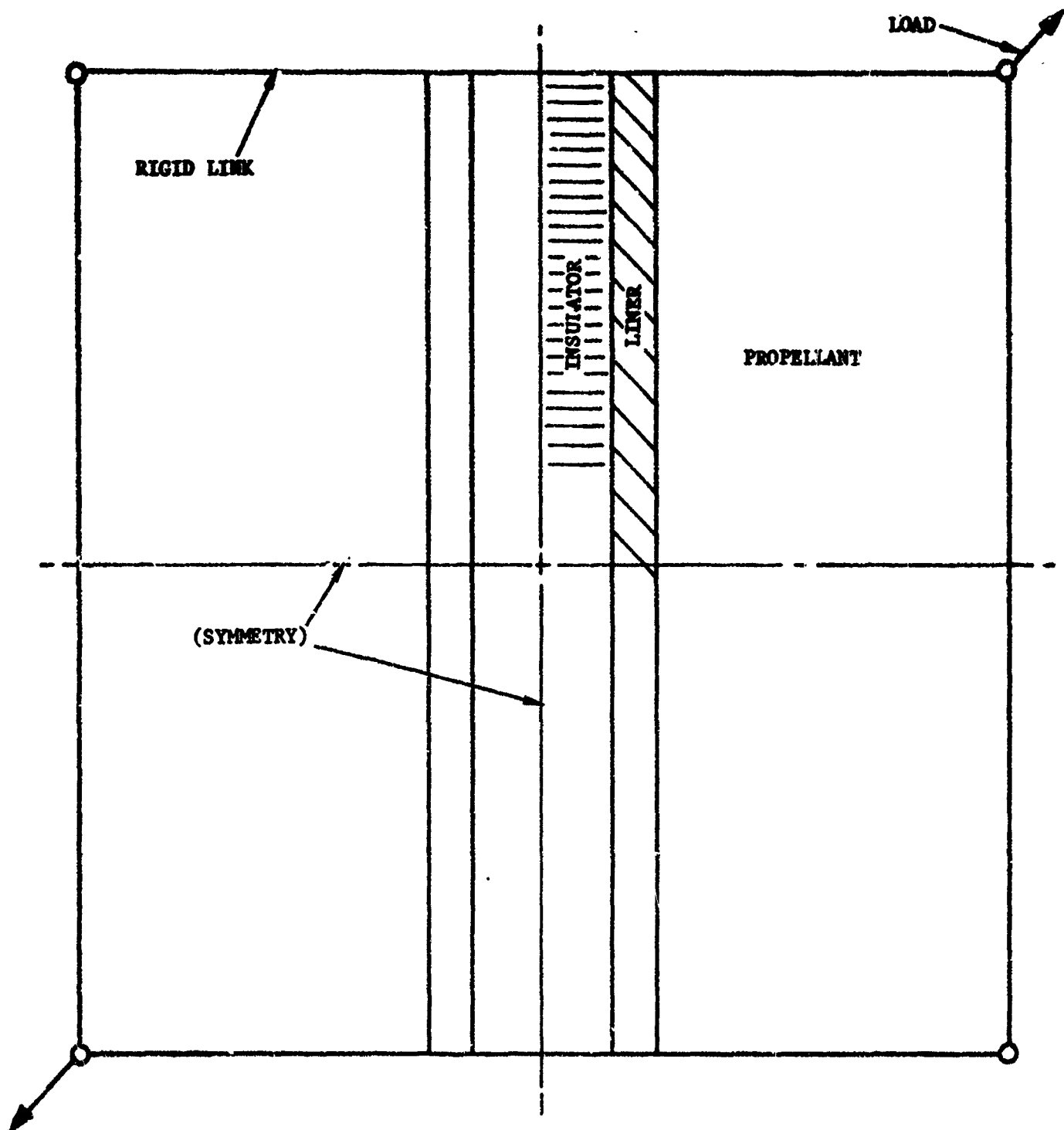
Figure 2-57. Picture-frame shear sample.

188

Figure 2-58. Lines of constant τ_{xy} shear stress for picture-frame shear sample.
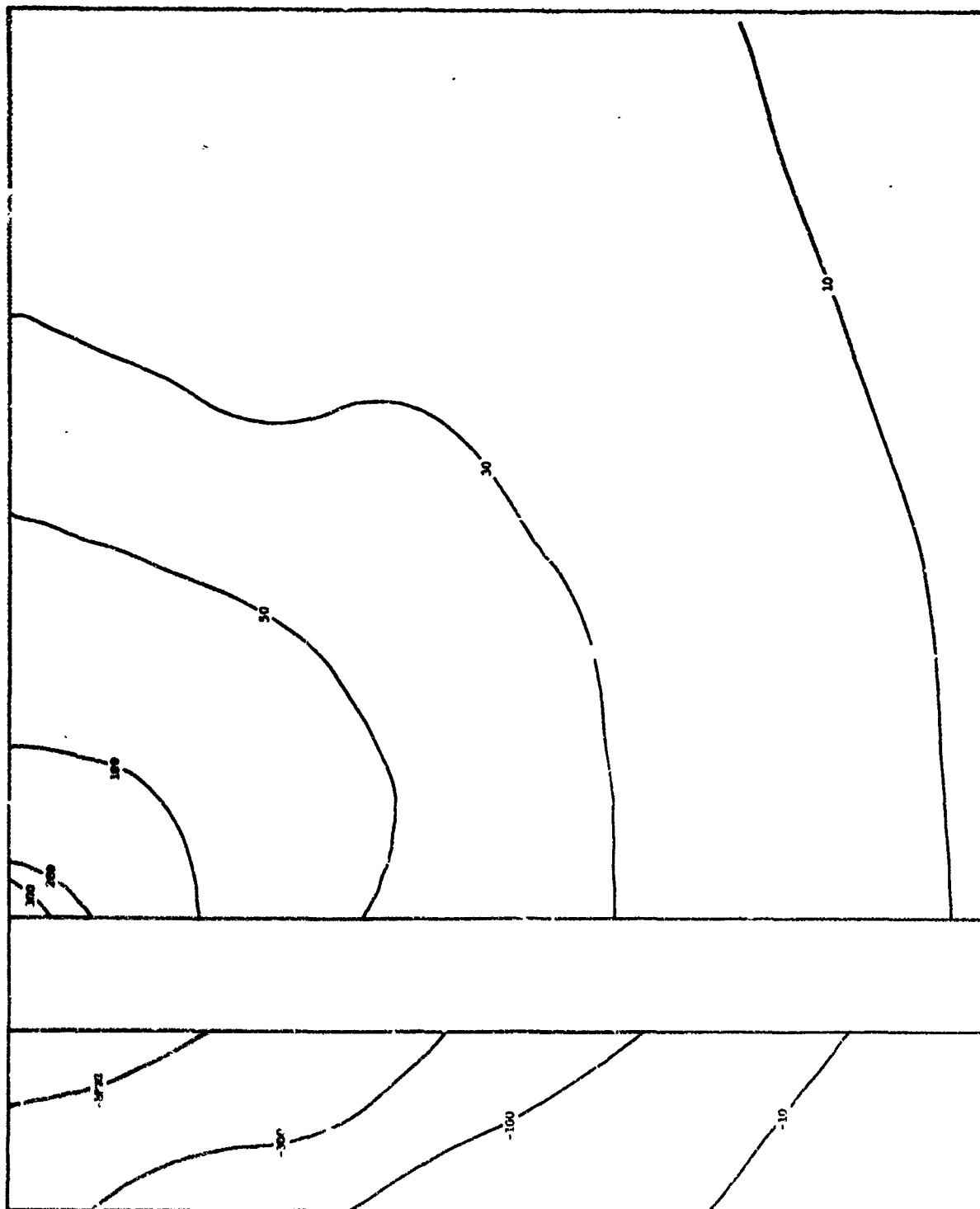
Figure 2-59. Lines of constant σ_y shear stress for picture-frame shear sample.
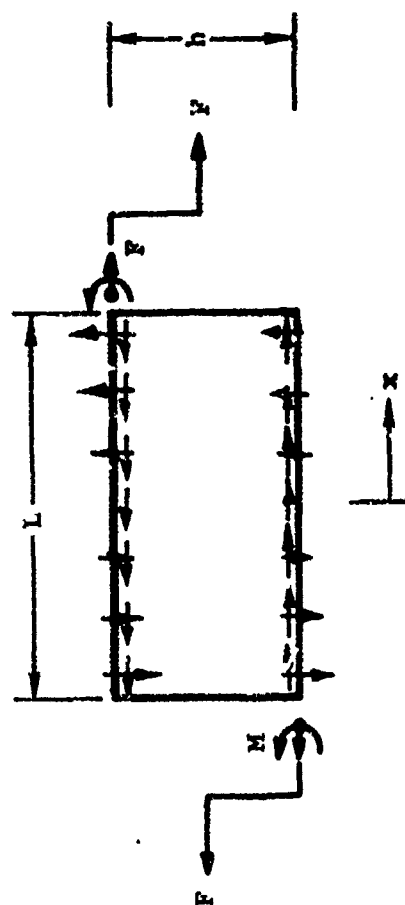
Figure 2-60. Lap shear force distribution.
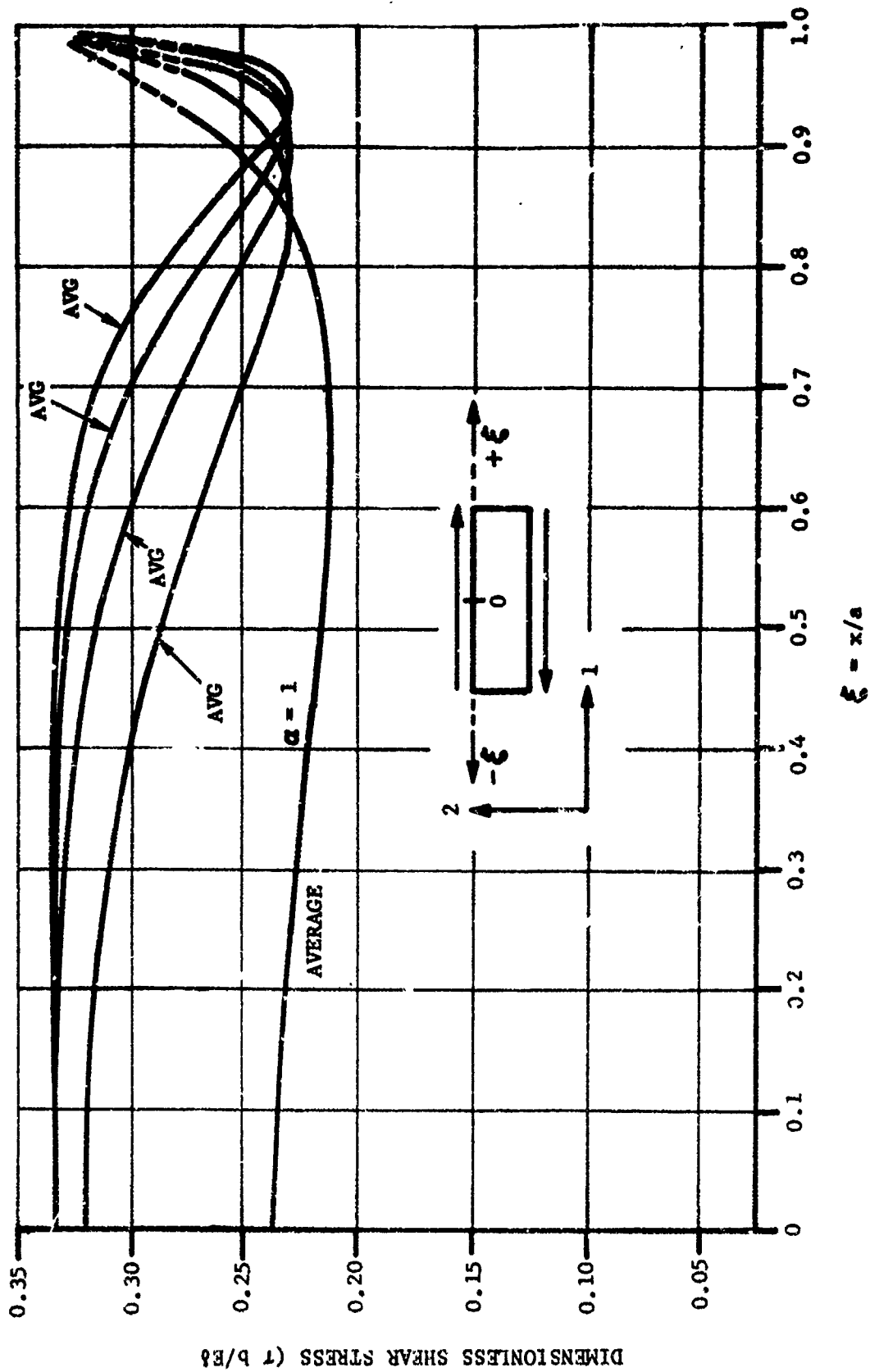
Figure 2-61. Shear stress along upper surface of shear lap specimens with $\beta = 90°$ for various values.
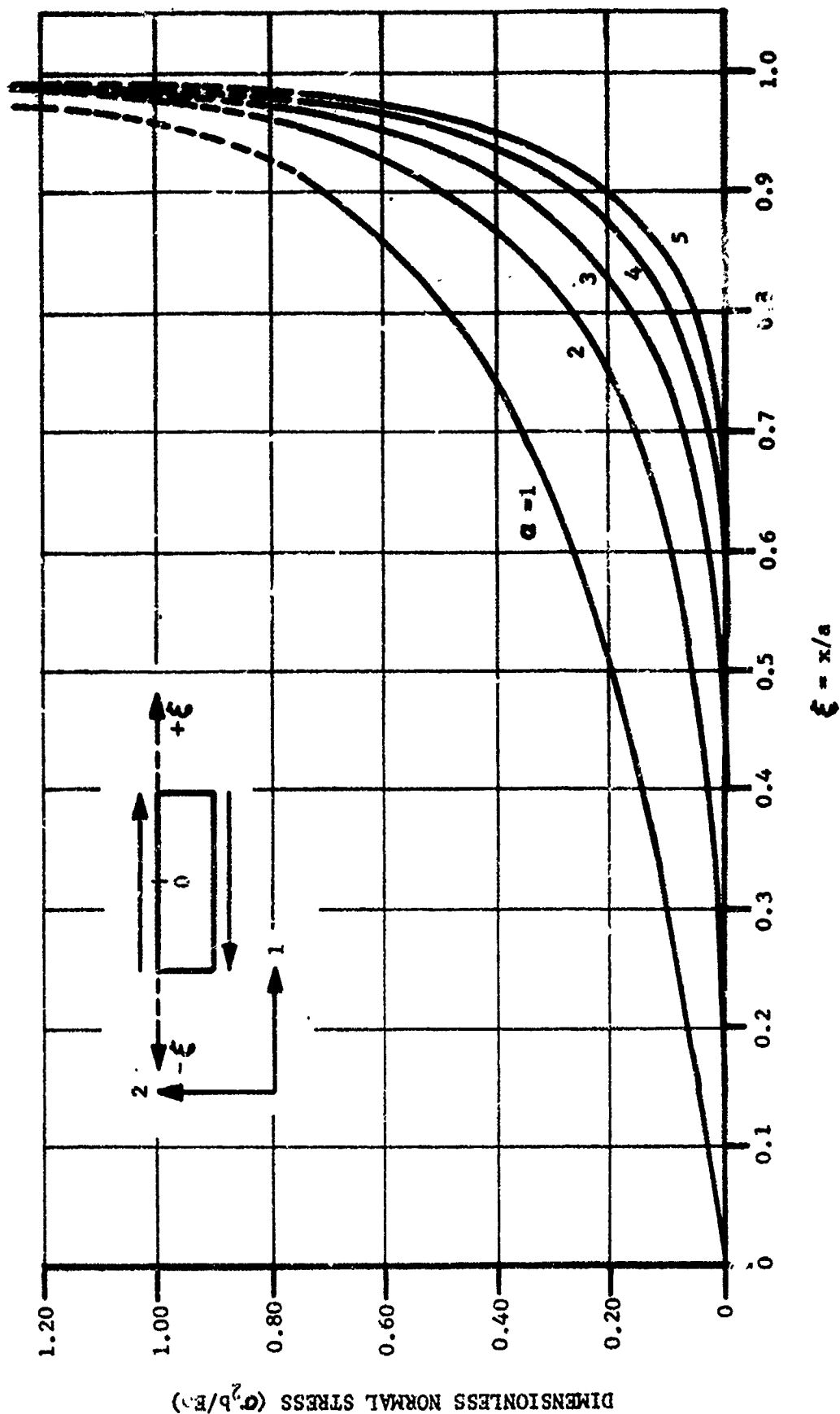
Figure 2-62. Normal stress along upper surface of shear lap specimens for $\beta = 90°$ and various values.

193
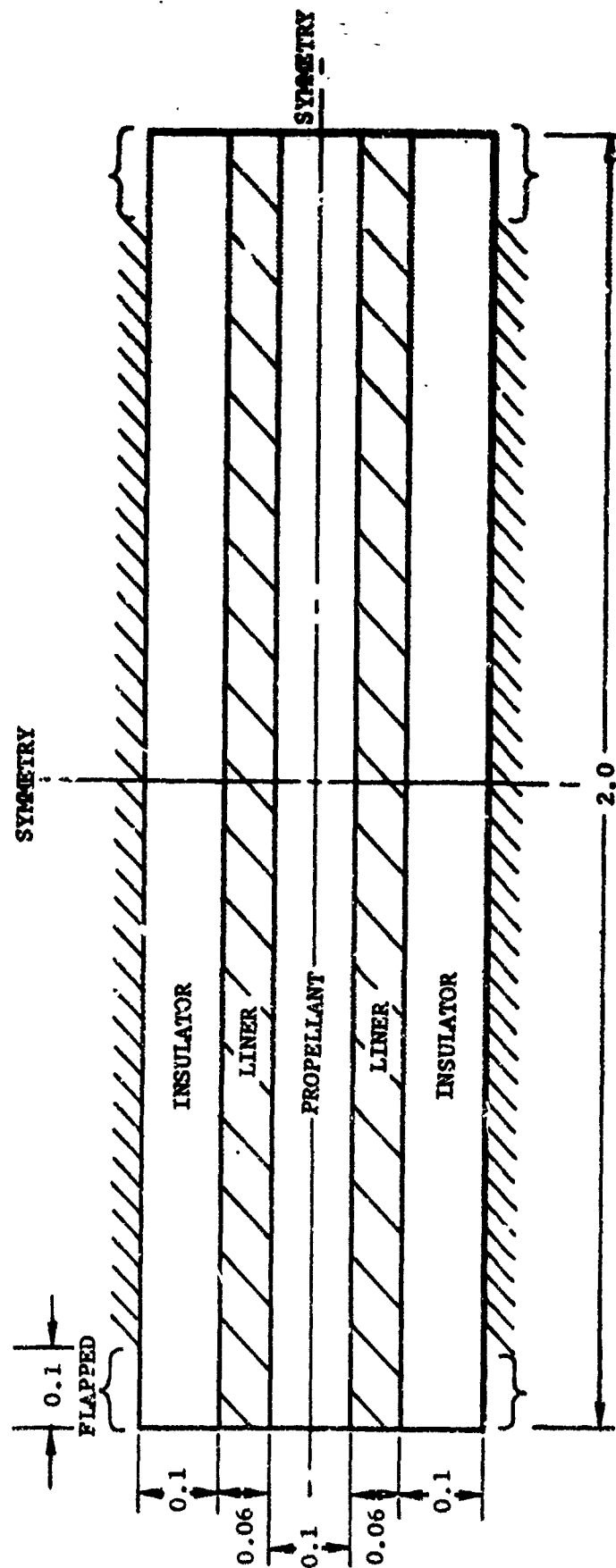
Figure 2-63. Basic case bond lap shear sample configuration used for preliminary studies.

INSULATOR

LINER

PROPELLANT

S-INFLAME
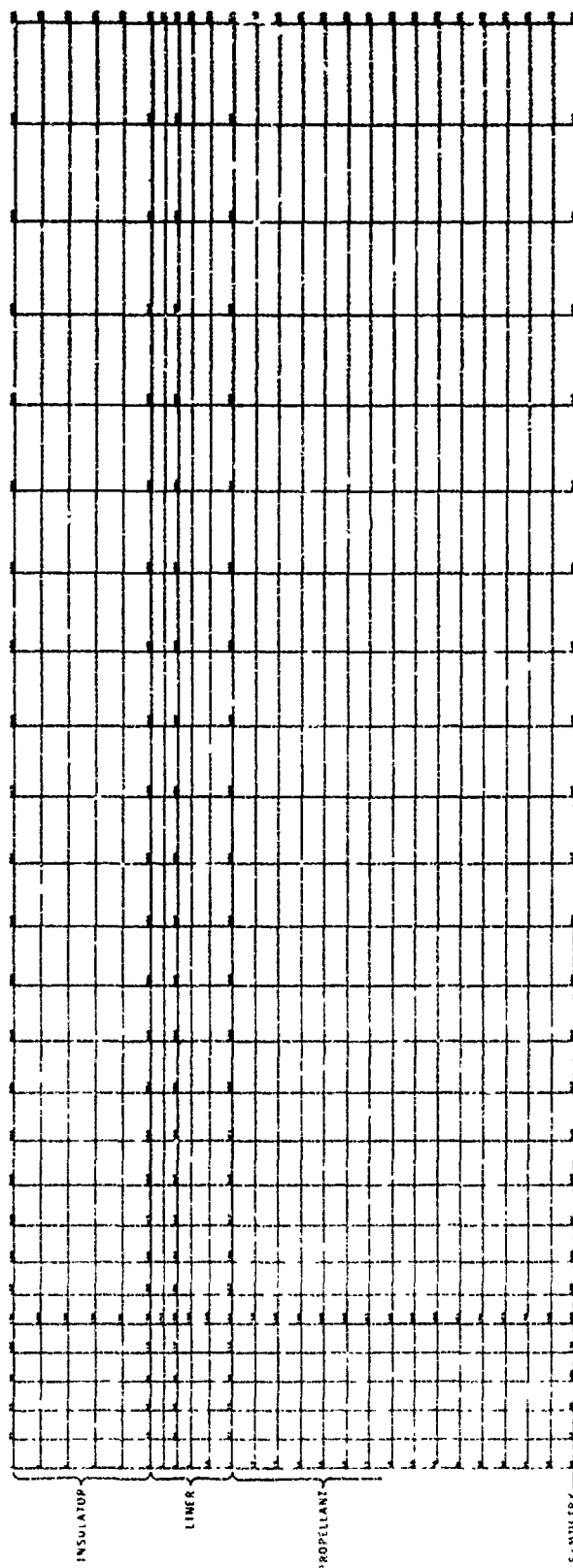
Figure 2-64. Finite-element model for 0.5-inch propellant height, case bond lap shear sample used in preliminary studies.

195
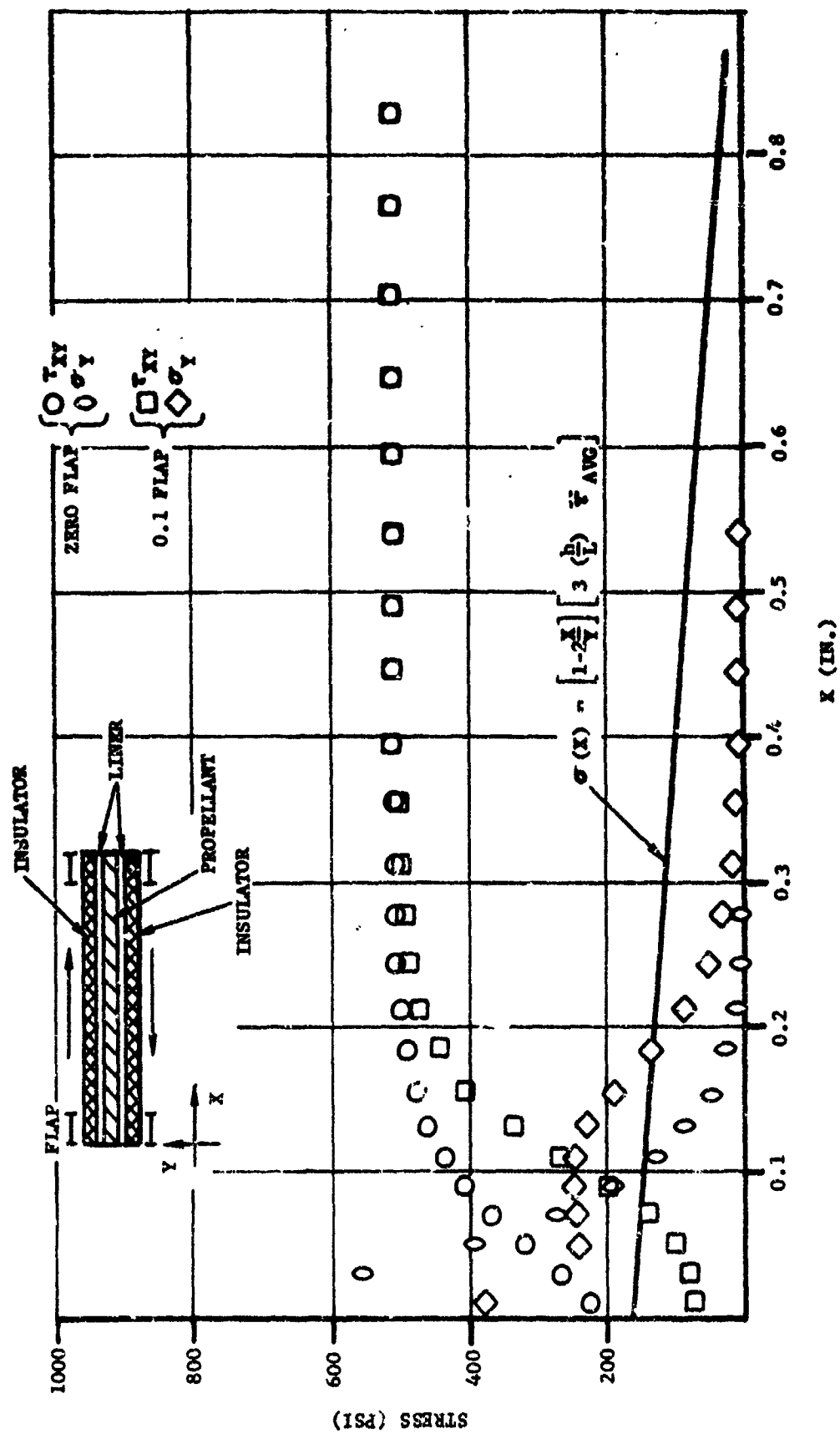
Figure 2-65. Normal and shear stresses in liner adjacent to insulator for zero and 0.1-inch flap length ($E_{liner} = E_{propellant} = 200$ psi).
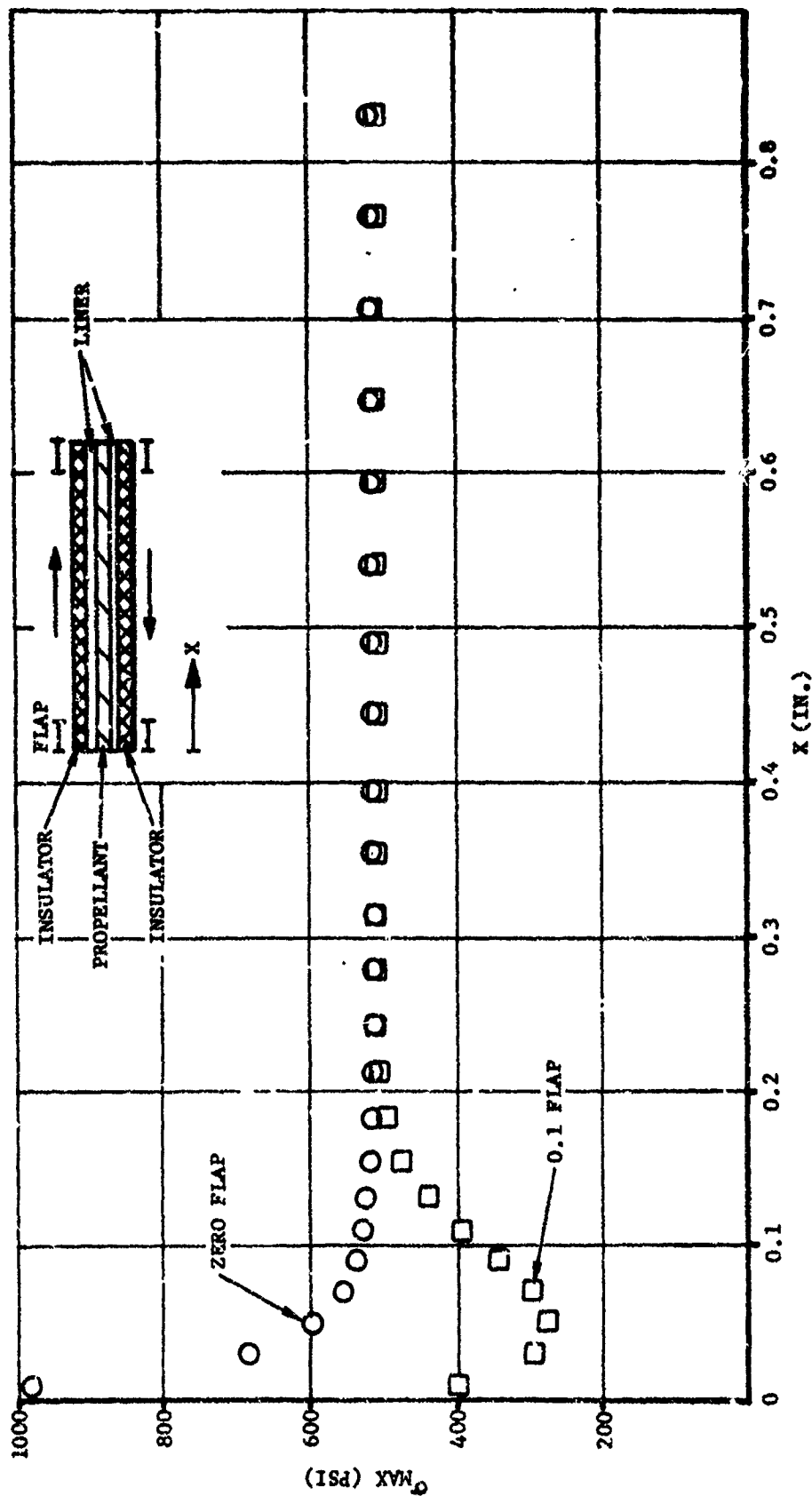
Figure 2-66. Maximum principal stress in the liner adjacent to the insulator for zero and 0.1-inch flap lengths ($E_{liner} = E_{propellant} = 200$ psi).

197
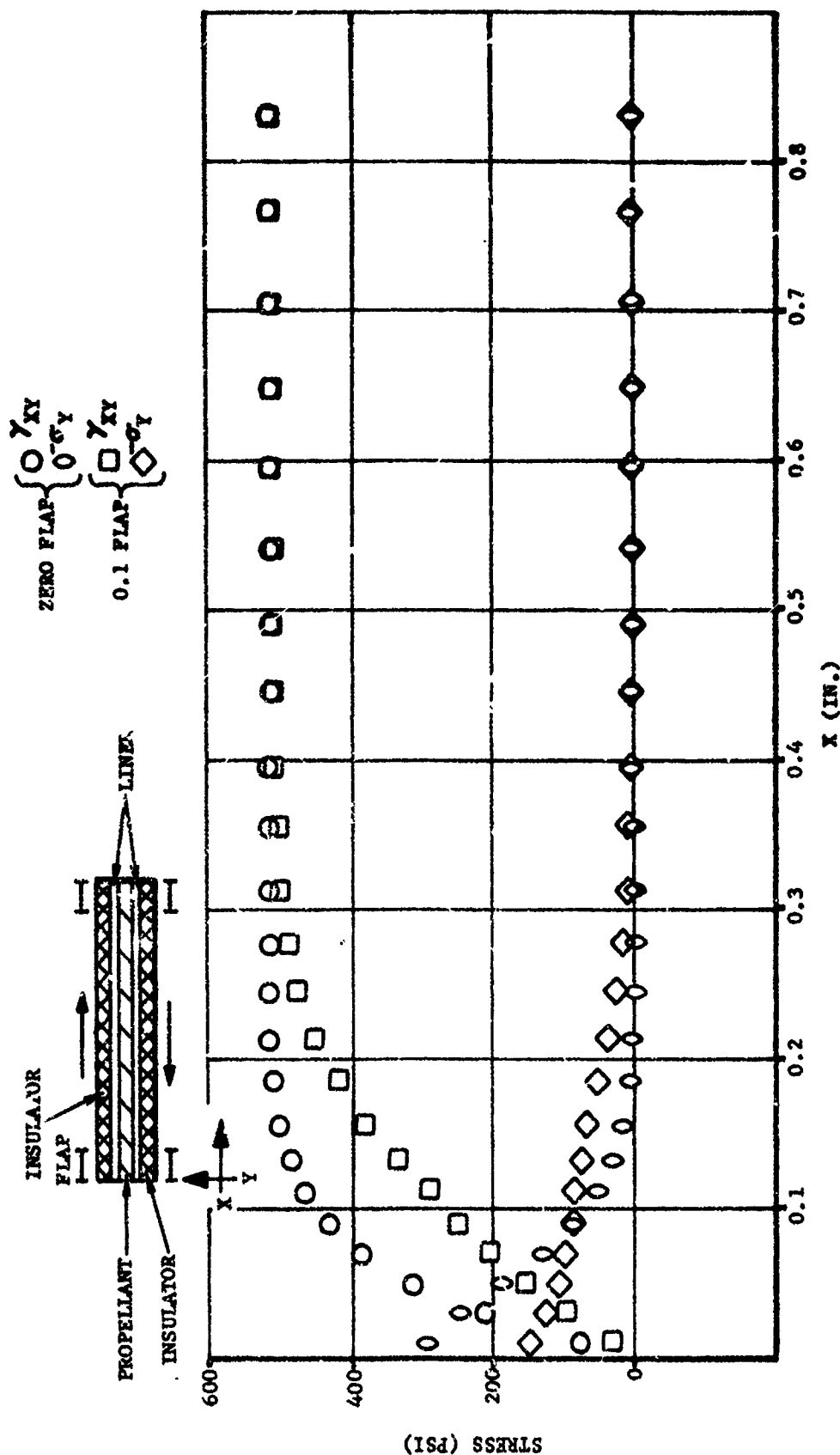
Figure 2-67. Normal and shear stresses in propellant adjacent to liner for zero and 0.1-inch flap lengths ($E_{liner} = E_{propellant} = 200$ psi).
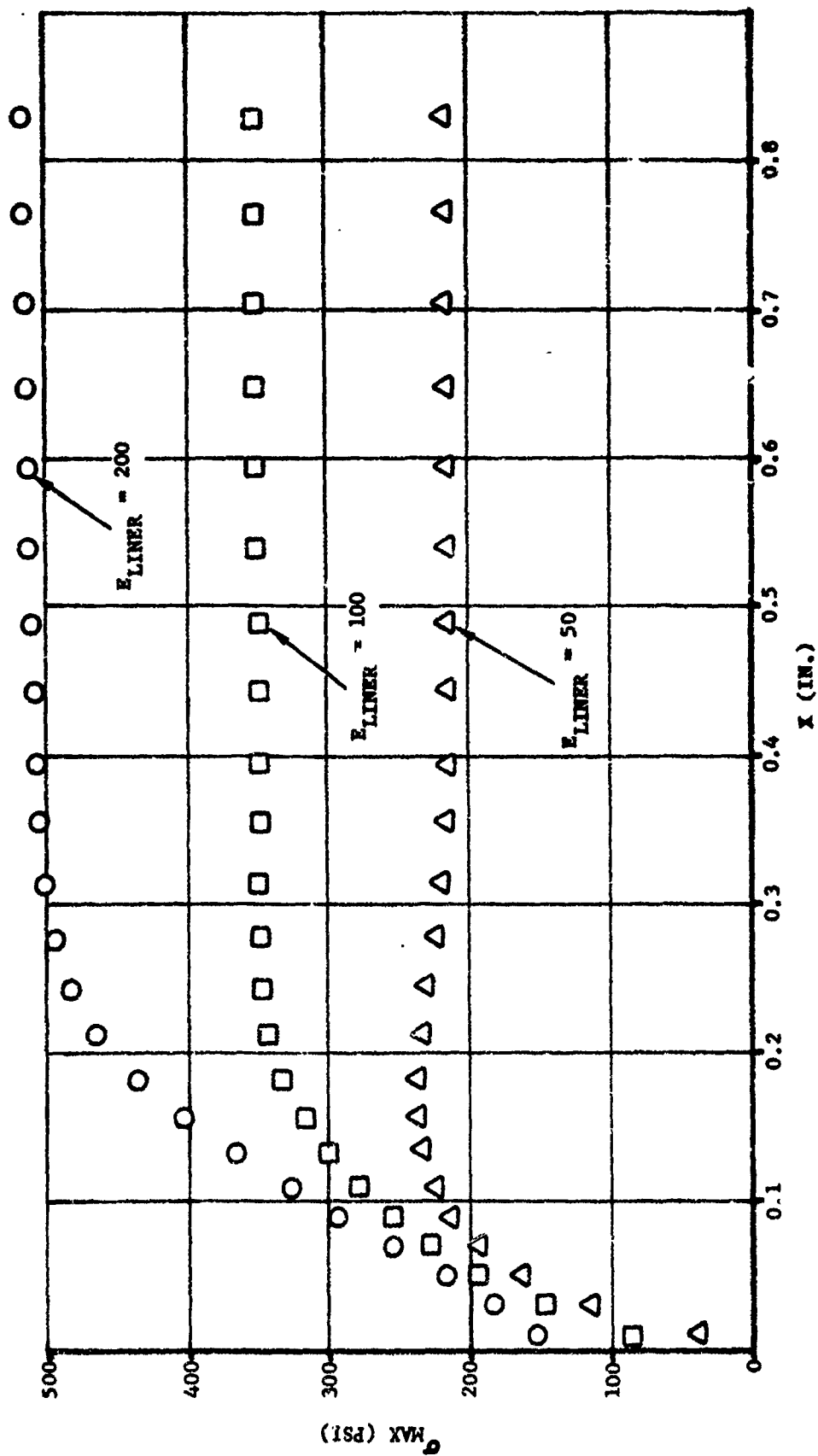
Figure 2-68. Maximum principal stress in the propellant adjacent to the liner for a 0.1-inch flap length with varying liner modulus.

199
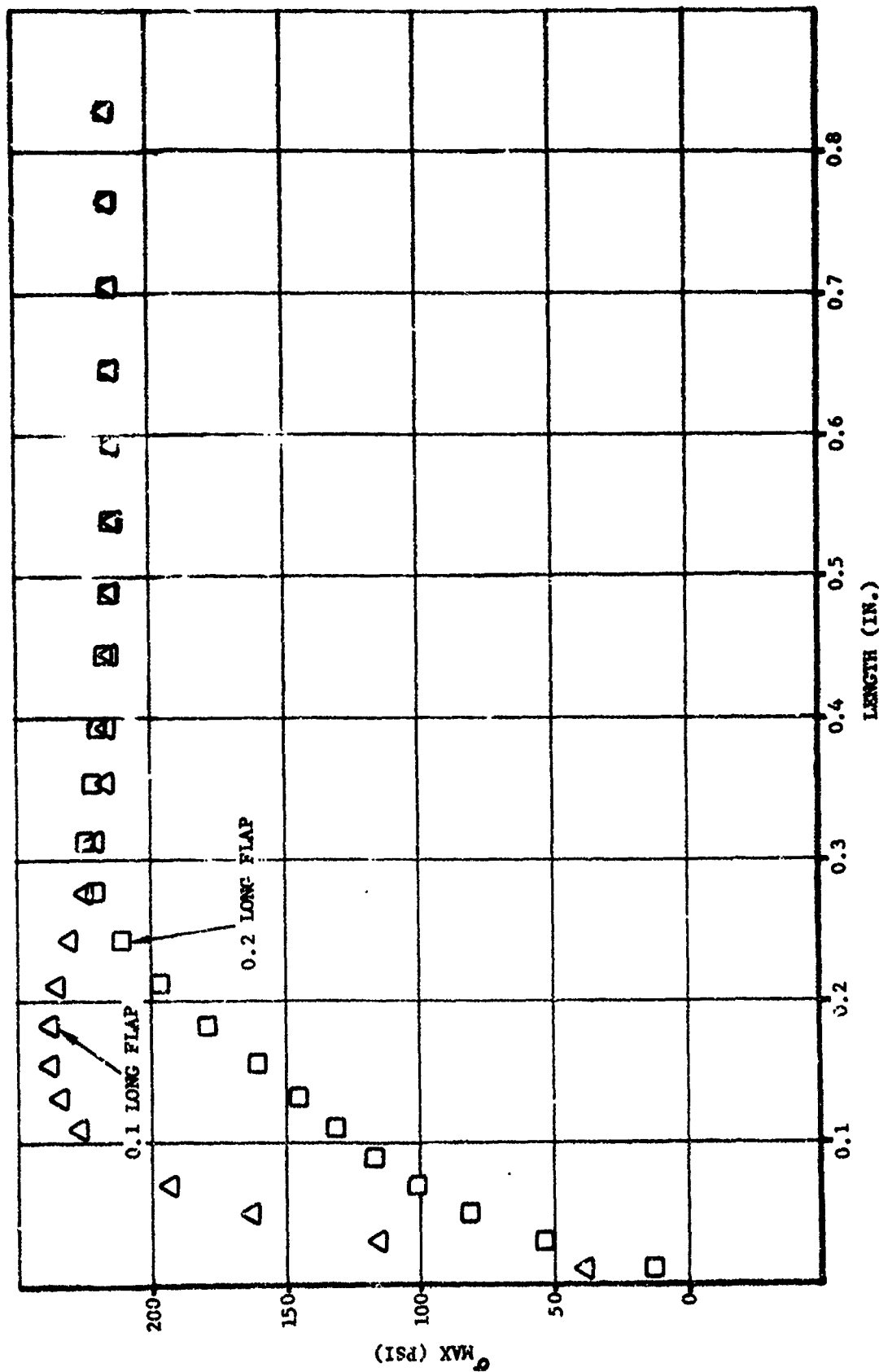
Figure 2-69. Maximum principal stress in the propellant adjacent to the liner for 0.1 and 0.2 flap length (E_{liner} = 50 psi).
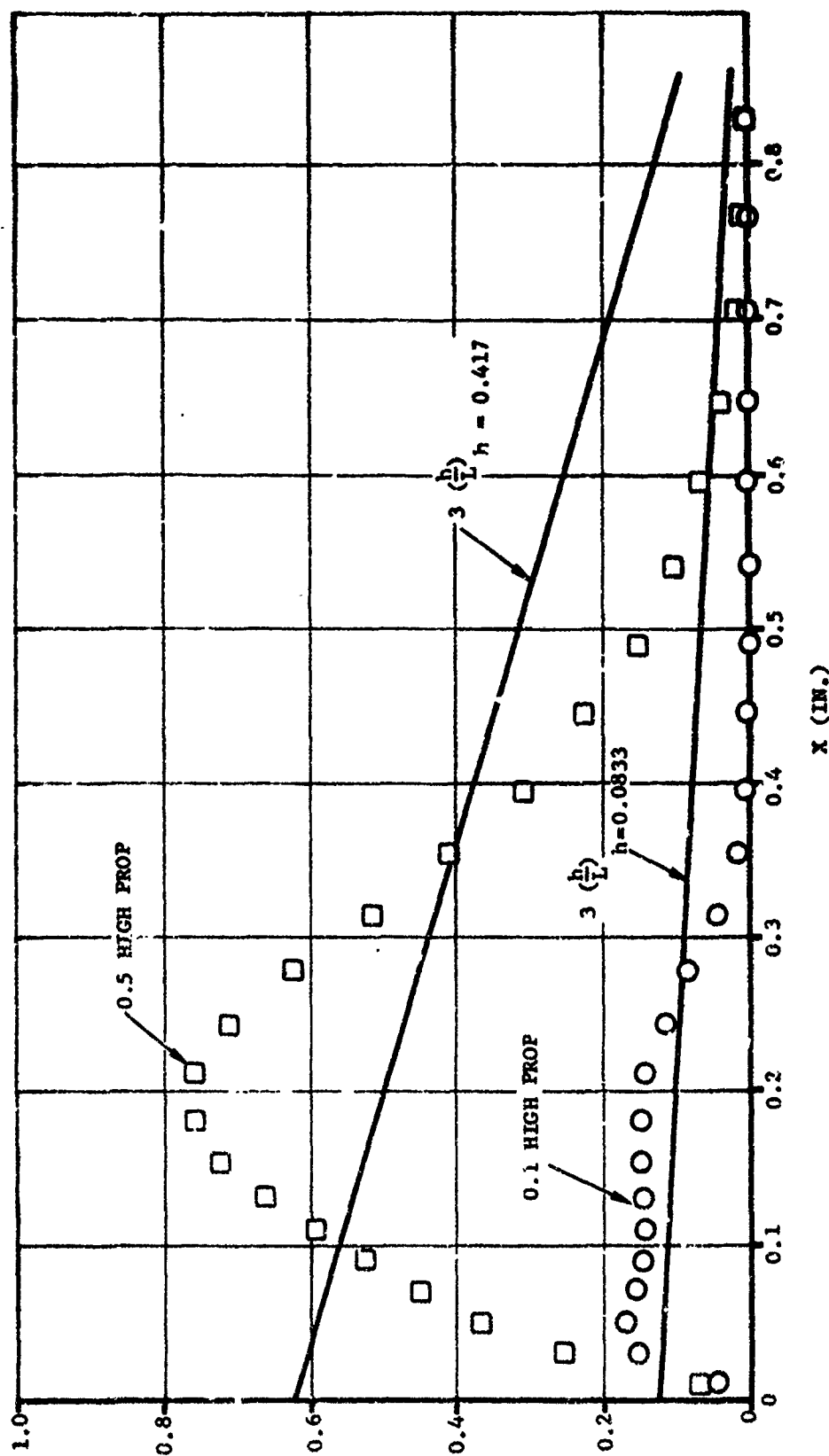
Figure 2-70. Nominal stress in the propellant adjacent to the liner, ratioed to the case bond shear stress near the axial midplane, for 0.1 and 0.5 inch propellant heights (E_{liner} = 50 psi).
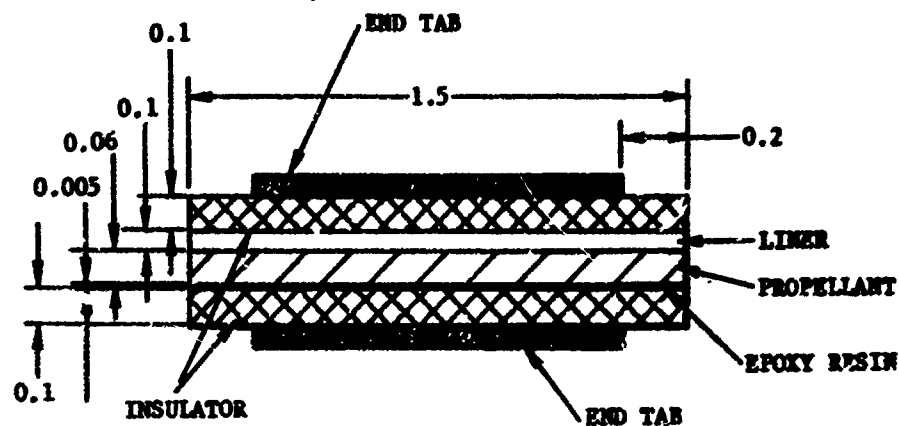
CONFIGURATION 1
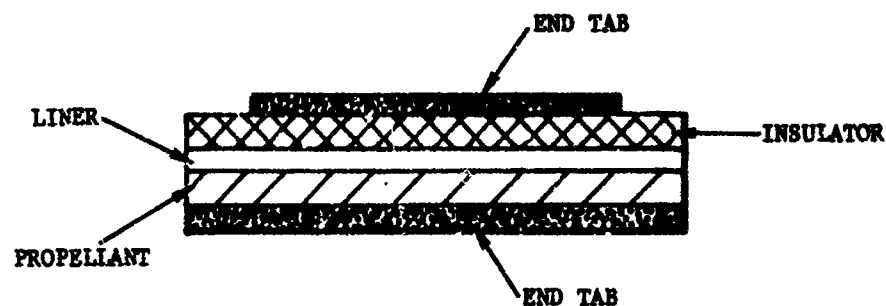
CONFIGURATION 2
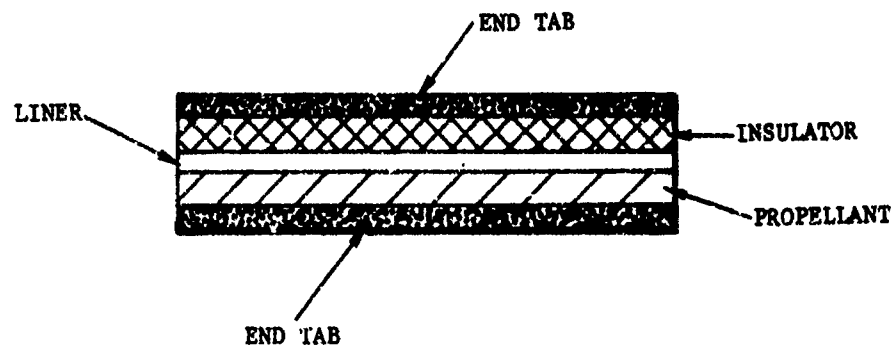
CONFIGURATION 3

Figure 2-71. Three candidate configurations for short lap-shear sample.
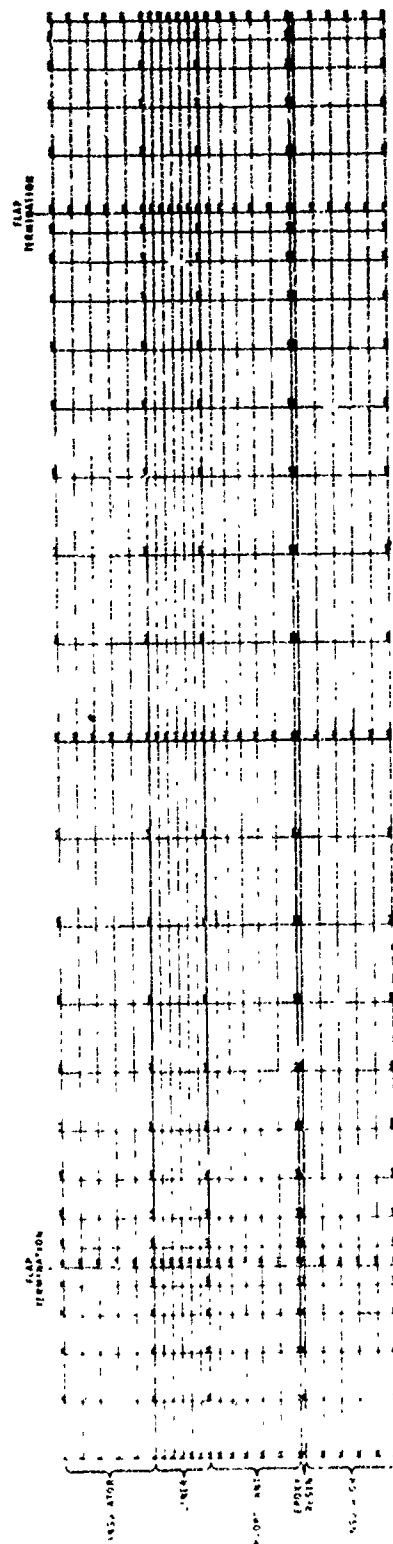
Figure 2-72. Finite-element model used for stress analysis of candidate short lap shear samples.
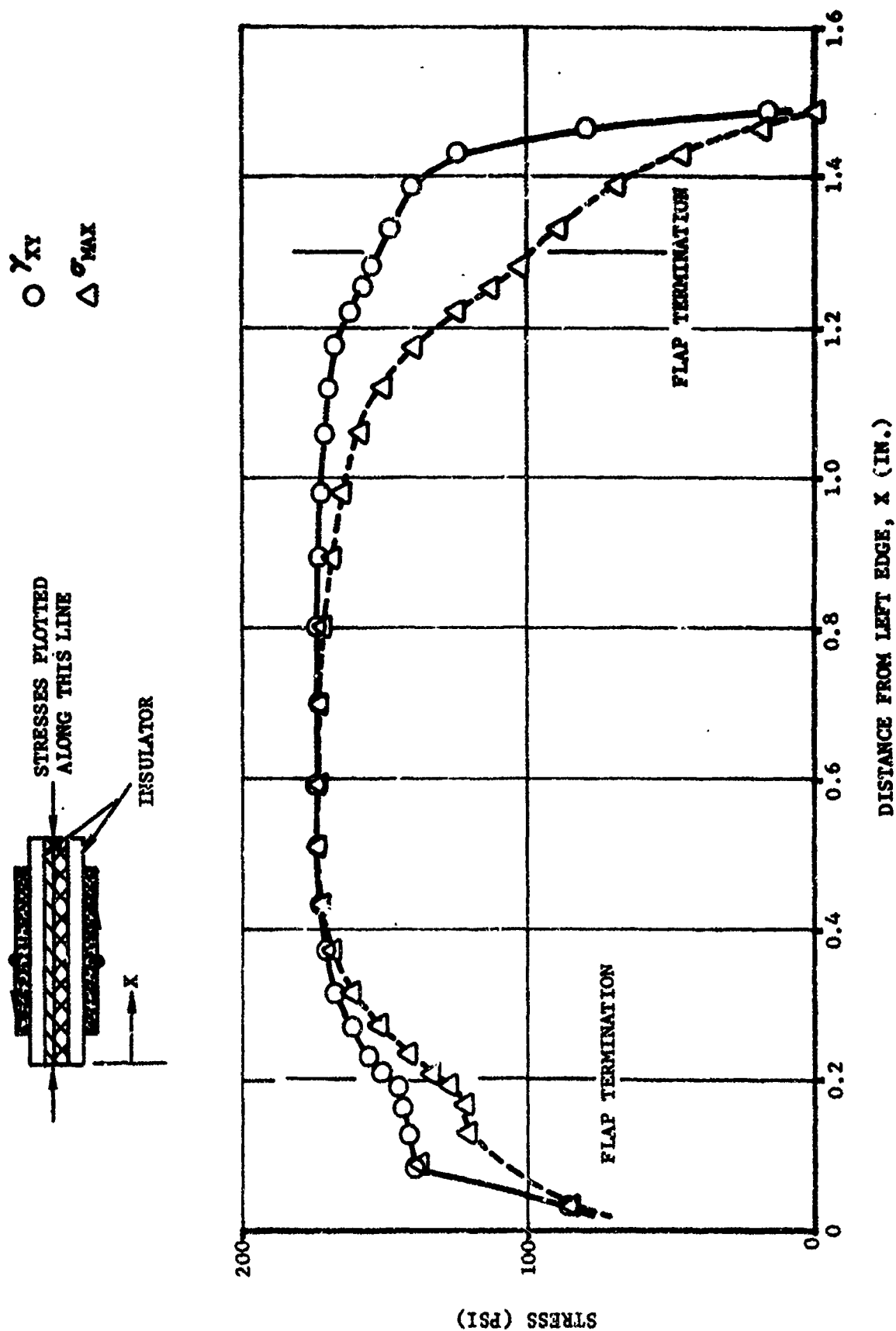
Figure 2-73. Propellant stresses adjacent to liner bondline for short lap shear sample of configuration 1.
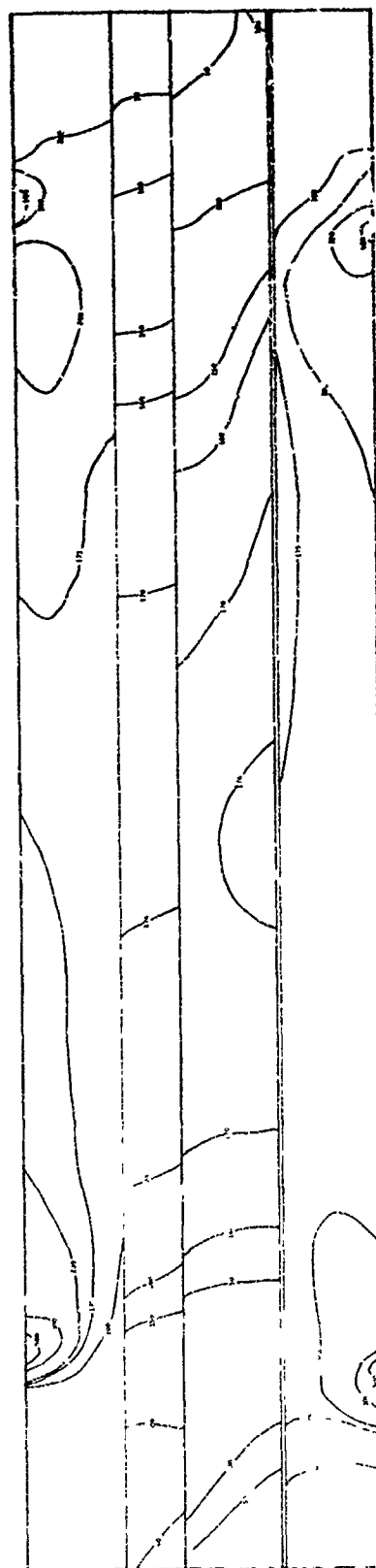
Figure 2-74. Lines of constant maximum principal stress for short lap
shear sample of configuration 1.

205
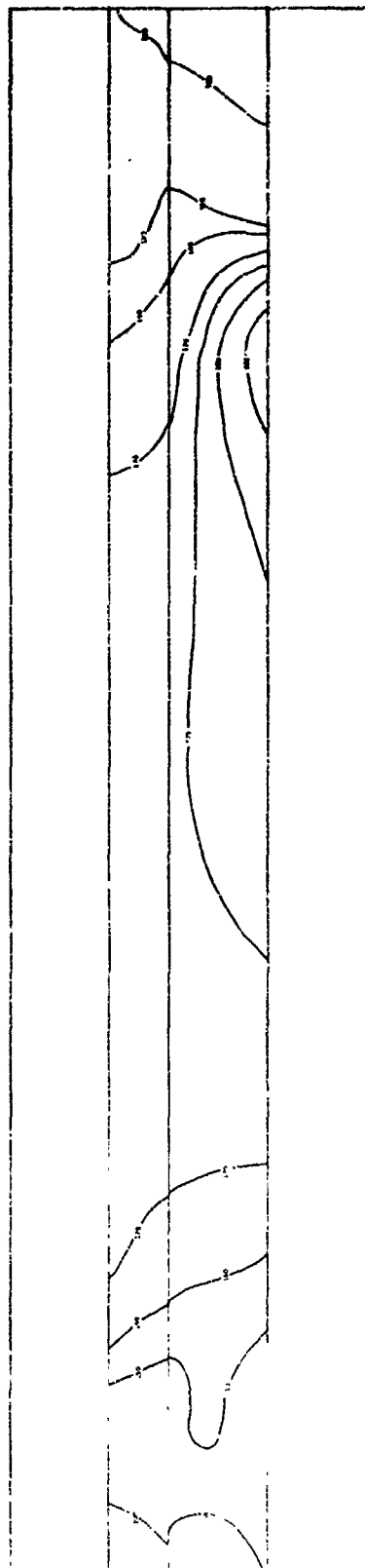
Figure 2-75. Lines of constant τ_{xy} shear stress for short lap shear sample of configuration 1.
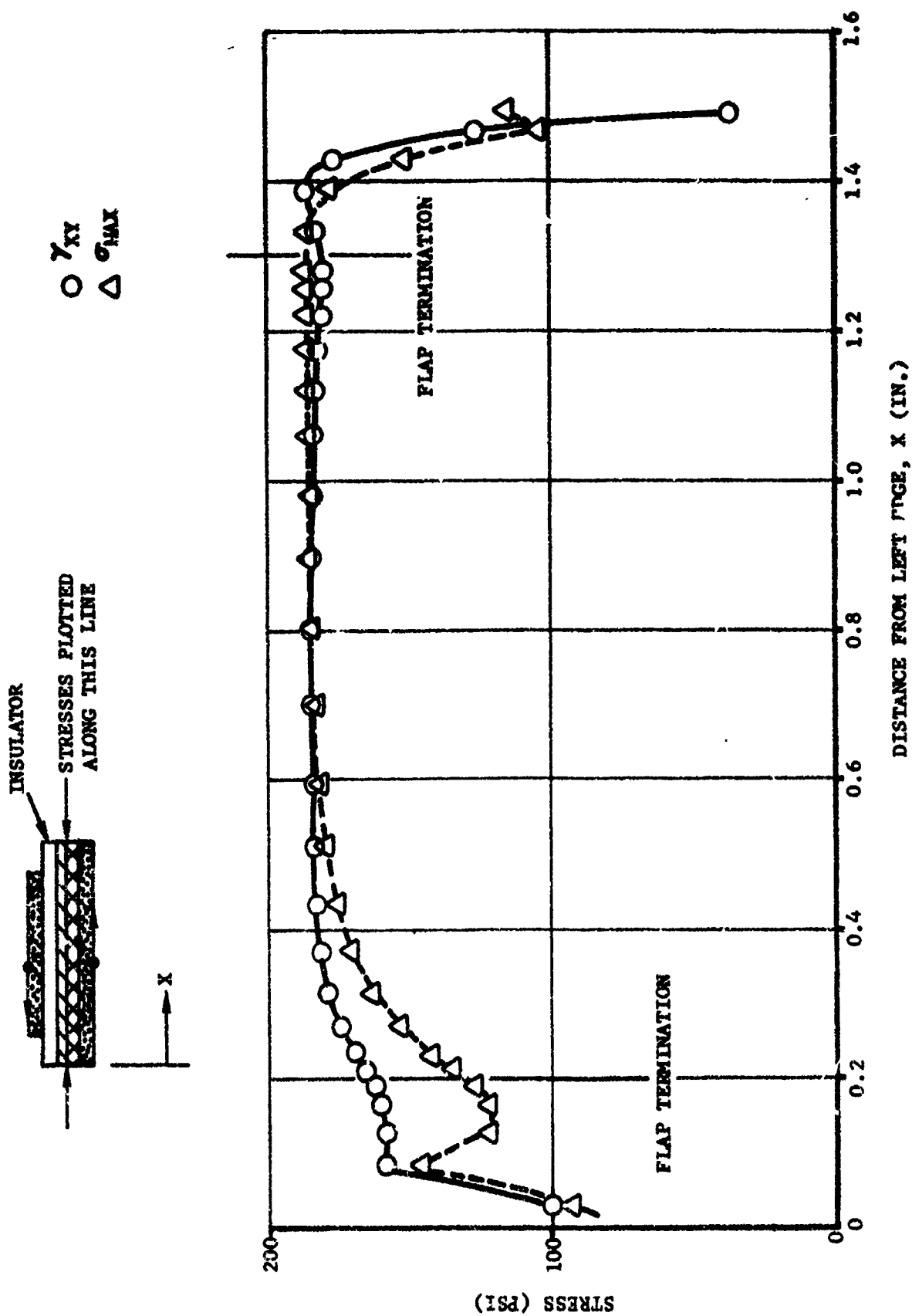
Figure 2-76. Propellant stresses adjacent to liner bondline for short lap shear sample of configuration 2.

207
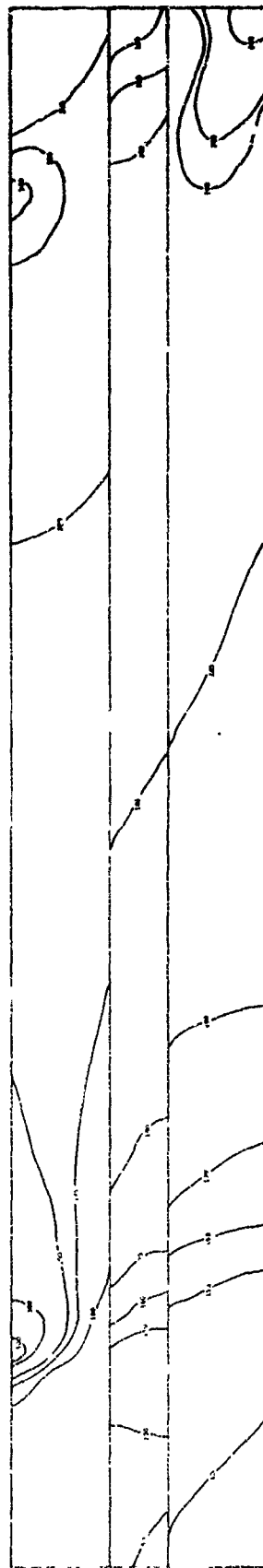
Figure 2-77. Lines of constant maximum principal stress for short lap
shear sample of configuration 2.

208
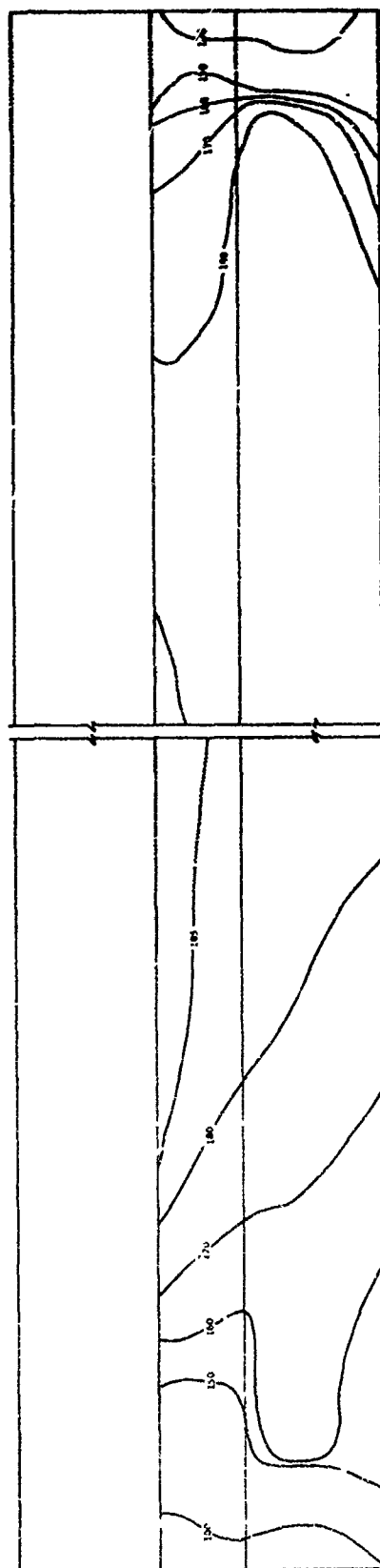
Figure 2-78. Lines of constant τ_{xy} shear stress for short lap shear sample of configuration 2.

209
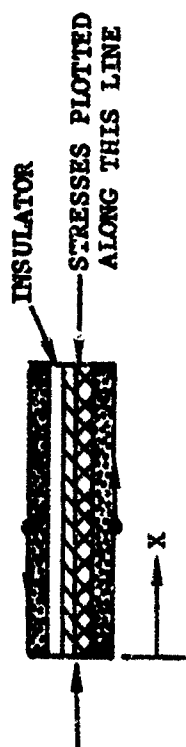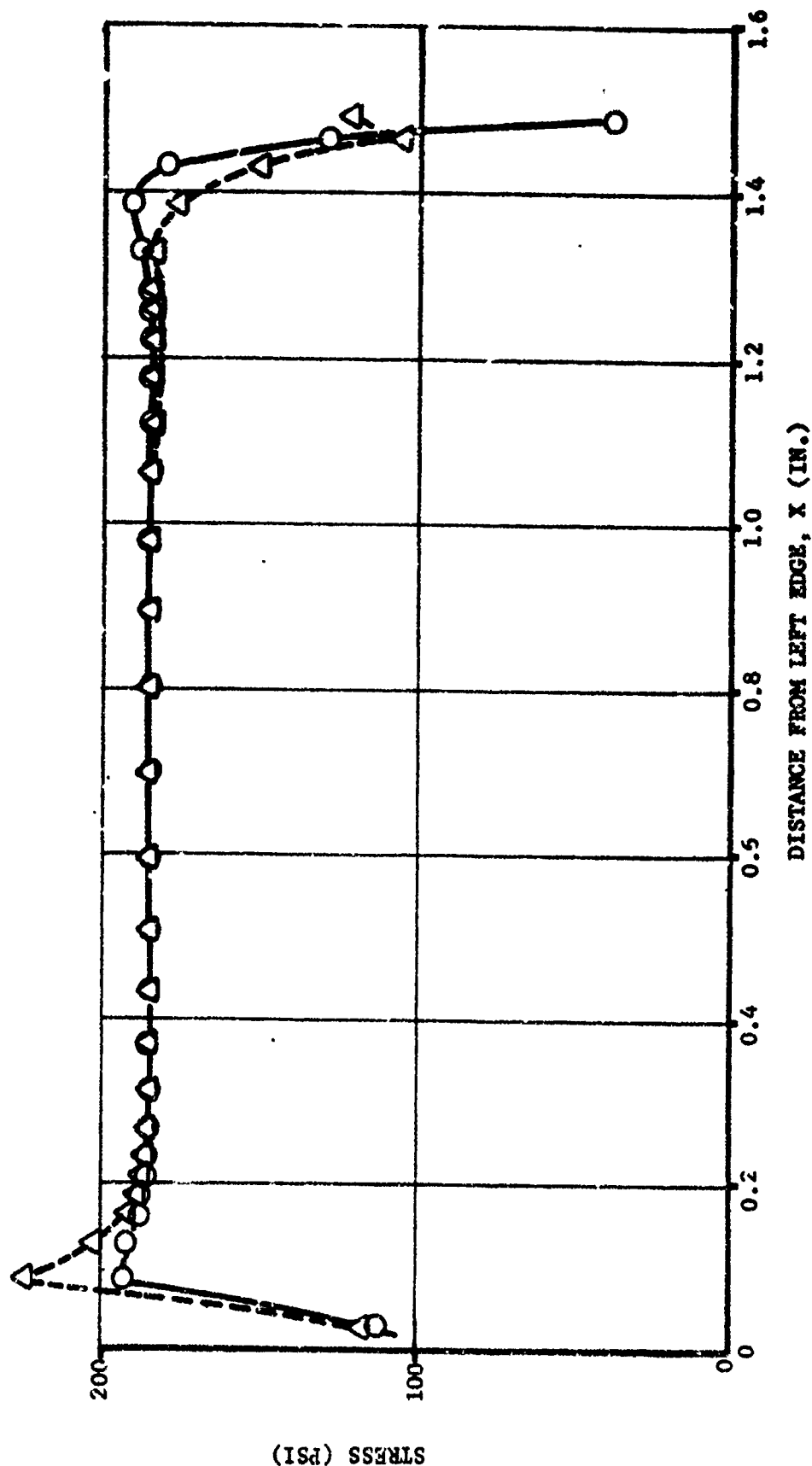
Figure 2-79. Propellant stress adjacent to liner bondline for short lap shear sample of configuration 3.

210
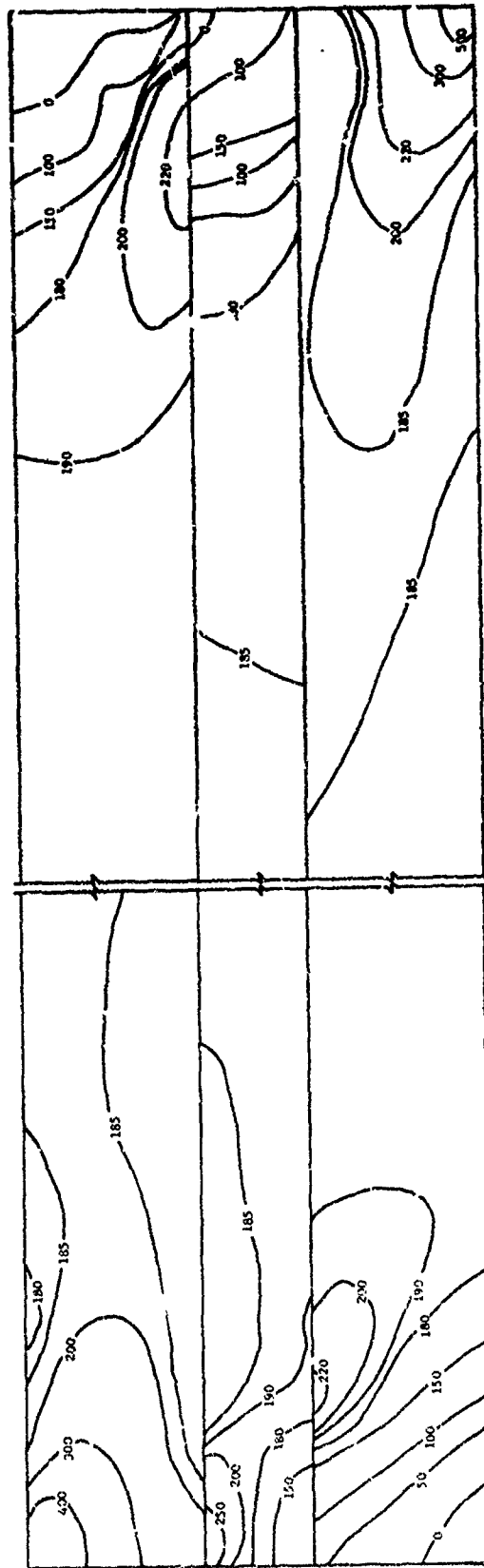
Figure 2-80. Lines of constant maximum principal stress for short
lap shear sample of configuration 3.

211
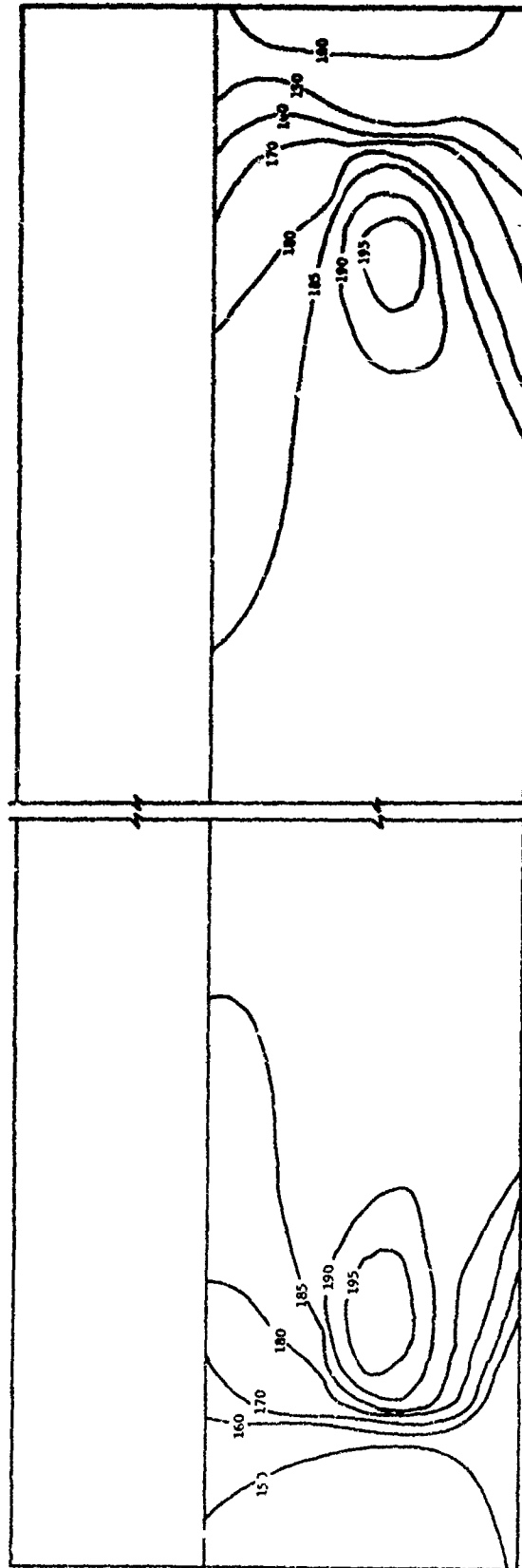
Figure 2-81. Lines of constant τ_{xy} shear stress for short lap shear sample of configuration 3.

Figure 2-82. Recommended configuration for short lap shear sample.

213
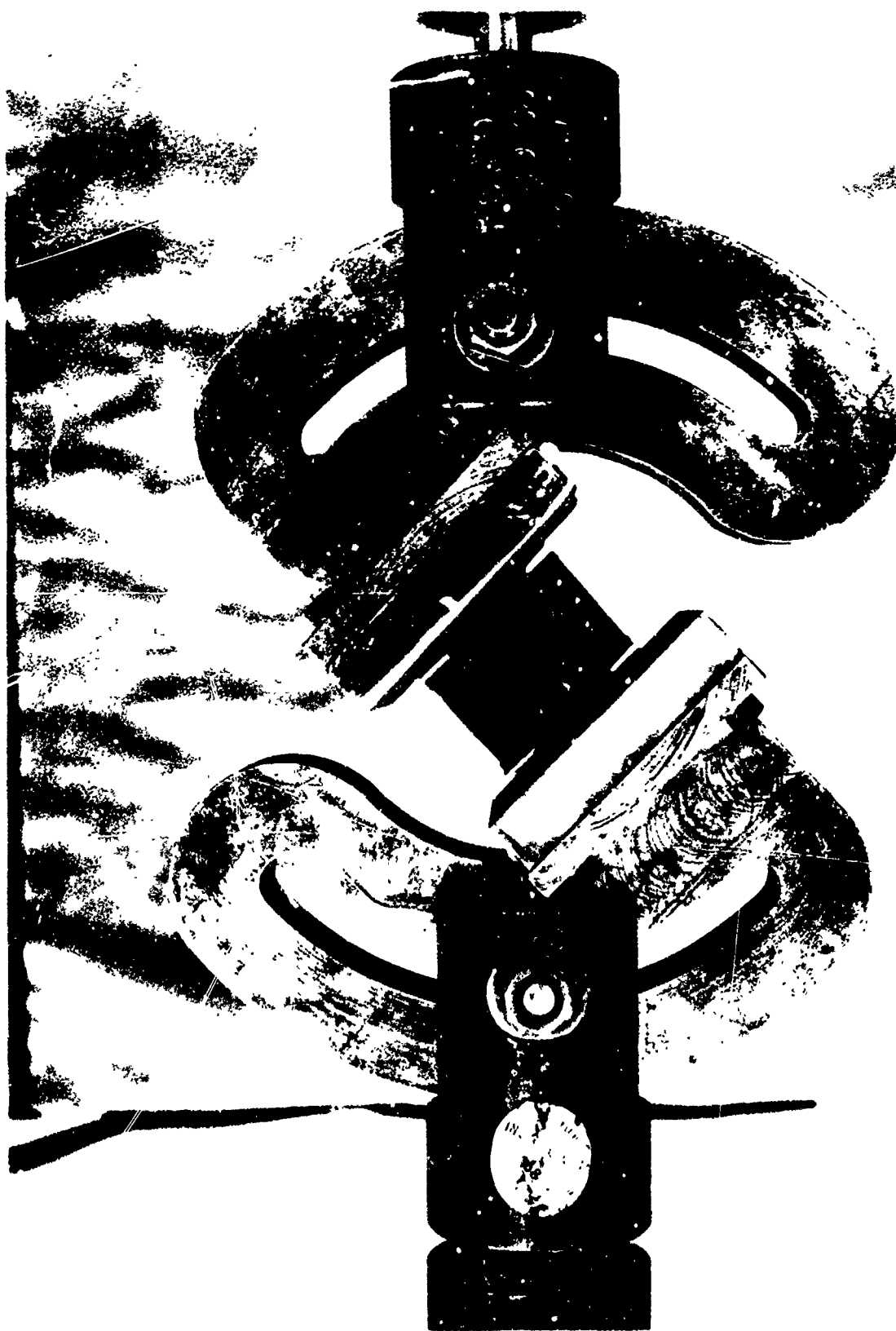
Figure 2-3. Ten-shear grips for testing lap shear and analog bond
termination samples.
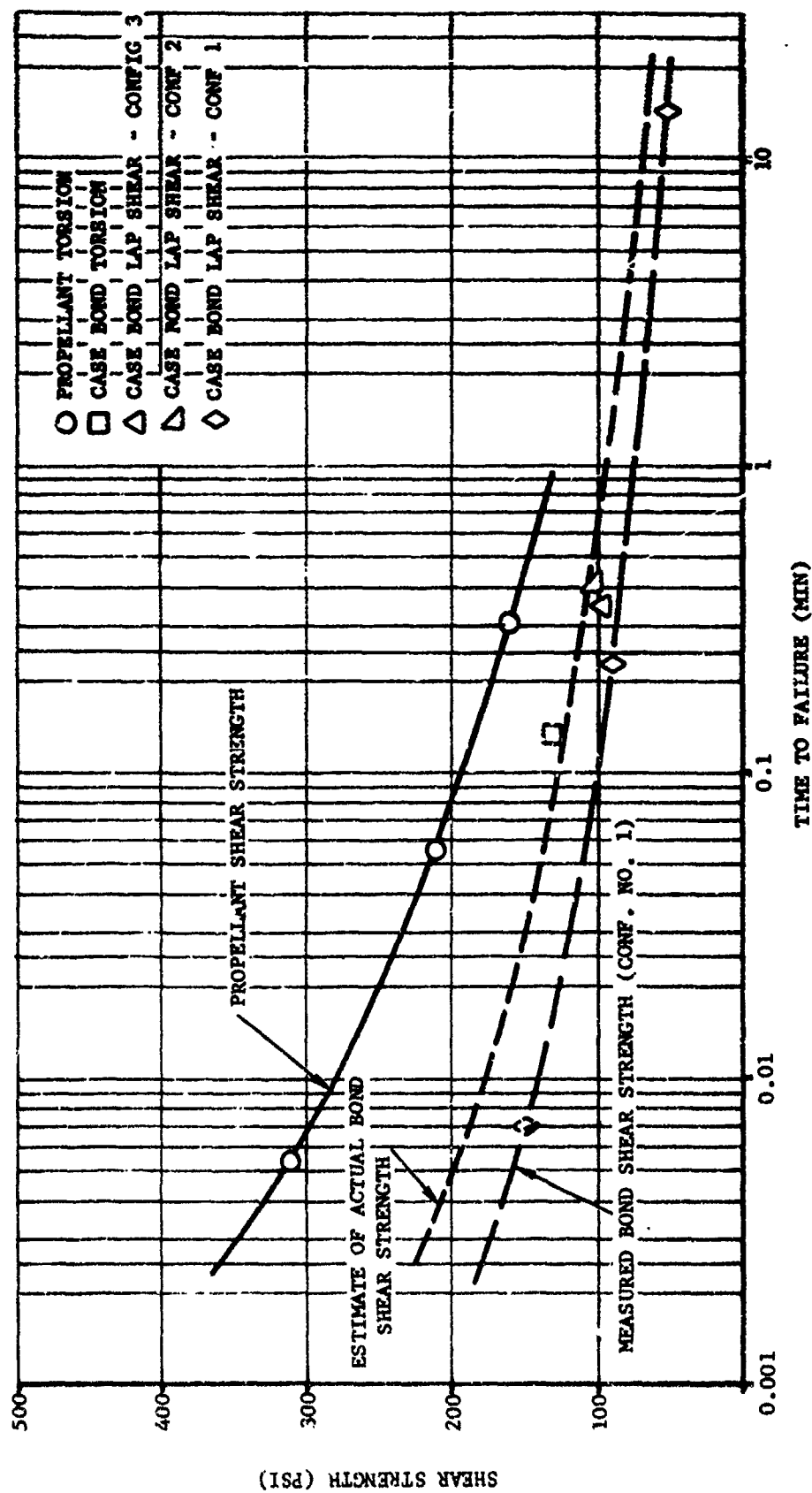
Figure 2-84. Shear strength for TP-H1123 propellant/case bond, 77° F, 50% R.H.

215
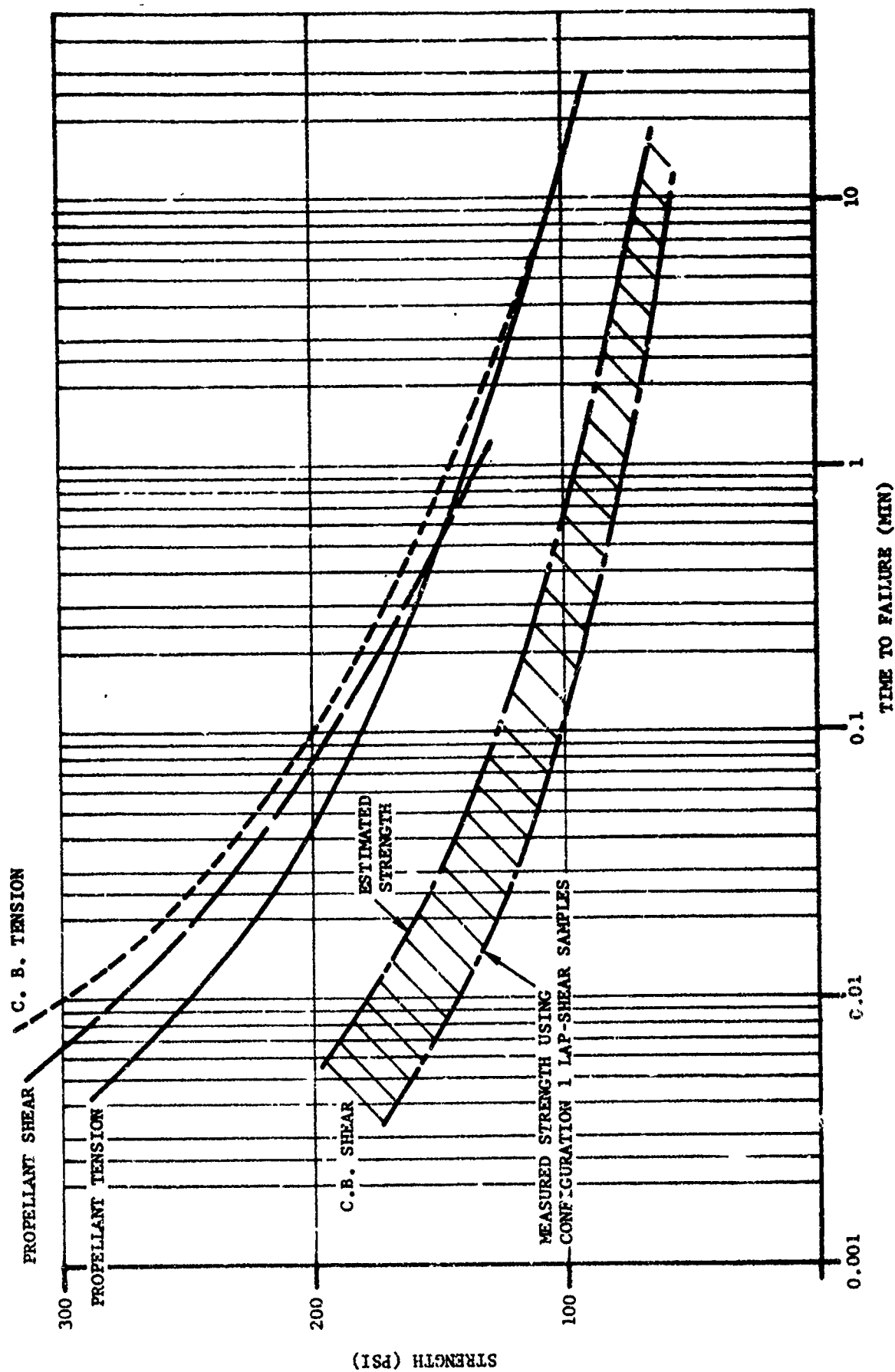
Figure 2-35. Strength comparison for TP-H1123 propellant and case bond material.
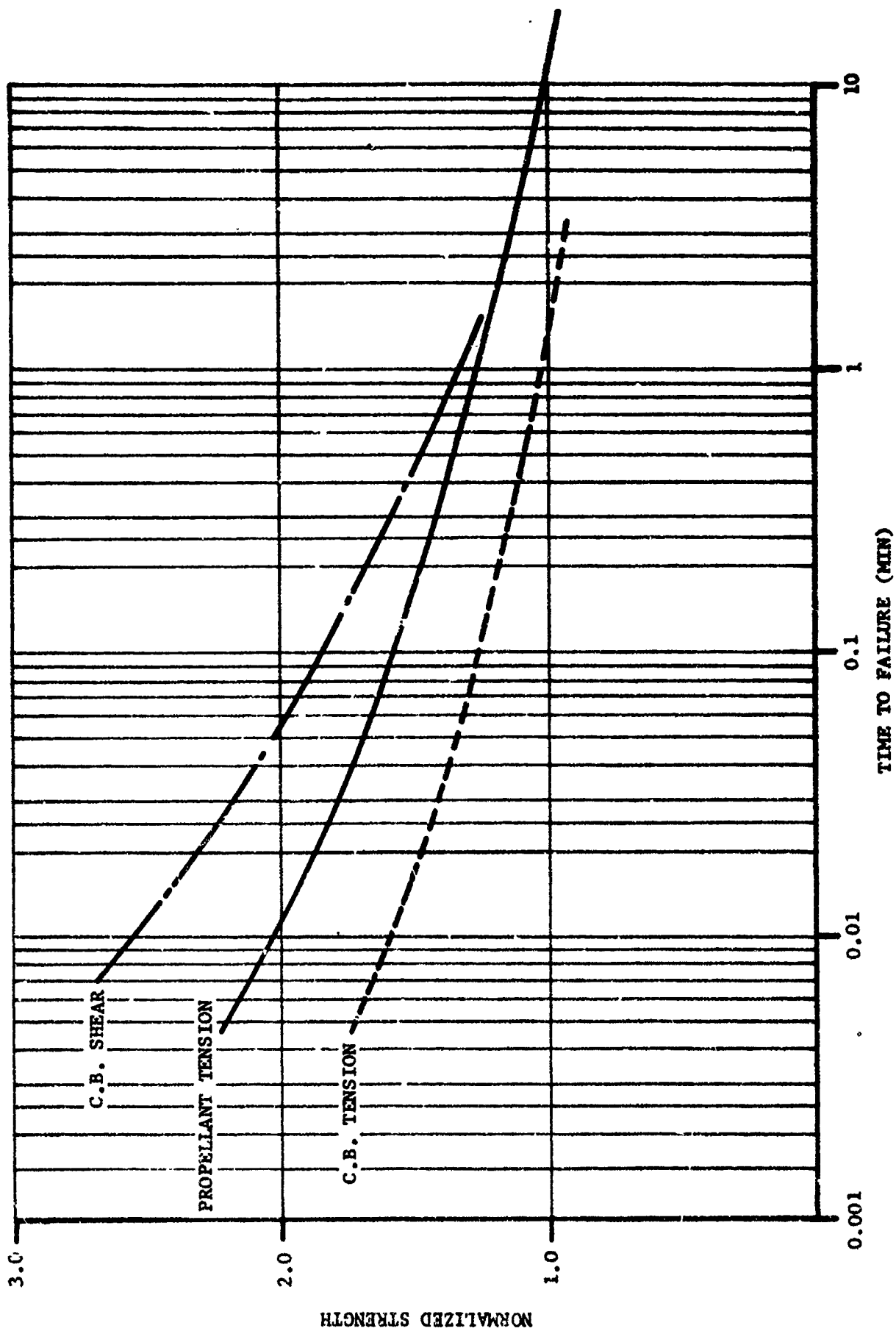
Figure 2-86. Strength comparison for AFB-3066 propellant and case bond material.

217
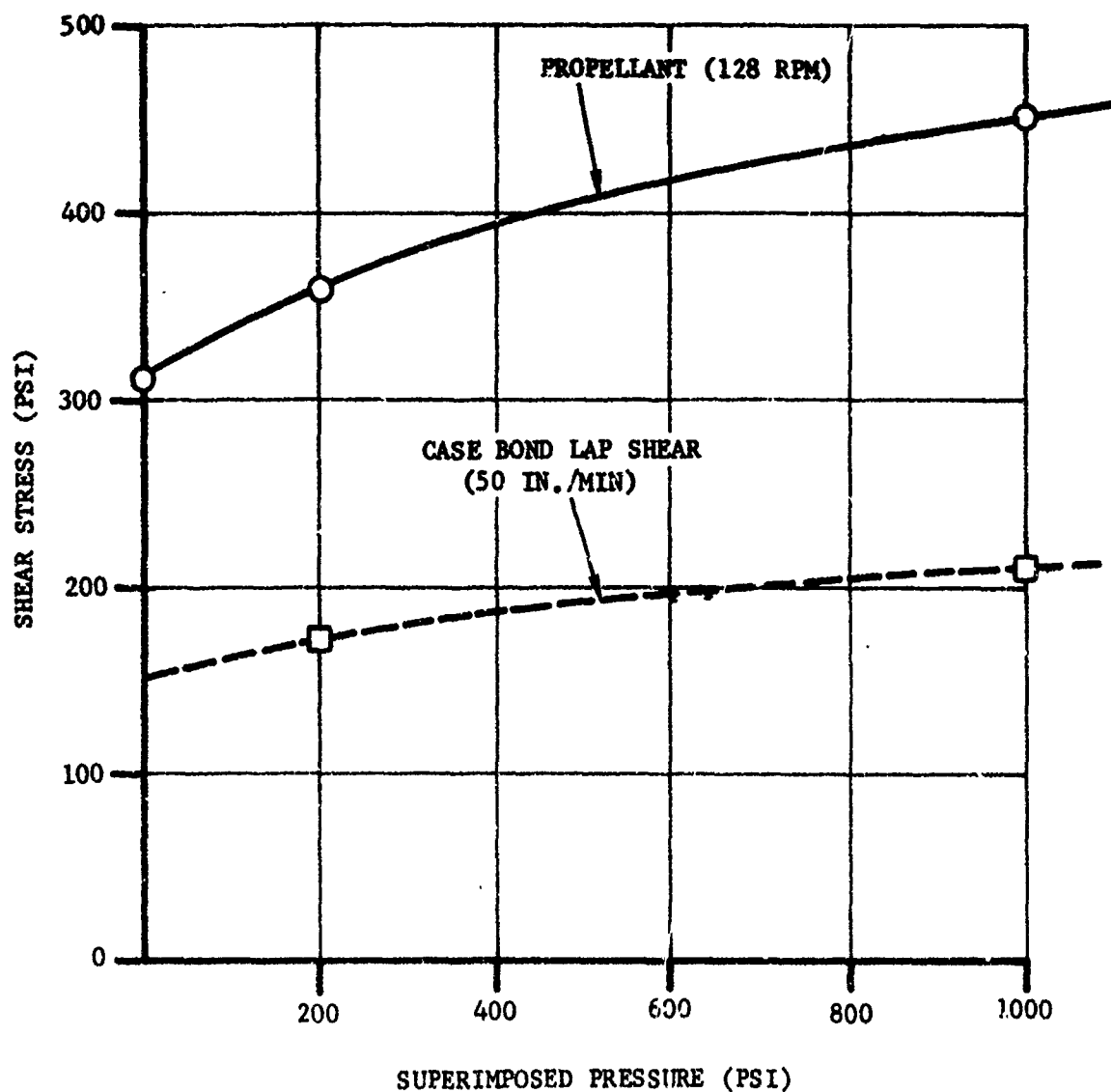
Figure 2-87. Effect of superimposed pressure on the shear strength of TP-H1123 propellant and case bond materials.

218
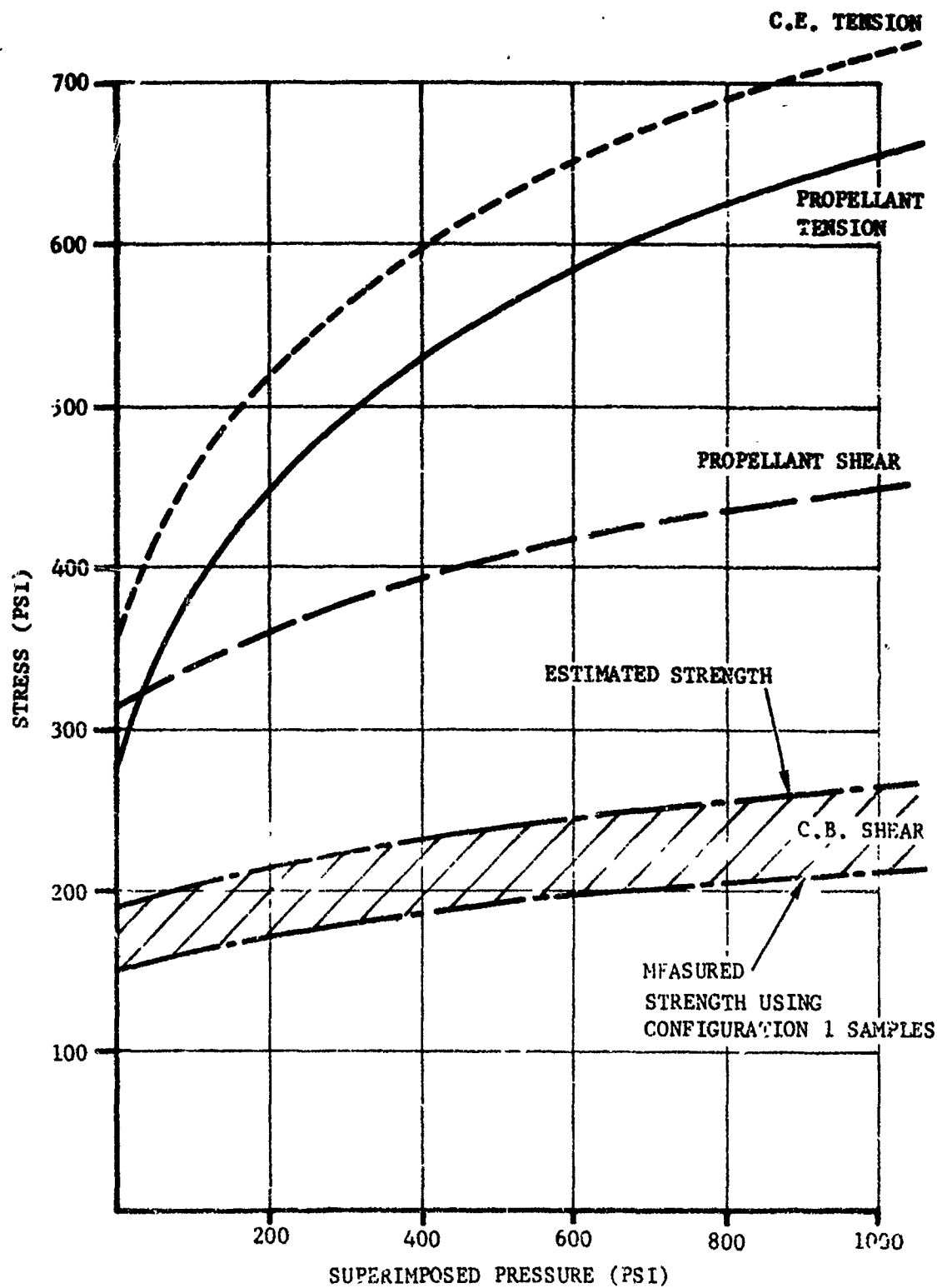
Figure 2-88. Comparison of the effect of superimposed pressure on the tensile and shear strength of TP-H1123 propellant and case bond materials.
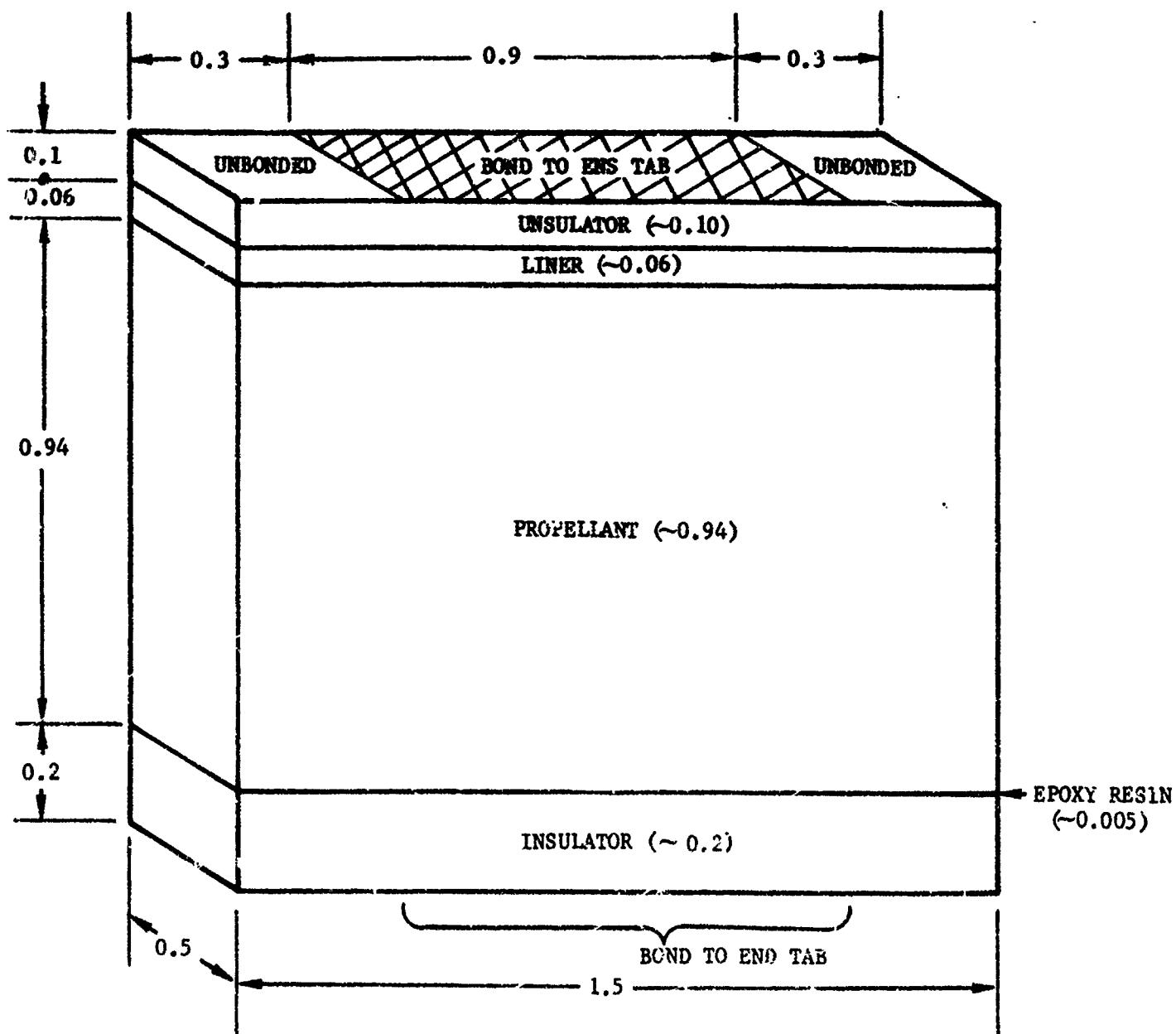
Figure 3-1. Analog flap termination sample.

220
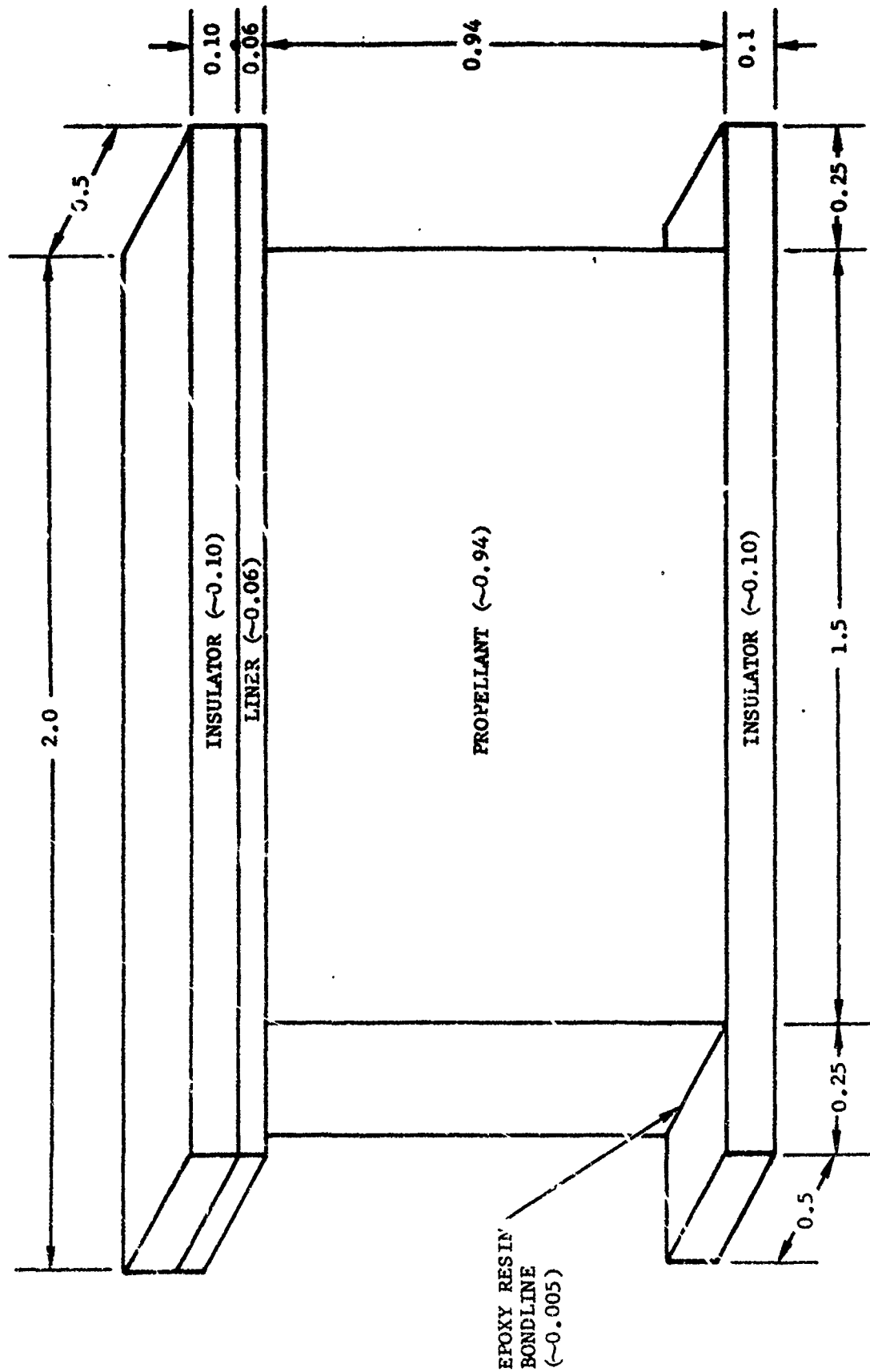
Figure 3-2. Analog discontinuity sample.

221
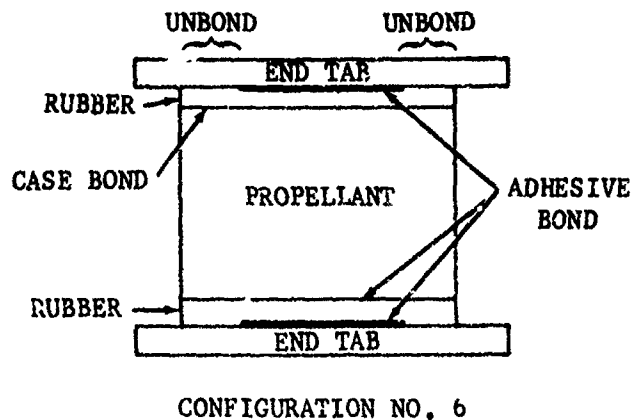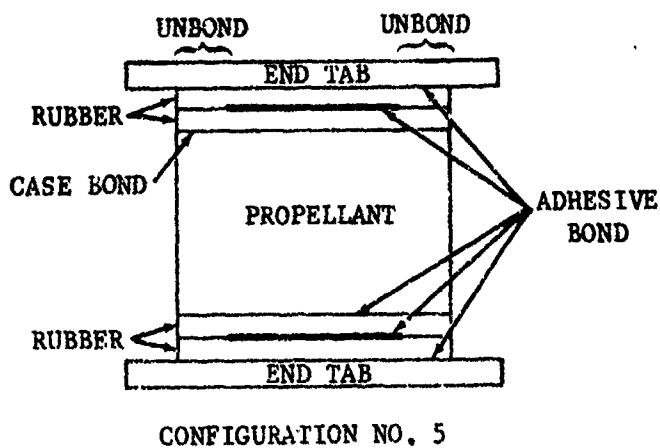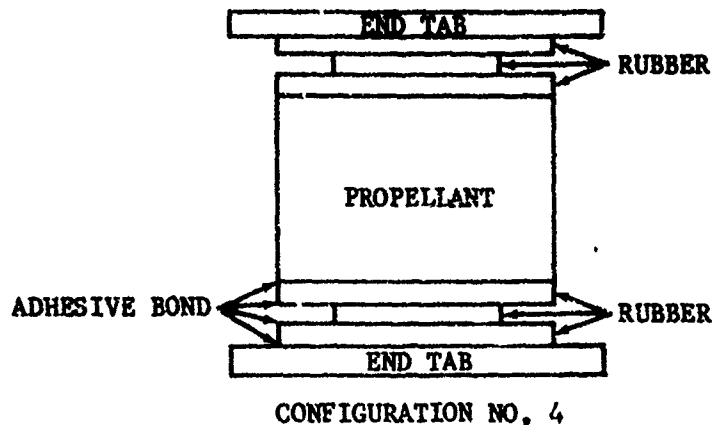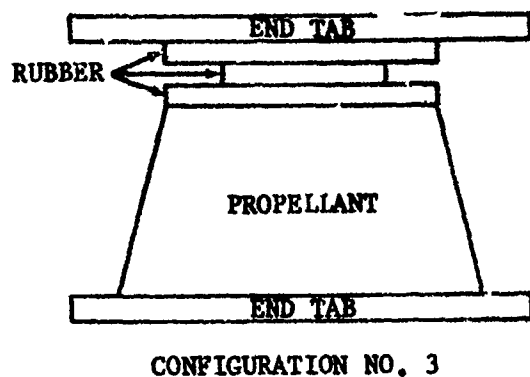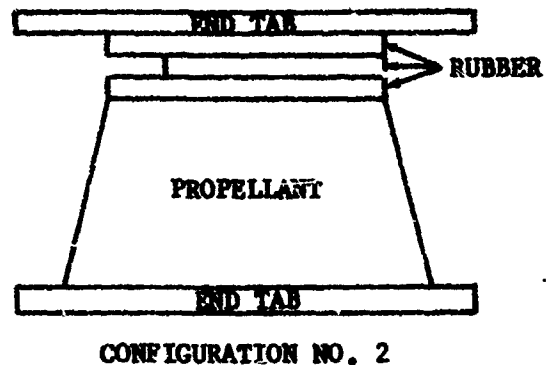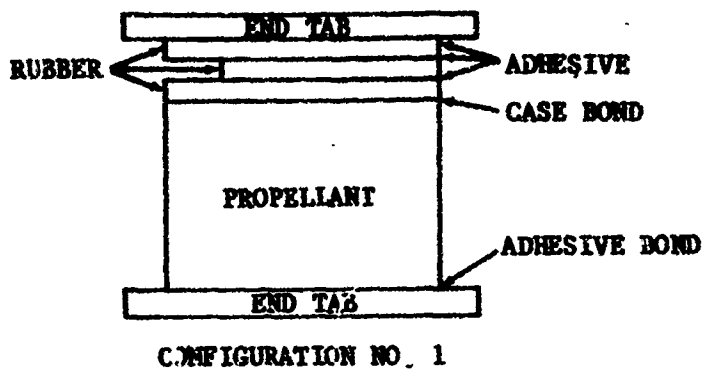
Figure 3-3. Evolution of analog flap termination sample.
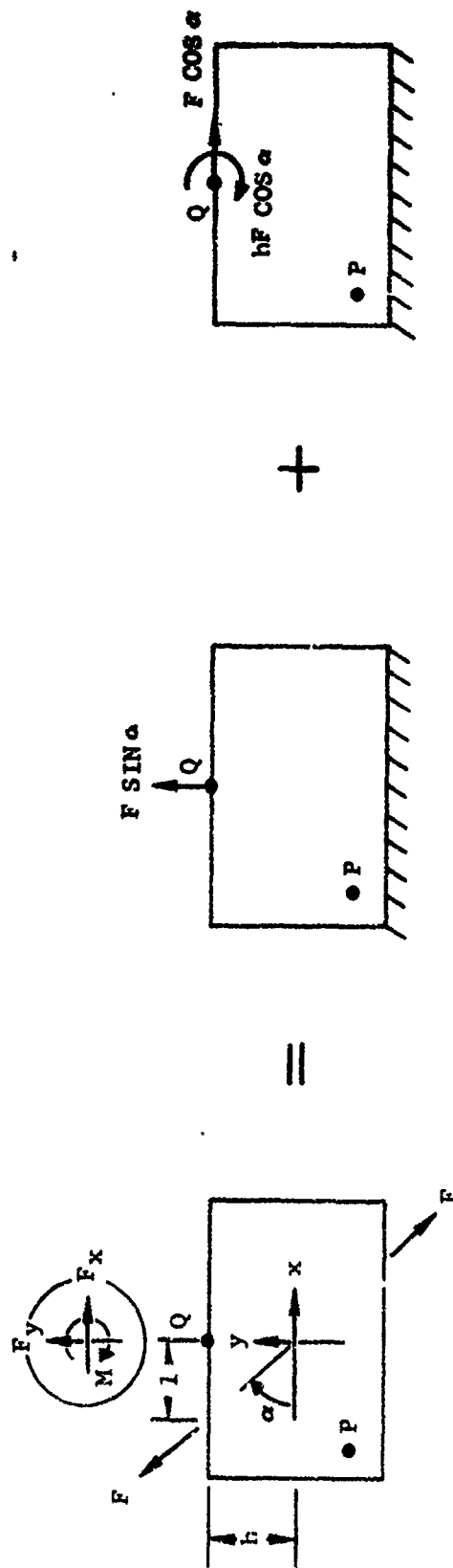
Figure 3-4. Force representation for a 2-D body pulled at on arbitrary angle relative to its midpoint.

223

1/8 SECTION (SYMMETRY)

-Z

Y

X

5

4
END

3
REAR

1

2

6
BOTTOM
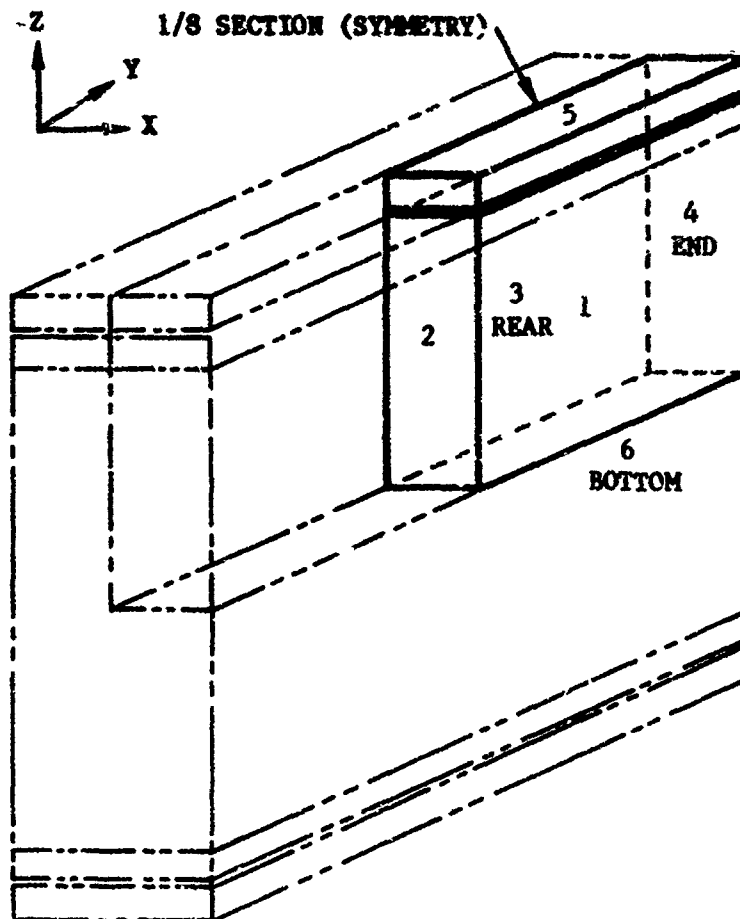
BOUNDARY CONDITIONS

LOADING CONDITION \ FACE NO.	1	2	3	4	5	6
TENSION		$U_Y = 0$	$U_X = 0$		$U_X = 0$ $U_Y = 0$ $U_Z = 1.0$	$U_Z = 0$
SHEAR	$U_X = 0$ $U_Z = 0$	$U_X = 0$			$U_X = 0$ $U_Y = 1.0$ $U_Z = 0$	$U_X = 0$ $U_Y = 0$

MATERIAL PROPERTIES

MATERIAL	E (PSI)	ν
INSULATOR	1000	0.4995
ADHESIVE	1000	0.4995
LINER	230	0.4999
PROPELLANT	700	0.499667

Figure 3-5. Eighth-section model for 3-D stress analysis of analog flap termination sample.

224

320C TOTAL NODES

TOP VIEW 128 NODES EDGE VIEW 25 PLANES

X

Z

15
14
13
12
11
10
9
8
7
6
5
4
3
2
1

SYM

ROW NO.

COLUMN NO.

1 2 3 4 5 6 7

0.25 OR 0.125

SYM

FLAP TERMINATION

0.75

25
24
23
22
21
20
19
18
17
16
15
14
13
12
11
10
9
8
7
6
5
4
3
2
1

0.67

NODE PLANE NO.

24
23
22
21
20
19
18
17
16
15
14
13
12
11
10
9
8
7
6
5
4
3
2
1

INSULATOR

ADHESIVE (OR GAP)

INSULATOR

LINER

PROPELLANT

ELEMENT PLANE NO.

SCALE 10:1
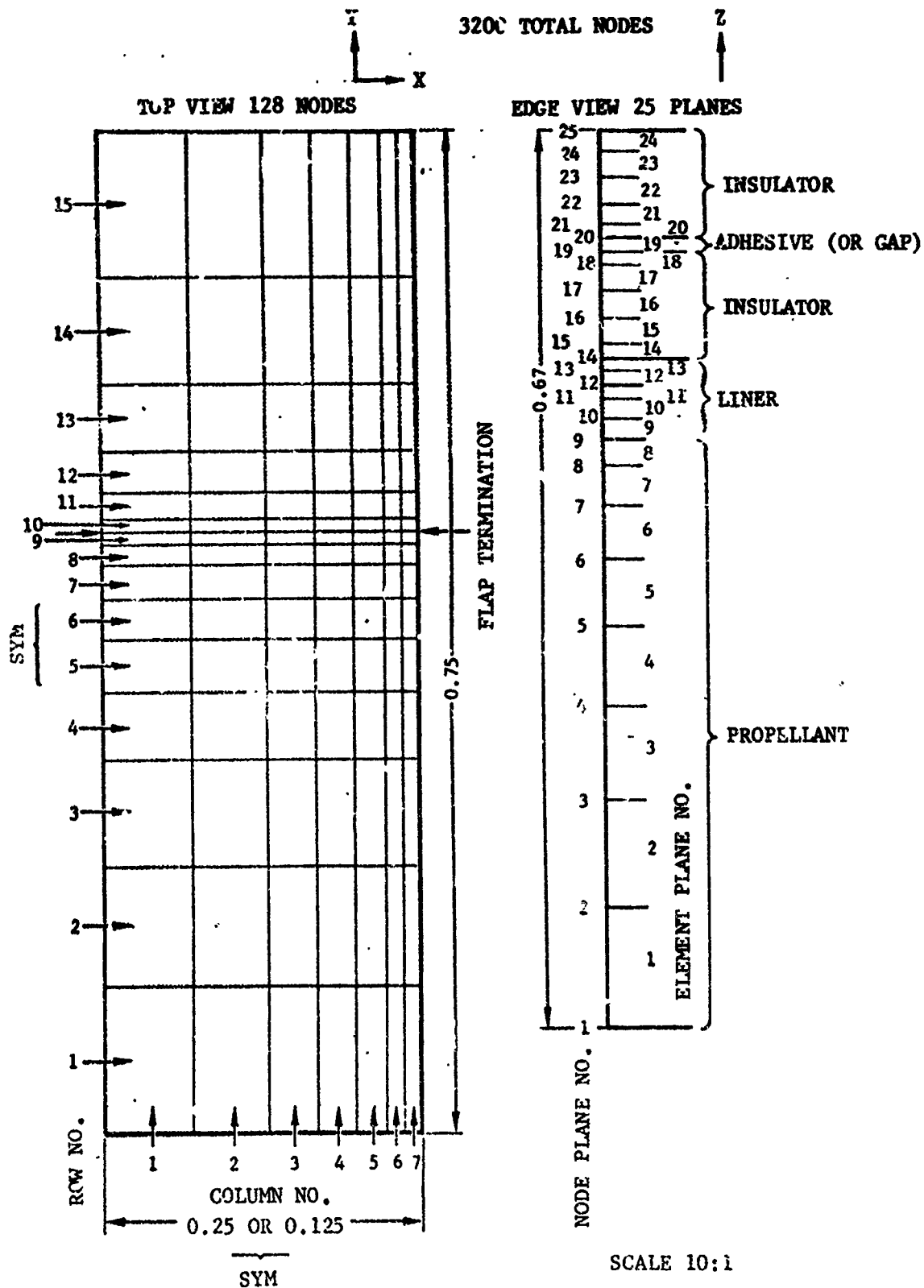
Figure 3-6.   Finite element model for 3-D stress analysis of
analog flap termination sample.

225
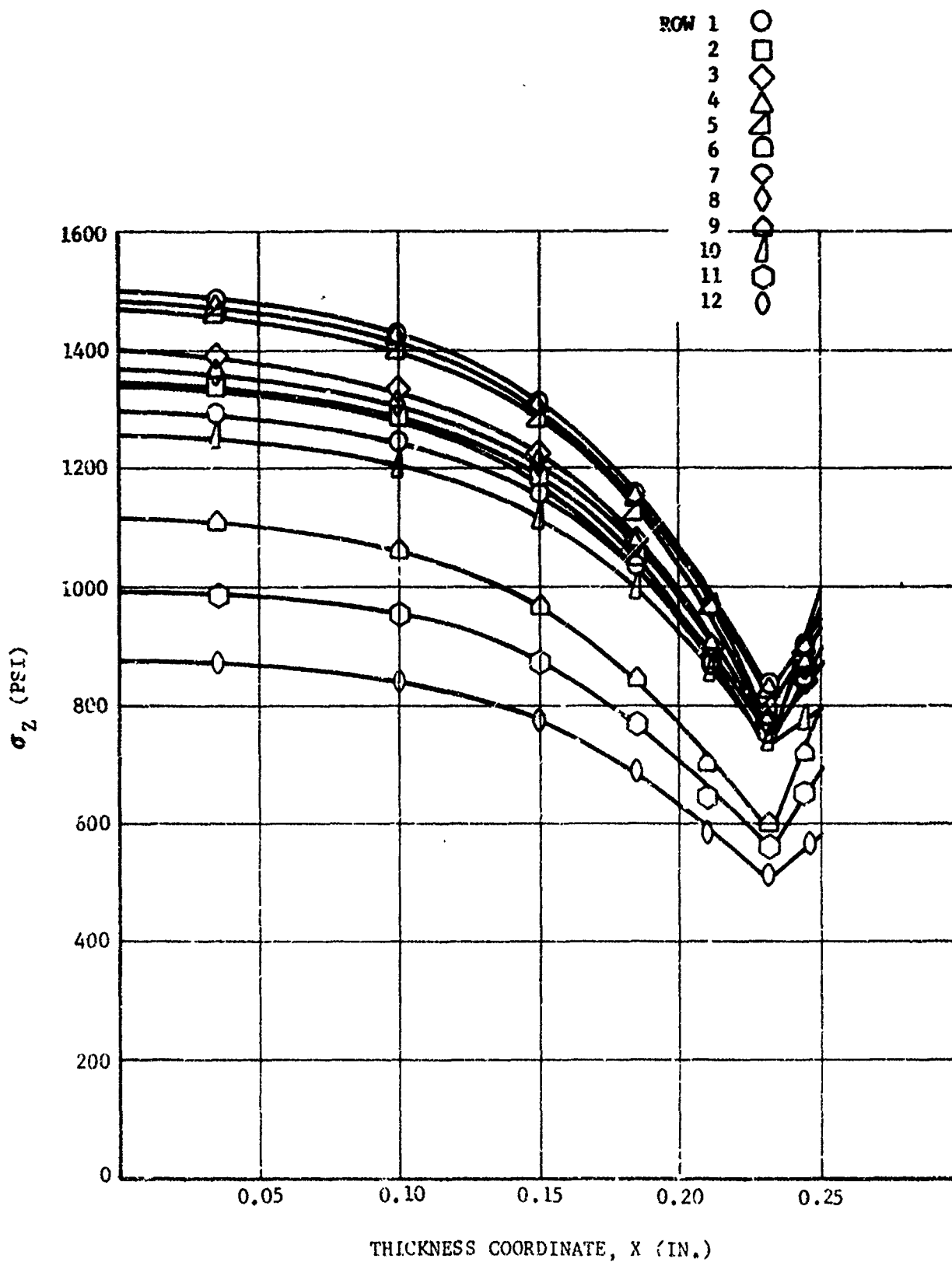
Figure 3-7. σ_z stress in element plane 8 for analog flap sample pulled in tension.

Figure 3-8. σ_z stresses in rows 1, 6, and 12 of element plane 8 for analog flap sample pulled in tension.

227

Figure 3-9. σ_z stresses in rows 1, 6, and 12 of element plane 11 for analog flap sample pulled in tension.

228
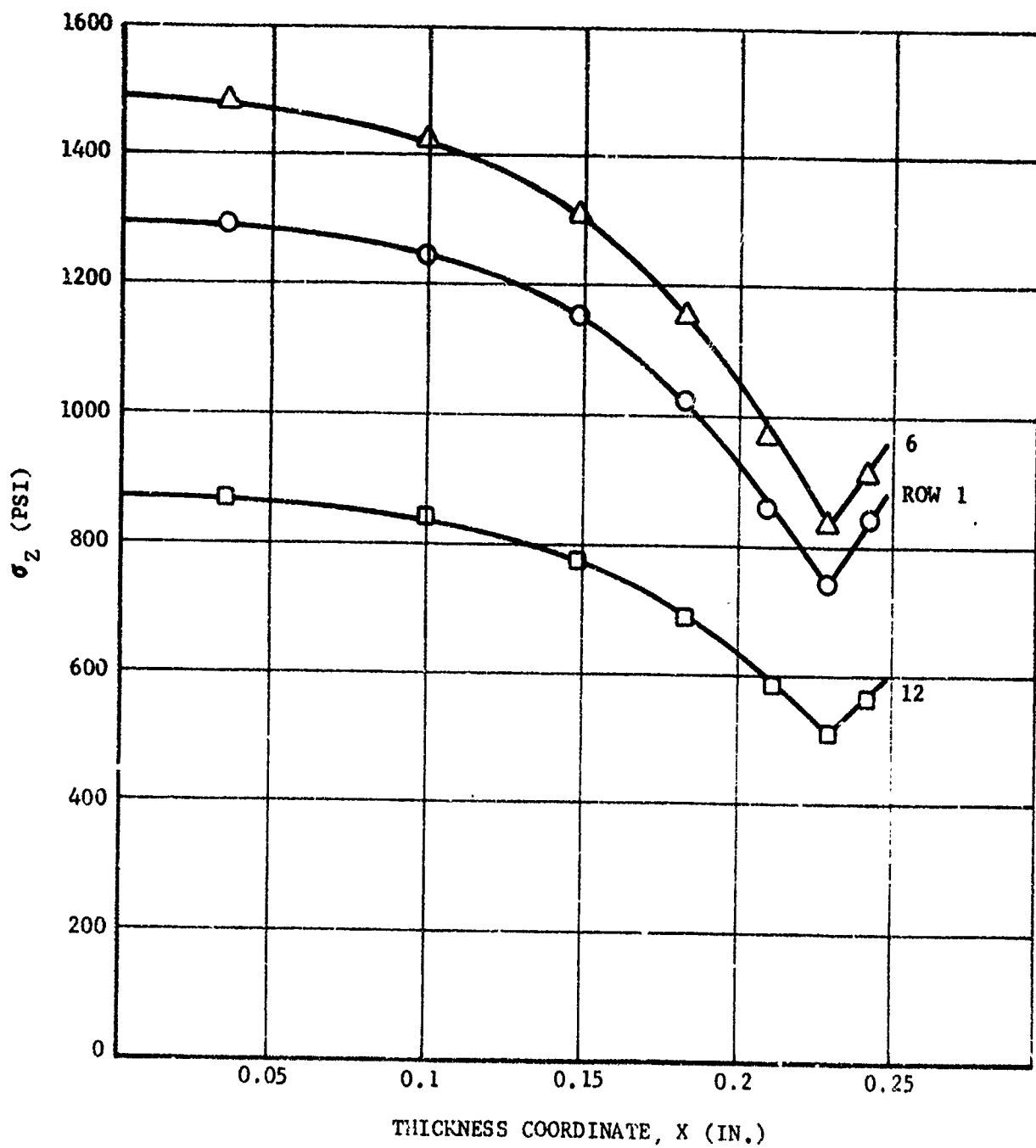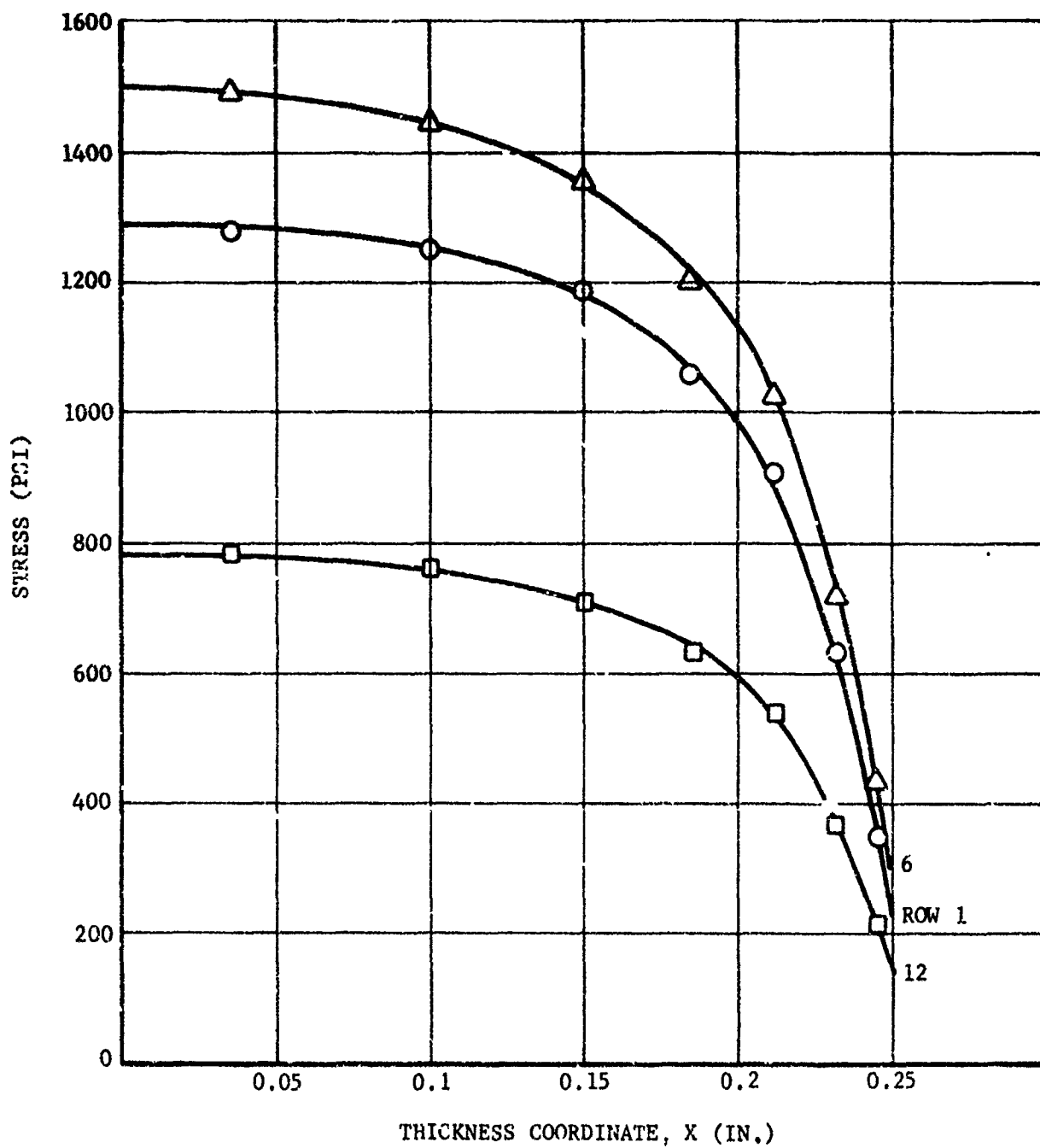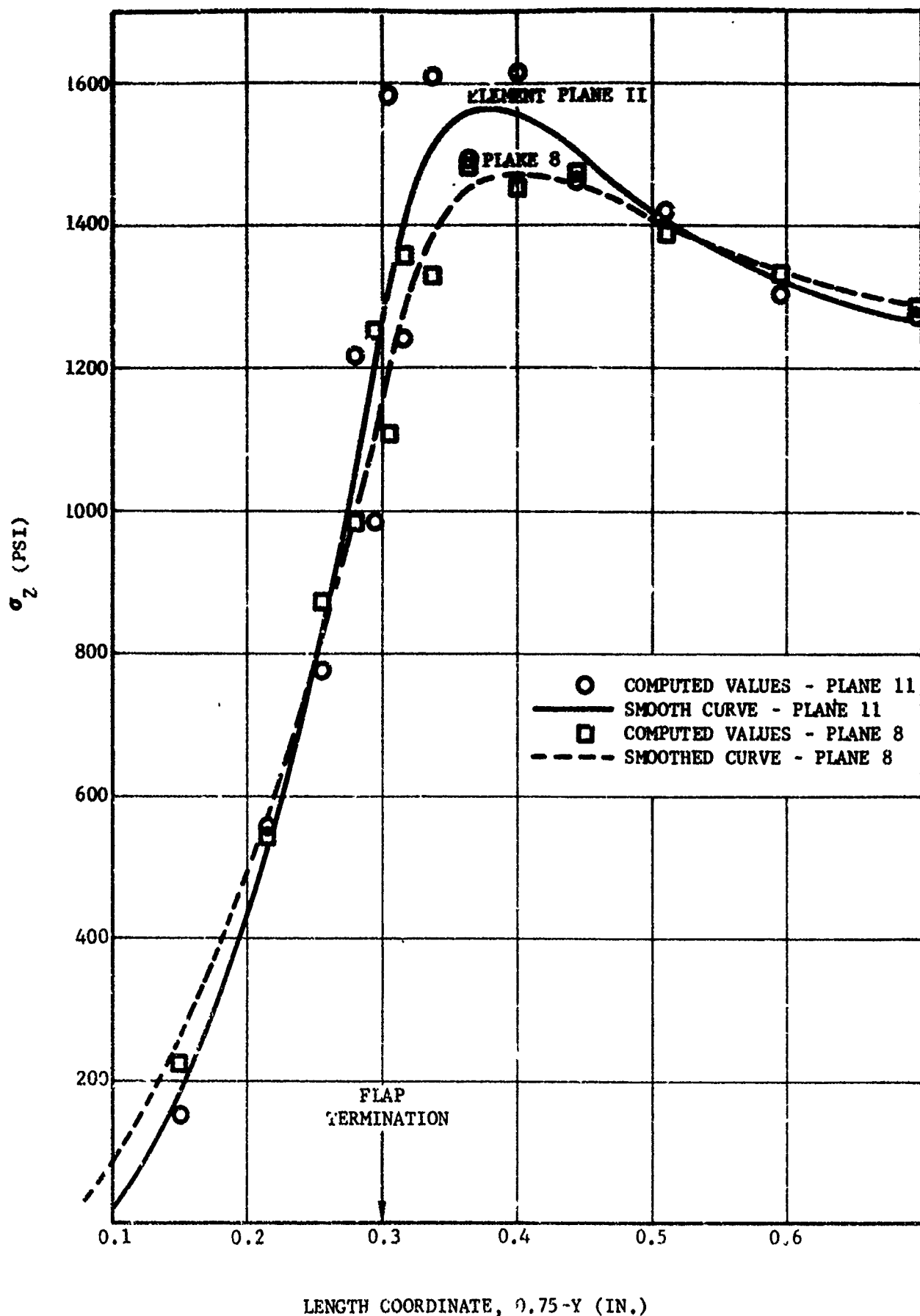
Figure 3-10. σ_z stress along column 1 in element plane 8 and 11 for analog flap sample pulled in tension.
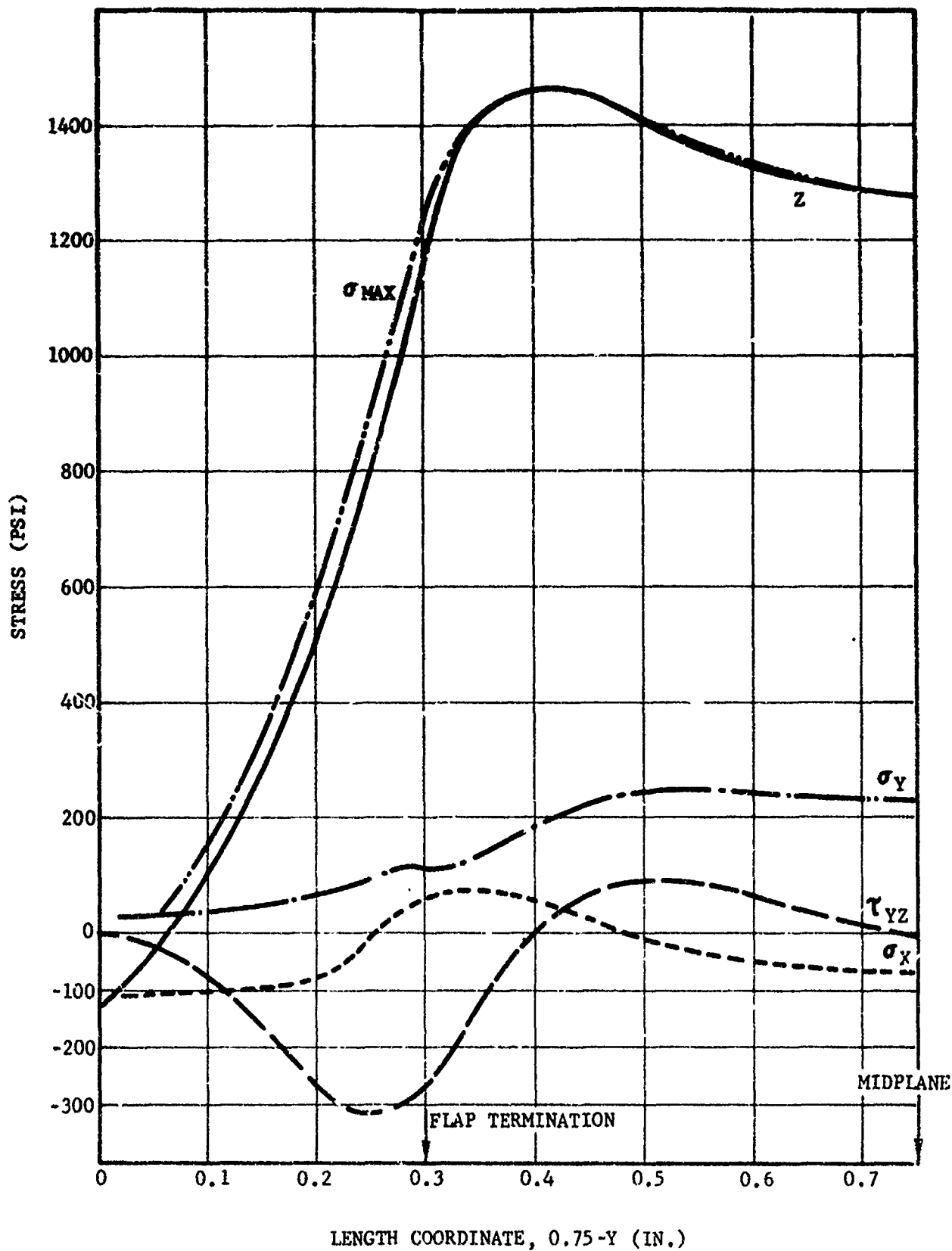
Figure 3-11. Stresses along column 1 in element plane 8 for
analog flap sample pulled in tension.
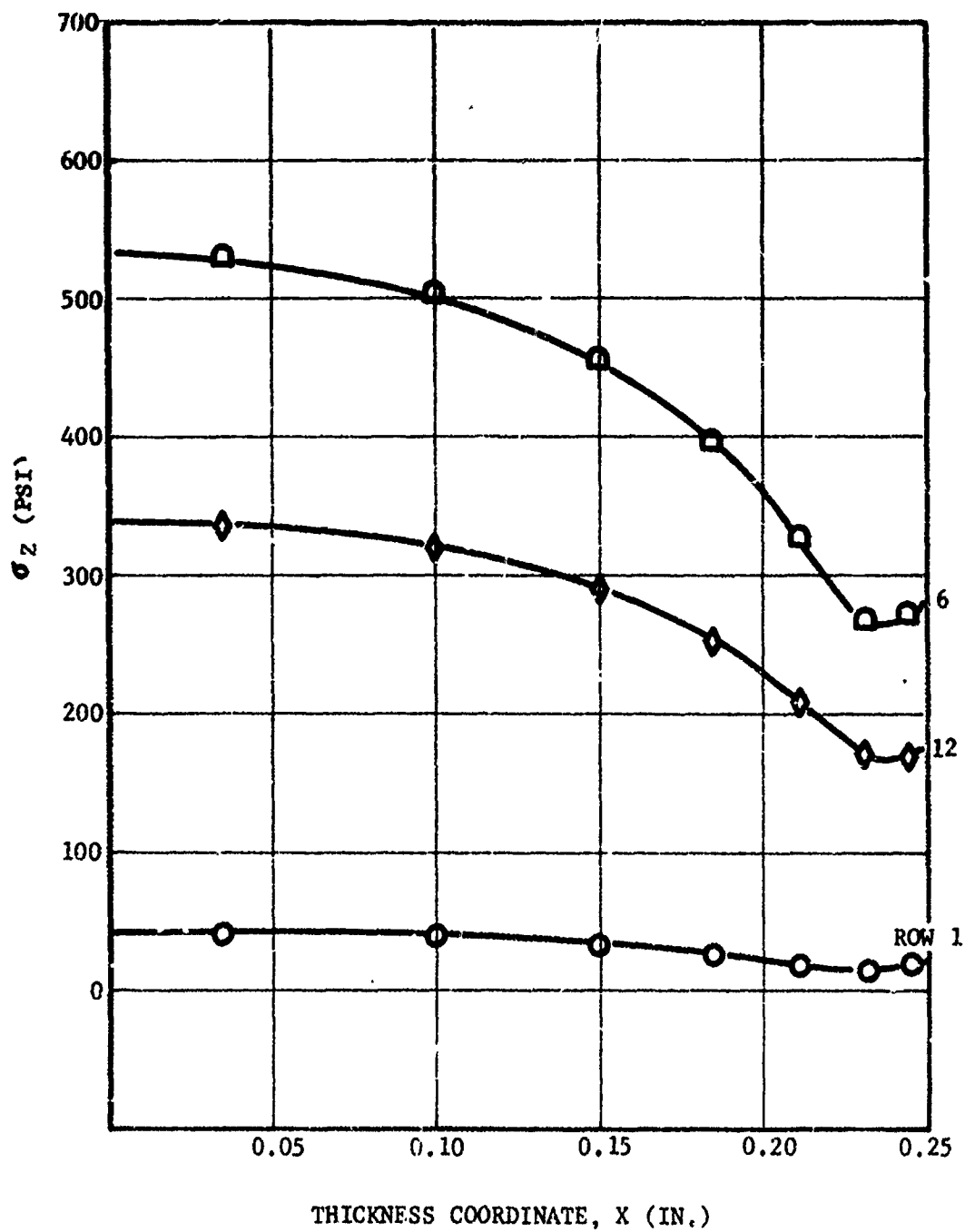
230

Figure 3-12. σ_z stresses in rows 1, 6, and 12 of element plane 8 for analog flap sample pulled in shear.

231
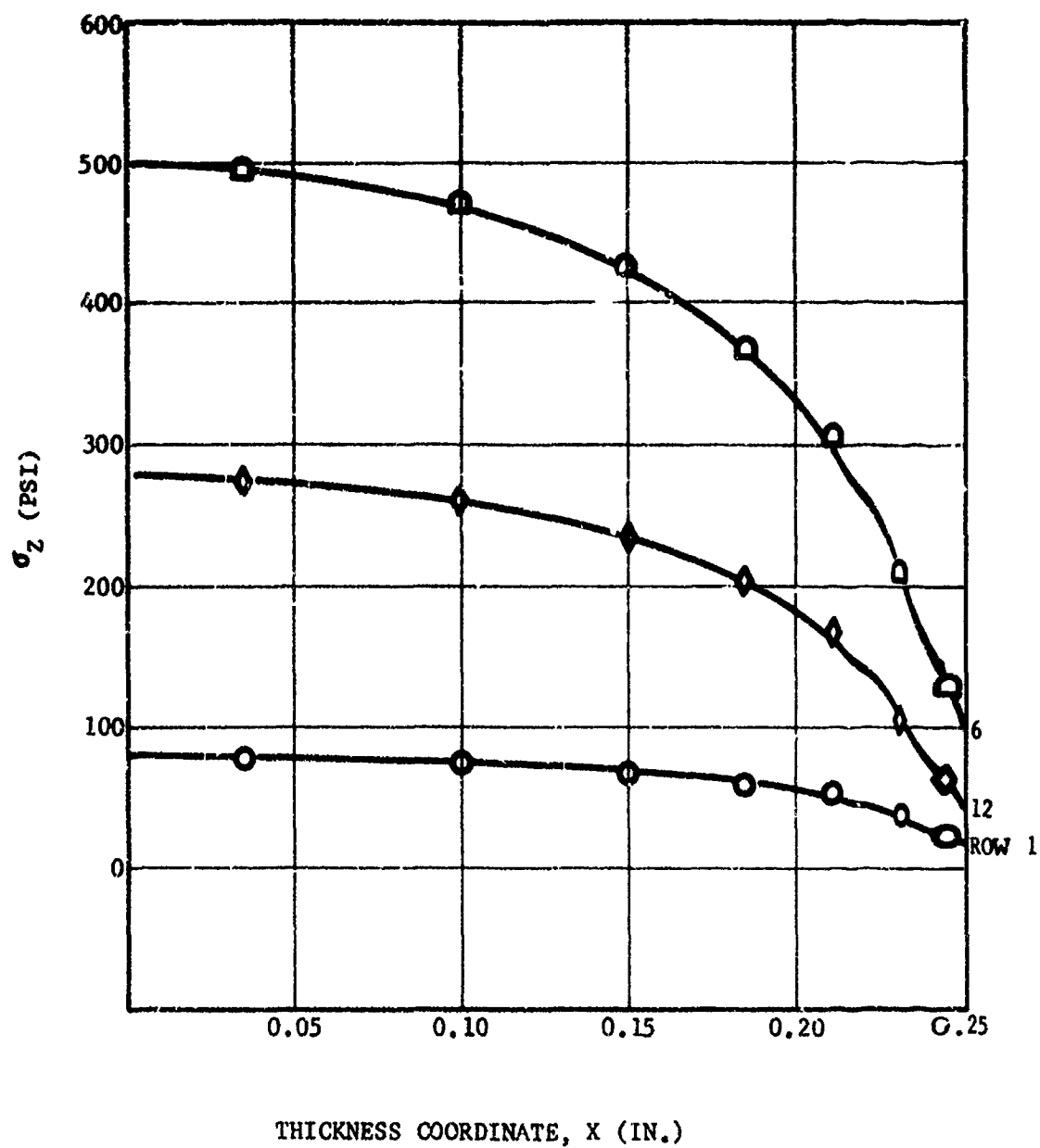
Figure 3-13. σ_z stress in rows 1, 6, and 12 of element plane 11 for analog flap sample pulled in shear.
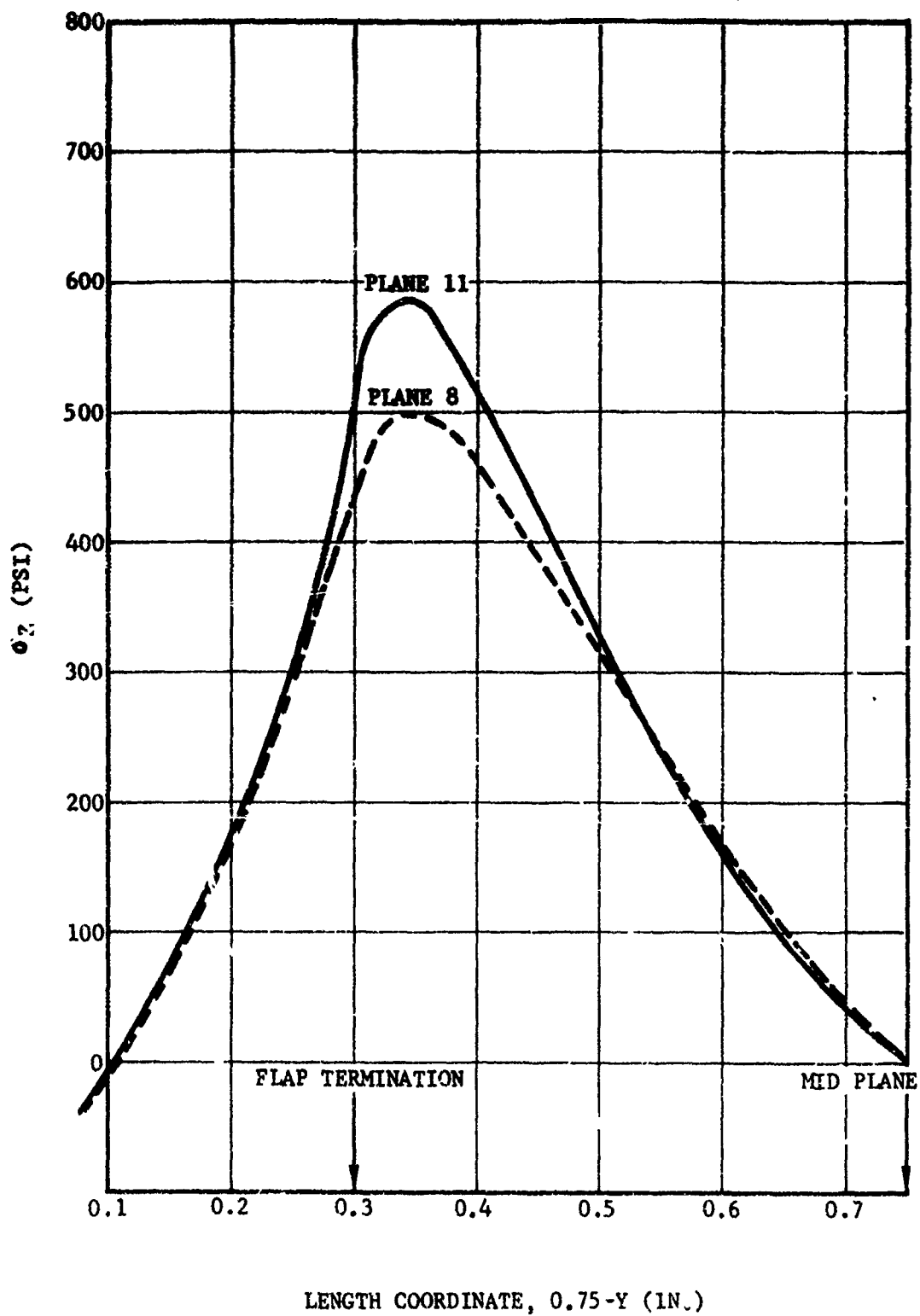
Figure 3-14. σ_z stress along column 1 in element planes 8 and 11 for analog flap sample pulled in shear.

233
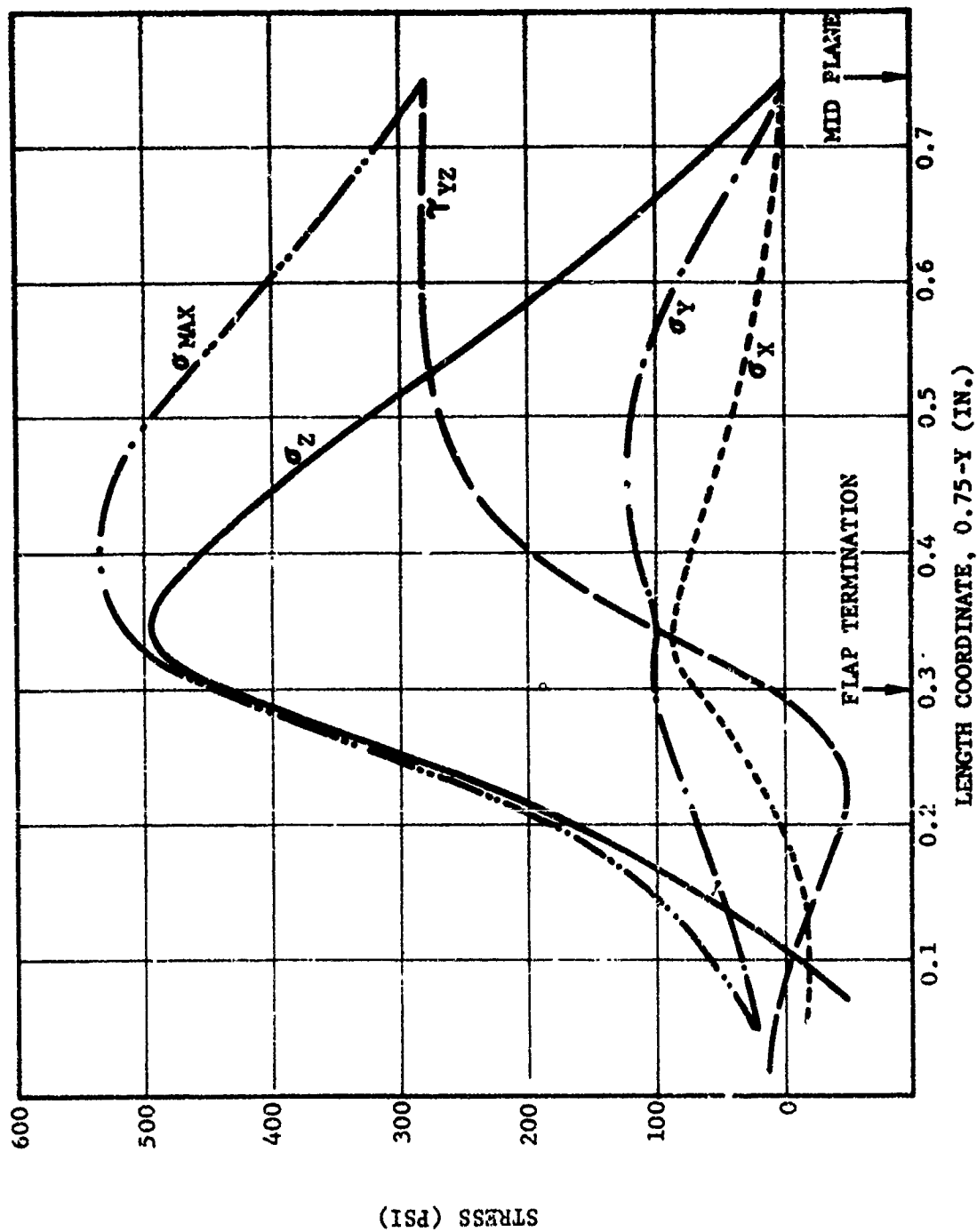
Figure 3-15. Stresses along column 1 in element plane 8 for analog flap sample pulled in shear.

234
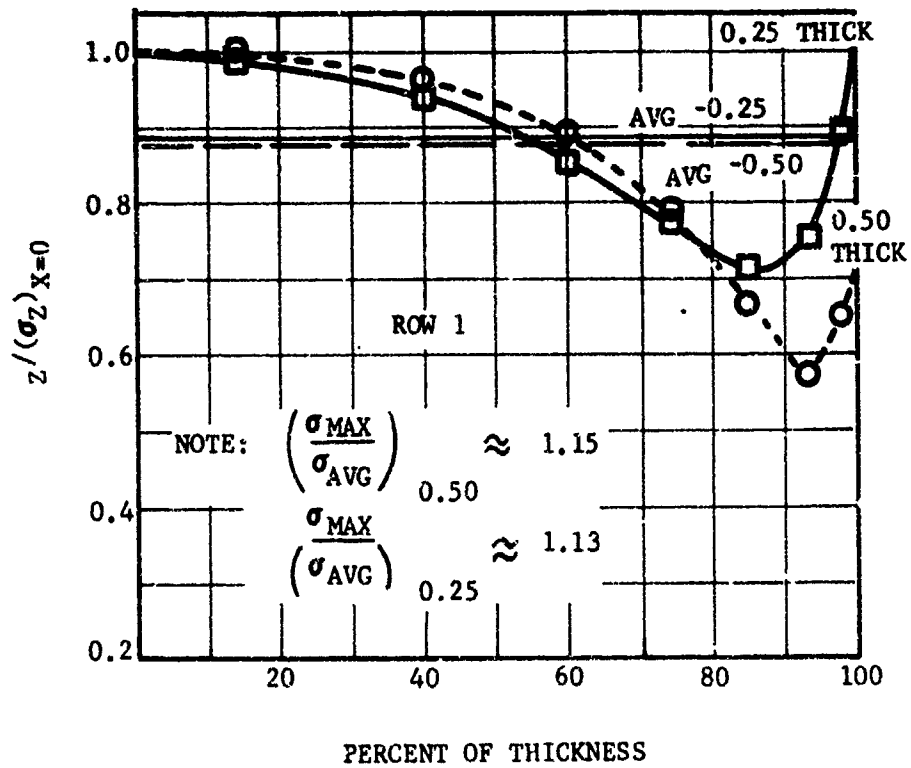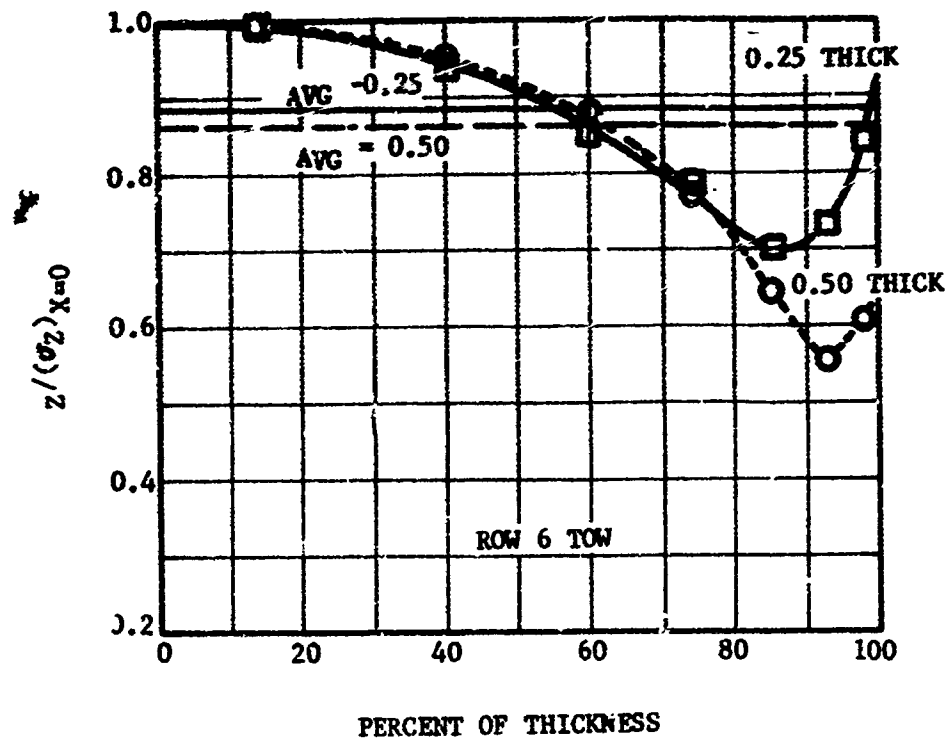
Figure 3-16. Normalized σ_z stress distribution through sample thickness, plane 8, for 0.25 and 0.50 thick analog flap samples pulled in tension.
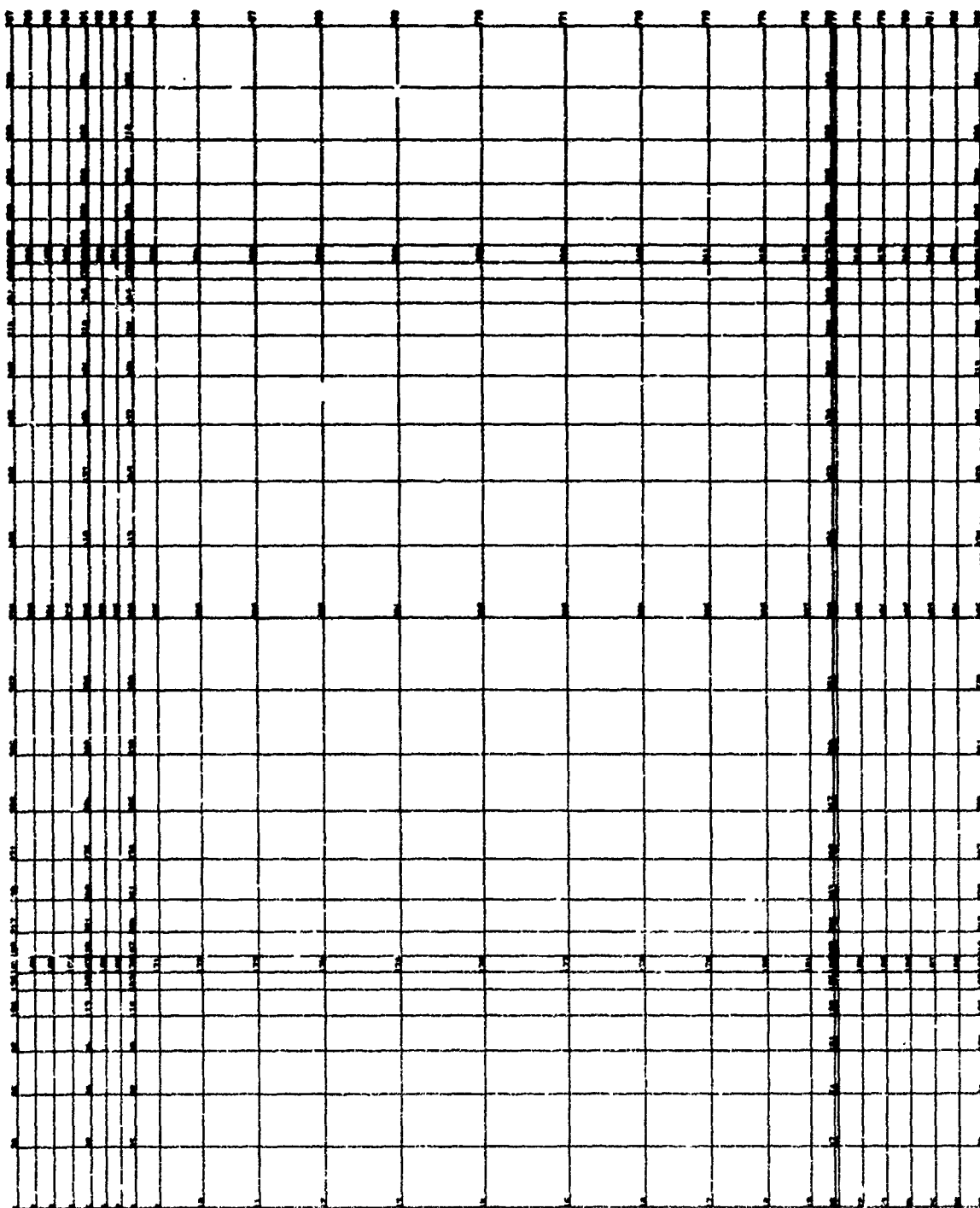
Figure 3-17. Full finite element model used for 2-D stress analysis of analog flap termination sample.
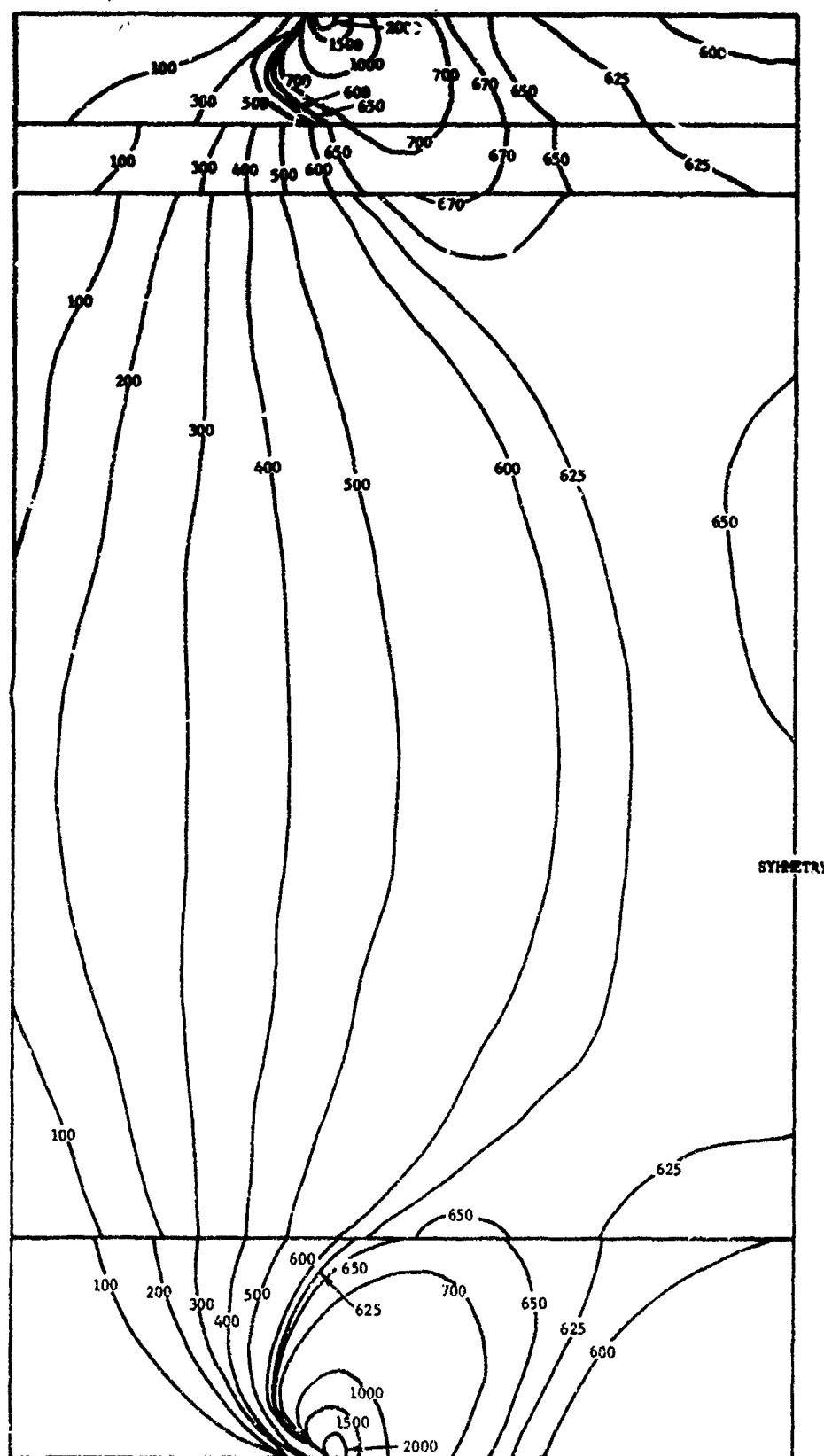
Figure 3-18. Lines of constant maximum principal stress in analog flap termination sample pulled in tension, $E_{liner} = 200$ psi.

237
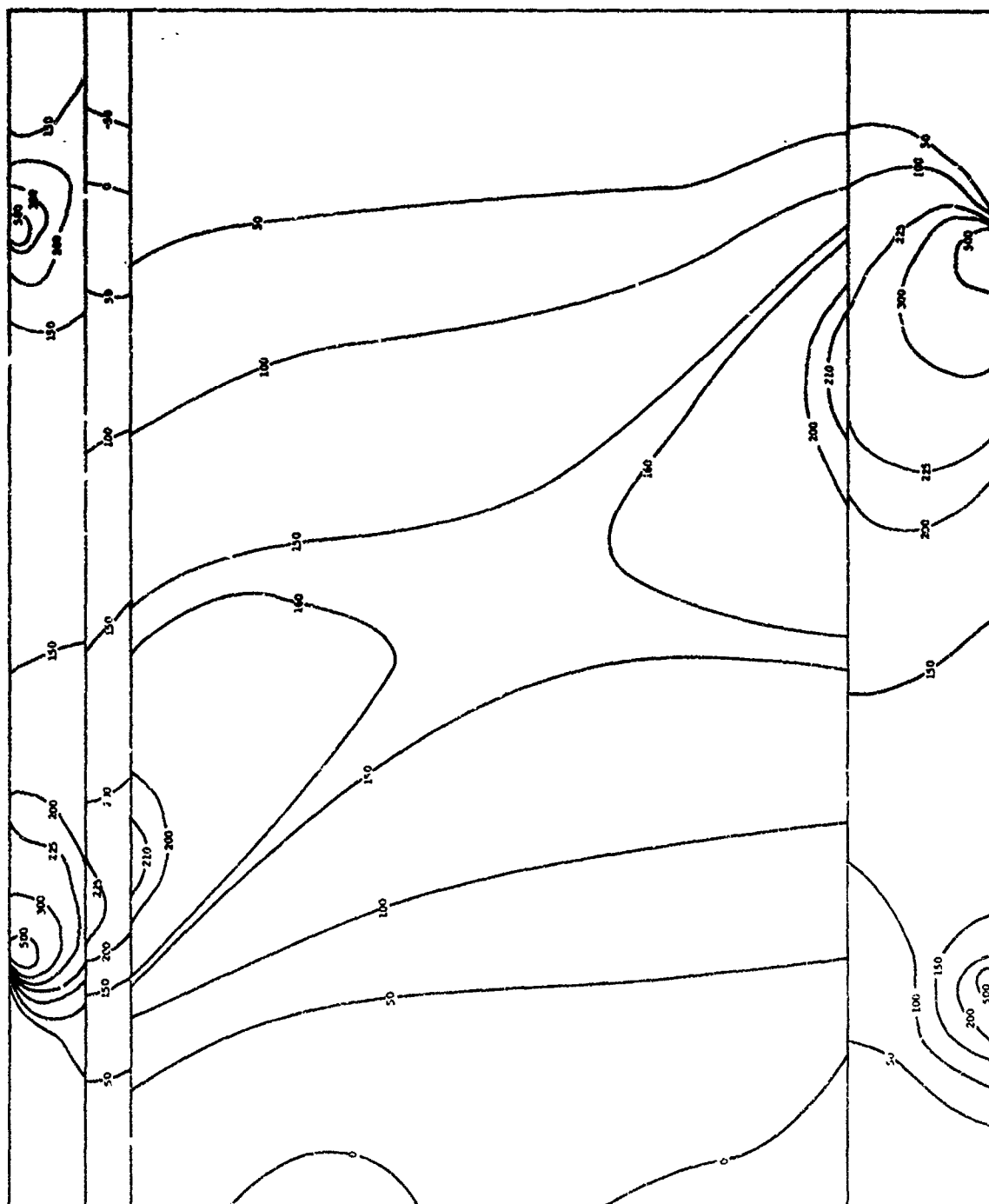
Figure 3-19. Lines of constant maximum principal stress in analog flap termination sample pulled in shear, $E_{liner} = 200$ psi and sliding boundary contact.

238
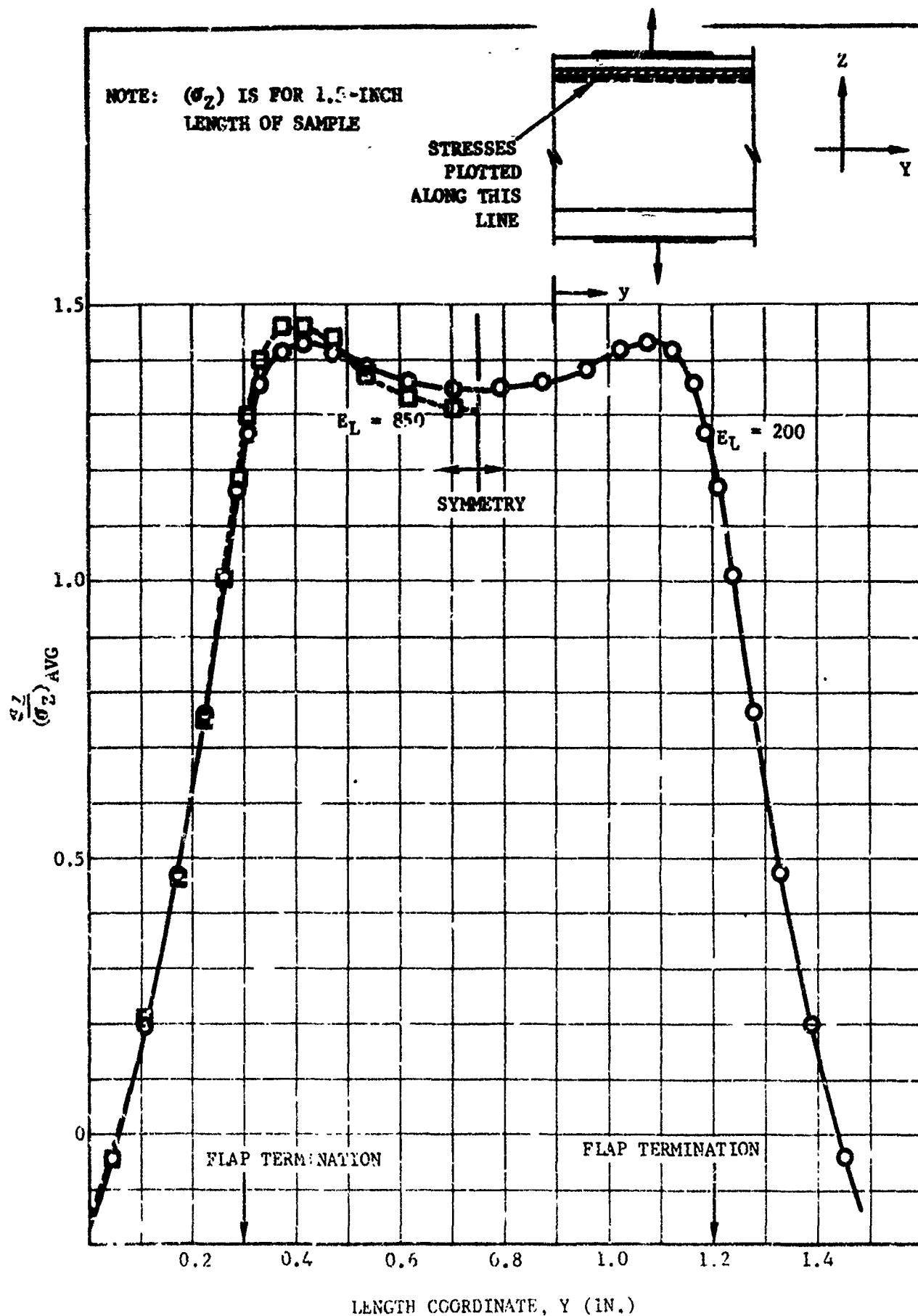
Figure 3-20. 2-D calculation for case bond normal stress distribution in the name flap termination sample pulled in tension.

239
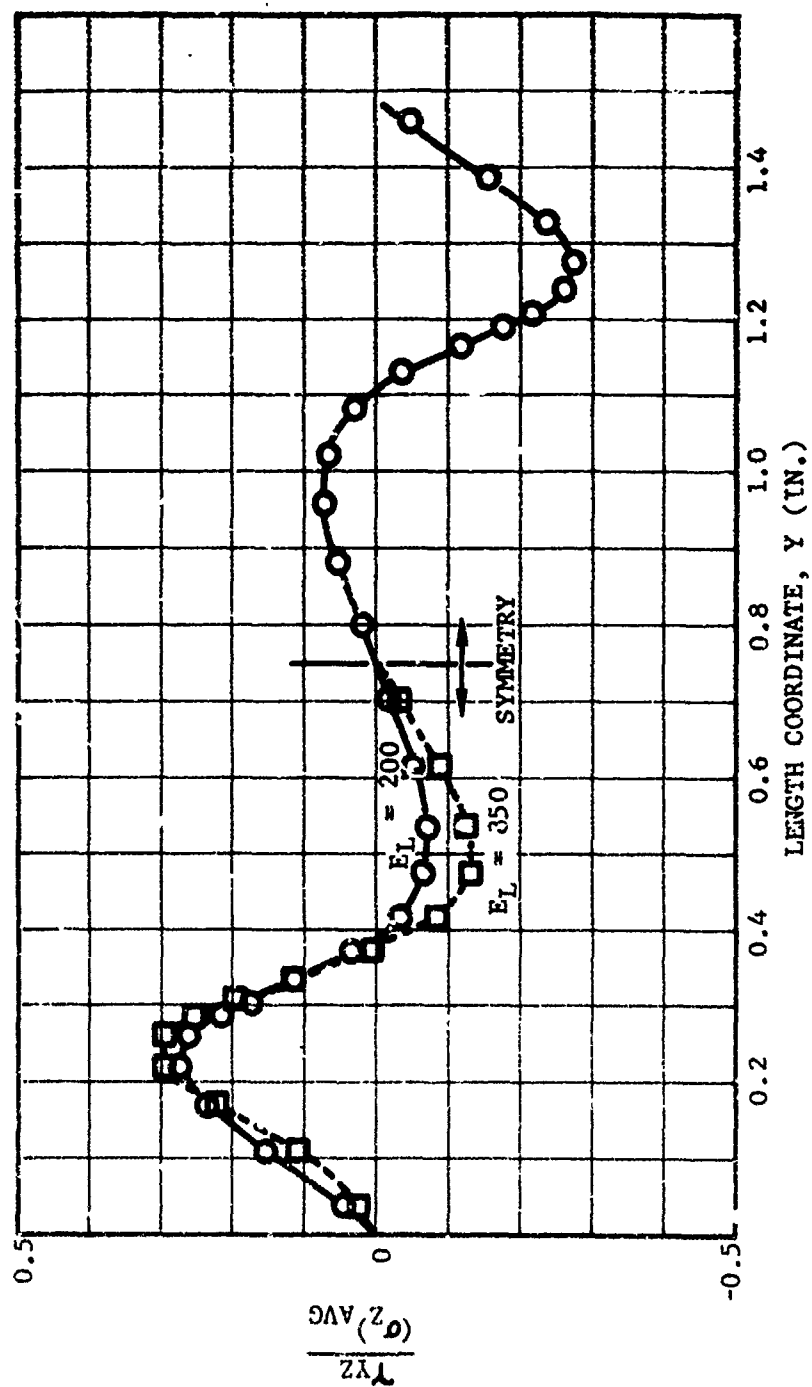
Figure 3-21. 2-D calculation for case bond shear stress distribution in the analog flap termination sample pulled in tension.
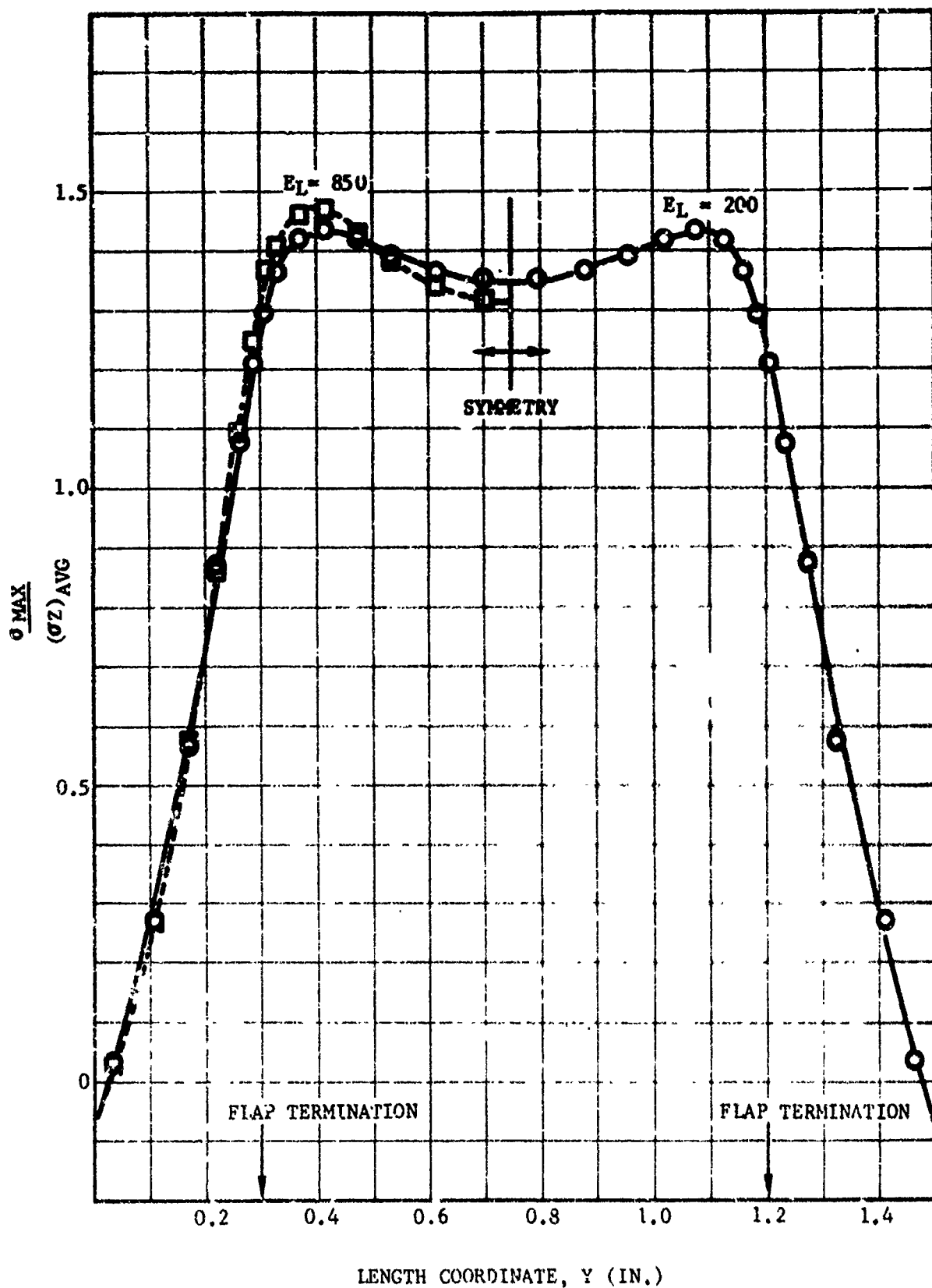
Figure 3-22. 2-D calculation for case bond principal stress
distribution in the analog flap termination sample
pulled in tension.
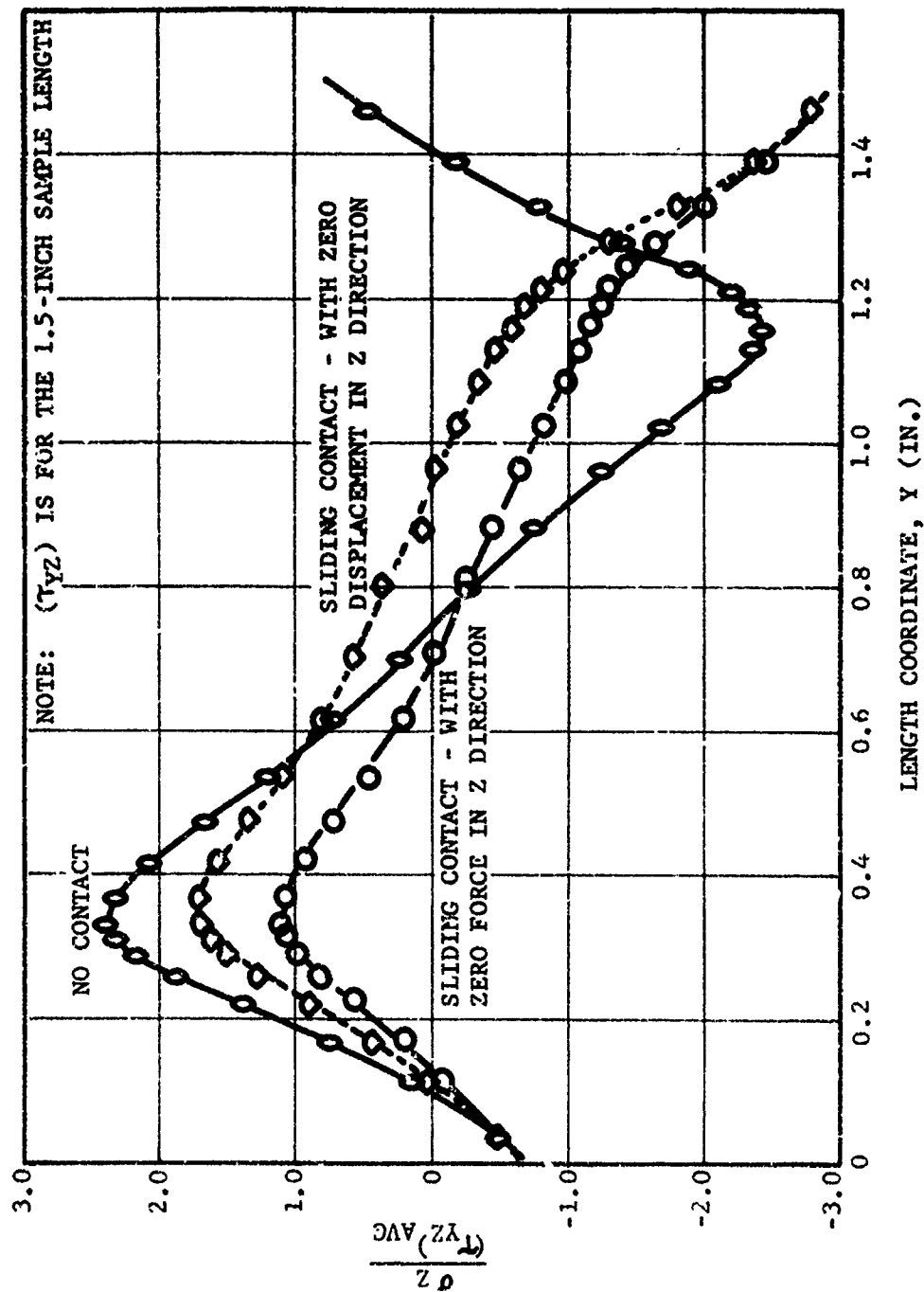
Figure 3-23. 2-D calculation for case bond normal stress distribution in the analog flap termination sample pulled in shear, $E_{liner} = 200$.
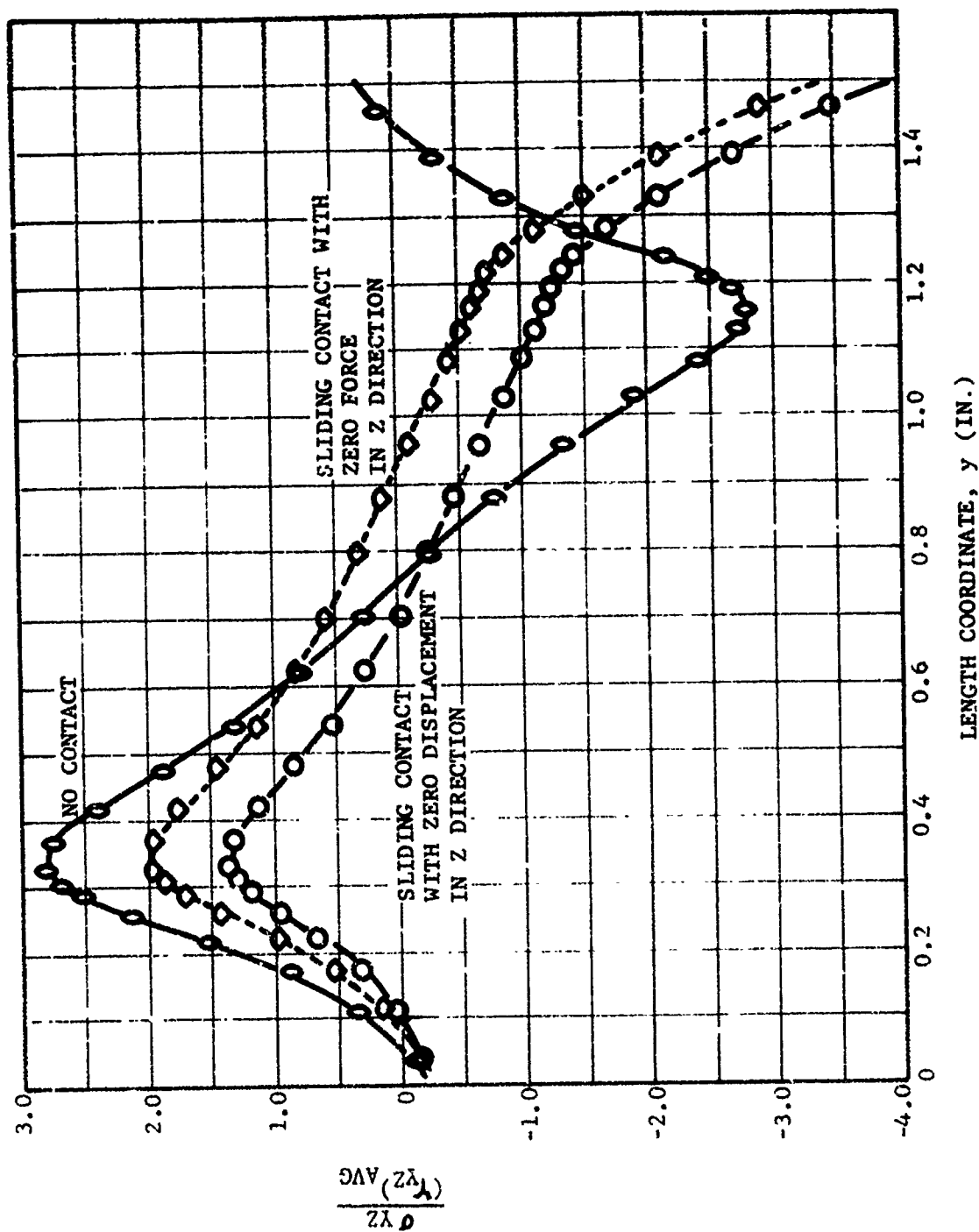
Figure 3-24. 2-D calculation for case bond normal stress distribution in the analog flap termination sample pulled in shear, $E_{liner} = 85C$.
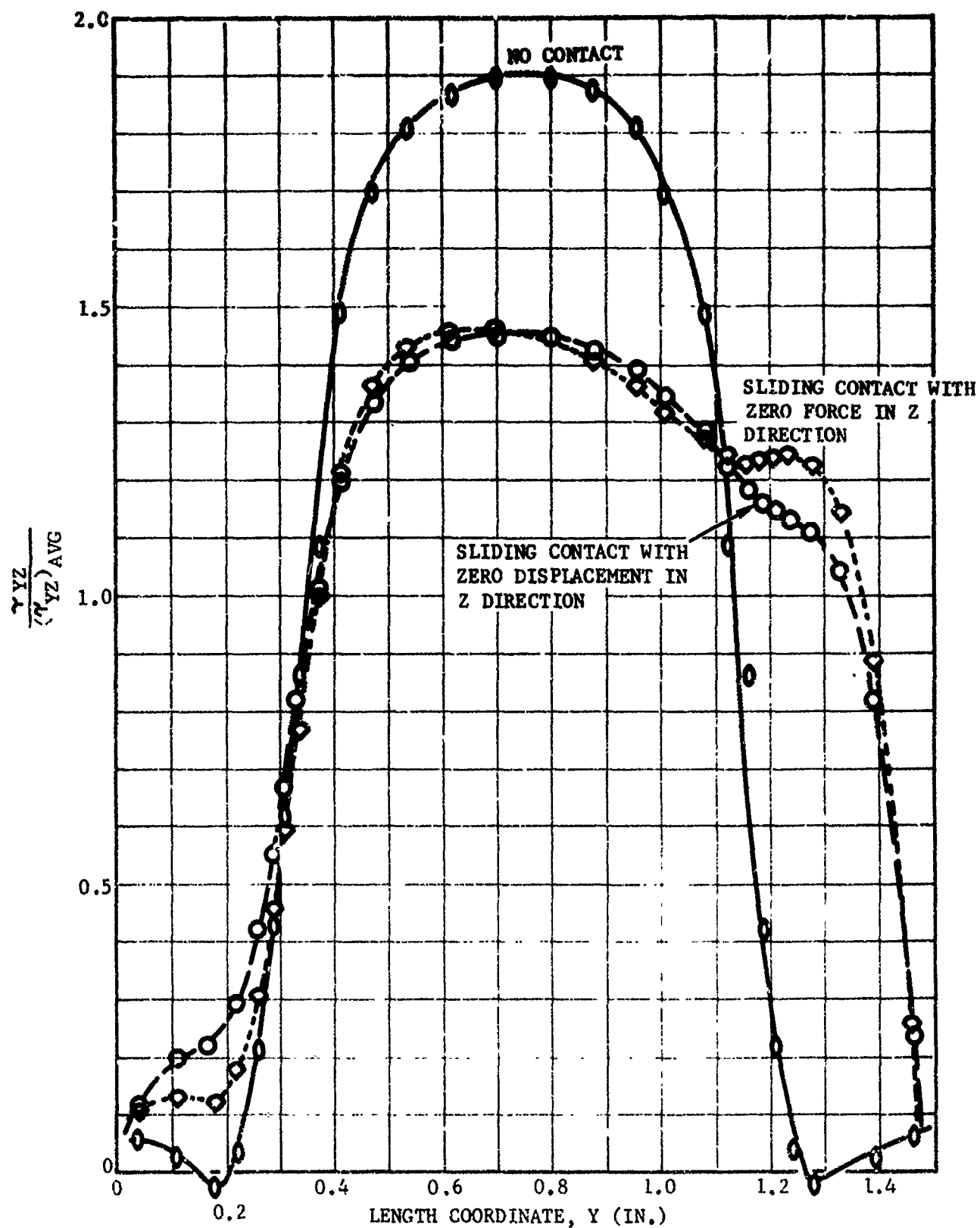
Figure 3-25.   2-D calculation for case bend shear stress distribution
in the analog flap termination sample pulled in shear,
E_{liner} = 200.

244
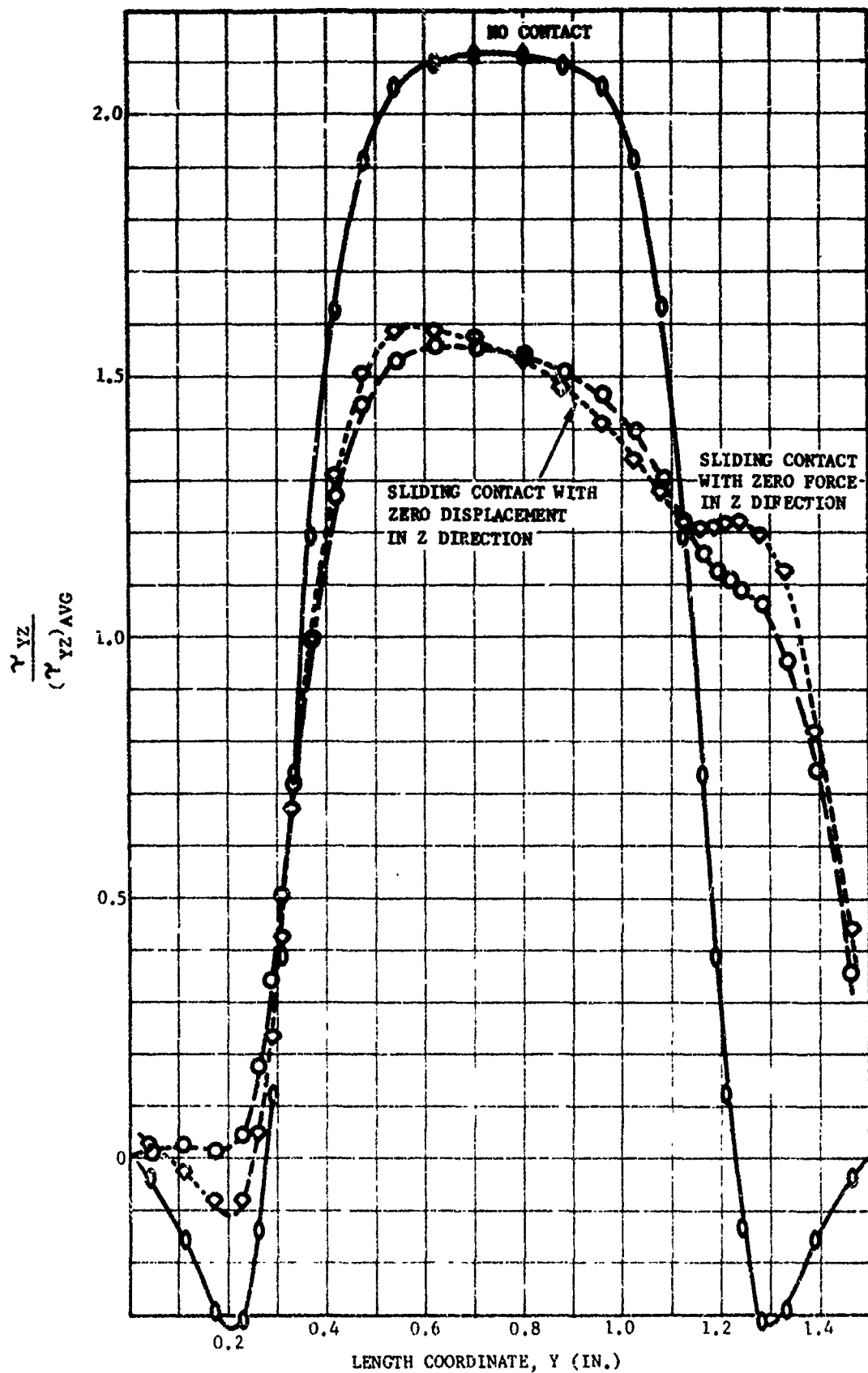
Figure 3-26. 2-D calculation for the case bond shear stress distribution
in the analog flap termination sample pulled in shear,
E_{liner} = 850.
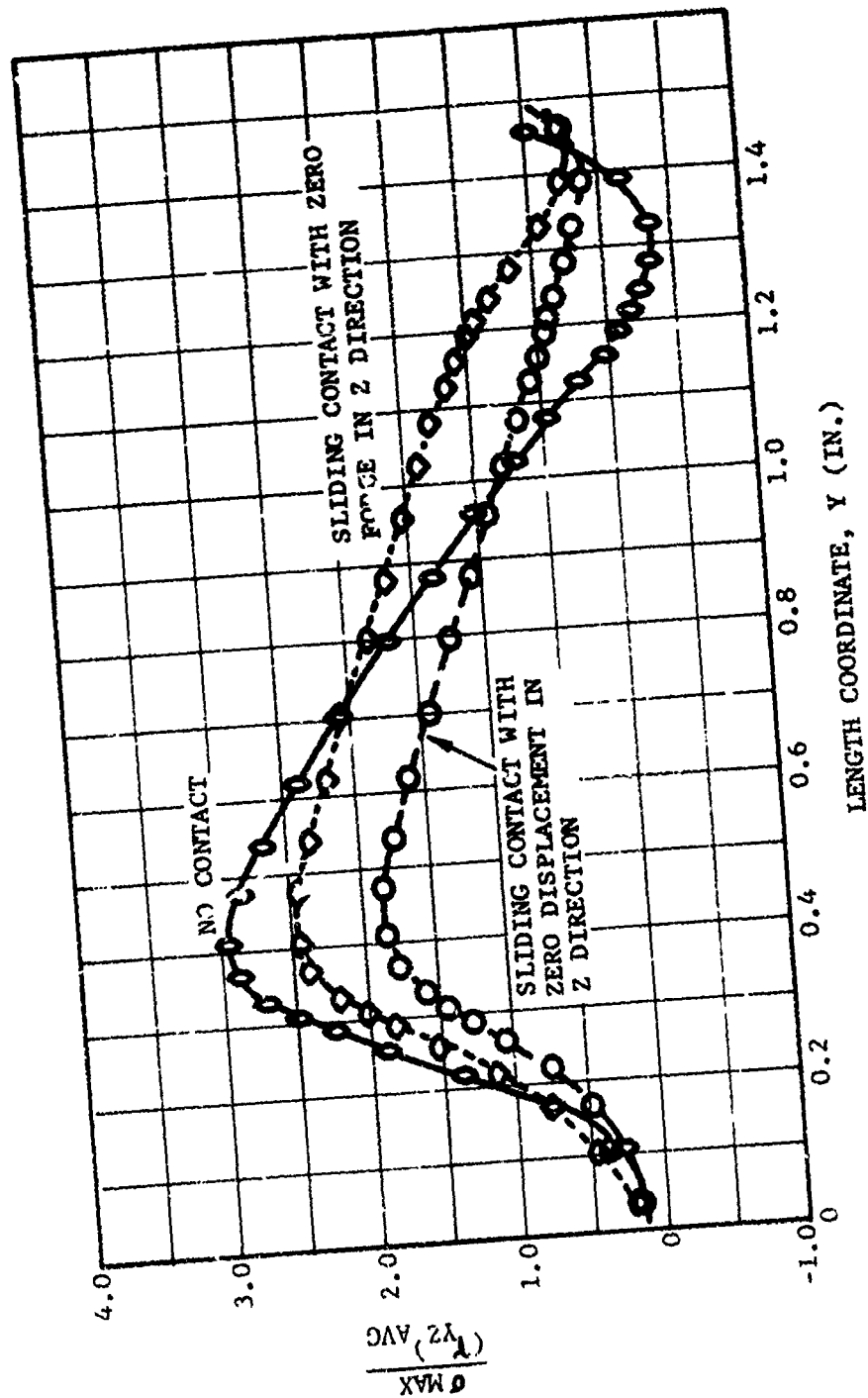
Figure 3-27. 2-D calculation for case bond principal stress distribution in the analog flap termination sample pulled in shear, $E_{liner} = 200$.
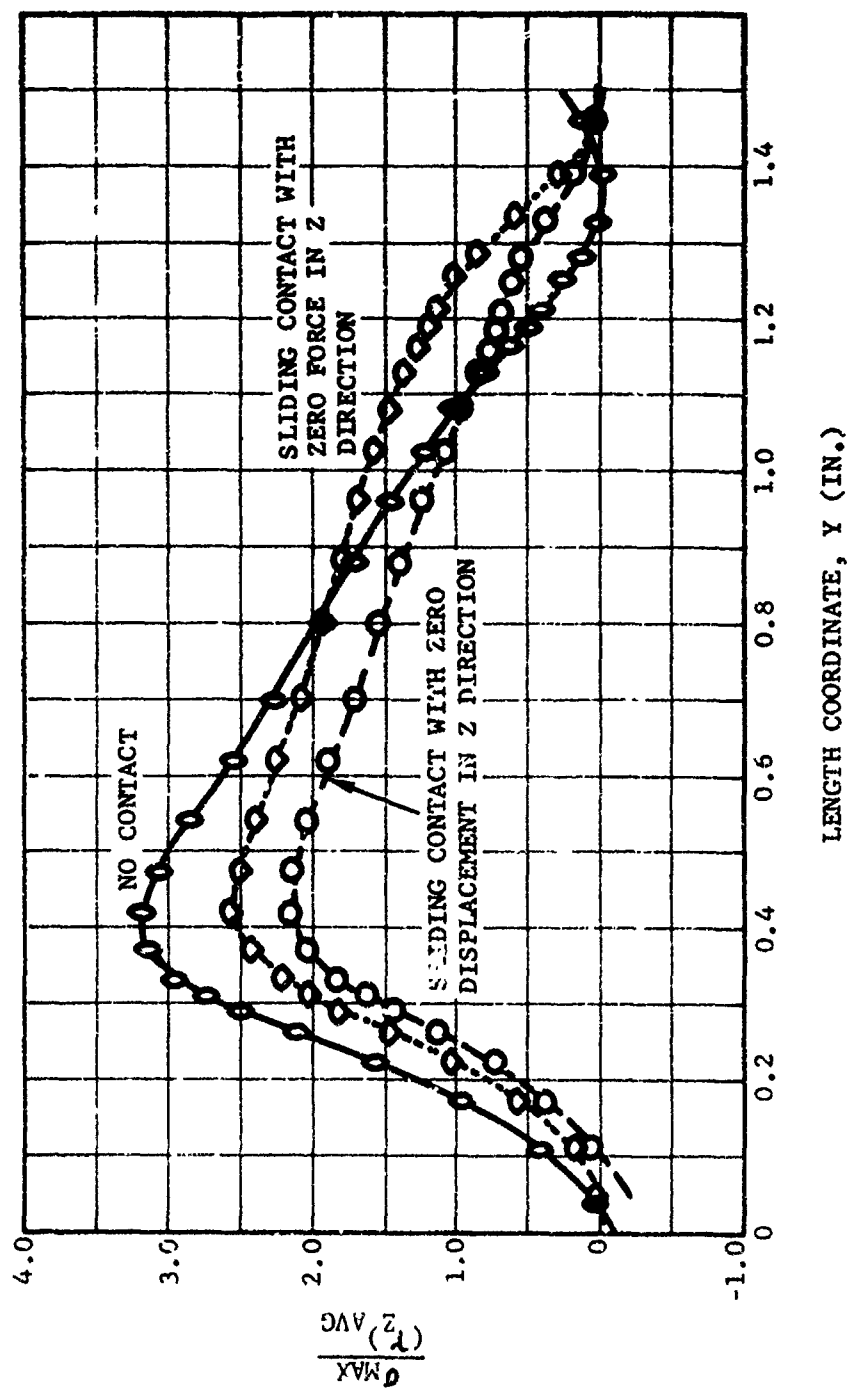
Figure 3-28. 2-D calculation for case bond principal stress distribution in the analog flap termination sample pulled in shear, $E_{liner} = 850$.
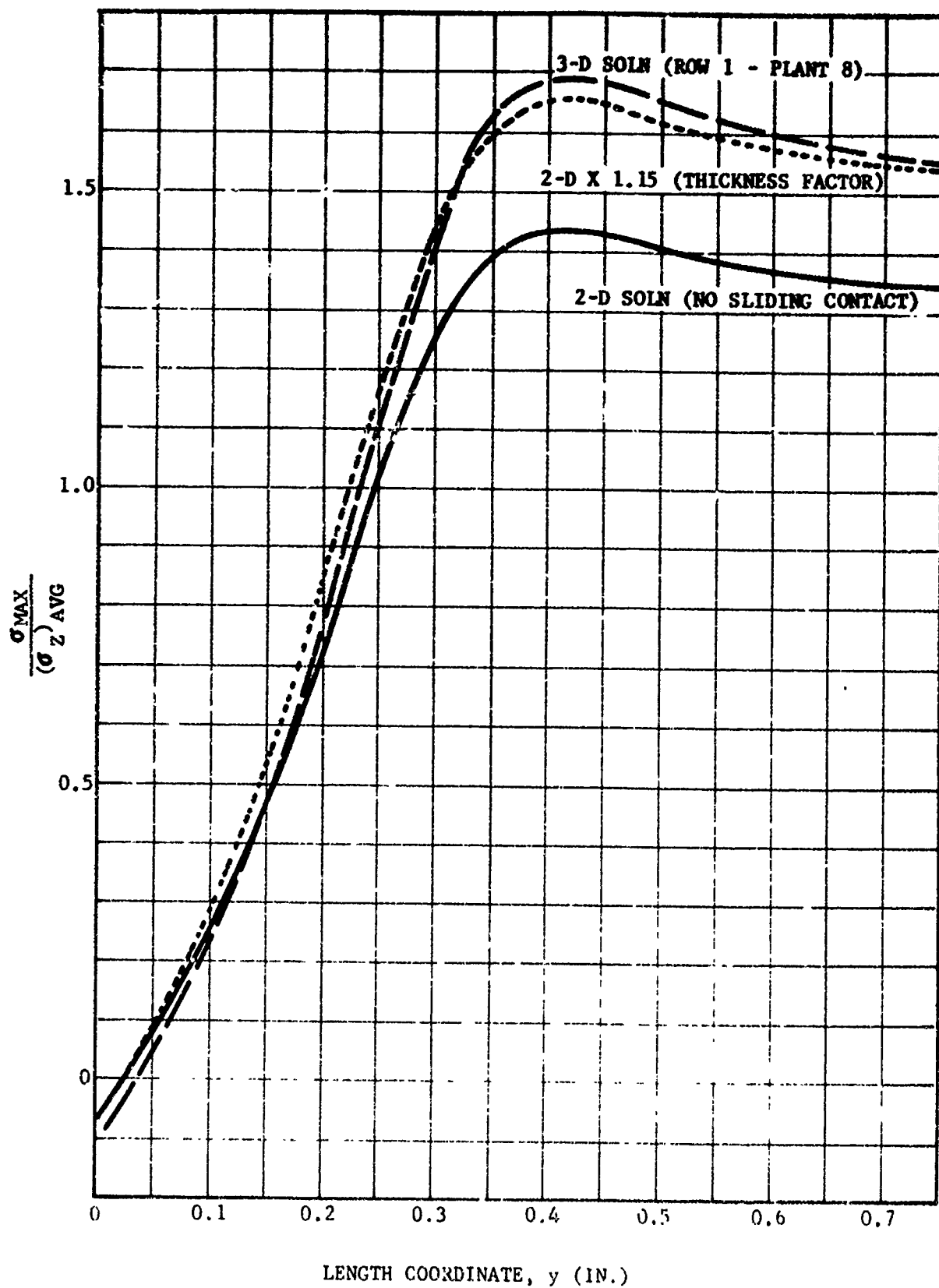
Figure 3-29. Comparison of 2-D and 3-D stress solutions for analog flap termination sample pulled in tension
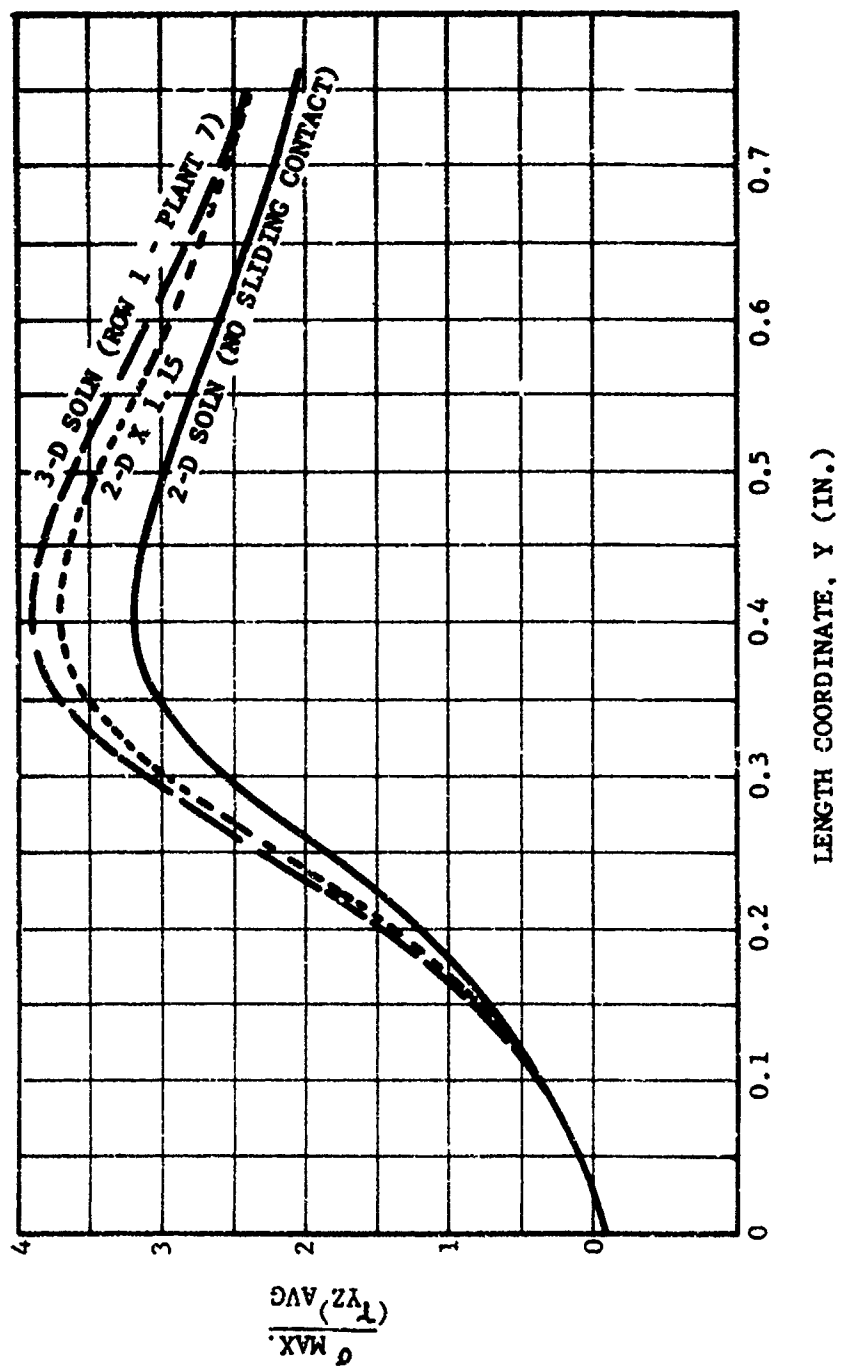
Figure 3-30. Comparison of 2-D and 3-D stress solutions for analog flap termination sample pulled in shear.
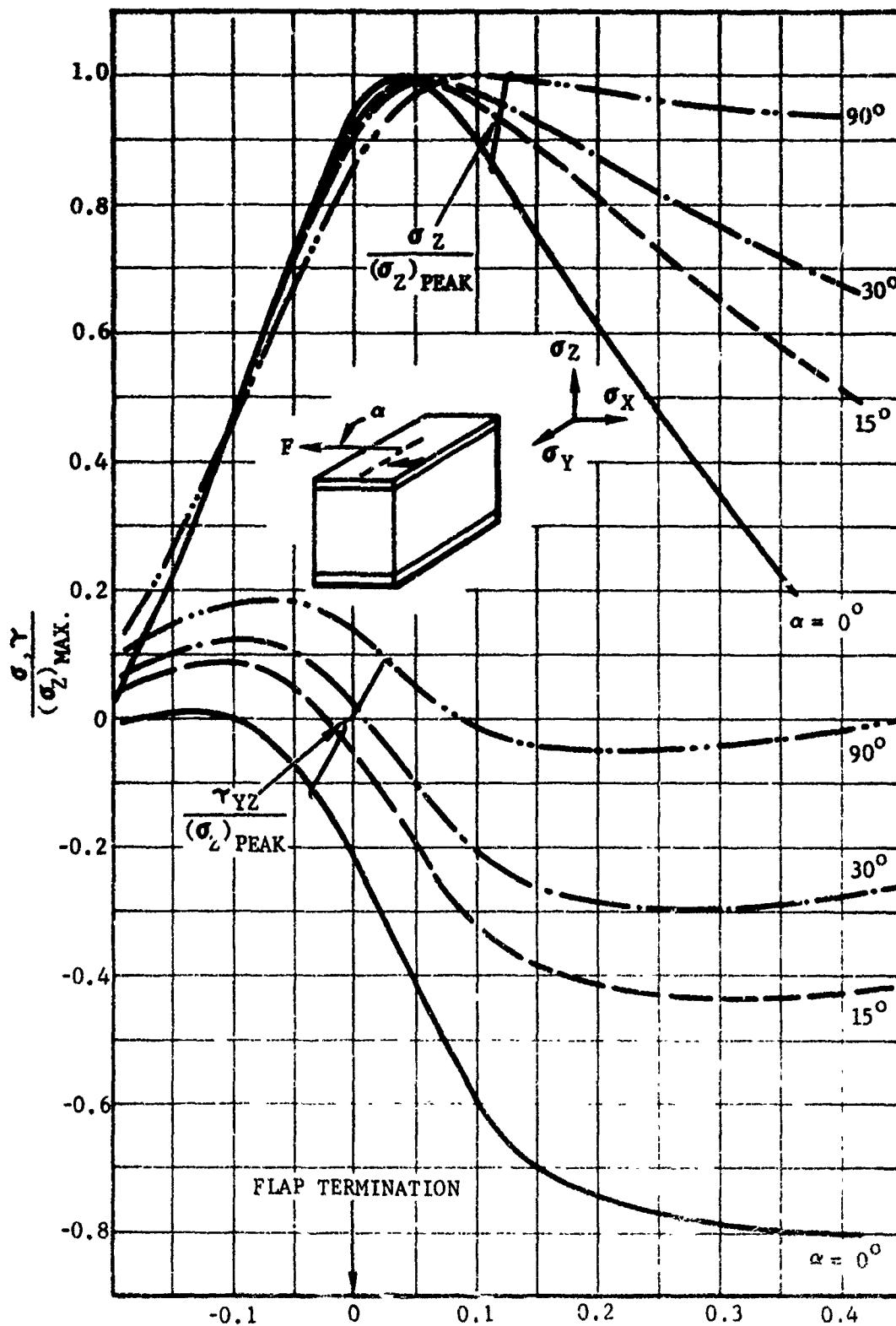
Figure 3-31. Effect of pull angle on case bond normal and shear
stress distribution in analog flap termination sample,
$E_{liner} = 200$ and no flap-end tab contact
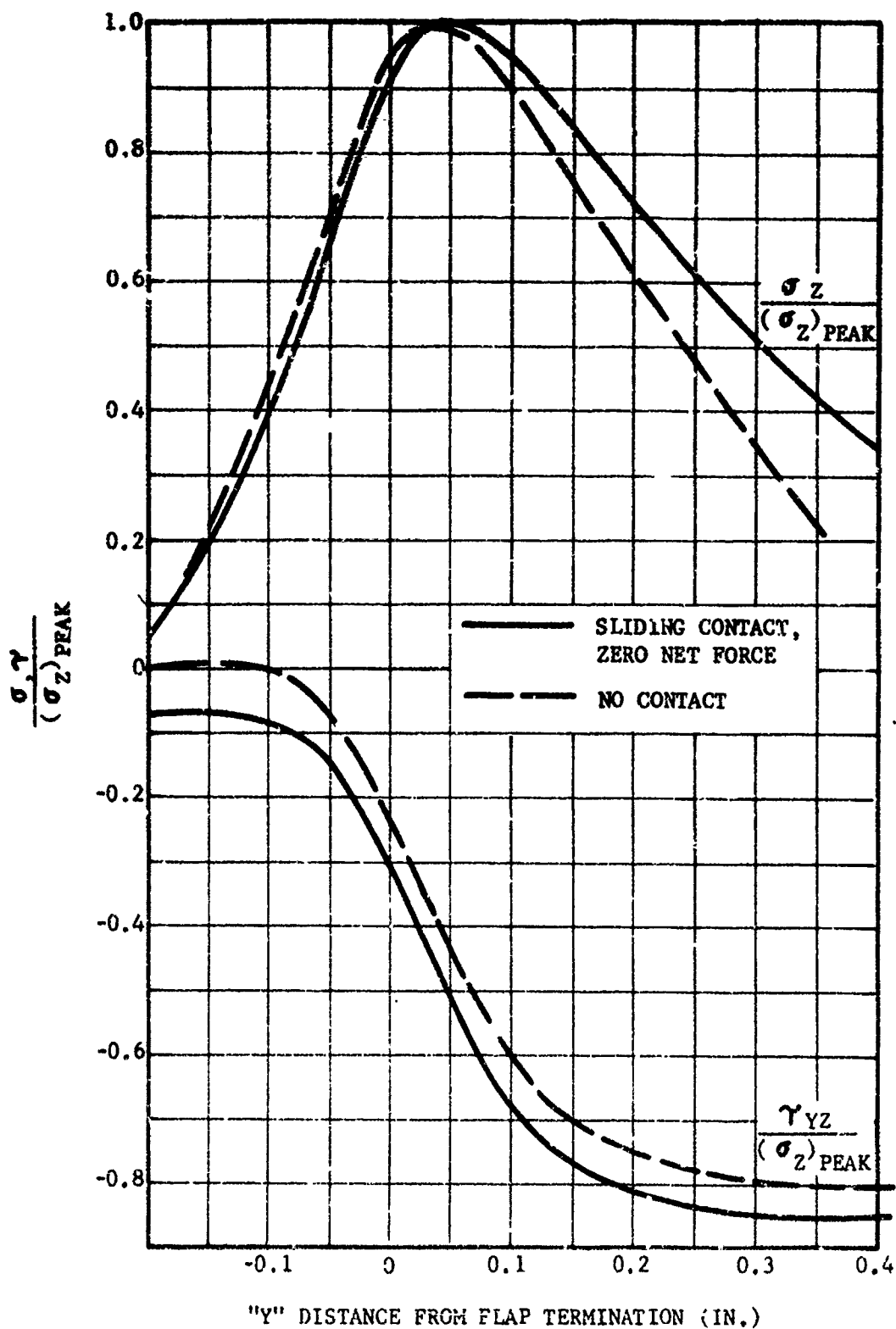
Figure 3-32. Comparison of case bond normal and shear stress distributions for analog flap termination sample pulled in shear with and without flap-end tab control, $E_{liner} = 200$ psi.
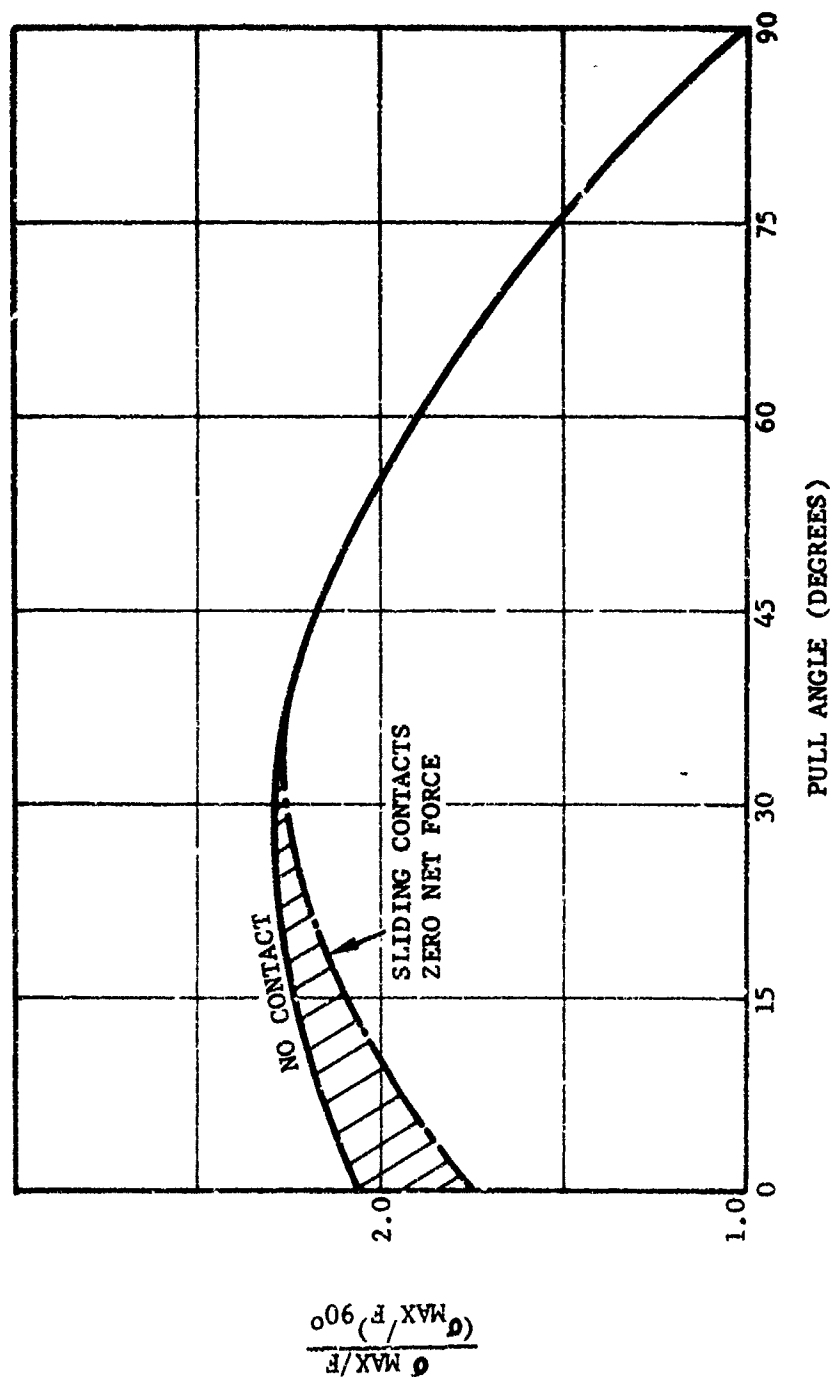
Figure. 3-33. Effect of pull angle on the maximum principal stress per unit force for the analog flap termination sample, E_{liner} = 200.
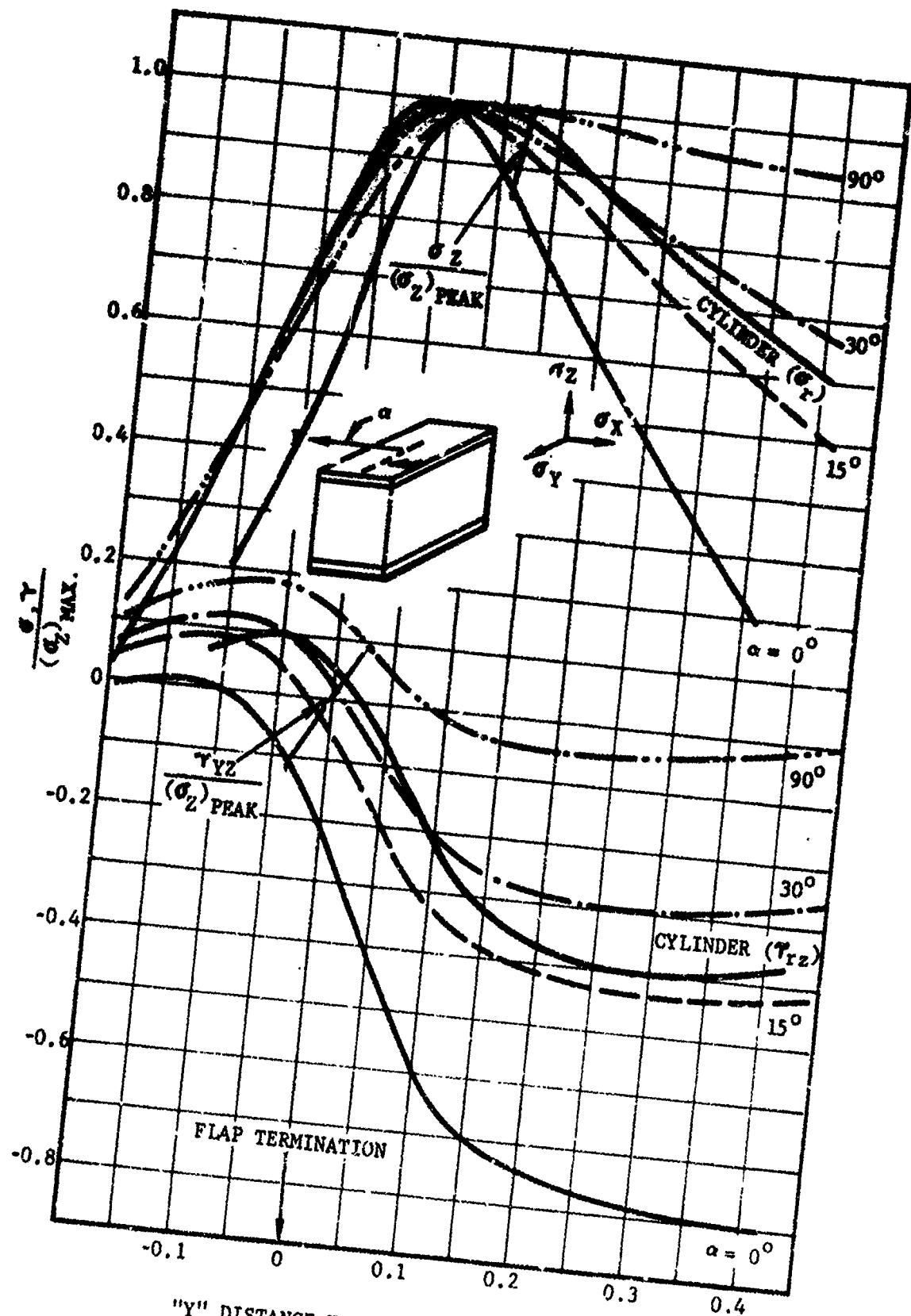
Figure 3-34. Comparison of case bond normal and shear stress distributions for cylindrical motor configurations and analog flap termination samples.
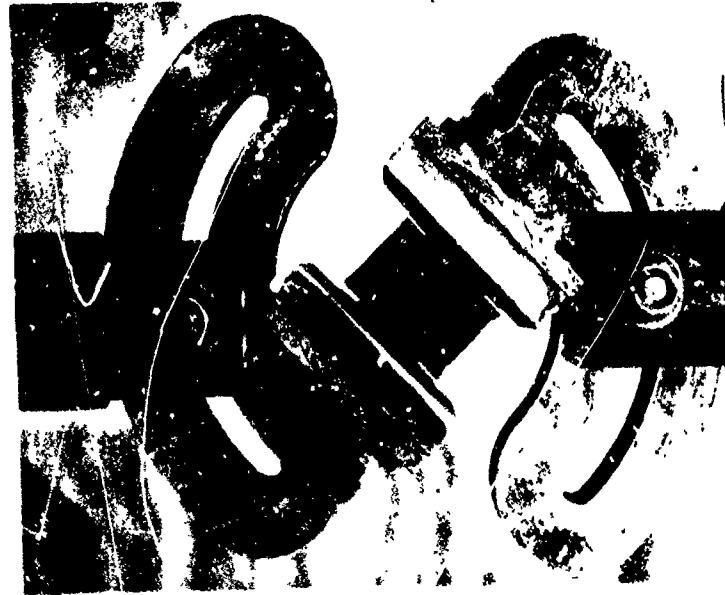
Figure 3-35. Photo sequence of double-base analog sample pulled at 45 degrees.
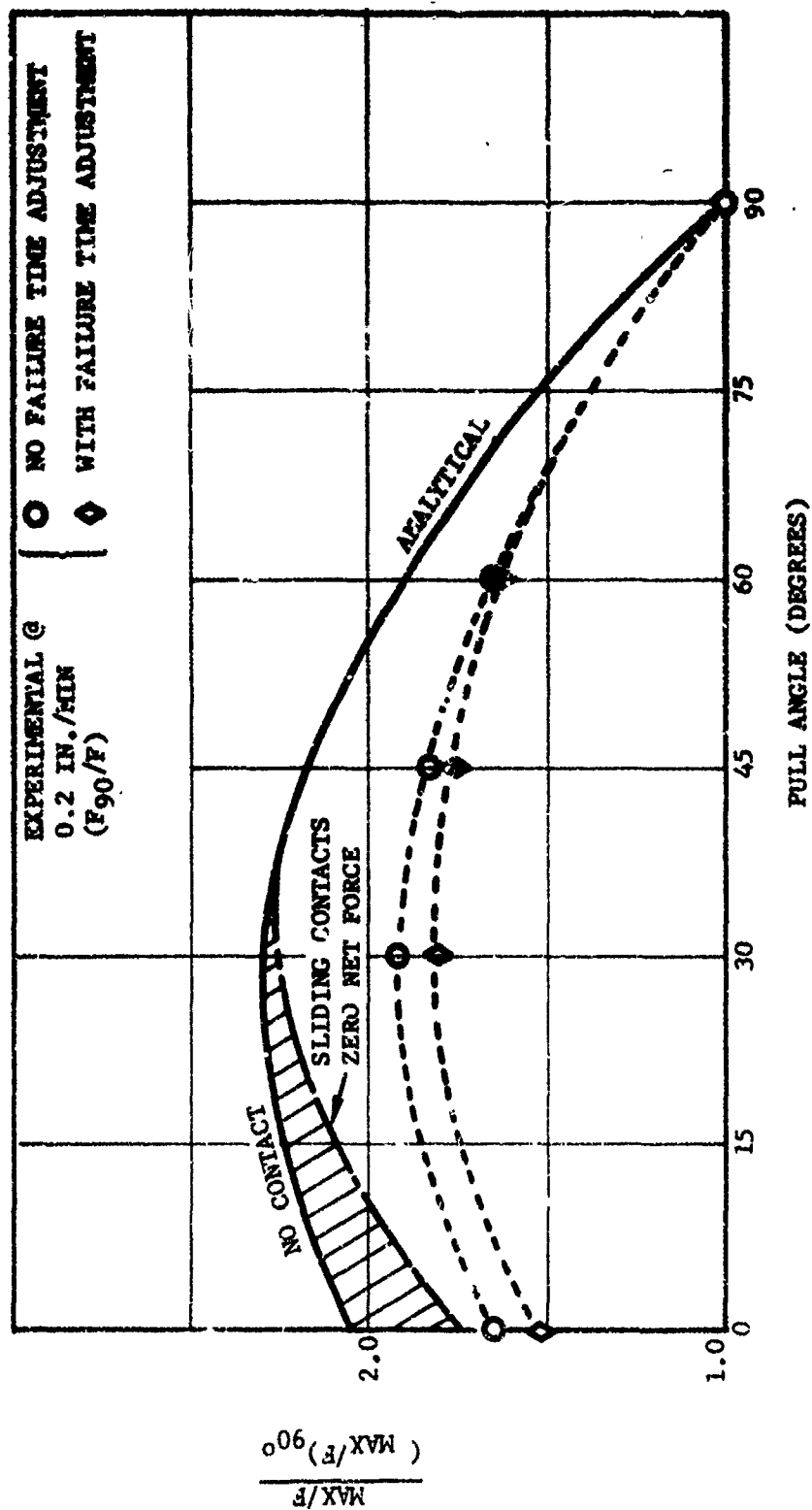
Figure 3-36. Effect of pull angle on failure of analog flap termination samples of TP-H1123 propellant, 0.2 in./min loading rate.

255
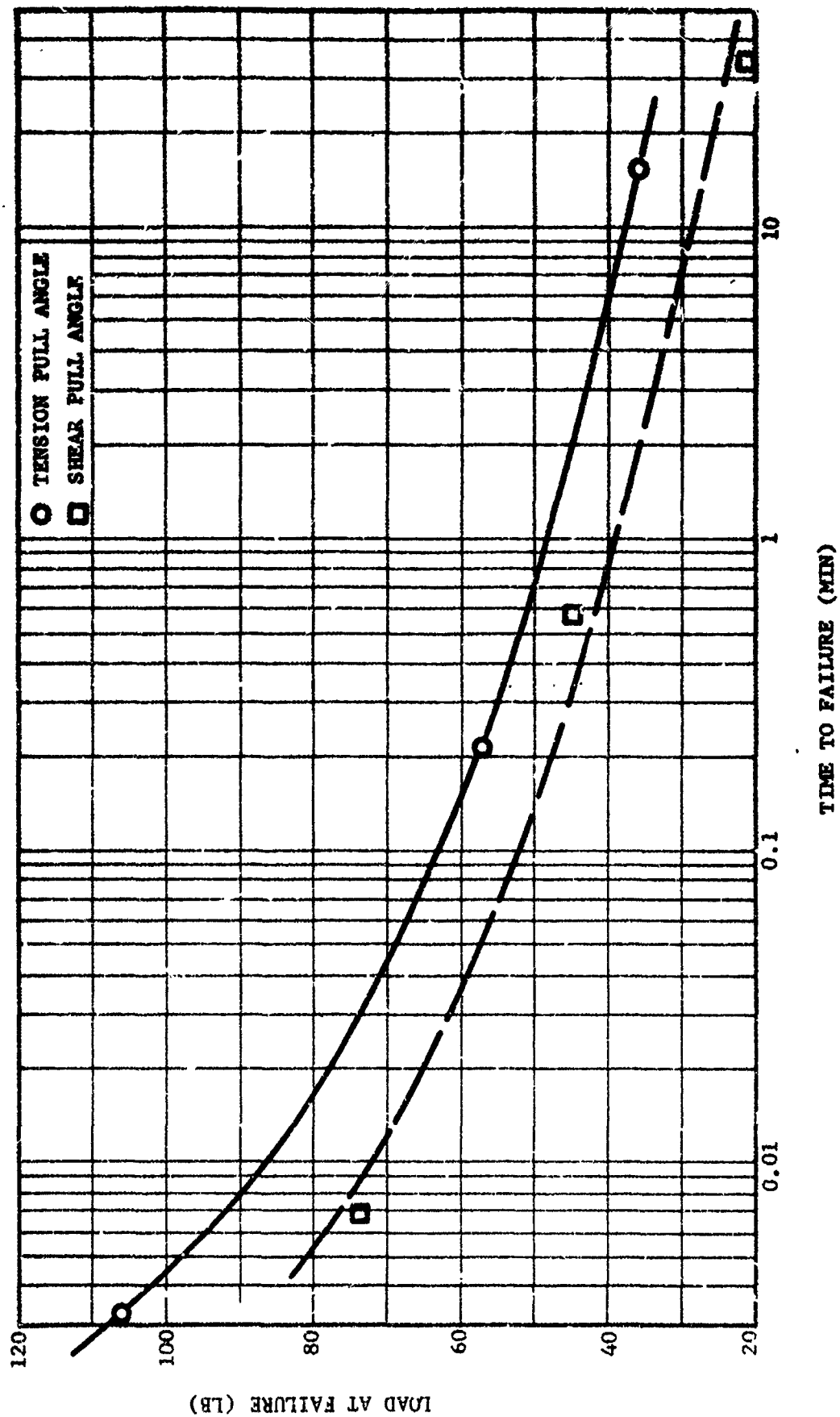
Figure 3-37. Failure load for analog flap termination samples pulled in tension and shear.
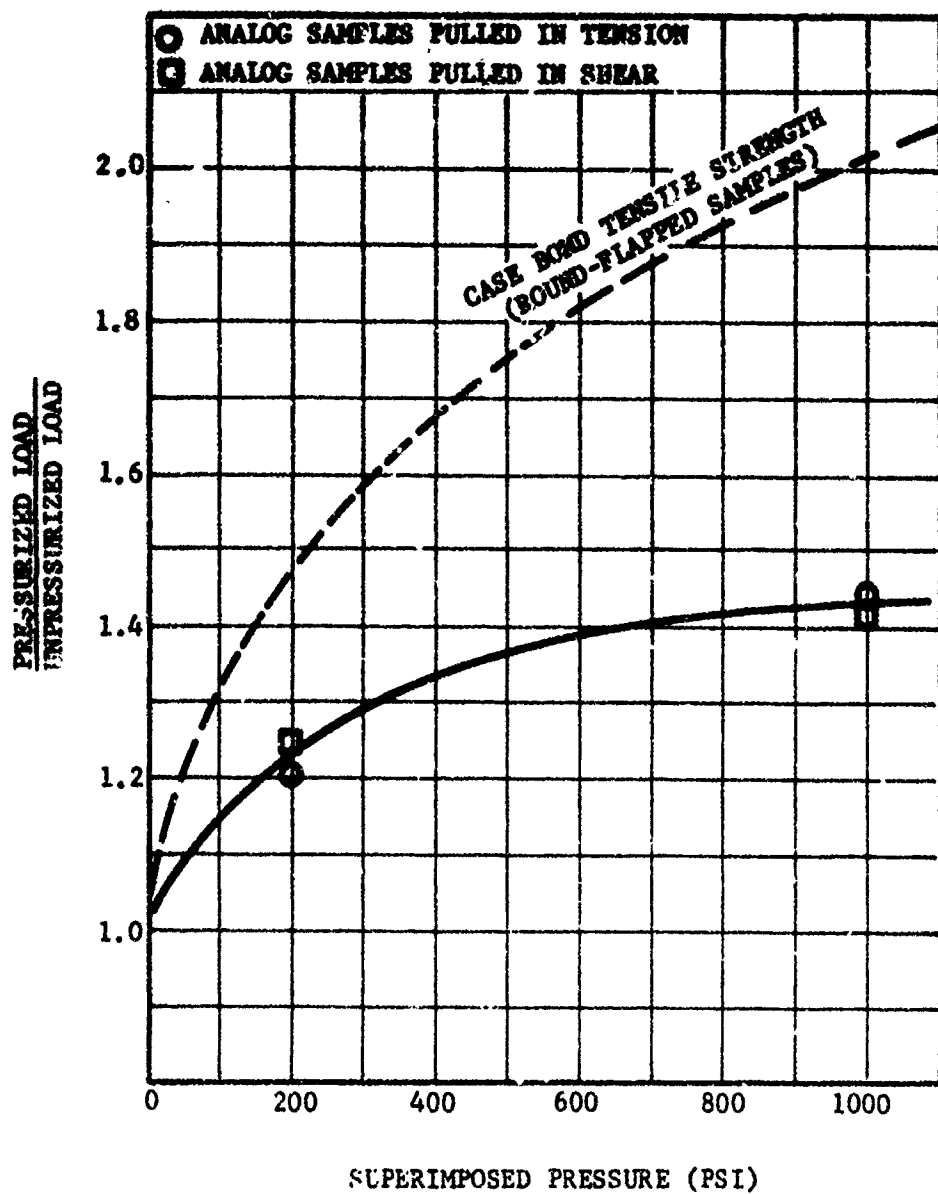
Figure 3-38.   Effect of superimposed pressure on the failure load.
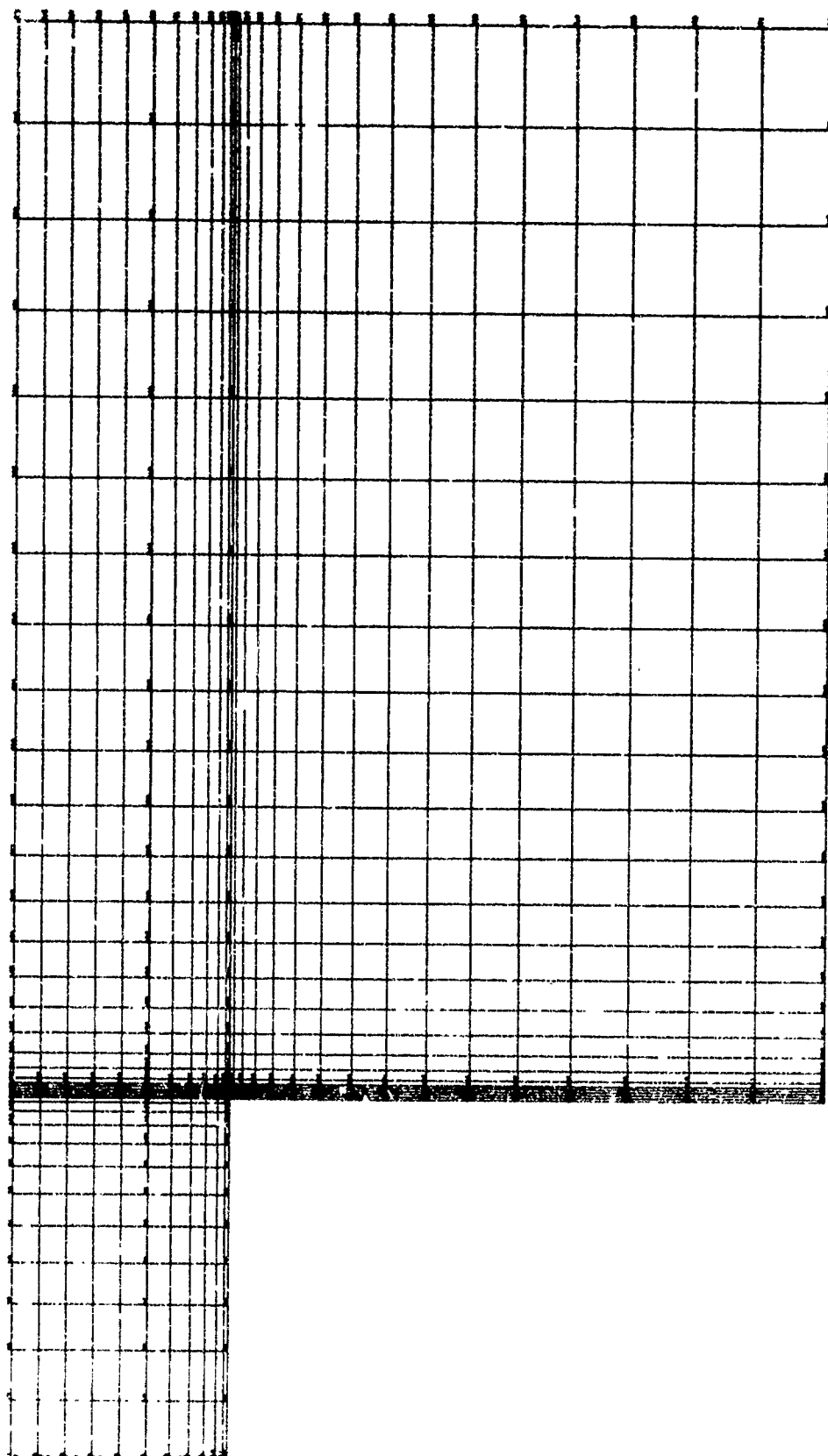
Figure 3-39. Finite element model used for stress analysis of the analog discontinuity sample.
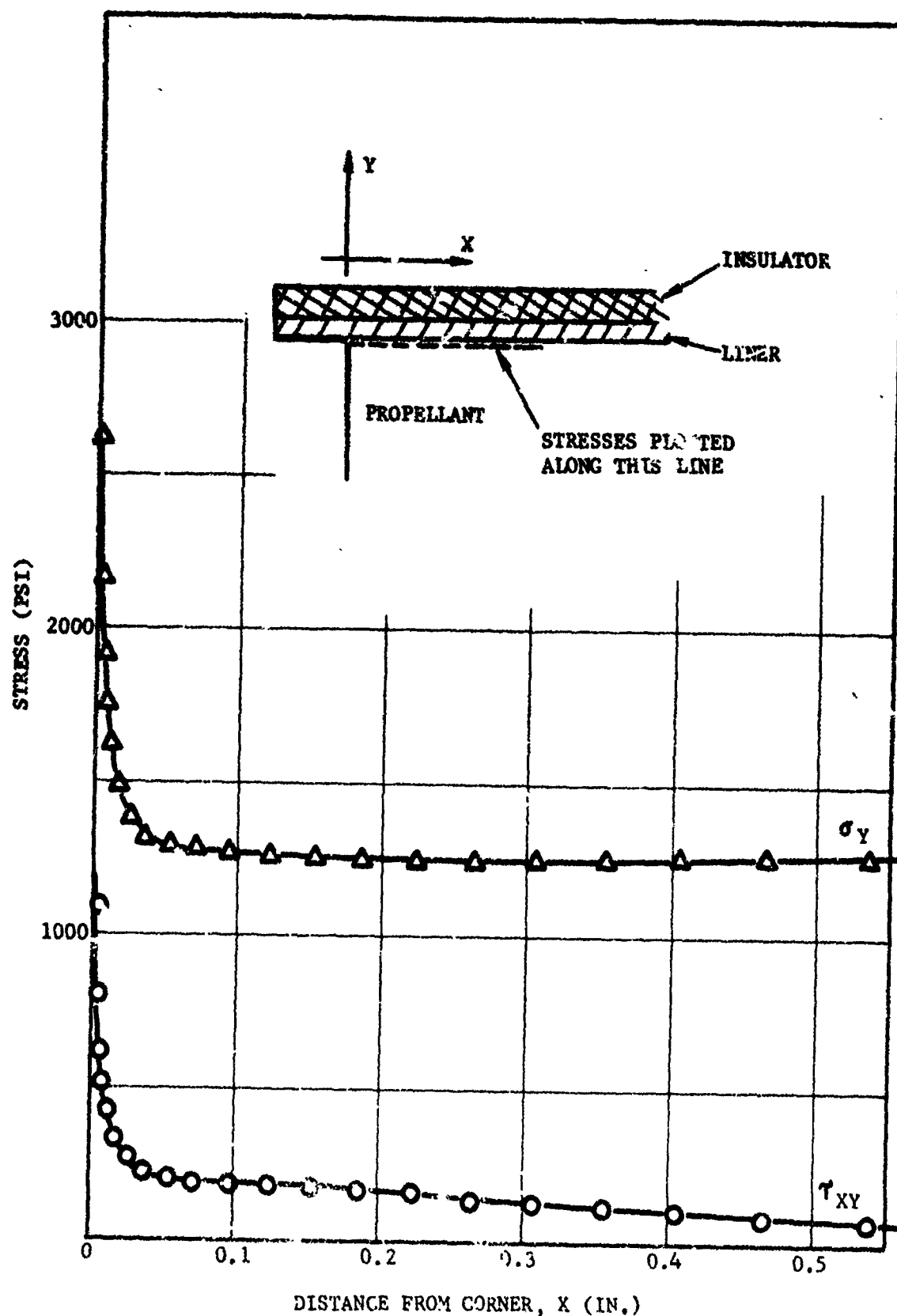
Figure 3-40. Stress distribution in propellant adjacent to liner interface for analog discontinuity sample pulled in tension (E_L = 200 psi).

259
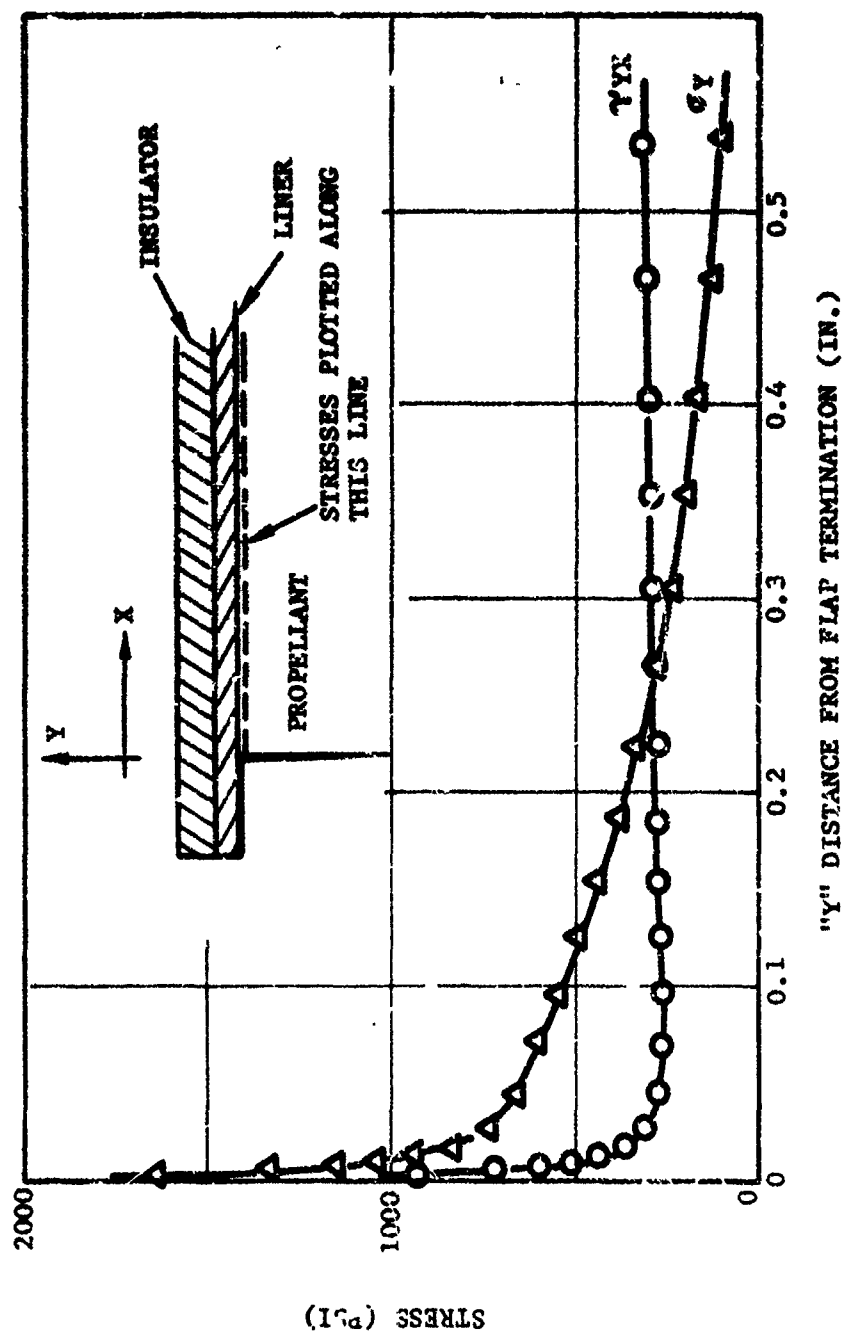
Figure 3-41. Stress distribution in propellant adjacent to liner interface for analog discontinuity sample pulled in shear ($E_L = 200$ psi).

260
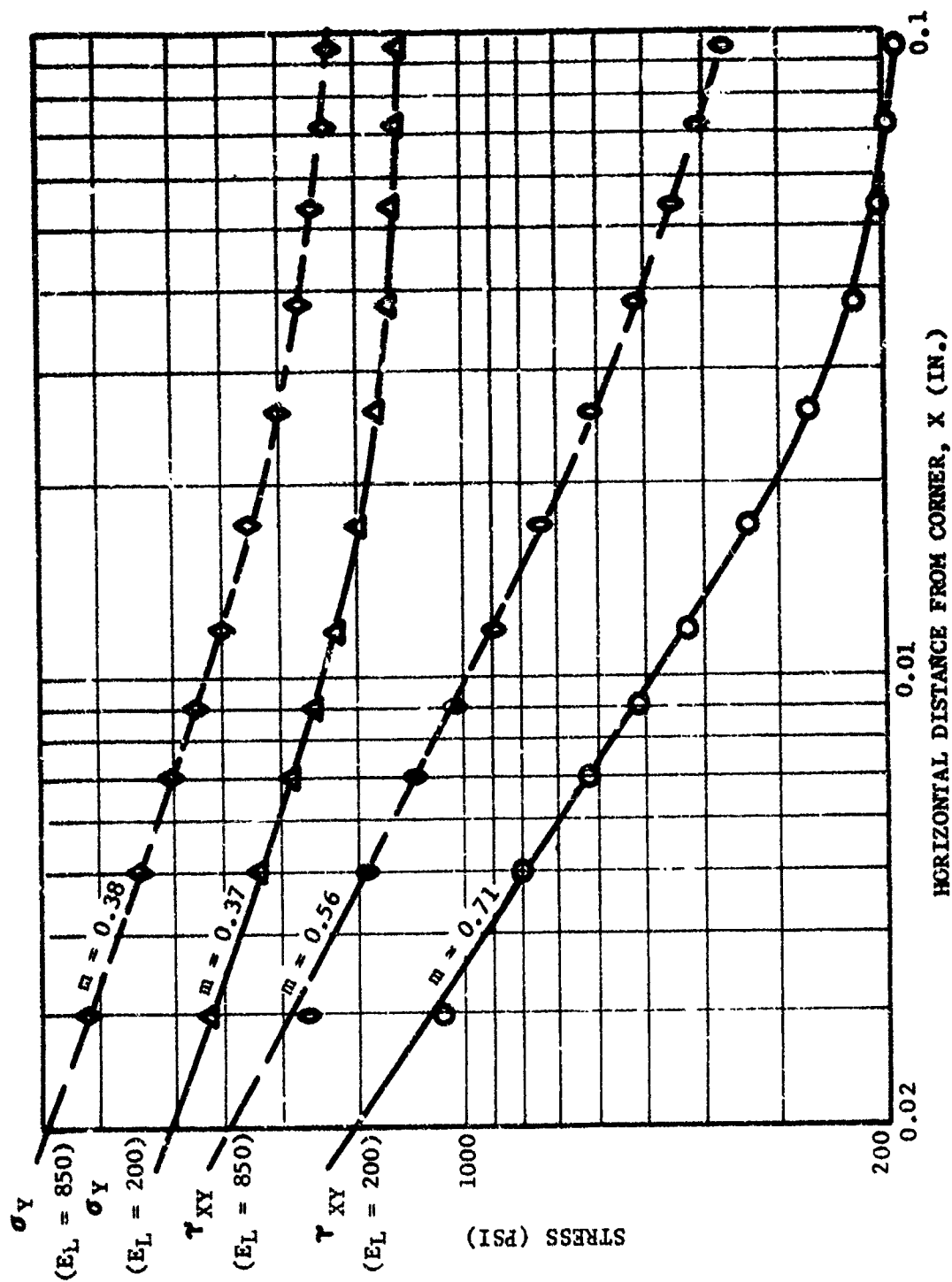
Figure 3-42. Stresses in propellant immediately adjacent to corner for analog discontinuity sample pulled in tension.

261
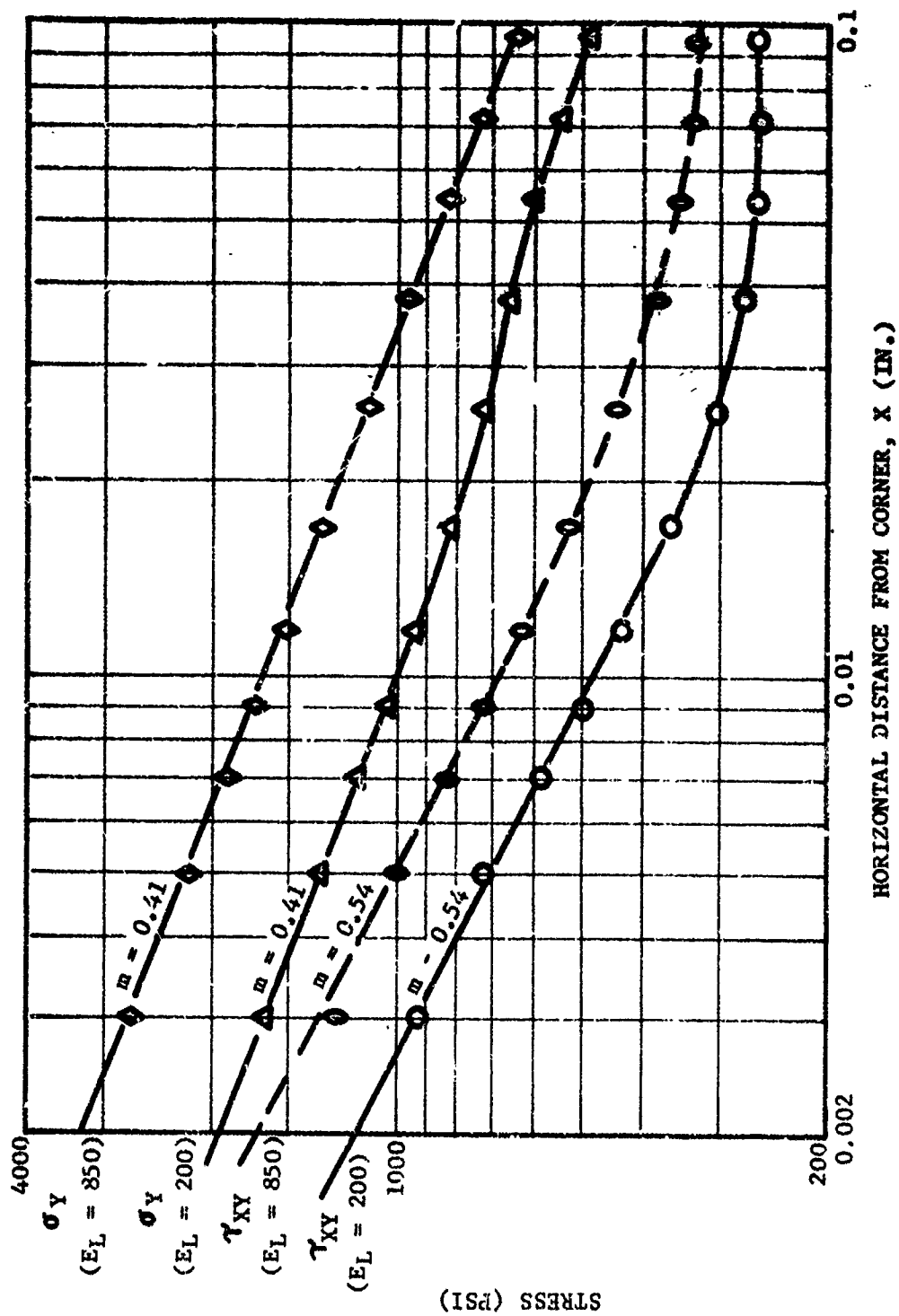
Figure 3-43. Stresses in propellant immediately adjacent to corner for analog discontinuity sample pulled in shear.

262

DISTANCE FROM CORNER (IN.)

MAXIMUM PRINCIPAL STRESS (PSI)
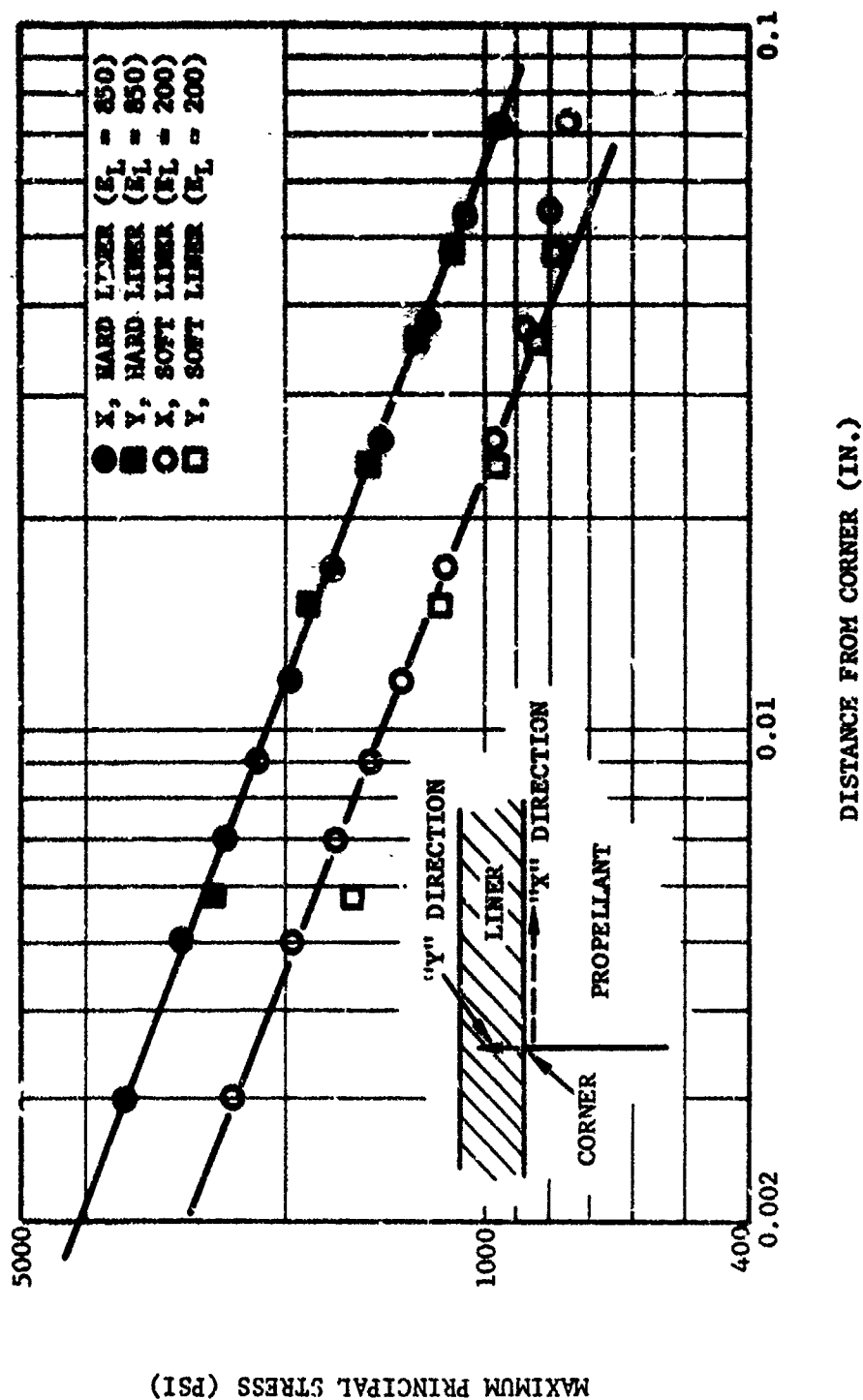
Figure 3-44. Maximum principal stress gradient in propellant along bond interface
(vs x) and in liner normal to bond interface (vs y) for analog
sample pulled in shear.

263
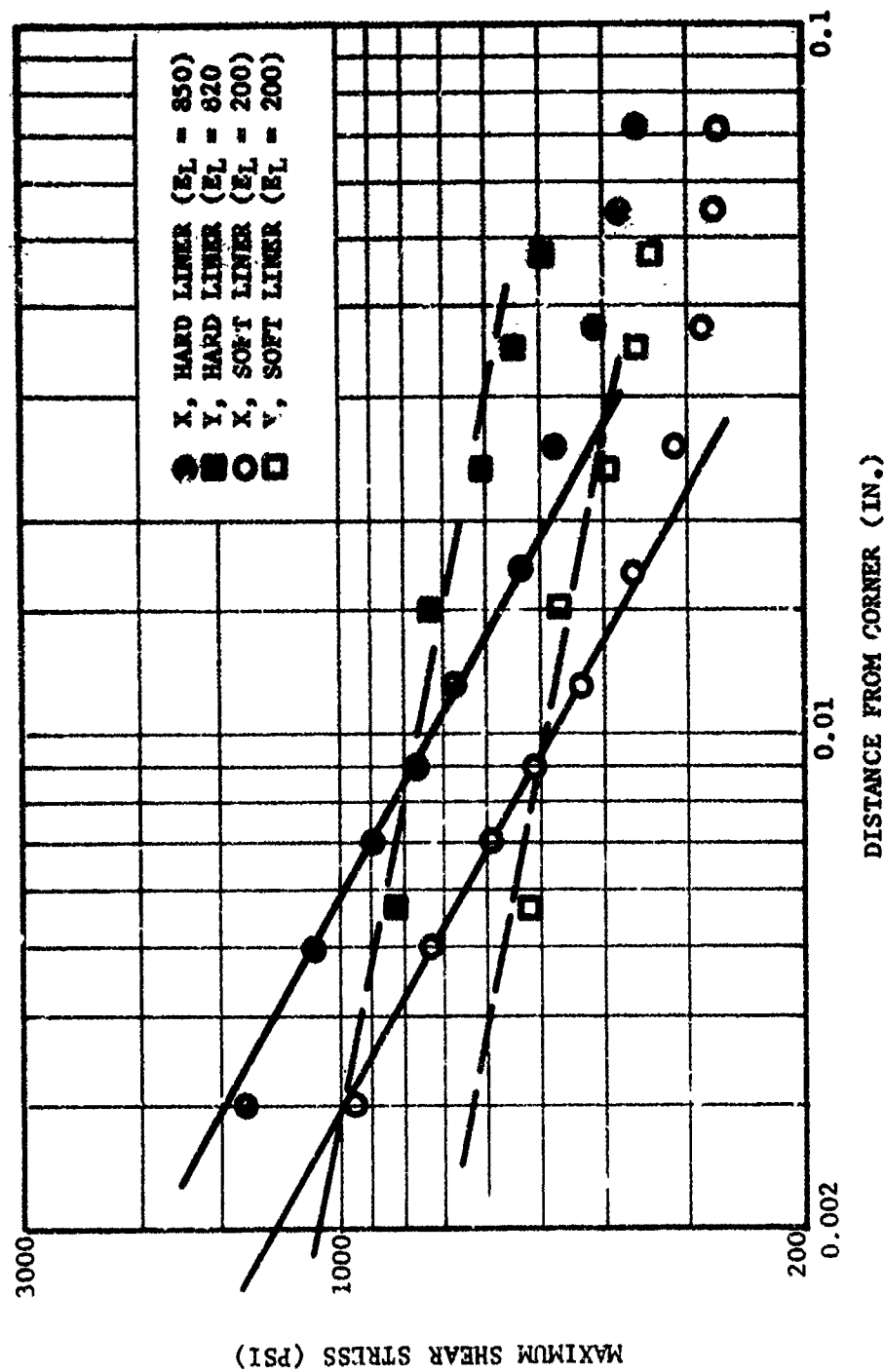
Figure 3-45. Maximum shear stress gradient in propellant along bond interface (vs x) and in liner normal to bond interface (vs y) for analog discontinuity sample.

264
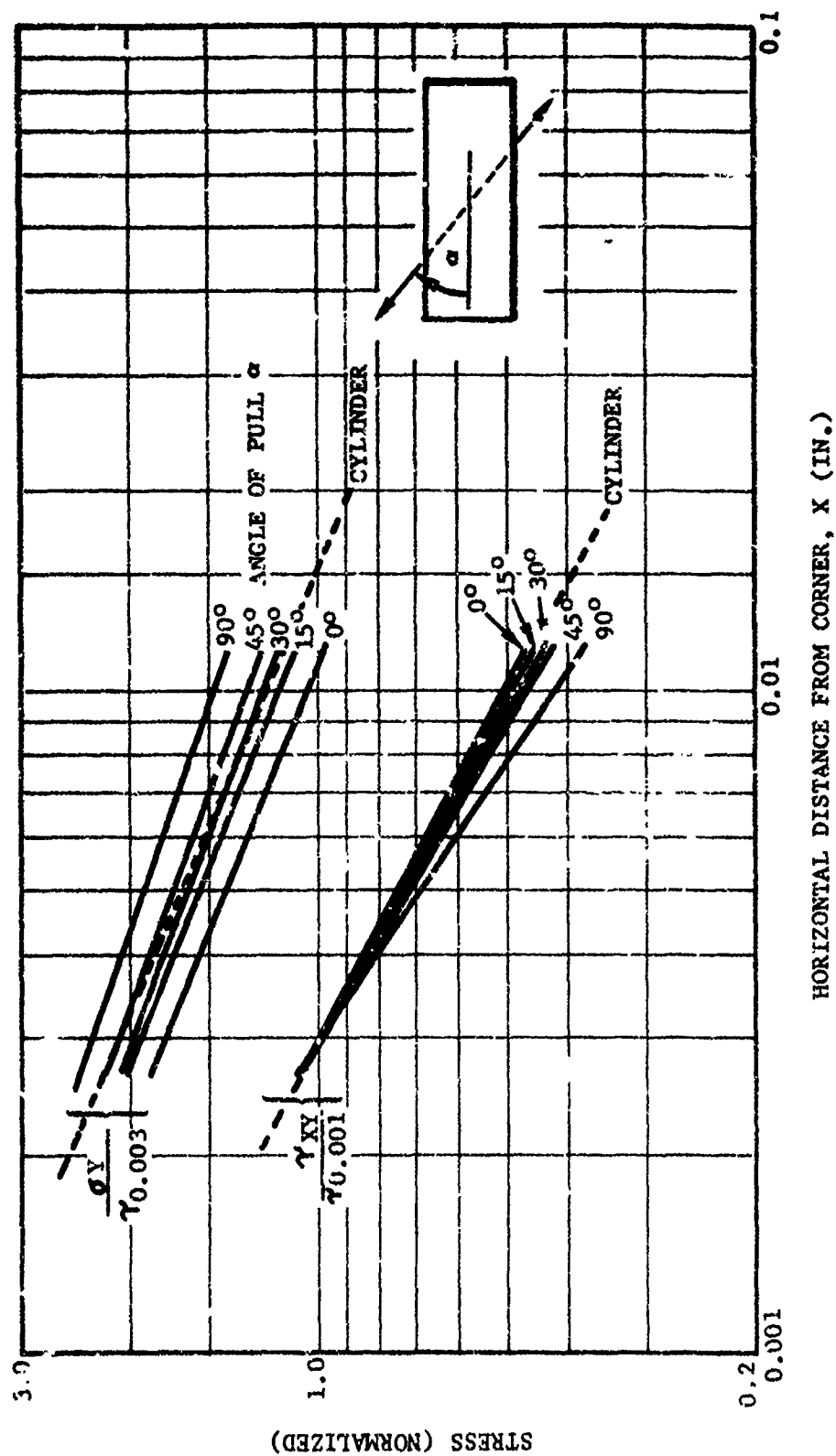
Figure 3-46. Normal and shear stress distribution adjacent to corner for analog discontinuity sample under various pull angles ($F_{liner} = 200$).

265
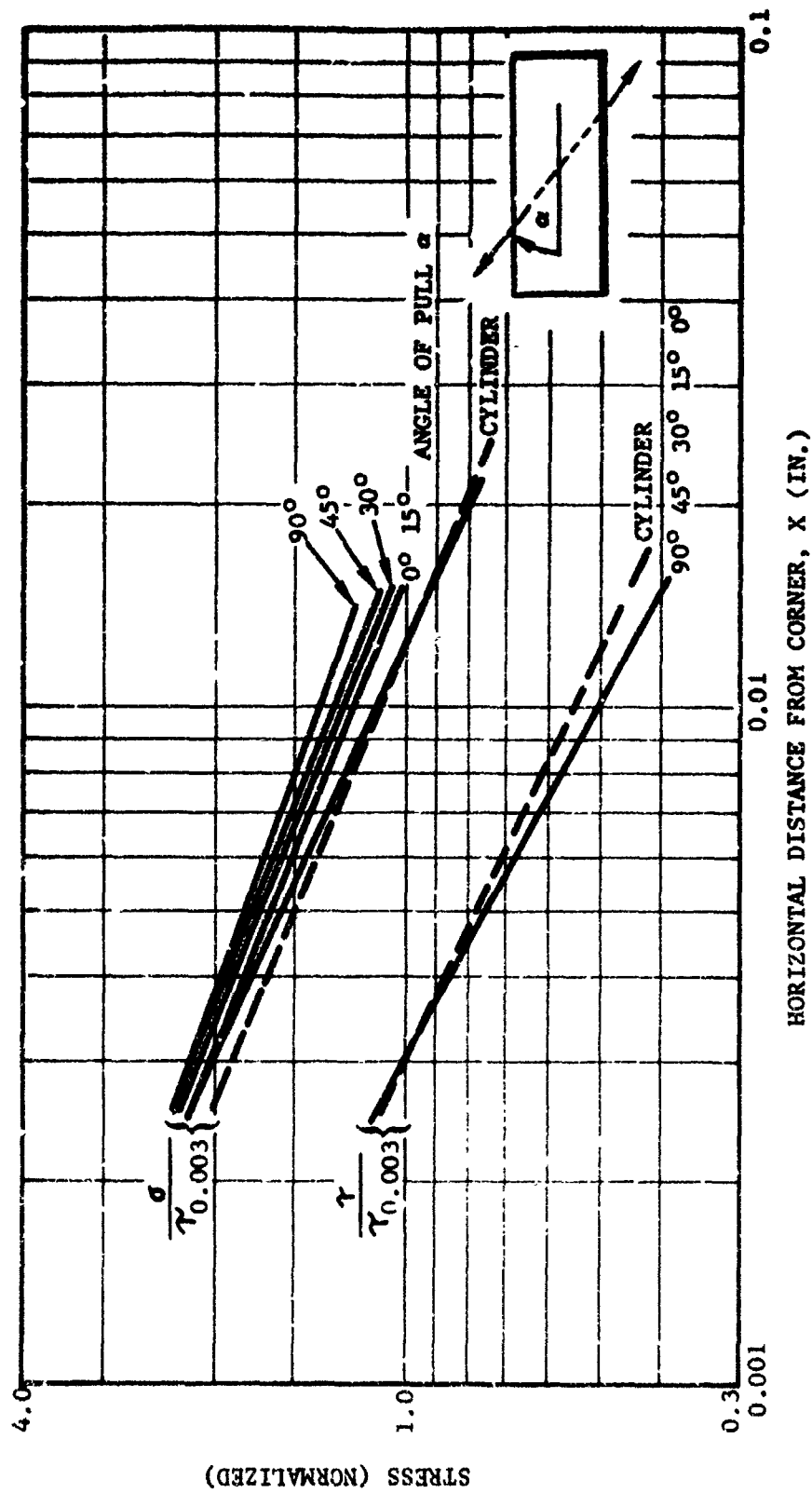
Figure 3-47. Normal and shear stress distribution adjacent to corner for analog discontinuity sample under various pull angles ($E_{liner} = 850$).

266
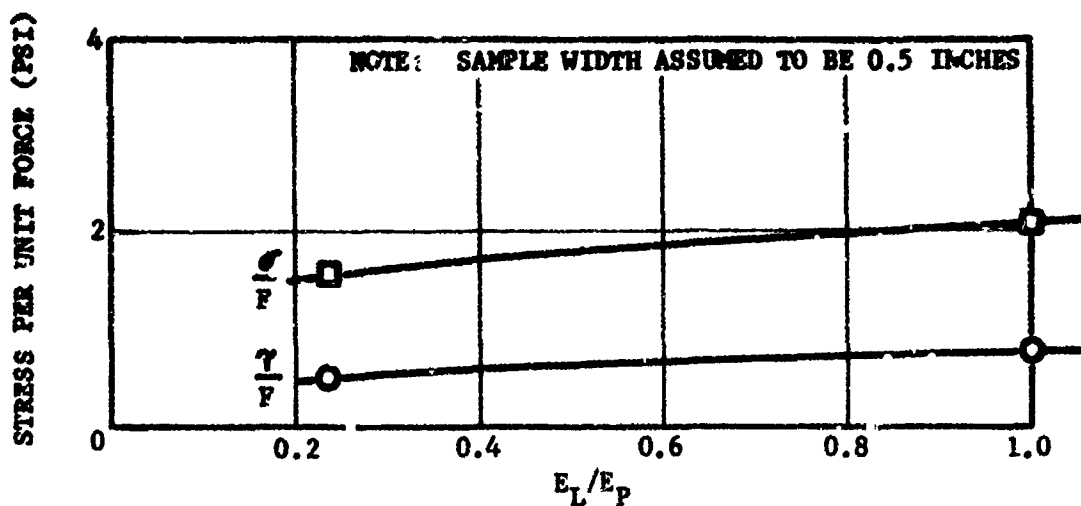
Figure 3-48a.   Stress magnitude 0.01 inch from corner for a
unit tensile force applied to analog discontinuity
sample
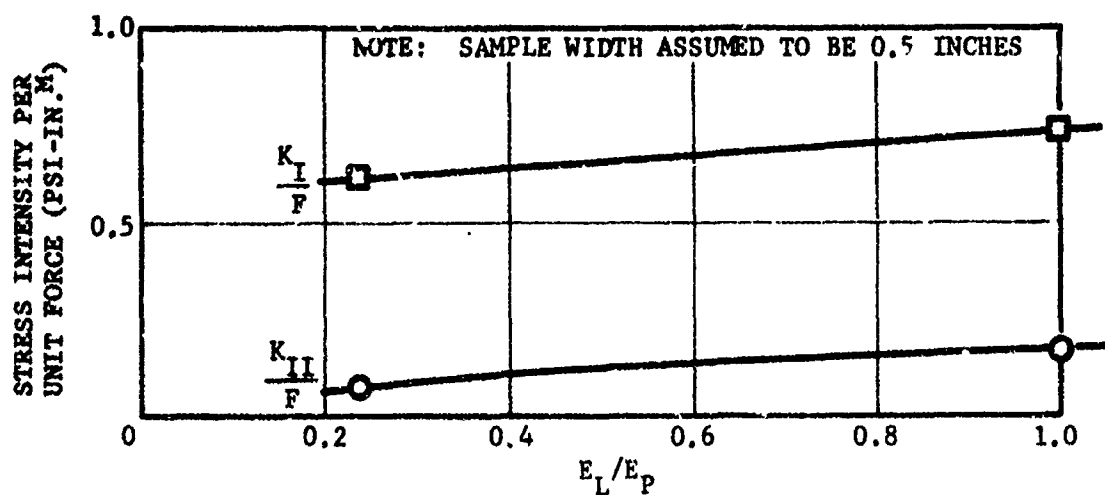
Figure 3-48b.   Stress intensity factor for a unit tensile force
applied to analog discontinuity sample.

267
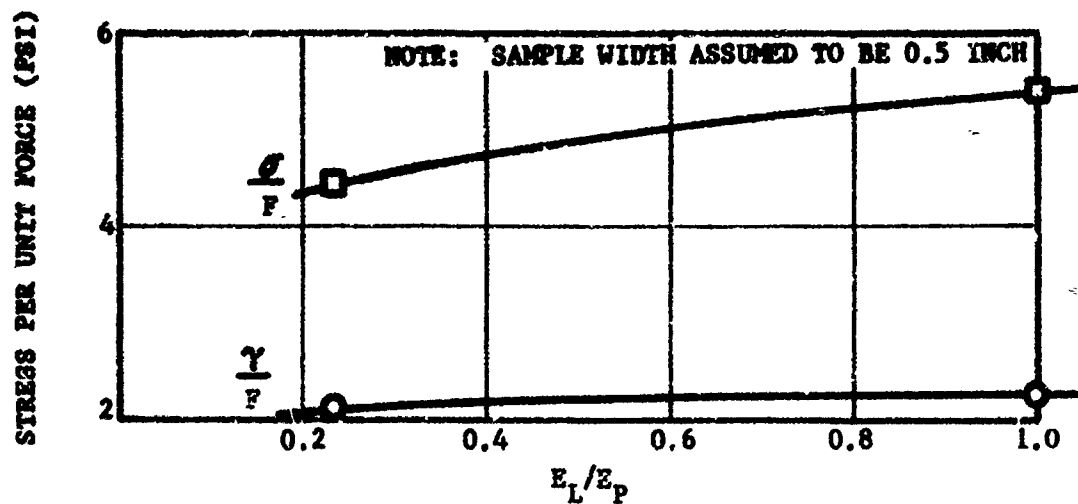
Figure 3-49a. Stress magnitude 0.01 inch from corner for a unit shear force applied to analog discontinuity sample.
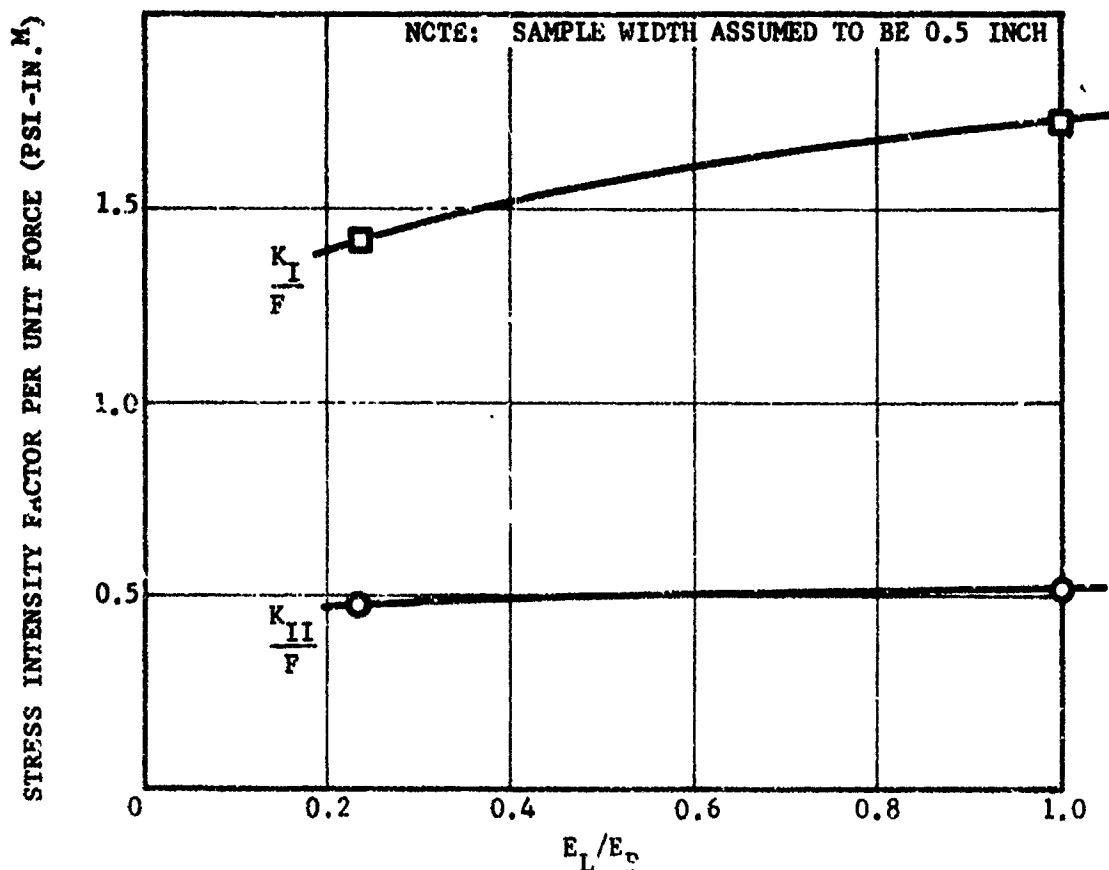
Figure 3-49b. Stress intensity factor for a unit shear force applied to analog discontinuity sample.
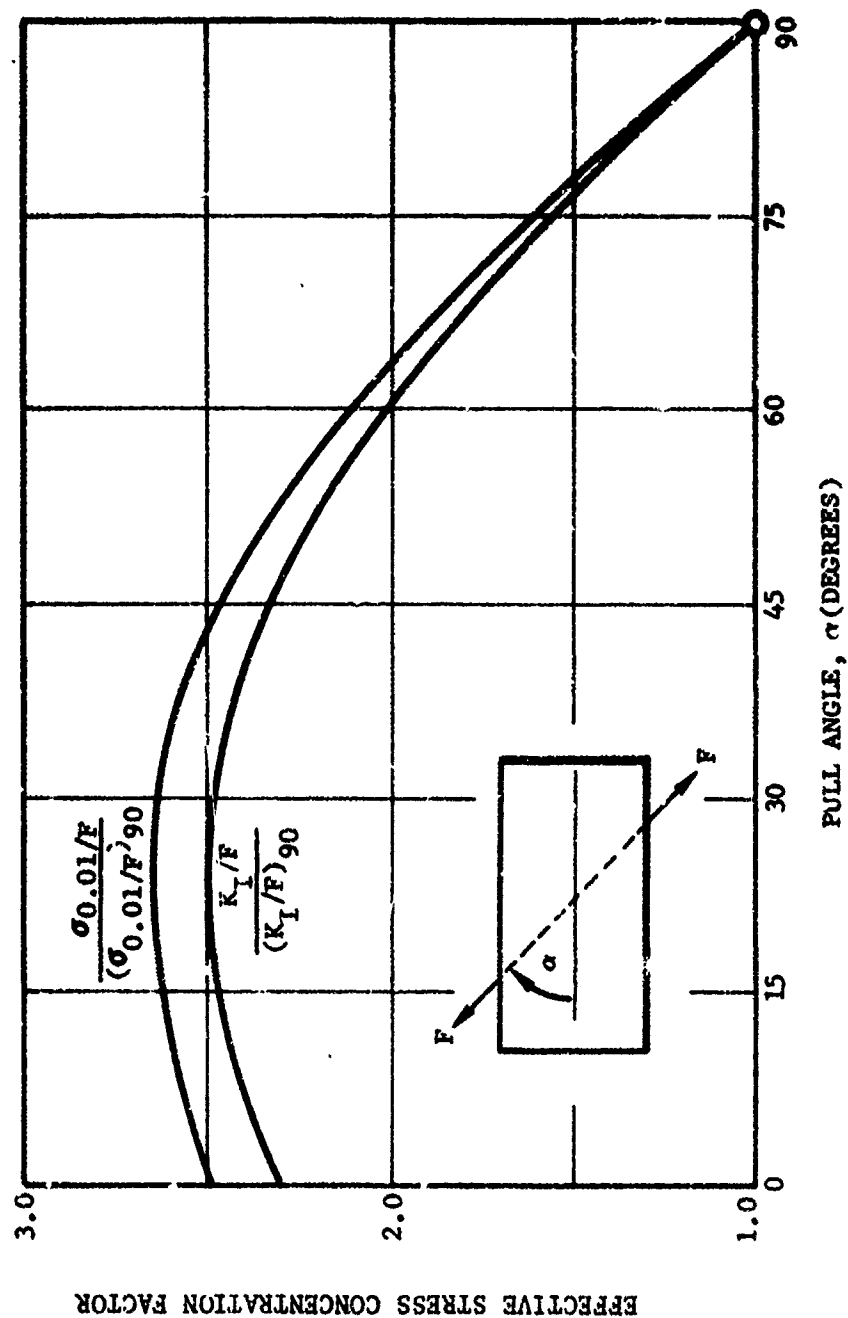
Figure 3-50. Effect of pull angle on the normal stress 0.01 inches from the corner and the K_I stress intensity factor for unit applied load on analog discontinuity sample ($K_L = 200$).
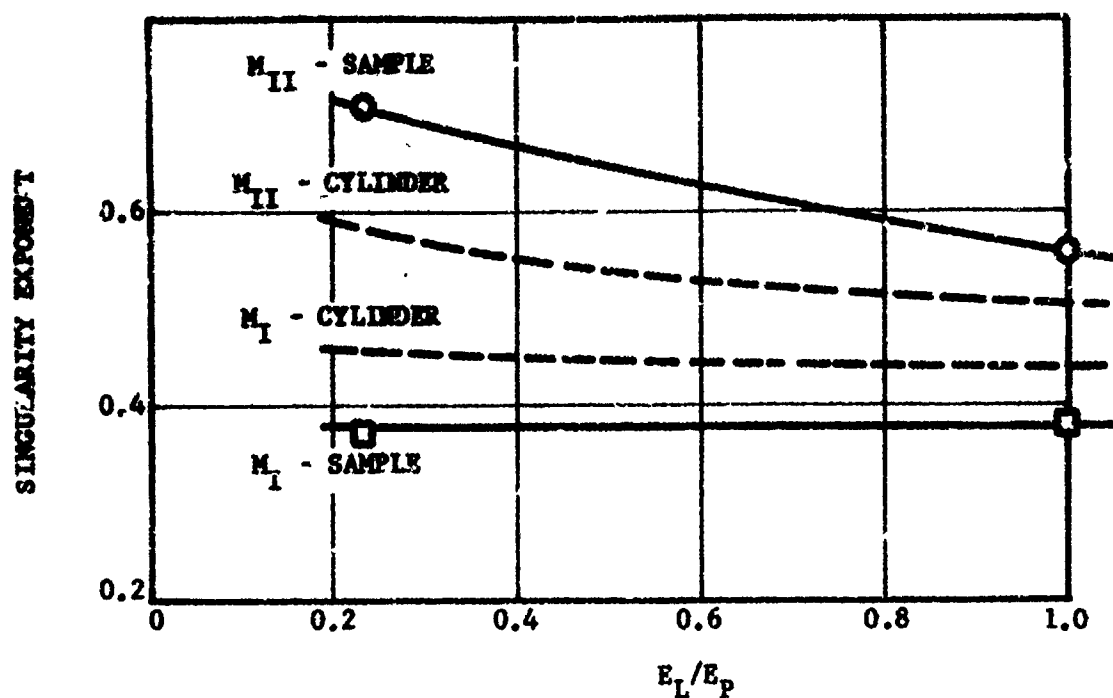
Figure 3-51a. Comparison of the effect of liner modulus on the singularity exponent for analog sample pulled in tension and cyliner.
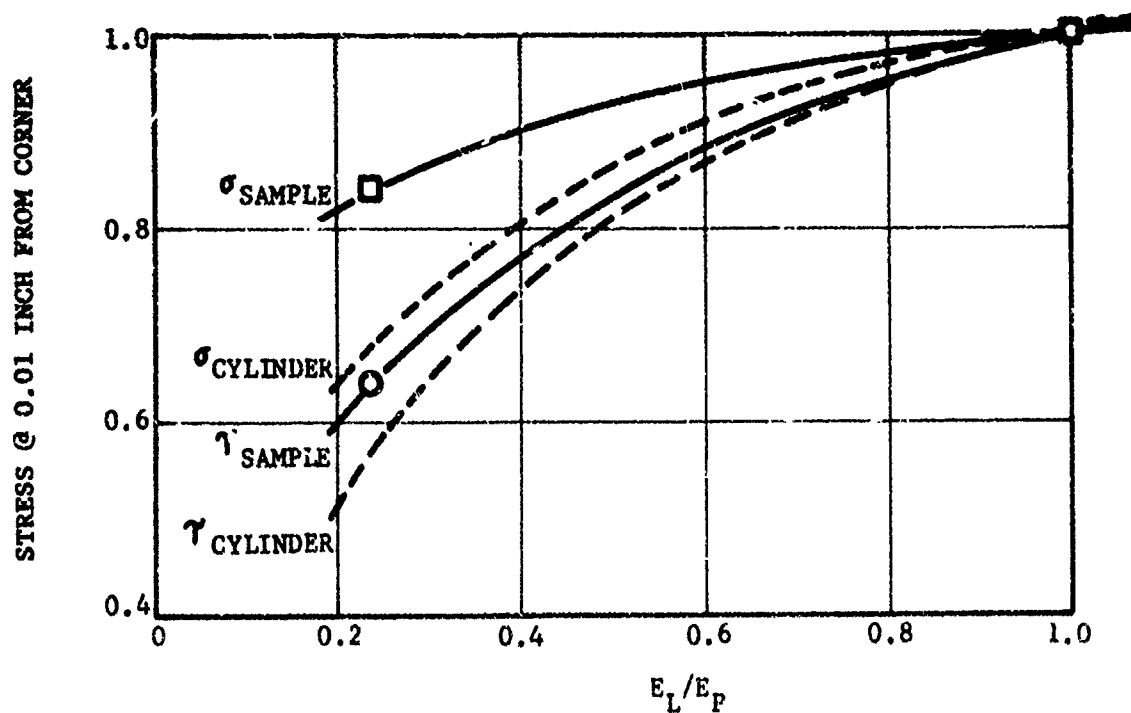
Figure 3-51b. Comparison of the effect of liner modulus on the normal and shear stresses at a distance 0.01 inches from the corner for analog sample pulled in tension and cylinder.
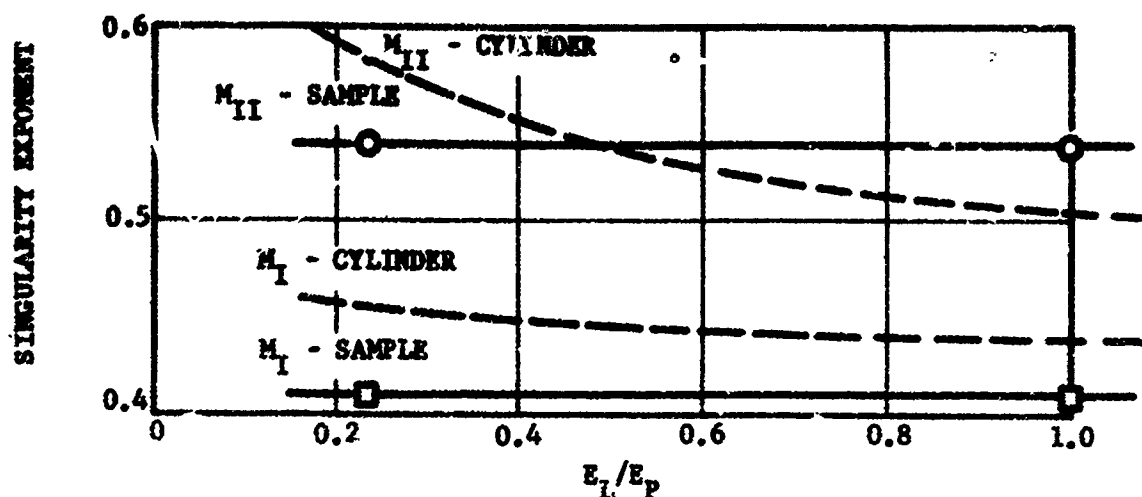
Figure 3-52a. Comparison of the effect of the liner modulus on the singularity exponent for analog sample pulled in shear and cylinder.
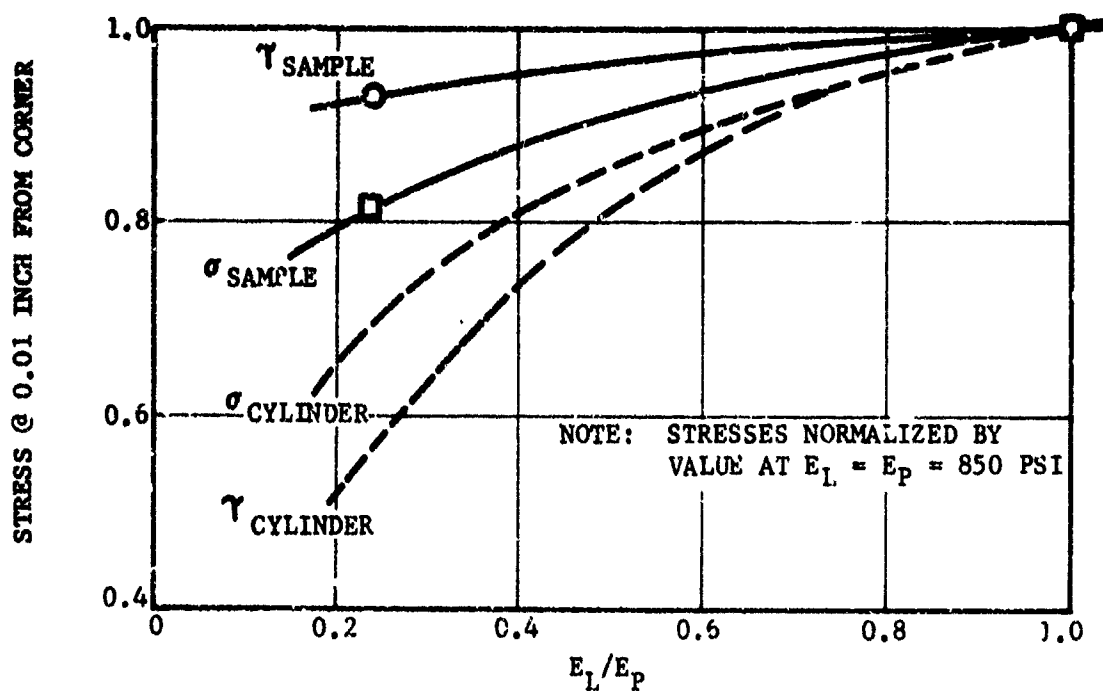
Figure 3-52b. Comparison of the effect of liner modulus on the normal and shear stresses at a distance 0.01 inches from the corner for analog sample pulled in shear and cylinder.

INSULATOR

LINER

PROPELLANT

NICK IN LINER

LINER NICK

INSULATOR

LINER

PROPELLANT

SMALL CORNER SEPARATION
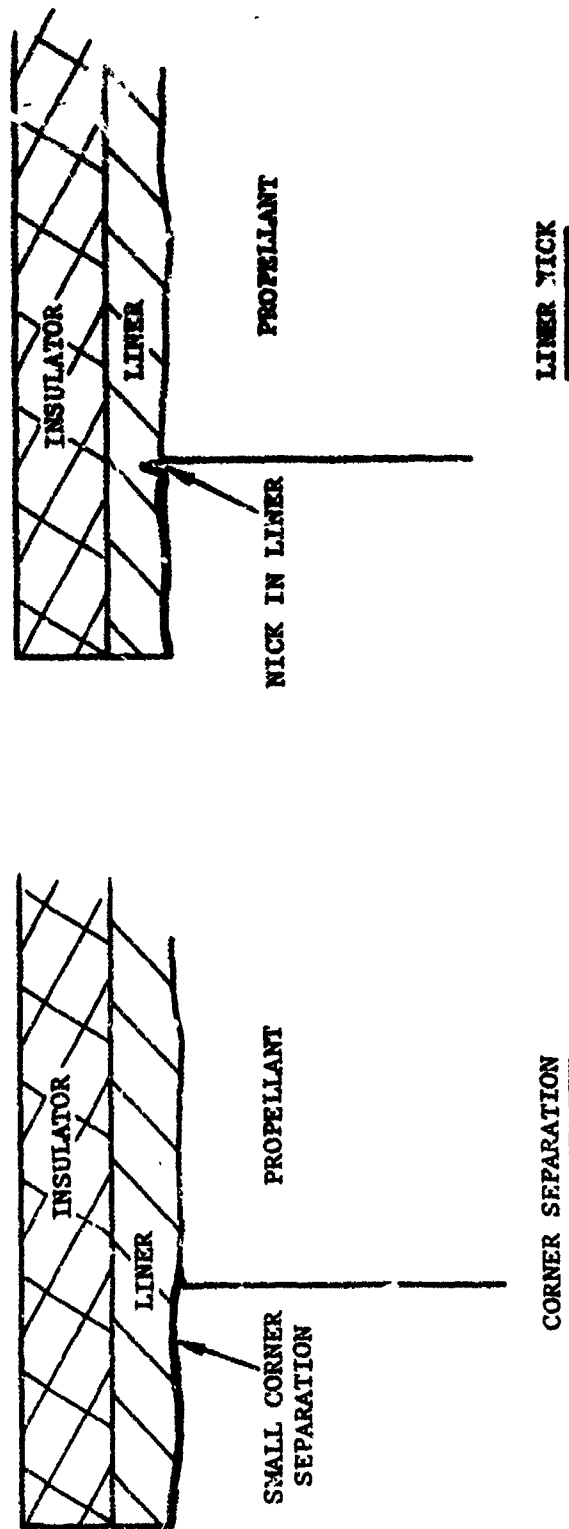
CORNER SEPARATION

Figure 3-53. Undesirable anomalies in the manufacturing of analog discontinuity samples.

BOND SEPARATION ∼ 0.5 INCH LONG

APPEARANCE OF BOND SEPARATION

LOAD

DISPLACEMENT

SAMPLE WITH INITIAL BOND SEPARATION

GOOD SAMPLE, WITHOUT INITIAL BOND SEPARATION
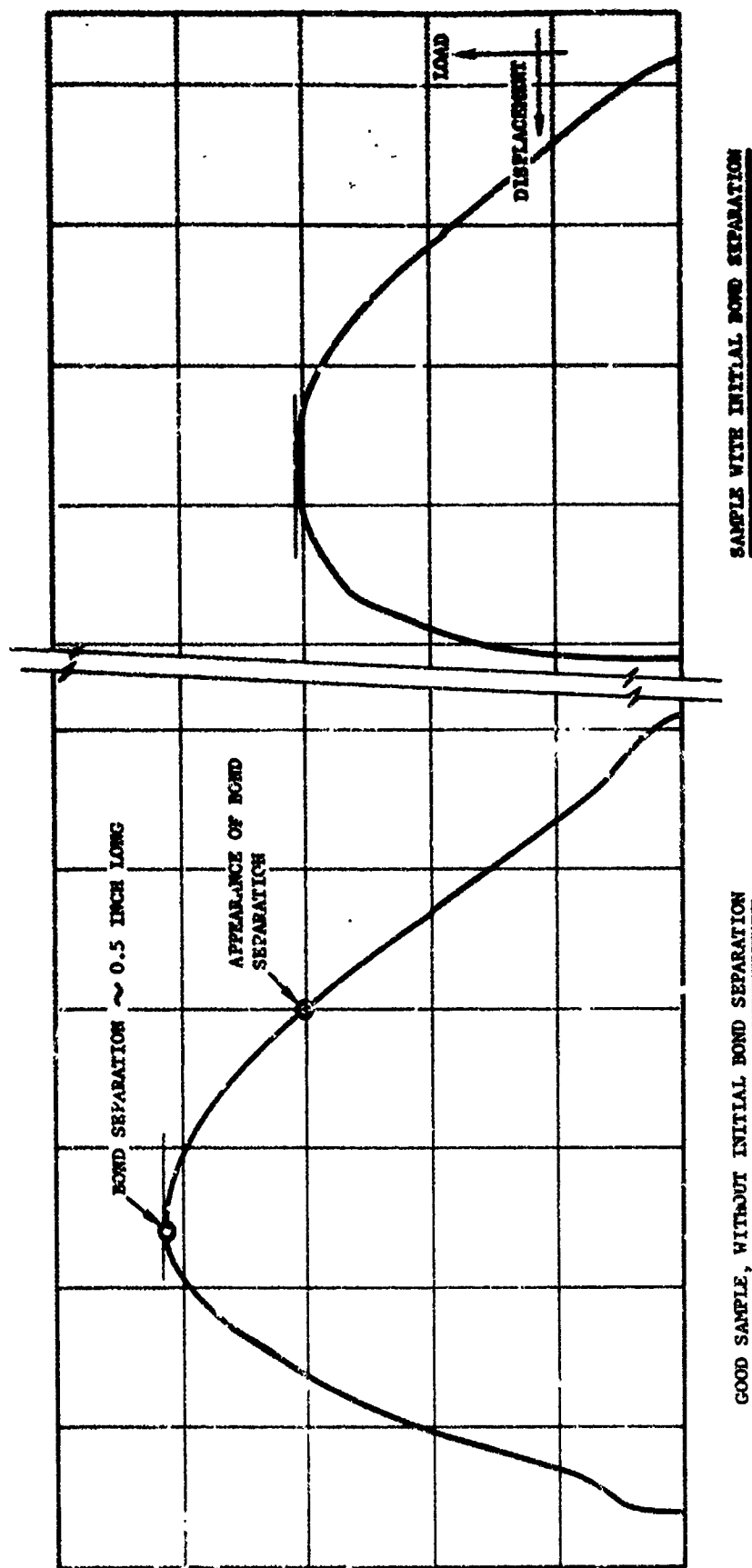
Figure 3-54. Comparison of strip-chart traces for TP-H1123 analog discontinuity samples with and without initial corner bond separations.
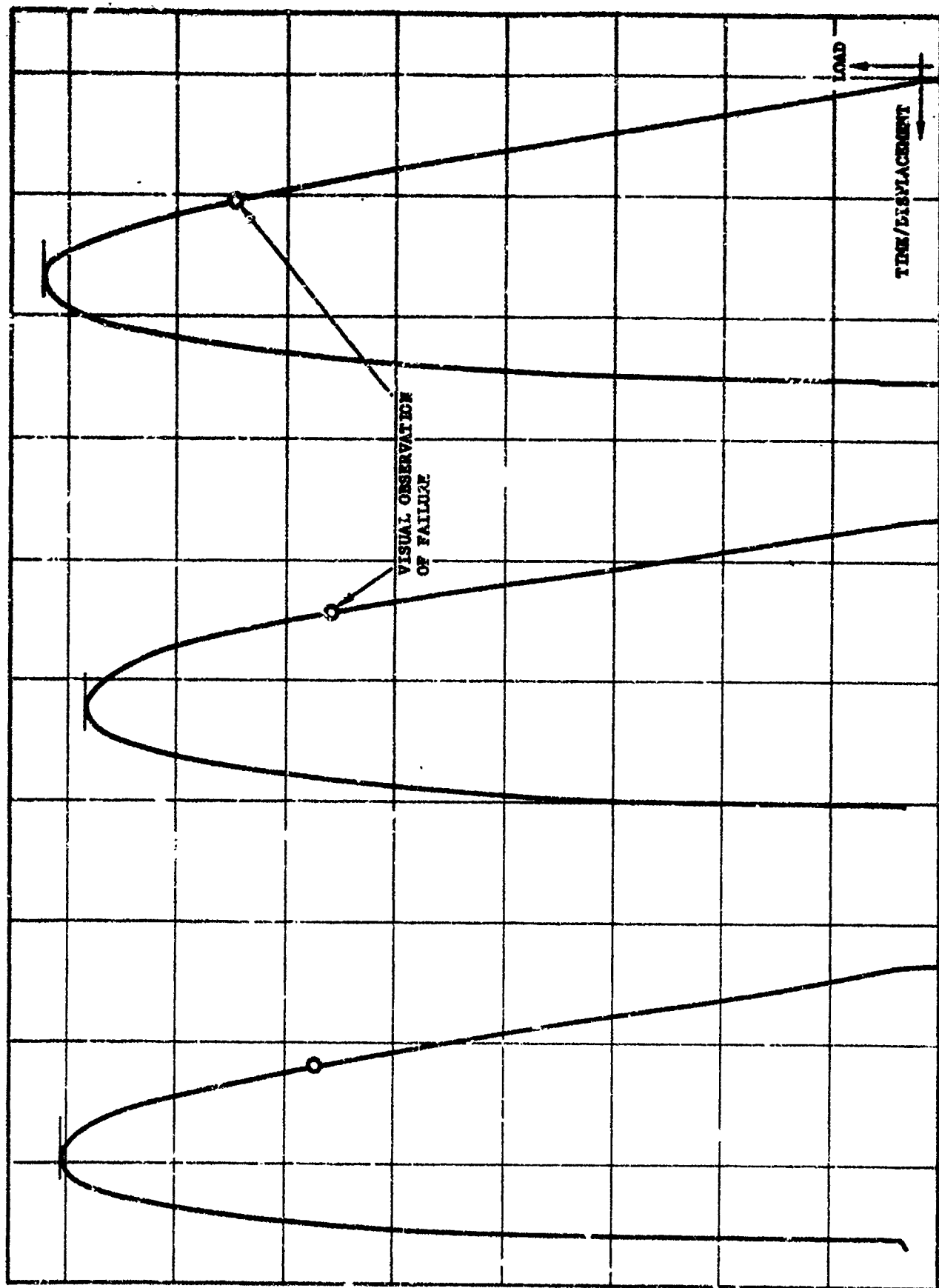
Figure 3-55. Strip-chart traces for analog discontinuity samples tested at 1.0 in./min.

200 PSI SUPERIMPOSED PRESSURE

NO SUPERIMPOSED PRESSURE

TIME TO FAILURE (MIN)
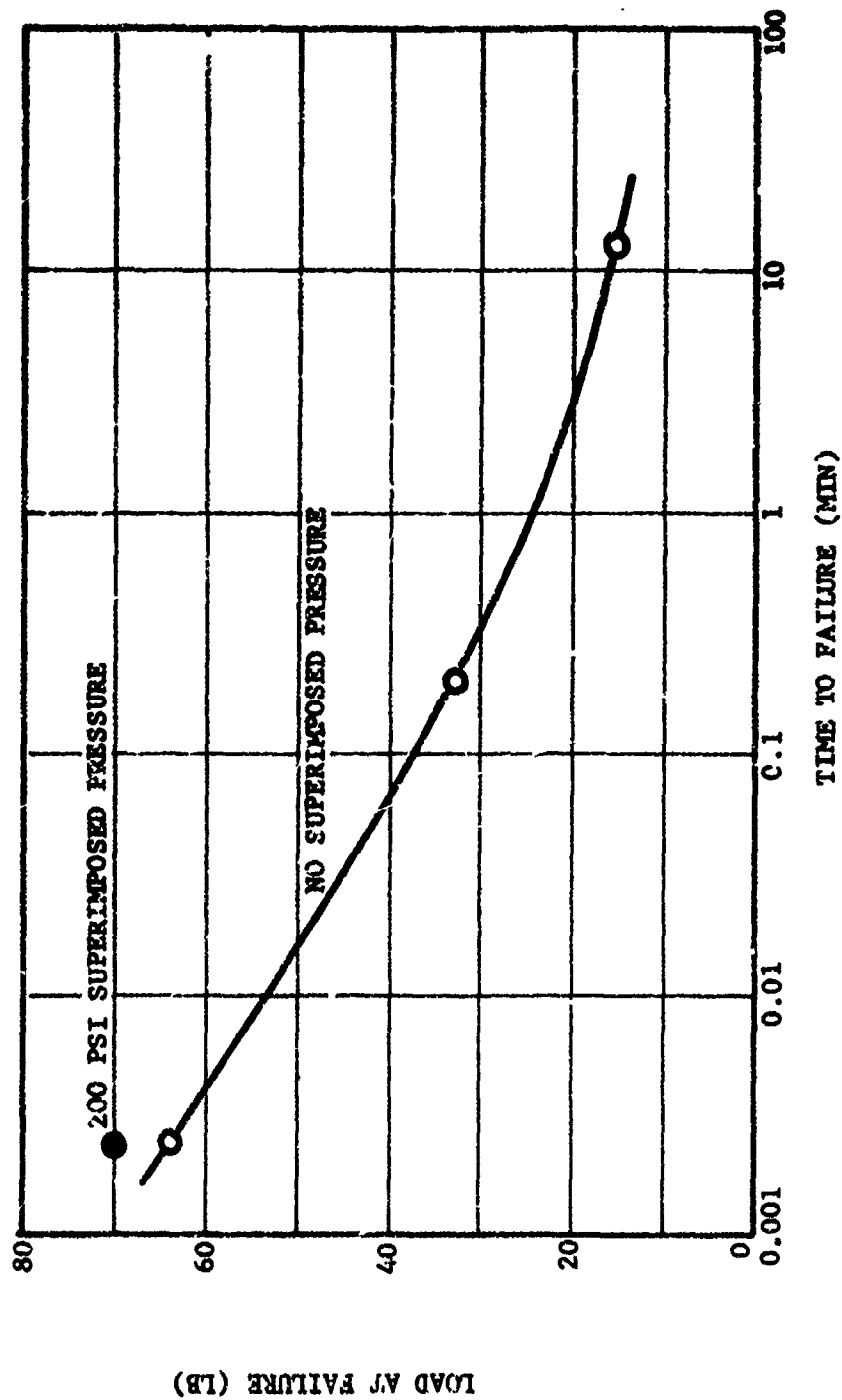
LOAD AT FAILURE (LB)

Figure 3-56. Load at failure for TP-H1123 analog discontinuity samples pulled in shear.
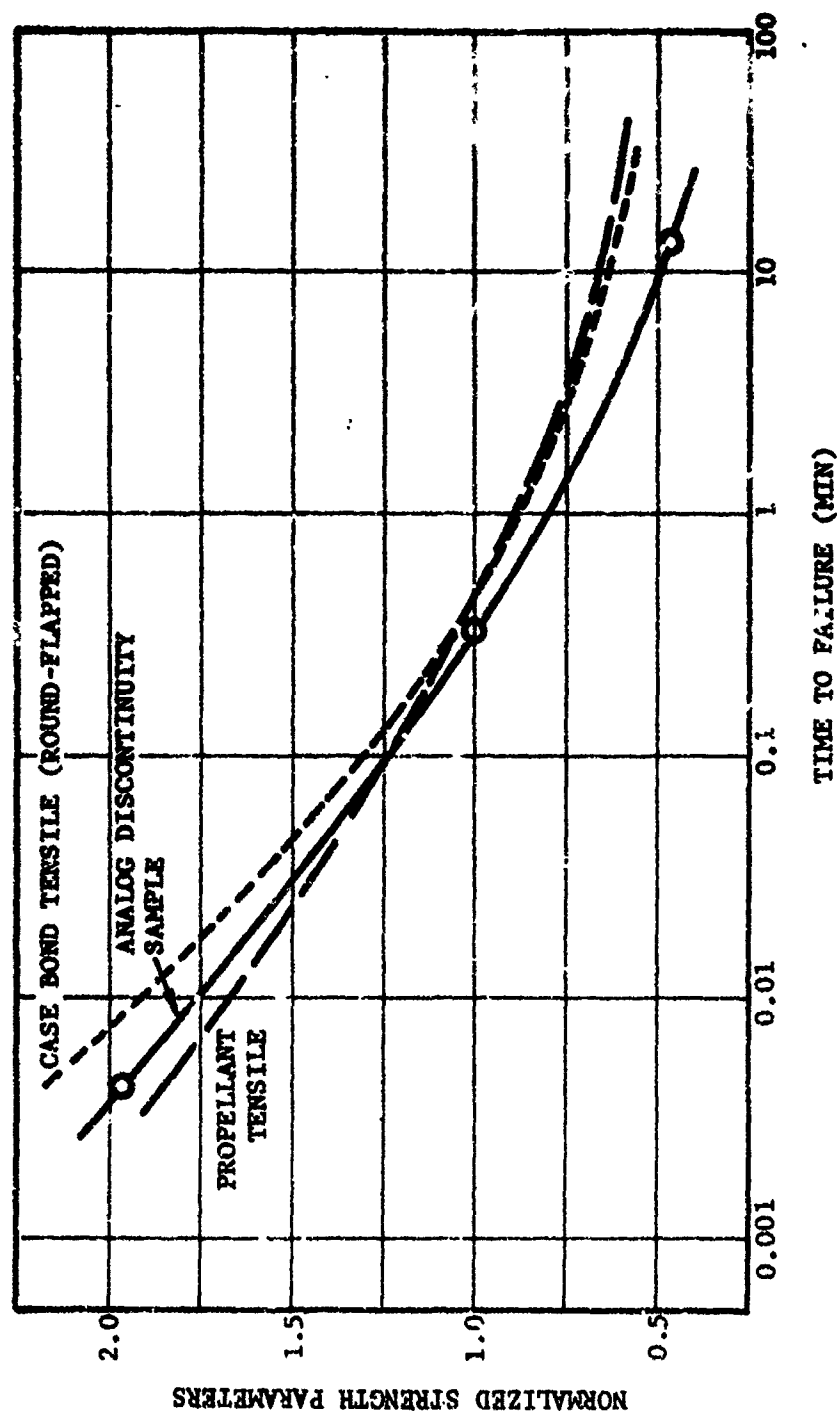
Figure 3-57. Time dependence of strength parameters for TP-H1123 propellant tensile, case bond tensile, and analog discontinuity samples.
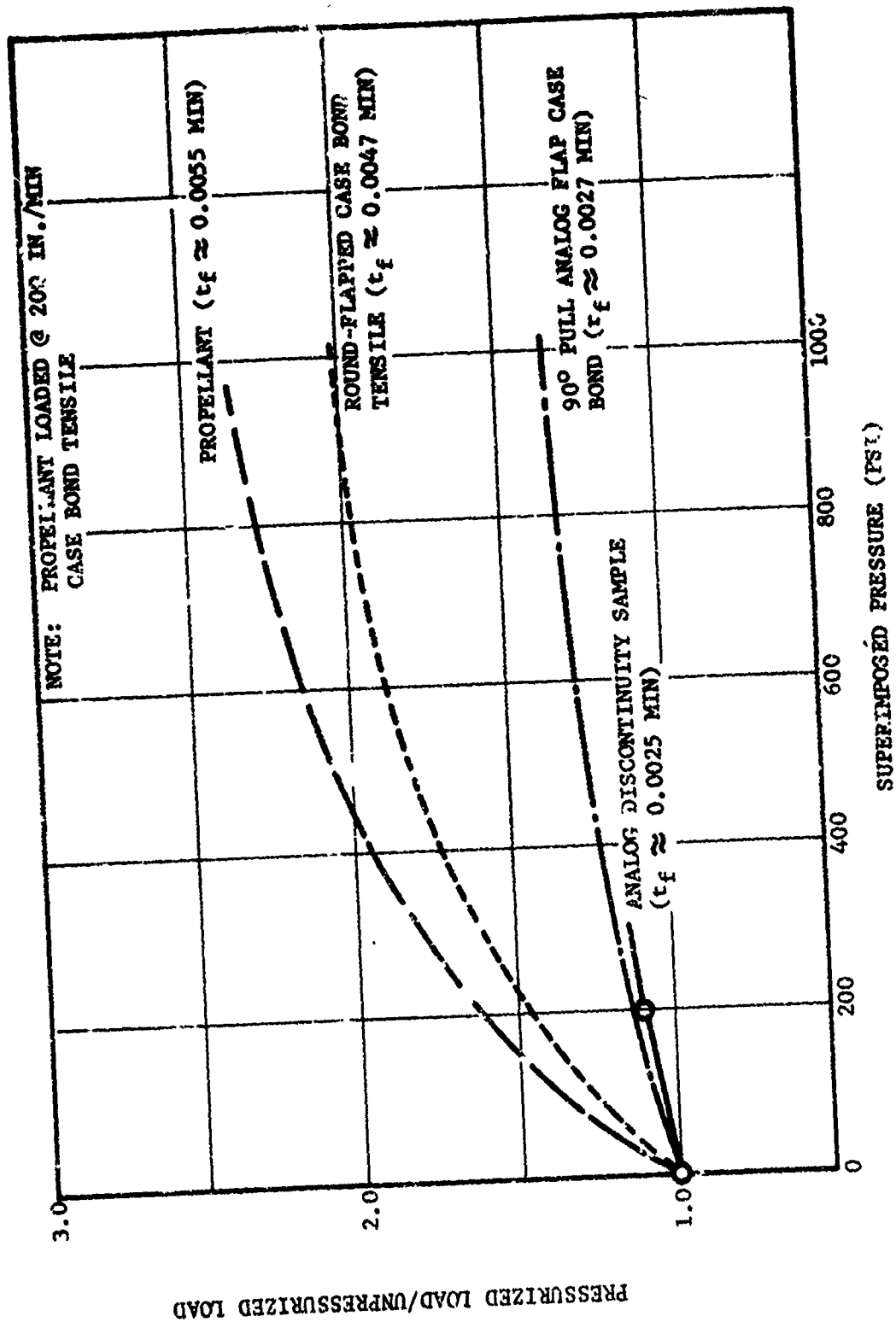
Figure 3-58. Effect of superimposed pressure on the load at failure for TP-H1123 propellant/case bond.

DETAIL A

INSULATOR

LINER

PROPELLANT

0.4

0.06

TP-H1123 PROPELLANT

DETAIL A

36

120

8
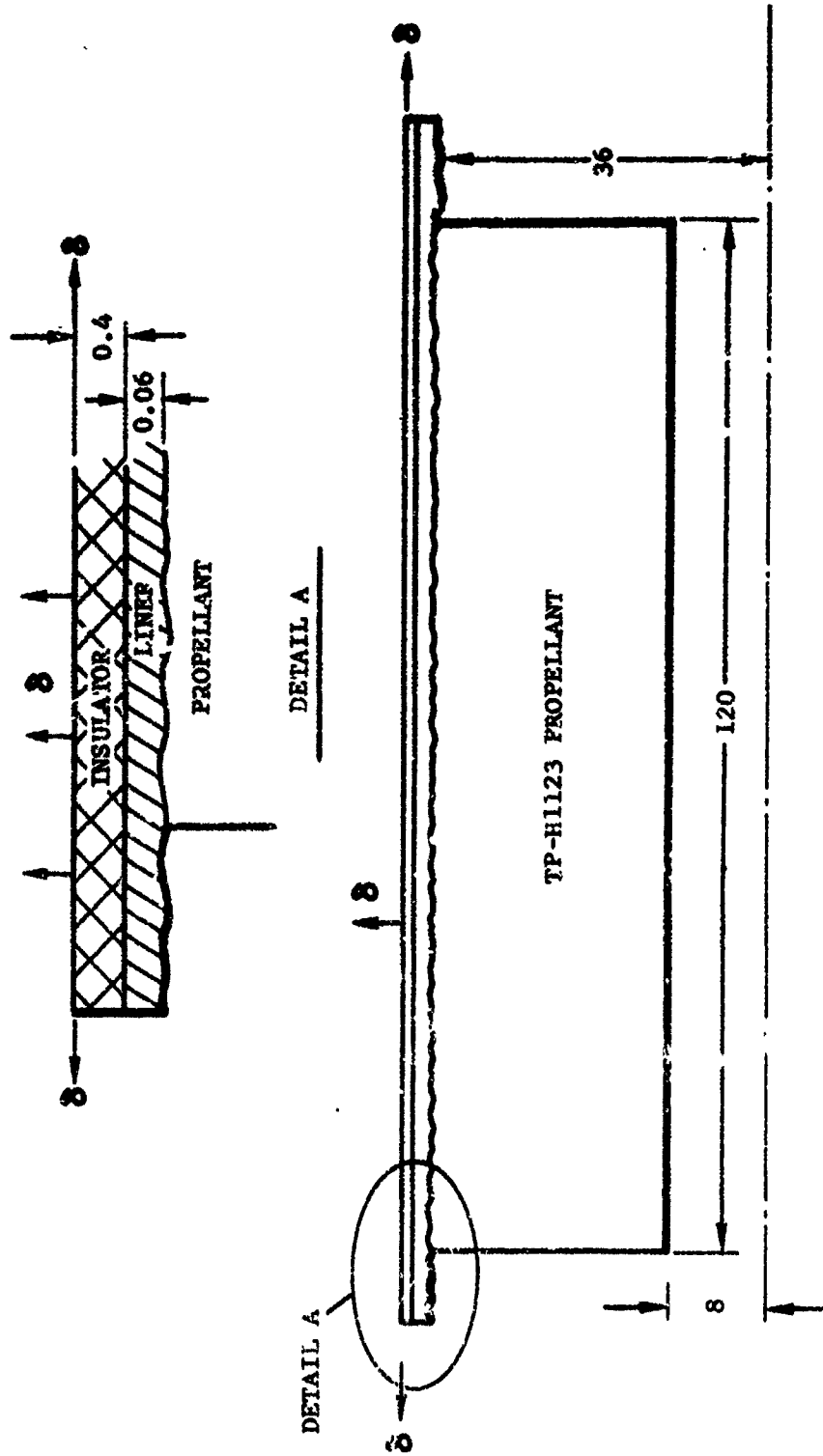
NOTES: 1. SUPERIMPOSED PRESSURE APPLIED AS A STRESS TO 200 PSI
2. $\delta(t) = 0.1t$ FOR t IN MINUTES

Figure 3-59. Motor example for determination of case bond integrity at right-angle corners.
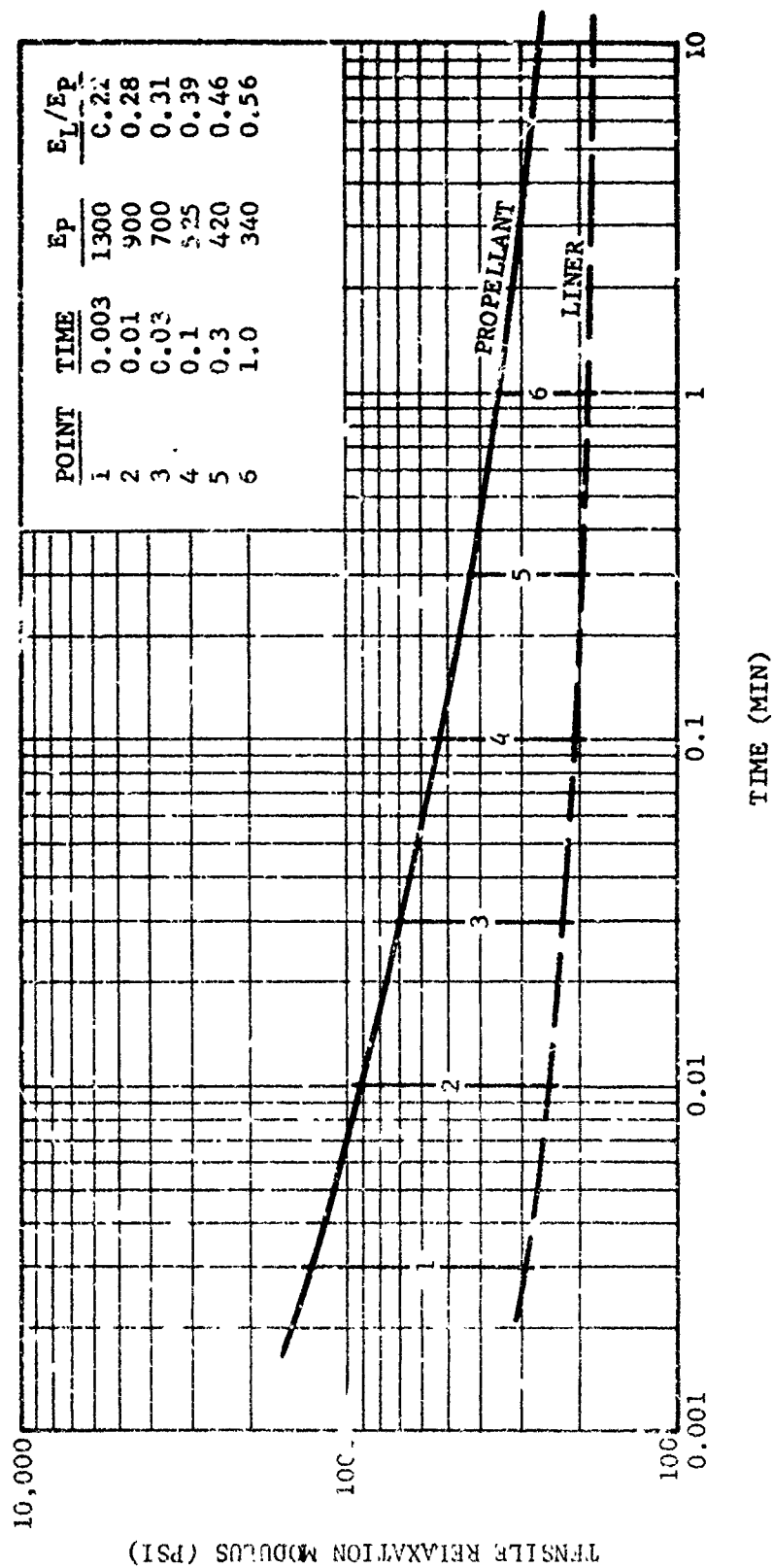
Figure 3-60. Assumed tensile relaxation moduli for propellant and liner in example motor.

POINT	TIME	E_P	E_L/E_P
1	0.003	1300	C.2?
2	0.01	900	0.28
3	0.03	700	0.31
4	0.1	525	0.39
5	0.3	420	0.46
6	1.0	340	0.56

TIME (MIN)

TENSILE RELAXATION MODULUS (PSI)
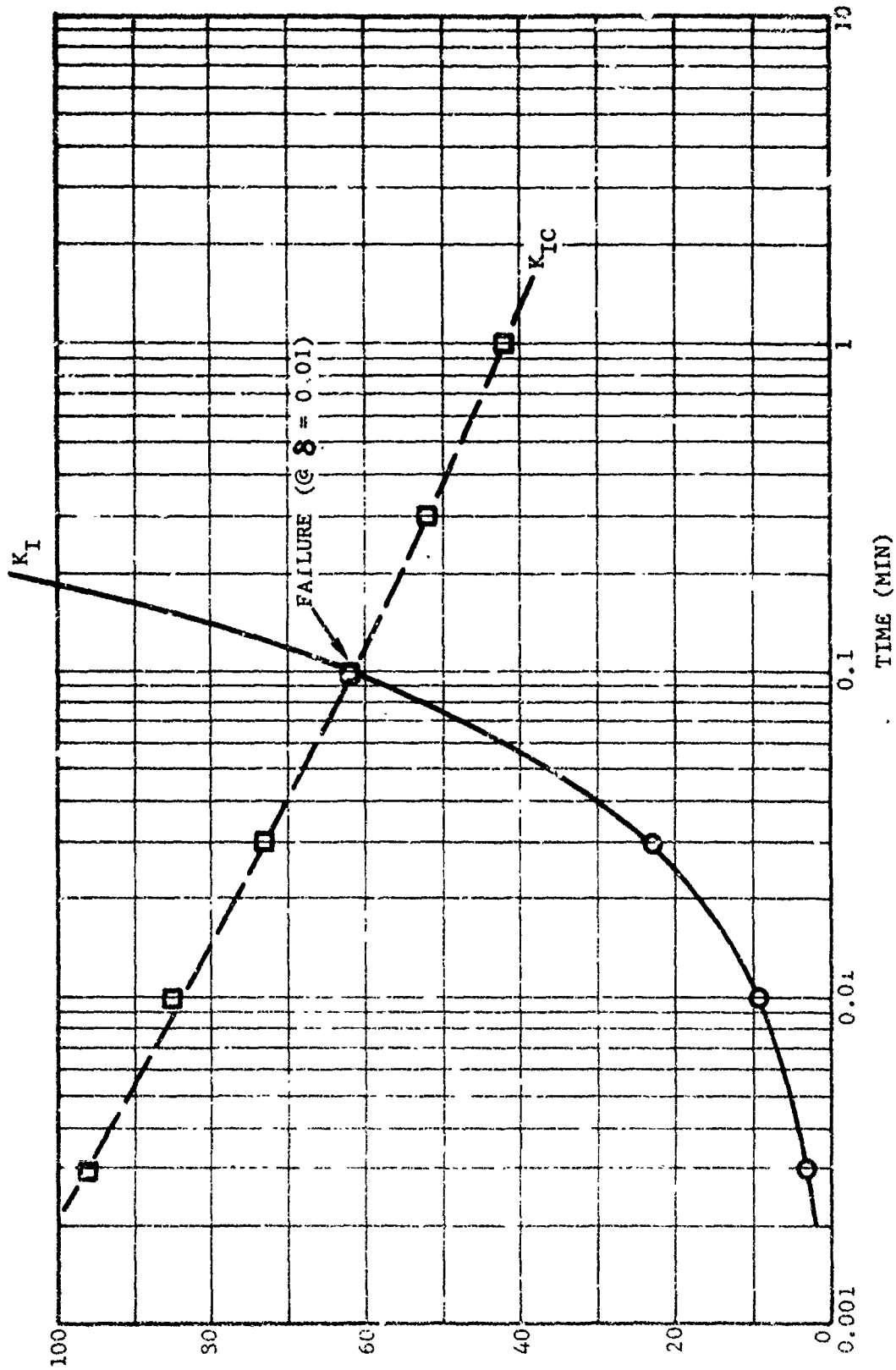
Figure 3-61. Time-dependent stress intensity factors for right-angle corner in example motor problem.
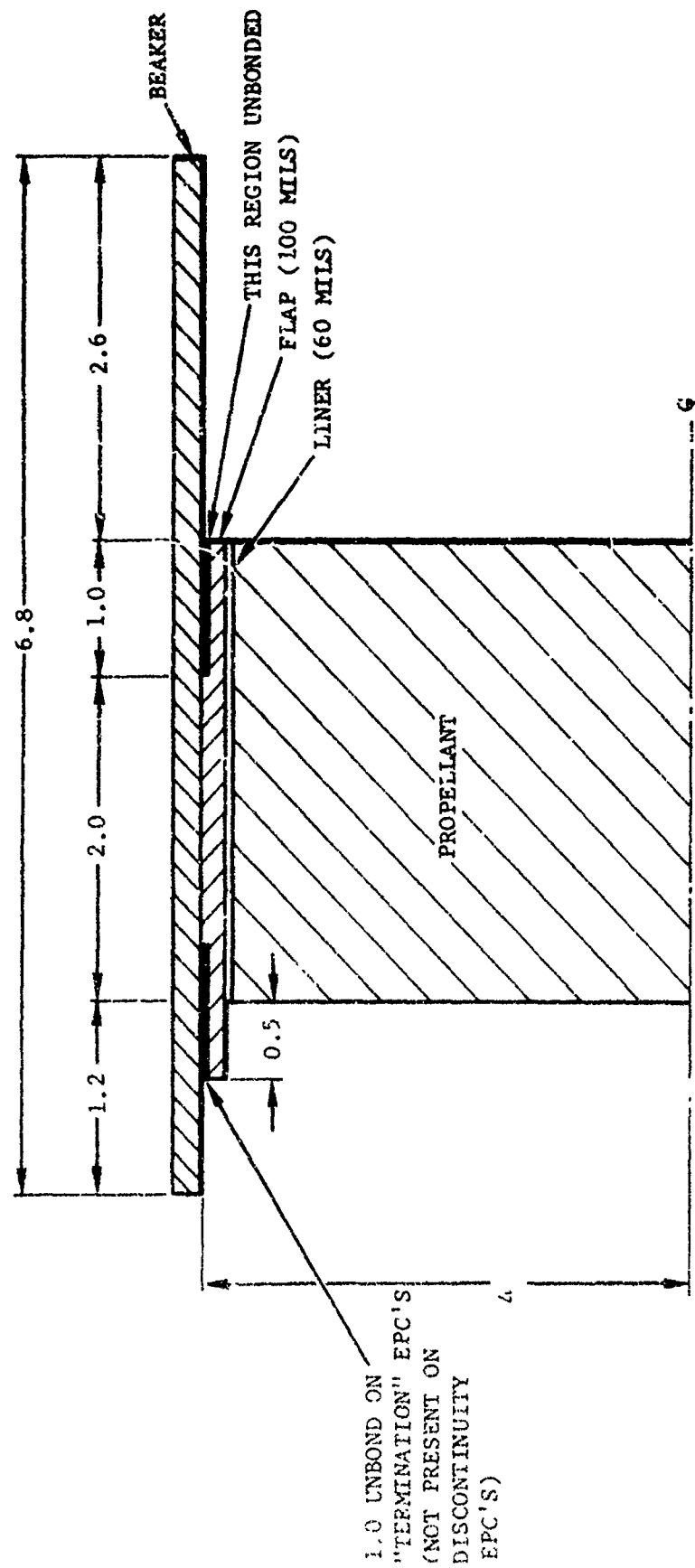
Figure 4-1. End-pressurized cylinder configuration.

BEAKER

THIS REGION UNBONDED

FLAP (100 MILS)

LINER (60 MILS)

PROPELLANT

6.8

2.6

1.0

2.0

1.2

0.5

NOTE: ALL DIMENSIONS ARE IN INCHES
UNLESS OTHERWISE SPECIFIED

1.0 UNBOND ON
"TERMINATION" EPC'S
(NOT PRESENT ON
DISCONTINUITY
EPC'S)
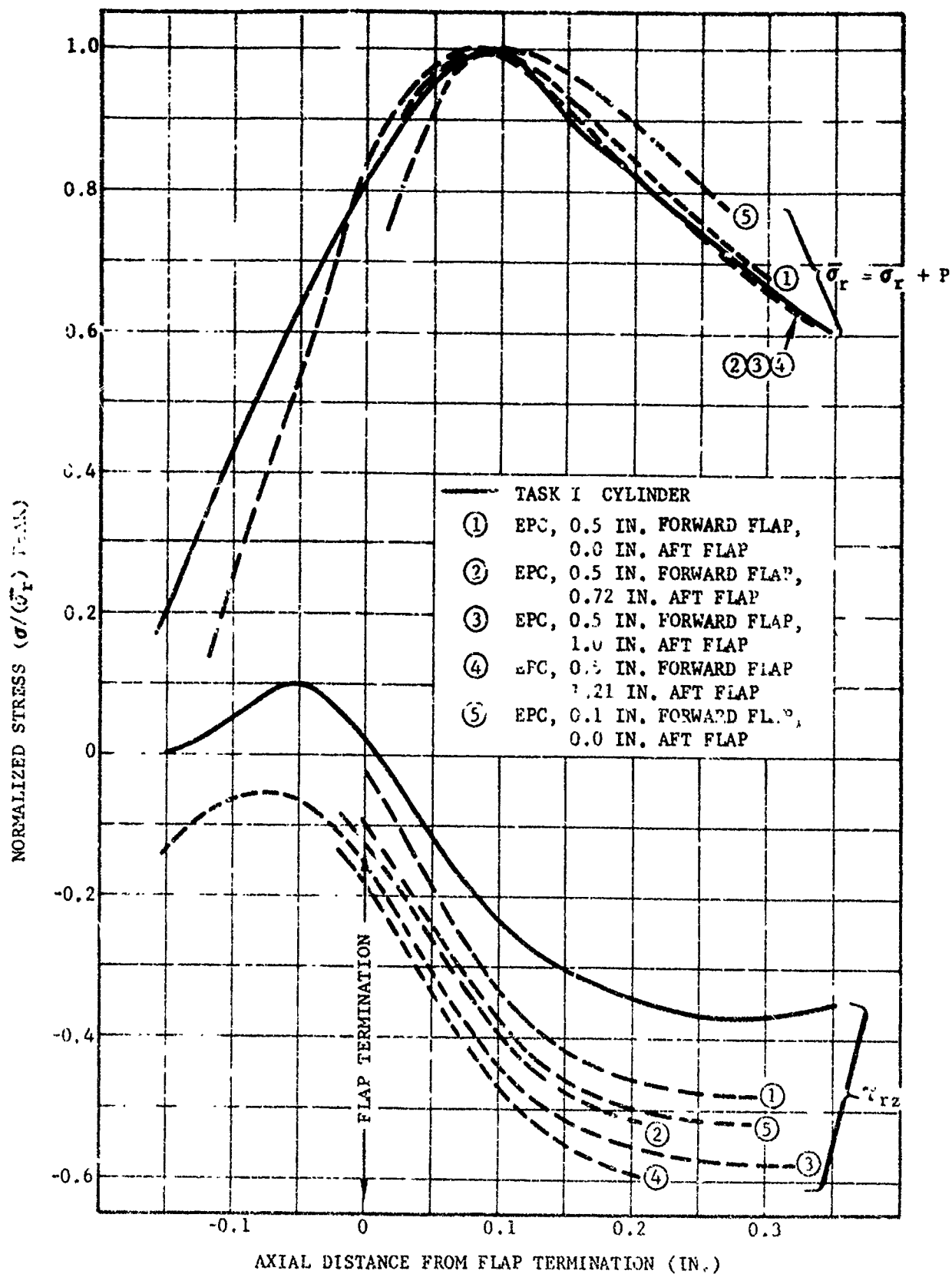
Figure 4-2. Comparison of stress distributions for various flapped EPC geometries with solution for Task I cylinder.
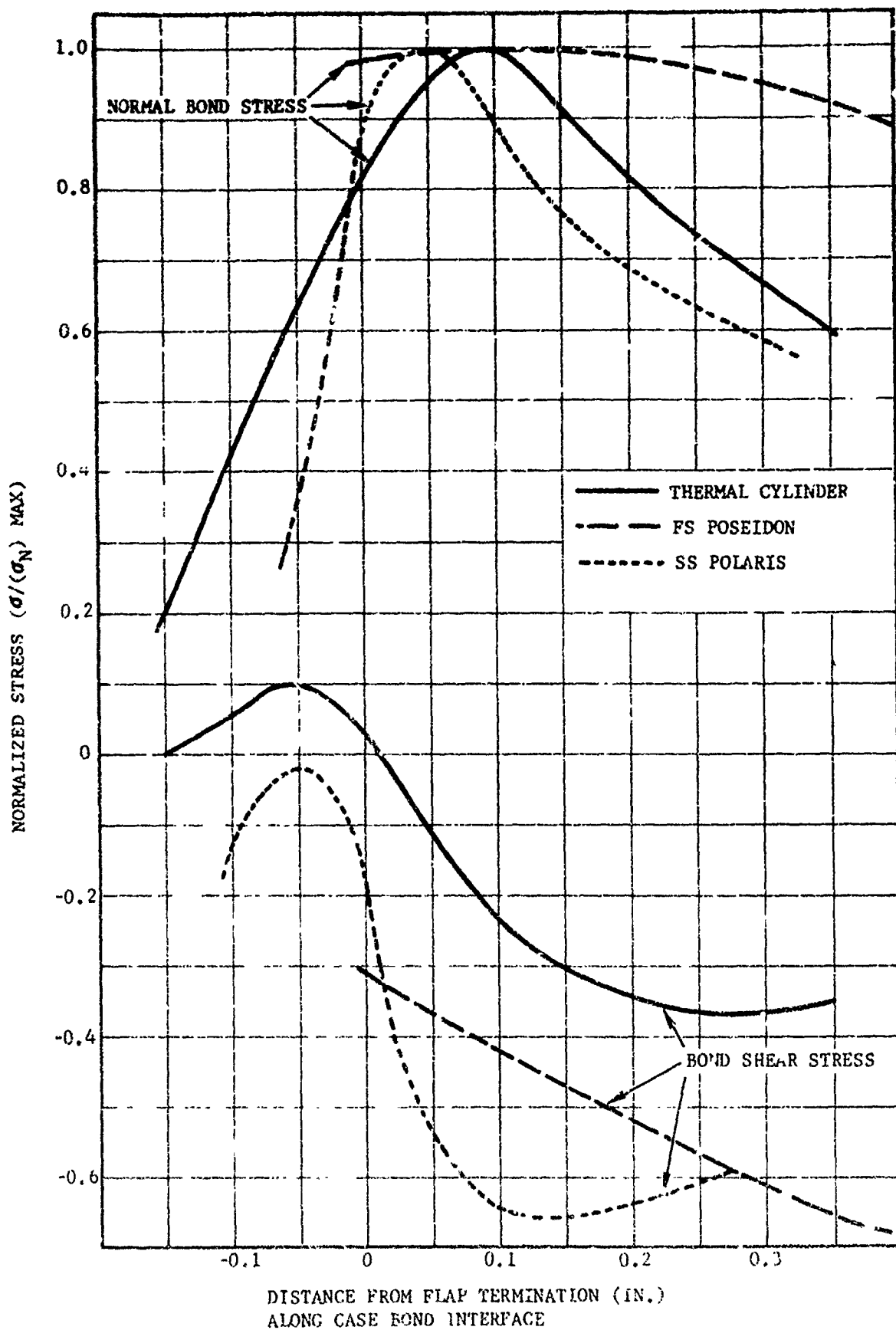
Figure 4-3. Comparison of case bond stress distributions in the FS Poseidon and SS Polaris motors with that of the thermal cylinder.
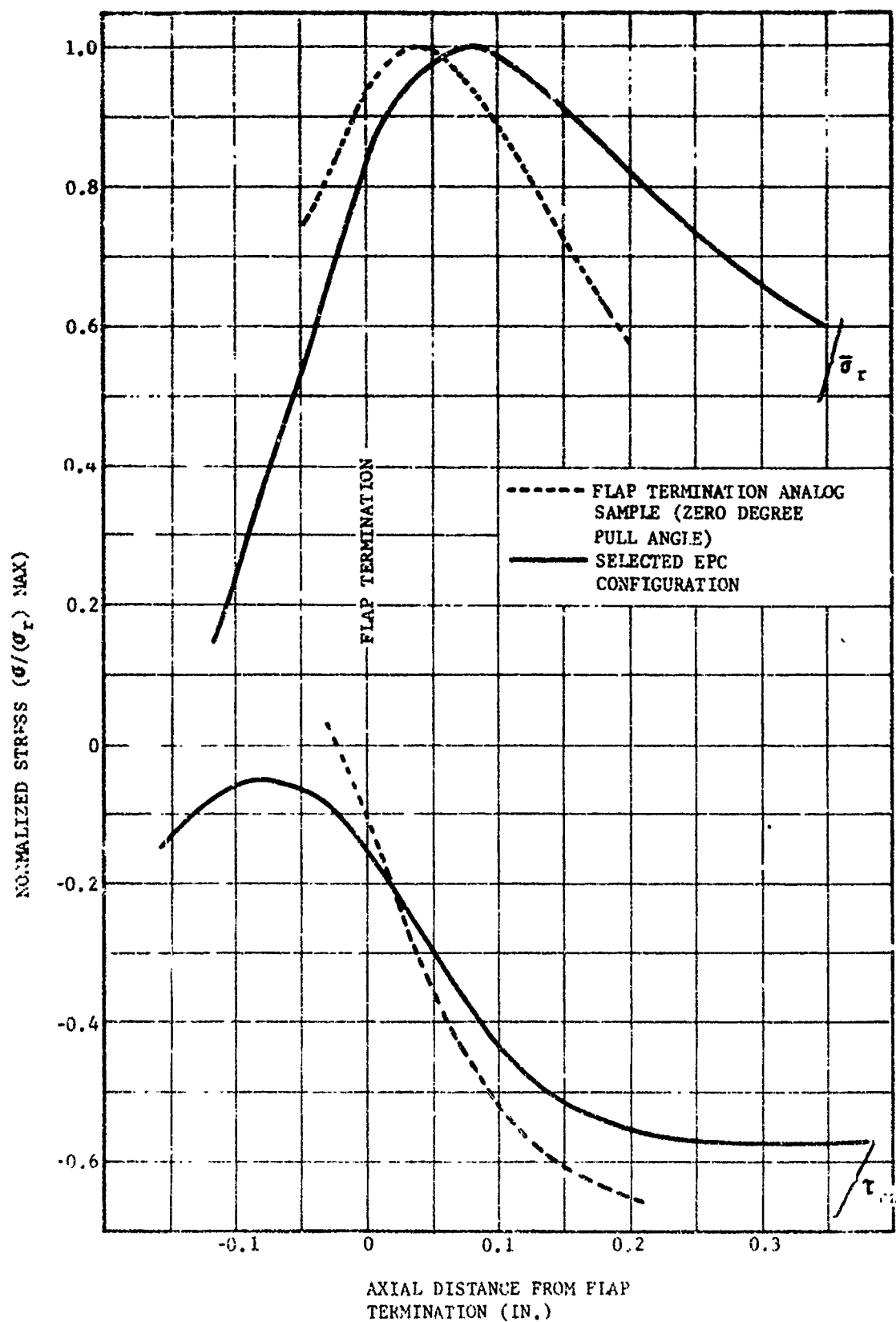
Figure 4-4. Comparison of stress distributions in selected EPC and analog flap termination sample (zero degree pull angle).
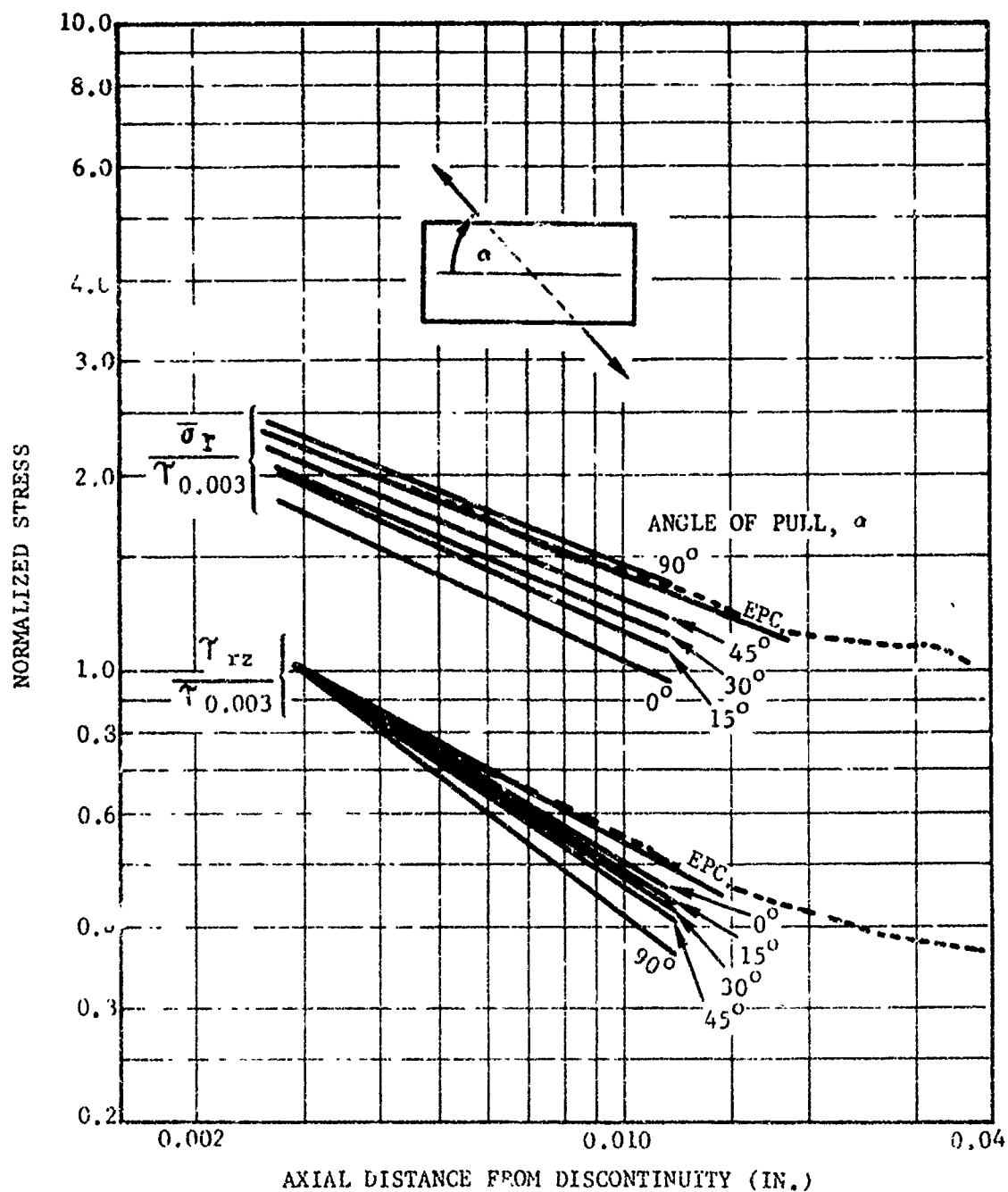
Figure 4-5. Normalized propellant stresses in analog discontinuity samples and discontinuity EPC as a function of axial distance from the discontinuity.

285
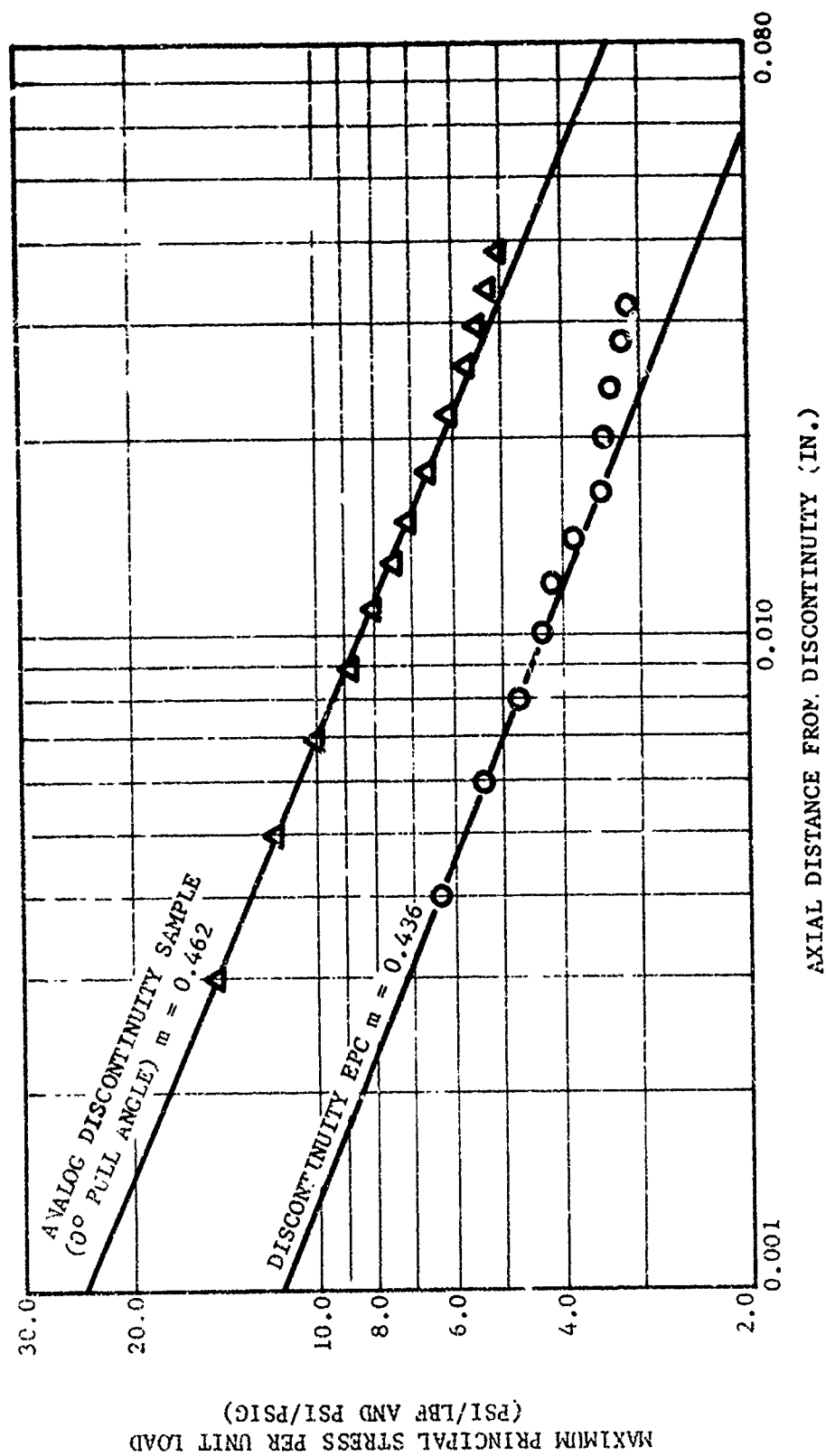
Figure 4-6. Propellant effective maximum principal stresses in analog discontinuity sample (zero degree pull angle) and discontinuity EPC as a function of axial distance from the discontinuity.

286

Figure 4-7. Details of EPC beakers following case preparation procedures.

DISCONTINUITY CYLINDER

TERMINATION CYLINDER
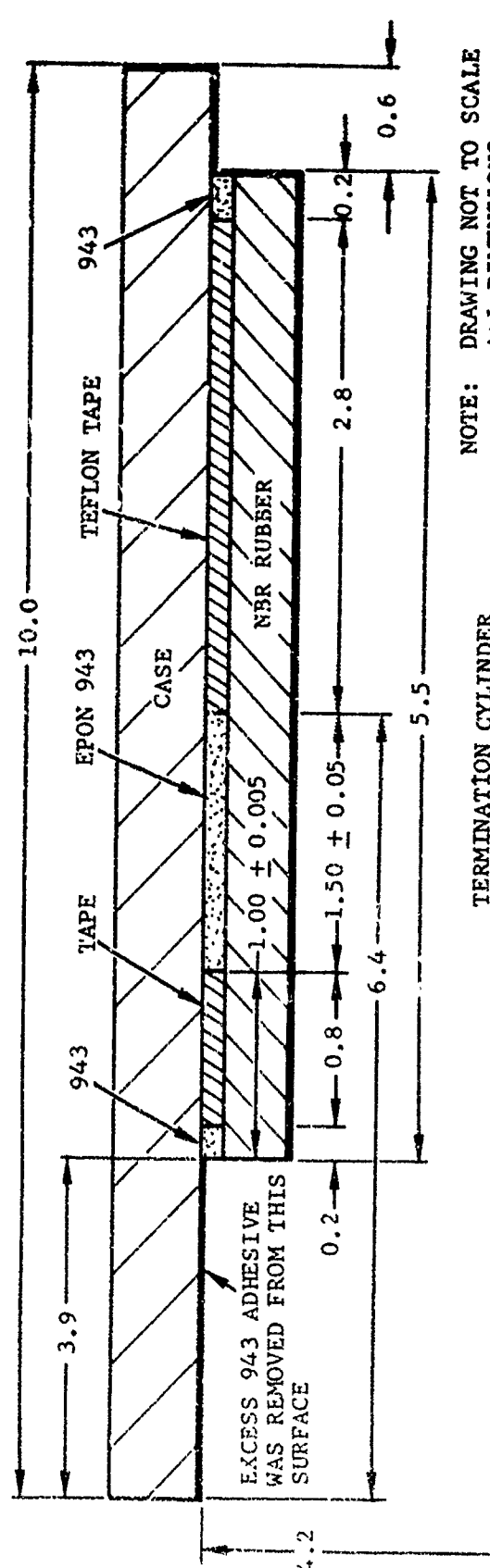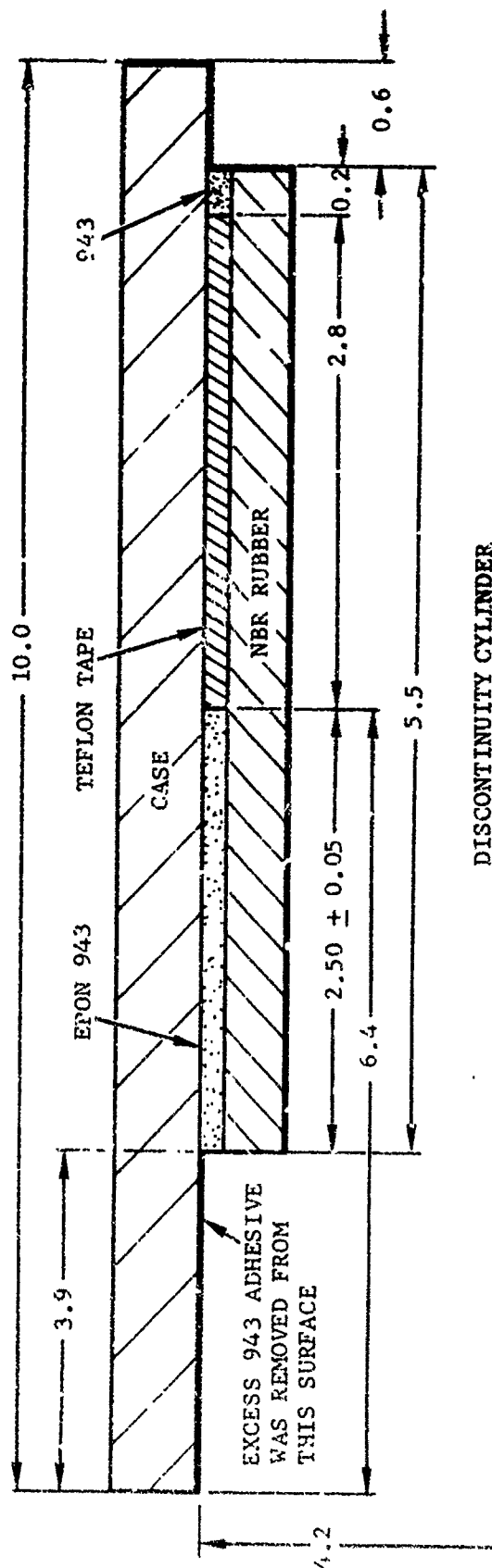
NOTE: DRAWING NOT TO SCALE
ALL DIMENSIONS
IN INCHES

NOTE: ALL DIMENSIONS ARE IN INCHES
UNLESS OTHERWISE SPECIFIED

1.75 ON "DISCONTINUITY" EPC'S
1.375 ON "TERMINATION" EPC'S

ITEM NO.   DESCRIPTION
1.   TABER PRESSURE GAGE
2.   HOOP STRAIN GAGES (8 PLACES. 45° APART)
3.   LINEAR POTENTIOMETER (4 PLACES, 90° APART)
4.   LINEAR POTENTIOMETER (1 PLACE)
5.   LINEAR POTENTIOMETER (1 PLACE)

Figure 4-10. EPC high rate pressurization instrumentation.
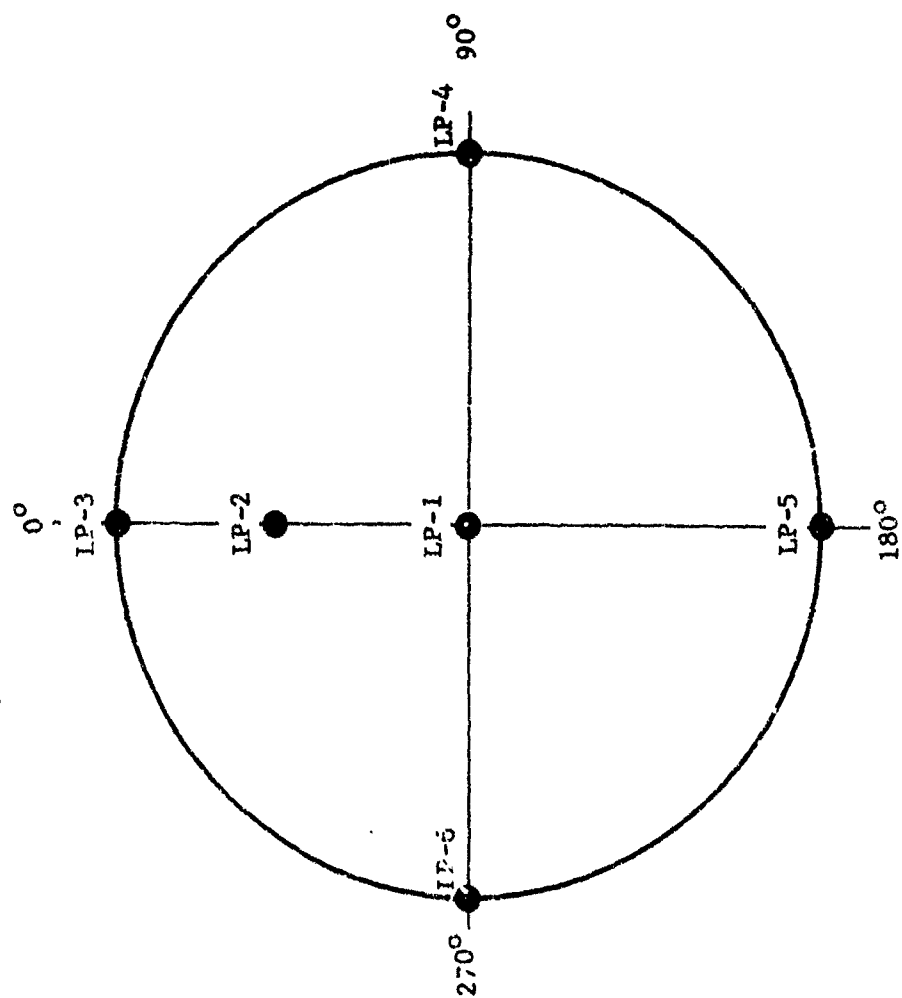
Figure 4-11. EPC linear potentiometer instrumentation location.

ITEM NO.	DESCRIPTION	FUNCTION
1	SUBSCALE MOTOR	TEST ITEM
2	AFT ALUMINUM END PLATE	HOLD MOTOR AND INSTRUMENTATION
3	FWD ALUMINUM END PLATE	HOLD MOTOR
4	TABER PRESSURE GAGE	CHAMBER PRESSURE
5	TEE AND PLUG	BLEED HOLE
6	FLEXIBLE HOSE	PIPING
7	NEEDLE VALVE	REGULATE PRESSURIZATION RATE
8	OIL FILL PIPE AND PLUG	FILL SYSTEM WITH OIL
9	ASCO SOLENOID	EXHAUST AND DRAIN SYSTEM
10	PNEUMATIC VALVE	PRESSURIZE MOTOR
11	ASCO SOLENOID	INITIATE PNEUMATIC VALVE REMOTELY
12	PRESSURE REGULATOR	CONTROL PRESSURE TO PNEUMATIC VALVE
13	NITROGEN TANK	SUPPLY DRIVING PRESSURE
14	TABER PRESSURE GAGE	DRIVING PRESSURE
15	ASCO SOLENOID	CONTROL DRIVING PRESSURE REMOTELY
16	PRESSURE VESSEL	PROVIDE DRIVING FORCE
17	PRESSURE REGULATOR	REGULATE DRIVING PRESSURE

BRIEF DESCRIPTION OF OPERATION

THE SYSTEM IS FILLED WITH MINERAL OIL ON THE MOTOR SIDE OF VALVE 10. THIS IS DONE BY FILLING AT 8 AND BLEEDING AT 5. PRESSURE VESSEL 16 IS THEN PRESSURIZED WITH NITROGEN TO THE DESIRED DRIVING PRESSURE BY ACTUATING VALVE 15 REMOVELY AND MONITORING THE PRESSURE RISE ON 14. WHEN 16 REACHES THE PRESSURE DESIRED, 15 IS CLOSED AND MOTOR PRESSURIZATION IS ACCOMPLISHED BY ACTUATING THE RAPID OPENING VALVE 10. THE SYSTEM IS THEN EXHAUSTED BY OPENING VALVE 9.
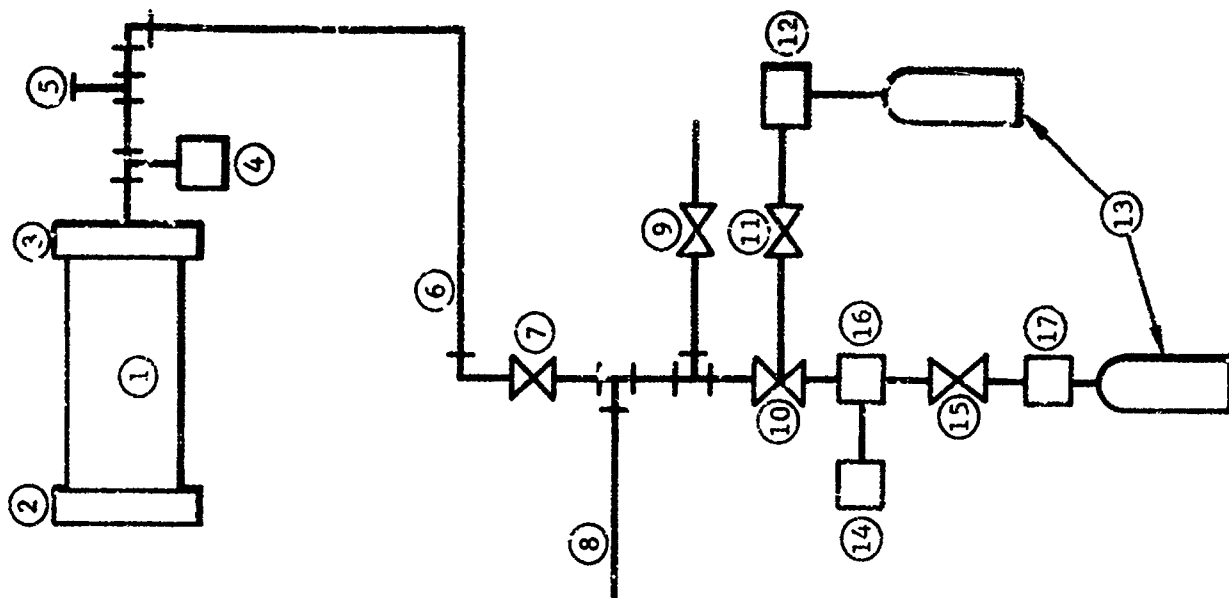
Figure 4-12. EPC pressurization system.

292
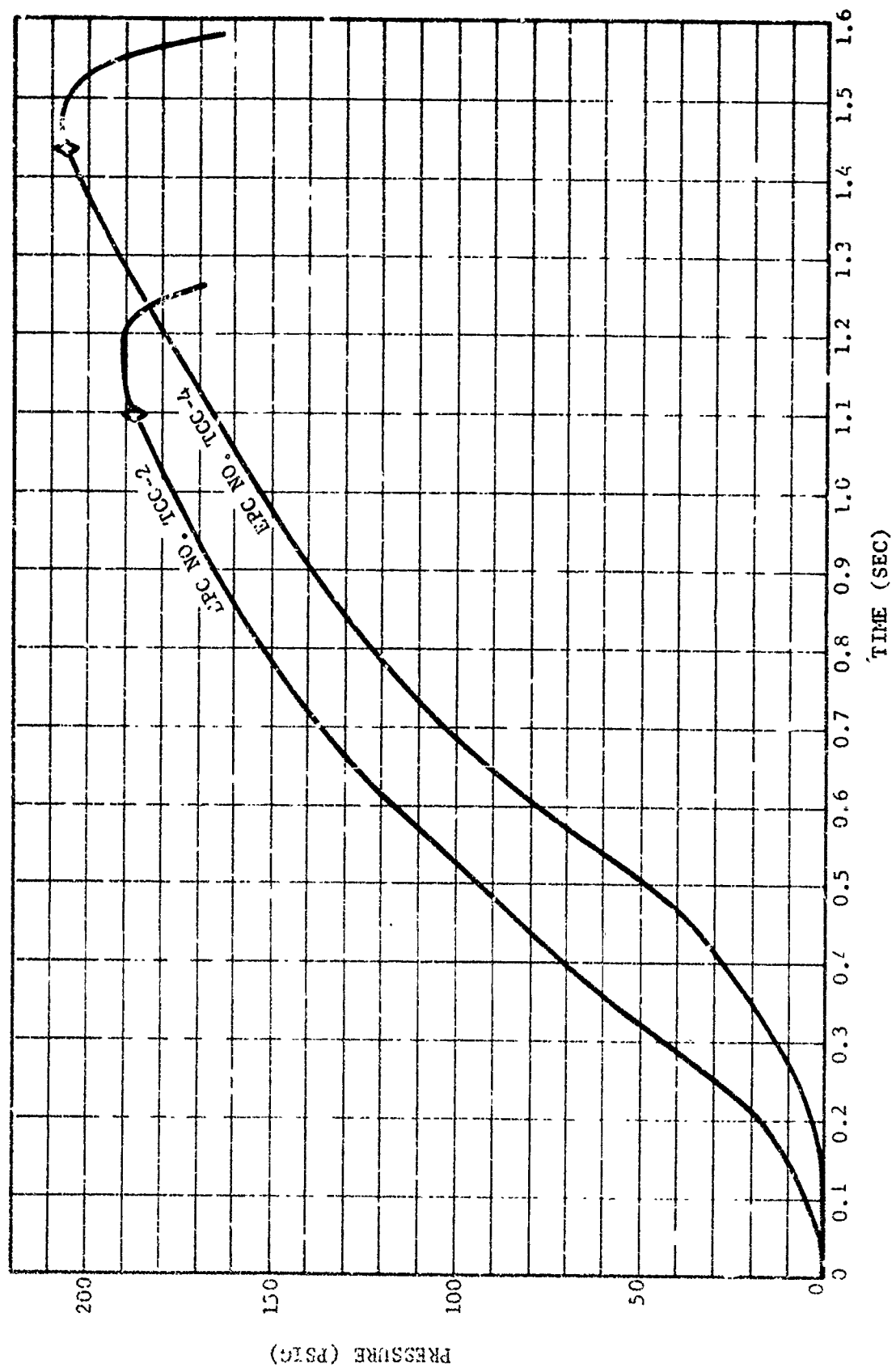
Figure 4-13. Hydrostatic pressure transients for flap termination EPC tests.

293
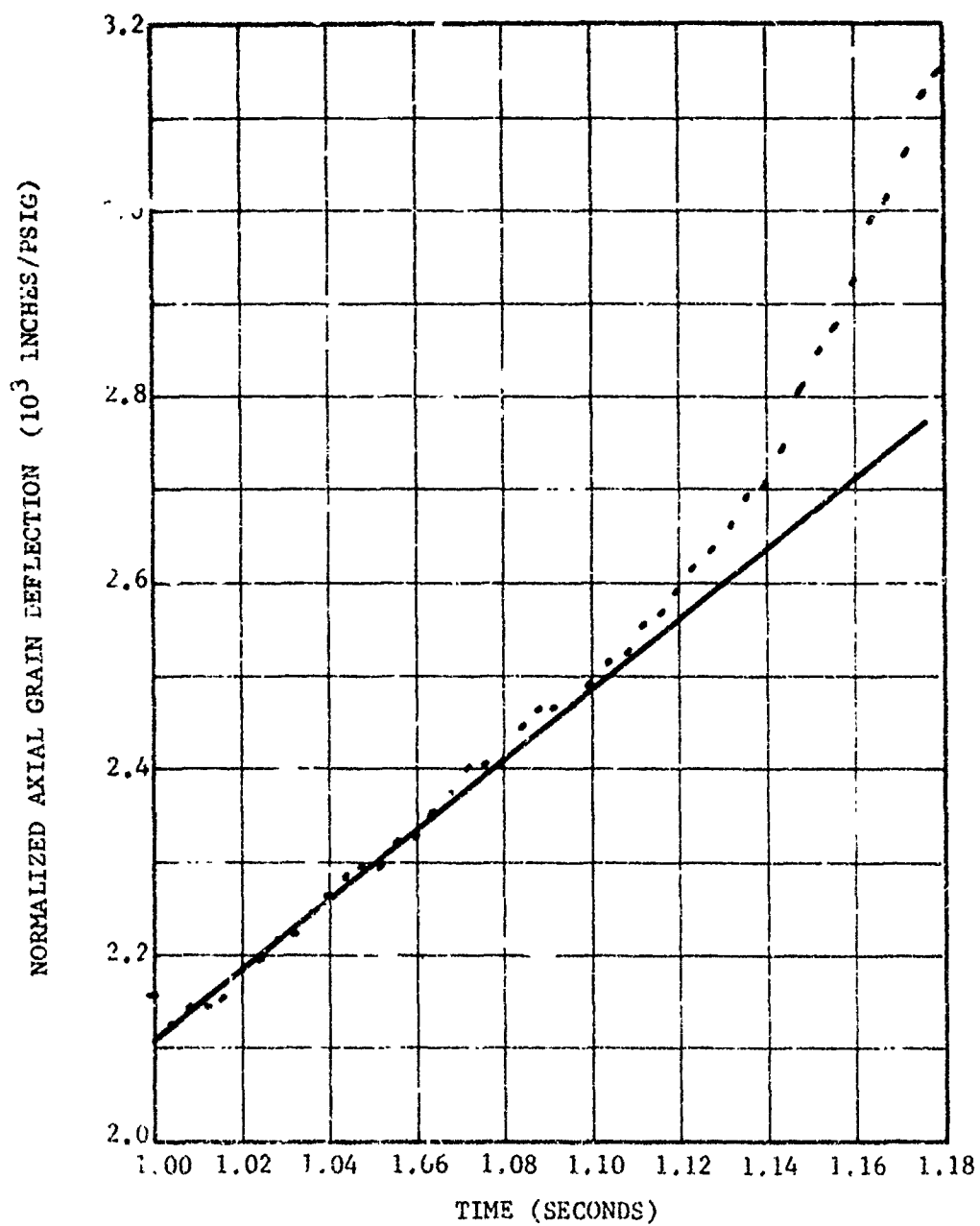
Figure 4-14. Normalized axial grain deflection versus time from linear potentiometer number five on flap termination EPC TCC-2.
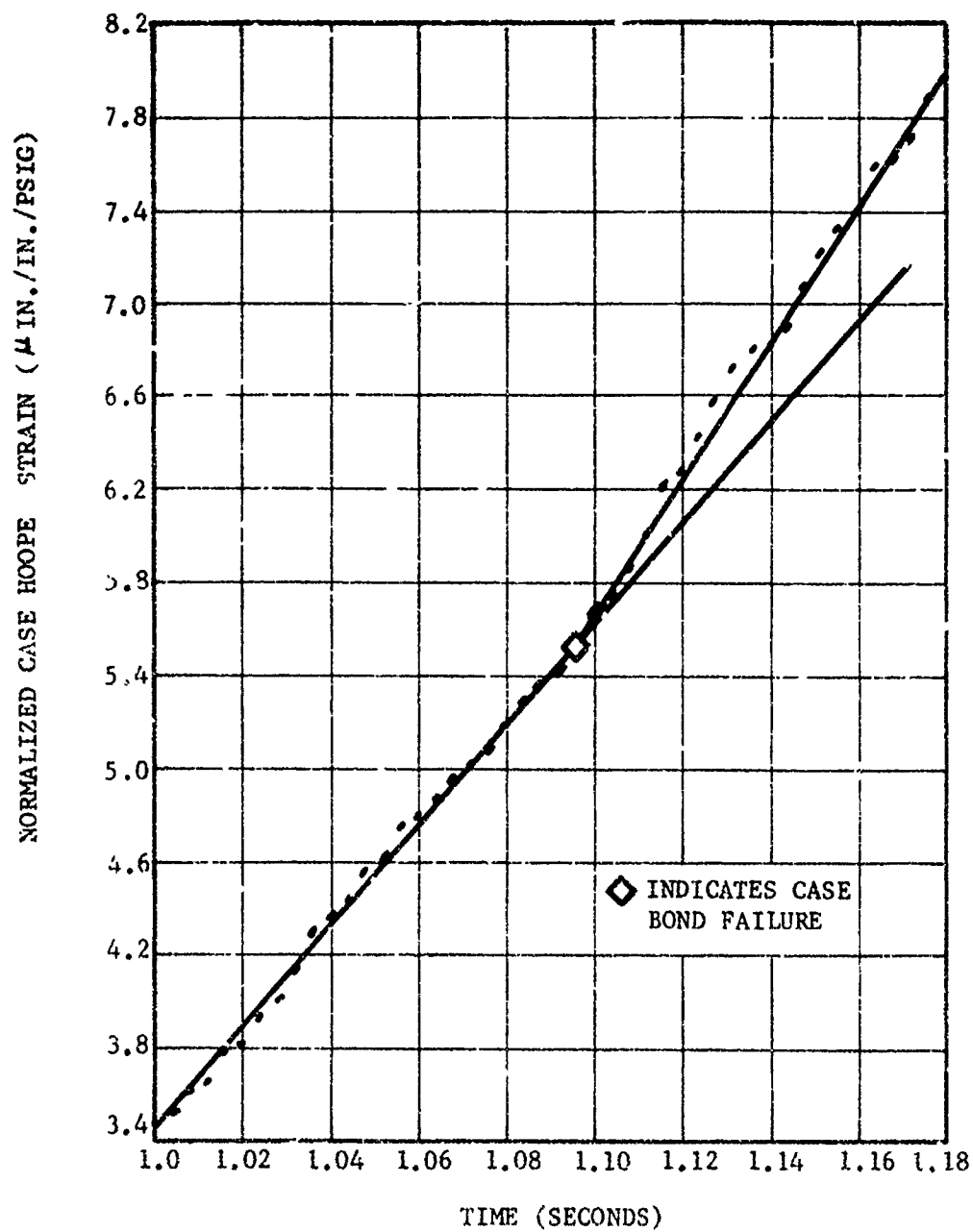
Figure 4-15. Normalized case hoop strain versus time from strain gage number four on flap termination EPC TCC-2.
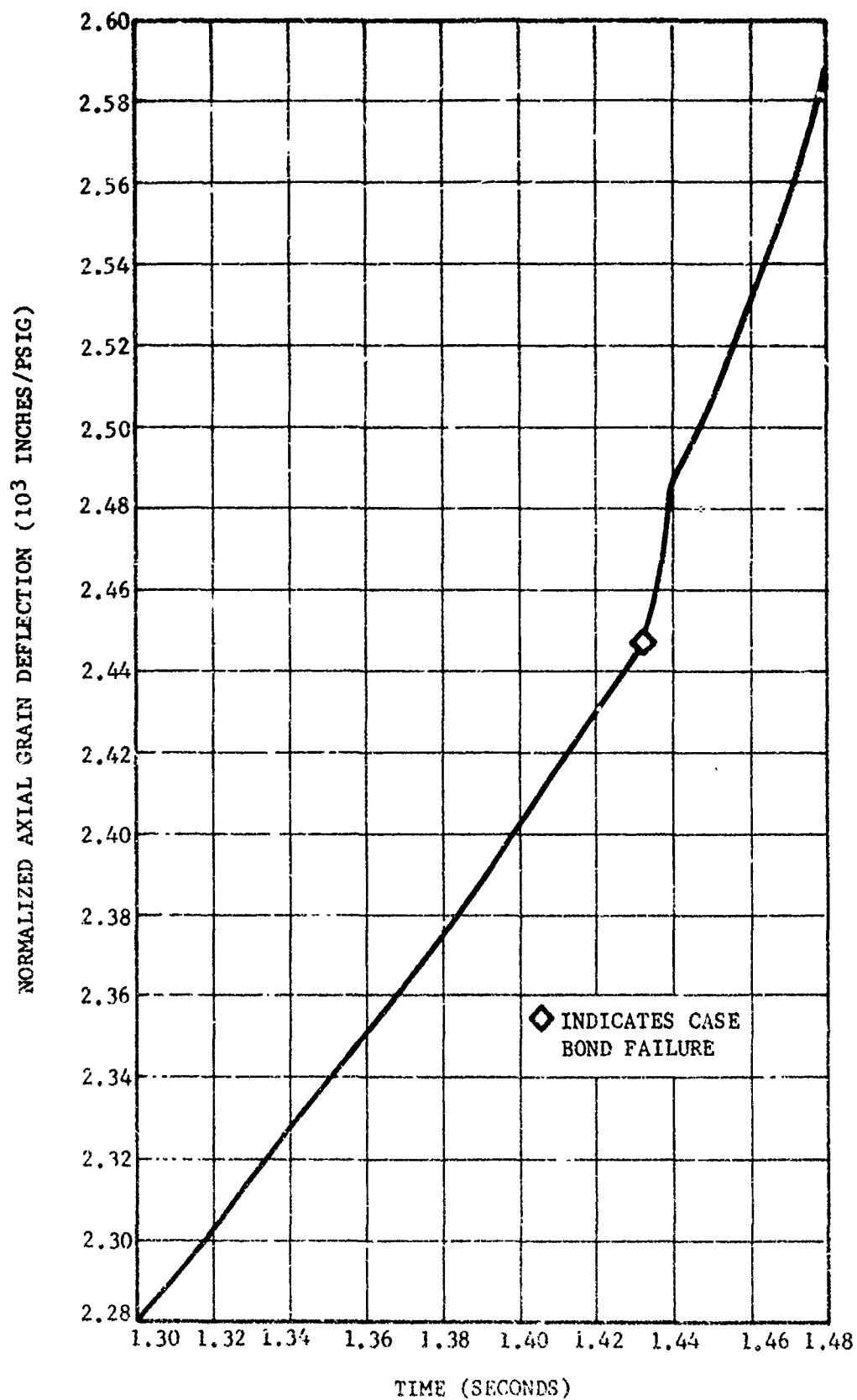
Figure 4-16. Normalized axial grain deflection versus time from linear potentiometer number six on flap termination EPC TCC-4.
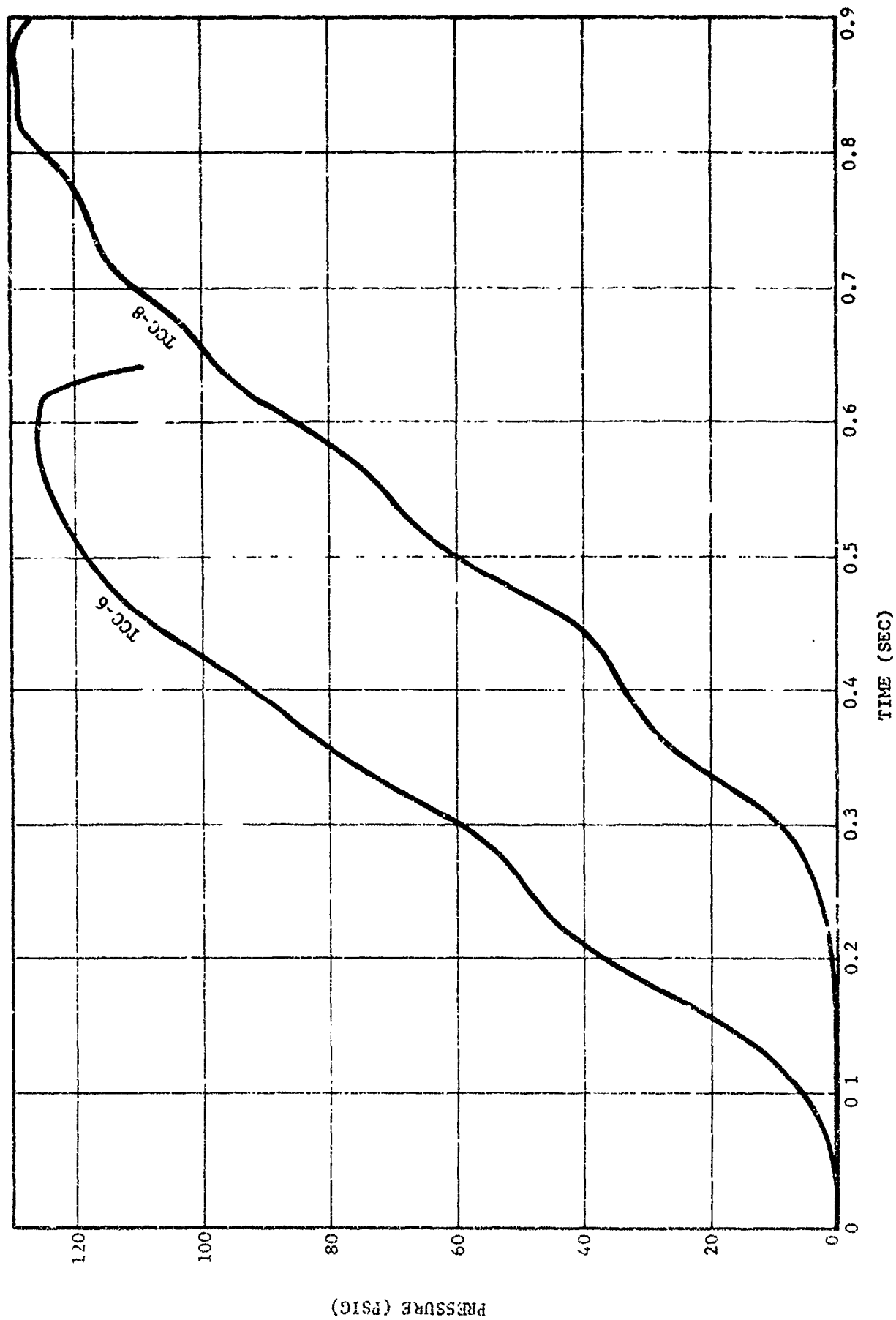
Figure 4-17. Hydrostatic pressure transients for discontinuity EPC tests.

PRESSURE (PSIG)

TIME (SEC)

TCC-8
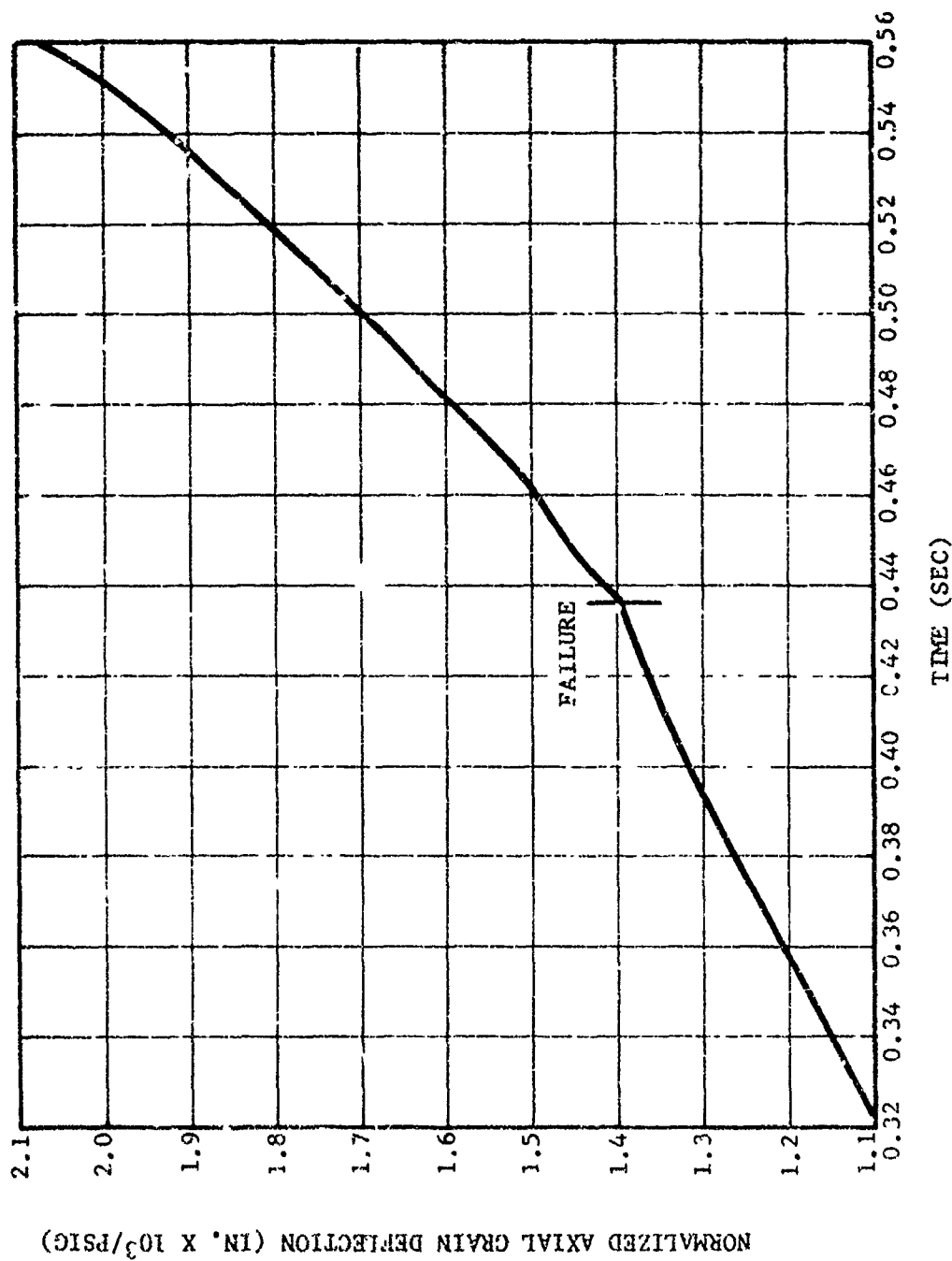
TCC-6

Figure 4-18. Normalized axial grain deflection versus time from linear potentiometer number four on discontinuity EPC TCC-6.

TIME (SEC)

NORMALIZED AXIAL GRAIN DEFLECTION (IN. X 10³/PSIG)

FAILURE
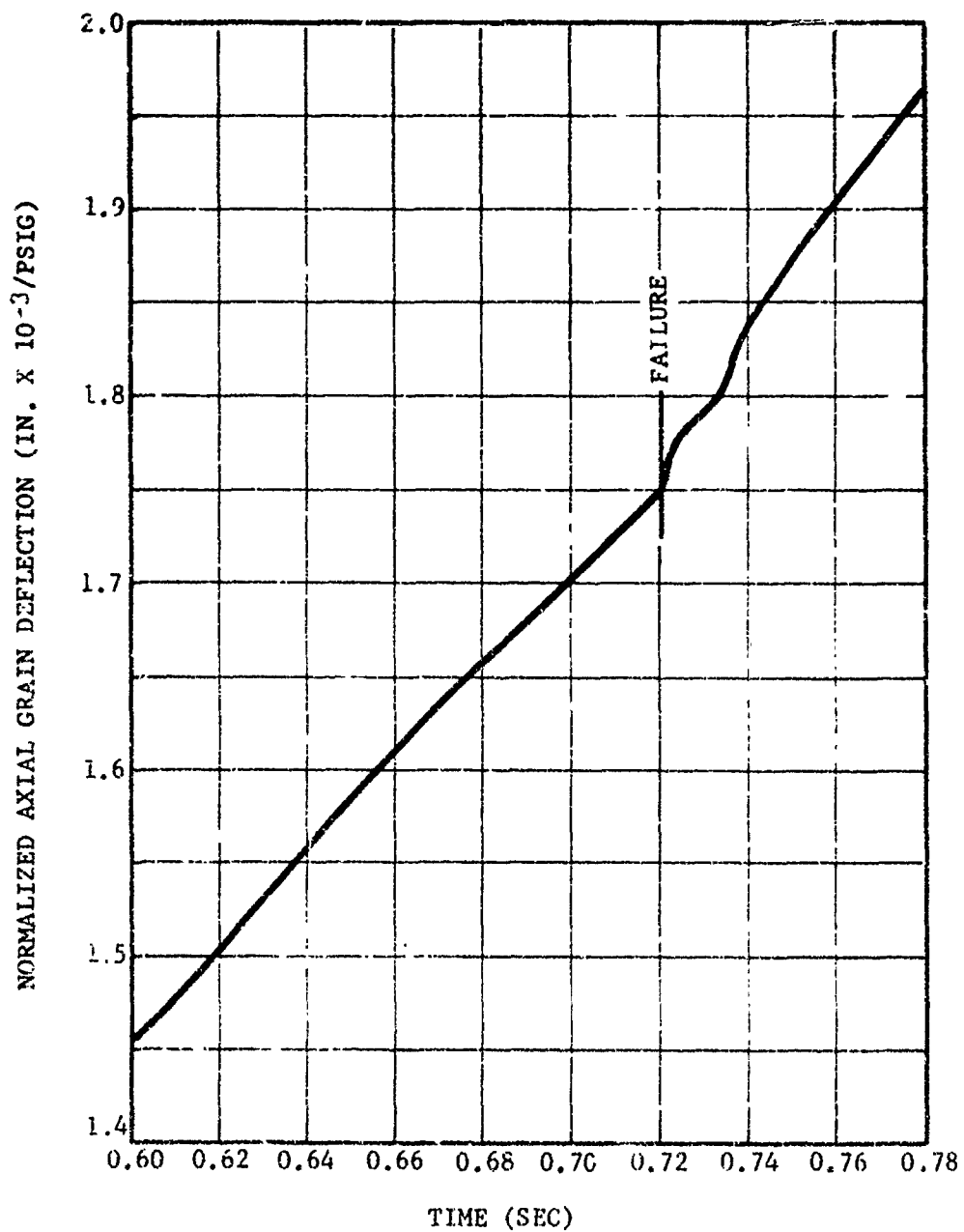
Figure 4-19. Normalized axial grain deflection versus time from linear potentiometer number three on discontinuity EPC TCC-8.
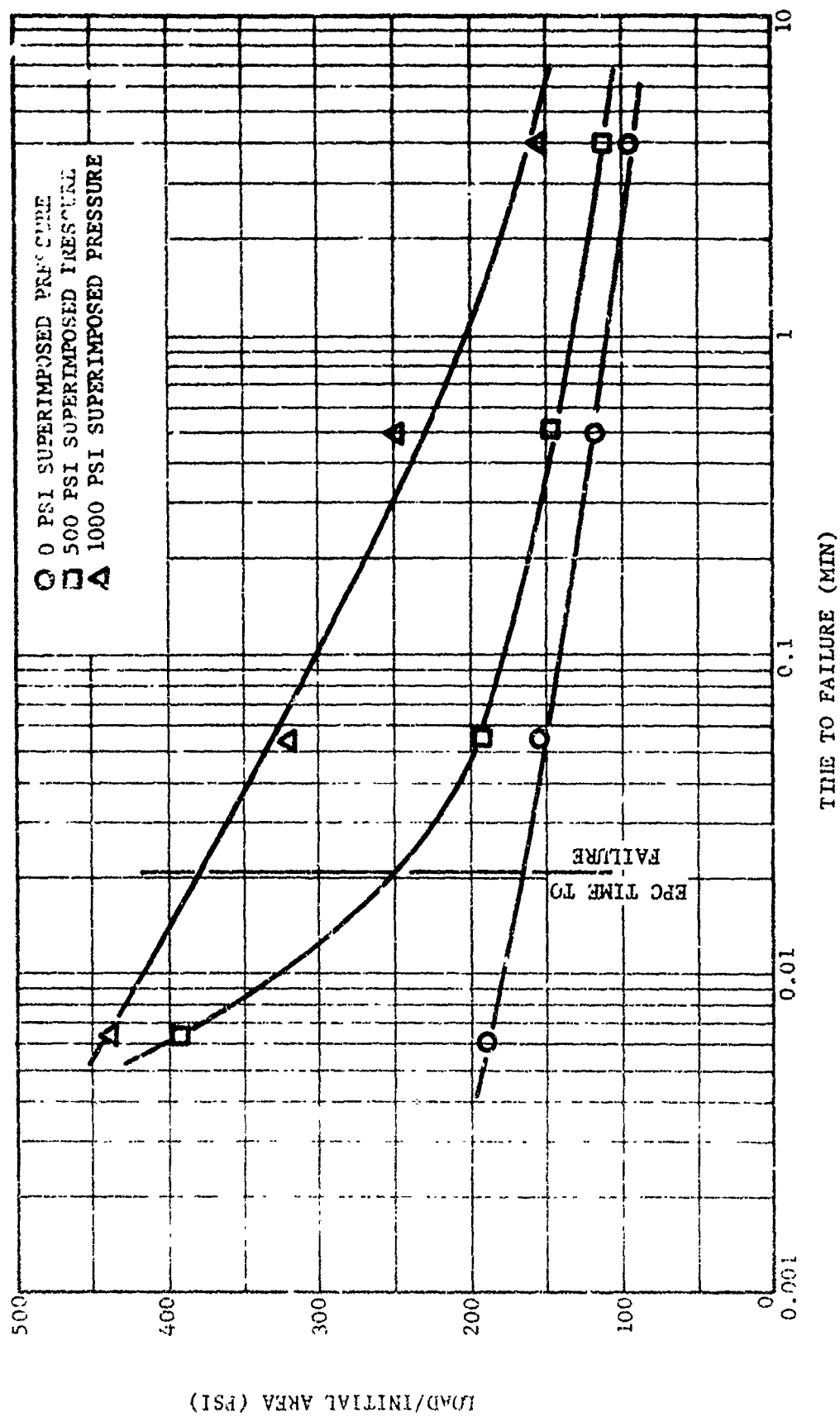
Figure 4-20. Effect of loading rate and superimposed pressure on TP-H1123 "effective" propellant tensile strength.

NOTE: PRESSURE FACTOR = $\frac{196}{165}$ = 1.19

SUPERIMPOSED PRESSURE (PSI)

LOAD/INITIAL AREA (PSI)
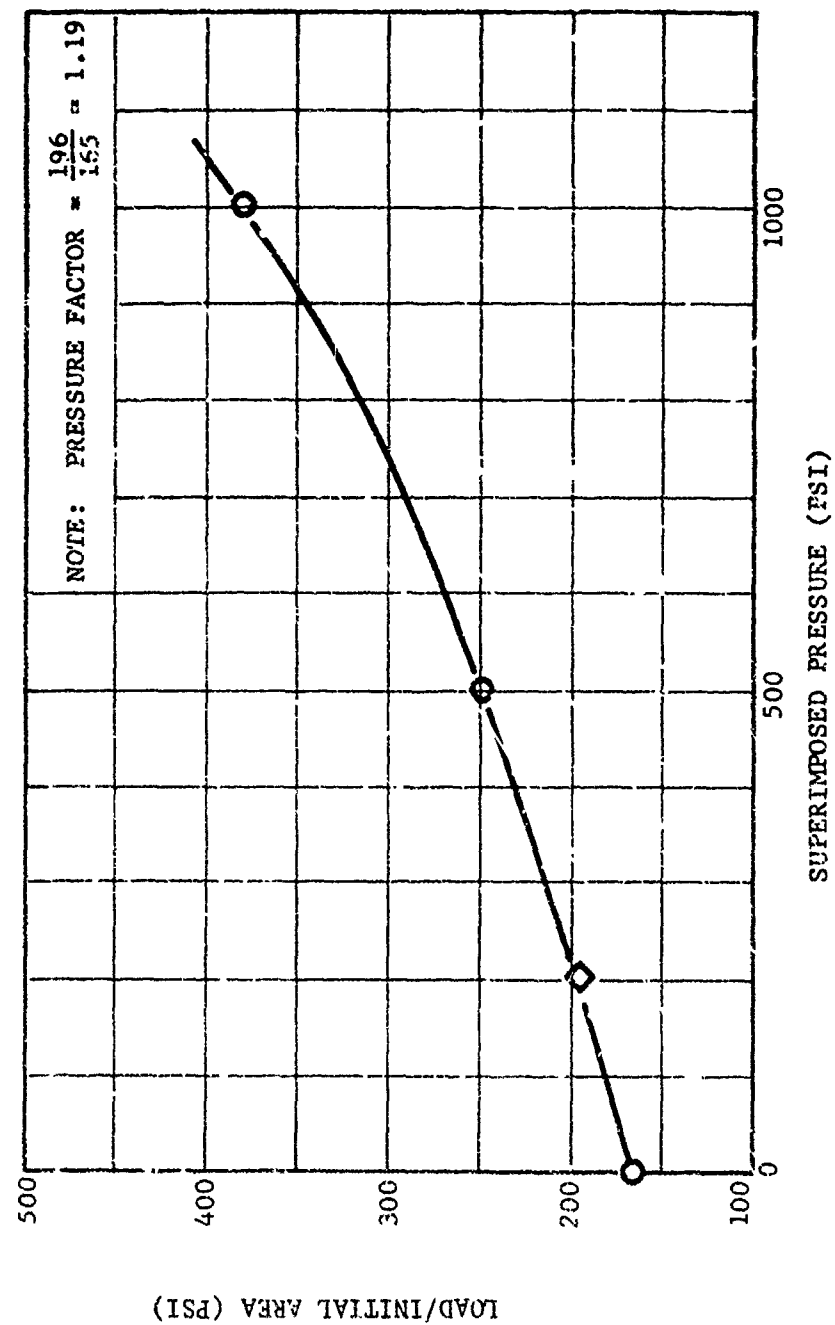
Figure 4-21. Effect of superimposed pressure on TP-H1123 propellant tensile strength at 0.021 minutes time to failure.
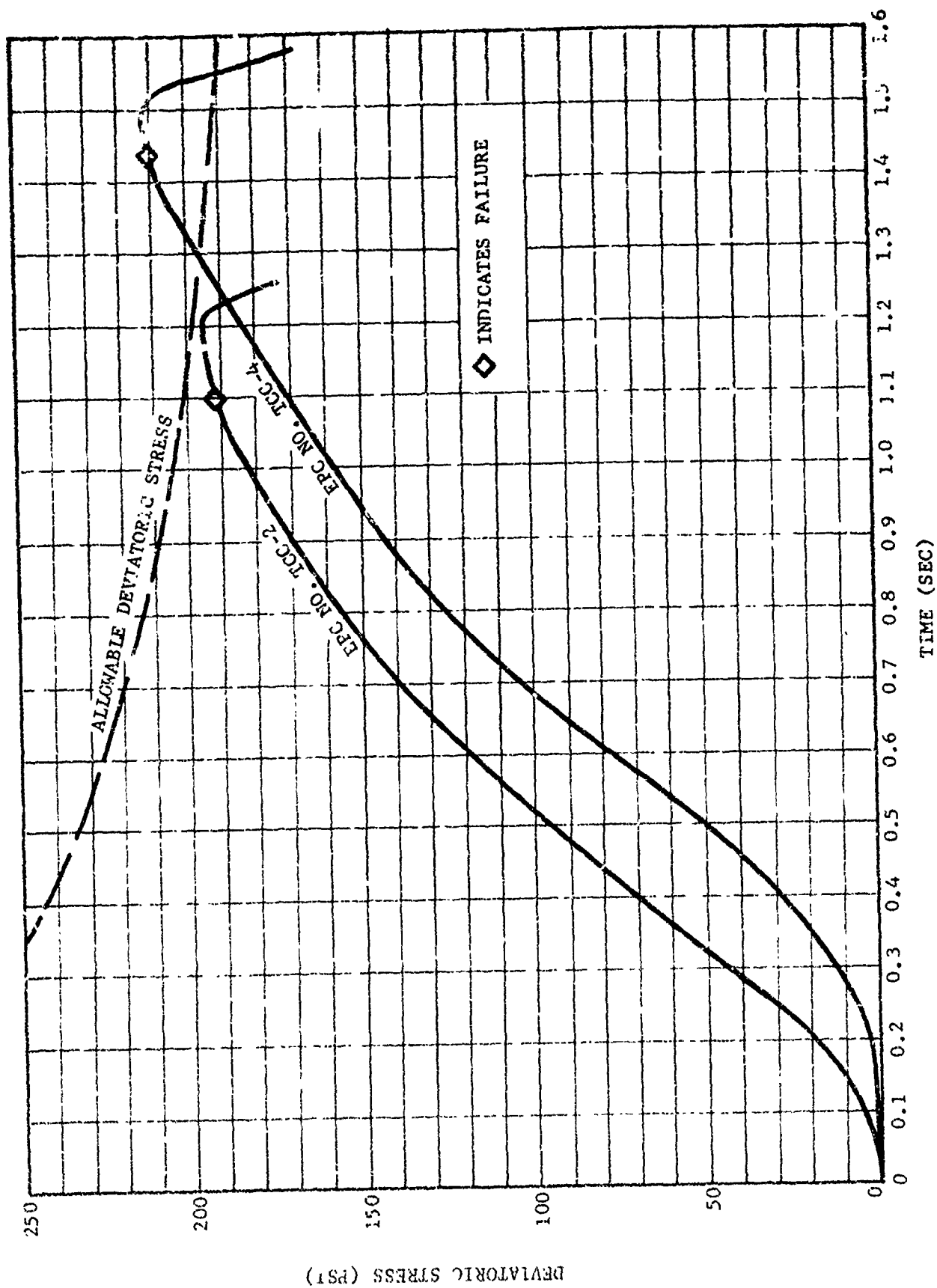
Figure 4-22. Comparison of experimental deviatoric stress with predicted maximum allowable deviatoric stress for flap termination EPC's.

302
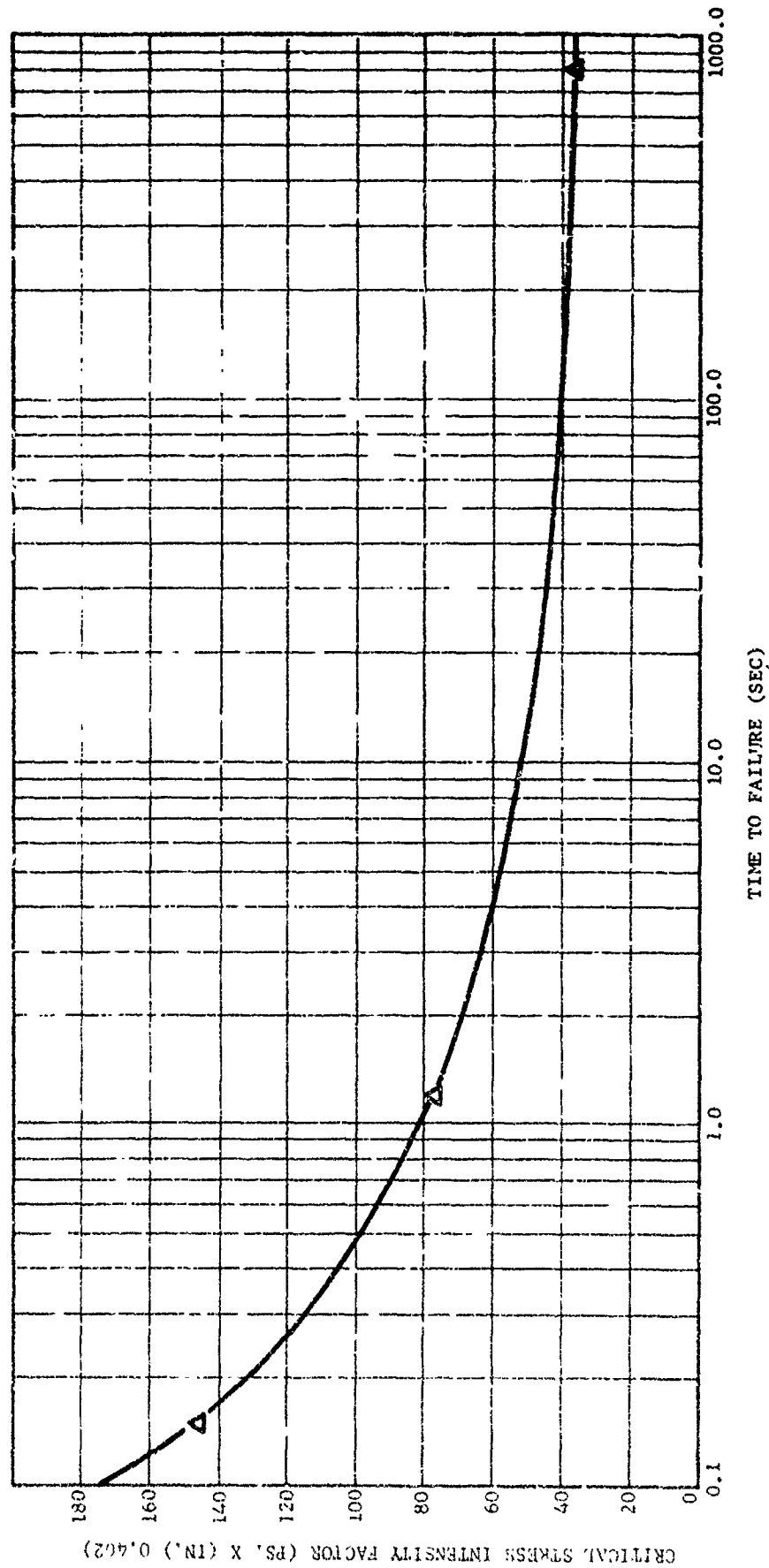
Figure 4-23. Critical stress intensity factor (based upon maximum principal stress) as a function of time to failure from unpressurized analog discontinuity sample tests.
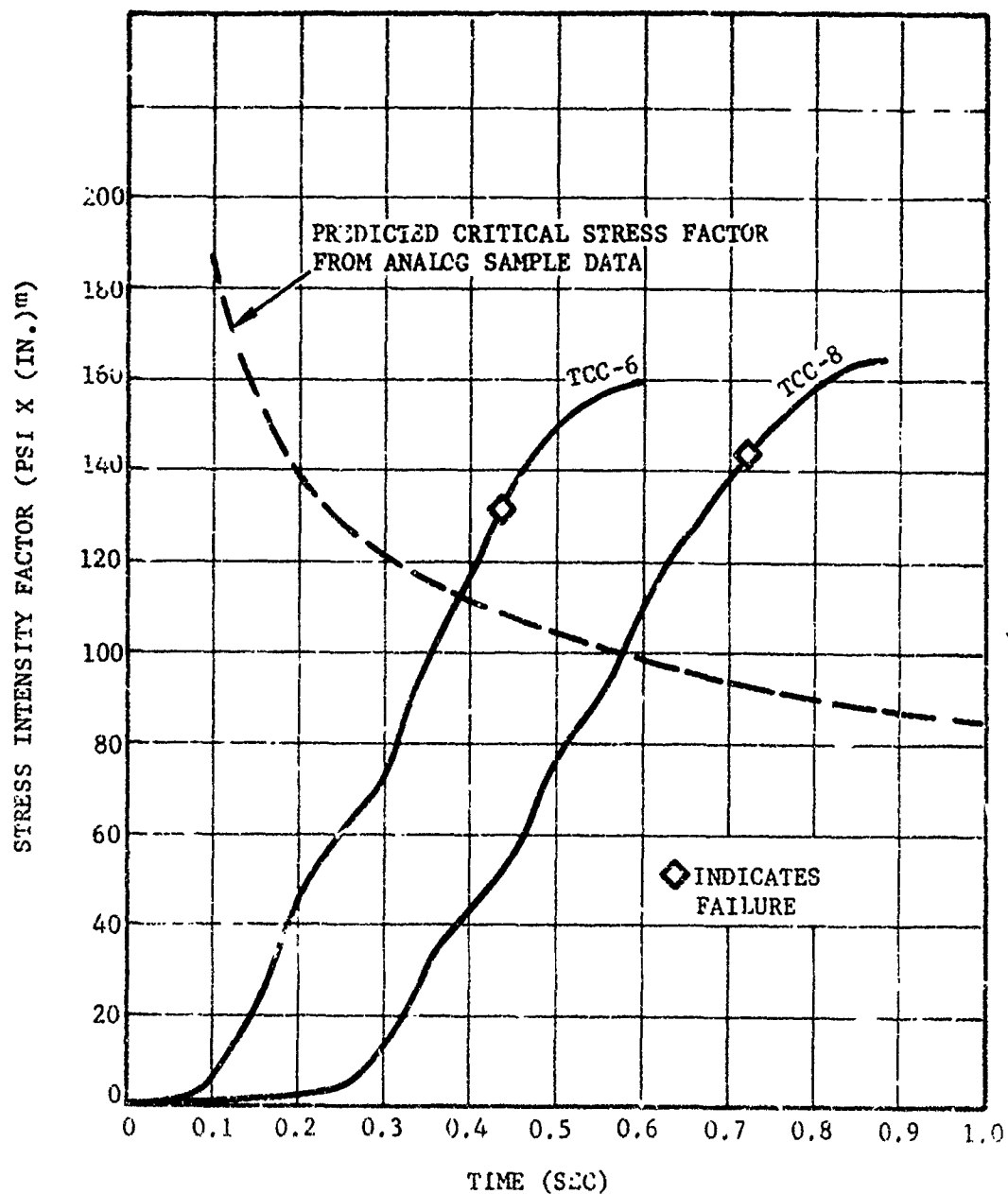
Figure 4-24. Comparison of predicted critical stress intensity factors with stress intensity factors indicated from discontinuity EPC testing.

REFERENCES

1. Anderson, J. M., "Case Bond Stress Calculations for Flapped Cylindrical Analogs of Solid Propellant Rocket Motors," AFRPL-TR-72-55 (May 1972).

2. Bills, K. K., Jr., et al, "Solid Propellant Cumulative Damage Program," Final Report, AFRPL-TR-68-131 (October 1968).

3 Robinson, ., et al, "Effect of Grain End Shape on Stress Concentrations . - . Case-Propellant Interface," Technical Report AFRPL-TR-69-_24 - Vol. I, Contract F04611-68-C-0015, Atlantic Research Corp. (May 1969).

.. Messner, A. M., and D. Schiessmann, "Parameter Calculation of Simple Propellant Grains for Temperature Cycling, Pressurization, and Acceleration," Appendix D, Study of Mechanical Properties of Solid Propellants, Aerojet-General Report No. 0411-10F (March 1962), and Lockheed Propulsion Company Structures Manual (December 1969).

. Shearly, R. N., and A. M. Messner, "Stresses in Propellant Grain Bond Systems," Bulletin of the 3rd Meeting ICRPG Working Group on Mechanical Behavior, Vol. I (October 1964 .

6. Williams, M. L., "Stress Singularities Resulting from Various Boundary Conditions in Angular Corners of Plates in Extension," J. Applied Mechanics, Vol. 19, Transactions of the ASME, Vol. 74, p. 26 (1952).

7. Zak, A. R., "Stresses in the Vicinity of Boundary Discontinuities in Bodies of Revolution," J. Applied Mechanics, Vol. 31, No. 1, p 150 (March 1964).

8. Zak, A. R., "Elastic Analysis of Cylindrical Configurations with Stress Singularities," J. Applied Mechanics, Vol. 39, No. 2, p. 501 (June 1972).

9. Williams, M. L. "The Stresses Around a Fault or Crack in Dissimilar Media," Bulletin of the Seismological Society of America, Vol. 49, p. 199 (April 1959).

10. Hein, V. L., and F. Erdogan, "Stress Singularities in a Two-Material Wedge," International Journal of Fracture Mechanics, Vol. 7, No. 3 (September 1971).

11. Irwin, G. R., "A Critical Energy Rate Analysis of Fracture Strength," Welding Journal (Research Supplement) (1954).

12. "Fracture Toughness Testing and Its Application," ASTM STP-381 (1965).

13. Deverall, L. I., and G. H. Lindsey, "A Comparison of Numerical Methods for Determining Stress Intensity Factors," 8th Meeting JANNAF Working Group on Mechanical Behavior, CPIA Publication No. 193, Vol. 1 (March 1970).

REFERENCES (Continued)

14. Zak, A. R., and M. L. Williams, "Crack Point Stress Singularities at a Bi-Material Interface," J. Applied Mechanics, Vol. 30, No. 1, p. 142 (March 1963).

15. Sih, G. C., "A Review of the Three-Dimensional Stress Problem for a Cracked Plate," International J. Fracture Mech., Vol. 7, No. 1 (March 1971).

16. Anderson, J. M., "Final Report Cumulative Damage Studies of Conventional-Cast, Composite-Modified, Double-Base Propellant," Report No. AFRPL-TR-69-258 (February 1970).

17. Bennett, S. J., "Carton/Motor Sample Correlation," Technical Report AFRPL-TR-72-117 (30 October 1972).

18. Corley, B. M., et al, "Evaluation of Propellant-to-Substrate Bonds in a Multiaxial Stress Field," Bulletin 6th Meeting ICRPG Working Group on Mechanical Behavior, Vol. II (March 1968).

19. "ICRPG Solid Propellant Mechanical Behavior Manual," CPIA Publication No. 21 (September 1963).

20. Swanson, S. R., and A. K. Phifer, "Case Bond Failure Criteria Study," Specific Data Report No. S44/6/40-153, Hercules Incorporated (31 October 1966).

21. Cost, T. L., and C. H. Parr, "Analysis of the Biaxial Strip and Shear Lap Tests for Solid Propellant Characterization," Rohm and Haas Company, Report No. S-73 (May 1967).

22. "Final Report on Poseidon Propellant Long Term Loads and Grain Structural Analysis Methods," FY 1973 TES Program, Data Item No. SA015-B3A00IITJ-15 (27 June 1973).

NOMENCLATURE

a	= Radius to inside of cylindrical grain
b	= Radius to outside of cylindrical grain
L	= Length of cylinder
D	= Diameter of cylinder
P	= Applied pressure
F	= Applied force
t	= Thickness
A	= Area
u	= Displacement
U	= Strain energy
E	= Tensile modulus
K	= Bulk modulus
K_I	= Stress intensity factor for crack opening
K_{II}	= Stress intensity factor for crack shearing
$\bar{K}_I$	= Crack opening intensity factor with rigid liner
$\bar{K}_{II}$	= Crack shearing intensity factor with rigid liner
H_I	= Radial stress reduction factor at 0.01 inches
H_{II}	= Shear stress reduction factor at 0.01 inches
ΔT	= Temperature change
x,y,z	= Cartesian coordinates
r,θ,z	= Cylindrical coordinates
I,L,F,P subscripts	= Insulator, liner, flap, propellant
σ	= Normal stress
τ	= Shear stress

NOMENCLATURE (Cont)

ϵ = Normal strain

$\sigma_1, \sigma_2, \sigma_3$ = Principal stresses

α = Coefficient of expansion, multiaxiality factor, scale factor

μ = Microns

ζ = Shrinkage coefficient; i.e., = - T

ν = Poisson's ratio

σ_{max} = Maximum principal stress, σ_1

APPENDIX

CASE BOND STRESS CALCULATIONS FOR FLAPPED CYLINDRICAL
ANALOGS OF SOLID PROPELLANT ROCKET MOTORS

BONDLINE PARAMETRIC STUDIES

ERRATA SHEET

This appendix was published separately in May 1972 as AFRPL-TR-72-55. Investigations since that time have resulted in minor corrections which have been made in this appendix. These corrections are listed as follows:

Page No.	Description
3	In last paragraph, thickness of insulator elements changed from "0.5 to 0.05-in."
6	In fourth paragraph, "Radial stress values . . . "sentence was deleted.
16	In first paragraph, " $\frac{P}{3K}$ " changed to " $-\frac{P}{3K}$ ".
	In last paragraph, "a" deleted from "a filament-wound glass."
18	In first paragraph " $\epsilon_z = \bar{\epsilon}_\theta - C_{\theta\theta} \frac{b}{t_c} \sigma_{bond}$ " changed to

$$\text{"}\epsilon_z = \bar{\epsilon}_z - C_{z\theta} \frac{b}{t_c} \sigma_{bond}\text{"}$$

Page No.	Description
23	Paragraph C(1) " $\bar{\epsilon}_{z_{case}} = \frac{\nu_{\theta z}}{E_\theta} \sigma_\theta$ . . . " changed to

$$\text{"}\bar{\epsilon}_{z_{case}} = -\frac{\nu_{\theta z}}{E_\theta} \sigma_\theta \cdot \cdot \cdot \text{"}$$

Page No.	Description
25	Last line on page, "Pressure Loading Result, 0.0074" changed to 0.00074"
33	"INSULATOR" callout added to top grid
50	"SOFT" callout added to "LINER IN MODEL" and " $\frac{b - r}{t}$ " changed to

$$\text{"} \frac{b - t_I - r}{t_f} \text{"}$$

CASE BOND STRESS CALCULATIONS
FOR FLAPPED CYLINDRICAL ANALOG
OF SOLID PROPELLANT ROCKET MOTORS

BONDLINE PARAMETRIC STUDIES

TASK I

TECHNICAL (INTERIM) REPORT, AFRPL-TR-72-55

May 1972

HERCULES INCORPORATED
SYSTEMS GROUP
Bacchus Works ● Magna, Utah

"Approved for public release;
distribution unlimited".

AIR FORCE ROCKET PROPULSION LABORATORY
AIR FORCE SYSTEMS COMMAND
UNITED STATES AIR FORCE
EDWARDS, CALIFORNIA

NOTICES

312

ABSTRACT

Numerical stress solutions were obtained for finite-length cylinders bonded to a flexible case and subjected to thermal shrinkage, axial acceleration, and internal pressure loading. Finite-element models contained insulator, flap, case-bond liner, and propellant layers typical of solid propellant rocket motors. Grid structure in the region of the flap termination was highly refined to provide accurate estimates for the maximum case-bond stresses.

The stress solutions indicated that flap length, flap modulus, and liner modulus do not significantly affect the case-bond stresses. The most important parameter relative to the maximum stresses is the thickness of material between the flap-insulator bondline and the liner-propellant bondline. Parametric studies were performed over a range of web-fractions and length-to-diameter ratios. These studies indicate that the stress distribution adjacent to the end termination is insensitive to the overall cylinder configuration, and sensitive only to the local end termination geometry. However, the maximum stresses at the end termination increase with web-fraction and length-to-diameter ratio for internal pressure and thermal shrinkage loading.

An equivalence was established between the stress solutions for internal pressure loading and thermal shrinkage loading. This equivalence provided highly accurate estimates for internal pressure stresses using the results for restrained thermal shrinkage loading.

314

TABLE OF CONTENTS

315

LIST OF FIGURES

317

LIST OF FIGURES (Cont)

348

319

LIST OF TABLES

321

x

NOMENCLATURE

a	Radius to inside of grain
b	Radius to inside of case
L	Cylinder length
D	Cylinder diameter
H	Case-Grain stiffness ratio $\left(H = \dfrac{Kb}{E_\theta t_c}\right)$
H_σ	Bond stress gradient factor (See Figure 25)
P	Internal pressure
t_c	Case thickness
r	Radial coordinate
θ	Hoop coordinate
Z	Axial coordinate
E	Tensile modulus
K	Bulk modulus
E_θ	Hoop modulus of case
E_Z	Axial modulus of case
$C_{\theta\theta}$, $C_{\theta Z}$, $C_{Z\theta}$, C_{ZZ}	Orthotropic stress-strain coefficients
ν	Poisson's ratio
$\nu_{\rho Z}$	Poisson's ratio of case in r-Z direction
δ	Shrinkage coefficient $(\delta = \alpha\Delta T)$
ϵ	Total normal strain
$\bar{\epsilon}$	Stress-producing normal strain
σ	Normal stress
τ	Shear stress
σ_{max}	Maximum principal stress
ϵ_{max}	Maximum principal strain

322

SECTION I

INTRODUCTION

Propellant grain survivability depends upon the structural integrity of the grain and all bonded interfaces. Probably more structural failures of motors have occurred at the case bond than in the propellant proper. This is true for at least two reasons: (1) The case bond is inherently weaker than the propellant, and (2) the stresses are highest at the bond lines, particularly at the bond terminations.

Case bonds impose challenges to the structural analyst which are somewhat greater than those imposed by the propellant. These challenges primarily result from geometrical considerations. Layers comprising typical case-bond systems, including insulator and flap components, are very thin compared with the propellant web. While these thin layers do not normally influence bond/propellant stresses over most of the motor, they are important at the critical bond termination locations.

Only limited information has been published which depicts typical case-bond stress distributions in rocket motors. Experimental studies have been accomplished using photoelasticity to evaluate stress distributions at bond terminations.[1] However, these studies did not consider case-bond detail and were restricted to configurations involving fillets and grooves in the propellant grain adjacent to the bond termination. Numerical stress analyses published to date have considered the case bond in varying degrees. Reference 2 contains case-bond stress distributions in cylinders with flat ends; no attempt was made to deal with the actual termination geometry or bond constituents. In later studies,[3] however, some consideration was given to the case-bond liner and bond termination configurations. Fracture mechanics theory has been applied to the case-bond problem, with the bond termination considered as a singularity[4]; information derived from these studies has been used to establish the length of flaps. Finite-element stress analyses of motors often consider the case bond; however, stress values obtained at the terminations are often of questionable value because of the lack of adequate grid refinement.

Hercules Incorporated and United Technology Center (UTC) are currently working on RPL-funded programs to develop improved methods for predicting initiation and propagation of failures in case-liner-bond systems. The Hercules program involves initiation of case-bond failure; whereas, the UTC program primarily involves propagation of case-bond failures. The Hercules program consists of four tasks involving: (1) Bondline Parametric Studies, (2) Test Sample Development for Simple States of Stress, (3) Failure Criteria for Bond Terminations, and (4) Subscale Motor Testing. This report documents studies performed under Task 1.

1

The objective of Task 1, Bondline Parametric Studies, is to establish case-bond stress distributions in basic motor configurations, with emphasis on bond terminations. The study involved simple cylinders containing flapped ends. Finite-element models were developed with highly refined grids in the vicinity of the flap terminations so that variations in case-bond constituents could be evaluated. Loading conditions considered were thermal shrinkage, internal pressurization, and axial acceleration. Information obtained under Task 1 will be used to develop meaningful case-bond failure criteria and associated test sample configurations, as outlined in the remaining three tasks. However, because of its applicability to propellant grain stress analysis in general, information gained under Task 1 is being published as an interim report.

This report first describes the modeling procedure. Results are then presented for thermal shrinkage loading. An equivalence is developed for thermal and pressure loading conditions such that thermal solutions can be used for internal pressure loading conditions as well. Results are subsequently presented for internal pressure loading and compared with predictions based on the thermal loading solutions. Finally, results are presented for axial acceleration loading.

324

2

SECTION II

MATHEMATICAL MODELING

The parameter study was restricted to flat-ended cylinders, which are symmetric about the axial mid-plane, as shown in Figure 1. The cylindrical propellant grains were bonded to the case, with flaps at the end terminations. Emphasis was placed on modeling local detail in the case-bond system, including the insulator, flap, and case-bond liner. Stress solutions were obtained for the three basic loading conditions: Thermal shrinkage, internal pressurization, and axial acceleration.

Stress solutions were obtained using a finite-element computer program based on the quadrilateral ring element, composed of four adjacent triangular elements. The program developed by Hercules is similar to the well-known Rohm & Haas program.[5] The Hercules program is reformulated for solution of problems with Poisson's ratio near 0.5. Since the reformulation variable is eliminated through partitioning at the element stiffness matrix level, solutions cannot be obtained for $v = 0.5$. The program capacity allows grid networks with up to 3,000 nodes. Double-precisioning is used in the program to obtain accurate stress solutions using the IBM System 360-370 series computers. Normal stress oscillations inherent in finite-element solutions using quadrilateral elements were minimized through grid refinement in areas of high stress gradient and through averaging of stresses in adjacent elements.

The parameter study considered nine cylinderical configurations consisting of three values of length-to-diameter ratio (L/D) and three values of web fraction (W/b). The grid network for L/D = 1, and W/b = 0.8 is shown in Figure 2. The basic cylinder diameter is 32 in. to the inside of the case. Symmetry conditions were imposed at the axial mid-plane such that only one half of the cylinder length was included in the model.

Local detail in the region of the flap termination is indicated in Figure 3. To facilitate modeling it was necessary to specify dimensions of the cylinders. The insulator is 0.2-in. thick, and the flap is 0.1-in. thick. The flap length (length of unbondedness between insulator and flap at the end termination) is 1.0 in., and the liner thickness is 0.06 in. Elements in the insulator are 0.05-in. thick (four elements to total 0.2 in.), elements in the flap are 0.025-in. thick, and elements in the liner graduated from a minimum of 0.01-in. to a maximum of 0.02-in. thick. Elements in the propellant adjacent to the liner are graduated in thickness away from the liner, with a minimum element thickness of 0.02 in. The element structure in the radial direction is carried through in a uniform manner along the total cylinder length. Element sizes in the axial direction are graduated to provide minimum element lengths of 0.02-in. in the region of the flap termination. The grid contains 2,420 total nodes.

325

3

Grid networks for web fractions and lengths different from W/b = 0.8 and L/D = 1.0 are similar to that shown in Figure 2. In all grids, the basic cylinder diameter and insulator and flap thicknesses were kept the same. The web fraction was changed by altering the port diameter, and the length-to-diameter ratio was changed by altering the length. The grid structure within 4-in. radially and 5-in. axially of the flap termination was kept the same in all grids for the various web fractions and length-to-diameter ratios. The grids for L/D = 3.0 were derived from the grids for L/D = 1.0 using the same number of nodes and increasing the lengths of the elements closest to the axial mid-plane, where stress gradients are minimum in the axial direction. The grids for L/D = 5.0 were derived from the grids for L/D = 3.0 by adding additional elements near the axial mid-plane, to provide a total of 2,640 nodes. Variations in the web fraction were obtained by decreasing radial spacing between nodes inboard of the 12-in. radial line in the grids for W/b = 0.8, without changing the total number of nodes. The thickest row of elements near the center port, 0.2-in. thick, occurred in the grid for W/b = 0.8.

Material property variations considered in the parameter study (Table I) were kept to a minimum. The propellant tensile modulus was selected as E = 200 psi, which is approximately the longterm (rubbery) tensile relaxation modulus of many solid propellants. The propellant bulk modulus was selected as K = 333,000 psi, which is the lower bound of published data for most propellants. The tensile/bulk modulus combination provides a value for Poisson's ratio of ν = 0.4999 for propellant.

The case-bond liner was assumed to have a tensile modulus equal to one half that of propellant for some stress solutions, but equal to that of the propellant in most solutions. The bulk modulus of the liner, flap, and insulator was considered to be the same as for propellant. (This choice for the flap and insulator is consistent with data for NBR/SBR rubber.[6]) The tensile modulus of the insulator and flap was considered to be equal to that of propellant in some solutions and equal to the approximate longterm tensile relaxation modulus of silica-filled NBR/SBR rubber (1000 psi) in most solutions. The shrinkage coefficient of the insulator, flap, and liner was considered to be the same as for propellant. For thermal shrinkage and axial acceleration loading, the motor case was assumed to be rigid. For internal pressure loading, approximate fiberglass-reinforced epoxy properties were used.

326

4

TABLE I

MATERIAL PROPERTIES USED IN PARAMETER STUDY

	Propellant	Case-Bond Liner	Flap	Insulator	Case
E (psi)	200	100, 200	200, 1000	200, 1000	4,000,000 (t = 0.1 in.), rigid
K (psi)	333,000	333,000	333,000	333,000	
ν	0.4999	0.49995, 0.4999	0.4999, 0.4995	0.4999, 0.4995	0.1
δ (in./in.)	1	1	1	1	0

NOTE: Values underlined were used in parameter study considering variable web fraction and length-to-diameter ratio for thermal loading conditions

RESULTS FOR THERMAL SHRINKAGE LOADING

Stress solutions for thermal shrinkage loading were obtained with the case (i.e., the outer diameter of the insulator) considered to be thermally and mechanically rigid. The propellant, liner, flap, and insulator were then assumed to shrink by the amount, δ.

Results will be first discussed for a typical set of motor parameters, with case-bond stresses shown as a function of axial position, and contour plots for the region of the bond termination. Effects of changes in the flap, liner, ar insulator moduli on the case-bond stresses will then be described. Results will be subsequently discussed for variations in the flap length. Case-bond and centerport stresses and strains will then be outlined for parametric variations in the grain web fraction and length-to-diameter ratio.

Cylinder parameters selected for the "typical" motor analysis are: $L/D = 1$, $W/b = 0.8$, $E_{insulator} = 1000$ psi, $E_{flap} = 1000$ psi, and $E_{liner} = 200$ psi (i.e., same as propellant). Stresses in the cylindrical coordinate directions for these properties are shown in Figure 4 for the row of elements in the case-bond liner next to the flap. As shown in Figure 3, the center of this element row is located 0.105 in. inboard of the insulator (0.005 in. into the liner). The stresses were made dimensionless by dividing by $E\delta$. These dimensionless stresses are strictly valid only for conditions wherein the insulator/flap modulus is five times as high as the propellant modulus, and for the given values of Poisson's ratio.

The stresses at the flap termination are shown in Figure 4; they are shown to be much higher than at the axial mid-plane of the cylinder ($Z = 16$ in., considering a 32.0-in. cylinder diameter). The dimensionless radial stress near the bond termination reaches a value of 17.5, while it is only 3.8 at the axial mid-plane. The dimensionless hoop stress peaks at 12.3 near the bond termination, while the dimensionless axial stress peaks at 8.3. The hoop and axial stresses are 60 percent greater than the radial stress at the axial mid-plane. The dimensionless shear stress peaks at 6.3 near the flap termination and goes through zero at mid-cylinder, as specified in the boundary conditions for symmetry.

Stress values in the immediate vicinity of the flap termination are shown in Figure 5. Gradients are well defined by the finite-element model. The radial stress peaks 0.05 in. aft of the flap termination (i.e., a distance approximately equal to one-half the flap thickness). The hoop stress is not shown, but it peaks at the same point as the radial stress. The axial stress is still increasing along the length after the

radial and hoop stresses have peaked. The shear stress changes direction at the flap termination, and peaks approximately 0.15 in. aft. The maximum principal stress peaks slightly to the right of the radial stress (as a result of the increasing shear stress) at a value of 18.7; the radial stress, as compared with the shear stress, is by far the largest contributor to the maximum principal stress. The maximum principal strain, ϵ_{max}/δ, is also shown in Figure 5; this quantity follows very closely the characteristics of the maximum principal stress.

Lines of constant maximum principal stress in the vicinity of the flap termination are shown in Figure 6. The discontinuity at the bond termination between the flap and insulator is well defined by the sharp stress gradient. Since the solution is linear, infinite stresses should be predicted at the discontinuity; however, the finite-element model provides stress values consistent with the grid detail utilized. The stress values at the flap-liner interface are accurately estimated with the chosen grid density, even though values become more in error as the discontinuity is approached. The principal stress is not necessarily continuous across material boundaries. However, since the radial and shear stresses, which must be continuous, are the major contributor to the maximum principal stress, the lines almost cross material boundaries.

Lines of constant maximum principal strain are shown in Figure 7. Unlike the stress values, the strain values are quite discontinuous across the flap-liner boundary. In the flap, there is the expected concentration at the flap-insulator bond termination discontinuity; however, there is also an unexpected concentration at the flap-liner interface. This results from a reduction in the triaxiality of the stresses, rather than by any stress concentration.

A. MATERIAL PROPERTY EFFECTS

The first variation from the basic solution involved softening of the flap material from E = 1000 psi to E = 200 psi, making it the same as propellant. Overall effects of this change were very small. Local effects at the flap termination, as shown in Figure 8, were most significant, but still relatively small. Radial and maximum principal stresses showed almost no change from the stiffer flap solution. The shear stress maximum increased approximately 6.3 percent over the stiffer flap solution. The largest effects were felt in the maximum principal strain and the axial stress. With the softer flap material, the axial stress decreased significantly at the flap termination, as shown in Figure 9, although it built up to the same level as for the stiff flap solution 0.5 in. further aft. This local reduction in axial stress caused a more uniaxial stress condition to occur near the location of the maximum strain, thus increasing its value from a maximum of 10.8 to 13.1. There was an insignificant change in the local hoop stress.

329

7

Lines of constant maximum principal stress and strain for the soft-flap solution are shown in Figures 10 and 11, respectively. The maximum principal stress values in the liner/propellant are almost identical for stiff and soft flap solutions. However, the stress concentration in both the flap and the insulator is significantly reduced near the bond termination by softening the flap. Thus, softening of the flap has a significant bearing on the stresses in the rubber goods even though the effect on the bond stresses is minimal. Lines of constant strain do not indicate the concentration effect in the flap adjacent to the liner evident in the stiff-flap solution. The strain contour lines tend to curve back toward the concentration more than the stress lines, indicating the increased triaxiality of the stresses further aft of the termination.

The next variation in material properties involved a decrease in the tensile modulus of the liner, reducing it from 200 to 100 psi. For this solution, the tensile modulus of the flap was kept at 200 psi, as opposed to the standard value of 1000 psi. Case-bond stresses and strains adjacent to the flap termination for the soft liner solution are shown in Figures 12 through 15; values are plotted for the row of elements in the propellant nearest the liner (i.e., 0.01 in. inboard of the liner-propellant interface, and 0.17 in. inboard of the flap-insulator interface). (See Figure 3.) Lines of constant maximum principal stress and strain for the soft-liner solution are shown in Figures 16 and 17, respectively. In general, the soft liner (in addition to the soft flap) had little effect on the stresses and strains in the propellant or at the liner-propellant interface. The maximum radial stress was reduced near the liner-propellant interface by 2 percent, the shear stress by 5 percent, the maximum principal stress by 2 percent, and the maximum principal strain by 7 percent, as compared with the soft flap solution.

The contour lines of maximum principal stress shown in Figure 16 for the soft liner solution indicate little change in the stresses in the liner itself, compared with the soft-flap solution. However, the contours for the maximum principal strain in Figure 17 indicate that the liner is shearing significantly, several flap thicknesses to the right of the flap termination. The larger liner shear strain, however, has little effect on the stresses and strain in the propellant or at the liner-propellant interface.

The final variation in material properties considered the insulator to have the same tensile modulus as the propellant, liner, and flap (E = 200 psi). Stresses and strains in the row of propellant elements immediately inboard of the liner are shown in Figures 12 through 15 for this solution. The soft-insulator solution provided the largest overall decrease in bond stresses and strains, i.e. a uniform 11-percent decrease in all the stresses and strains, as compared with the soft-flap solution.

330

Contour lines of maximum principal stress and strain for the soft insulator solution are shown in Figures 18 and 19, respectively. The stress contours indicate a significant reduction in the stress levels near the insulator-flap bond discontinuity, as compared with the other solutions. Both stress and strain contour lines are continuous across material interfaces since the material layers are assumed to have the same moduli.

In summary, none of the material property variations provided a significant change in the stresses at the case-bond interface adjacent to the flap termination, except perhaps softening of the insulator. Softening of the flap (and probably softening of the liner considering a stiffer flap) reduced the axial stress locally at the flap termination such that the maximum propellant strain increased significantly, without measurably affecting the radial/shear/maximum principal stresses. Softening of the liner increased the shear strain (and hence the maximum principal strain) in the liner for a distance to the right of the bond termination, but affected the liner/bond stresses very little.

Perhaps the most significant feature of the variable-modulus solutions is the large stress gradients, both radially and axially, with distance from the discontinuity at the insulator-flap bond termination. The maximum principal stresses in each row of elements are shown in Figure 20 as a function of the radial position, normalized to unity at the flap-liner interface, for the soft flap solution. The stress varies according to the ratio $\dfrac{K}{\sqrt{S}}$, where K is a constant and S is the distance from the discontinuity. This variation is consistent with the fracture mechanics theory. By doubling the flap thickness, the stress is reduced to 72 percent of that for the standard 0.1-in. flap thickness, and by tripling the flap thickness, the stress factor goes to 60 percent. Also shown in Figure 20 are stiff-flap stresses which have been normalized with respect to the stress at the flap-liner interface for the soft flap. Only two points are plotted for the stiff flap solution since these are sufficient to show that stiffening of the flap had no effect on the stresses inside the propellant. Corresponding normalized stresses for the soft liner solution indicate a similarly insignificant effect on the stress level inside the propellant. Thus, the propellant stresses are essentially a function of the radial distance from the flap-insulator bond discontinuity only, regardless of the material layers (within the range considered) between the propellant and the discontinuity. Case-bond stresses can be reduced by either thickening the flap or the liner. A similar conclusion cannot be reached for the maximum principal strain since it was shown to be sensitive to the flap modulus. The stress behavior, however, provides a valuable procedure for estimating the effects of flap/liner thickness on the bond stresses using stress solutions for a single flap thickness.

331

B. FLAP LENGTH EFFECTS

Adjustment of the flap length is a common technique for minimizing propellant/case-bond stresses. Information relating to flap length effects is available from several sources. A simple procedure for sizing flaps was outlined by Lockheed Propulsion Company[7], wherein grain end unbonding was observed in motors without release flaps. An empirical curve has been derived from motors with web fractions near 50 percent and length-to-diameter ratios between 1.0 and 3.0. Based on these data, a flap with an approximate length of 1.0 in. is desirable for a 32-in. diameter cylinder.

Information concerning flap length effects has been derived using fracture mechanics principles.[4] In fracture mechanics solutions, a singularity is assumed at the point of initial unbonding. The unbond is assumed to propagate when the strain energy in the loaded motor, released by a small increase in the unbond, exceeds the energy required to create a new bond surface of the same area. In general, as the amount of unbonding increases under thermal loading, the overall stresses and strains in the motor decrease, and hence, the strain energy decreases. However, as shown in Reference 4, the motor energy release rate is a complex function of the motor web fraction, length-to-diameter ratio, and length of unbond.

The primary objective of the study of flap length reported here is to evaluate the effect of varying flap length on the local case-bond stress distribution at the flap termination. The study is somewhat limited, with flap lengths of 0.1, 0.5, and 1.0 in. considered for a cylinder L/D of 1.0 and W/b of 0.8. Finite-element models for the two shorter flap conditions were very similar to that for the 1.0-in. flap model; special attention was given to keeping the grid sizes near the flap termination identical in all three models.

Case-bond radial and shear stresses adjacent to the flap termination are shown in Figures 21 and 22, respectively, for the three different flap lengths. Stresses are reported for the row of elements in the liner, closest to the flap. The radial stresses for the 0.1- and 0.5-in. flaps peak at the same level; whereas, the peak for the 1.0-in. flap is 3 percent lower. The shear stresses for the 0.5- and 1.0-in. flaps peak (negative peak) at values significantly less (13 percent) than for the 0.1-in. flap. Overall, however, it is surprising that the stresses for a flap only as long as its thickness are as close as they are to those for the longer flaps.

The largest value of the maximum principal stress in the row of elements in the liner closest to the flap is plotted in Figure 23 as a function of the normalized flap length. For the 0.1-in. flap, the largest stress value is only 6 percent greater than for the 1.0-in. flap. Thus, changes in the bond stresses are relatively insensitive to changes in flap length over the limited range studied and flap thickness has a much greater effect on the case-bond stresses at the flap termination than does flap length.

832

The strain energy in the finite-element model is shown in Figure 24 as a function of the normalized flap length. The three values calculated provide a straight line, indicating that the energy release rate is constant. This is consistent with local stresses being almost independent of flap length; differences between energy and local stress criteria can probably be explained by the limited number of solutions used to define the energy-versus-flap-length curve. Considering $S \leq 1.0$ in., flap length effects on the local case-bond stresses for cylinders with smaller web fractions and larger L/D ratios are expected to be less than those for the stubby cylinder which was studied, based on energy release rate curves contained in References 2 and 4.

C. WEB FRACTION AND LENGTH/DIAMETER (L/D) STUDIES

Overall case-bond stress distributions in cylinders have been shown to be sensitive to web fraction and length-to-diameter ratio. (See Reference 2 for example.) It is important, therefore, that the current study consider as an objective the evaluation of case bond stress distributions for variations in W/b and L/D. A secondary objective is to provide design charts which can be used to estimate maximum values of case-bond stresses at flap terminations.

The study considered nine cylinder configurations: L/D = 1, 3, and 5, for W/b = 0.5, 0.67, and 0.8. The cylinder diameter was held constant at 32 in. for these studies; thus, L/D was varied by changing L and W/b was varied by changing propellant bore diameter. The thickness and modulus of the flap and insulator, the length of the flap, and the modulus of the propellant were kept the same in all nine solutions. Modulus values used in the study are indicated in Table I. The insulator thickness of 0.2 in. is the same as for all previous solutions, and the flap thickness of 0.1 in. and the length of 1.0 in. is also the same as that used in previous solutions.

Data shown in Figure 20 indicate that the propellant stress adjacent to the flap termination is not strongly affected by the modulus of the flap or liner. Thus, the stresses obtained in a computer solution for a given flap/liner thickness can be made to apply to conditions in which the flap and liner thickness vary. Bond normal stresses are presented parametrically as $\frac{\sigma}{H_\sigma}$, where H_σ is a function of the radial distance, $\bar{t}$, of the propellant-to-liner bondine from the flap-to-insulator bondline; for a liner-bond system, $\bar{t} = t_{flap} + t_{liner}$ when the critical failure location is between the propellant and liner. The value for H_σ is presented in Figure 25 as a function of the normalized thickness, $\bar{t}/b$. The value H_0 was normalized such that it would be unity at a distance of 0.105 in. from the flap-insulator bondline, where stresses are obtained conveniently from the finite-element solutions. The value for H_σ may be a function of W/b and L/D; the value shown in Figure 25 is for L/D = 1.0 and W/b = 0.8. Figure 26 contains a comparison of H_σ for the extreme values of cylinder parameters studied (i.e., L/D = 1, W/b = 0.8, and L/D = 5, W/b = 0.5).

There is a negligible difference in H_σ for these extreme conditions, indicating that the stress distribution adjacent to the flap termination is a function of the local flap-insulator geometry and not the overall cylinder geometry. Furthermore, the radial stress gradient near the flap termination, as shown in Figure 26, is so close to that for the maximum principal stress that H_σ in Figure 25 applies to both stress components, although it was obtained from the maximum principal stress. As shown in Figure 26, H_σ for normal stresses does not apply to the τ_{rz} shear stress. The peak value of the shear stress does not decrease as rapidly with distance from the discontinuity as do the normal stresses.

A relationship for the strain components as a function of flap thickness cannot be obtained with confidence from a solution for one flap thickness since the flap modulus significantly affects the strain magnitude, as shown in Figures 5 and 8. Results are provided, however, for the basic flap thickness to indicate variations with cylinder web fraction and length.

The dimensionless radial stress adjacent to the flap termination is shown in Figure 27 as a function of L/D for the three web fractions. Values change significantly between L/D = 1.0 and 3.0, and little thereafter; the greatest effect occurs for the largest web fraction. Also indicated in Figure 27 is the ratio of the shear stress τ_{rz} to the radial stress at the location of the maximum radial stress for the standard flap/liner thickness, $\bar{t}$ = 0.105 in. The stress ratio changes very little with web fraction and length, indicating that the local stress distribution (shown in detail earlier) for L/D = 1.0 and W/b = 0.8 is characteristic of other cylinder configurations as well.

To illustrate the use of parametric information in Figure 27 for design purposes, consider a motor with the following dimensions:

Item	Value
Case Diameter, D	12 in.
Flap Thickness, t_f	0.08 in.
Liner Thickness, t_l	0.05 in.
L/D	2
W/b	0.75
$t_{insulator}/b$	0.2/16 = 0.0125
$E_{insulator}/E_{propellant}$	5
$\nu_{propellant}$	0.4999
$\nu_{insulator}$	0.4995
ν_{flap}	0.4999
ν_{liner}	0.4999

334

12

The interpolated value of $\left(\dfrac{\sigma_r}{H_\sigma E\delta}\right)_{bond}$ from Figure 27 is approximately 24.0. The normalized sum of the liner and flap thickness is,

$$\bar{t}/b = (0.08 + 0.05)/12 = 0.0108 \ ;$$

thus, H_σ from Figure 25 is 0.79. (The critical case-bond stress location is assumed to be between the liner and propellant, not between the flap and liner.) Assuming,

$$E = 500 \text{ psi}$$

$$\delta = \alpha\Delta T = 0.004 \text{ in./in.},$$

then

$$\sigma_r = (0.19)\ (500)\ (0.004)\ (24) = 37.9 \text{ psi}$$

The case-bond shear stress at this location is approximately

$$\tau_{rz} = (0.19)\ (37.9) = 7.2 \text{ psi}$$

The dimensionless maximum principal stress adjacent to the flap termination is shown in Figure 28 and the maximum principal strain is shown in Figure 29. The strain is located at $\bar{t}/b = 0.0066$ only, and varies with web fraction and length similar to the stresses. Also shown in Figure 29 are the ratio of the other two principal stresses to the maximum principal stress at the location of the maximum principal strain (same location as the maximum principal stress for $\bar{t}/b = 0.0066$). The hoop stress is approximately 65 percent of the maximum principal stress, and the smallest principal stress is approximately 20 percent of the maximum principal stress. There is only a small variation in the stress ratios with L/D and W/b.

For completeness, the centerport hoop stress and strain at the mid-cylinder is presented in Figures 30 and 31, respectively. These curves are almost identical to those presented in Reference 8, wherein finite difference methods were used for the calculations. The strain values are for the stress-producing strain, $\bar{\epsilon} = \epsilon + \delta$, as opposed to the total strain, $\epsilon = u_r/r$. The centerport stress and strain do not level off as quickly with increasing L/D as do the bond termination stresses and strains. The ratio of the axial stress (a principal stress) to the hoop stress at the mid-cylinder is indicated in Figure 31. This stress ratio changes dramatically with L/D and W/b, and is approximately 0.5 (i.e., 2:1 biaxial) for L/D, greater than 3.0, and approaches zero (uniaxial) for L/D equal to 1.0.

The ratio of the maximum principal stress at the flap termination to the maximum centerport hoop stress is shown in Figure 32. As the web fraction and length-to-diameter ratio decrease, the bond termination stress becomes much larger than the centerport hoop stress. For high L/D cylinders with large web fractions, the centerport hoop stress becomes larger than the bond termination stress, although the bond termination stress can be adjusted appreciably by the flap/liner thickness (H_σ).

The case-bond radial stress distribution as a function of motor length varies greatly with L/D, as indicated in Figure 33. For L/D = 1.0 and W/b = 0.08, the radial stress at the mid-cylinder is much less than at the flap termination. However, for L/D = 3.0, the radial stress increases significantly near the mid-cylinder, and a distinct saddle region of minimum stress occurs to the right of the flap termination. The ratio of the maximum case-bond radial stress at the flap termination to the case-bond radial stress at the mid-cylinder is shown in Figure 34 as a function of L/D and W/b. The trend for this ratio is similar to that for the flap-centerport hoop stress ratio; however, the radial bond stress is less than the centerport hoop stress at the mid-cylinder location. The ratio of the case-bond radial stress at the saddle to that at the mid-cylinder is shown in Figure 35. The saddle deepens with increasing L/D and W/b.

It was shown in Figure 4 that the hoop and axial stresses along the case-bond line are greater than the radial stress, except near the flap termination. This may be somewhat surprising at first glance. However, the plane strain cylinder solution for thermal loading predicts that

$$\left(\frac{\sigma_\theta}{\sigma_r}\right)_{r=b} = \frac{b^2 + a^2}{b^2 - a^2}$$

for $v = 0.5$ and a rigid case. Thus, as the web fraction decreases, the hoop stress at the bond becomes larger than the radial stress. The finite-element results for the ratio of the hoop stress to the radial stress at the mid-cylinder bond location are given in Figure 36. The dependence upon web fraction for large values of L/D (approaching plane strain) follows the plane strain predictions. In addition, the hoop stress increases in magnitude over the radial stress as L/D decreases. The axial stress at the mid-cylinder is equal (within 1-percent error) to the hoop stress.

The average case-bond radial stress is shown in Figure 37 for the various cylinder parameters. The distribution indicates an increasing average load on the case with increasing L/D and W/b.

336

14

SECTION IV

THERMAL-PRESSURE LOADING EQUIVALENCE

Much similarity exists between the stress solutions for continuums subjected to restrained thermal shrinkage and pressure loadings. (See Reference 9, for example.) This similarity can be used to advantage in both stress and strength analysis of solid propellant rocket motors. In particular, the number of stress solutions required to depict typical case-bond stress distributions in two-layered, finite-length cylinders can be reduced in the current parameter study by taking advantage of this equivalence.

A pictorial presentation of propellant (and case bond) stresses and strains in cylindrical rocket motors with free ends, subjected to thermal shrinkage and internal pressure loading, is given in Figure 38. During thermal shrinkage loading, propellant normal stresses (σ), shear stresses (τ), and stress-producing strains ($\bar{\epsilon}$) occur because the propellant has a higher coefficient of thermal expansion than the case.

The stresses, strains, and deformations for thermal loading can be separated into those resulting from two situations, free shrinkage and case expansion, as indicated in Figure 38-a. Assuming that the propellant is disconnected from the case and allowed to uniformly shrink, zero normal and shear stresses will result. By definition, the stress-producing strains ($\bar{\epsilon}$) will also be zero; the total strains (ϵ) will then be equal to the negative of the linear shrinkage coefficient (δ_p). The case will also shrink, but normally much less than the propellant. When the case and propellant are bonded together, interface stresses will occur at the case-bond line. The case deformation resulting from these stresses is usually small, but is dependent upon the relative grain-to-case stiffness ratio in the coupled system, as are the interface stresses. For convenience of presentation, consider that the case deformation due to the interface stresses is known and included in the free shrinkage solution. The propellant stresses for restrained shrinkage loading can then be viewed as those which occur when the outer boundary of the shrunk propellant cylinder is pulled out to make contact with the deformed case (i.e., case expansion loading), as indicated in the right side of Figure 38-a. Since the propellant grain under free shrinkage loading was assumed to uniformly shrink such that all total normal strains are equal to "$-\delta_p$", and the case deformation is usually small due to the interface stresses, the hoop strain (ϵ_θ) will be approximately equal to the axial strain (ϵ_z) all along the case-bond line for case expansion loading. Strength analysis is most logically carried out in terms of stress producing strains, $\bar{\epsilon}$, as opposed to total strains, ϵ.

337

During uniform internal pressure loading, propellant stresses (other than hydrostatic pressure stresses) and strains occur because the case expands and the grain follows to take up the increased volume inside the deformed chamber. The stresses, strains, and deformations for uniform internal pressure loading can be separated into those resulting from two situations, hydrostatic pressure and case expansion, as indicated in Figure 38-b. Assuming that the propellant is disconnected from the case and subjected to uniform hydrostatic pressure, all normal stresses will be equal to -P and all shear stresses will be zero; the normal strains will be equal to $-\frac{P}{3K}$. Consider now a strain definition corresponding to that for the stress-producing strain, $\bar{\epsilon}$, under thermal loading. In the pressure loading situation, this "stress-producing strain," $\bar{\epsilon}$, corresponds to that required to produce normal stresses different from -P; thus, $\bar{\epsilon}$ by definition is zero for hydrostatic pressure loading.

For convenience of presentation, consider that the case deformation due to interface stresses and end forces is known for internal pressure loading, even though it is a function of the coupled grain/case system. The propellant stresses considering the propellant and case are bonded together can then be viewed as those for hydrostatic pressure loading, plus those which occur when the outer boundary of the compressed propellant cylinder is pulled out to make contact with the deformed case. The case strains for an empty metal chamber will be such that $\epsilon_Z \approx \frac{1}{2} \epsilon_\theta$; considering filament-wound glass, ϵ_Z will be typically as large as ϵ_θ. Considering a case designed to produce a hoop strain of 0.01 in./in. at 1000 psi internal pressure, and a propellant with a bulk modulus of 333,000 psi, the propellant strain due to uniform hydrostatic compression will be $\epsilon = \frac{-1000}{1 \times 10^6} = -0.001$ in./in., which is 10 percent of the empty case hoop strain. The empty case expansion component of loading can usually be expected to dominate the propellant compressibility component of loading.

338

16

LOAD SHARING OF CASE AND GRAIN

The interface stresses between the case and grain are a function of the relative grain-to-case stiffness. A procedure for estimating the case deformation which results from the interface stresses is derived in the following paragraphs. Pressure loading, which produces the most complex case-grain coupling, is discussed in detail; then, case-grain coupling is summarized for thermal loading.

A. INTERNAL PRESSURE LOADING

Consider a two-layered cylinder subjected to internal pressure loading. The case hoop and axial stresses can be approximately expressed as:

$$\sigma_\theta = (P - \sigma_{bond}) \frac{b}{t_c}$$

$$\sigma_z = \frac{Pb}{2t_c} - \tau_{bond}$$

The term "σ_{bond}" represents the average internal pressure load carried by the grain, and τ_{bond} relates to the shear stress at the interface. The pressure load carried by the grain is highest near the end terminations, where there is a sharp stress concentration, and near the axial mid-plane where gross end relief effects diminish. The shear stress is highest near the end terminations and changes sign at the axial mid-plane such that the integral of the shear is zero over the total length. Shear is secondary compared with the radial stress effect, and will be ignored in further considerations.

For a membrane case, the orthotropic stress-strain relationships are:

$$\epsilon_\theta = C_{\theta\theta}\,\sigma_\theta + C_{\theta z}\,\sigma_z$$

$$\epsilon_z = C_{z\theta}\,\sigma_\theta + C_{zz}\,\sigma_z$$

Substitution of the above stress-load relationships (minus the shear) into the stress-strain relations provides:

$$\epsilon_\theta = C_{\theta\theta}(P - \sigma_{bond})\frac{b}{t_c} + C_{\theta z}\left(\frac{Pb}{2t_c}\right)$$

$$\epsilon_z = C_{z\theta}(P - \sigma_{bond})\frac{b}{t_c} + C_{zz}\left(\frac{Pb}{2t_c}\right)$$

339

Upon regrouping these expressions, the following are obtained:

$$\epsilon_\theta = \bar{\epsilon}_\theta - C_{\theta\theta} \frac{b}{t_c} \sigma_{bond}$$

$$\epsilon_z = \bar{\epsilon}_z - C_{z\theta} \frac{b}{t_c} \sigma_{bond}$$

where $\bar{\epsilon}_\theta$ and $\bar{\epsilon}_z$ are the case strains in the absence of the grain.

The average interface radial stress carried by the grain, σ_{bond}, is a function of both the radial and axial case strains. Consider functions

$$\left(\frac{\sigma_r}{E\epsilon_\theta}\right)_{avg} \quad \text{and} \quad \left(\frac{\sigma_r}{E\epsilon_z}\right)_{avg} ,$$

which are the average dimensionless bond radial stresses for arbitrary (case expansion loading) hoop and axial case strains. Further, recognize $C_{\theta\theta} = \frac{1}{E_\theta}$ and $C_{z\theta} = -\frac{\nu_{\theta z}}{E_\theta}$. Then the hoop and axial case strains are related as:

$$\epsilon_\theta = \bar{\epsilon}_\theta - \frac{Eb}{E_\theta t_c} \left[\left(\frac{\sigma_r}{E\epsilon_\theta}\right)_{avg} \epsilon_\theta + \left(\frac{\sigma_r}{E\epsilon_z}\right)_{avg} \epsilon_z \right] .$$

$$\epsilon_z = \bar{\epsilon}_z + \nu_{\theta z} \frac{Eb}{E_\theta t_c} \left[\left(\frac{\sigma_r}{E\epsilon_\theta}\right)_{avg} \epsilon_\theta + \left(\frac{\sigma_r}{E\epsilon_z}\right)_{avg} \epsilon_z \right]$$

These equations can be solved for ϵ_θ and ϵ_z, as:

$$\epsilon_\theta = \frac{(1 - \nu_{\theta z} H \sigma_{rz}) \bar{\epsilon}_\theta - (H \sigma_{rz}) \bar{\epsilon}_z}{(1 - \nu_{\theta z} H \sigma_{rz})(1 + H \sigma_{r\theta}) + \nu_{\theta z} H^2 \sigma_{rz} \sigma_{r\theta}}$$

and

$$\epsilon_z = \frac{\bar{\epsilon}_z + (\nu_{\theta z} H \sigma_{r\theta}) \epsilon_\theta}{1 - \nu_{\theta z} H \sigma_{rz}}$$

340

18

where:

$$H = \frac{Eb}{E_\theta t_c}, \quad \sigma_{r\theta} = \left(\frac{\sigma_r}{E \, \epsilon_{\theta_{case}}}\right)_{avg}, \quad \text{and} \quad \sigma_{rZ} = \left(\frac{\sigma_r}{E \, \epsilon_{Z_{case}}}\right)_{avg}$$

B. THERMAL SHRINKAGE LOADING

Case axial and hoop stresses for thermal shrinkage loading can be approximately expressed as:

$$\sigma_\theta = (-\sigma_{bond}) \frac{b}{t_c}$$

$$\sigma_Z = 0$$

The stress producing case strains are related to the average bond radial stress as:

$$\bar{\epsilon}_\theta = \frac{1}{E_\theta} (-\sigma_{bond}) \frac{b}{t_c}$$

$$\bar{\epsilon}_Z = \frac{-\nu_{\theta Z}}{E_\theta} (-\sigma_{bond}) \frac{b}{t_c} = -\nu_{\theta Z} \bar{\epsilon}_\theta$$

The average bond radial stress, $\left(\frac{\sigma_r}{E\delta}\right)_{avg}$, is presented in Figure 37 for variations in L/D, W/b, E, and δ of a cylinder with a rigid case. Thus,

$$\sigma_{bond} \approx \left(\frac{\sigma_r}{E\delta}\right)_{avg} E\delta,$$

and;

$$\bar{\epsilon}_\theta \approx -H\left(\frac{\sigma_r}{E\delta}\right)_{avg} \delta \; ; \quad \bar{\epsilon}_Z \approx -\nu_{\theta Z} \bar{\epsilon}_\theta$$

341

The stresses for thermal shrinkage loading, considering a flexible case, are then approximately equal to those for a rigid case plus those for case expansion loading of the amount estimated above. Since the case strains are negative, however, the flexible case solution will provide lower stresses than the rigid case solution.

342

RESULTS FOR INTERNAL PRESSURE LOADING

A. DIRECT INTERNAL PRESSURE LOADING RESULTS

The case-bond stress distribution for a typical set of cylinder parameters was obtained for internal pressure loading applied to the finite-element model. The propellant, liner, and insulator properties used are those underlined in Table I. However, the flap modulus was 200 psi and the motor case was not assumed to be rigid; a case with thickness, t_c = 0.1 in. (t_c/b = 0.00625), a tensile modulus, E_c = 4 x 10^6 psi, and Poisson's ratio, ν_c = 0.1 were used. These case properties provide a mid-cylinder case hoop strain of 1.85 percent at 500 psi internal pressure, which is typical of fiberglass-reinforced epoxy cases.

Case-bond stresses in the row of elements in the case-bond liner next to the flap in the immediate vicinity of the flap termination are shown in Figure 39 for P = 1.0 psi. This stress distribution is virtually identical with the companion solution for thermal shrinkage loading shown in Figure 5. Lines of constant maximum principal strain are shown in Figure 40 for the immediate vicinity of the flap termination; gradients are almost identical with those for the corresponding shrinkage solution in Figure 11. Thus, there is little value in presenting more of the stress distributions for internal pressure loading since they are similar to those already presented for thermal shrinkage loading.

B. CASE HOOP EXPANSION COMPONENT OF LOADING

Stress/strain values already presented for thermal shrinkage loading can be interpreted as case expansion solutions for ϵ_θ = ϵ_z = δ at the case-insulator interface. By obtaining additional stress solutions for a unit value of ϵ_θ of the case and a zero ϵ_z, the stresses for arbitrary combinations of ϵ_θ and ϵ_z can be derived. Key stresses for ϵ_θ case expansion loading of the cylinder with an 80-percent web fraction are presented in Table II. They are compared with the corresponding stresses for thermal shrinkage loads; however, the shrinkage stresses were reduced through division by a factor of 1.5. The 1.5 factor is based on the assumption that the cylinder stresses for a unit axial strain are equal to Poisson's ratio (~ 0.5) times those for a unit hoop strain. For thermal shrinkage loading, the axial and hoop strains were assumed to be equal at the case, considering shrinkage to be case expansion loading. Thus, stresses for hoop case expansion loading only should be two-thirds those for shrinkage loading. The comparison between the (reduced) shrinkage values and the hoop case expansion values is surprisingly good, with deviations generally less than 10 percent. The largest deviations occur for the centerport hoop stress and strain for L/D = 1 (14 percent), and

343

21

TABLE II

COMPARISON OF KEY STRESS PARAMETERS IN CYLINDERS WITH W/b = 0.8 FOR CASE RADIAL EXPANSION AND THERMAL SHRINKAGE LOADINGS

Loading Condition / L/D Stress Parameter	(σ_θ)Case Loading $\dfrac{(\sigma_\theta)\text{Bore}}{E(\sigma_\theta)\text{Case}}$	Thermal Shrinkage Loading $\dfrac{(\sigma_\theta)\text{Bore}}{1.5\ E\delta}$	(σ_θ)Case Loading $\dfrac{(\sigma_\theta)\text{Bore}}{(\sigma_\theta)\text{Case}}$	Thermal Shrinkage Loading $\dfrac{(\sigma_\theta)\text{Bore}}{1.5\ \delta}$	(σ_θ)Case Loading $\dfrac{(\sigma_{max})\text{Flap}}{E\,(\sigma_\theta)\text{Case}}$	Thermal Shrinkage Loading $\dfrac{(\sigma_{max})\text{Flap}}{1.5\ E\delta}$	(σ_θ)Case Loading $\dfrac{(\sigma_r)\text{Flap}}{(\sigma_r)\text{Mid-Cylinder}}$	Thermal Shrinkage Loading $\dfrac{(\sigma_r)\text{Flap}}{(\sigma_r)\text{Mid-Cylinder}}$	(σ_θ)Case Loading $\dfrac{(\sigma_r)\text{Saddle}}{(\sigma_r)\text{Mid-Cylinder}}$	Thermal Shrinkage Loading $\dfrac{(\sigma_r)\text{Saddle}}{(\sigma_r)\text{Mid-Cylinder}}$
1	7.2	(6.4)	7.1	(6.1)	13.4	(12.5)	4.2	(4.5)	0.84	(0.82)
3	21.8	(22.1)	17.2	(16.6)	22.6	(24.0)	2.3	(2.1)	0.36	(0.33)
5	29.6	(29.8)	22.3	(21.9)	22.9	(23.4)	1.9	(1.6)	0.30	(0.25)

314

for ratios of the flap and saddle stresses to the mid-cylinder radial stress at the bond for L/D = 5.0 (16 percent). The critical propellant and bond stresses for case hoop expansion loading can be predicted with good accuracy from the thermal shrinkage solutions. Therefore, case hoop expansion solutions were not obtained for the other two web fractions.

C. PROCEDURE FOR PREDICTING PRESSURE SOLUTIONS FROM THERMAL SOLUTIONS

Stresses and strains for internal pressure loading can be predicted completely from corresponding values for thermal shrinkage loading. The procedure for predicting stress solutions for internal pressure loading is as follows:

(1) Calculate axial and hoop strains for the case, without the grain:

$$\bar{\epsilon}_{\theta_{case}} = \frac{1}{E_\theta} \sigma_\theta - \frac{\nu_{\theta z}}{E_\theta} \sigma_z$$

$$\bar{\epsilon}_{z_{case}} = - \frac{\nu_{\theta z}}{E_\theta} \sigma_\theta + \frac{1}{E_z} \sigma_z$$

where $\sigma_\theta = \frac{Pb}{t_c}$ and $\sigma_z = \frac{Pb}{2t_c}$

(2) Determine average case strains for coupled case and grain:

$$\epsilon_{\theta_{case}} = \frac{\left[1 - \nu_{\theta z} \frac{H}{3} \left(\frac{\sigma_r}{E\delta}\right)_{avg}\right] \bar{\epsilon}_{\theta_{case}} - \left[\frac{H}{3}\left(\frac{\sigma_r}{E\delta}\right)_{avg}\right] \bar{\epsilon}_{z_{case}}}{\left[1 - \nu_{\theta z} \frac{H}{3}\left(\frac{\sigma_r}{E\delta}\right)_{avg}\right]\left[1 + \frac{2}{3} H \left(\frac{\sigma_r}{E\delta}\right)_{avg}\right] + \frac{2}{9} \nu_{\theta z} H^2 \left(\frac{\sigma_r}{E\delta}\right)^2_{avg}}$$

$$\epsilon_{z_{case}} = \frac{\bar{\epsilon}_z + \left[\frac{2}{3} \nu_{\theta z} H \left(\frac{\sigma_r}{E\delta}\right)_{avg}\right] \epsilon_{\theta_{case}}}{1 - \frac{1}{3} \nu_{\theta z} H \left(\frac{\sigma_r}{E\delta}\right)_{avg}}$$

where $H = \frac{Eb}{E_\theta t_c}$, and $\left(\frac{\sigma_r}{E\delta}\right)_{avg}$ is obtained from Figure 37.

345

(3) Calculate critical stresses and strains for pressure loading:

$$\sigma_{pressure} + P = E\left(\frac{2}{3}\,\epsilon_{\theta_{case}} + \frac{1}{3}\,\epsilon_{z_{case}} + \frac{P}{3K}\right)\left(\frac{\sigma}{E\delta}\right)_{shrinkage}$$

$$\epsilon_{pressure} = \left(\frac{2}{3}\,\epsilon_{\theta_{case}} + \frac{1}{3}\,\epsilon_{z_{case}} + \frac{P}{3K}\right)\left(\frac{\epsilon}{\delta}\right)_{shrinkage}$$

Note: Case strains for the empty case must apply for pressure, P.

This procedure will now be demonstrated for the cylinder with W/b = 0.8 and L/D = 3.0, considering an isotropic case.

(1) Empty case strains:

$$\sigma_\theta = \frac{Ph}{t_c} = \frac{(1.0)\,(16.05)}{0.1} = 160.5$$

$$\sigma_z = \frac{Pb}{2t_c} = 80.25$$

$$\bar{\epsilon}_\theta = \frac{1}{E_\theta}\,\sigma_\theta - \frac{\nu_{\theta z}}{E_\theta}\,\sigma_z = \frac{160.5}{4 \times 10^6} - \frac{0.1}{4 \times 10^6}\,(80.25) = 38.1 \times 10^{-6}$$

$$\bar{\epsilon}_z = -\frac{\nu_{\theta z}}{E_\theta}\,\sigma_\theta + \frac{1}{E_z}\,\sigma_z = -\frac{0.1}{4 \times 10^6}\,(160.5) + \frac{80.25}{4 \times 10^6} = 16.04 \times 10^{-6}$$

(2) Case strains considering grain reinforcement:

$$H = \frac{Eb}{E_\theta\,t_c} = \frac{(200)\,(16)}{(4 \times 10^6)\,(0.1)} = 0.0080$$

$$\left(\frac{\sigma_r}{E\delta}\right)_{average} = 11.2$$

346

24

$$\frac{H}{3}\left(\frac{\sigma_r}{E\delta}\right)_{average} = 0.0298$$

$$\epsilon_{\theta_{case}} = \frac{\left[1 - (0.1)(0.0298)\right](38.1 \times 10^{-6}) - (0.0298)(16.04 \times 10^{-6})}{\left[1 - (0.1)(0.0298)\right](1 + 0.0596) + (2)(0.1)(0.0298)^2}$$

$$= 35.6 \times 10^{-6}$$

$$\epsilon_{z_{case}} = \frac{16.04 \times 10^{-6} + (2)(0.0298)(35.6 \times 10^{-6})}{1 - 0.1(0.0298)} = 18.2 \times 10^{-6}$$

(3) Calculate critical stresses and strains:

$$(\sigma_{\theta} + P)_{bore} = 200\left[(0.667)(35.6 \times 10^{-6}) + (0.333)(18.2 \times 10^{-6})\right.$$

$$\left. + 1 \times 10^{-6}\right](32.6) = 0.201$$

$$(\sigma_{max} + P)_{flap} = 200(30.8 \times 10^{-6})(33.0) = 0.203$$

$$(\epsilon_{\theta})_{bore} = (30.8 \times 10^{-6})(24.9) = 0.00077$$

A finite-element solution, obtained directly for internal pressure loading, correlated with the above prediction as follows:

Stress Parameter	Pressure Loading Result	Predicted Value from Thermal Solution	Error (percent)
$(\sigma_{\theta} + P)_{bore}$	0.191	0.201	+5.2
$(\sigma_{max} + P)_{flap}$	0.200	0.203	+1.5
$(\epsilon_{\theta})_{bore}$	0.00074	0.00077	+3.5

347

The maximum error of 5.2 percent occurs in the centerport hoop stress. In al. cases, the thermal prediction is high. The predicted case hoop strain of 35.6×10^{-6} compares with pressure loading results of 35.7×10^{-6} at the flap termination, 36.6×10^{-6} at the saddle (maximum case hoop strain), and 34.5×10^{-6} at the mid-cylinder; the predicted case axial strain of 18.2×10^{-6} compares with pressure loading results of 16.6×10^{-6} at the flap termination, 16.1 at the saddle, and 15.0×10^{-6} at tne mid-cylinder. Thus, the average hoop strain in the case compares quite well with the prediction, while the predicted axial strain is too high. Omission of the bond shear stress in the grain-case coupling equations is probably to blame for the high axial strain prediction. Overall, the directly calculated pressure solution compares very favorably with the prediction based on thermal shrinkage loading.

SECTION VII

RESULTS FOR AXIAL ACCELERATION LOADING

Stress solutions for axial acceleration loading were obtained with the case considered to be rigid. The propellant, liner, flap, and insulator were given the same weight density, $\rho_w = 0.064$ lb/in.^{3} and subjected to a 1.0 g axial acceleration. Stress solutions were obtained only for $E_{insulator} = E_{flap} = 1000$ psi and $E_{liner} = E_{propellant} = 200$ psi. The flap length was 1.0 in.

Calculated radial and shear stresses for the cylinder with L/D = 3.0 and W/b = 0.8 are shown in Figure 41 for the row of elements in the case-bond liner next to the flap. The center of this element row is located 0.105 in. inboard of the insulator (0.005 in. into the liner). The shear stress reaches an average value of -0.50 psi at the mid-axial location (Z = 48 in.). Near the flap termination the shear stress has a negative peak of -0.68 psi and a positive peak of 0.23 psi. The peak radial stress at the flap termination, 3.4 psi, is much higher than the shear stress. Both the low value of the peak shear stress and the high value of the peak radial stress are somewhat surprising. Currently-used handbook methods for approximating stresses at the bond termination assume that the peak shear stress is 3.0 times the average shear stress.[10] In the sample given here, the calculated concentration factor for the peak shear stress is only 1.4. However, the peak radial stress is 4.3 times the average shear stress.

Stress values in the immediate vicinity of the flap termination are shown in Figure 42. The shear stress and maximum principal strain approach their average values to the right of the flap termination rather than approaching zero, as in the thermal solution.

Lines of constant maximum principal stress and strain in the vicinity of the flap termination are shown in Figures 43 and 44, respectively. The stress values are normalized in terms of $(\tau_{rz})_{avg}$ and the strain values are shown in terms of $\dfrac{E\,\epsilon_{max}}{(\tau_{rz})_{avg}}$ (a bond length of 94.0 in. and a radial distance of 15.895 in. were used in calculating the average shear stress). The stress values indicate a high stress concentration at the flap-insulator bond termination as expected. The overall gradient is similar to that for thermal shrinkage loading. This similarity holds quantitatively, as shown in Figure 45, wherein the ratio of the maximum principal stress inside of the liner/propellant to that at the liner-flap bondline (H_σ) decreases almost identical to that for shrinkage loading. Lines of constant maximum principal strain are essentially the same for axial acceleration and thermal shrinkage loading, as shown in Figures 7 and 44.

349

47

Finite-element stress solutions were obtained for W/b = 0.5, 0.67, and 0.8 for the cylinder with L/D = 3.0. Computed results for the critical stresses at the flap termination are shown in Figure 46. The peak stresses, when normalized with respect to the average case-bond shear stress, are essentially independent of web fraction. The peak value of the maximum principal stress (for a unit value of H_σ) is approximately equal to 4.6 times the average bond shear stress; whereas, peak value for the radial stress is approximately 4.4 times the average bond shear stress. The peak value of the bond shear stress is approximately 1.4 times the average bond shear stress. The shear stress at the location of the peak radial stress is only 0.17 times as large as the peak radial stress.

Finite-element stress solutions for W/b = 0.8 were obtained for L/D = 1.0, 3.0, and 5.0. The key stresses at the flap termination are shown in Figure 47 as a function of L/D. These critical (normalized) stress parameters are essentially independent of length-to-diameter ratio, as well as web fraction. Values for L/D = 1.0 are only 7 percent higher than those for L/D = 3.0 and 5.0. One would anticipate higher stresses relative to the average for shorter cylinders; however, dependence upon L/D is very moderate for values 1.0 and greater.

It appears that the normalized bond termination stresses for axial acceleration loading are basically dependent upon the local flap termination geometry and are independent of L/D and W/b. In this regard, the cylinder behavior is much different than for thermal shrinkage and internal pressure loadings. The peak bond stresses for axial acceleration are sensitive to flap-liner thickness in the same quantitative manner as for thermal shrinkage and internal pressure loadings. No study was performed for variations in flap length or liner-flap-insulator modulus. However, since the same stress-strain patterns exist near the flap termination for all three loading conditions, it is expected that variations for thermal shrinkage loading are representative of axial acceleration loading as well.

350

SECTION VIII

SUMMARY AND CONCLUSIONS

The important results and conclusions obtained from the parameter study are as follows:

(1) Case-bond stresses for thermal shrinkage and internal pressure loading become larger as web fraction and length-to-diameter ratio increase. However, as L/D and W/b increase, the end termination stresses decrease relative to the centerport hoop stress and the radial bond stress at the mid-cylinder location.

(2) Case-bond stress distributions at flap terminations are a function of the local geometry only and are relatively insensitive to changes in W/b and L/D for the loadings studied.

(3) Modest changes in flap and case-bond liner stiffness have little effect on local case-bond stress levels.

(4) Flap length is a less significant factor than flap thickness in determining stresses at the flap terminations.

(5) Case-bond and propellant stresses can be predicted quite accurately for internal pressure loading using thermal shrinkage solutions.

(6) The case-bond radial stress at flap terminations is much larger than the shear stress under axial acceleration loading, as well as under thermal shrinkage and internal pressure loading.

(7) Flap termination stresses relative to the average case-bond shear stress are insensitive to L/D and W/b for axial acceleration loading.

351

REFERENCES

1. Durelli, A. J., et al., "Study of Stress Concentrations at the Ends of Solid Propellant Grains Subjected to Restrained Shrinkage," Catholic University, Final Report, Contract No. AF-04(611)-10378, May 1966.

2. Messner, A. M., and Schiessmann, D., "Parameter Calculation of Simple Propellant Grains for Temperature Cycling, Pressurization, and Acceleration," Appendix D, Study of Mechanical Properties of Solid Propellants, Aerojet-General Report No. 0411-10F, March 1962, and Lockheed Propulsion Company Structures Manual, December 1969.

3. Shearly, R. N., and Messner, A. M., "Stresses in Propellant Grain Bond Systems," Bulletin of the 3rd Meeting ICRPG Working Group on Mechanical Behavior, CPIA Publication No. 61V, Vol. I, October 1964.

4. Noel, J. S., and Webb, L. D., "The Role of Fracture Mechanics in the Design of Optimum Grain-Case Terminations," Bulletin of the 5th Meeting ICRPG Working Group on Mechanical Behavior, CPIA Publication No. 119, Vol. I, October 1966.

5. Becker, E. B., and Brisbane, J. J., "Application of the Finite Element Method to Stress Analysis of Solid Propellant Rocket Grains," Rohm & Haas Report No. S-76, November 1965.

6. Bridgeman, P. W., "The Compression of 46 Substances to 50,000 kg/cm^3," 8 November 1930.

7. Jones, J. W., "Engineering Methods for Grain Structural Integrity Analysis," LPC Report No. 578/556-F-3, Lockheed Propulsion Company, Redlands, California, May 1963.

8. Parr, C. H., "Deformations and Stresses in a Case-Bonded Solid Propellant Grain of Finite Length by Numerical Methods," Rohm & Haas Quarterly Progress Report on Engineering Research, Report No. P-61-17, 25 June 1962.

9. Holsapple, K. A., Schmidt, W. F., and Fourney, M. E., "Some Pressure-Temperature Equivalences in Elasticity, with Applications to Case-Bonded Solid Propellant Rocket Grains," Journal of Applied Mechanics, Vol. 37, No. 4, December 1970.

10. Fitzgerald, J. E., and Hufferd, W. L., "Handbook for the Engineering Structural Analysis of Solid Propellants," CPIA Publications 214, May 1971.
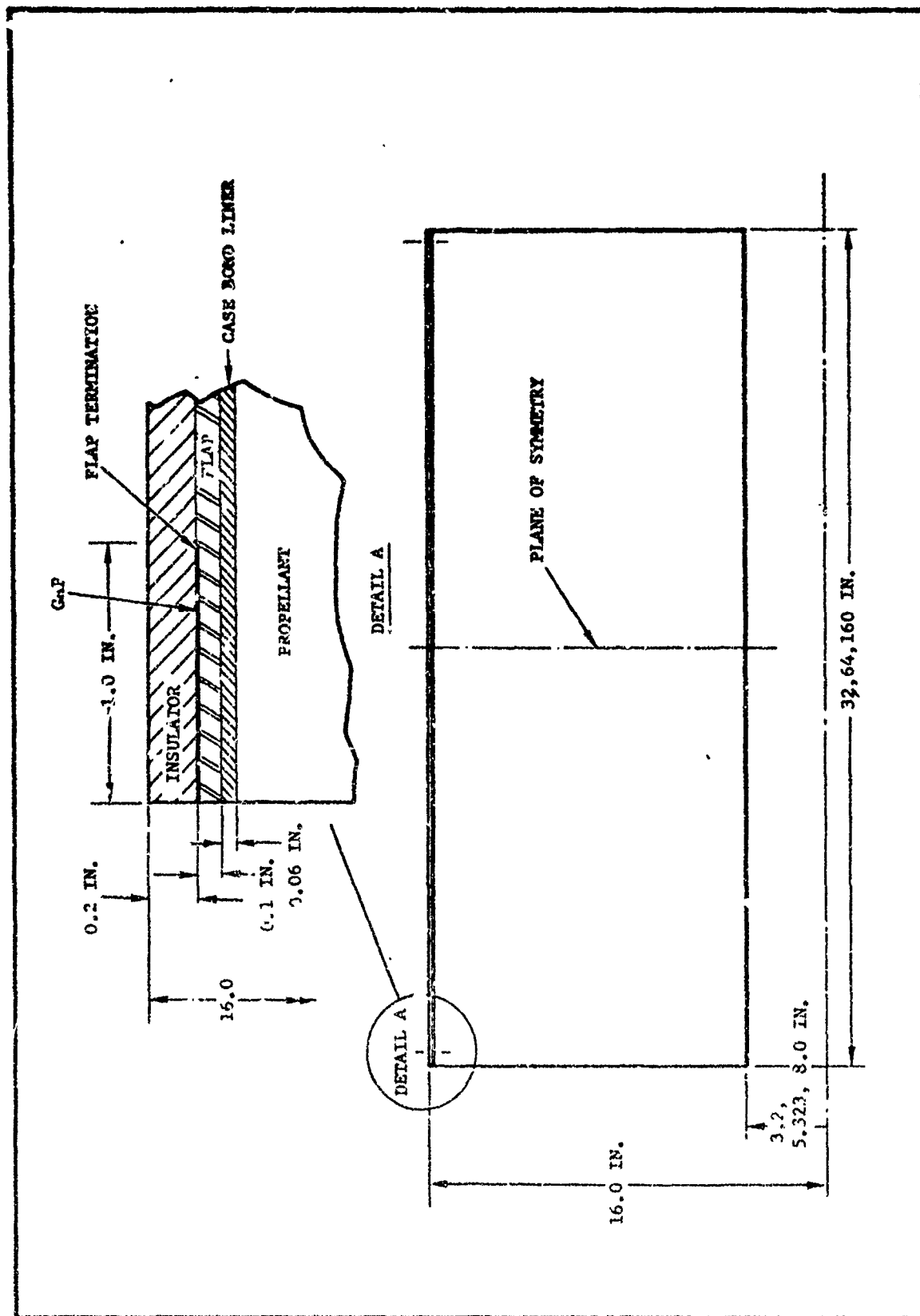
Figure 1. Cylinder Model for Flap Termination Studies

31
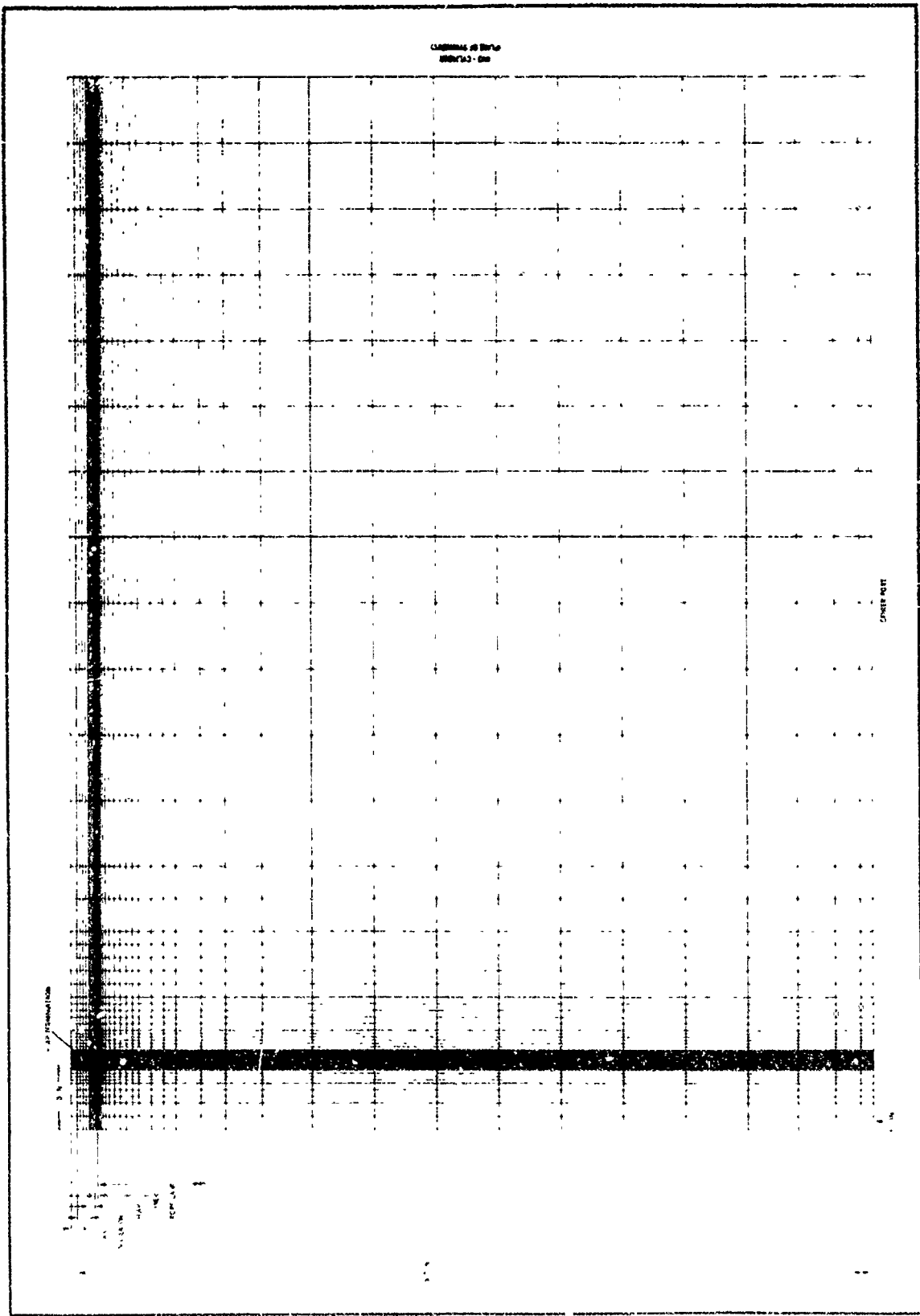
Figure 2. Finite Element Model for Cylinder with L/D = 1.0 and W/b = 0.8
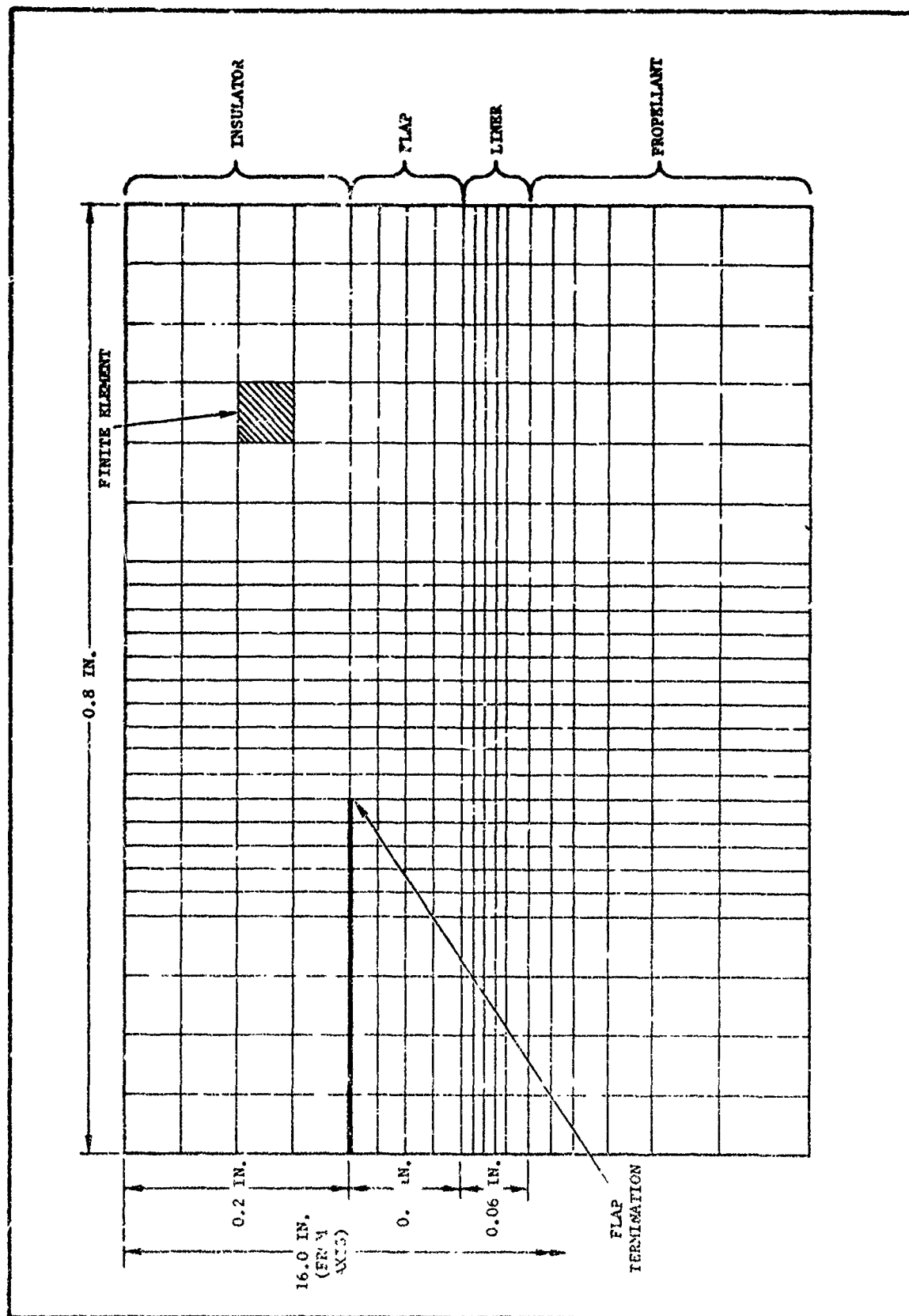
Figure 3. Finite Element Grid Detail Adjacent to Flap Termination
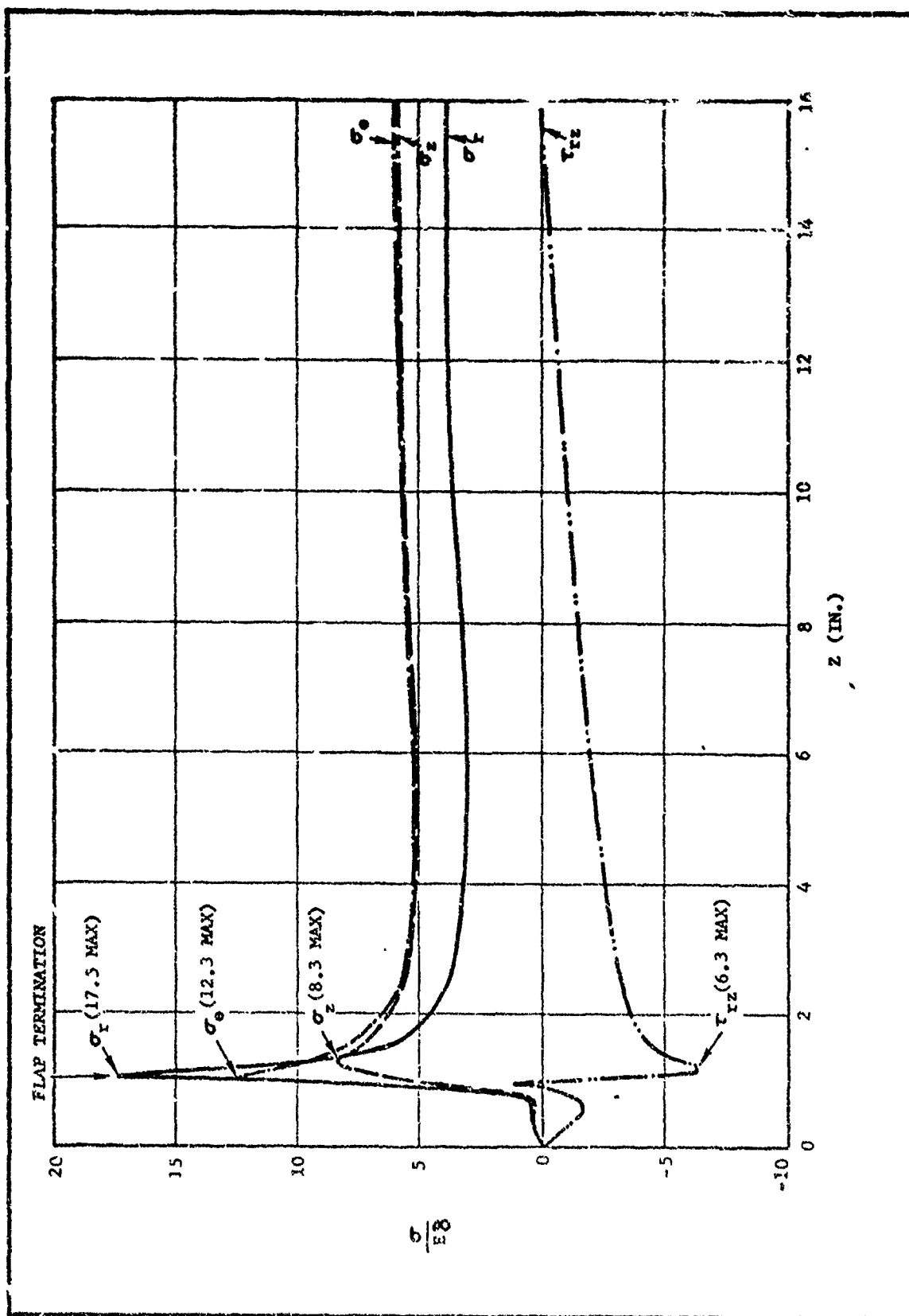
Figure 4. Case Bond Liner Stresses for a Cylinder with L/D = 1.0 and W/b = 0.8 Under Thermal Shrinkage Loading
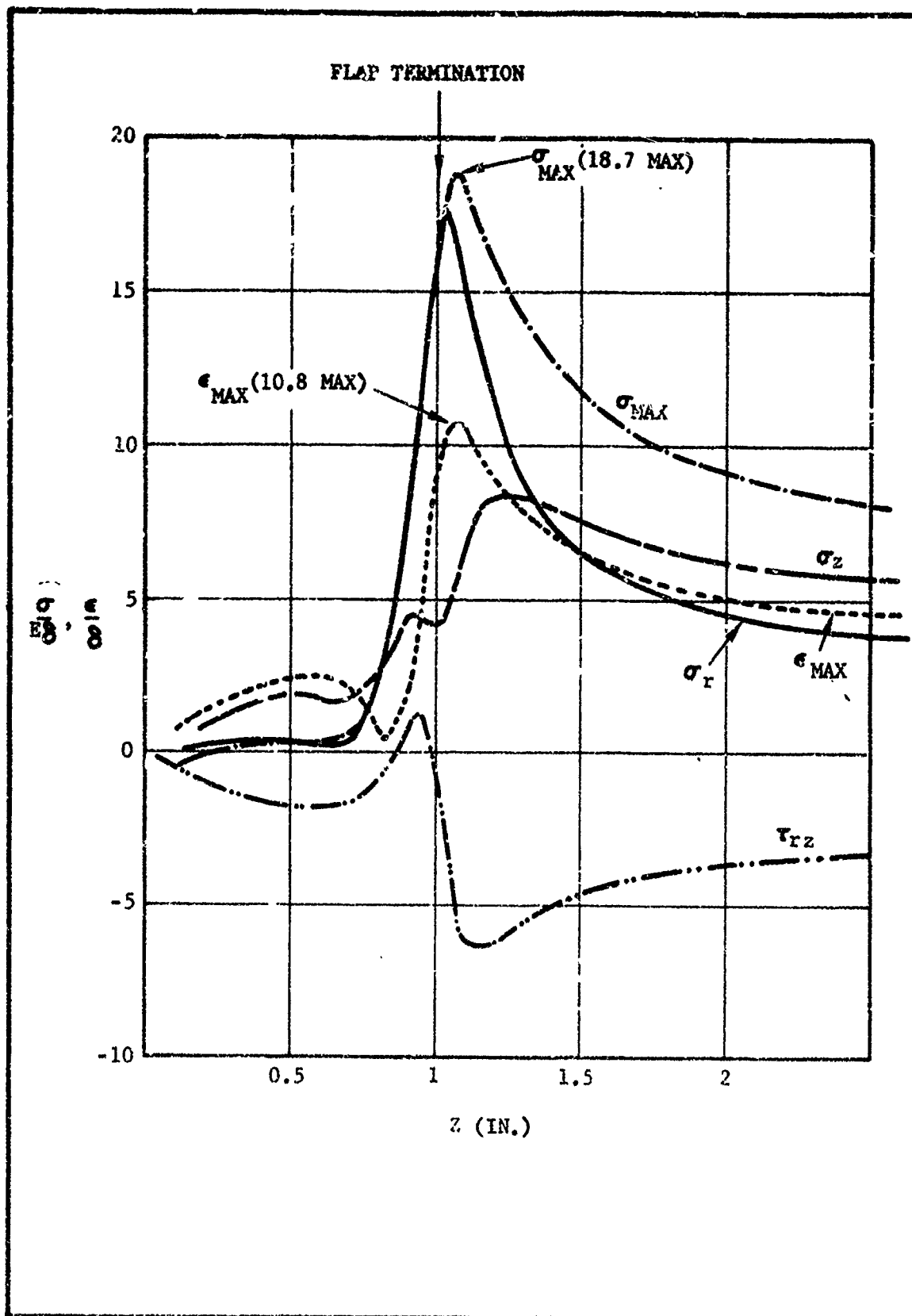
Figure 5.   Case Bond Liner Stresses Near the Flap Termination for a
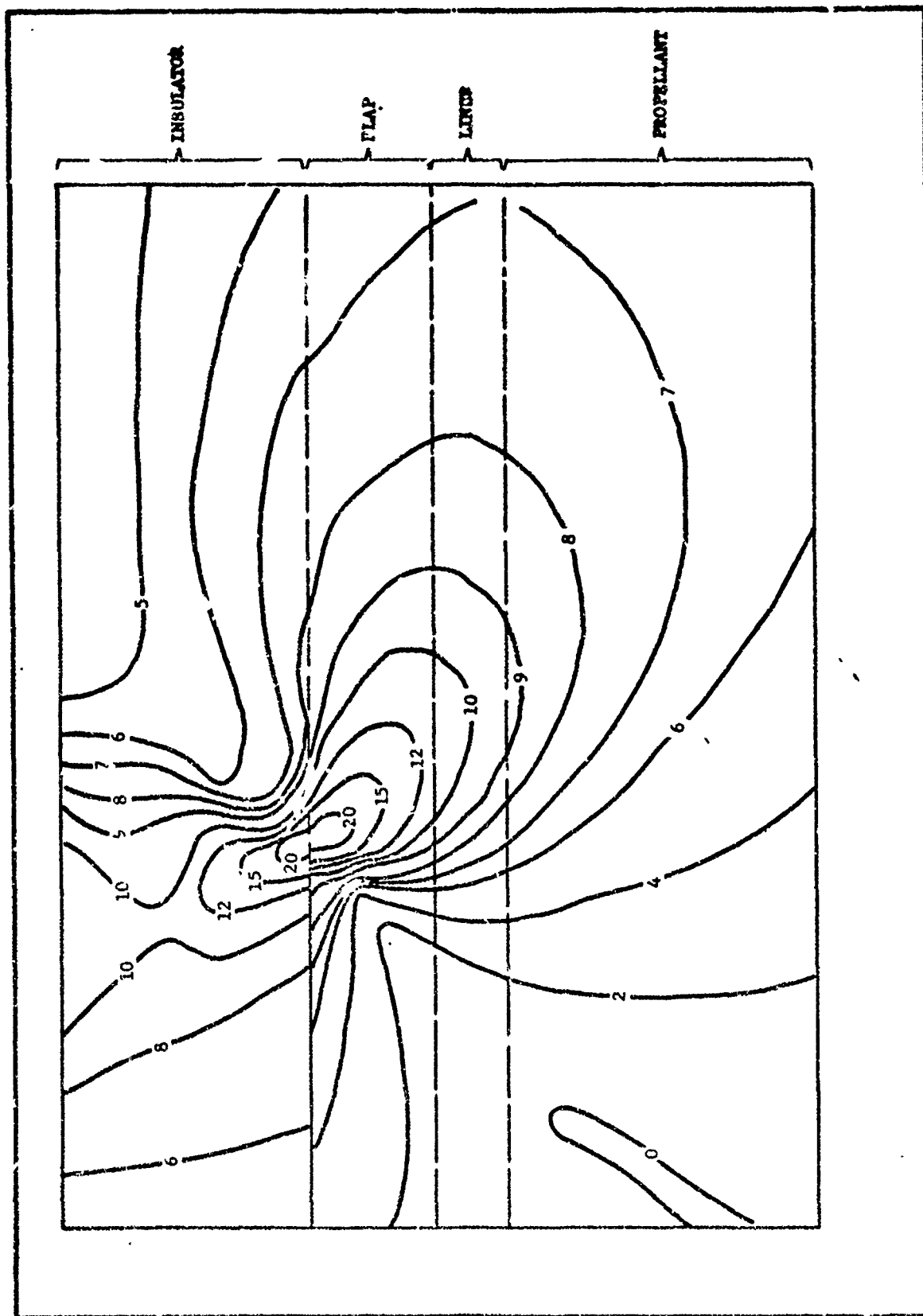Cylinder with L/D = 1.0 and W/b = 0.8 Under Thermal
Shrinkage Loading

357
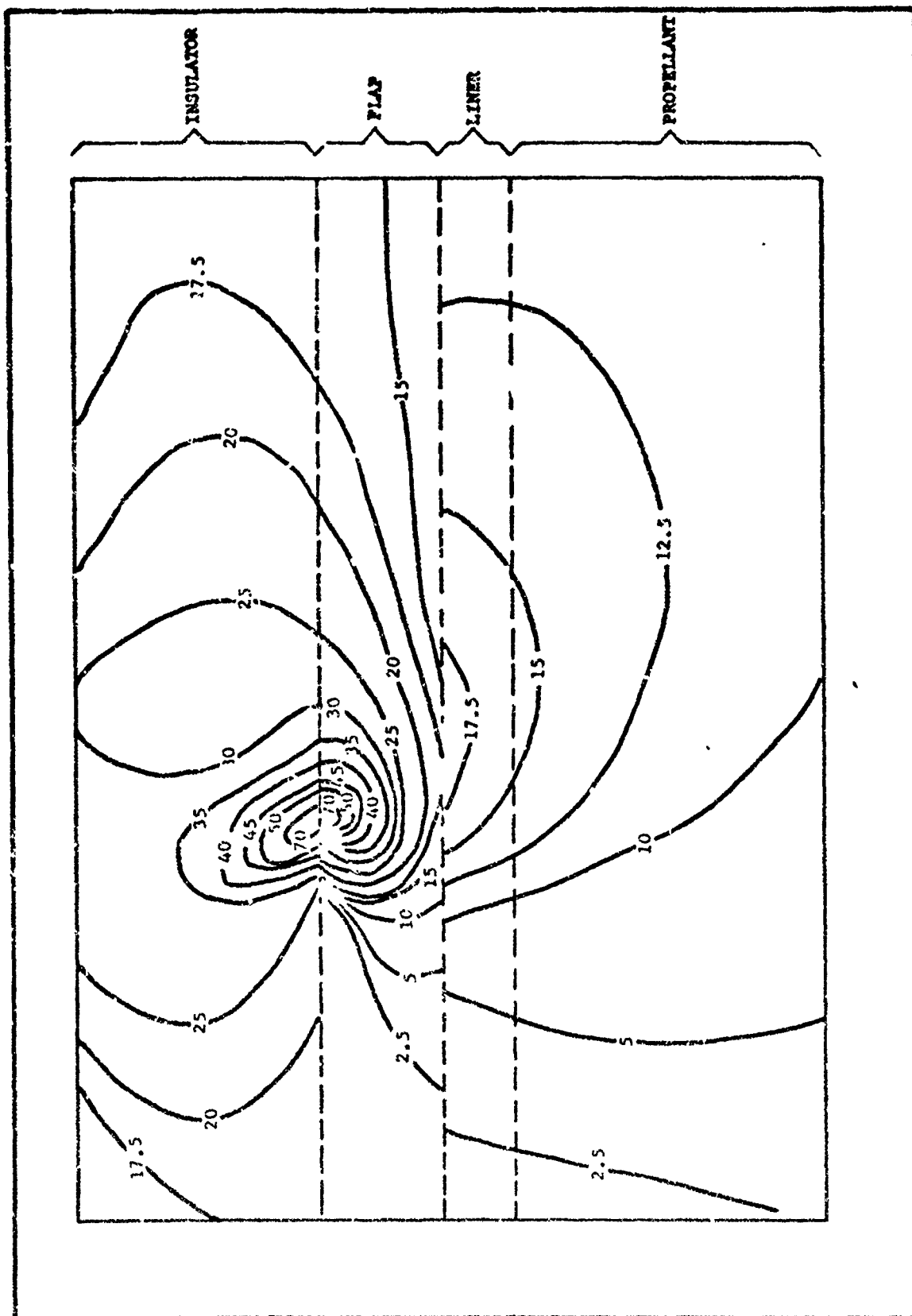
Figure 6. Lines of Constant Maximum Principal Stress $\left(\dfrac{\sigma_{max}}{E_0}\right)$ in the Vicinity of the Flap Termination for a Cylinder with L/D = 1.0 and W/b = 0.8 Under Thermal Shrinkage Loading
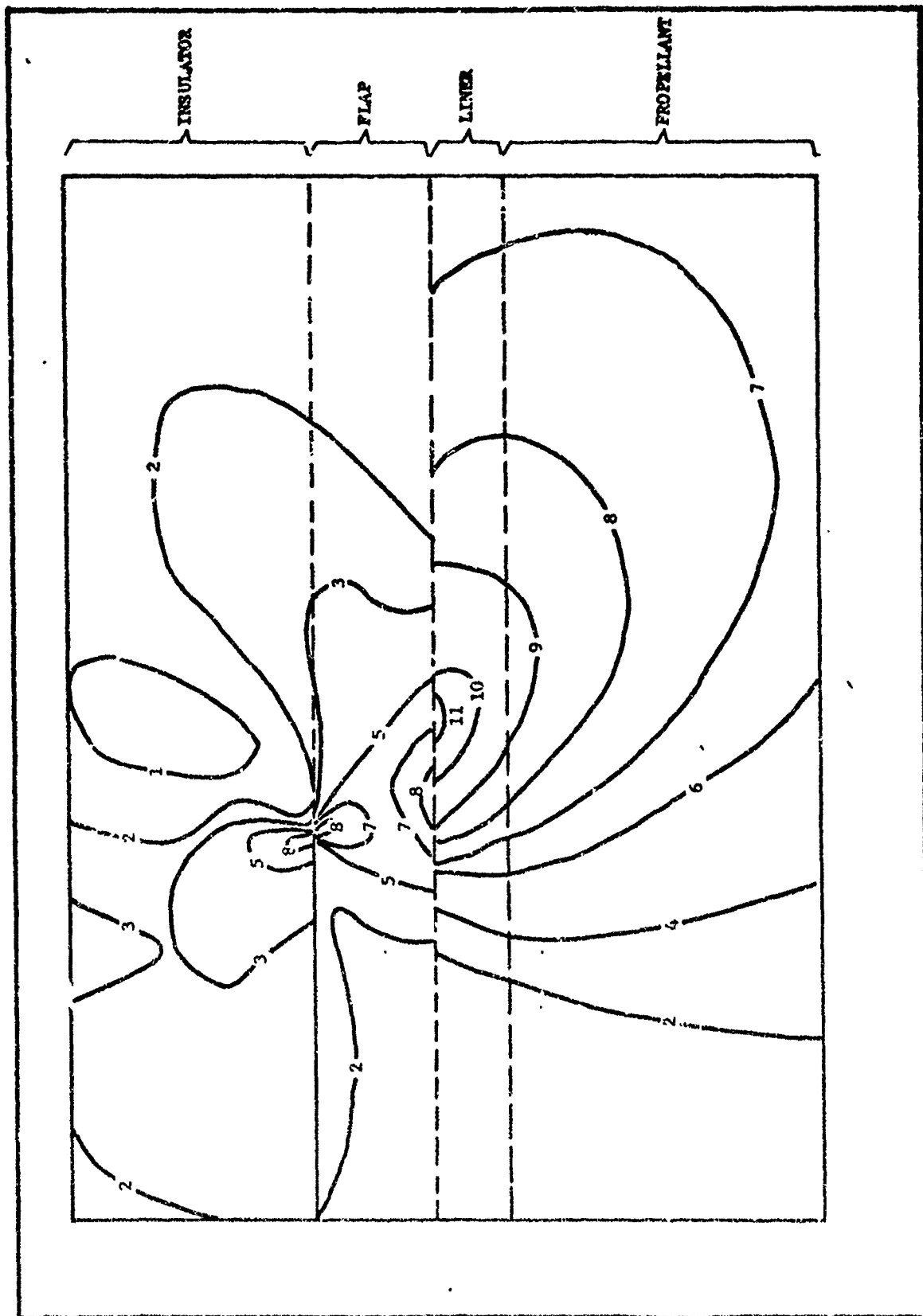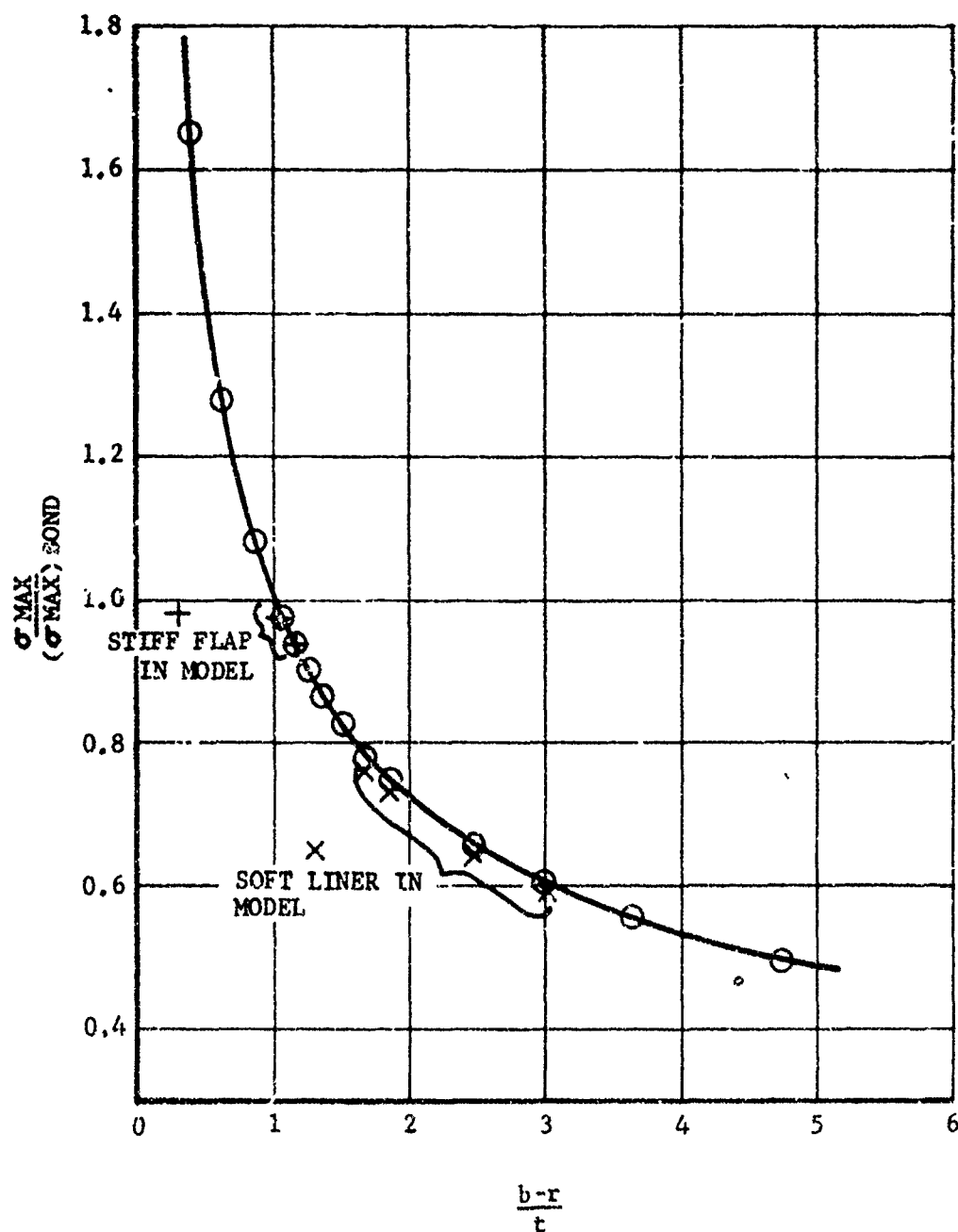
Figure 7. Lines of Constant Maximum Principal Strain $\left(\frac{\epsilon_{max}}{8}\right)$ in the Vicinity of the Flap Termination for a Cylinder with L/D = 1.0 and W/b = 0.8 Under Thermal Shrinkage Loading

359
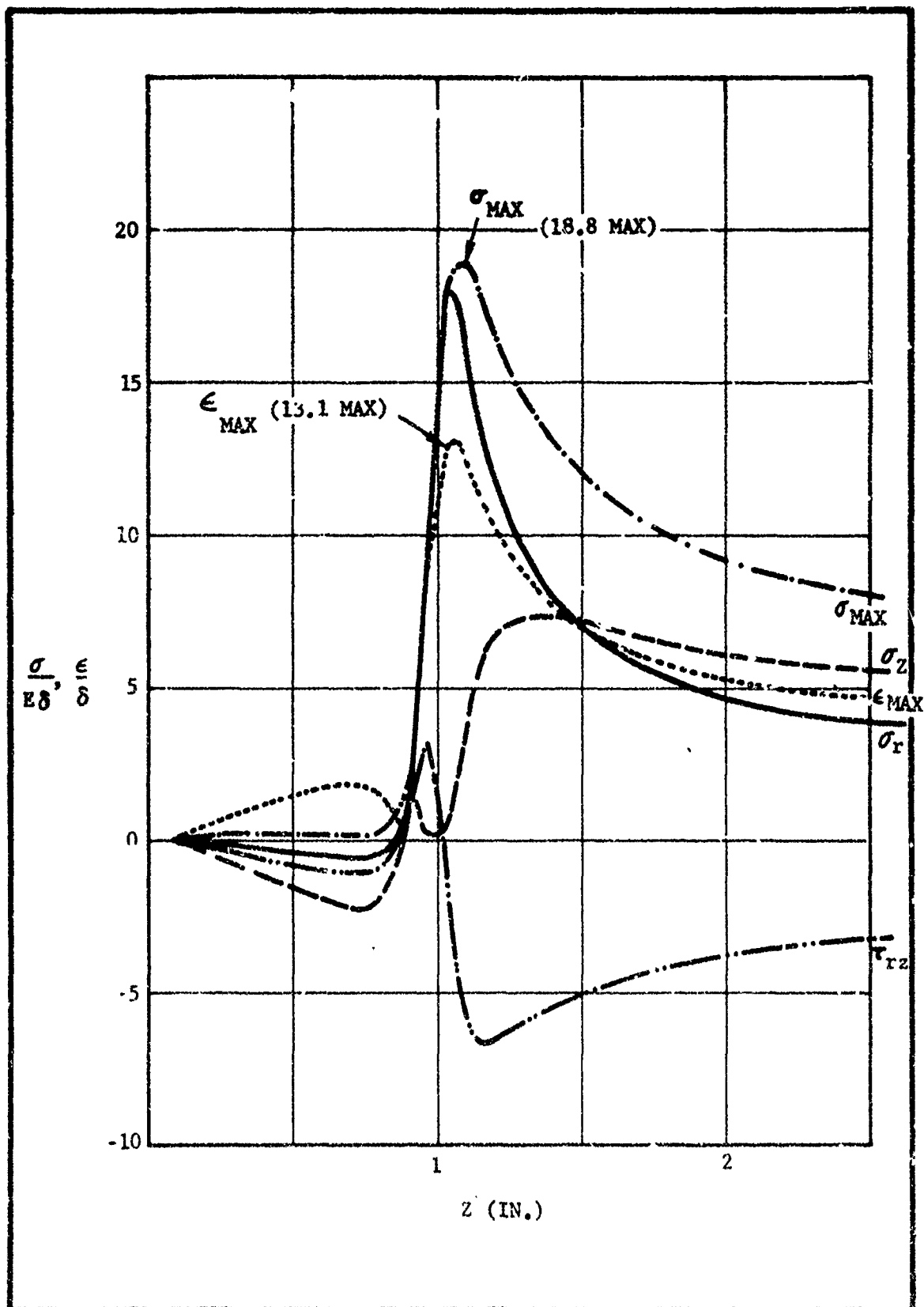
Figure 8. Case Bond Liner Stresses Near the Flap Termination for a
Cylinder with L/D = 1.0 and W/b = 0.8 (E_{flap} = 200 psi) Under
Thermal Shrinkage Loading
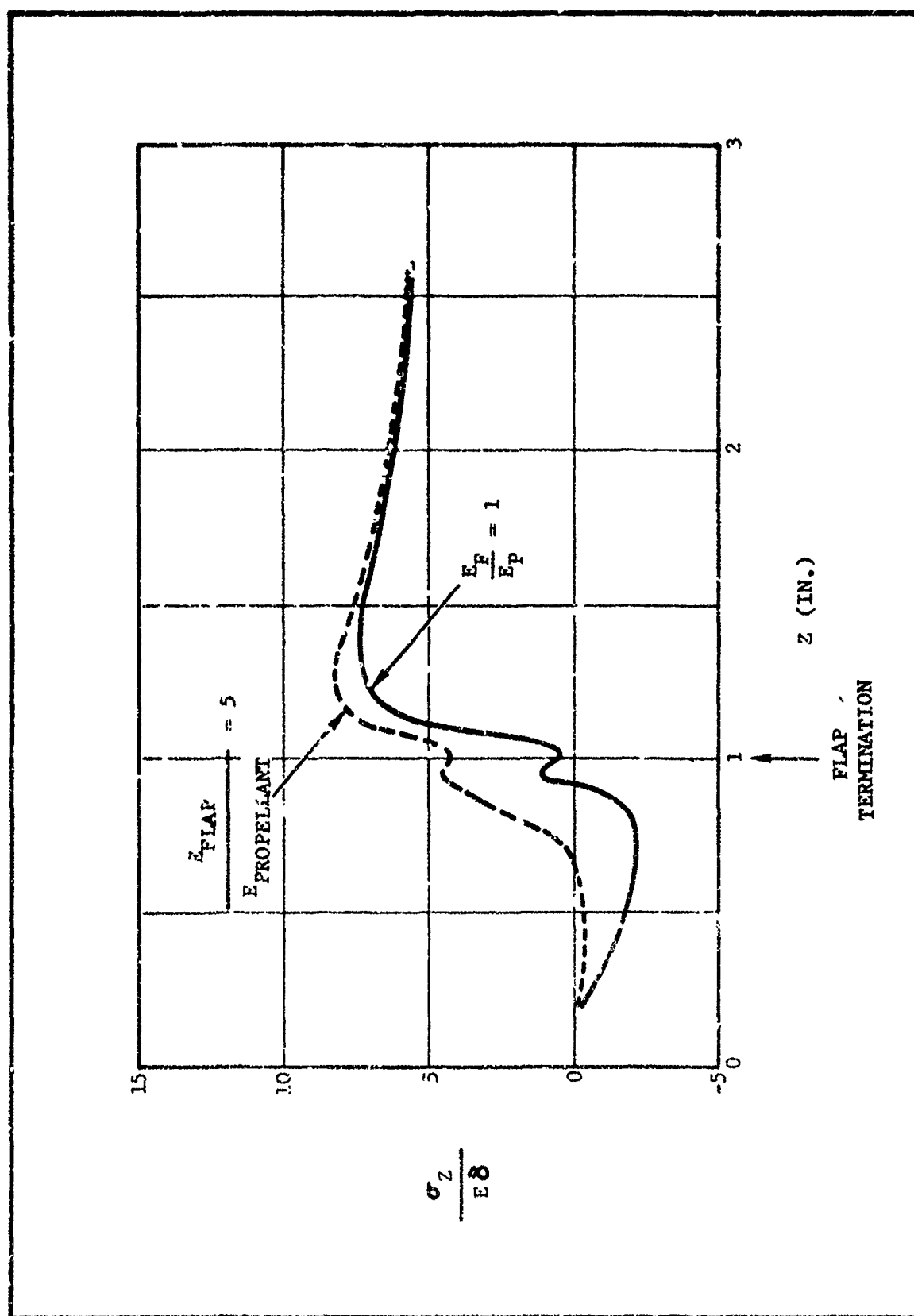
Figure 9 Case Bond Axial Stresses in the Liner Near the Flap Termination for a Cylinder with L/D = 1.0 and W/b = 0.8 Under Thermal Shrinkage Loading

361

39
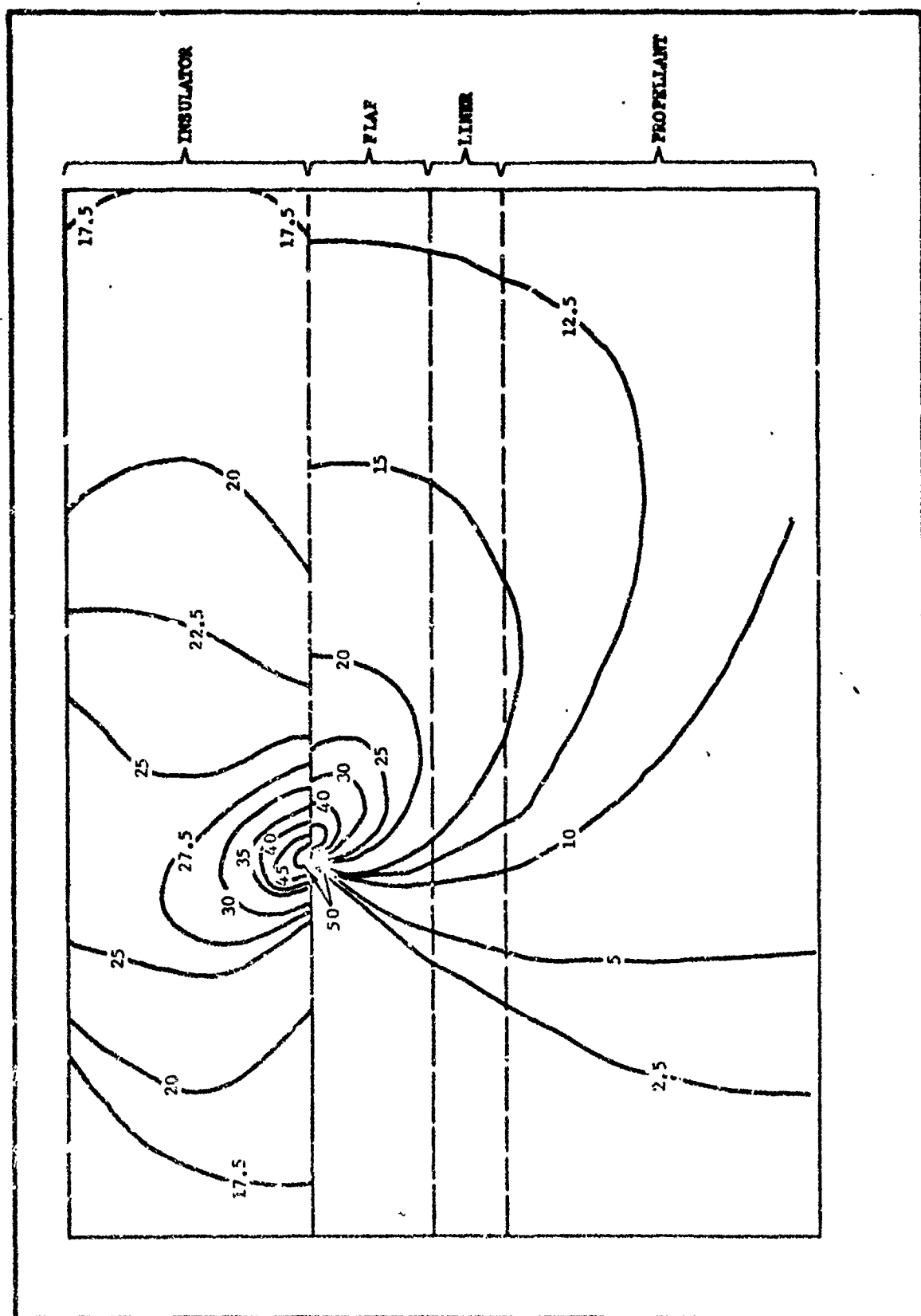
Figure 10. Lines of Constant Maximum Principal Stress $\left(\frac{\sigma_{max}}{E8}\right)$ in the Vicinity of the Flap Termination for a Cylinder with $L/D = 1.0$ and $W/b = 0.8$ ($E_{flap} = 200$ psi) Under Thermal Shrinkage Loading
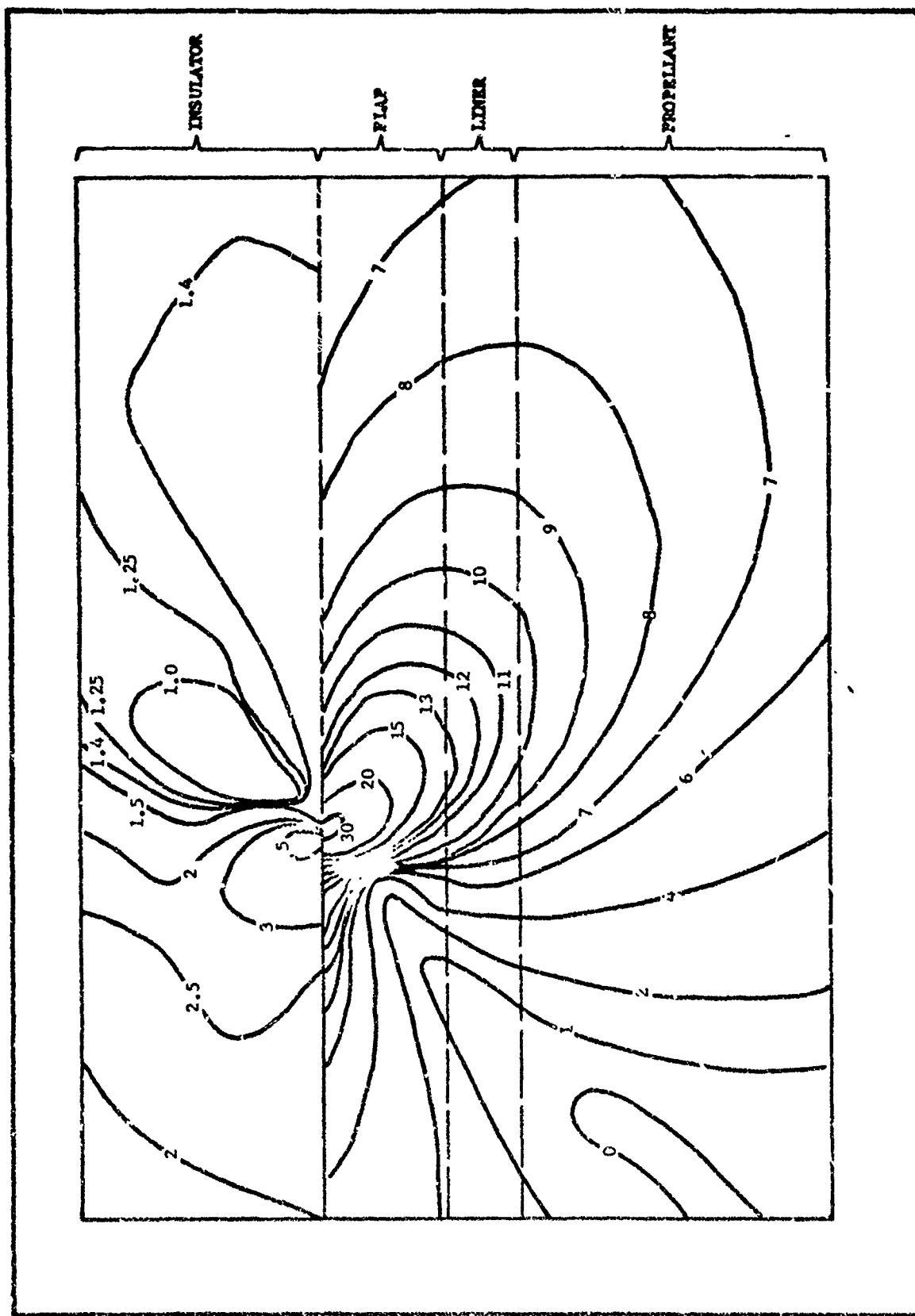
Figure 11. Lines of Constant Maximum Principal Strain $\left(\frac{\varepsilon_{max}}{8}\right)$ in the vicinity of the Flap Termination for a Cylinder with L/D = 1.0 and W/b = 0.8 (E_{flap} = 200) Under Thermal Shrinkage Loading

41
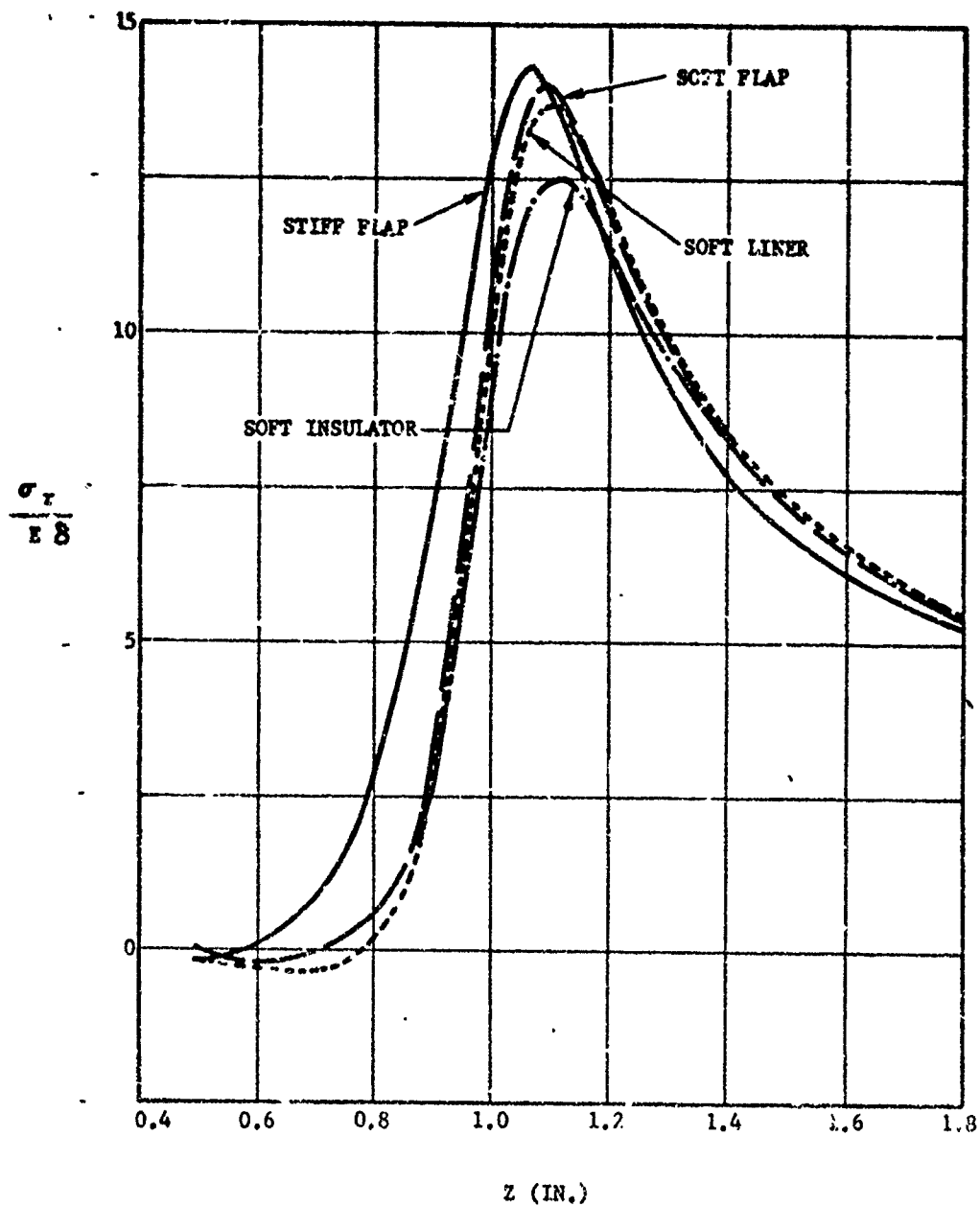
Figure 12. Propellant Radial Stresses at the Propellant-to-Liner Bond Adjacent to the Flap Termination for a Cylinder with $L/D = 1.0$ and $W/b = 0.8$ Under Thermal Shrinkage Loading

364
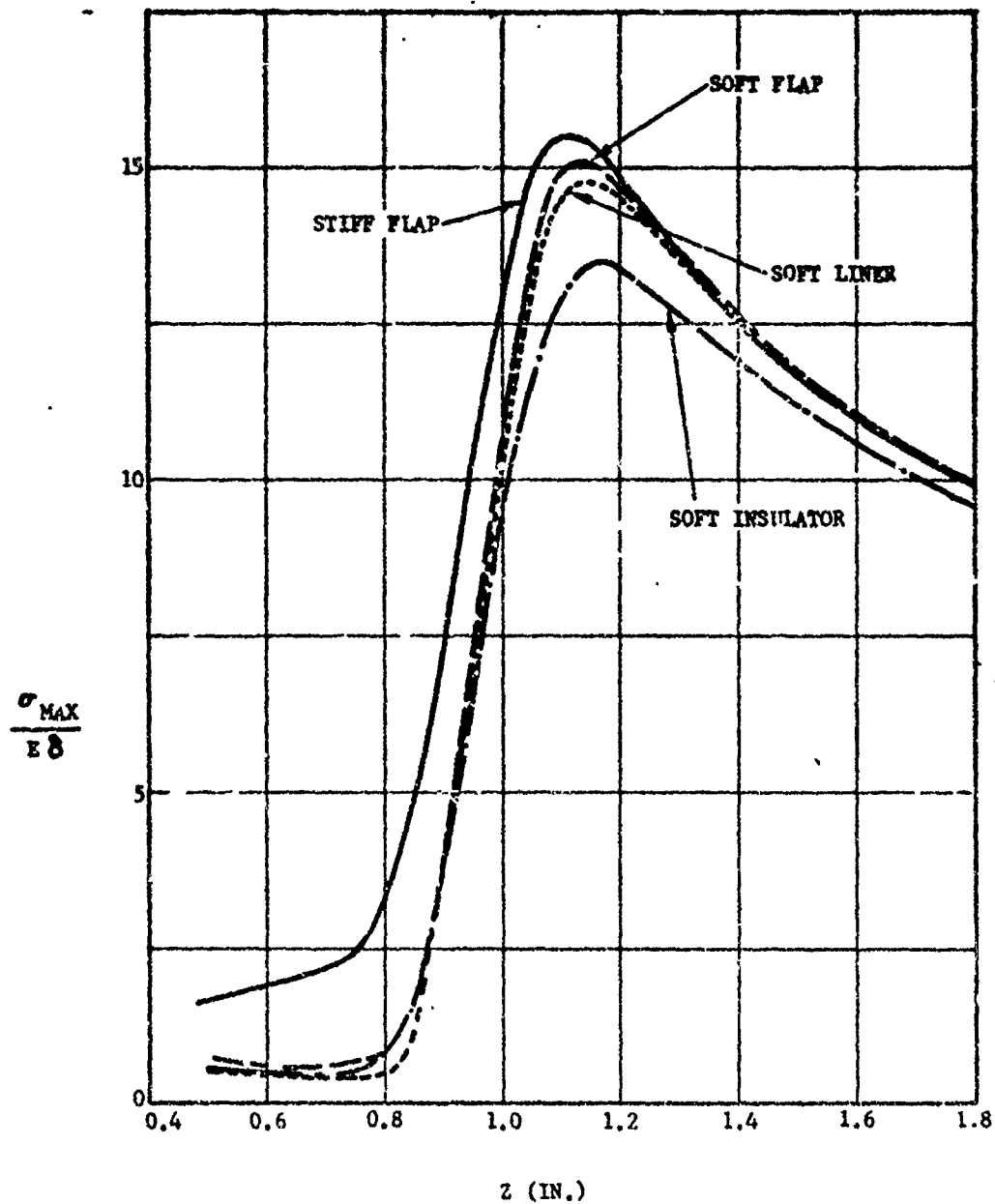
Figure 13. Propellant Maximum Principal Stresses at the Propellant-to-Liner Bond Adjacent to the Flap Termination for a Cylinder with L/D = 1.0 and W/b = 0.8 Under Thermal Shrinkage Loading

43   365
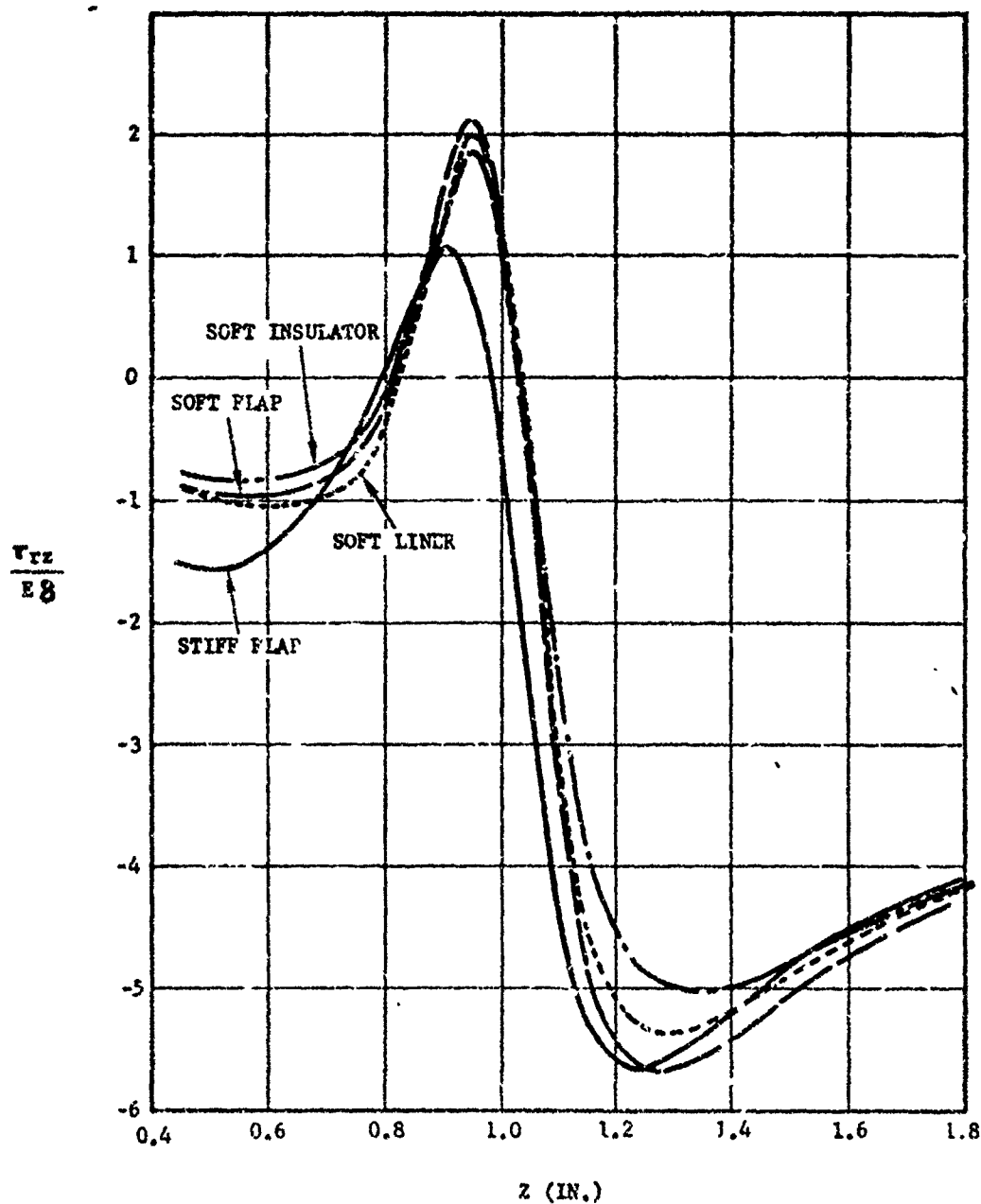
Figure 14.   Propellant Shear Stresses at the Propellant-to-Liner Bond Adjacent to the Flap Termination for a Cylinder with L/D = 1.0 and W/b = 0.8 Under Thermal Shrinkage Loading

366
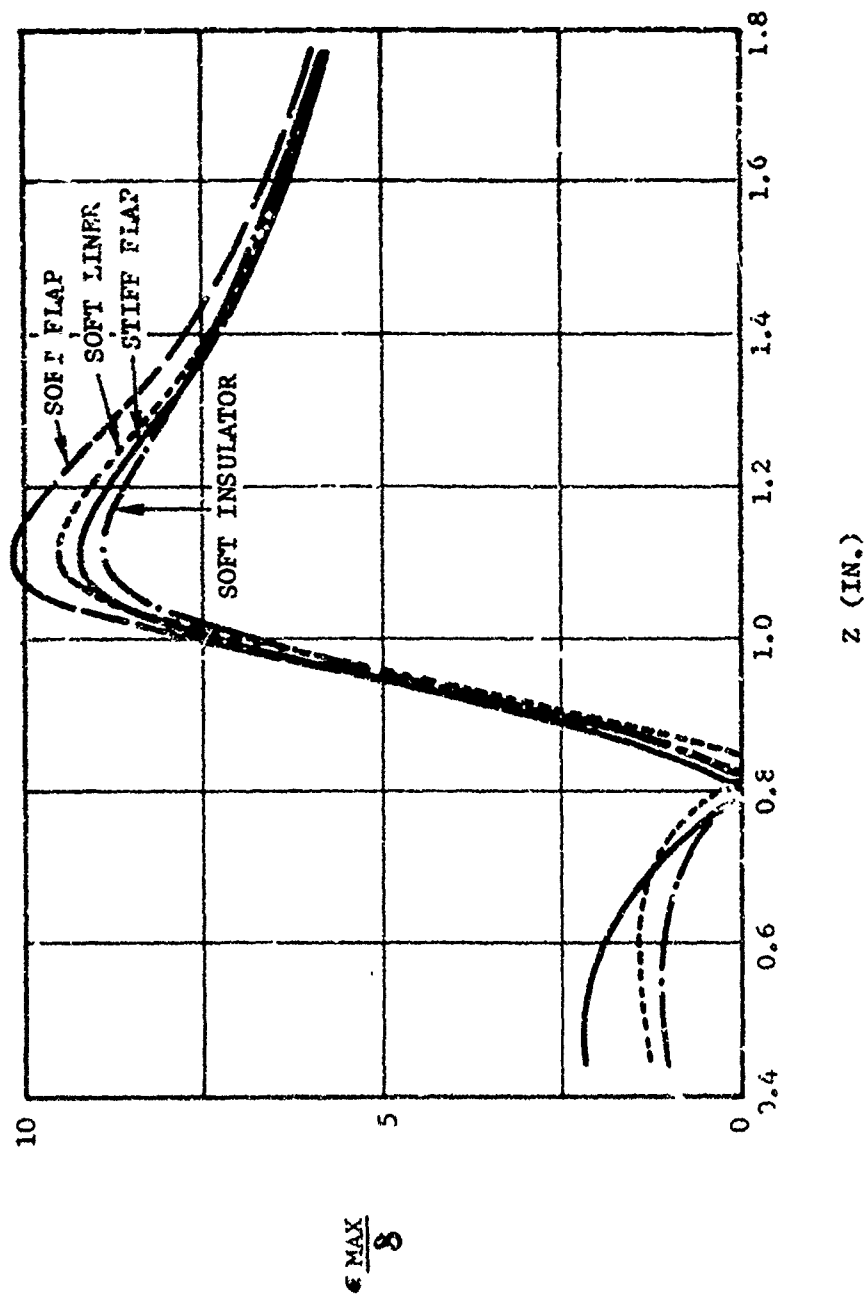
Figure 15. Propellant Maximum Principal Strains at the Propellant-to-Liner Bond Adjacent to the Flap Termination for a Cylinder with L/D = 1.0 and W/b = 0.8 Under Thermal Shrinkage Loading
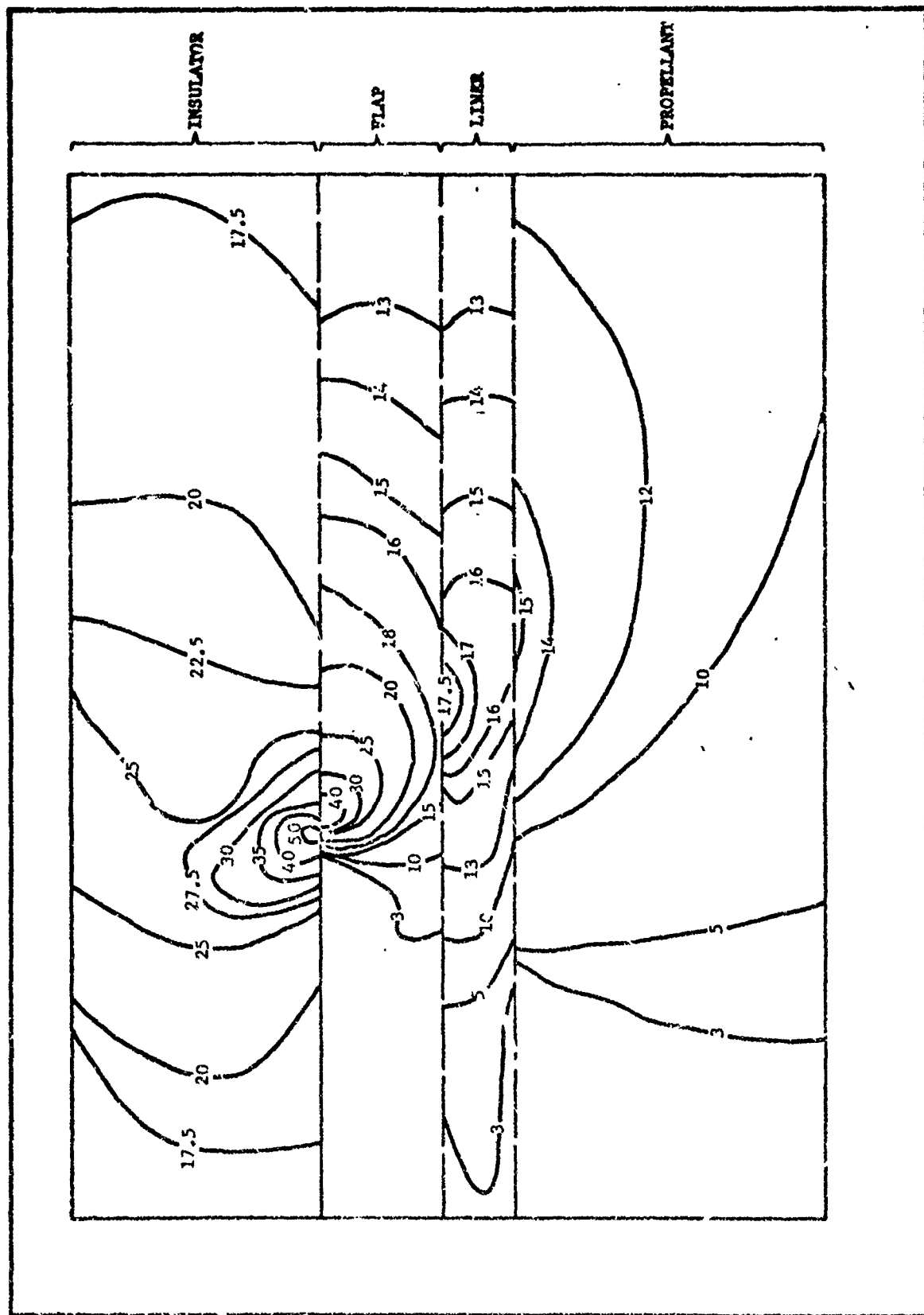
Figure 16. Lines of Constant Maximum Principal Stress $\left(\frac{\sigma_{max}}{E\beta}\right)$ in the Vicinity of the Flap Termination for a Cylinder with L/D = 1.0 and W/b = 0.8 (E_{flap} = 200 psi, E_{liner} = 100 psi) Under Thermal Shrinkage Loading

368
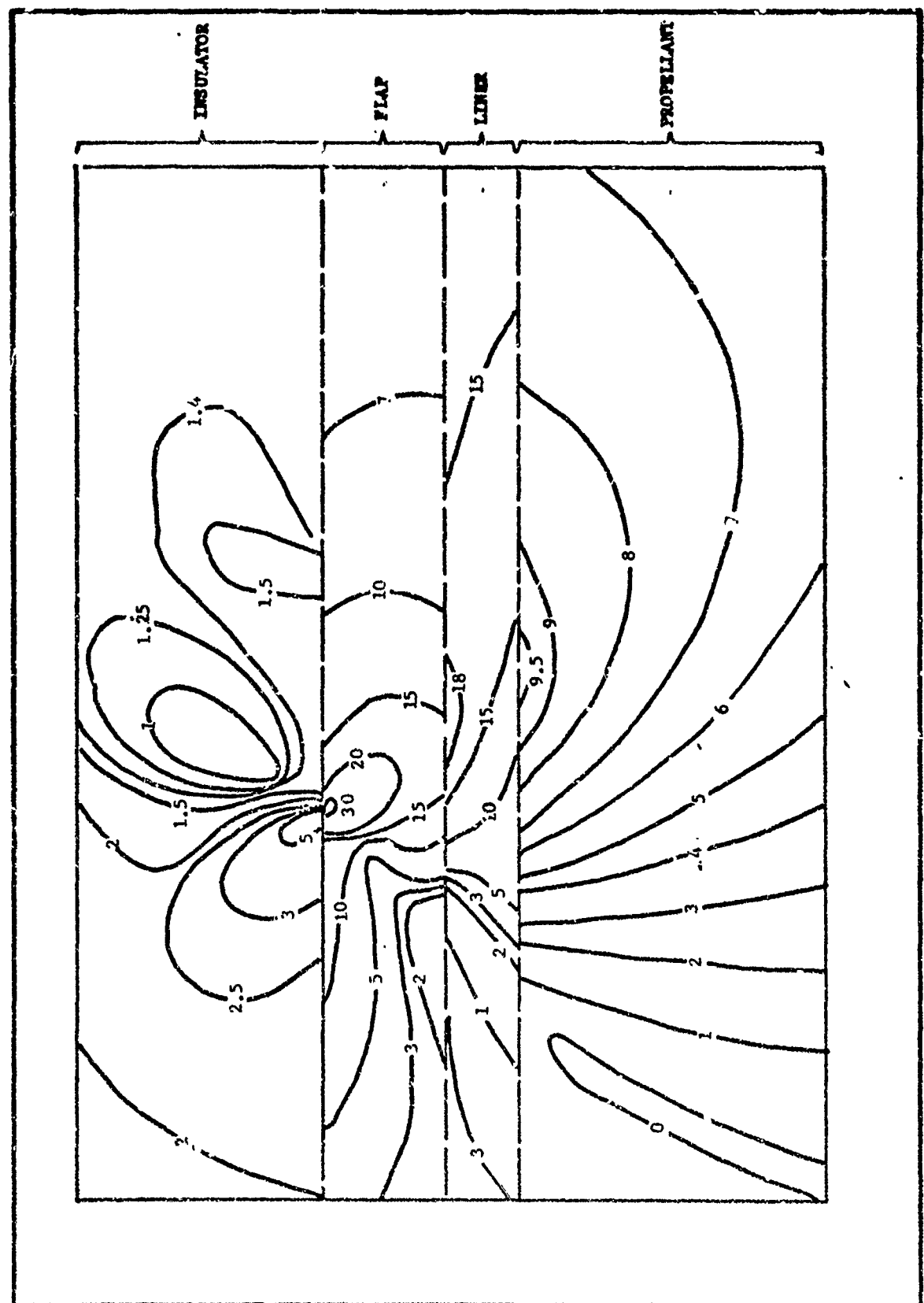
Figure 17. Lines of Constant Maximum Principal Strain $\left(\frac{\epsilon_{max}}{\delta}\right)$ in the Vicinity of the Flap Termination for a Cylinder with $L/D = 1.0$ and $W/b = 0.8$ ($E_{flap} = 200$ psi, $E_{liner} = 100$ psi) Under Thermal Shrinkage Loading

369
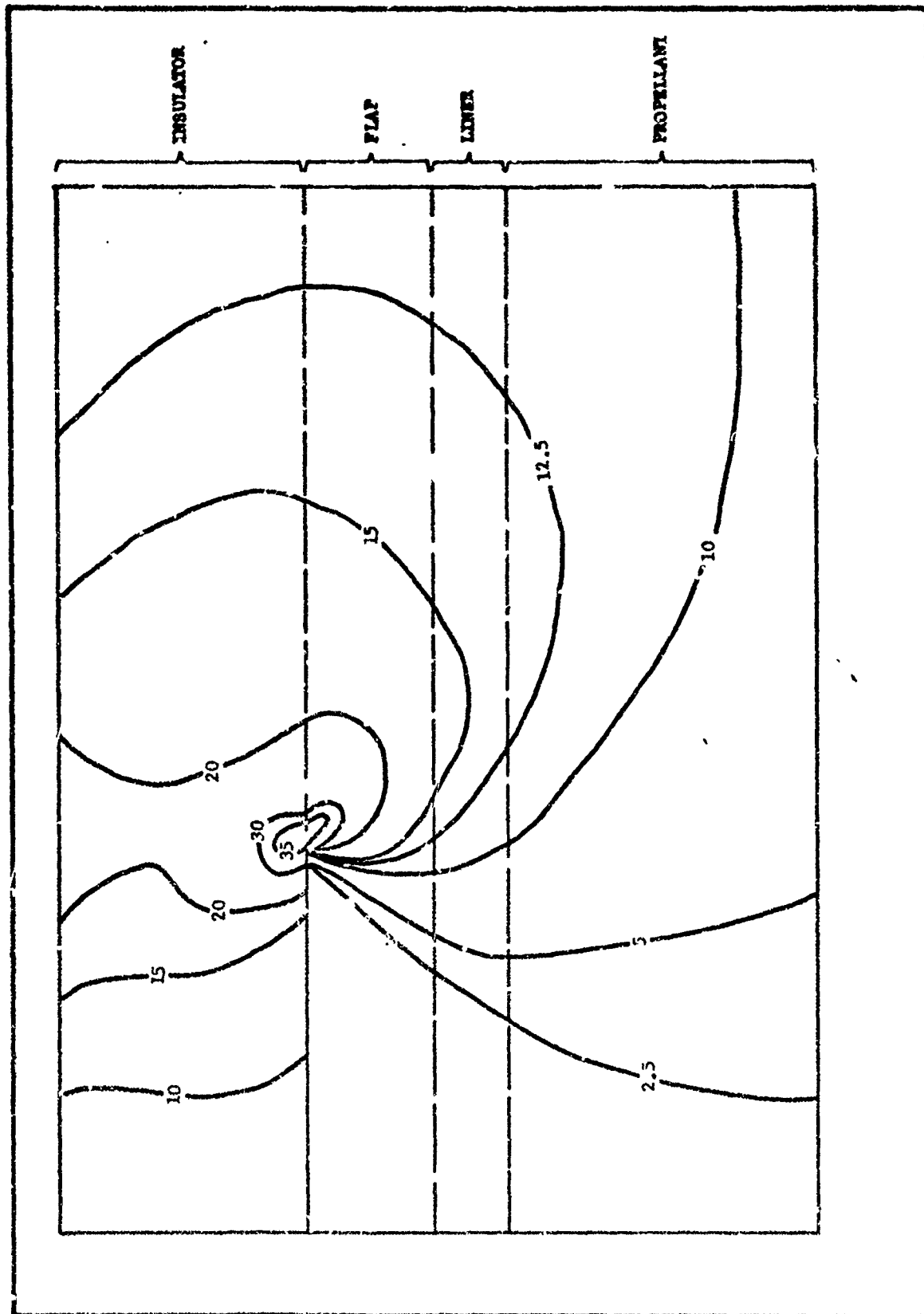
Figure 18. Lines of Constant Maximum Principal Stress $\left(\frac{\sigma_{max}}{E8}\right)$ in the Vicinity of the Flap Termination for a Cylinder with L/D = 1.0 and W/b = 0.9 (E_{flap} = $E_{insulator}$ = E_{liner} = 300 psi) Under Thermal Shrinkage Loading

Figure 19. Lines of Constant Maximum Principal Strain $\left(\frac{\epsilon_{max}}{\delta}\right)$ in the Vicinity of the Flap Termination for a Cylinder with L/D = 1.0 and W/b = 0.8 (E_{flap} = $E_{insulator}$ = E_{liner} = 200 psi) Under Thermal Shrinkage Loading.

371

Figure 20. Ratio of the Maximum Principal Stress in the Flap, Liner, and Propellant to that at the Flap-Liner Interface in the Vicinity of the Flap Termination for a Cylinder with L/D = 1.0 and W/b = 0.8 Under Thermal Shrinkage Loading
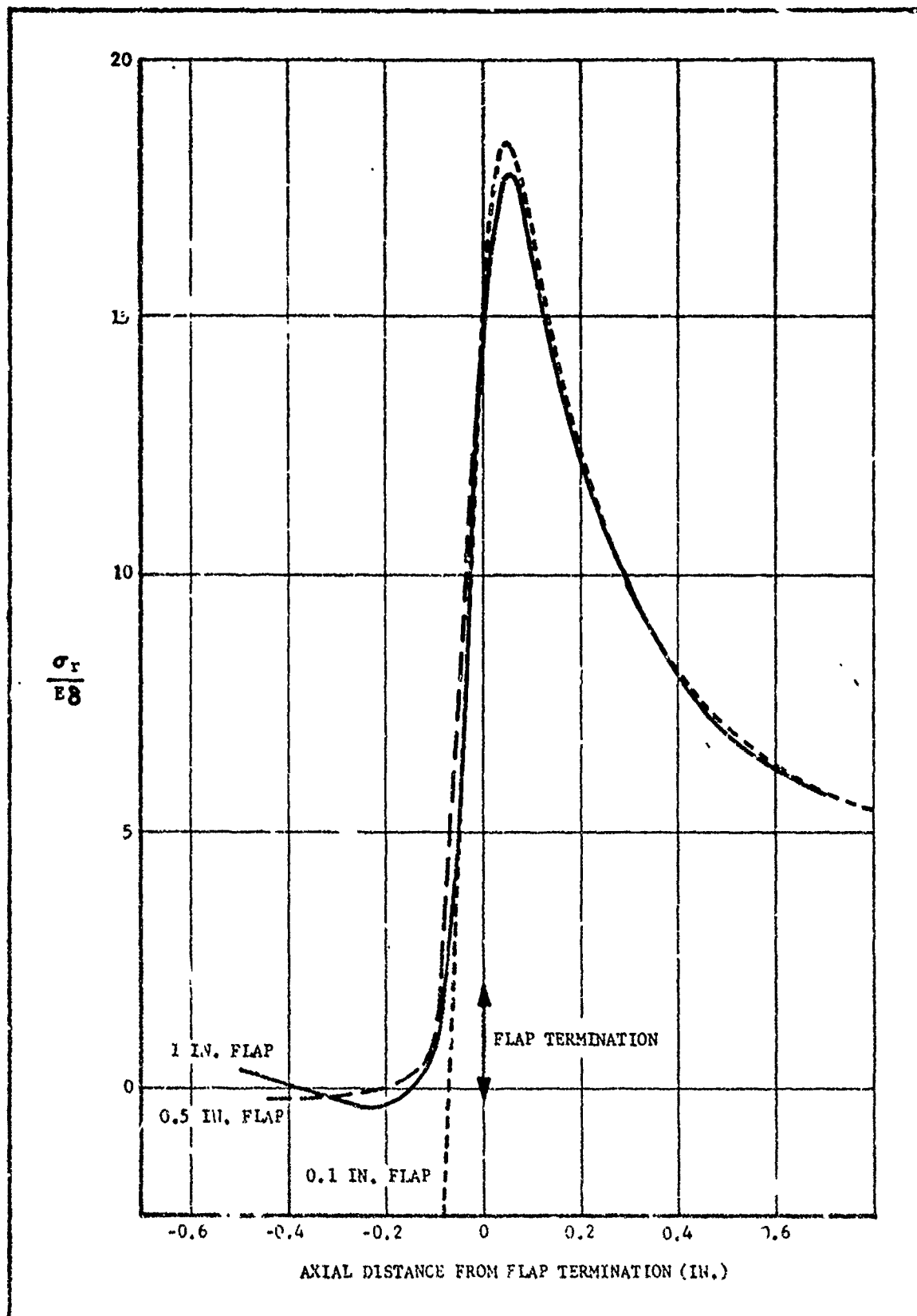
Figure 21. Radial Stress in the Case Bond Liner for a Cylinder with L/D = 1.0
and W/b = 0.8 and a Variable Flap Length Under Thermal Shrinkage
Loading   373
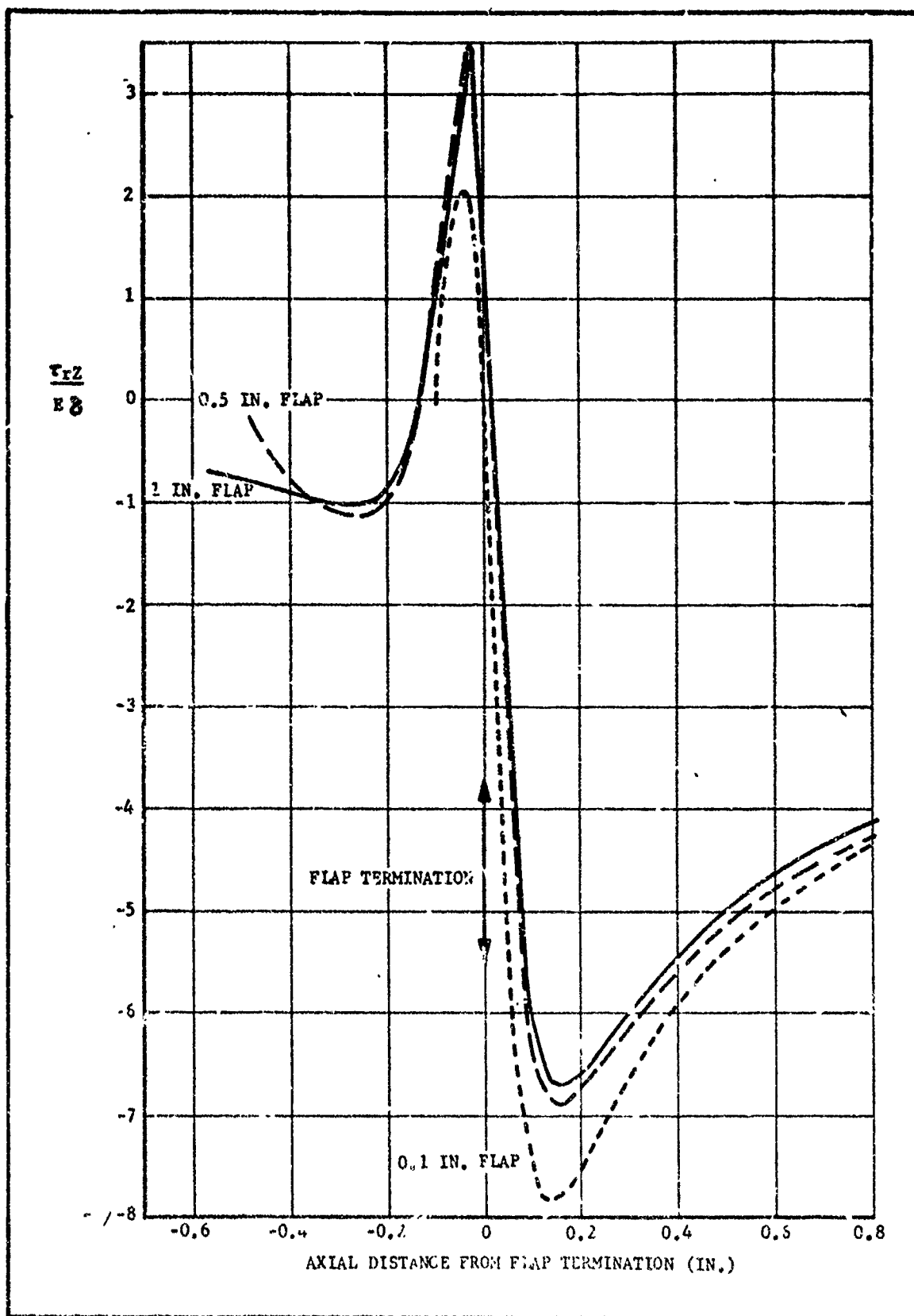
Figure 22. Shear Stress in the Case Bond Liner for a Cylinder with L/D = 1.0 and W/b = 0.8 and a Variable Flap Length Under Thermal Shrinkage Loading

374
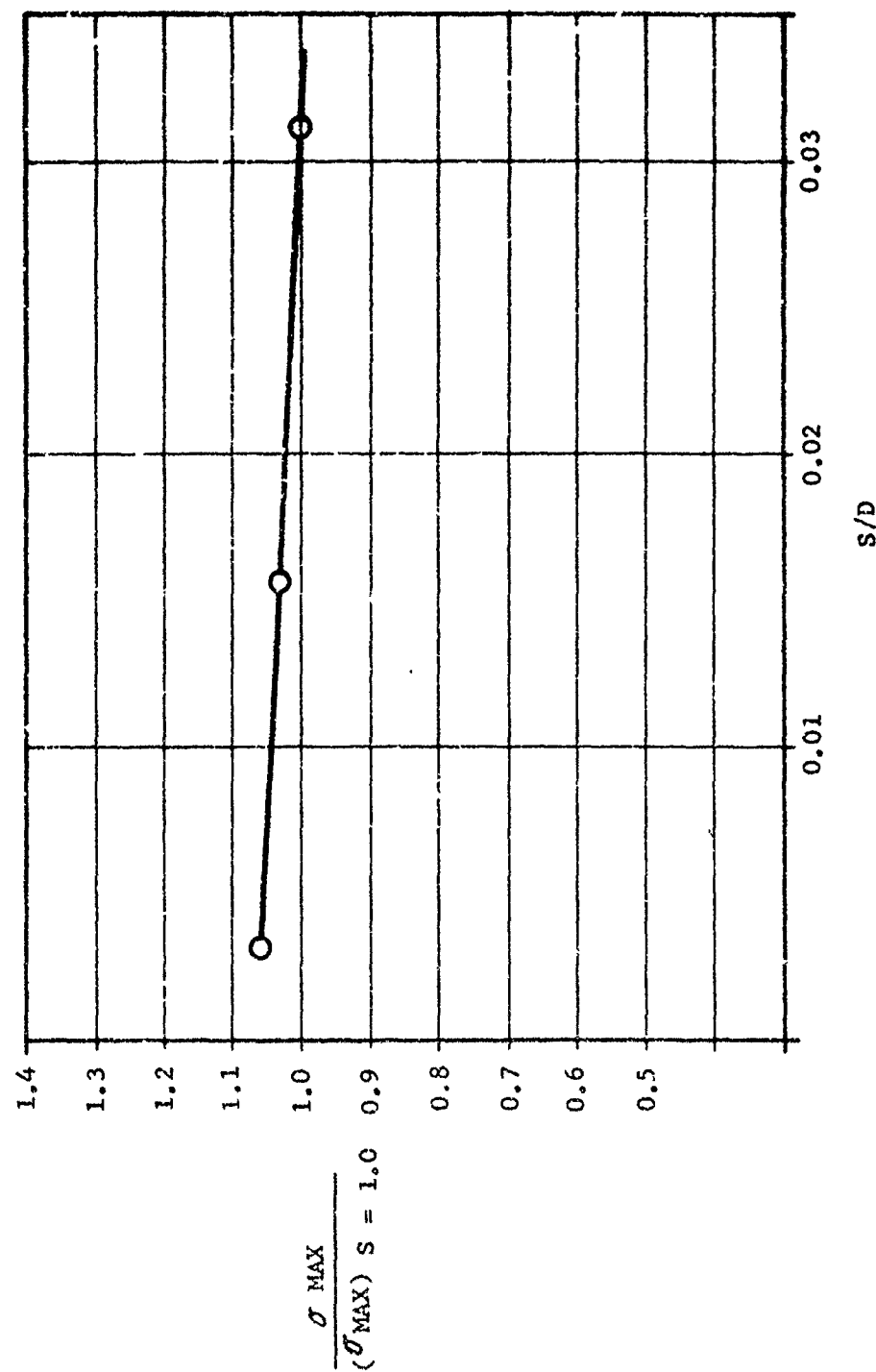
Figure 23. Maximum Principal Stress Adjacent to the Flap Termination for Flap Lengths of 0.1 and 0.5 In. Relative to that for a Flap Length of 1.0 In.

375
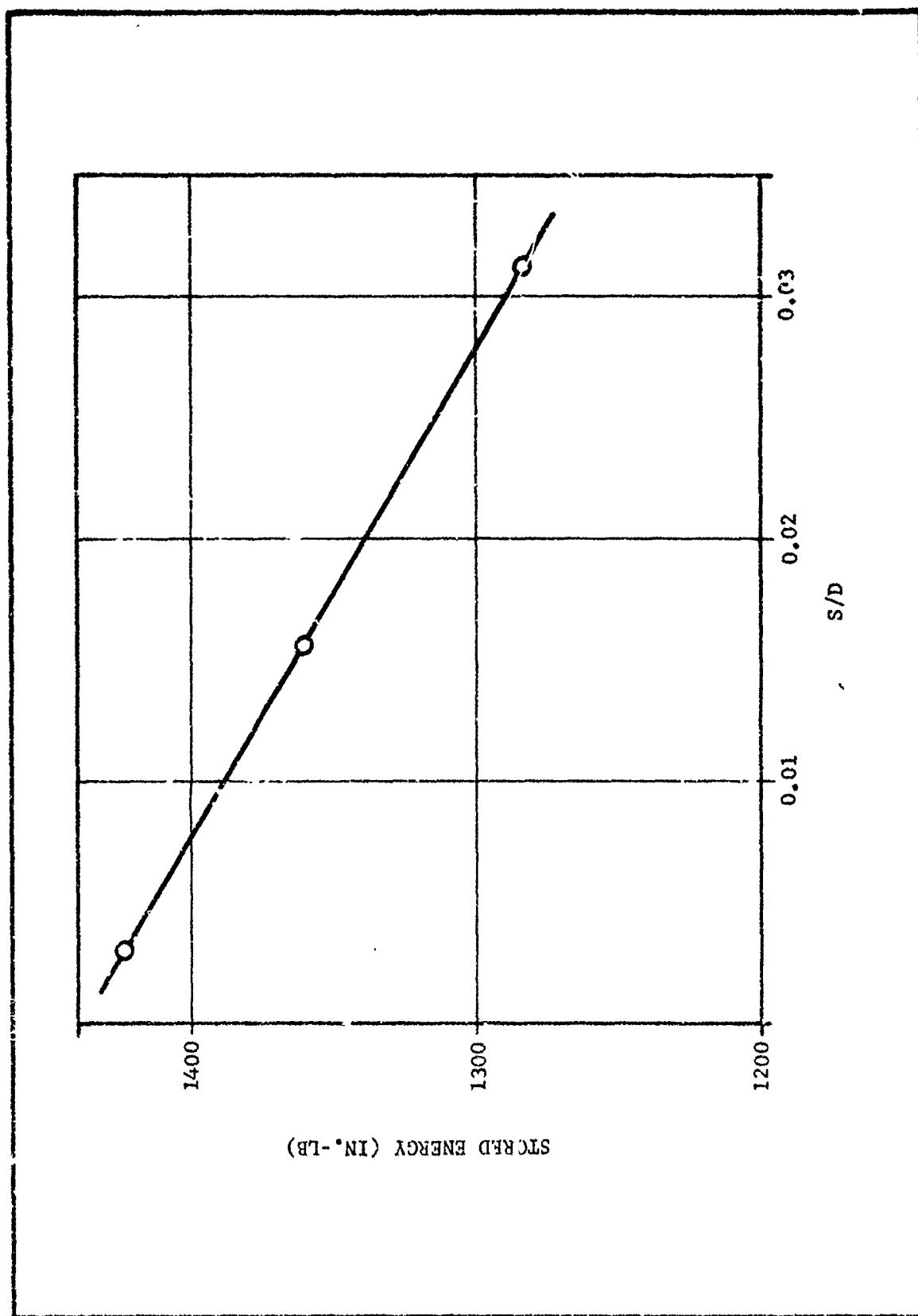
Figure 24. Strain Energy in Cylinder under Thermal Shrinkage Loading, with
L/D = 1.0 and W/b = 0.8, as a Function of Flap Length

376
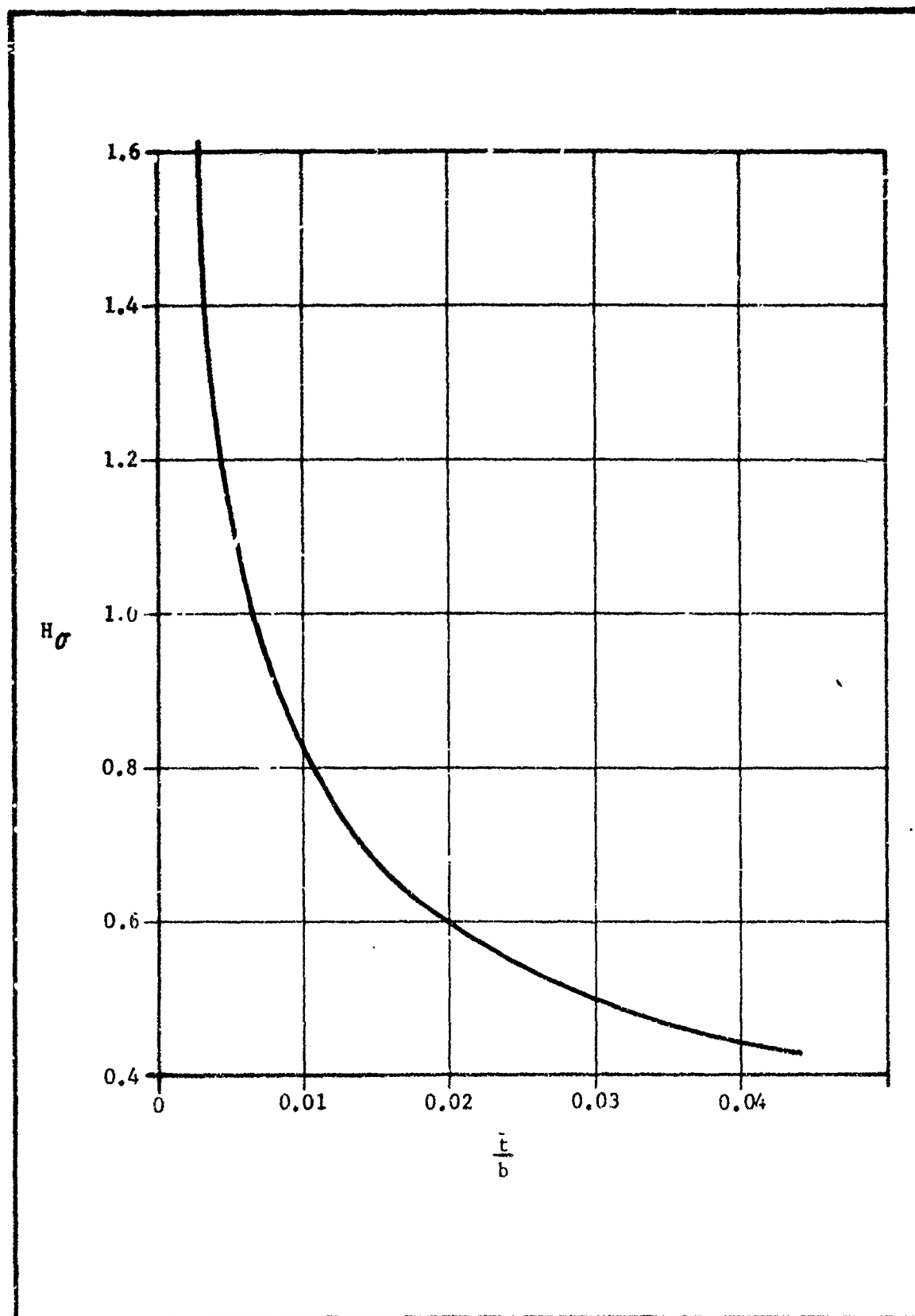
Figure 25. Gradient in Maximum Principal Stress as a Function of Normalized Radial Distance from Flap-Insulator Bond Discontinuity for Cylinder with L/D = 1.0 and W/b = 0.8
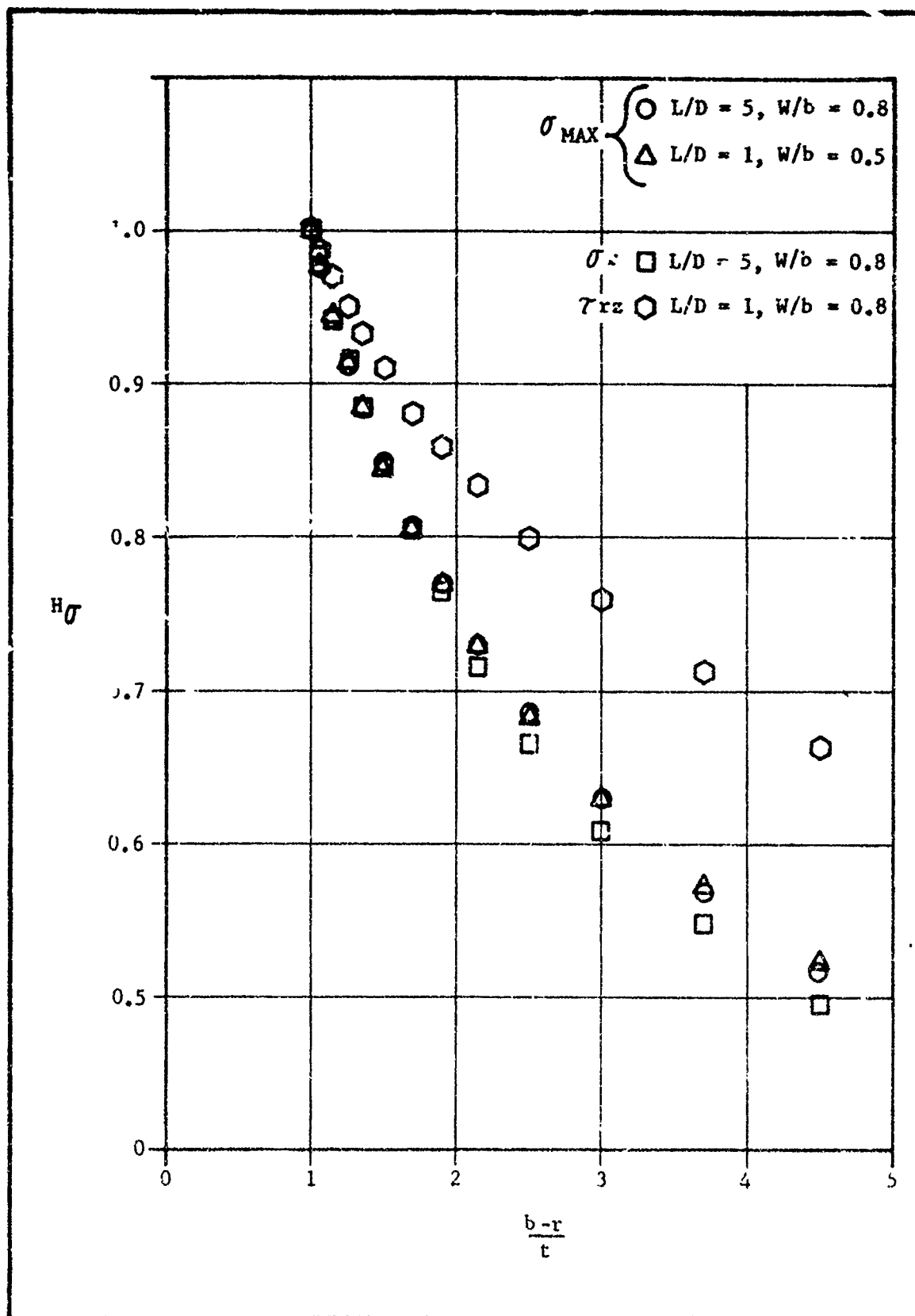
Figure 26. Stress Gradient as a Function of Radial Distance from Flap-Insulator Bond Discontinuity

$$\frac{W}{b} = 0.8$$

$$(0.18)$$

$$\left(\frac{\mathcal{T}_{rz}}{\sigma_r}\right)_{@ \text{ MAX } \sigma_r} \left(\frac{\vec{t}}{b} = 0.0067\right)$$

$$(0.18)$$

$$\left(\frac{\sigma_r}{H_0 E \delta}\right)_{BOND}$$

$$(0.19)$$

$$\frac{W}{b} = 0.67$$

$$(0.19)$$

$$(0.20)$$

$$(0.21)$$

$$(0.22)$$

$$\frac{W}{b} = 0.5$$

$$(0.22)$$

$$(0.23)$$

L/D
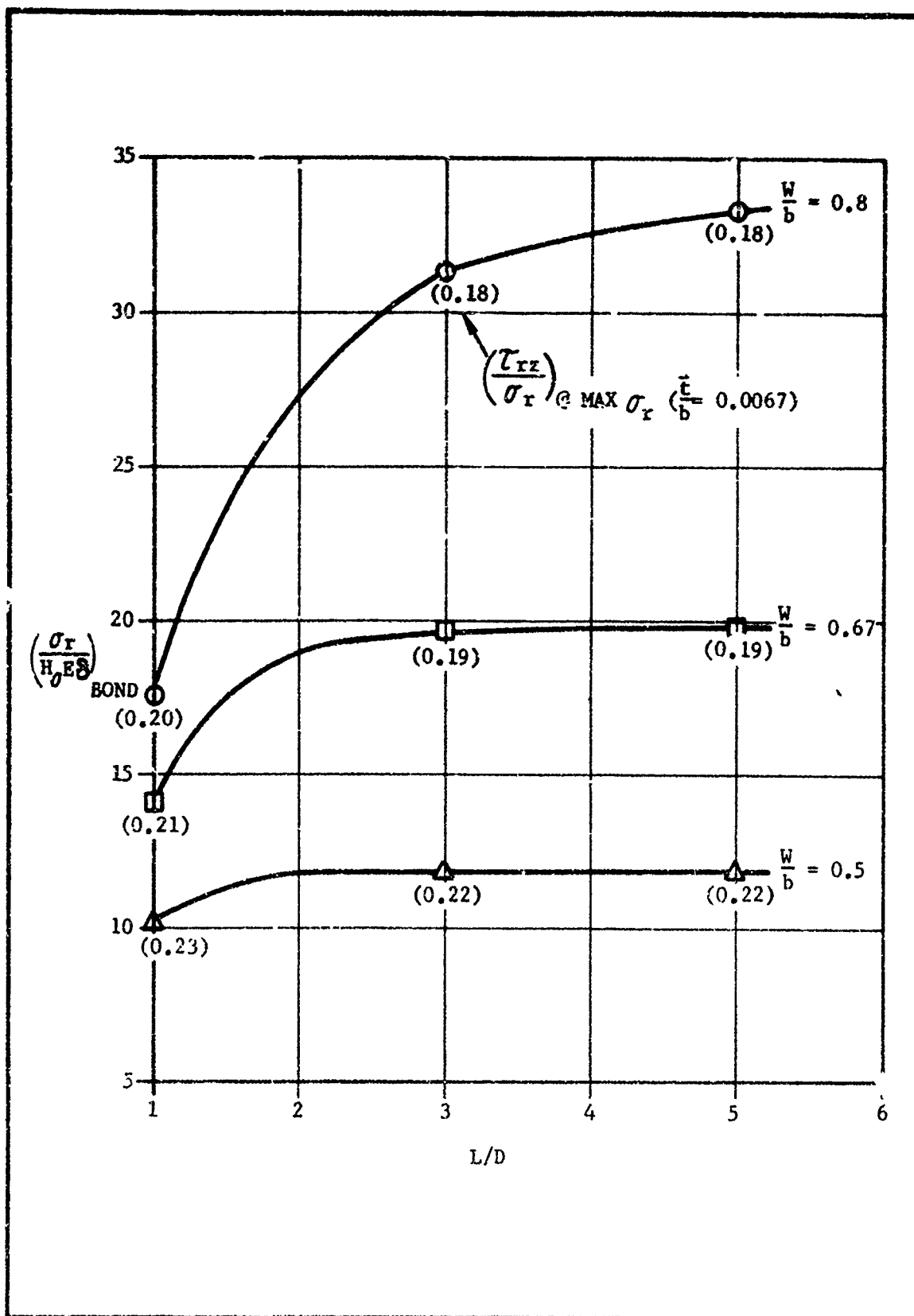
Figure 27. Peak Radial Stress Adjacent to Flap Termination for Cylinder
Under Thermal Shrinkage Loading

379

57
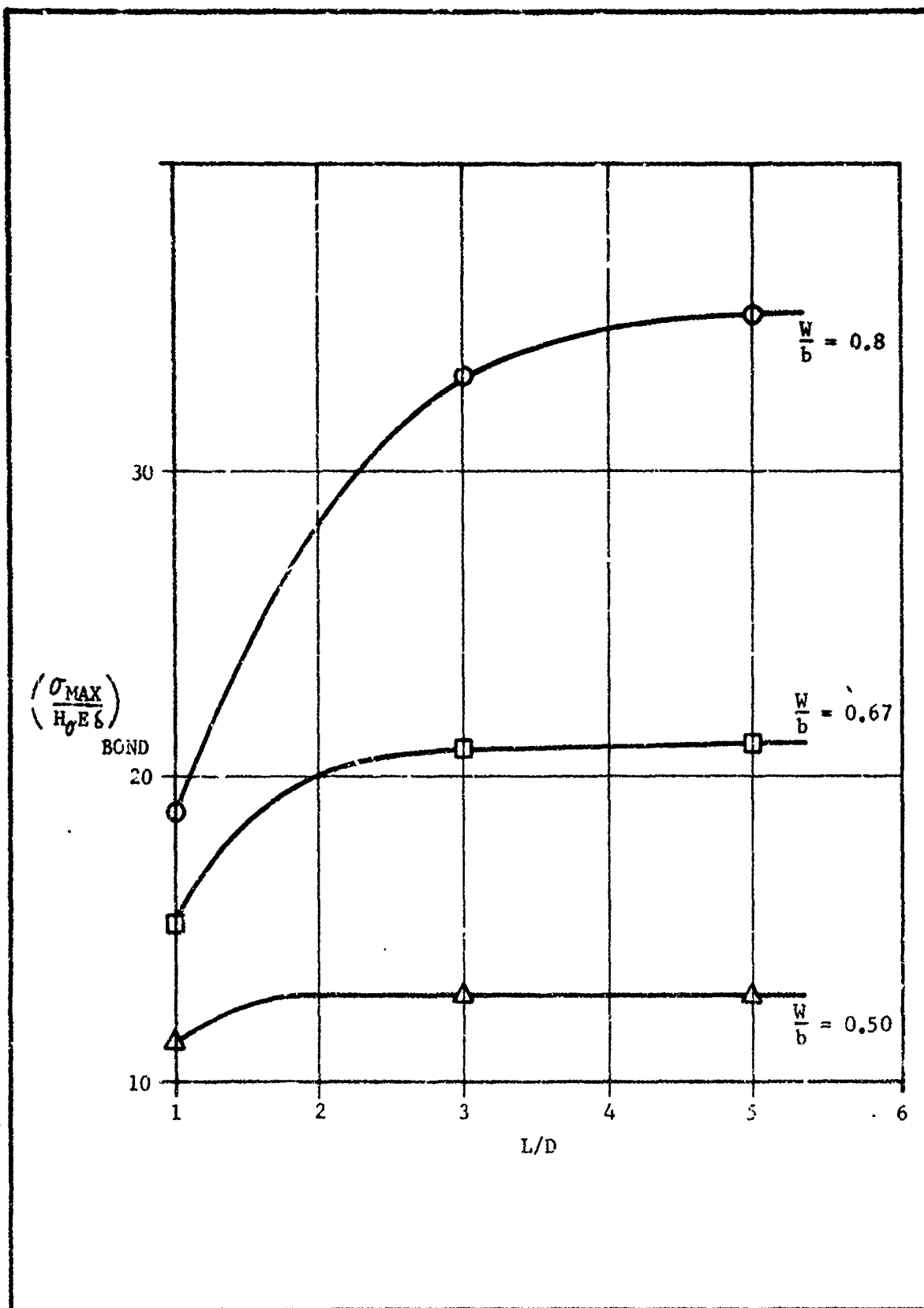
Figure 28. Peak Maximum Principal Stress Adjacent to Flap Termination for Cylinder Under Thermal Shrinkage Loading
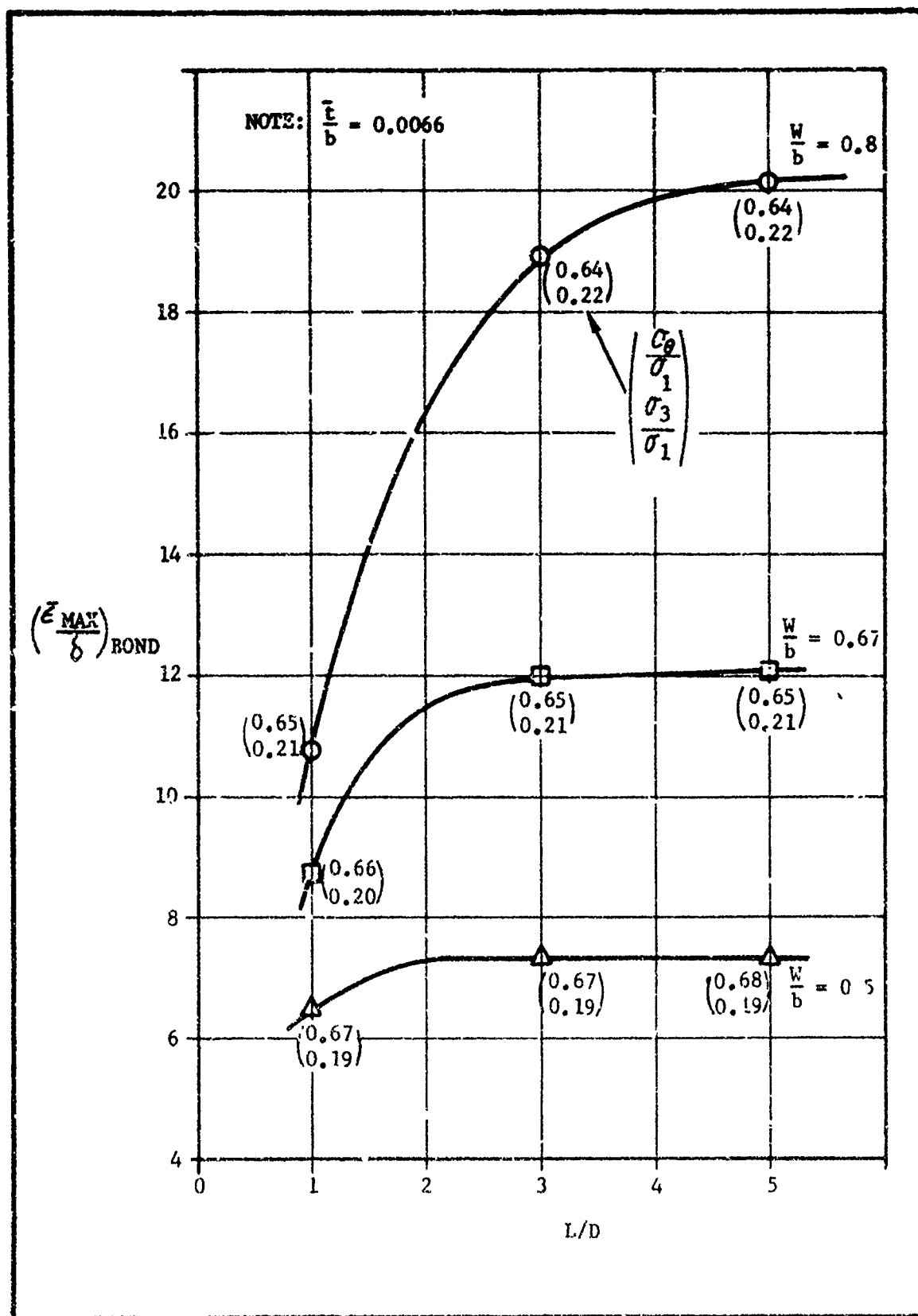
Figure 29. Peak Maximum Principal Strain in Propellant Adjacent to
Flap Termination for Cylinder Under Thermal Shrinkage Loading
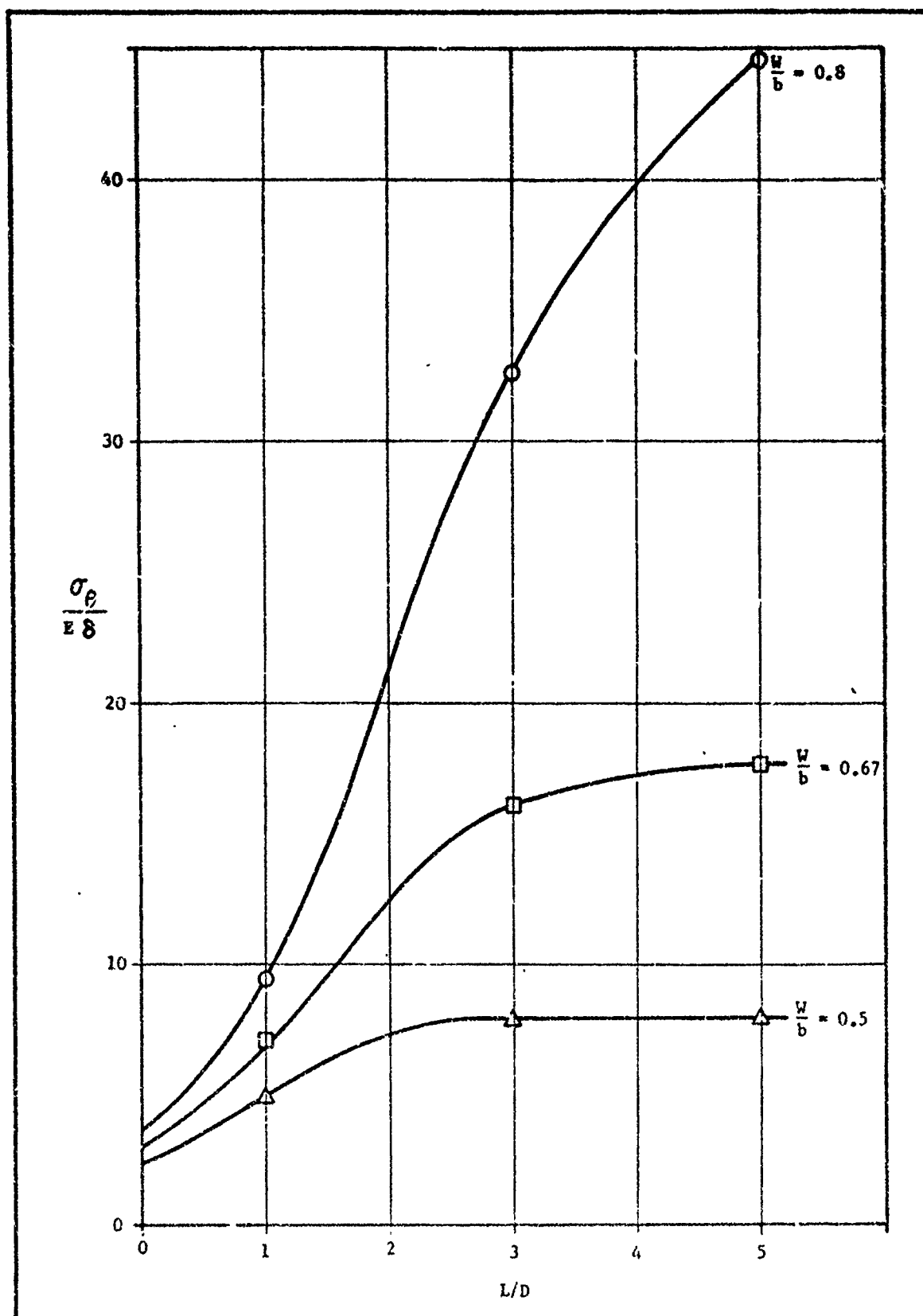
Figure 30.   Peak Center Port Hoop Stress for Cylinder Under Thermal
Shrinkage Loadⁱ g   382
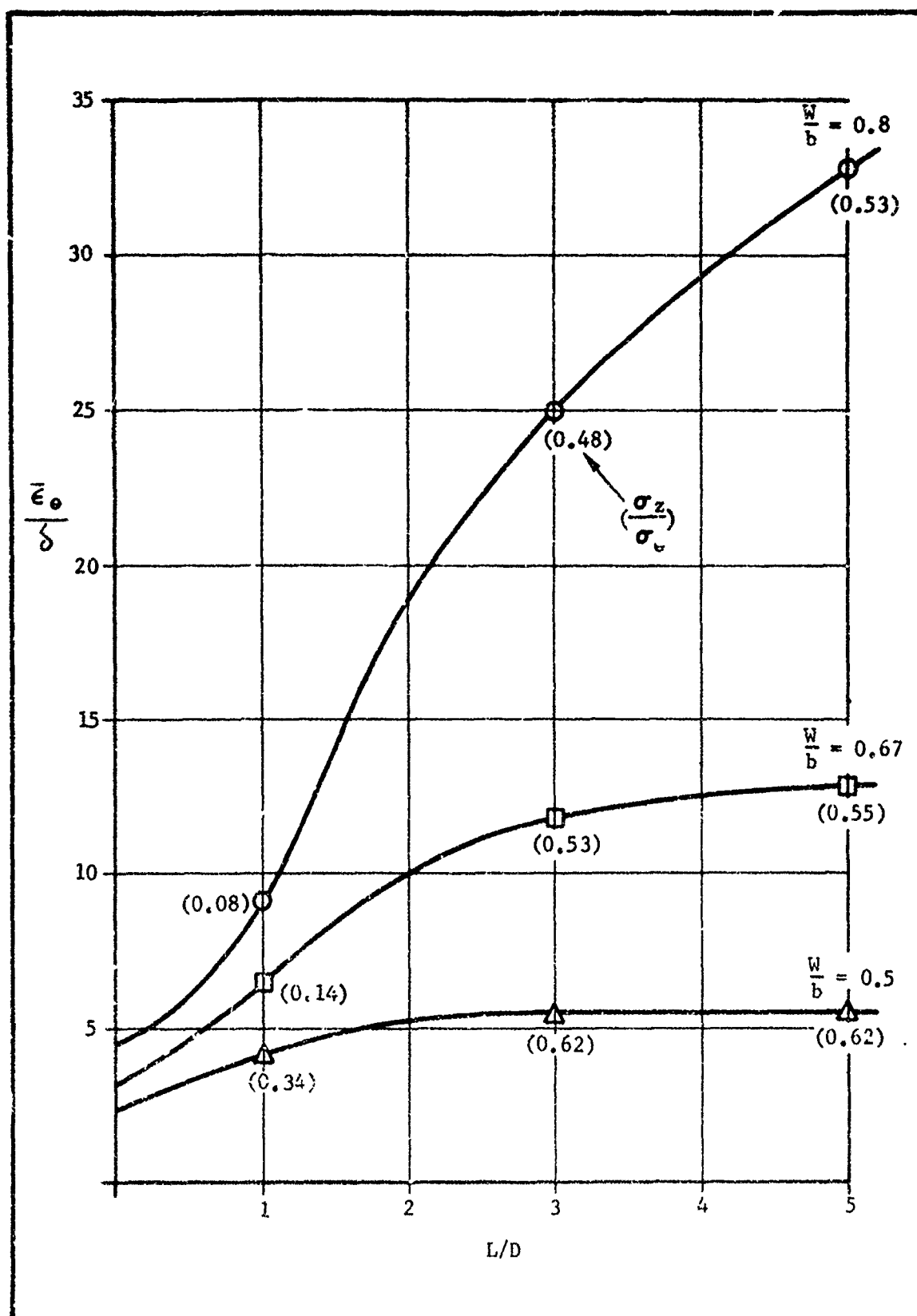
Figure 31. Peak Center Port Hoop Strain for Cylinder Under Thermal
            Shrinkage Loading   383
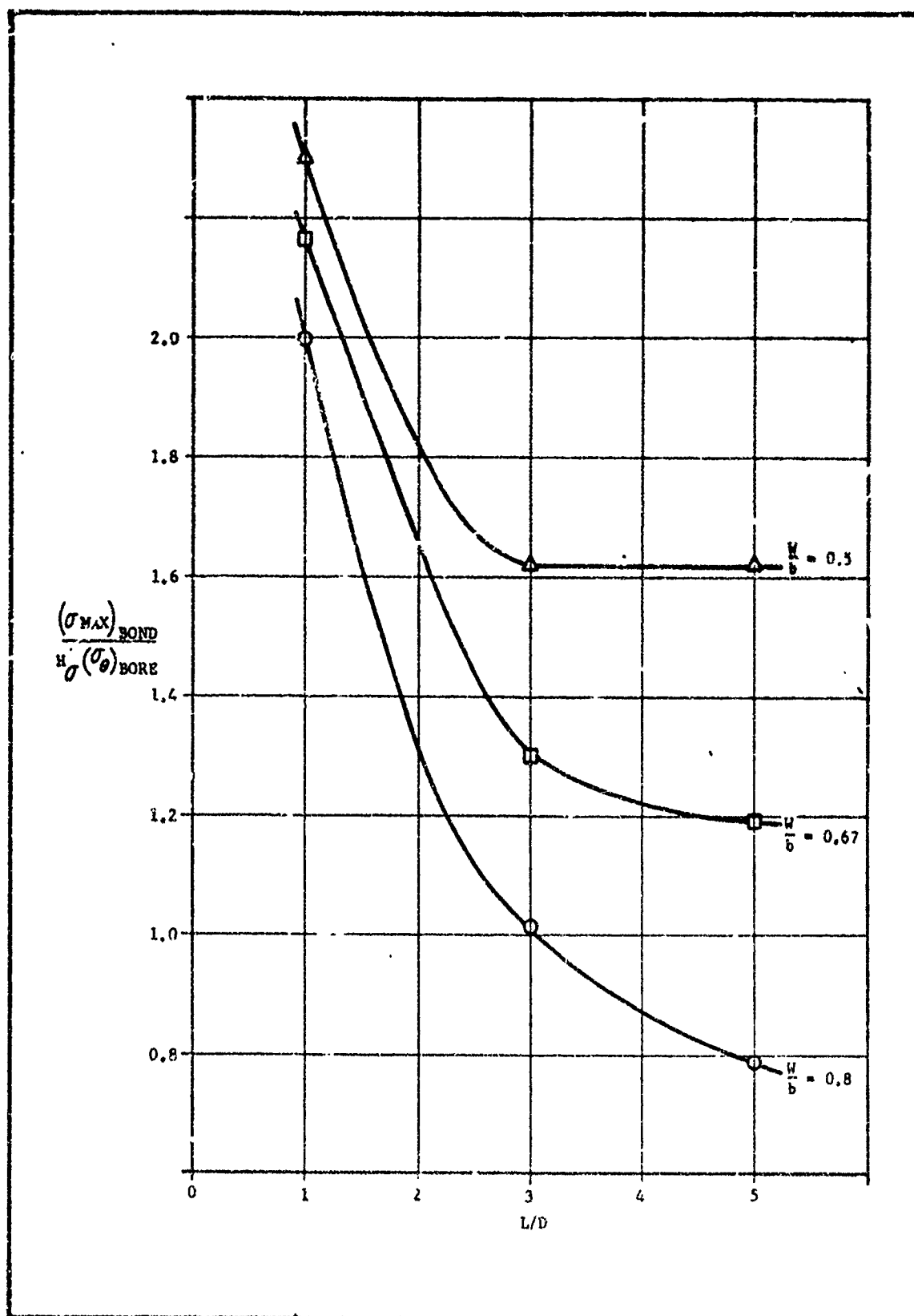
Figure 32. Ratio of Peak Maximum Principal Propellant Stress Near Flap Termination to Maximum Center Port Hoop Stress for Cylinder Under Thermal Shrinkage Loading

62
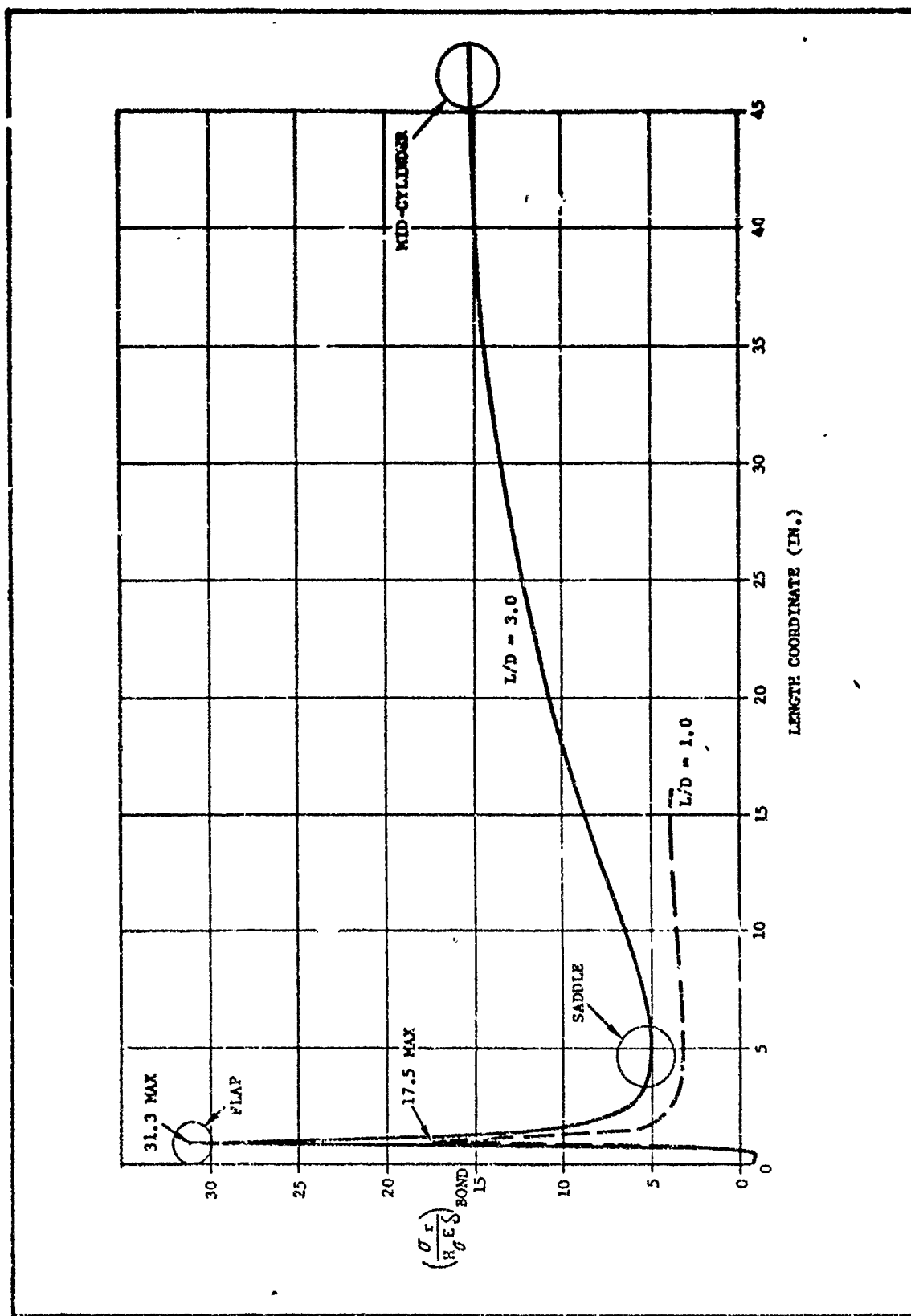
Figure 33. Case Bond Liner Stress in Radial Direction for Cylinder with L/D = 1.0 and 3.0, W/b = 0.8, Under Thermal Shrinkage Loading

385
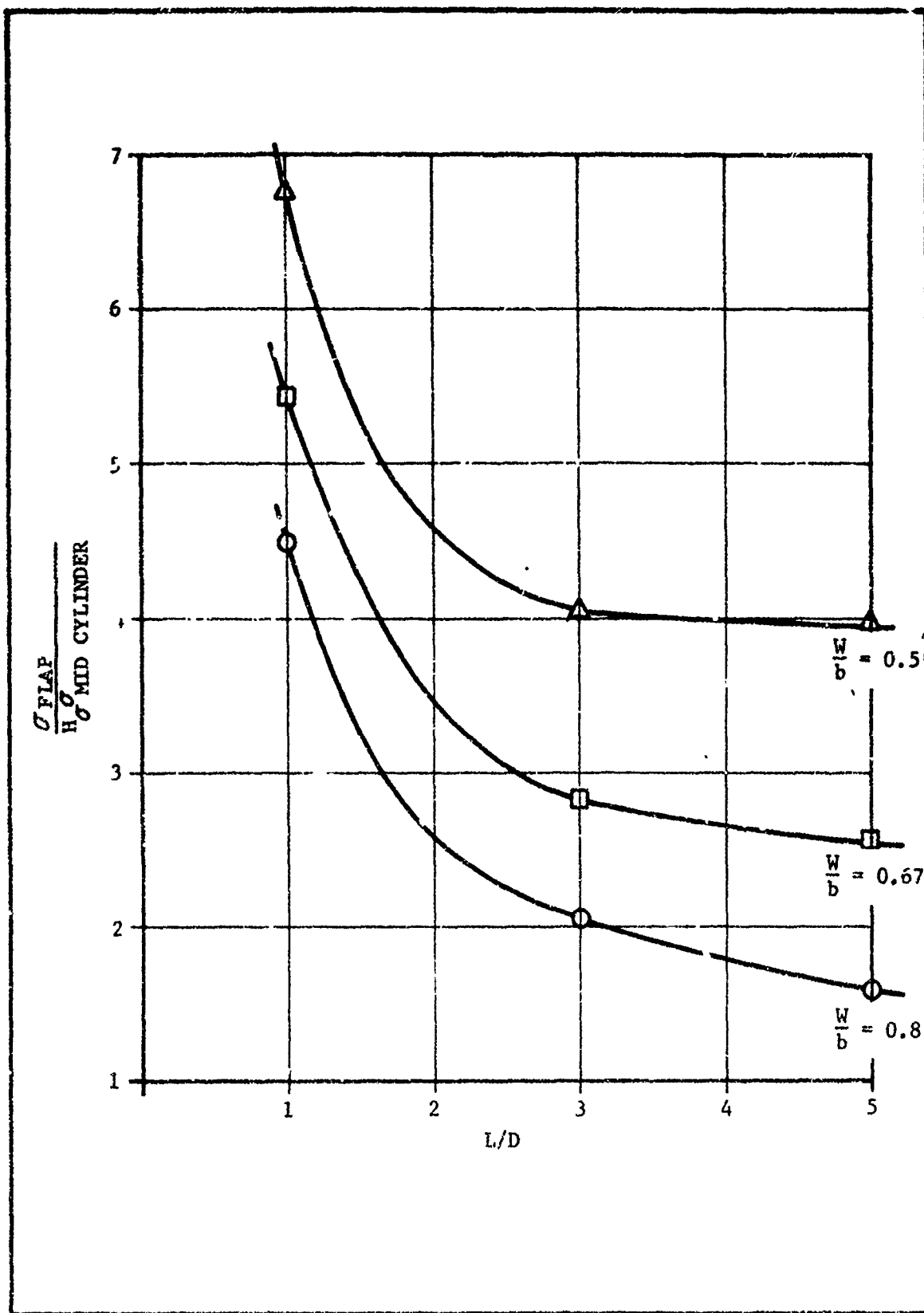
Figure 34. Ratio of the Peak Radial Liner Stress Near Flap Termination to
Mid-Cylinder Value for Cylinder Under Thermal Shrinkage Loading

386

64
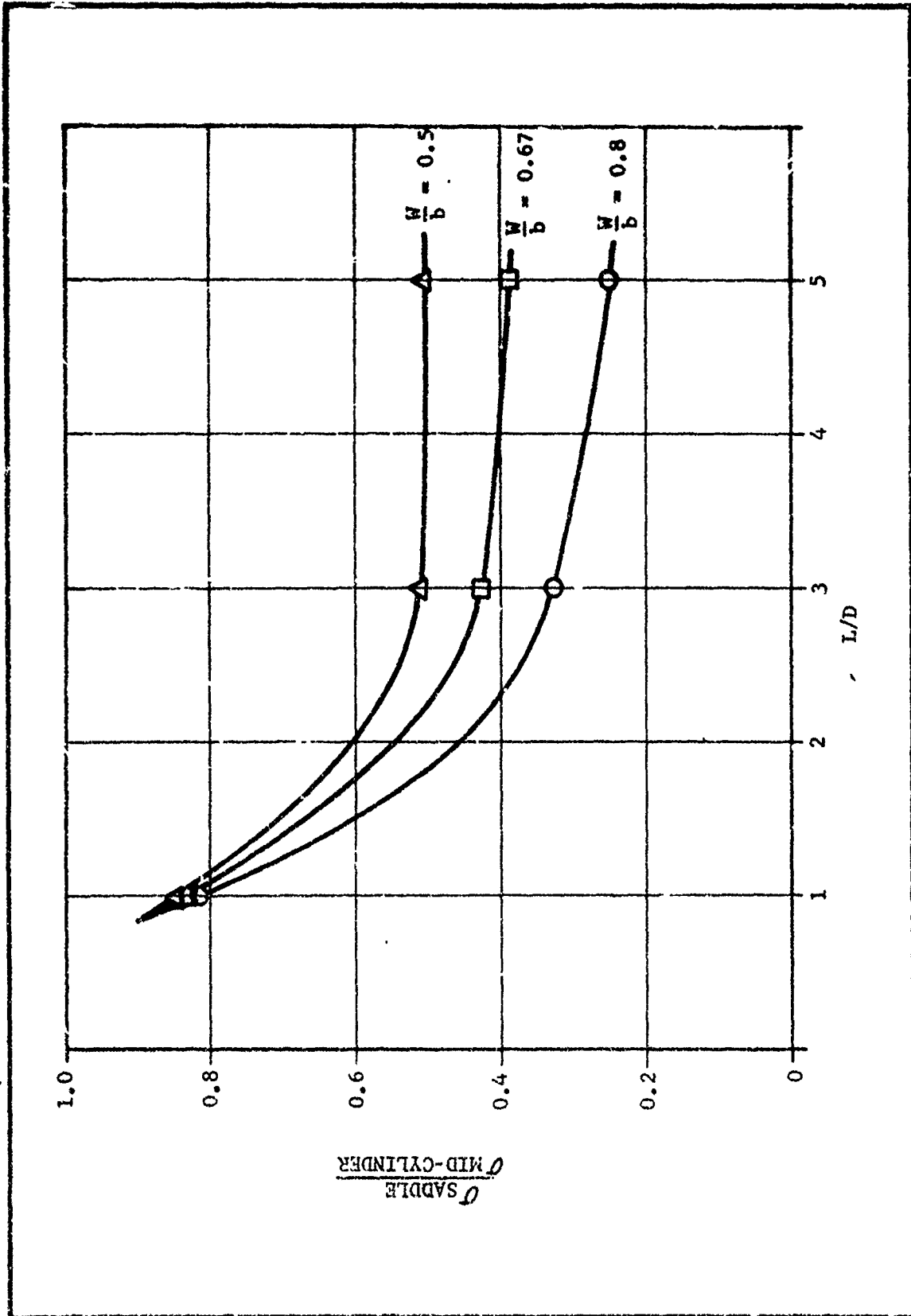
Figure 35. Ratio of Radial Liner Stress in Saddle to Mid-Cylinder Value for
Cylinder Under Thermal Shrinkage Loading

387
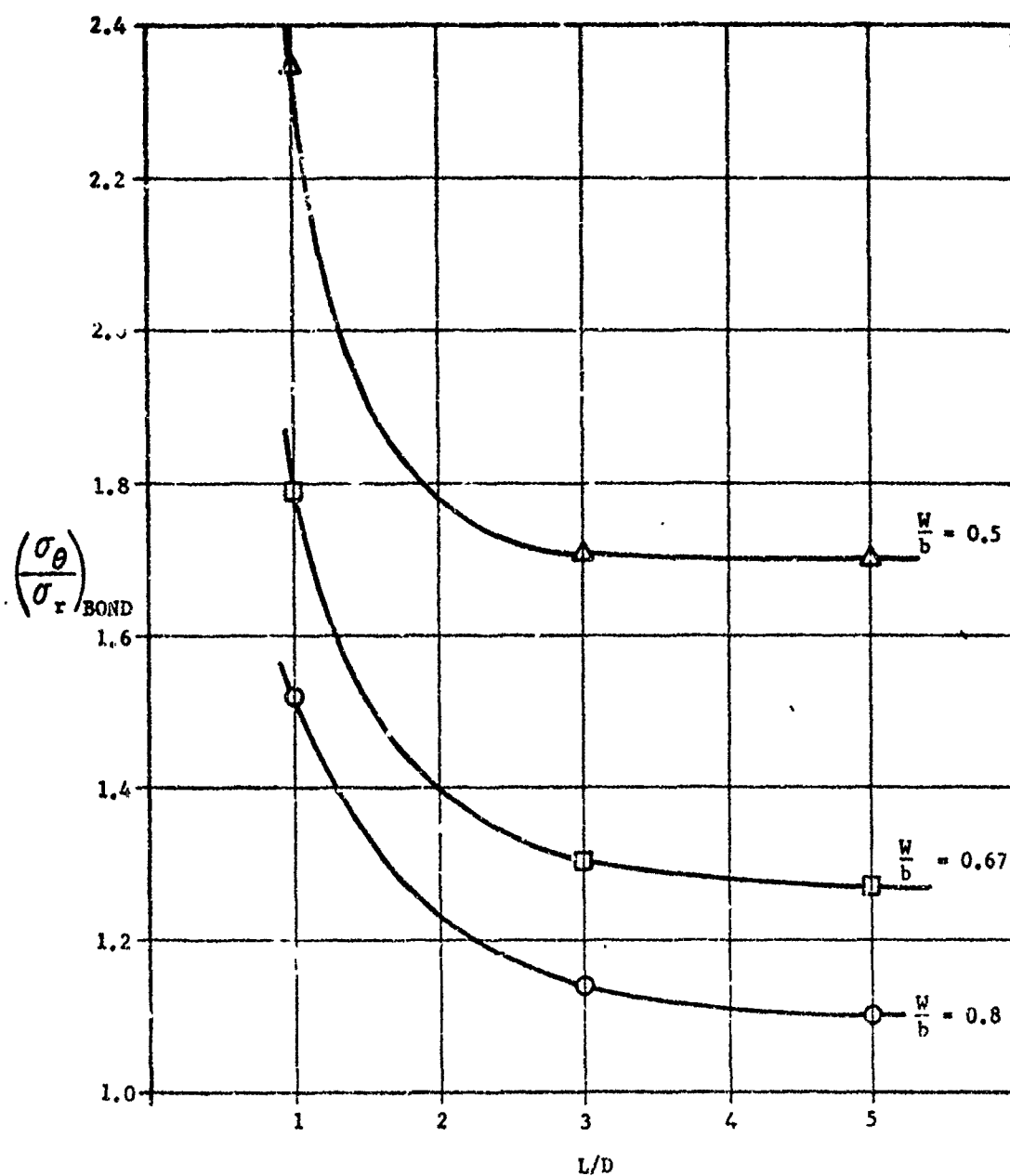
Figure 36. Ratio of Liner Hoop to Radial Stress at Mid-Axial Position in Cylinder Under Thermal Shrinkage Loading

66   388
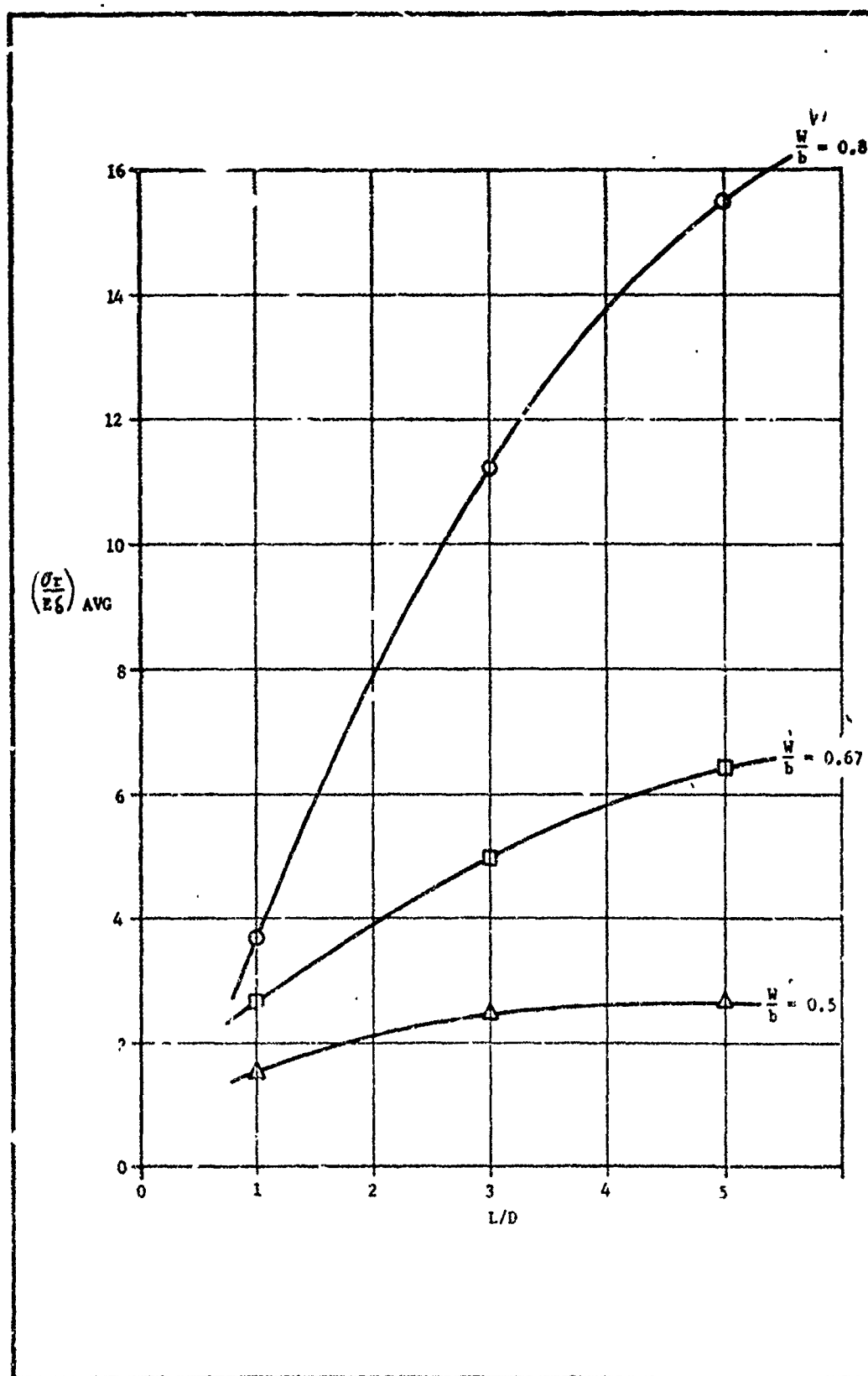
Figure 37. Average Case Bond Radial Stress in Cylinder Under Thermal Shrinkage Loading

389
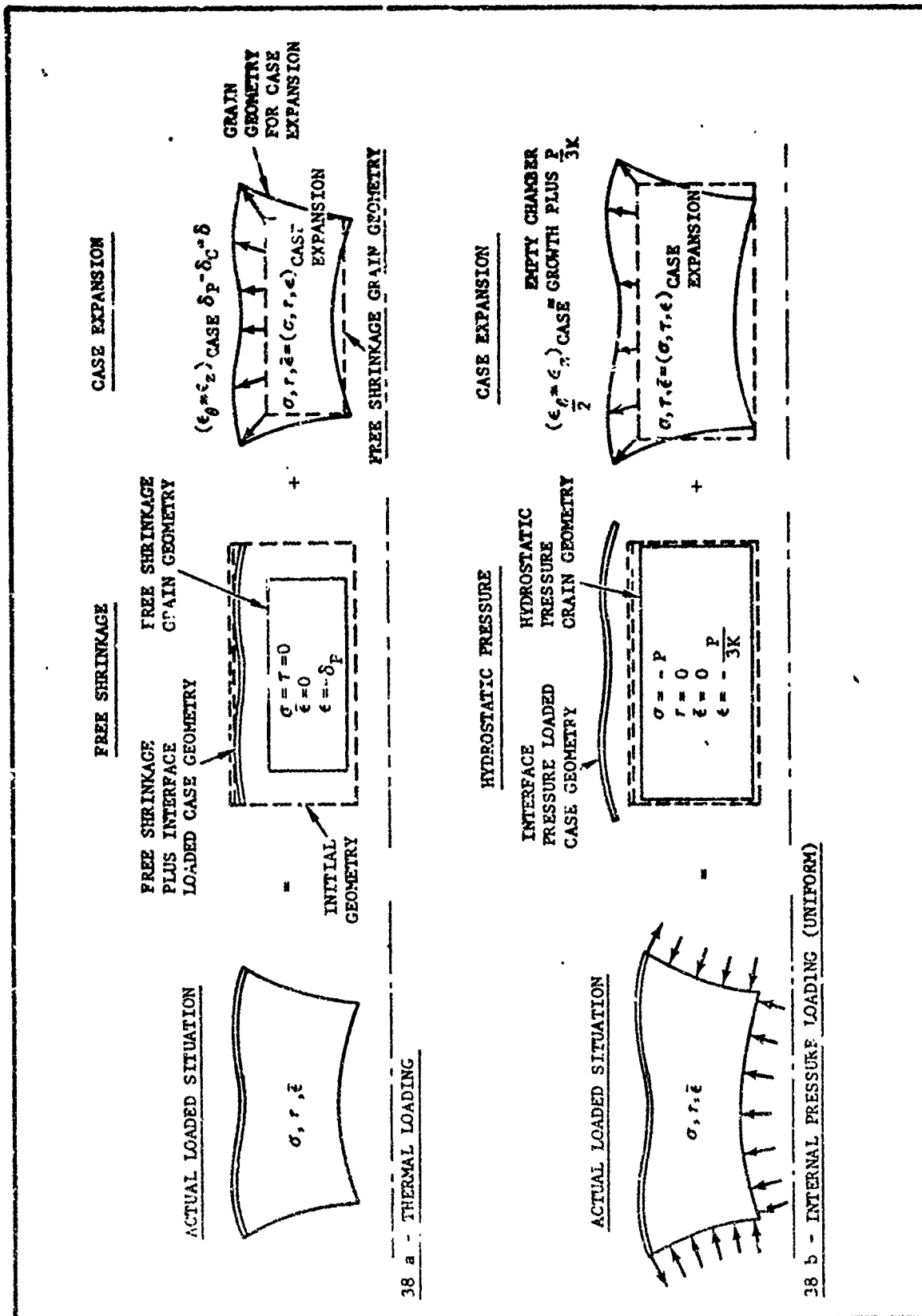
Figure 38. Correspondence of Stresses and Strains Resulting from Thermal Shrinkage and Internal Pressurization of Two-Layered Cylinders

390

68
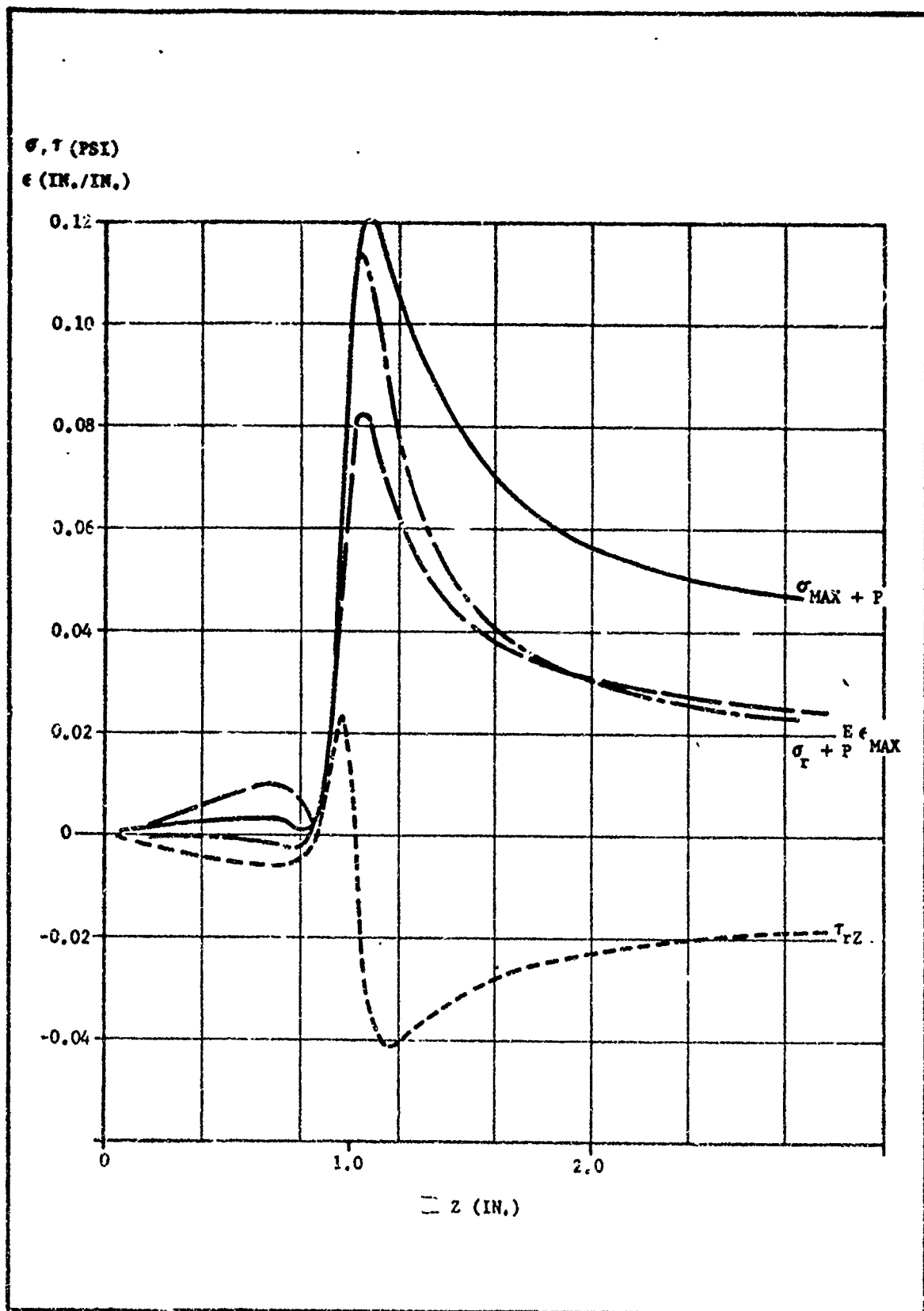
Figure 39. Case Bond Liner Stresses Near the Flap Termination for a Cylinder with L/D = 1.0 and W/b = 0.8 Under 1.0 psi Internal Pressure Loading

391

69
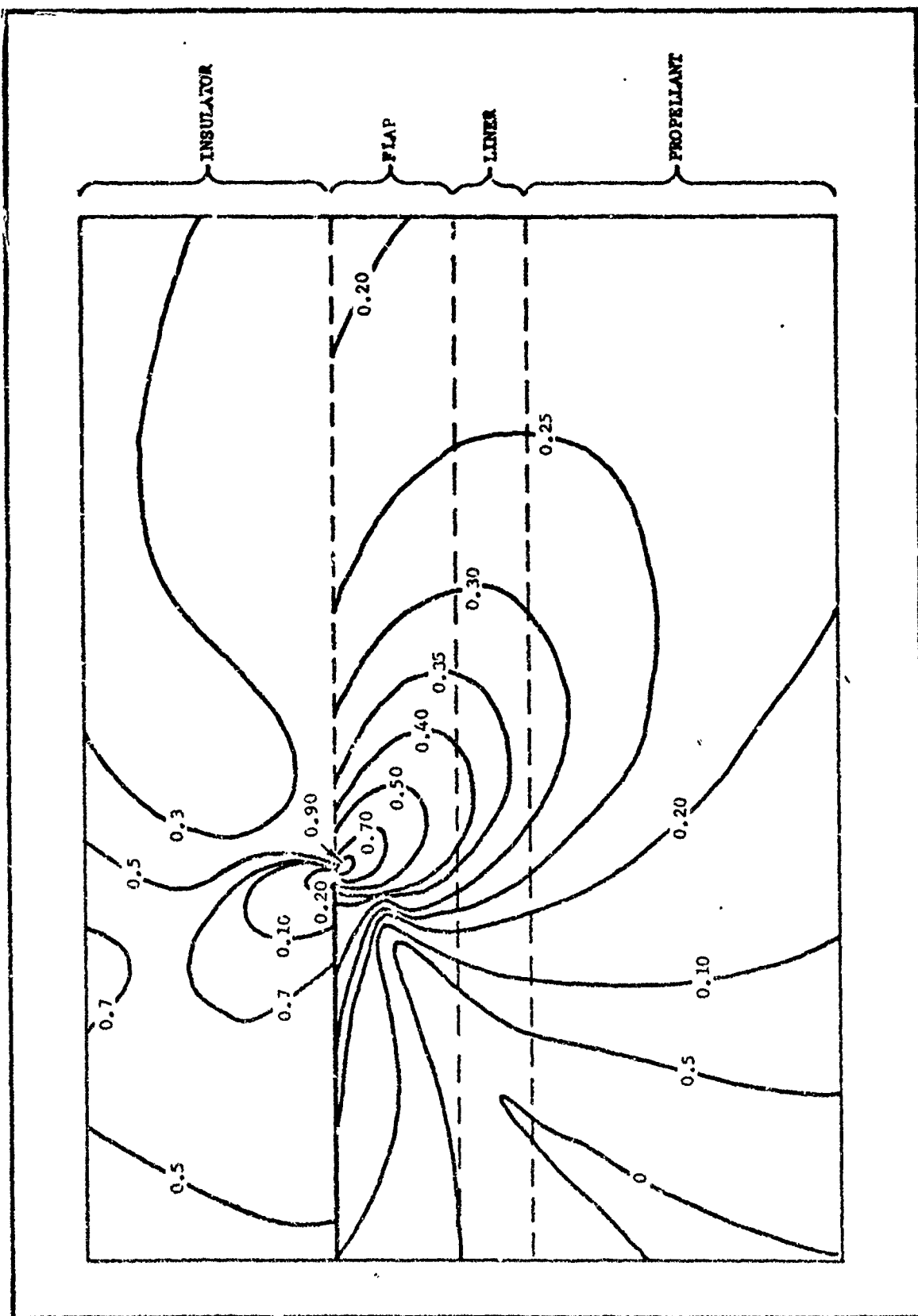
Figure 40. Lines of Constant Maximum Principal Strain (ϵ_{max}) in the Vicinity of the Flap Termination for a Cylinder with L/D = 1.0 and W/b = 0.8 Subjected to 1000 psi Internal Pressure Loading

392
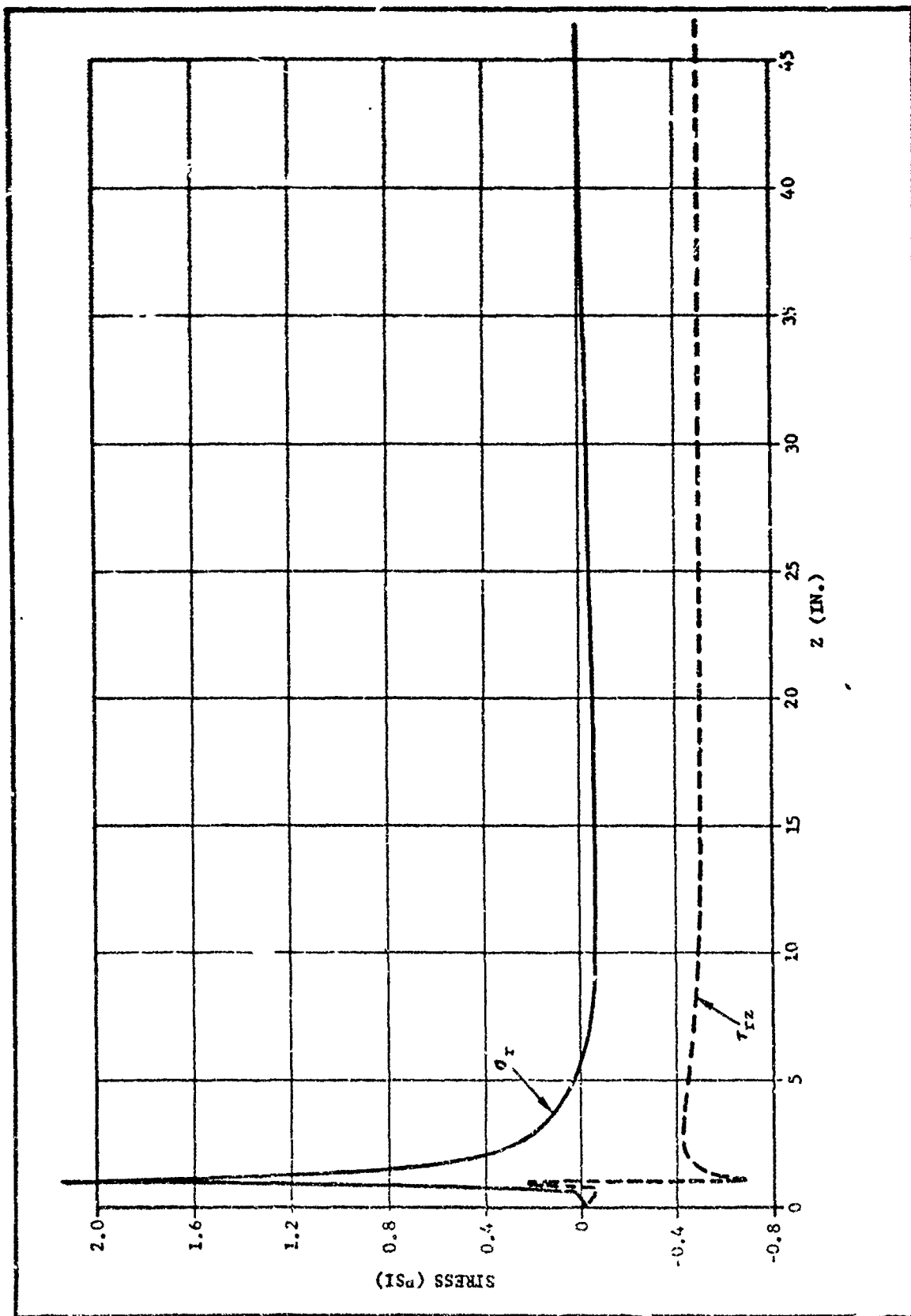
Figure 41. Case Bond Liner Stresses for a 32-Inch Diameter Cylinder with L/D = 3.0 and W/b = 0.8 Under 1 g Axial Acceleration Loading (P_W = 0.064 lb/in.³)
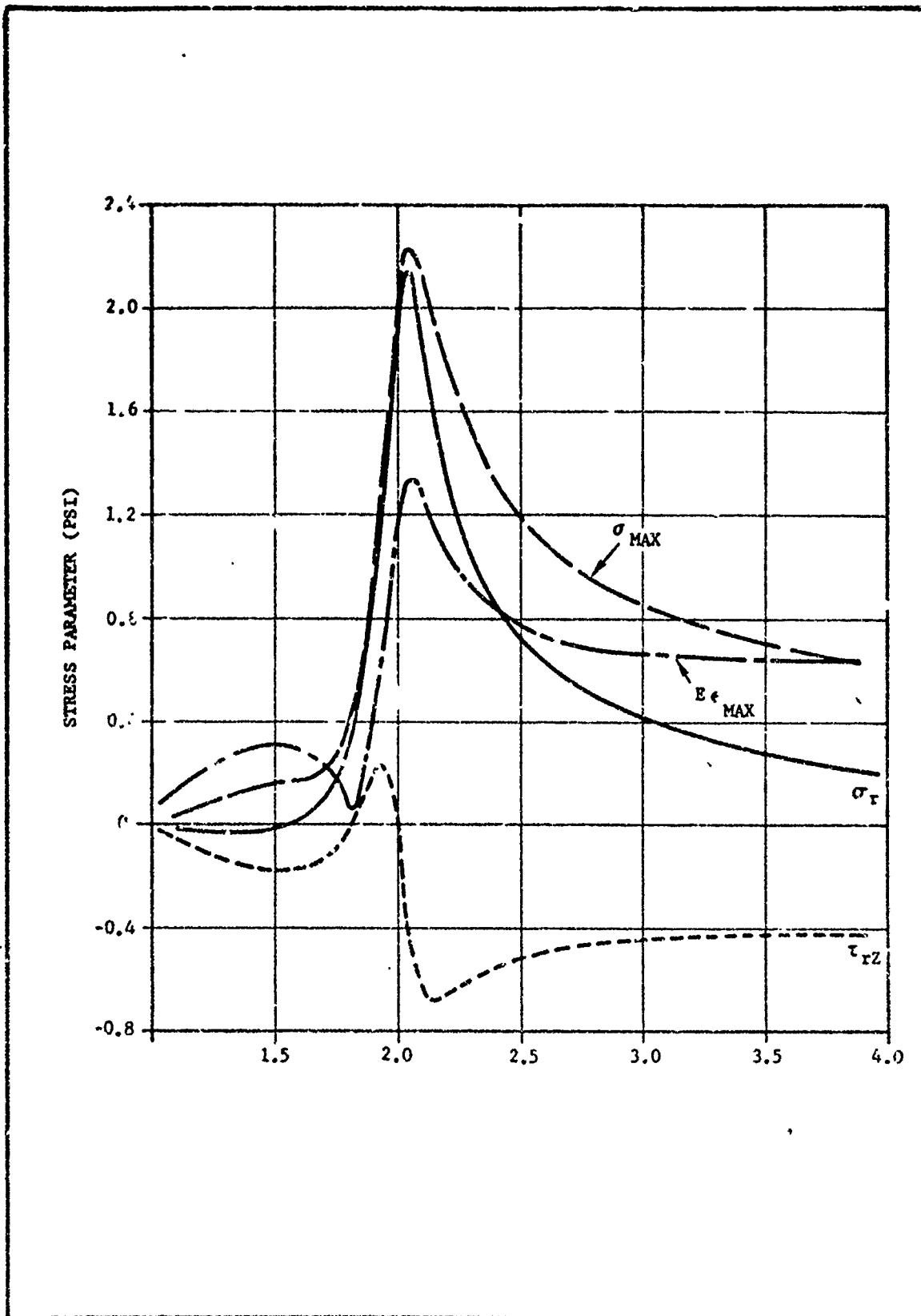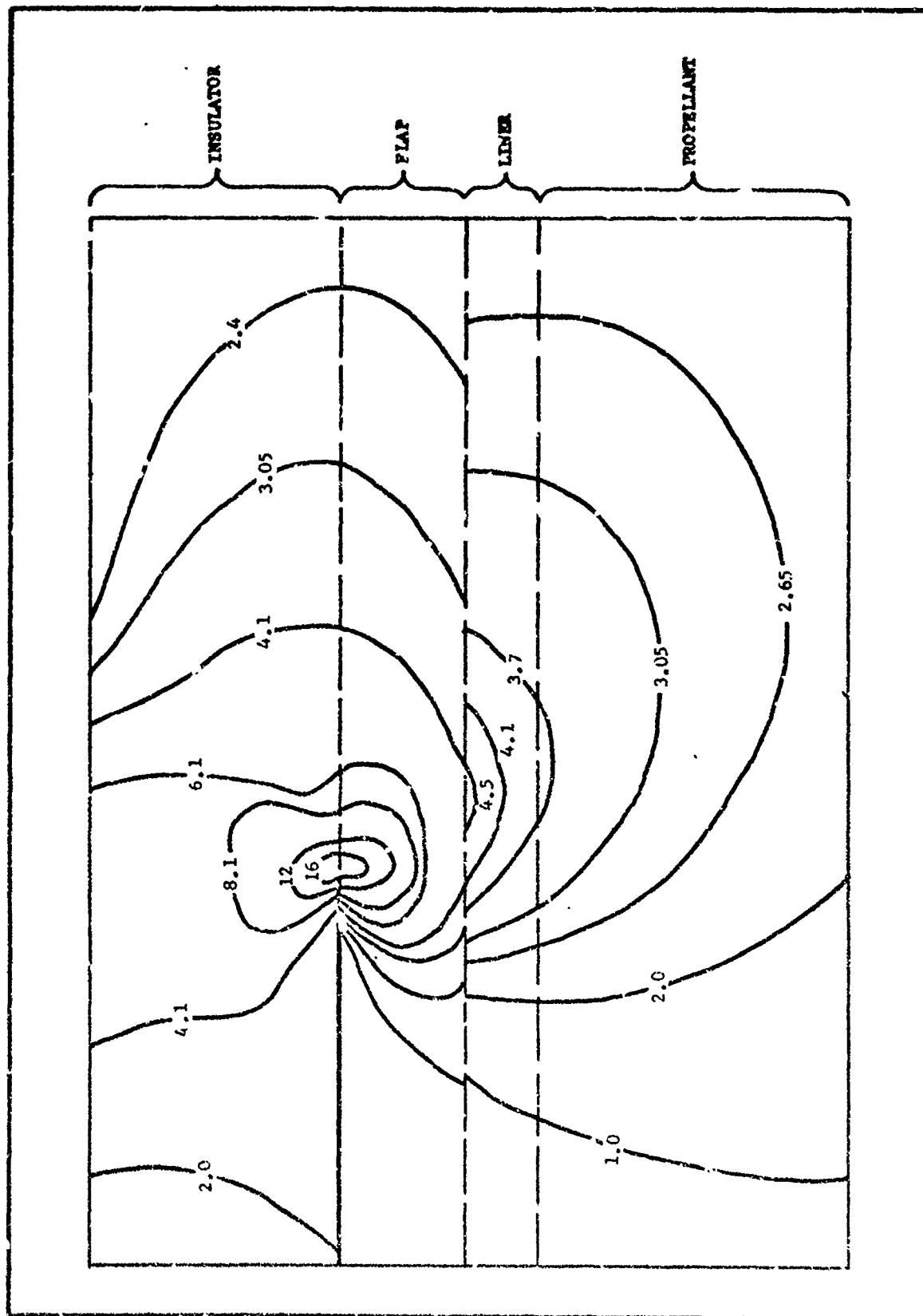
Figure 42. Case Bond Liner Stresses Adjacent to Flap Termination in a 32-Inch Diameter Cylinder with L/D = 3.0 and W/b = 0.8 Under 1 g Axial Acceleration Loading (ρ_W = 0.064 lb/in.^{3})

394

72

Figure 43. Lines of Constant Maximum Principal Strain $\left(\frac{\sigma_{max}}{\tau_{avg}}\right)$ in the Vicinity of the Flap

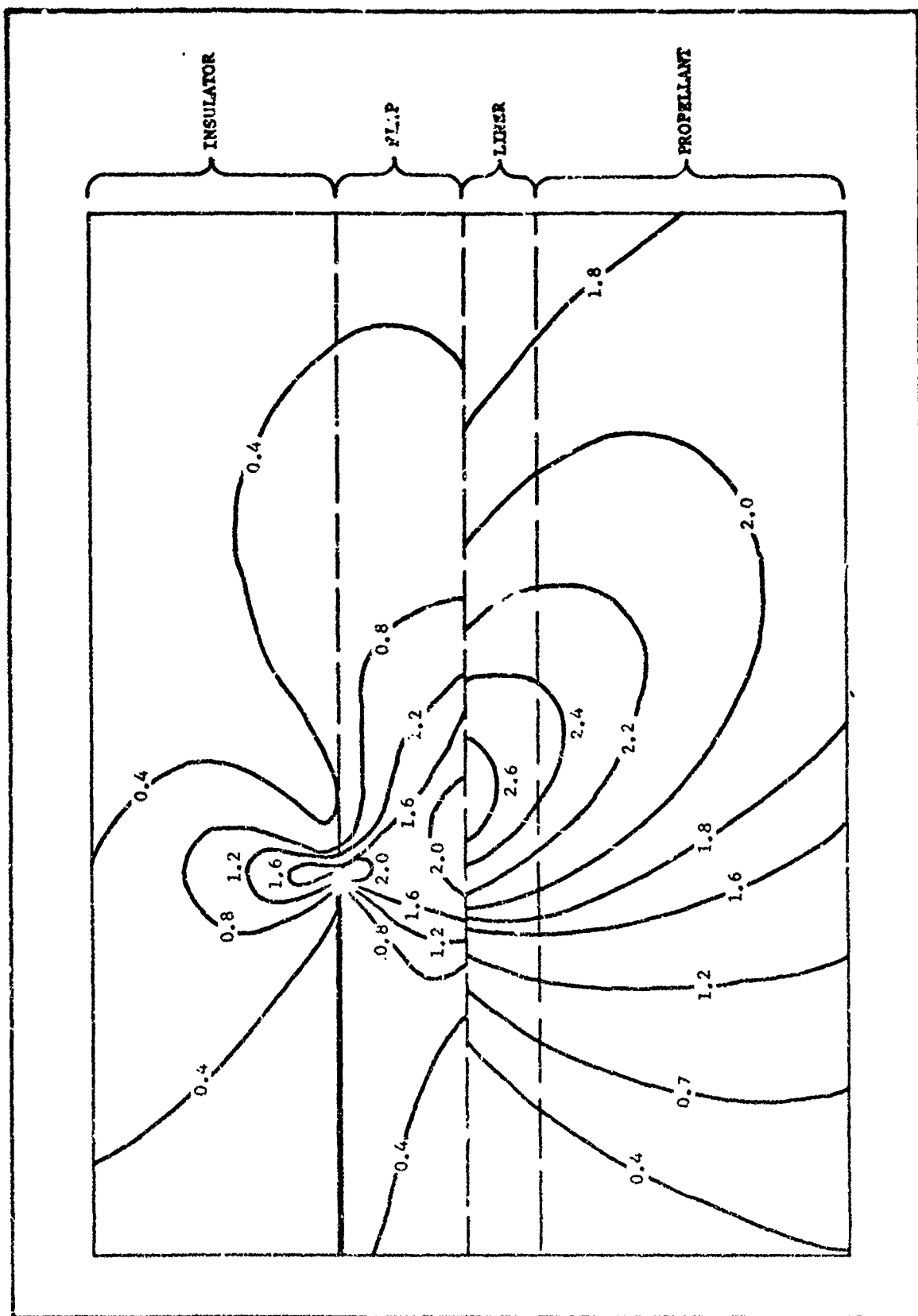Termination for a Cylinder with $L/D = 3.0$ and $W/b = 0.8$ Under Axial Acceleration Loading

395

73

Figure 44. Lines of Constant Maximum Principal Strain $\left(\dfrac{E\,\epsilon_{max}}{\tau_{avg}}\right)$ in the Vicinity of the

Flap Termination for a Cylinder with L/D = 3.0 and W/b = 0.8 Under Axial Acceleration Loading
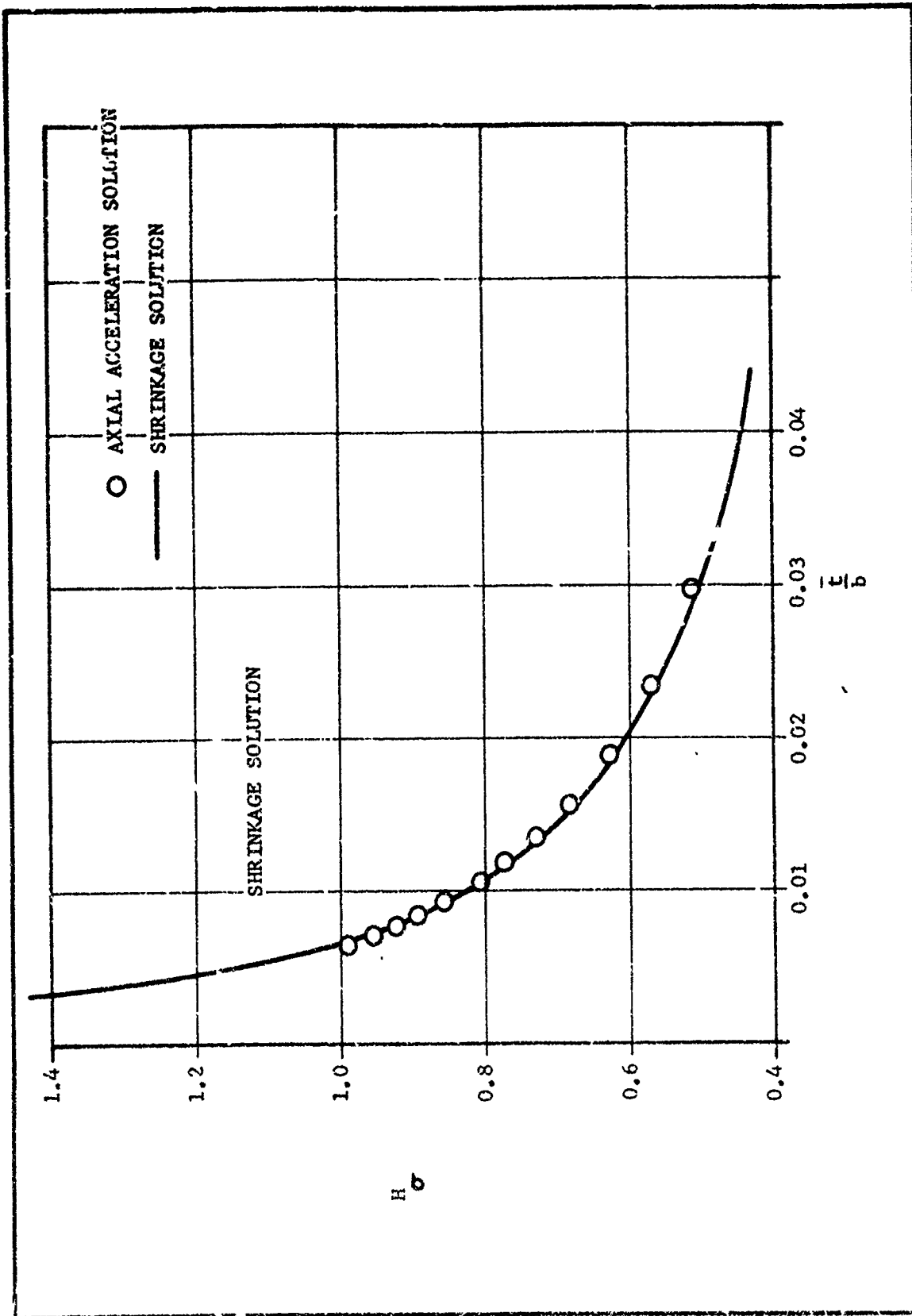
Figure 45. Comparison of Gradient in Maximum Principal Stress as a Function of Normalized Radial Distance from Flap-Insulator Bond Discontinuity for Cylinders Under Thermal Shrinkage and Axial Acceleration
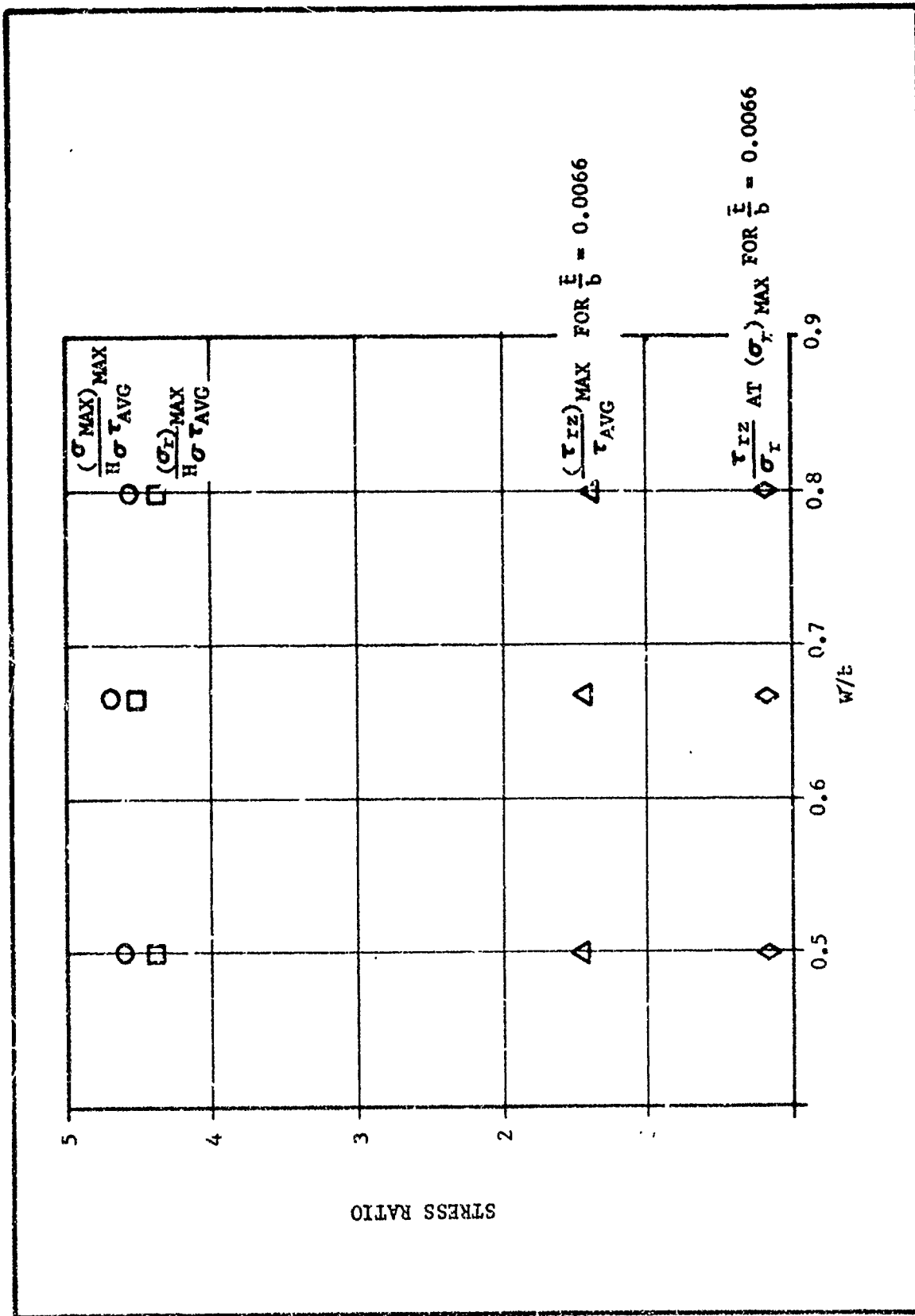
Figure 46. Normalized Case Bond Liner Stresses Adjacent to Flap Termination for Cylinder with L/D = 3.0 Subjected to Axial Acceleration Loading
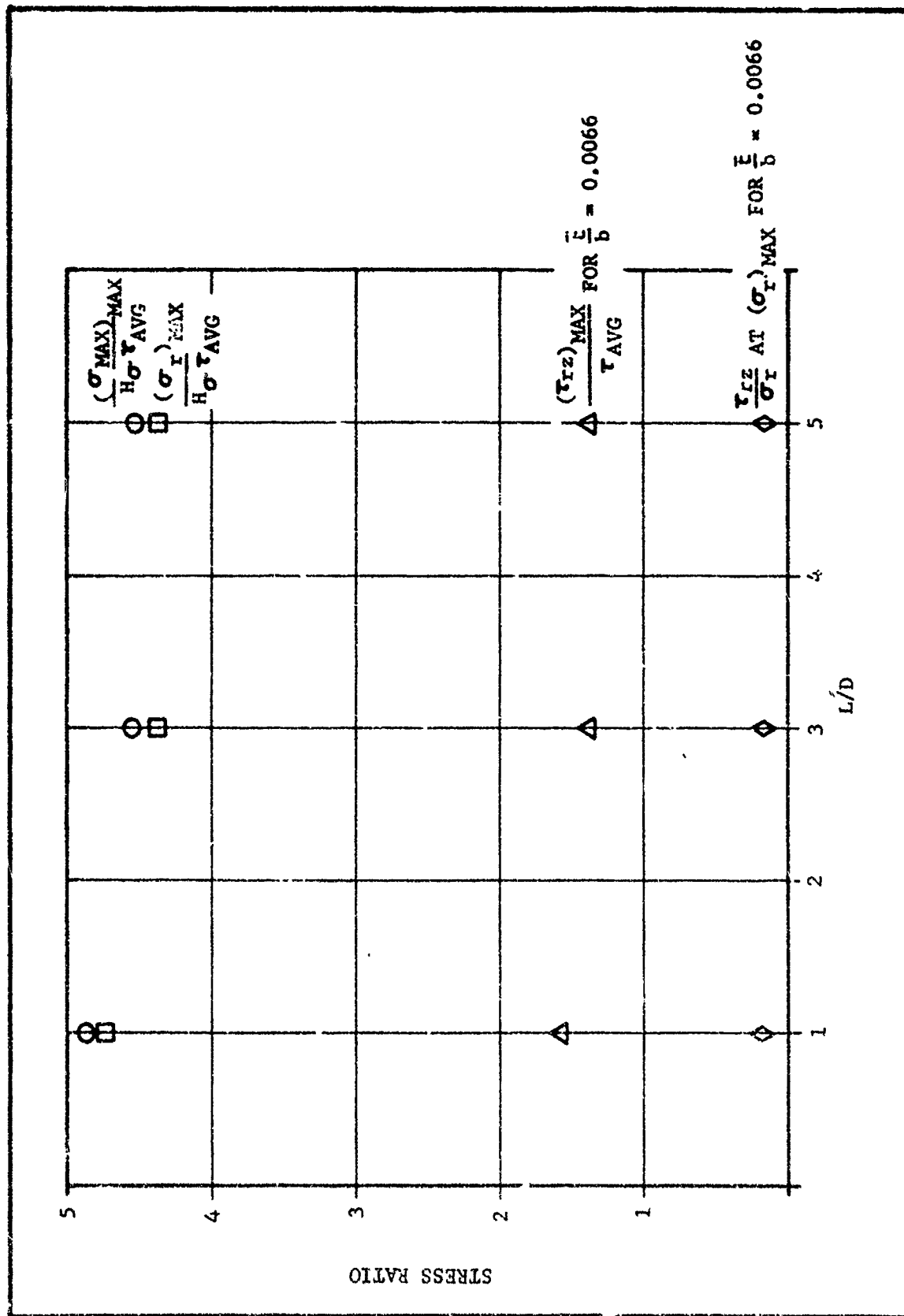
Figure 47. Normalized Case Bond Liner Stresses Adjacent to Flap Termination for Cylinder with $W/b = 0.8$ Subjected to Axial Acceleration Loading